Polycyclic Aromatic Dicarboximides as NIR Chromophores, Solid-State Emitters and Supramolecular Host Platforms

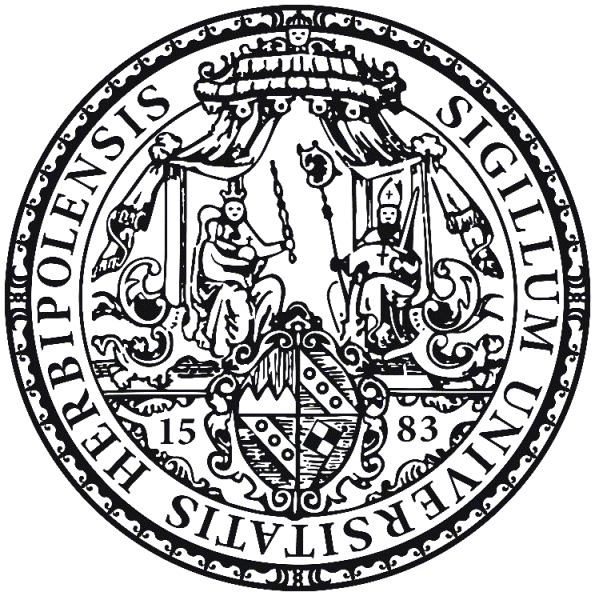

Dissertation zur Erlangung des
naturwissenschaftlichen Doktorgrades der
Julius-Maximilians-Universität Würzburg

vorgelegt von

Magnus Mahl
aus Roth

Würzburg 2021

Eingereicht bei der Fakultät für Chemie und Pharmazie:

02.02.2021

Gutachter der schriftlichen Arbeit:

1. Prof. Dr. Frank Würthner
2. Prof. Dr. Matthias Lehmann

Prüfer des öffentlichen Promotionskolloquiums:

1. Prof. Dr. Frank Würthner
2. Prof. Dr. Matthias Lehmann
3. Prof. Dr. Holger Helten
4. Prof. Dr. Claudia Höbartner
5. Prof. Dr. Roland Mitric

Datum des öffentlichen Promotionskolloquiums:

08.04.2021

Doktorurkunde ausgehändigt am:

_____

List of Abbreviations

A	acceptor
Ac	acetyl
ACN	acetonitrile
Ad	adamantyl
ALMO	absolutely localized molecular orbitals
APCI	atmospheric-pressure chemical ionization
bpy	2,2′-bipyridine
BSA	benzeneseleninic anhydride
Bu	butyl
BuLi	butyllithium
CD	circular dichroism
CPP	cyclo-*para*-phenylene
CPPA	cyclo-*para*-phenyleneacetylene
CT	charge-transfer
CV	cyclic voltammetry
Cy	cyclohexyl
D	donor
dba	dibenzylideneacetone
DBN	1,5-diazabicyclo[4.3.0]non-5-ene
DBPO	dibenzoyl peroxide
DBU	1,8-diazabicyclo[5.4.0]undec-7-ene
DCB	dichlorobenzene
DCC	*N*,*N*′-dicyclohexylcarbodiimide
DCM	dichloromethane
DCTB	*trans*-2-[3-(4-*tert*-butylphenyl)-2-methyl-2-propenylidene]malononitrile
DDQ	2,3-dichloro-5,6-dicyano-1,4-benzoquinone
DFT	density functional theory
DGDEE	bis(2-ethoxyethyl) ether
DMA	dimethylacetamide
DME	dimethoxyethane
DMF	*N*,*N*-dimethylformamide
DMSO	dimethyl sulfoxide
DOSY	diffusion ordered spectroscopy
EDA	energy decomposition analysis
EI	electron ionization
equiv	equivalent(s)

ESI	electrospray ionization
ET	electron-transfer
Et	ethyl
Fc^+/Fc	ferrocenium/ferrocene redox couple
GPC	gel permeation chromatography
HOMO	highest occupied molecular orbital
HPLC	high-performance liquid chromatography
HRMS	high-resolution mass spectrometry
IRF	instrumental response function
ISC	intersystem crossing
ITC	isothermal titration calorimetry
KHMDS	potassium bis(trimethylsilyl)amide
LDA	lithium diisopropylamide
LiTMP	lithium 2,2,6,6-tetramethylpiperidide
LUMO	lowest unoccupied molecular orbital
MALDI	matrix-assisted laser desorption ionization
Me	methyl
m.p.	melting point
MS	mass spectrometry
NBS	*N*-bromosuccinimide
NIR	near-infrared
NMP	*N*-methyl-2-pyrrolidone
NMR	nuclear magnetic resonance
PADI	polycyclic aromatic dicarboximide
PAH	polycyclic aromatic hydrocarbon
PBI	perylene bisdicarboximide
Ph	phenyl
PIFA	phenyliodine bis(trifluoroacetate)
ppm	parts per million
Pr	propyl
PT	proton-transfer
SPhos	2-dicyclohexylphosphin-2′,6′-dimethoxybiphenyl
SWV	square wave voltammetry
TBAHFP	tetrabutylammonium hexafluorophosphate
t-BuXPhos	2-di-*tert*-butylphosphin-2′,4′,6′-triisopropylbiphenyl
TD	time-dependent
Tf	triflate

THF	tetrahydrofuran
TMEDA	*N*,*N*,*N*′,*N*′-tetramethylethylenediamine
TOF	time of flight
Ts	tosyl
UV	ultraviolet
vis	visible

Physical Constants, Variables and Units

δ	chemical shift
ε	molar extinction coefficient
$\Delta\varepsilon$	molar circular dichroism coefficient
θ	ellipticity
κ	statistical transmission coefficient
λ	wavelength
$\Delta\sigma_{CT}$	charge-transfer distance parameter based on spread of positive and negative electron density upon excitation
τ	fluorescence lifetime
Φ_{fl}	fluorescence quantum yield
A	absorbance
Å	ångström
a.u.	arbitrary unit
c	concentration
E	energy
E_{ox}	oxidation potential
E_{red}	reduction potential
D_{CT}	charge-transfer distance parameter based on spatial separation of electron density upon excitation
ΔG	Gibbs free energy
$\Delta G^{\#}$	free enthalpy for the activation of the racemization
g_{abs}	dissymmetry factor
h	hour(s)
h	Planck constant
ΔH	molar enthalpy
I_{fl}	fluorescence intensity
J	coupling constant
K	association constant
k_B	Boltzmann constant

k_{rac}	rate constant of the racemization
min	minute(s)
R	ideal gas constant
Δr	charge-transfer distance parameter based on the displacement of molecular orbital centeroids upon excitation
rpm	revolutions per minute
ΔS	molar entropy
T	temperature
t	time
$t_{1/2}$	half-life time
v/v	volumetric ratio

Table of Contents

Chapter 1

Introduction and Aim of the Thesis

Ever since prehistoric times, the diversity, brilliant hues and tinctorial strength of dyes and pigments have fascinated humankind. Already our prehistoric ancestors extracted natural colorants, e.g. indigo from dyer's woad or alizarin from bloodwood trees, and used these as vat dyes for textiles or pigments for cave drawings (Figure 1).[1-2] However, only in 1856 Perkin succeeded in the accomplishment of the first synthetic colorant namely mauveine. Since then, this field has tremendously developed and an enormous number of new synthetic dyes and pigments is accessible with the help of modern (organic) synthetic chemistry. In addition to their early use as colorants or vat dyes, they continuously emerge into various high-technology applications and are for example important for cancer targeting and (bio)imaging,[3-5] lasing[6-8] or organic (opto)electronics.[9-11] In this regard, new functional dyes and pigments are interesting not only due to their optical properties or (photo-) stability, but also due to their electronic properties, interaction with external stimuli or intermolecular interactions.[1-2, 12-14] Therefore, the iterative process of designing, developing and subsequent revealing of (fundamental) structure–property relationships is indispensable to obtain dyes and pigments with tailor-made properties.

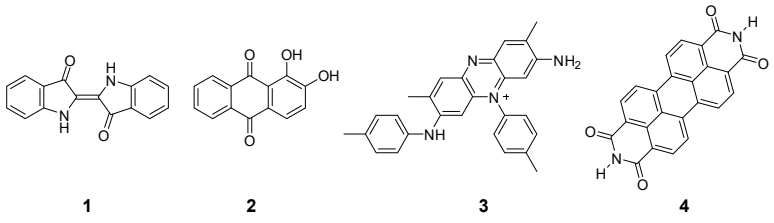

Figure 1. Chemical structures of the colorants indigo (**1**), alizarin (**2**), mauveine (**3**) and a perylene bisdicarboximide (**4**).

In this regard, rylene dicarboximide dyes are one of the most studied classes of organic chromophores.[15-17] They are due to their excellent optical properties, high chemical and mechanical resistance, easy functionalization and electron-deficient character a valuable chromophoric scaffold in (functional) dye research.[18-20] Such characteristics lead to countless applications of these dyes such as n-type semiconductor in organic field-effect transistors[18, 21] and photovoltaics,[22] in organic lasers,[23] as near-infrared (NIR) chromophores[15, 24] or fluorescence probe in (bio)imaging.[25] Furthermore, these dyes are used in various fundamental studies, for

instance in electron-transfer[26] as well as energy-transfer[27] dynamics or in light-harvesting systems for artificial photosynthesis.[28] Especially, perylene bisdicarboximides (PBIs, Figure 1) are with their strong and distinct visible light absorption and fluorescent quantum yields up to unity in solution of special interest.[16] In addition, they exhibit strong interchromophoric interactions, which can lead to fascinating (functional) supramolecular architectures.[29-30] However, such interactions lead often to an almost complete quenching of the fluorescence in the solid-state.[31-32] This can be overcome by enwrapping the π-surface with sterically demanding groups,[33-35] which opens applications as solar-light concentrators,[36] solid-state emitters[33] or lasing dyes.[23] In this context, introduction of bulky substituents at the imide-position is of special interest since they preserve the optical properties of the monomeric dyes in solution.[35-36] However, synthetic access to these materials is hampered by low-yielding multi-step synthesis. Considering the lack of detailed studies of the solid-state properties of rylene dicarboximide structures, easy synthetic access to these scaffolds with bulky substituents is of great interest. For this purpose, one aim of this thesis was the development of a new direct, simplified imidization reaction protocol, which gives easy and straightforward access towards new sterically crowded rylene dicarboximides (Figure 2), and the subsequent evaluation of structure–property relationships in the solid-state.

In contrast to PBIs, the further longitudinal π-extended rylene bisdicarboximide homologs have the advantage of systematic bathochromically shifted absorption and fluorescence spectra reaching the NIR region,[19] while unfortunately the fluorescence quantum yield significantly diminishes for longer rylenes (terrylene bisdicarboximides ≤90%[37-38] and quaterrylene bisdicarboximides ≤5%[39-40]). These properties result from the energy gap narrowing mainly caused by an increase of the HOMO (highest occupied molecular orbital) levels due to the linear π-extension.[41-42] Beside the increase of the conjugation length, a minimized bond-length alternation in the π-conjugated system and the introduction of donor/acceptor moieties have major effects on the narrowing of the frontier orbitals.[43-44] The resulting NIR dyes are of significant importance due to implementation in applications like bioimaging that requires tissue-penetrating NIR light,[3, 45] light-harvesting in organic photovoltaics,[46-47] NIR organic light-emitting diodes[48] or security measures.[12] However, the number of available organic NIR chromophores is limited and they still suffer challenges like low stabilities.[44] In this regard, dicarboximide containing polyaromatics, like rylene bisdicarboximides, are valuable compounds, because their frontier energy levels and with this their optical as well as electronic properties can be easily tuned by the spatial extension of their aromatic scaffold,[49] introduction of additional functional groups[50] or incorporation in donor–acceptor[44, 51] motifs.[43-44, 52] In general, such structures can be termed as polycyclic aromatic dicarboximides (PADIs), which are polycyclic aromatic hydrocarbon (PAH) scaffolds containing dicarboximide groups at their peripheries.[53] In addition, the electron-poor character induced by the electron-withdrawing dicarboximide groups makes such NIR dyes also interesting as n-type semiconductor

for organic electronics.[18, 48] However, the synthesis of PADIs is often achieved by a consecutive multi-step synthesis.[54-56] This drawback can be attributed to the electron-deficient character of these systems, which omits synthetic strategies, e.g. Scholl reaction, as applied for electron-rich polyaromatics.[57] Only recently, the group of Würthner[53, 58-59] introduced a new convergent palladium-catalyzed annulation strategy for the rapid and easy construction of novel PADIs, which show strong visible light absorption. Based on this synthetic strategy, another major aim of this thesis was the development of new electron-deficient NIR absorbers and emitters based on narrow HOMO–LUMO gaps. In the first approach, this should be accomplished with a broad variety of π-enlarged and tetrachlorinated PADIs (Figure 2). Optical spectroscopy of these chromophores should reveal the correlation between absorption/emission properties and structure. In addition, disclosure of the electronic properties should give insights into the electron-deficient character of these dyes. Next, optical properties of these NIR dyes should be carefully modulated and tuned (Figure 2) and for this purpose, the attached chlorides should be substituted with aryloxy and aryl groups. Again, absorption and emission spectroscopy should reveal substituent-dependent optical features. In addition, the introduction of the four aryl groups should lead to an inherent chirality,[60-61] which might be interesting in terms of their chiroptical properties. In the last attempt, a narrowing of the HOMO–LUMO gap should be achieved by the incorporation of electron-deficient naphthalene dicarboximide acceptors in fused acceptor–donor(–acceptor) structures. These compounds should possess, in addition to low-lying LUMO levels, a pronounced charge-transfer character, which should result in a broad absorbance up to the NIR region. In-depth investigation with different donor-moieties as well as multiple acceptor units should provide systematic insights in the corresponding optical and electronic properties.

Further, the strong interchromophoric interactions, easy and precise functionalization, and electron-deficient character of rylene dicarboximide dyes lead to their comprehensive investigation in supramolecular chemistry.[19, 29] In this context, the concept of host–guest chemistry is of immense importance for chemistry as well as biology in understanding fundamental non-covalent interactions[62-64] and (bio)molecular recognition,[65-66] and had found utilization in applications such as catalysis,[67] supramolecular materials[68] and sensors.[69-70] In this regard, chemists have thoroughly designed artificial host structures like macrocycles,[71-72] tweezers/clips,[73-74] cage compounds[75] or more recently nanohoops[76] for the uptake of various guest molecules. However, the number of available general host scaffolds is limited and such structures are often branded by an intricate design principle, tedious synthesis and a rather rigid structure, which limits the number of suitable guests.[71] For this purpose, another major goal of this thesis was the implementation of a new host design. Therefore, based on a recently published π-extended tetrakisdicarboximide by the group of Würthner,[58] a rational electron-deficient host structure should be devised (Figure 2), whose charge-transfer interaction with electron-rich guest molecules should support the guest

binding. Thereby, four bulky imide substituents at the periphery of the nanographene scaffold should build-up two molecular cavities, which allow the encapsulation of (electron-rich) guests with various sizes. Detailed spectroscopic and crystallographic investigations should disclose structural features of the host–guest complexes and reveal insights into the intermolecular interactions between electron-rich guests and ditopic, electron-deficient nanographene host.

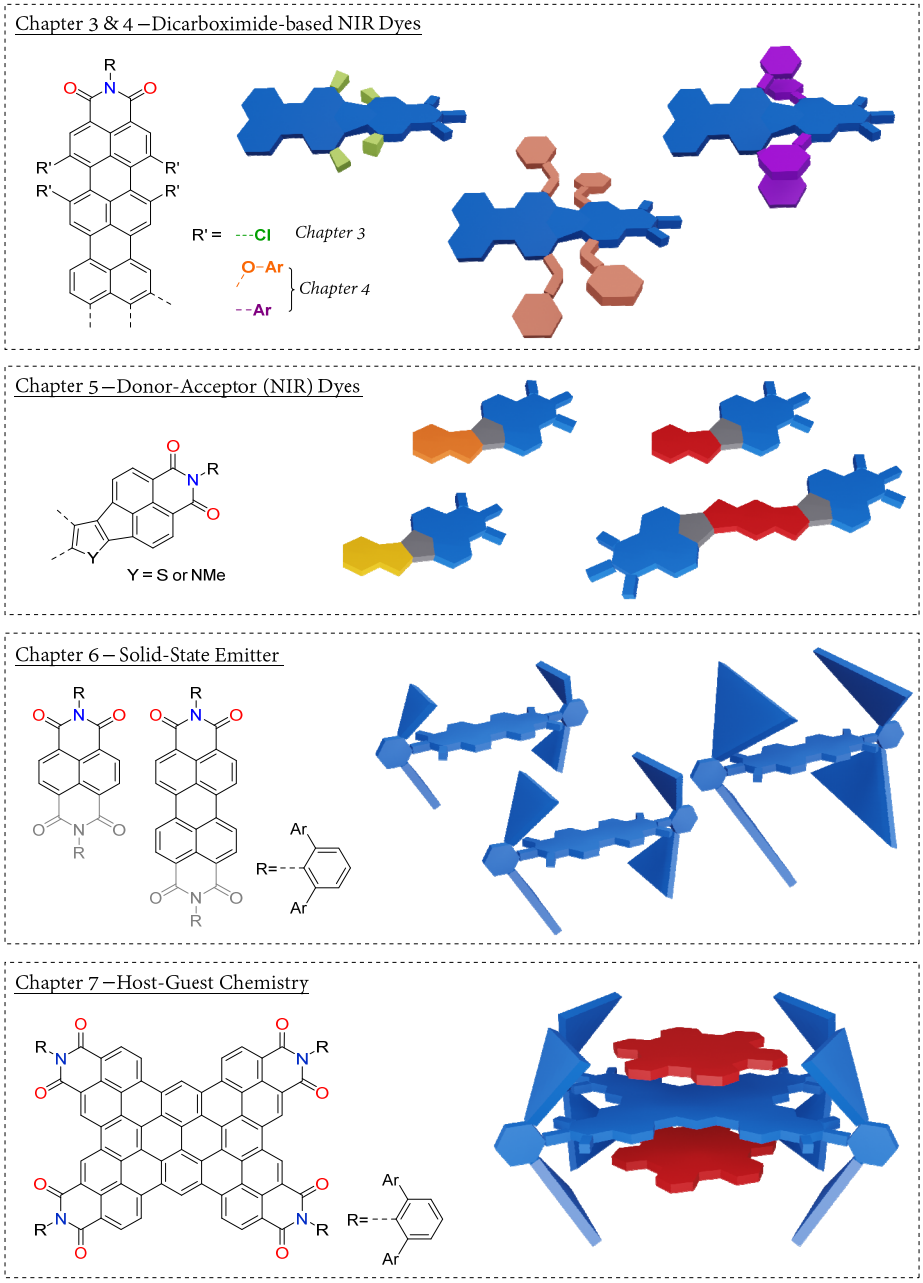

Figure 2. General chemical structures of molecules described in this thesis and their schematic representations.

In *Chapter 2*, first, synthetic concepts for the preparation of polycyclic aromatic dicarboximides are summarized and their resulting properties briefly discussed. Then, design principles and frequently

used scaffolds of organic NIR dyes are described. Finally, supramolecular, solution-state, organic donor–acceptor complexes are reviewed and categorized with respect to their host design.

Chapter 3 deals with novel π-extended, tetrachlorinated polycyclic aromatic dicarboximides as NIR absorber and emitter. First, a versatile synthetic annulation methodology towards these dyes is explored. Optical absorption and fluorescence spectroscopy, and electrochemical analysis were used to study the respective properties, which were correlated with the spatial extension of the π-scaffold. The obtained results were further rationalized with density functional theory (DFT) calculations.

The following *Chapter 4* builds on the results of the NIR dyes from *Chapter 3* and describes the modulation of the absorption and fluorescence properties by chemical modification. For this purpose, aryloxy- and aryl-substituted counterparts of the dicarboximide molecules in *Chapter 3* were synthesized. Absorption and emission spectroscopy was used to reveal the influence of the introduced substituents and circular dichroism spectroscopy to study the inherent chirality of a tetraaryl-substituted PADI.

In *Chapter 5,* the synthesis and properties of new fused donor–acceptor chromophores are described. Optimized reaction conditions provided access to dicarboximide acceptors fused to a broad variety of donor structures. The influence and correlation of the donor-strength and the number of fused acceptors on the charge-transfer character were studied with the help of optical spectroscopy, electrochemical investigations and DFT calculations.

The subsequent *Chapter 6* describes the synthesis and influence of bulky dicarboximide substituents of rylene mono- and bisdicarboximides on the packing and optical properties in the solid-state. For this purpose, a direct base-assisted imidization was developed and the resulting sterically crowded dyes were studied with crystallographic analysis as well as optical spectroscopy in the solid-state to disclose structure–property relationships.

In *Chapter 7*, the complexation capabilities of an electron-deficient ditopic nanographene host – equipped with four bulky dicarboximide substituents from *Chapter 6* – were investigated. The host–guest complexes with various electron-rich PAHs were analyzed with detailed spectroscopic, computational and crystallographic studies to gain systematic insights into the formation of these organic donor–acceptor complexes in solution and solid-state.

Chapter 8 and *Chapter 9* summarize and conclude the work described herein in English and German, respectively.

Chapter 2

State of Knowledge

The first part of this chapter will provide an overview of polycyclic aromatic hydrocarbons containing six-membered ring dicarboximide functionalities. After a brief description of the term polycyclic aromatic dicarboximides, synthetic concepts and general properties are discussed. The second part discloses general design strategies as well as commonly applied scaffolds of organic NIR absorbers and/or emitters. Further, the optical properties of exemplary NIR dyes are depicted and discussed. The last part focuses on finite, organic supramolecular donor–acceptor assemblies in solution. For this purpose, this part is arranged into subdivisions, which correspond to the host design. Selected recent literature examples of organic charge-transfer complexes and their resulting properties and applications are presented. Foldamer- or template-based structures are not included.

2.1. Polycyclic Aromatic Dicarboximides

2.1.1. Terminology

Polycyclic aromatic hydrocarbons are an essential class of compounds in (organic) chemistry, which possess due to their aromatic character interesting properties and in particular high stability.[77] Extended PAHs represent small cutouts of graphene and can therefore be termed as nanographenes, which are ideal model compounds to study the properties of graphene.[78] Further, the size of the aromatic scaffold, linkage of the benzenoid rings, introduction of different ring sizes, incorporation of heteroatoms and functionalization at the peripheries are powerful tools to tune the (opto)electronic properties of these compounds.[77, 79-80] The dicarboximide group as edge functionalization is of special interest as it can be used not only to alter the properties of the aromatic hydrocarbons but also to introduce additional substituents, like solubilizing chains, or act as binding site through the dicarboximide substituent.[57, 81-82] Therefore, PAHs, which contain dicarboximide groups, can be termed as polycyclic aromatic dicarboximides (PADIs).[53] This is not only limited to parent PAHs but also to heteroaromatics that further alter the resulting characteristics, like the possible induction of an intramolecular charge-transfer.[57, 80]

2.1.2. Synthetic Concepts

Rylene dicarboximides are the most prominent representative from the class of PADI dyes.[15-16, 19] In 1913, Kardos synthesized the first PBI, which accounts to the most well-studied rylene bisdicarboximide homolog, and due to its low solubility this chromophore found application as pigment and vat dye.[83-84] In 1959, soluble PBI derivatives were developed for the first time and their outstanding fluorescent properties were revealed.[85] Over the last decades, functionalization at the perylene scaffold using the *peri*-, *ortho*- and *bay*-position yielded applications in a broad variety of fields for PBIs ranging from simple use as dyes to application in modern high-performance organic electronics (Figure 3).[16, 86-87]

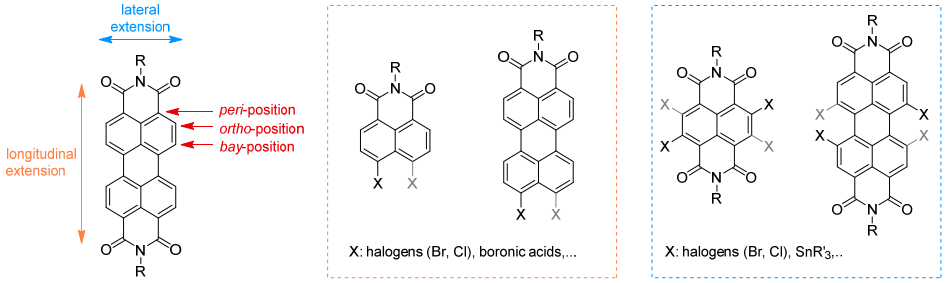

Figure 3. Depiction of a perylene bisdicarboximide scaffold with relevant positions (left) and general structures of important precursors for the synthesis of PADIs (orange box: monodicarboximides; blue box: bisdicarboximides).

These positions display also an important starting point for two main strategies for the synthesis of (other) polycyclic aromatic dicarboximides (Figure 3, orange and blue box). In general, it can be differentiated between three major synthetic strategies:

(a) monodicarboximide-based approach

(b) bisdicarboximide-based approach

(c) postimidization approach

Synthetic strategies based on monodicarboximides represent one of the most common ones (Figure 3, orange box). This approach has the benefit of a broad versatility of possible substrates for the annulation with a rylene monodicarboximide and beside a linear π-extension, also more complex systems are easily accessible. Hereby, only naphthalene and perylene monodicarboximides precursors are of significant importance. This might be due to scarce availability/circuitous synthesis of higher rylene homologs. The second approach uses functionalized rylene bisdicarboximides as starting materials, which are also readily available (Figure 3, blue box). Due to the high reactivity of the (typically) used *ortho*- and *bay*-positions, this approach provides the advantage for the simple and fast construction of large PADIs. However, this strategy is rather

limited to a lateral extension of the used rylene bisdicarboximide and reduces a possible two-dimensional extension in an additional longitudinal fashion. In contrast to these two approaches, the last strategy does not rely on the fusion of various substrates towards functionalized rylene mono- and bisdicarboximides. This strategy rather uses (functionalized) polyaromatic hydrocarbons and build-up the dicarboximide groups at their peripheries. This approach often has the disadvantage of a linear, multi-step synthesis, however, it gives access to PADIs which might be not accessible *via* the other two strategies.[10, 19, 57]

Monodicarboximide-based approach

Synthetic access to PBIs are feasible using two main strategies (Scheme 1, n, m = 1).[19, 57] The first strategy is a two step-procedure, whereby in the first step two complementary functionalized naphthalene monodicarboximide moieties are connected by a C–C cross-coupling reaction, such as Suzuki–Miyaura, Stille or Yamamoto coupling. Subsequently, an oxidative cyclization lead to the corresponding PBI. The second strategy is a simple one-step oxidative annulation of two naphthalene dicarboximide units. For this purpose, typically rather harsh reaction conditions like molten alkali hydroxides or elevated temperatures in combination with a strong base are required. Both strategies can be easily transferred to the longitudinal extended rylene mono- as well as bisdicarboximides like terrylene ($n + m$ = 3)[37-38], quaterrylene ($n + m$ = 4)[40] or pentarylene ($n + m$ = 5)[24] dicarboximides. However, the higher homologs are substituted with additional aryloxy groups due to synthetic reasons and to provide sufficient solubility.

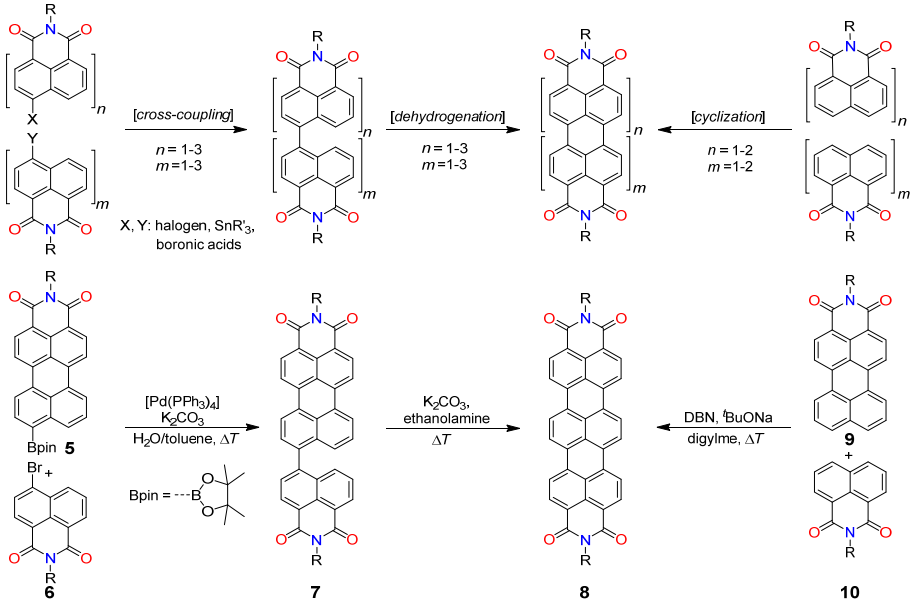

Scheme 1. Synthetic strategies towards linear, longitudinal extended rylene bisdicarboximides (top) and synthesis of terrylene bisdicarboximide **8** (bottom) as an example (R, R′ = alkyl or aryl groups).

The two pathways are exemplarily depicted for the synthesis of terrylene bisdicarboximide **8** (Scheme 1). Hereby, the functionalized perylene dicarboximide **5** and naphthalene dicarboximide **6** are first used in a Suzuki–Miyaura cross-coupling reaction towards intermediate **7**, which is subsequently fused under basic conditions to the target product **8**.[38] The other strategy uses under harsh reaction conditions unfunctionalized **9** and **10** as well as a strong base, sodium *tert*-butoxide, in a direct oxidative annulation reaction.[38] However, the latter strategy can lead to additional undesirable side-products of homo-coupled starting materials. The linear, longitudinal extension of the π-scaffold leads to a pronounced bathochromic shift in the UV–vis absorption spectrum as well as a decrease of the energy gap mainly due to an increase of the HOMO levels.[10, 24, 41] Unfortunately, the fluorescence quantum yields in solution drops from unity for PBIs[16] to ~0.9 for terrylene bisdicarboximides[37] to ≤0.05 for quaterrylene bisdicarboximides.[39]

Beside the linear, longitudinal π-extension, the non-linear elongation is also known. Such modification strongly alter the properties of the corresponding rylene dicarboximides derivatives. A famous example is the zethrene bisdicarboximide **12** from the group of Wu (Scheme 2).[88] Synthetic access to the desired zethrene **12** gave a one-pot cascade reaction, consisting of a Stille cross-coupling followed by an *in-situ* transannular cyclization reaction, with dibromo-functionalized naphthalene dicarboximide **11**. Dilute and carefully adjusted reaction temperature reduced the formation of hardly separable oligomers and other side-products. Furthermore, **12** could be oxidized with *N*-bromosuccinimide (NBS) into the corresponding dione **13**. The introduction of the dicarboximide groups resulted in both compounds in an enhanced photostability and solubility. The same group could also realize in a comparable manner the higher homolog heptazethrene bisdicarboximide **14**,[89] which has an open shell singlet biradical character in the ground state.

Not only dibromo-functionalized naphthalene dicarboximide is a valuable precursor for the synthesis of PADIs, but also the monobromo-substituted naphthalene dicarboximide **15**. In this context, Ortiz and Segura[90] reported the synthesis of heteroatom containing PADI **21** starting from **15** (Scheme 2). For this purpose, the intermediate product **17** from a Suzuki–Miyaura reaction of **15** and boronic acid **16** was cyclized under basic conditions in an oxidation reaction to **18**. The subsequent oxidation yielded dione **19**, which was applied in a condensation reaction with diamino-thiophene **20** to give perylene monodicarboximide annulated thieno[3,4-*b*]pyrazine **21**. The strong electron-accepting character and low-lying LUMO level allowed the implementation of **21** as n-type semiconductor in organic field-effect transistors.

The fusion of rylene monodicarboximides is applicable not only to planar substrates, but also to bowl-shaped PAHs. An example is reported by Wang and coworkers,[91] in which *peri*-brominated perylene monodicarboximide **22** and corannulene derivative **23** are coupled towards intermediate **24** and a subsequent five-ring cyclization gave the desired product **25** (Scheme 2). The possible six-

membered ring side-product was not observed, probably due to the easier accessible position for the formation of a pentagon. Annulated compound **25** shows an antiparallel packing motif in the solid-state due to strong dipole–dipole interaction and its low-lying LUMO level makes it a promising material for application in organic electronics. Beside the annulation with corannulene, mono-brominated **15** and **22** can be further directly fused towards spherical C_{60}-fullerene to yield **26**[92] and **27**[93], respectively. These compounds possess interesting electronic properties and a derivative of **27** showed a power conversion efficiency up to 8% in organic solar cells.[94]

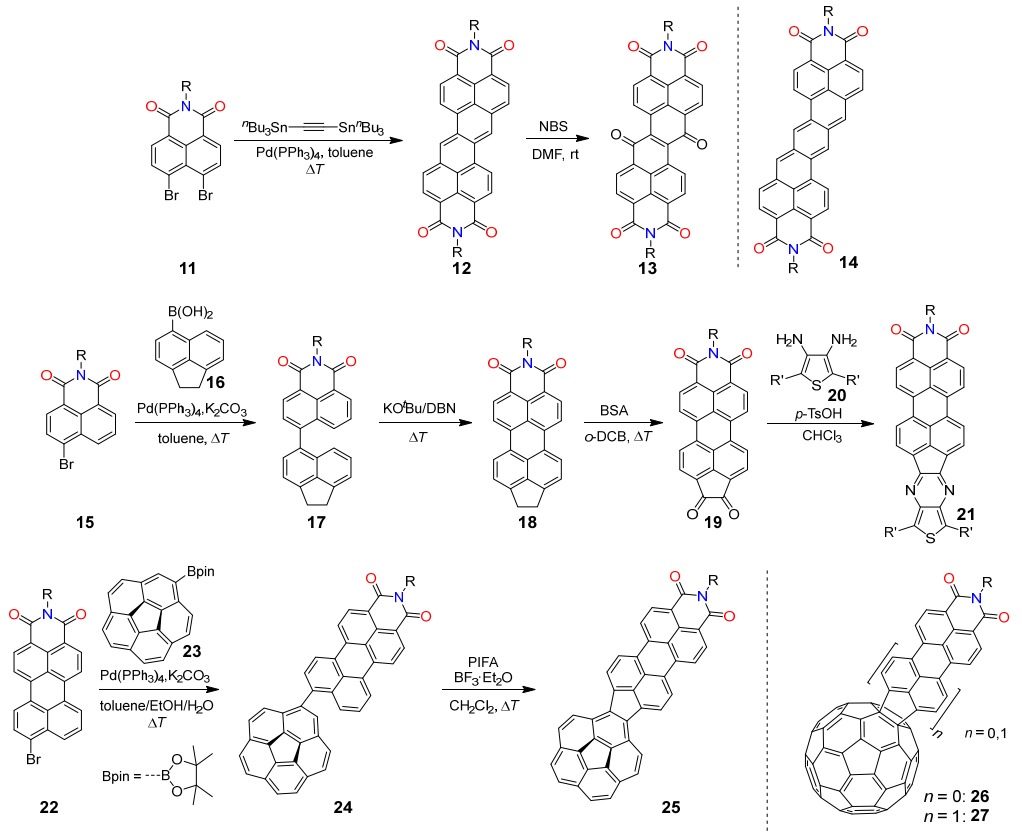

Scheme 2. Examples for the synthesis of PADIs starting from rylene monodicarboximides (R, R′ = alkyl or aryl groups).

Beside these mainly two-step procedures, first a C–C cross-coupling and second a cyclization reaction, the group of Würthner[53, 58-59] devised an elegant direct annulation reaction with dibromo-functionalized naphthalene monodicarboximide **11** for the fast construction of (extended) PADIs (Scheme 3). A palladium-catalyzed cascade reaction sequence, consisting of a Suzuki–Miyaura cross-coupling followed by a Heck-type C–H arylation, of **11** with PAH boronic acid esters (e.g. **28**) gave access to a broad variety of new PADIs (e.g. **30**).[53, 59] In addition, they observed a base-dependent preference for either six- (e.g. **30**) or five-membered (e.g. **31**) ring products, which was attributed to different base-induced cyclization pathways.[53] The obtained products display strong differences in their (opto)electronic properties, whereby five-ring compounds showed a pronounced charge-transfer character from rather electron-rich annulated PAHs to electron-deficient

naphthalene dicarboximide units, while six-ring products exhibited an homogenous conjugation over the entire π-scaffold. Their synthetic strategy was also applicable towards multi-fold annulation reactions.[58-59, 95] Thus, the tetrakisdicarboximide nanographene **32** consisting of 64 sp^2-hybrized carbon atoms could be synthesized in a one-pot reaction (Scheme 3).[58] In this remarkable cascade sequence ten bonds are formed, of which the last two bonds (highlighted in blue) are the result of additional oxidation reactions. Nanographene **32** showed distinct visible light absorption, strong emission and multiple reduction potentials. Modified reaction conditions and a step-wise procedure yielded in a five-fold annulation towards corannulene the bowl-shaped pentakisdicarboximide **33**, which represents the first synthesis of a carbon nanocone.[95]

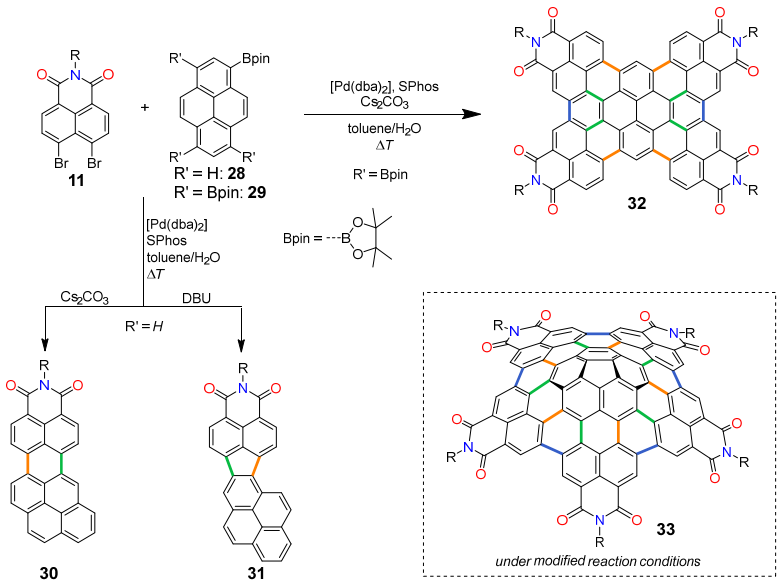

Scheme 3. Developed palladium-catalyzed annulation strategy by the group of Würthner (R = aryl group). The colored bonds represent the different involved reaction types (orange: Suzuki–Miyaura; green: C–H arylation; blue: oxidation).

Bisdicarboximide-based approach

In contrast to the first strategy, which uses the *peri*-position of rylene monodicarboximides, the second approach employs functionalized rylene bisdicarboximides as starting point for the construction of PADIs. The *bay*- and *ortho*-functionalized rylene bisdicarboximides are readily accessible and ideal starting materials for the fast extension in a lateral fashion.[10, 19] Typically, reaction sequences contain aryl–aryl C–C cross-coupling reactions and subsequent oxidative cyclization reactions (Scheme 4). Dibromo and tetrabromo naphthalene bisdicarboximides **34** and **35**, respectively, represent valuable precursors. In contrast to the above mentioned reaction sequence, tetracene bisdicarboximide **37** was obtained in a one-pot double cross-coupling reaction of **35** with silole **36**.[96] Further, the tetrabenzo-derivative **38** could be synthesized in a similar

manner.[96] The obtained products show broad absorption up to the NIR region, low-lying LUMO levels, good solubility and stability, and making them promising candidates as NIR dyes as well as n-type semiconductors. The elongation is not only restricted to pure benzenoid systems, but also the introduction of heteroatomic structures is feasible. In this context, Würthner and Klauk could demonstrate the one-pot synthesis of diindole-annulated **41** starting from dibromo naphthalene dicarboximide **34**.[97-98] A nucleophilic substitution with 1-bromoaniline (**39**) followed by a palladium-catalyzed cyclization reaction afforded PADI **41**, which is planar, fully conjugated and showed n-type as well as p-type semiconducting behavior in transistors. With the same synthetic strategy benzofuran-annulated **42**[98] could be obtained, however, the respective benzothiophene-fused **43**[99] required a multi-step procedure.

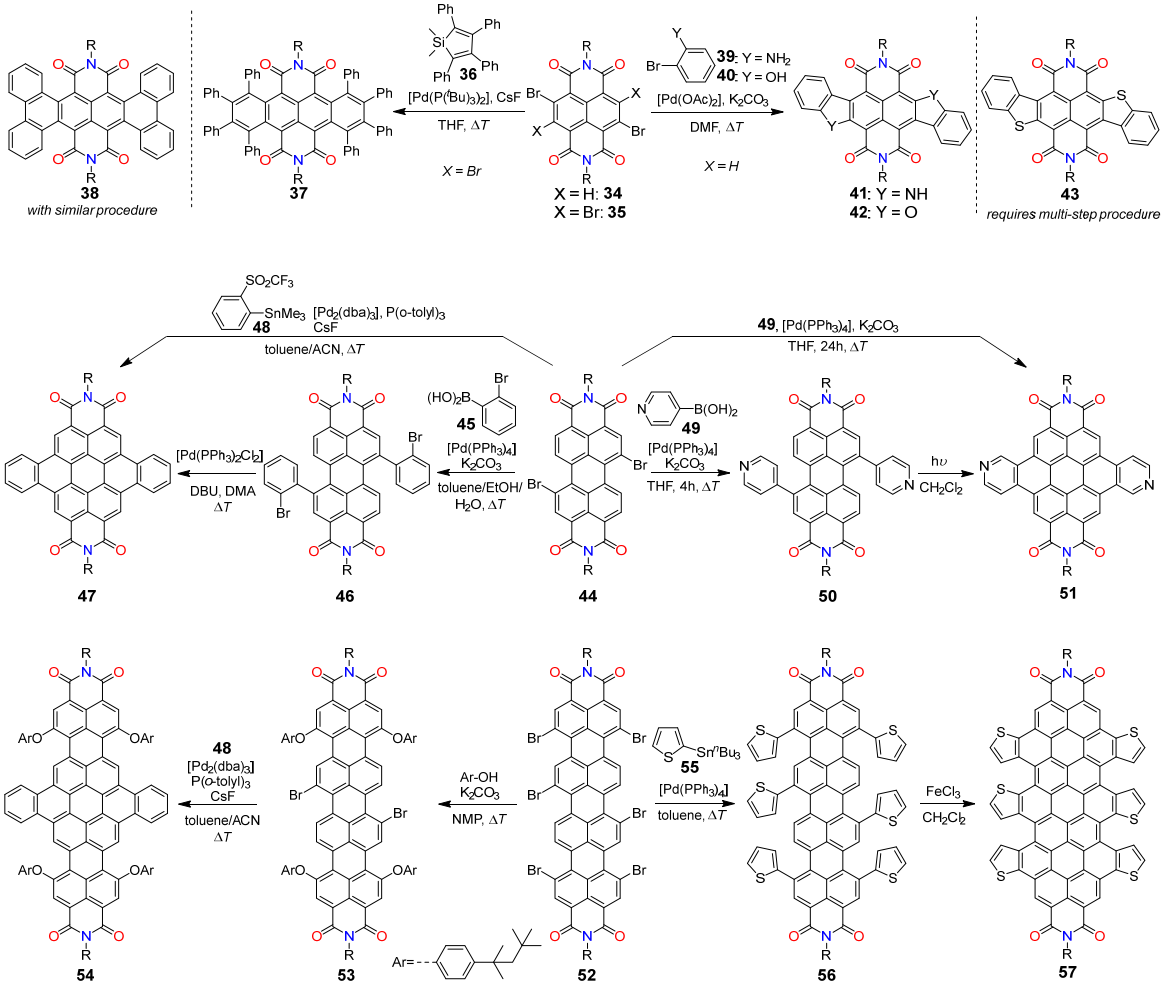

Scheme 4. Examples for the lateral π-extension of rylene bisdicarboximides (R = alkyl or aryl groups).

Beside brominated naphthalene bisdicarboximides, *bay*-brominated perylene bisdicarboximides, e.g. **44**, are also versatile precursor for a lateral π-extension. In this regard, two-step procedure of **44** with boronic acid **45** afforded intermediate **46**, which was subsequently converted by a palladium-catalyzed dehydrohalogenation to fused perylene bisdicarboximide **47** (Scheme 4).[100]

In addition, one-step reaction of **44** with *in situ* generated benzyne (from **48**) yielded directly **47**. Furthermore, Suzuki–Miyaura reaction of **44** with pyridine boronic acid **49** followed by a photocyclization gave nitrogen containing counterpart **51**.[101] Prolonged reaction of PBI **44** with **49** furnished directly the pyridine-annulated product **51**. Such lateral extension lead, in contrast to the longitudinal extension, to a hypsochromic shift in the absorption spectrum.[100-101] The second strategy is also regularly applied to higher rylene bisdicarboximide homologs, like quaterrylene bisdicarboximides. Similar to perylene bisdicarboximide **47**, the corresponding lateral extended quaterrylene bisdicarboximide **54** is accessible in a direct annulation with *in-situ* generated benzyne from **53**.[100] Such extension induced similar to **47** an hypsochromic shift in the absorption spectrum of **54** and, interestingly, afforded emission properties (toluene, λ_{max} = 726 nm, Φ_{fl} = 0.40) that are superior to those of regular quaterrylene bisdicarboximides. Negri and Wong reported the effective lateral extension of **52** with thiophenes.[102] For this purpose, a six-fold Stille cross-coupling reaction of **52** with stannyl thiophene **56** and subsequent oxidative cyclization under Scholl-type reaction conditions gave thiophene decorated quaterrylene bisdicarboximide **57**.

In addition to the fusion with polyaromatic hydrocarbons and heteroaromatics, *bay*-halogenated perylene bisdicarboximides are also highly versatile starting materials for the construction of multidicarboximide containing PADIs (Scheme 5).[19] In this context, the group of Wang has developed a facile synthetic procedure.[20, 103-105] A copper mediated Ullmann coupling and C–H arylation reaction of tetrachloro-perylene bisdicarboximide **59** lead to homo-coupled tetrakisdicarboximide **60**.[103] Further, more elevated reaction temperatures can be used to obtain the non-chlorinated counterpart of **60**. These structures are highly electron-deficient and show strong and broad absorption in the visible range. Furthermore, the devised reaction sequence can be extended for the construction of multidicarboximide compounds containing three[104] or four[105] PBI units. The same group developed an annulation procedure for the fusion of naphthalene bisdicarboximides and PBIs.[106-107] For this purpose, a one-pot annulation consisting of a Stille cross-coupling and a subsequent intramolecular cyclization gives direct access to hybrid rylene dicarboximide arrays **62** and **63**.[106] This procedure was applied in a step-wise manner for the synthesis of linear extended dodecakisdicarboximide **64**.[107] Such hybrid arrays are twisted due to the steric demand of adjacent rylene bisdicarboximide units, and have a strong electron-poor character and broad visible light absorption.

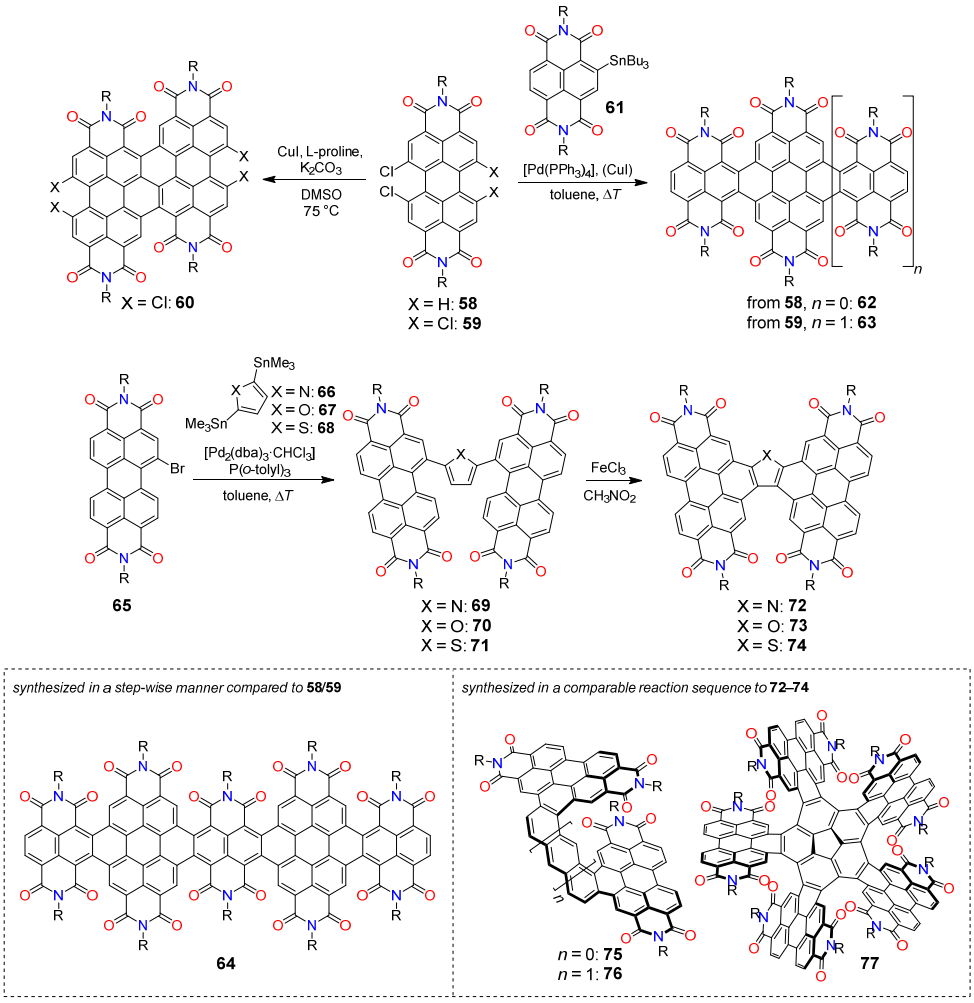

Scheme 5. Examples for the synthesis of multidicarboximide containing PADIs (R = alkyl or aryl groups). Only one enantiomer is depicted for PADIs **75**–**77**.

Another prominent and elegant approach towards multidicarboximide-based systems is the fusion of multiple rylene bisdicarboximide units towards a central (hetero)aromatic unit (Scheme 5).[57] Therefore, a typical reaction sequence consists of a C–C cross-coupling followed by an oxidative cyclization reaction. Monobromo-PBI **65** is a valuable and readily available precursor. For instance, the group of Jen reported the synthesis of thiophene/furan/selenophene fused PBIs **72**–**74**, respectively.[108] After two-fold Stille coupling of **65** with the corresponding coupling partner (**66**–**68**), a Scholl reaction yielded the desired annulated products **72**–**74**. Thereby, the fusion rigidifies the π-scaffold, which enhanced the power conversion efficiency in organic solar cells compared to a non-fused system. This is rationalized by a decreased reorganization energy as well as a stronger conjugation in the fused system. Therefore, such structures are heavily studied in organic photovoltaics.[18, 109-111] In addition, this synthetic strategy can be easily transferred for the introduction of chirality as shown by the group of Nuckolls. They synthesized in a comparable reaction sequence the helicene containing dicarboximides **75** and **76**.[112] The high steric demand of the PBI units in **75** prohibited an interconversion of the separated enantiomers even at elevated

temperatures (250 °C, 60 min, diphenylether), while **76** racemized at room temperature due to the extended distance between the PBI subunits. In addition, a shorter spacer unit (n = 0; **75**) lead to through-space electronic delocalization of the single PBI moieties. Furthermore, **65** can be employed in the synthesis of even more complex systems like bowl-shaped penta-PBI fused corannulene **77** (Scheme 5).[113] The steric demand of the five PBI-subunits lead to five axial chirality centers, however, under the chosen reaction conditions only D_5- (*P*,*P*,*P*,*P*,*P* or *M*,*M*,*M*,*M*,*M*) or C_2- (*M*,*P*,*P*,*P*,*P* or *P*,*M*,*M*,*M*,*M*) symmetry products are formed and yielding different, highly interesting packing motifs.

Postimidization approach

In contrast to the first two strategies, which rely one pre-formed rylene mono- and bisdicarboximides, the last approach relies on the functionalization of the PAH with six-membered dicarboximide groups at a later stage of the reaction sequence. In this context, the group of Wudl has devised a synthetic pathway towards trisdicarboximide **82** (Scheme 5).[55] First, the parent PAH decacyclene (**78**) is treated in a six-fold Friedel–Crafts carbamylation with **79** to give **80** and second a hydrolyzation and cyclization yielded the trisdicarboxlic anhydride **81**. Finally, an imidization reaction gave the desired trisdicarboximide **82**. The radial extended PADI forms interesting self-assembled structures and was employed as n-type semiconductor in organic photovoltaics.

The same group developed a five-step strategy towards anthracene bisdicarboximide **88** (Scheme 5).[114] For this purpose, **83** was converted into the corresponding acid chloride and subsequently a Friedel–Crafts alkylation gave dione **84**. After tetrabromination, a solvolysis with DMSO and a following oxidation bisdicarboxylic anhydride **87** was obtained. Lastly, an imidization furnished the desired product **88**. Yamada and coworkers could simplify the synthesis towards **88** (Scheme 5).[115] Analogues to the procedure of Wudl, first an acid chloride is formed, but a subsequent Lewis-acid mediated cyclization with an isocyanate directly yielded bisdicarboximide **88**. Furthermore, the procedure was applicable for the synthesis of tetracene and pentacene bisdicarboximides **90** and **91**, respectively. The introduction of the dicarboximide groups lead to a lowering of the LUMO levels compared to their parent PAH counterparts, thereby making them n-type semiconductors.

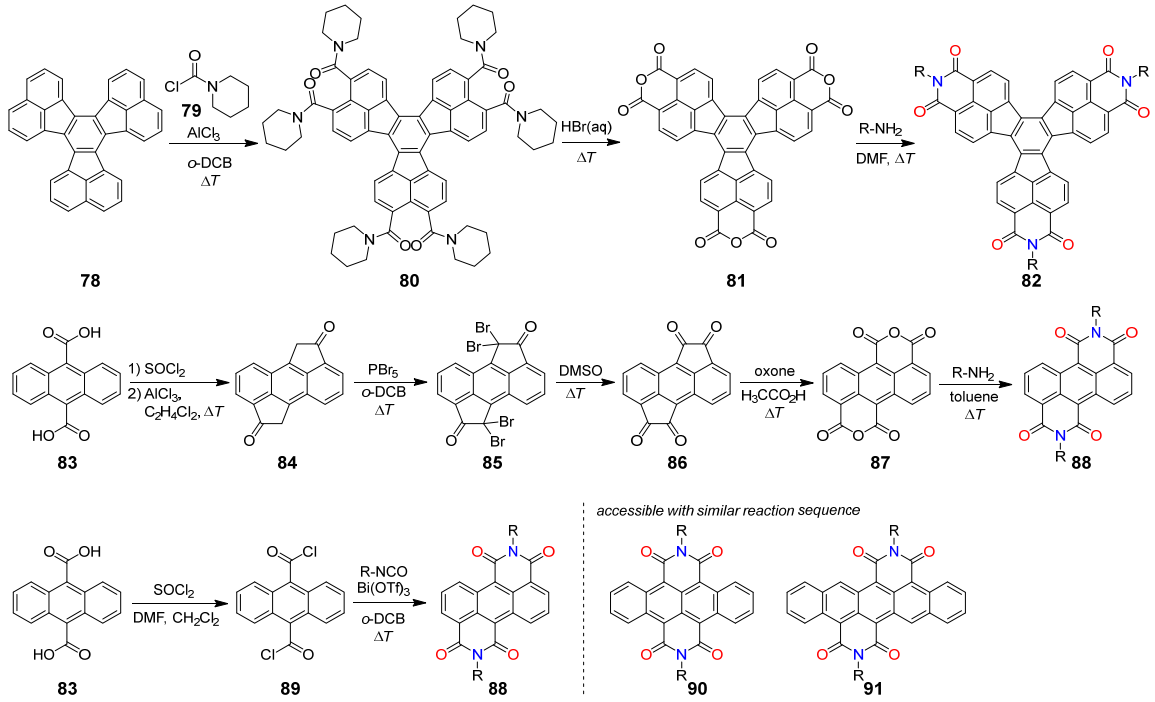

Scheme 5. Examples for the synthesis of PADIs using the postimidization approach (R = alkyl or aryl groups).

The group of Stępień devised another elegant and versatile strategy towards large multi-dicarboximide containing nanographenes (Scheme 6).[116-121] The approach is based on the valuable pyrrole-fused naphthalene dicarboximide **97**.[116] For this purpose, acenaphthene derivative **92** is first oxidized (**93**) and subsequently equipped with a tosyl group (**94**). A Zard–Barton reaction with the help of isocyanate is used for the formation of the pyrrol-ring to give **95**. Cleavage of the remaining ester group under basic conditions and a subsequent imidization reaction yielded precursor **97**. The high reactivity of the pyrrol-subunit in **97** is ideal for the construction of extended multi-dicarboximide systems. For instance, deprotonation and nucleophilic substitution gave six-fold substituted benzene derivative **99**.[117] A Scholl reaction yielded the respective fused azacoronene hexakisdicarboximide **100**, which shows multiple (consecutive) reduction potentials. Moreover, Stepien and coworkers could install under modified reaction conditions bulky groups at the naphthalene dicarboximide subunits to introduce an inherent chirality (**105**).[119, 122] The optical as well as electronic properties were strongly altered due to the steric constrain in **105** compared to **100**. In addition, **97** can be applied in a condensation reaction with benzaldehyde (**101**) to give a porphyrin with four fused naphthalene dicarboximide groups (**102**).[116] Further, a stepwise procedure can be used to obtain partial decoration with electron-withdrawing dicarboximide groups (**103** and **104**), which lead to systematically changes in the (opto)electronic properties.[120]

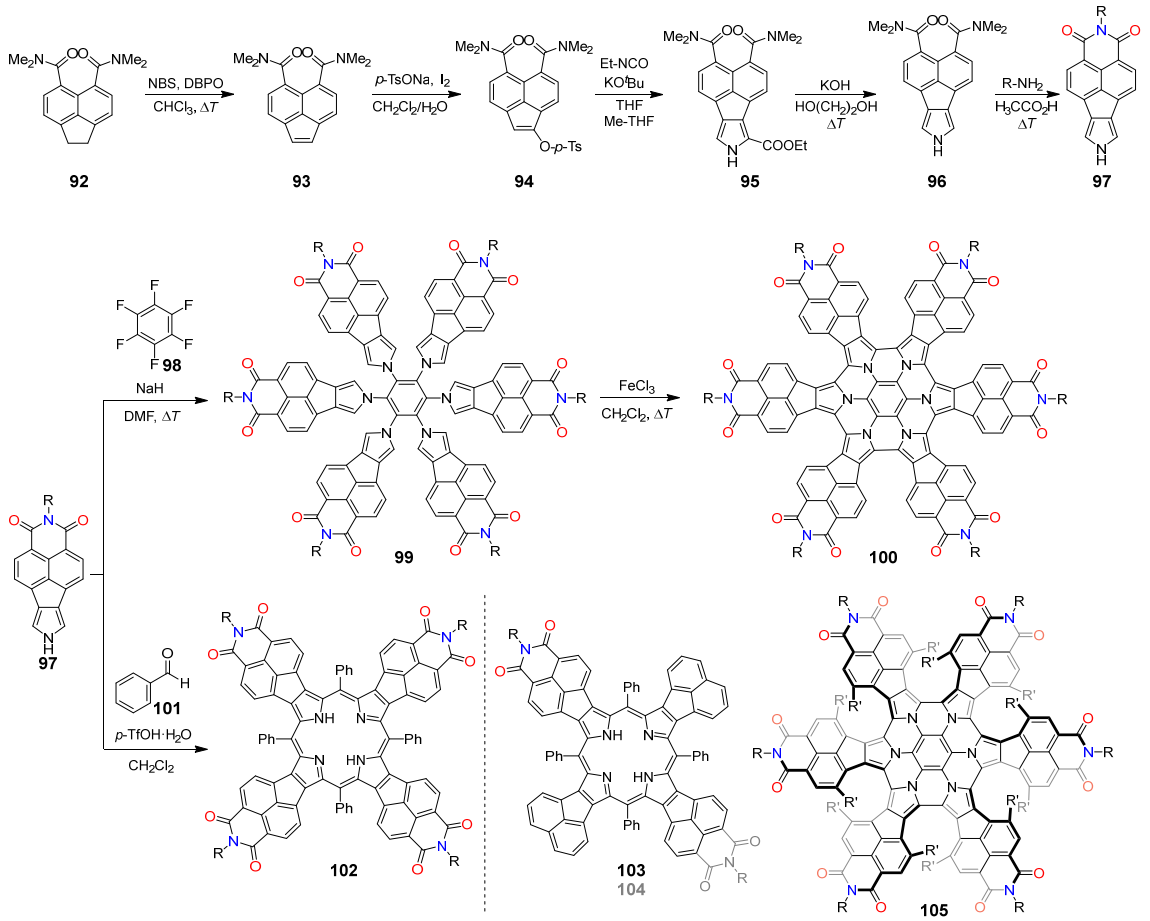

Scheme 6. The developed strategy by the group of Stępień for the synthesis of large PADIs (R, R′ = aryl groups). Structure of **105** represents only D_6-symmertic *P*,*P*,*P*,*P*,*P*,*P*-enantiomer.

2.1.3. Properties and Characteristics

In general, PADIs typically possess a pronounced electron-deficient character due to the electron-withdrawing dicarboximide group. They are mostly chromophores with high tinctorial strength and show good thermal and chemical stability.[10, 15, 19, 57] The electronic and optical properties of PADIs are strongly influenced by the spatial extension of their aromatic surface, which is revealed by a comparison of longitudinal as well as lateral extended rylene bisdicarboximides. In the former case, the extension in a longitudinal fashion led to a bathochromic shift in the UV–vis absorption spectrum as well as an increase in absorption strength (extinction coefficient) of the corresponding bisdicarboximide (Figure 4a).[19, 24] However, the fluorescence quantum yields drops from unity (perylene bisdicarboximide[16]) dramatically when reaching the NIR range (quaterrylene bisdicarboximides ≤0.05[39-40]). The bathochromic shift in the absorption spectrum upon elongation in longitudinal direction can be attributed to a narrowing of the energy gap. This is a result of the (significant) rise of the HOMO levels upon longitudinal extension, whereas the LUMO levels decrease only slightly.[41-42]

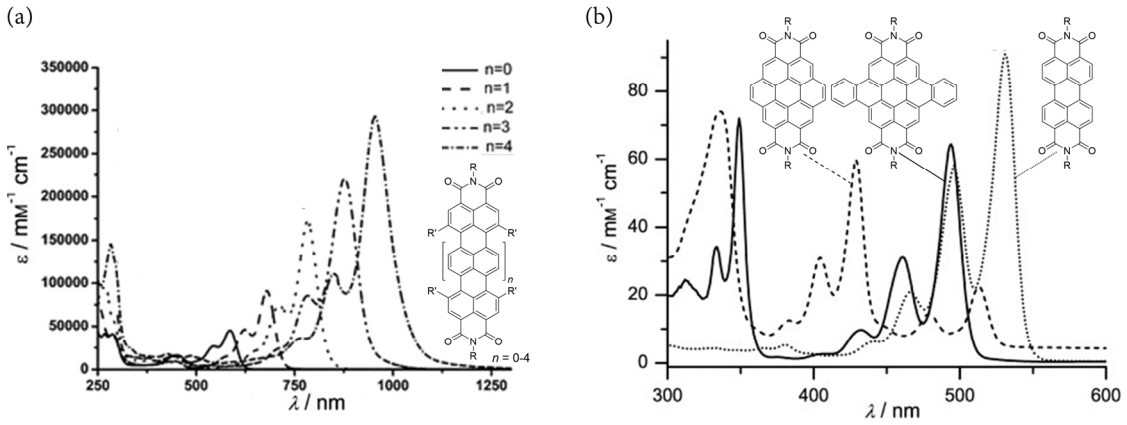

Figure 4. UV–vis absorption spectra of (a) longitudinally and (b) laterally [coronene bisdicarboximide: dashed line; dibenzocoronene bisdicarboximide: solid line; perylene bisdicarboximide: dotted line] extended rylene bisdicarboximides in solution (R = alkyl or aryl group; R′ = aryloxy group). (a) reprinted and adapted with permission from ref. [10]. Copyright 2010 The Royal Society of Chemistry. (b) reprinted and adapted with permission from ref. [100]. Copyright 2007 Wiley-VCH Verlag GmbH & Co. KGaA.

In contrast, the lateral extension of a parent perylene bisdicarboximide along the *bay*-positions led to an hypsochromic shift as well as decreased absorptivity (Figure 4b).[100] These observations can be directly linked to the orbital-mixing of the related rylene bisdicarboximide scaffold and the corresponding PAH, which led to changes in the frontier orbital localization as well as their coefficients. For instance, in the case of coronene bisdicarboximide (Figure 4b) the HOMO–LUMO transition originates from a coronene-like HOMO to a perylene bisdicarboximide-like LUMO. Therefore, a lateral extension does not give directly related higher analogues with incremental changes. Similar observations are described for laterally extended quaterrylene bisdicarboximides.[100, 123] However, a lateral extension in the non-*bay* regions led to strongly altered characteristics. First, such extension induce a torsion in the aromatic scaffold due to neighboring hydrogen atoms and second, the acene-like HOMOs cause a bathochromic shift in the absorption spectra.[10, 124-125] The introduction of multiple dicarboximide moities, like in fused rylene bisdicarboximides, typically led to a pronounced electron-deficient character with several reduction potentials, a decreased HOMO–LUMO gap and strong as well as broad absorption bands in the visible range, when compared to a parent perylene bisdicarboximides.[58, 95, 103, 105-106] Furthermore, incorporation of non-benzenoid rings,[53, 55] hetereoatoms,[102, 126] curvature[91, 95, 113] or additional substituents[10, 15-16] are known to (drastically) influence the resulting properties of the PADIs in solution as well as in the solid-state. For instance, an insertion of five-membered rings often disturbs the aromatic conjugation.[53, 55] This can result in donor–acceptor systems, whereas a charge-transfer from electron-rich subunits to electron-deficient moieties (dicarboximide containing parts) occur. This charge-transfer character causes a rather broad and weak absorption as well as a low fluorescence quantum yield.[53] The incorporation of heteroatoms in the aromatic scaffold has a similar effect, which often results in a localization of electron-density on a certain moiety and entail a donor–acceptor structure.[126-128] Therefore, the optical and electronic properties of the resulting

PADIs are strongly dependent on their spatial extension and modifications at their aromatic scaffold. In contrast, the dicarboximide substituent has only a negligible influence on these properties due to typical nodes of the HOMO and LUMO orbitals at the dicarboximide nitrogen.[16, 53] However, the nitrogen represents not only an additional binding site[72, 129] for the construction of covalently bonded systems but also heavily influences the solubility in organic media[130-131] or even water.[132-133] Furthermore, rational design of the dicarboximide substituent allows the control of aggregation processes[29, 55, 131] in supramolecular chemistry or induces liquid crystallinity.[56, 134] Moreover, the arrangement in the solid-state is strongly induced and influenced by the substituent, for example in the packing for organic electronics[18, 135] or the construction of shielded PADIs, which crystallize in isolated molecules.[31, 35-36]

2.2. Organic Near-Infrared Dyes

2.2.1. General Aspects

Dyes that absorb and/or emit light between 700–2000 nm are called near-infrared (NIR) chromophores. This window can be further divided into the NIR I (700–1000 nm) and NIR II (1000–2000 nm) range, while the latter one can be also termed as short-wave infrared region. However, a strict classification is not given in the literature.[5, 44] Organic NIR chromophores are highly interesting dyes, because the tissue-penetrating window for biomedical implementations falls in this range (650–1450 nm),[45] thereby offering applications for NIR dyes in bioimaging[3, 136] or photothermal therapy.[25, 137] In addition, panchromic absorption of the sunlight spectrum with absorbance in the visible up to the NIR light is of significant importance for an efficient light-harvesting in organic photovoltaic devices and high power conversion efficiencies.[44] Further fields of applications of NIR dyes are for example optical data storage,[138] security measures,[12] or NIR organic light-emitting diodes.[48] NIR chromophores can be categorized based on their composition/structure in three main classes: organic, polymeric and inorganic materials.[44] The longwave absorption of NIR dyes is a result of a narrowing of the HOMO–LUMO gap. In this regard, organic NIR dyes typically require a π-conjugated system with strong delocalization or pronounced charge-transfer interactions. However, as a result of the narrow energy gaps, organic NIR dyes suffer often from low stabilities.[43-44]

This chapter focuses on small organic NIR dyes and in the following common design principles and regularly used dye scaffolds of organic NIR chromophores are reviewed and discussed. For this purpose, it will be differentiated between these three major dye classes: cyclic polyene dyes, polymethine dyes and donor–acceptor dyes. Chromophores such as azo-dyes[139-140] or quinone dyes,[141] which are only rarely used as NIR dyes, are not considered in this section.

2.2.2. Cyclic Polyene Dyes

The use of extended cyclic polyene scaffolds is a well-established strategy to achieve a longwave absorption and/or emission. Such extended aromatic structures provide the required small energy gap for NIR dyes due to strong delocalization of the frontier orbitals.[44] Popular representatives of cyclic polyene dyes are porphyrins,[142] phthalocyanines,[143] or π-extended naphthocyanines[144] (Figure 5). These chromophores offer strong and distinct absorption up to the NIR, which can be easily tuned by additional substituents or incorporation of metal cations. Similar advantages, like systematic tunable optical properties in the NIR region, are provided by the already mentioned higher rylene bisdicarboximide homologs (Figure 4a and Figure 5).[24, 39] Due to their polyaromatic structure, these can also be assigned to the group of cyclic polyene dyes.

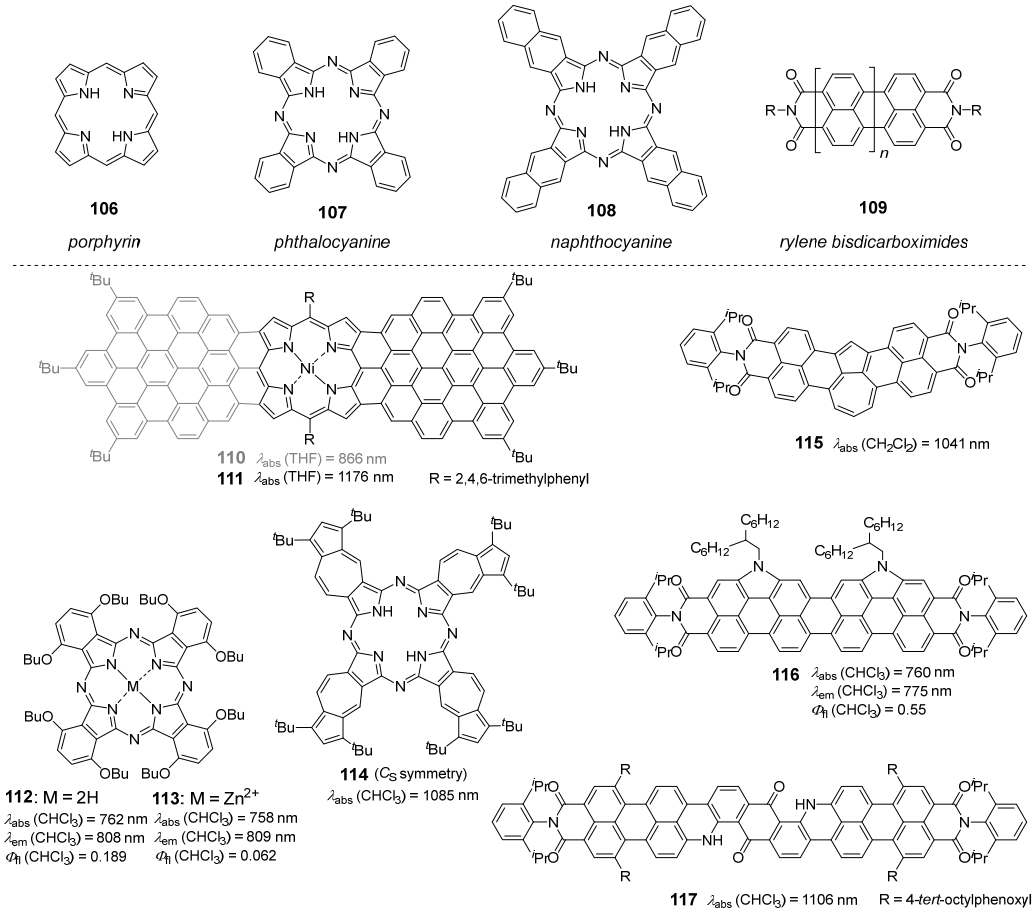

Figure 5. General (top) and specific (bottom) chemical structures of some important cyclic polyene dyes.

By extending this concept, the groups of Narita and Müllen reported the porphyrin containing nanographenes **110** and **111**, which show extraordinary absorption properties in solution (Figure 5).[145] The absorption maximum of mono-fold fused conjugate **110** is located at 866 nm and tails to roughly 1000 nm. Two-fold extended nanographene **111** with its absorption maximum at 1176 nm, which tails up to 1400 nm, offers an absorption in the deep NIR region. Both compounds are non-fluorescent, which was attributed to the heavy-atom effect from nickel. The NIR absorption

could be rationalized with calculated small HOMO–LUMO gaps of 1.78 eV (**110**) and 1.35 eV (**111**). The easy and diverse substitution pattern make also phthalocyanines an attractive scaffold for tailor-made NIR dyes. Whereas undecorated phthalocyanine (**107**) offers an absorption maximum at 699 nm and a fluorescence maximum at 705 nm with a fluorescence quantum yield of 60% (in THF), substituted derivatives show strongly altered properties.[146] For instance, octa-butoxy substituted phthalocyanines **112** and **113** show a pronounced redshifted absorption maximum of 762 nm and 758 nm, respectively (Figure 5). Further, the emission maxima are with 809 nm (**112**) and 808 nm (**113**) also strongly bathochromically shifted. Their fluorescence quantum yields are with 18.9% (**112**) and 6.2% (**113**) reduced but still quite good for this emission range.[146] Therefore, such dyes found broad applications, for example a silicon-derivative has been used as NIR fluorescence label for tumors.[147]

Muranaka *et al.* reported a new class of azulene containing NIR absorbers, e.g. **114** (Figure 5).[148] In analogy to naphthocyanines (**108**), they named these compounds azulenocyanines. The structural isomers of naphthocyanines differ strongly in their optical characteristics. Hereby, **114** shows not only panchromic behavior in the visible range, but also with an absorption maximum of 1085 nm absorption far into the NIR region ($CHCl_3$). This maximum is compared to a naphthocyanine[149] >300 nm redshifted, which can be explained by calculated frontier orbital energies. These reveal a decreased HOMO–LUMO gap for **114** compared to its naphthocyanine counterpart, which could be attributed to the electron-accepting character of the azulene moieties. Another azulene incorporated NIR dye (**115**) was reported by the group of Würthner (Figure 5).[150] The bisdicarboximide **115** represents a structural isomer of a terrylene bisdicarboximide, itself a well-established NIR chromophore. Hereby, PADI **115** exhibit highly interesting absorption properties into the far NIR region. The absorption maximum for the lowest energy transition of **115** is located at 1041 nm (CH_2Cl_2), which is ~400 nm bathochromically shifted compared to the corresponding terrylene bisdicarboximide analog (650 nm). The observed and strongly altered optical characteristics are a result of the retained aromatic character of the azulene subunit in **115** as revealed by DFT calculations.

Instead of the introduction of non-benzenoid rings, the group of Wu annulated donor groups to alter the optical properties of a rylene bisdicarboximide scaffold. Hence, they reported the two-fold *N*-annulated quaterrylene bisdicarboximide **116**,[151] whereas the fused pyrrole groups function as donor and the dicarboximide groups as acceptor moieties (Figure 5). In this regard, the resulting PADI **116** can be interpreted as an acceptor–donor–donor–acceptor dye based on a cyclic polyene scaffold (quaterrylene). This molecular design lead to a small energy gap of 1.56 eV, which resulted in NIR optical properties exceeding typical values for quaterrylene bisdicarboximides. In this context, dye **116** exhibited with an absorption maximum of 760 nm and an extinction coefficient of ~ 90000 $M^{-1}cm^{-1}$ a pronounced NIR absorption ($CHCl_3$). More interestingly, the fluorescence

quantum yield of 55% at an emission maximum of 775 nm is remarkably high.[151] A further example of a cyclic polyene dye on the basis of a rylene bisdicarboximide is reported by the group of Müllen.[152] Their PADI **117** showed with an absorption maximum of 1106 nm ($CHCl_3$) an even more redshifted absorption compared to **116** (Figure 5). This is a consequence of the incorporation of a strong donor moiety, diaminoanthraquinone, into a quaterrylene bisdicarboximide scaffold to give an acceptor–donor–acceptor scaffold. Hence, the longwave absorption could be attributed to a pronounced intramolecular charge-transfer character.

2.2.3. Polymethine Dyes

Beside cyclic polyene dyes, polymethine dyes also represent an important scaffold of organic NIR chromophores. The simplest and most popular representatives are the positively cyanine dyes,[153] which are two nitrogen atoms connected by an odd-number of conjugated carbon atoms (Figure 6). In this context, merocyanine dyes[154] show a comparable composition, however, they are uncharged and one nitrogen is replaced by an oxygen atom. The optical properties of cyanine and merocyanine dyes can be easily modified by the variation of the terminal groups and/or extension of the conjugated chain. The latter one typically lead to a redshift of ~100 nm/vinylene unit. However, an increasing chain length results in a decreased stability, which often can be overcome by the introduction of fused rings into the polymethine chains.[44, 153] Also zwitterionic squaraine dyes,[155] which have a squaric acid core in the centre of their polymethine chain, account to the class of polymethine dyes. They are characterized by sharp and strong absorbance and emission, which can easily reach the NIR region. By exchanging the squaric acid with a croconic acid core, croconic acid dyes can be obtained.[156] These dyes offer a general redshift of ~100 nm compared to their squaraine analogs. Dyes with dipyrrometheneboron difluoride (BODIPY) core structures are another prominent example of polymethine dyes.[157] These are characterized by their strong emitting properties, however, mainly below 600 nm. Various substitution strategies can be employed to redshift the emission and make BODIPY dyes valuable NIR emitters.

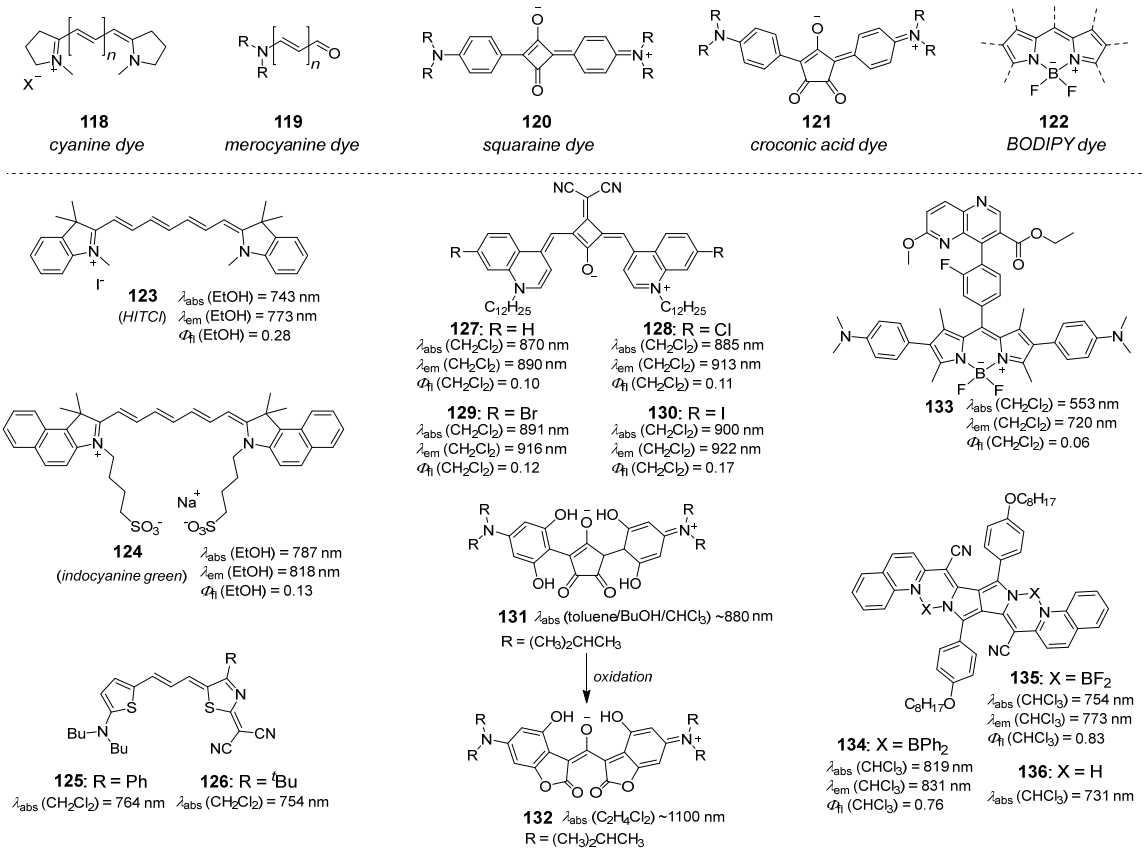

Figure 6. General (top) and specific (bottom) chemical structures of some polymethine dyes.

Cyanine dyes are due to their high fluorescence quantum yields excellent fluorescence reference compounds for the determination of fluorescence quantum yields in the NIR region.[158-159] Two of them are **123** and **124**, which are commercially available as HITCI and indocyanine green/IR-125, respectively (Figure 6). The absorption (743 nm) and emission (773 nm) maximum of HITCI are both located in the beginning of the NIR region and HITCI offer a high fluorescence quantum yield of 28% (ethanol).[158] Indocyanine green shows with an absorption maximum at 787 nm and fluorescence maximum at 818 nm more redshifted values, while the fluorescence quantum yield is with 13% still high (ethanol).[158] In DMSO solutions a fluorescence quantum yields of 23% can be obtained.[159] Further, NIR dyes are valuable compounds for light-harvesting in photovoltaic devices. In this context, the groups of Meerholz and Würthner reported a series of extended merocyanine dyes with absorption in the NIR, e.g. **125** and **126** (Figure 6).[160] Both compounds exhibited with absorption maxima at~760 nm and molar extinction coefficients >140000 $M^{-1}cm^{-1}$ a strong absorbance in the NIR region (CH_2Cl_2), which are results of small HOMO–LUMO gaps (**125**: 1.62 eV, **126**: 1.65 eV). In addition, both dyes could be applied as donor materials in organic photovoltaic devices with power conversion efficiencies of up to 1.4% (**126**).

The series of squaraine dyes **127**–**130** offer a pronounced redshifted absorption compared to the merocyanines **125** and **126** (Figure 6).[161] These dyes are based on dicyanovinyl-substituted squaric

acid units, which differ in their attached halogens (**127**: F; **128**: Cl; **129**: Br; **130**: I). These resulted in an unexpected halogen effect concerning the optical properties of these dyes. In this context, the absorption maximum bathochromically shifts with increasing size of the halogen from 870 nm for (**127**) to 900 nm for (**130**). Furthermore, the emission maxima are shifted in the same way from 890 nm (**127**) to 922 nm (**130**) and more interestingly, the fluorescence quantum yield increases from 10% (**127**) to 17% (**130**). The origin of the halogen effect was assigned to the increased polarizability of the halogens (I > Br > Cl), which led to a pronounced relocation of electron density form the halogens to the squaraine chromophore. Croconic acid dyes are closely related to squaraine dyes, however, with a typically redshifted absorption.[43] In this context, Tian *et al.* reported the croconic acid dye **131** (Figure 6), whose absorption maximum is located at ~880 nm (mixture of toluene/1-butanol/$CHCl_3$).[162] However, **131** could not be isolated in pure form due to fast decomposition. More interestingly, further heating of **131** in a toluene/1-butanol mixture furnished the new dye **132**. This chromophore offers not only good thermal stability (>200 °C), but also a pronounced bathochromically shifted absorption maximum of ~1100 nm (1,2-dichloroethane), making such dyes interesting in terms of nonlinear optical applications.

In contrast to the aforementioned examples, BODIPY dye **133** is not characterized by a pronounced absorption or emission in the NIR region, but rather by an extremely large Stokes shift, pushing the emission into the NIR range (Figure 6).[163] An absorption maximum of 553 nm and emission maximum of 720 nm lead to an extraordinary large Stokes shift for BODIPY dyes of 4200 cm^{-1} (CH_2Cl_2). This results in a negligible overlap of absorption and emission spectrum, which prohibits reabsorption and is therefore interesting for applications such as imaging or multi-labeling. The pronounced redshifted emission and the resulting Stokes shift was attributed to an emissive charge-transfer transition between the BODIPY core and the naphthyridyl moiety.

In contrast to these dyes with a clear chromophoric unit, the group of Daltrozzo reported the hybrid dyes **134** and **135**, which can be interpreted as combination of BODIPY and diketopyrrolopyrrole dyes (Figure 6).[164] Absorption and emission of both compounds are with absorption maxima of 754 nm (**134**) and 819 nm (**135**) and emission maxima 773 nm (**134**) and 831 nm (**135**) located in the NIR region ($CHCl_3$). More interestingly, both compounds offer outstandingly high fluorescence quantum yields of 83% (**134**) and 76% (**135**). In contrast, reference compound **136** without BF_2 or BPh_2 groups is non-emissive, which can be attributed to non-radiative relaxations pathways due to conformational freedom and the lack of rigidity in **136**.

2.2.4. Donor–Acceptor Dyes

The connection of donor and acceptor units can lead to dyes with a pronounced redshifted absorption due to charge-transfer transitions caused by the interplay of electron-rich to electron-deficient moieties.[43-44] This valuable strategy could already be disclosed in some of the above-mentioned examples of cyclic polyene and polymethine dyes e.g. merocyanine dyes **125** and **126**. In these cases, either the acceptor or the donor unit could be accounted to one of these dye classes. However, NIR dyes can be also obtained by using strong donor and acceptor units, which are themselves not considered as chromophores. These groups are often connected by a bridging unit, which can be conjugated or not. Widely applied electron-rich donor moieties contain often a sp^3-hybridized nitrogen as in **137**, **138** or **140**, or are carbon-rich scaffolds e.g. **141** and **142** (Figure 7). Electron-deficient acceptors are for example benzothiodiazol-like units (**143**–**145**) or dicyanomethylene containing structures, e.g. **147**, **149** and **150**.[43-44] The resulting donor–acceptor dyes are also often termed as push–pull dyes.

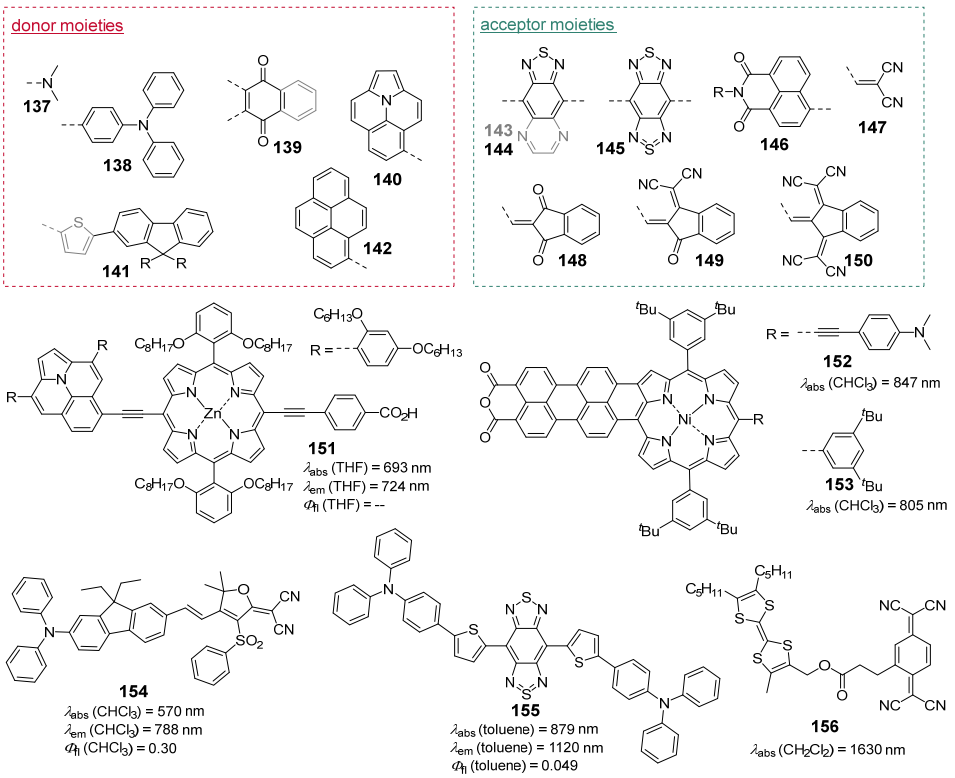

Figure 7. Commonly applied donor (red box) and acceptor (blue box) moieties for the construction of NIR dyes based on donor–acceptor structures and some examples of such dyes.

Porphyrins are frequently applied as bridging units in donor–acceptor based NIR dyes, especially for light-harvesting in dye-sensitized solar cells due to a pronounced visible light absorption, which can be extended into the NIR by appropriate substituents.[47] In this context, Mathew *et al.* reported porphyrin containing dyad **151** (Figure 7).[165] The push–pull chromophore utilizes an ullazine donor and an ethynylbenzoic acid as acceptor moiety. The dye possess a broad panchromic

absorption with a maximum at 693 nm, which tails into the NIR region (THF). In addition, it offers an emission maximum located at 724 nm. Due to its strong absorbing features, **151** could be applied in a dye-sensitized solar cell with a power conversion efficiency up to 7.35% and showing to comparable dyes an improved light-harvesting of NIR (>700 nm) light. Jiao *et al*. reported another example of a porphyrin-bridged push–pull dye (**152**, Figure 7).[166] They attached the electron-donating diamino-phenylethynylene group to a porphyrin, which is fused with a perylene monoanhydride unit. The latter one serves not only as an acceptor unit, but also as an anchor group for the implementation in dye-sensitized solar cells. Dye **152** shows strong absorbance far into the NIR with an absorption maximum of 847 nm, which tails up to 1000 nm ($CHCl_3$). Moreover, compared to **153**, which lacks the strong donor group, the absorption maximum is 42 nm redshifted, disclosing the importance of a strong donor moiety for efficient light-harvesting in the NIR region. This trend is also apparent with a smaller HOMO–LUMO gap for **152** compared to **153**.

In contrast to these rather large structures, the group of Kim reported the much smaller NIR emitter **154** (Figure 7).[167] This dye consists of a diphenylamine donor which is bridged by a fluorene unit with a dicyanomethylene containing acceptor moiety. The resulting push–pull dye shows with an absorption maximum of 570 nm ($CHCl_3$) only visible light absorption, but more interestingly an emission maximum of 788 nm. Further, the quantum yield in solution is with 30% remarkably high and the emission could be even retained in the solid-state (λ_{max} = 800 nm, Φ_{fl} = 9%, thin-film). The obtained large Stokes shift as well as the observed solvatochromism are characteristic for push–pull dyes due to the intramolecular charge-transfer. The chromophore **154** was successfully implemented in an NIR light-emitting electrochemical cell. Another strategy combines multiple donor and/or acceptors in a single dye. In this context, the group of Wang reported donor–acceptor–donor dye **155** (Figure 7).[168] The strong intramolecular charge-transfer arising from the two triphenylamine donors and the benzobis(thiodiazol) acceptor resulted in an absorption in the NIR region with an absorption maximum at 879 nm (toluene). Moreover, compound **155** exhibits with an emission maximum of 1120 nm and a fluorescence quantum yield of 4.9% extraordinary strong emission in the NIR region. These optical features allowed the utilization of **155** in a NIR organic light-emitting diode, which solely emitted NIR light. In contrast to these structures with rigid bridges, Perepichka *et al.* reported the dyad **156** with a non-conjugated and more flexible ester-bridge (Figure 7).[169] Further, the applied strong donor, tetrathiofulvalene, and acceptor, 7,7,8,8-tetracyanoquinodimethane, yielded a remarkably small HOMO–LUMO gap for dye **156** (electrochemical: 0.17 eV). The push–pull dye shows with an absorption maximum at 1630 nm, which tails up to ~2700 nm, a pronounced NIR absorbance (CH_2Cl_2). This observation was attributed to an intramolecular through-space charge-transfer from a folded arrangement resulting in a larger HOMO–LUMO gap (optical: 0.75 eV). The difference between optical and electrochemical HOMO–LUMO gap is a result of a second, non-folded, conformation during the

electrochemical measurements. This non-folded structure is easier to reduce, which was proven by DFT calculations.

2.3. Hosts for Finite, Solution State Organic Donor–Acceptor Complexes

2.3.1. General Aspects

The concept of host–guest chemistry is a key section in the field of supramolecular chemistry and has therefore attracted tremendous attention in the last decades.[62, 170] Thereby, it emerges continuously into new aspiring applications like sensing, (photo)catalysis or supramolecular material science.[67-68, 171-172] Furthermore, it contributed to the understanding in non-covalent interactions between host and guest molecules.[62, 170] Such (weak) interactions include for instance electrostatic, dispersion or charge-transfer interactions. While the latter one cannot only contribute to the complex formation but can also strongly alter the optical as well as electronic properties of the resulting supramolecular assemblies.[173-174] Hereby, a charge-transfer complex is formed by a non-covalent interaction induced by the interplay of electron-rich donor and electron-deficient acceptor molecules. The resulting charge-transfer complex has interacting donor-HOMO and acceptor-LUMO orbitals, thereby leading to a narrowing of the energy gap, compared to its components.[173] Prerequisites for an efficient charge-transfer are close proximity of donor and acceptor, energetic complementary of HOMO and LUMO levels as well as planarity of each component.[173, 175-178] Therefore, organic host–guest complexes based on charge-transfer interactions can be obtained by opposite electron-rich (donor) and electron-deficient (acceptor) structures (host/guest). Parent PAHs like pyrene (**162**) or coronene (**163**), but also porphyrins (**164**) or tetrathiofulvalene (**157**) are prominent electron-rich donors, while tetracyanoquinodimethane (**165**), fullerenes (**168**) or rylene bisdicarboximides (**169** and **170**) represents frequently applied electron-poor acceptors (Figure 8).[176, 179]

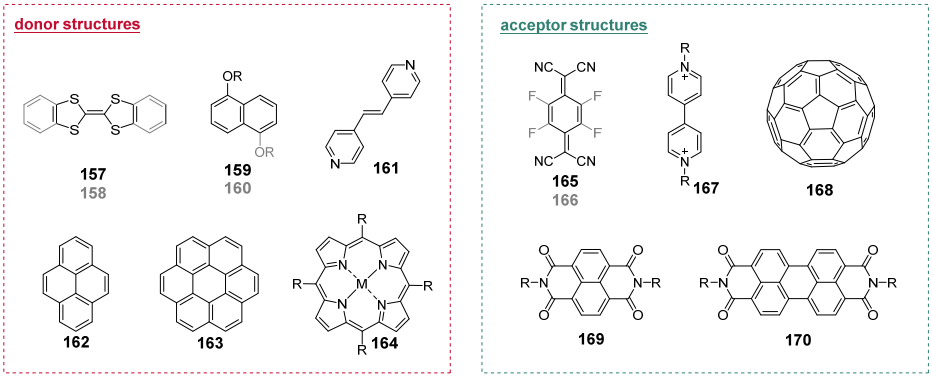

Figure 8. Examples of donor and acceptor structures utilized in charge-transfer complexes.

The use of such donor–acceptor combinations afford supramolecular assemblies[30, 174] in the solid-state with new emerging properties. Indeed, most examples are found in the solid-state as co-crystals.[176, 179-180] However, in solution the interaction of such donors and acceptors are often too weak and no complex formation can be observed.[181-182] Therefore, solution state complexation typically requires the encapsulation of the guest molecules in a defined cavity where the guest molecule interacts with both π-faces.[64] For this purpose, chemists have developed numerous host structures, which can be classified in the following general host categories:

(a) cyclophanes and macrocycles[71]

(b) molecular containers[75, 183]

(c) nanohoops[76]

(d) tweezers and clips[73-74]

A host structure may possess characteristics of two or more categories and cannot in all cases exclusively be assigned to a single category. The contribution of a charge-transfer interaction to the complex formation between donor and acceptor in solution is usually identified by a bathochromically shifted absorption band in the UV–vis absorption spectrum as well as a quenching of the fluorescence of the host. Furthermore, investigation of solvatochromism and shift of the redox-potentials, infrared (IR) or Raman spectroscopic studies as well as the use of ultrafast spectroscopy and theoretical calculations are routinely applied to disclose the involvement of charge-transfer interactions.[63, 173-175, 184]

In the following sections, the focus is on some of the latest developments in solution-state, organic host–guest systems, which are (partially) governed by charge-transfer interactions, as well as their application in solution or solid-state. For this purpose, this part is divided into four subchapters that correspond to the above-mentioned host designs.

2.3.2. Cyclophanes and Macrocycles

Cyclophanes and macrocycles account to the most frequently used host structures in supramolecular chemistry.[71-72, 185-186] The former one usually consists of two parallel (aromatic) surfaces that are kept at a rather fixed distance by spacer units and therewith span a rigid cavity for guest molecules. On the other hand, macrocycles are (often) larger structures with multiple (aromatic) surfaces as binding sites, which are arranged in a cyclic structure to build-up an inner cavity for guest encapsulation. However, the terms cyclophanes and macrocycles are often used as synonyms. To the most prominent and widely applied macrocycles account crown ethers,[187] cyclodextrins,[188]

calix[*n*]arenes,[189] cucurbit[*n*]urils[190] and pillar[*n*]arenes[191] (Figure 9). Such structures typically encapsulate substrates mainly by hydrogen bonds, halogen bonds, hydrophobic and/or electrostatic effects.[71]

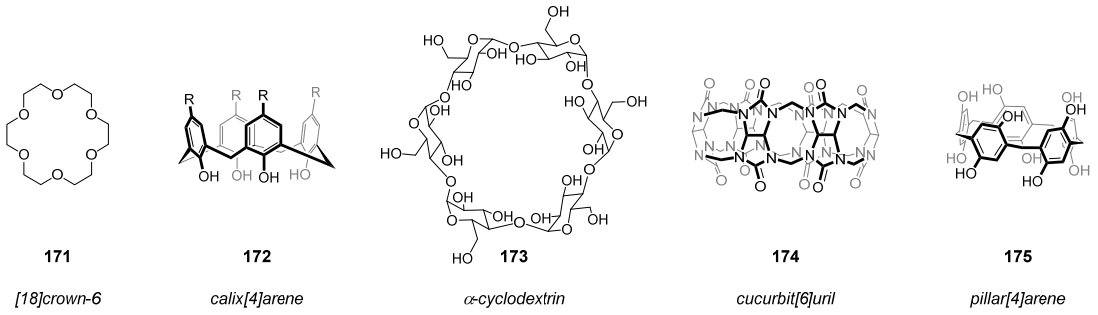

Figure 9. Exemplary structures of a crown ether (**171**), calix[*n*]arene (**172**), cyclodextrin (**173**), curcurbit[*n*]uril (**174**) and pillar[*n*]arene (**175**).

A significant contribution of a donor–acceptor interaction to the complexation can be achieved by the incorporation of (strong) acceptor or donor moieties (Figure 8) into the macrocyclic or cyclophane scaffold. In this context, the group of Stoddart has contributed enormously in the design of new (functional) electron-deficient host structures.[185] Based on their famous *Blue Box* (**176**)[192] reported for the first time in 1988, a tetracationic cyclobis(paraquat-*p*-phenylene) cyclophane, the group has developed numerous related cyclophanes, like **177**–**179**,[193-195] for the tailor-made encapsulation of various guest molecules and investigated the resulting diverse properties/applications of these host–guest systems (Figure 10).

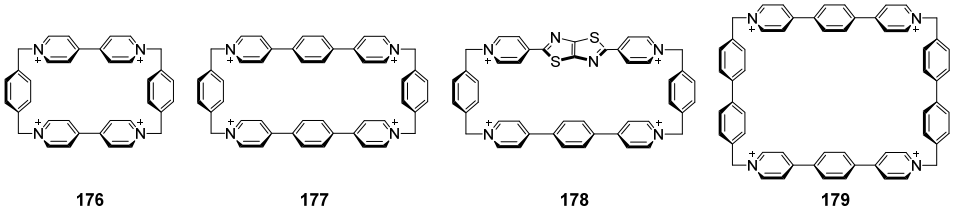

Figure 10. Chemical structures of some cyclophanes developed by the group of Stoddart (counterions are not depicted).

In 2013, Stoddarts group described the template-directed synthesis of cyclophane **177**, which contains an additional phenyl group in the paraquat units compared to *Blue Box* **176**.[193] The inner cavity of **177** allowed the complexation of eleven different PAHs ranging from small naphthalene over non-planar [4]helicene to large coronene (Figure 11a). In nearly all host–guest titration experiments, the emergence of a charge-transfer band could be observed in the solution-state UV–vis absorption spectrum upon addition of guest molecules. Furthermore, almost all obtained co-crystals of inclusion complexes are colored compared to colorless crystals of pure host **177**. These observations could be rationalized with pronounced donor–acceptor interactions due to the strong electron-deficient character, as proven by cyclic voltammetry measurements, of cyclophane **177**

and the electron-rich PAHs. In 2019, the same group could use host **177** for the encapsulation of the photosensitizer 5,12-diphenylporphyrin in water, which was also supported by charge-transfer interactions as indicated by UV–vis absorption spectroscopy.[196] The inclusion lead to a photoprotection of the porphyrin and prohibited the formation of toxic triplet oxygen. However, the photosensitizer could be released upon protonation due to electrostatic repulsion with cationic cyclophane **177**. On this basis, **177** was utilized as a carrier for the diphenylporphyrin into the lysosomes of cancer cells. Subsequently, the acidic cell-environment released and thereby restored the phototoxicity of the porphyrin.

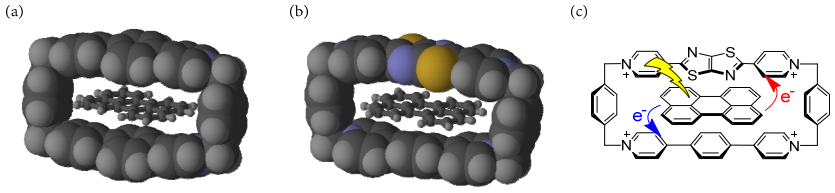

Figure 11. Solid-state inclusion complexes of (a) perylene⊂**177** (generated from CCDC deposition number: 893559; counterions omitted for clarity) and (b) perylene⊂**178** (generated from CCDC deposition number: 1872160; counterions omitted for clarity). (c) Schematic illustration of electron-transfer pathways from photoexcited perylene (counterions are not depicted.) (c) is reprinted and adapted with permission from ref. [197]. Copyright 2019 The Royal Society of Chemistry.

The incorporation of an additional strong electron-deficient dipyridylthiazolothiazole-subunit into the cyclophane-scaffold lead to the less symmetric but even more electron-poor host **178** (Figure 10).[194, 197] The cyclophane was capable to encapsulate perylene (Figure 11b), although the determined binding constant in acetonitrile is only slightly increased compared to perylene⊂**177**. Similarly, upon addition of perylene the emergence of a charge-transfer band was detected in the UV–vis absorption spectrum of **178**. The resulting (asymmetric) supramolecular acceptor–donor–acceptor´ system was investigated with the help of femtosecond transient absorption spectroscopy, while competing photoinduced electron-transfer pathways could be revealed (Figure 11c). Thereby, either electron transfer from the photoexcited perylene donor to the phenylene extended viologene unit (Figure 11c, blue arrow) or to the dipyridylthiazolothiazole containing viologene part (Figure 11c, red arrow) was disclosed. Furthermore, detailed studies indicated an electron transfer process between the two different acceptor units with the help of perylene. Stoddarts group reported even further elongation of the bipyridyl unit, which allowed the uptake of multiple guest molecules and more extended guests, whereas the complex formation is – dependent on the electronic nature of the guest molecules – also supported by charge-transfer interactions.[198]

An extension of the spacer unit in cyclophane **177** by one phenylene group gave the more square-shaped host **179** (Figure 10).[195] The enlarged cavity of **179** allowed the encapsulation of larger, three-dimensional substrates like C_{60}-fullerene in solution. DFT calculations revealed the location of the frontier orbitals on the host–guest complex, whereby the LUMO is mainly located at the

cyclophane scaffold while the HOMO resides at the C_{60}. This counterintuitive observation is a consequence of the stronger electron-accepting character of **179** compared to C_{60}, which pushes the fullerene into the role of a donor. Nevertheless, a mainly entropy-driven complexation was indicated by isothermal titration calorimetry (ITC) experiments, although theoretical calculations actually supported a contribution of charge-transfer interactions to the complex formation. The inclusion could be unambiguously confirmed by crystallographic analysis (Figure 12a,b). More interestingly, the 1:1 complexes arrange in a linear fashion forming columnar stacks and leading to an unusual long-range order for C_{60} arrays. Conductivity measurements of these supramolecular assemblies under ambient conditions (without the exclusion of oxygen) showed electrical conductivity comparable to high-grade pure C_{60}-based materials (Figure 12c). Kaur *et al.* also reported such increased conductivities, however, within three-dimensional, supramolecular donor–acceptor frameworks consisting of an electron-rich host and electron-deficient fullerenes.[199]

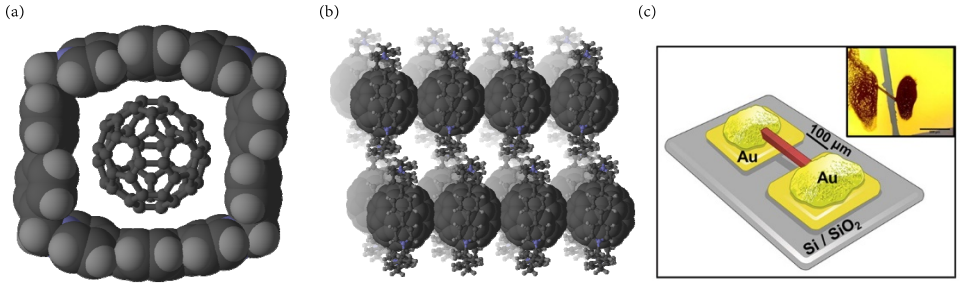

Figure 12. (a) Solid-state structure and (b) packing arrangement of inclusion complex C_{60}⊂**179** (generated from CCDC deposition number: 1022765; counterions omitted for clarity). (c) Schematic device structure of co-crystal C_{60}⊂**179**. (c) is reprinted with permission from ref. [195]. Copyright 2015 American Chemical Society.

In 2015, the group of Würthner reported the PBI-cyclophane host **180** (Figure 13).[200] Similar to Stoddarts *Blue Box* (**177**) a xylylene-spacer unit was utilized, however, the viologene moieties were exchanged by electron-poor PBI units. The dye-based host was capable to encapsulate various PAHs, while the complexation events could be easily followed by absorption and emission spectroscopy. Most interestingly, the electronic nature of the applied guest drastically influenced the observed changes in the UV–vis absorption and fluorescence spectrum. On the one hand, rather electron-poor guests, like carbazole or anthraquinone, caused a pronounced emission enhancement and only small changes in the absorption spectrum of host **180**. On the other hand, electron-rich guests, like perylene or anthracene, quenched the fluorescence and an additional charge-transfer band emerged in the absorption spectrum (Figure 13b,d). These results were rationalized by an oxidative fluorescence quenching mechanism, where guests with higher HOMO levels (more electron-rich) than host **180** quenched the fluorescence due to an intermolecular charge-transfer from guest to photoexcited host (Figure 13c, blue arrow). In contrast to this, guests with a lower HOMO level (more electron-poor) than host **180** increased the fluorescence due to inhibition of

non-emitting relaxation pathways of excited **180**. Therefore, dependent on the electronic nature of the applied guest molecules the fluorescence of the devised host was turned on or off. Subsequent detailed investigation with transient absorption spectroscopy gave further insights into the relaxation pathways of photoexcited cyclophane and its complexes.[201] Recently, a water-soluble derivative of **180** could be applied for the encapsulation of alkaloids, while the observed fluorescence-quenching upon guest addition was rationalized with a charge-transfer interaction between cyclophane and alkaloids.[202]

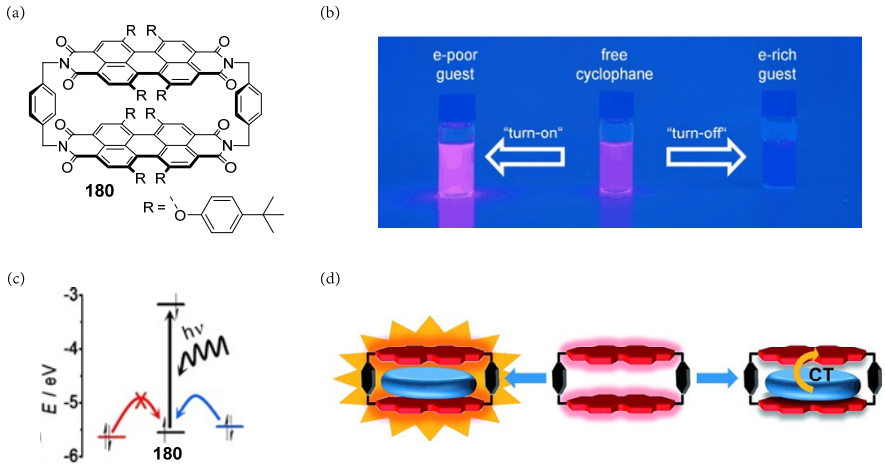

Figure 13. (a) Chemical structure of cyclophane **180**. (b) A photograph illustrates the fluorescence turn-on and turn-off depending on the electronic nature of the encapsulated guest. (c) Depiction of the oxidative fluorescence quenching mechanism (red arrow: electron-poor guest; blue arrow: electron-rich guest). (d) Graphical illustration of the fluorescence enhancement (left pathway) or quenching (right pathway) upon guest encapsulation (CT: charge-transfer). (b–d) are reprinted and adapted with permission from ref. [200]. Copyright 2015 Wiley-VCH Verlag GmbH & Co. KGaA.

In 2020, Barendt and Beer reported the PBI-based macrocycle **181** (Figure 14a).[203] In contrast to **180**,[200] host **181** differs in three main characteristics: rigidity, cavity size and electronic properties. With regard to the electronic properties, the pyrrolidine substituents at the PBI scaffold induce with their electronic-donating effect a rather electron-rich character of **181** compared to the electron-deficient aryloxy-substituted host **180**. Furthermore, the spacer units in **181** are considerably extended and more flexible, which results in a less rigid system with higher flexibility and larger cavity. Thus, the macrocycle host was capable for the complexation of electron-deficient fullerenes C_{60} and C_{70}. Thereby, upon addition of fullerenes the emergence of a new bathochromically shifted band in the UV–vis absorption spectrum could be observed, which was attributed to a ground-state intermolecular charge-transfer (in toluene and *ortho*-dichlorobenzene). Furthermore, the fluorescence quenching as well as a potential shift in cyclic voltammetry measurements due to guest encapsulation underlined the contribution of a charge-transfer interaction to the complexation event. Femtosecond transient absorption spectroscopy in toluene revealed a full electron-transfer between donor host **181** and acceptor-guest fullerene in the excited state (toluene). More interestingly, titration experiments in more polar solvent nitrobenzene resulted not only in higher

association constants but also in a rare thermally allowed, reversible, and complete ground-state electron transfer from **181** to the fullerene guest (Figure 14b).

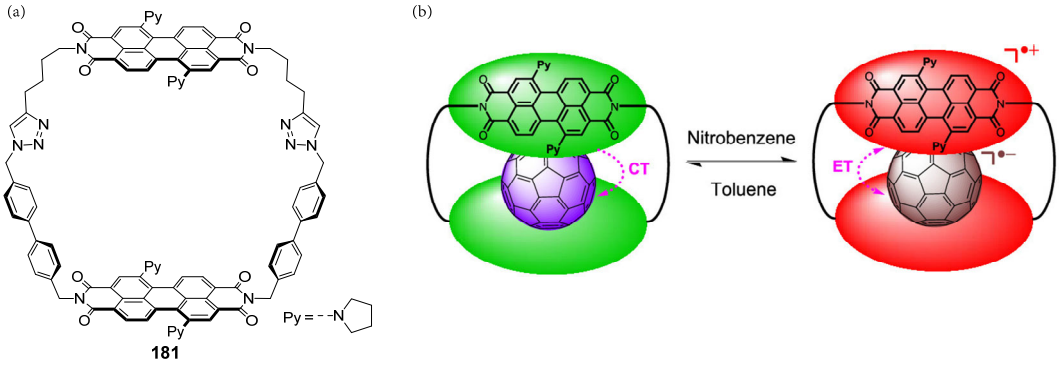

Figure 14. (a) Chemical structure of macrocycle **181**. (b) Schematic illustration of switching between ground-state charge-transfer (CT) in toluene and complete electron-transfer (ET) in nitrobenzene within the macrocycle **181** as donor and fullerene as acceptor. (b) is reprinted and adapted with permission from ref. [203]. Copyright 2020 American Chemical Society.

The group of Iwasawa designed the significantly smaller difluorobenzothiadiazole-based cyclophane **182** (Figure 15a).[204] These units cause an electron-deficient character of **182**, which assists the encapsulation of electron-rich anthracene (**183**) by charge-transfer interactions as shown by UV–vis absorption spectroscopy. This charge-transfer interaction could be utilized in a supramolecular photocatalyzed [4+2] cycloaddition (Figure 15b). For this purpose, the anthracene⊂**182** complex was excited at its charge-transfer band. The resulting charge-separated singlet state gave after intersystem crossing a triplet-excited anthracene. The latter was released from the host and utilized with a diene (**184**) in a cycloaddition reaction to yield **185**. This reaction mechanism was proposed based on several control experiments as well as triplet-quenching studies and was also applied for anthracene-derivatives and other dienes.

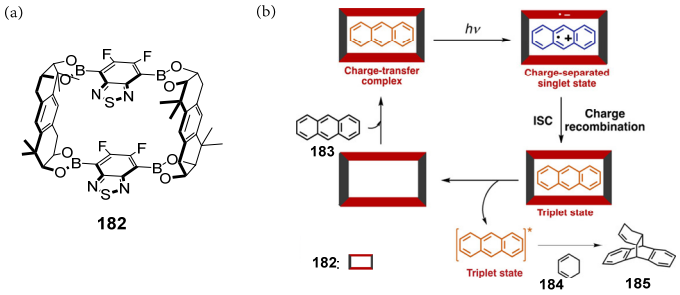

Figure 15. (a) Chemical structure of cyclophane **182**. (b) Proposed catalytic cycle for a [4+2] cycloaddition using cyclophane **182** as catalyst. First, charge-transfer inclusion complex anthracene⊂**182** is formed. Second, photoexcition of charge-transfer complex lead to a charge-separated singlet state, which gave after intersystem crossing (ISC) a triplet-excited anthracene. Release of latter one from the host-cavity yielded after cycloaddition with **184** the desired product **185**. (b) is reprinted and adapted with permission from ref. [204]. Copyright 2020 Wiley-VCH Verlag GmbH & Co. KGaA.

2.3.3. Molecular Containers

While macrocycle and cyclophane hosts have two connecting points at their units to construct their cyclic two-dimensional scaffolds, cage structures are characterized by at least three connecting points to build-up a three-dimensional scaffold.[75, 183, 205] Due to their defined spatial topology, cage structures are often termed as molecular containers. Important and well-known structures among others are cryptands from Lehn,[206] carcerands from Cram[183, 207] and self-assembling and non-covalently bonded capsules from Rebek[208-209] (Figure 16). Such structures typically do not employ pronounced charge-transfer interactions with their guest molecules, and substrate encapsulation is often driven by solvophobic effects, electrostatic effects and/or hydrogen bonds.[71, 183] Another prominent way for the construction of container structures are (self-assembling) coordination cages.[205] Thereby, a broad variety of different architectures, depending on the applied ligands and (transition) metals, can be obtained. This results in three-dimensional, highly stable and rigid structures with large cavities and often with spatial expansion. This allows the encapsulation of larger as well as multiple guests with strong binding. Therefore, the spanned inner hollows of cages are excellent confined reaction spaces for catalyzing reactions.[67, 210] Thus, such hosts are sometimes termed as molecular flasks or nanoreactors.

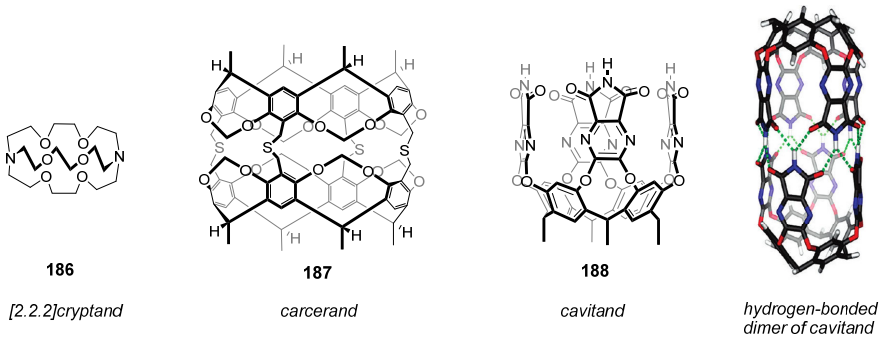

Figure 16. Exemplary structures of a cryptand (**186**), carcerand (**187**) and a cavitand (**188**) with its calculated self-assembled dimer (in the presence of a suitable guest; simplified structure). Calculated structure is reprinted with permission from ref. [208]. Copyright 2009 American Chemical Society.

A prime example is the multifunctional, electron-deficient cage **189** from Fujita *et al.* reported in 1995 (Figure 17a).[75, 211] This cage can be synthesized quantitatively *via* self-assembly of the corresponding starting materials. This molecular container or its derivatives found among others application in molecular recognition,[212] stabilization of reactive/labile guests[213] and in the supramolecular catalysis of various reactions, for instance condensation reactions,[214] oxidation of alkanes[215] or photodimerization of olefins[216] and others.[75] A prominent example is the catalyzed Diels–Alder reaction of anthracene-derivative **191** with maleimide **190** towards selectively non-bridgehead fused product **192** (Figure 17b,d).[217] A recent example is the photo-induced oxidation due to the formation of a charge-transfer complex of cage **189** and the respective substrate (Figure

17c,e).[218] In this context, host **189** and the small organic molecule toluene (**193**) formed in water inclusion complexes, while UV–vis absorption spectroscopy disclosed the contribution of a charge-transfer interaction between the electron-donating toluene and the electron-accepting **189**. Excitation of the resulting charge-transfer complex induced an ultrafast C–H-activation of toluene due to charge separation as tracked by femtosecond transient absorption spectroscopy. Subsequent proton transfer and oxidation with molecular oxygen yielded the product benzaldehyde (**101**). Finally, exchange of product with a new substrate (toluene) reoccurred the catalytic cycle. Additional studies revealed the impact of substituents at **193** and explored other possible substrates like methylated naphthalene.

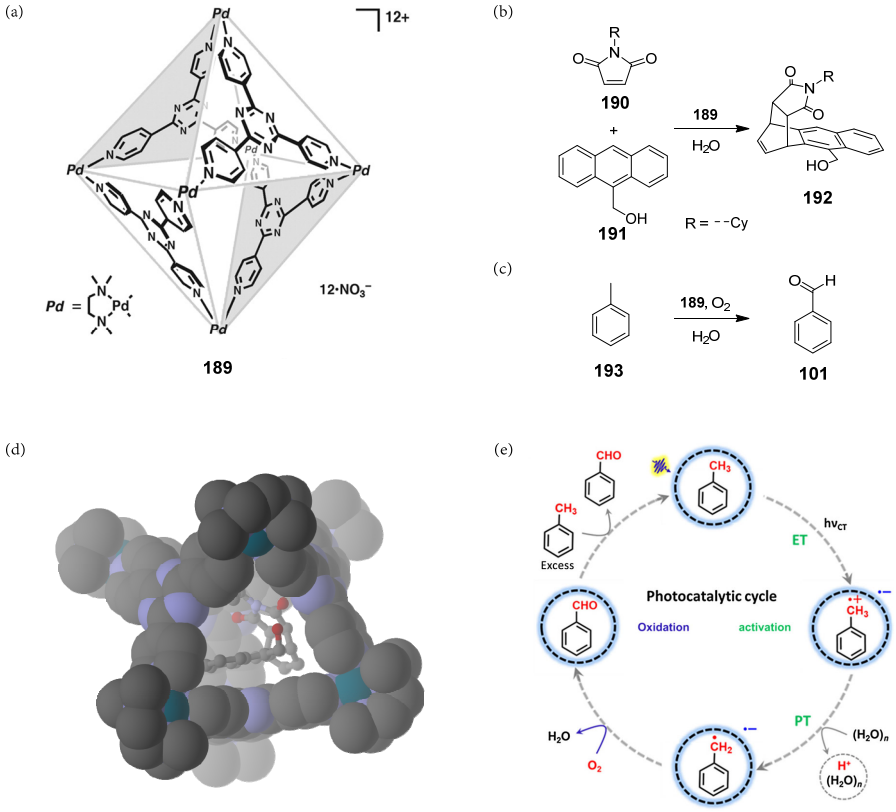

Figure 17. (a) Chemical structure of cage **189**. (b) Diels–Alder[217] and (c) photooxidation[218] reaction catalyzed by cage **189**. (d) Solid-state structure of inclusion complex **192⊂189** (generated from CCDC deposition number: 293777; counterions omitted for clarity). (e) Proposed reaction cycle of photocatalytic oxidation of toluene to benzaldehyde by cage **189** (blue circle). First, photoexcitation of charge-transfer complex caused an electron-transfer (ET) and subsequent proton-transfer (PT). Oxidation to product benzaldehyde and displacement with new substrate restored the catalytic cycle. (a) is reprinted and adapted with permission from ref. [217]. Copyright 2006 American Association for the Advancement of Science. (e) is reprinted with permission from ref. [218]. Copyright 2019 The Authors. Published by American Association for the Advancement of Science.

Stoddart's group reported not only the two-dimensional extension of their *Blue Box* (**176**), but also the expansion in three-dimensions to obtain cage structures.[185] One example is the D_3-symmetric *para*-xylylene linked **194** (Figure 18a).[219] Similar to the viologene-based cyclophanes,[185] cage **194** has a strong electron-accepting character, however, is less electron-deficient than cyclophane

host **177**.[193] This fact was attributed to the *meta*- (**194**) and not *para*-substitution (**177**) of the central benzene ring with pyridinium units. The cavity of **194** could be utilized for the complexation of various (electron-rich) PAHs (Figure 18b), while the contribution of donor–acceptor interactions could be disclosed by UV–vis absorption spectroscopy with charge-transfer bands. This was supported by X-ray crystallographic analysis of the inclusion complexes, where the electron-rich guests arrange close to the electron-deficient moieties (pyridinium subunits) of host **194**. The estimated binding constants for the PAH guests with **194** are in all cases higher than those of cyclophane host **177**, which can be attributed to the macro-bicyclic effect of host **194** (Figure 18c). Kinetic studies revealed fast complexation of smaller guests (like pyrene), while larger guests (like coronene) showed slower binding due to a larger complexation barrier caused by steric effects. However, high decomplexation barriers for larger guests led to highly stable host–guest complexes.

The same group reported cage **195** with triazine units at the core-position of the two triangular panels (Figure 18a).[220] In comparison to cage **194**, host **195** showed as expected a more pronounced electron-deficient character, which was anticipated to facilitate stronger binding with electron-rich guests. However, a decrease in binding strength with the tested guest, pyrene, was observed. This was attributed to the competing inclusion of the counterion *via* anion–π-interactions with the triazine units as revealed by crystallographic analysis.

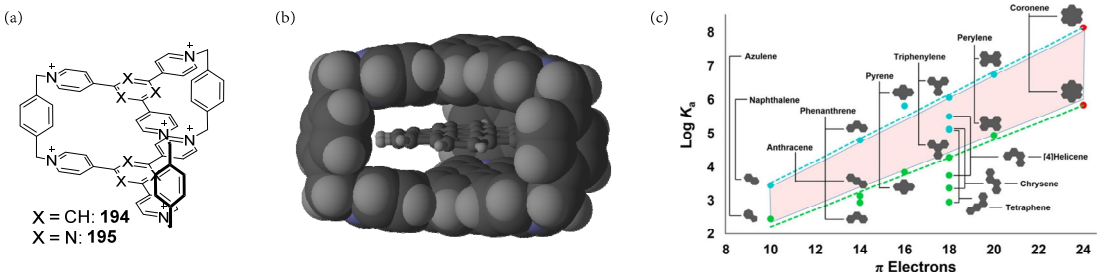

Figure 18. (a) Chemical structures of cages **194** and **195** (counterions are not depicted). (b) Solid-state structure of inclusion complex coronene⊂**194** (generated from CCDC deposition number: 988443; counterions omitted for clarity). (c) Correlation of binding constants (as log K_a) and number of π-electrons of various PAHs with cyclophane host **177** (dotted green line) and cage host **194** (dotted blue line). (c) is reprinted with permission from ref. [185]. Copyright 2016 American Chemical Society.

Cao and coworkers reported the D_{2h}-symmertic cage **196**, which has in comparison to **194**/**195** four instead of three *para*-xylylene linkers (Figure 19a).[221] The electron-deficient cage **196** could not only encapsulate PAHs (Figure 19c) in organic solvents, but also the electron-rich fluorescence dye SR101 (Figure 19b). In the latter case, involvement of charge-transfer interactions between host and guest are evidenced by a charge-transfer band in the UV–vis absorption spectrum of **196** upon titration with guest SR101. On the contrary, a typically fluorescence quenching due to the formation of a charge-transfer complex was not observed, instead, stronger as well as purer emission with prolonged fluorescence lifetime and an increased excitation–emission gap was obtained. This unusual emission properties were accounted to the formation of the inclusion complex, which

avoided fluorescence self-quenching and increased rigidity in the excited state. Furthermore, the enhanced offset between excitation and emission was attributed to the charge-transfer interactions. A comparable cage structure was reported at the same time by Stoddart's group, which showed a fluorescence turn-on of an encapsulated PBI dye.[222]

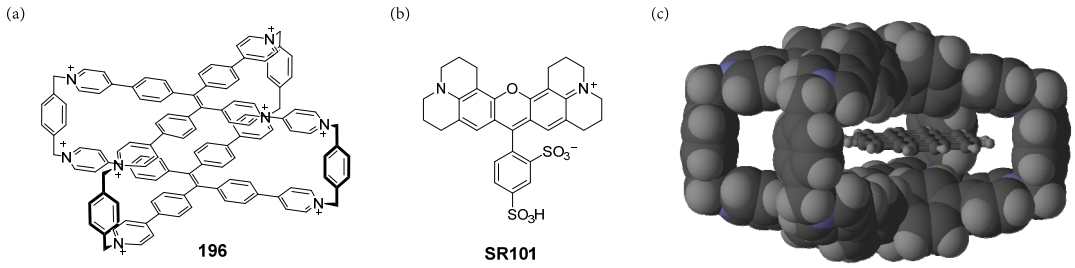

Figure 19. (a) Chemical structure of cage **196** (counterions are not depicted). (b) Chemical structure of fluorescence dye SR101. (c) Solid-state structure of inclusion complex coronene⊂**196** (generated from CCDC deposition number: 1923331; counterions are omitted for clarity).

Zhao *et al.* devised the three triangular prismatic hosts **197**–**199** (Figure 20a–b).[223] The cages assemble from six cobalt ions and three tridendate ligands and form a hydrophobic cavity for the uptake of guest molecules. In this regard, the inclusion of a quinhydrone cofactor in **197** caused the emergence of a charge-transfer band in the absorption spectrum and the ITC experiment provide high association constants (>10^5 M^{-1}, H_3CCN, 298 K).

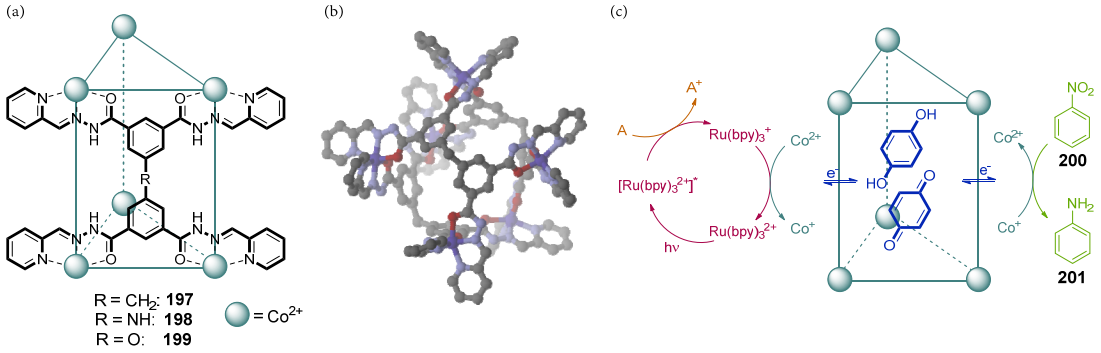

Figure 20. (a) Structure of hosts **197**–**199**. (b) Solid-state structure of **197** (generated from CCDC deposition number: 1558243, hydrogens and counterions are omitted for clarity). (c) Schematic tandem catalytic cycle for the hydrogenation of nitrobenzene (**200**). First, photoredox active $Ru(bpy)_3^{2+}$ is excited and reduced with an sacrificial electron donor (A: ascorbic acid). The following reduction of Co^{2+} due to efficient electron transfer by the encapsulated quinhydrone cofactor could be utilized in the reduction of **200**. (c) is reprinted and adapted with permission from ref. [223]. Copyright 2020 Wiley-VCH Verlag GmbH & Co. KGaA.

The combination of the charge-transfer complex with the photoredox catalyst $Ru(bpy)_3^{2+/+}$ was utilized in the generation of hydrogen, where the encapsulated cofactor acted as proton source (Figure 20c). A control experiment without the cofactor was ten times less efficient and disclosed the efficient electron transfer due to the encapsulated quinhydrone cofacator. The devised catalytic cascade system could be directly used in the reduction of nitrobenzene (**200**) to aniline (**201**) with

high turnover numbers (340000 per mol catalyst) at mild conditions. The isostructural cages **198** and **199** showed weaker binding affinity towards the quinhydrone cofactor and resulted in a decreased hydrogen evolution compared to **197**. Therefore, the formation of the strong charge-transfer complex was a prerequisite for the efficient generation of hydrogen and the designed system represents a step towards artificial photosynthetic catalysis.[224-225]

2.3.4. Nanohoops

In contrast to cyclophanes, macrocycles and molecular containers, carbon nanohoops represent in the context of host structures a newer but aspiring scaffold.[76, 226] This is a consequence of their challenging synthesis, which still limits the available scaffolds. Such nanohoops are strained cyclic structures typically consisting of sp- and sp^2-hybridized carbon atoms and often contain acetylene units and/or phenylene-rings. The most prominent examples are cyclo-*para*-phenyleneacetylenes ([CPPA]) and cyclo-*para*-phenylenes ([CPP]) (Figure 21). The high strain energy in nanohoops spans a stable shape-persistent, cyclic cavity for the encapsulation of guest molecules. Due to their cyclic structure, they are well established for the complexation of spherical guests like fullerenes[226] *via* π–π-interactions or planar[227] and bowl-shaped[228] guests *via* C–H interactions. However, the explicit involvement of charge-transfer interaction in the complexation event is rather rare.[229-230] Related names of nanohoops are nanorings or nanobelts, which often refer to the degree of the longitudinal extension of the respective nanohoops. Thereby, the term nanoring is commonly used for linked arene systems, while nanobelts is used for fused arene systems (Figure 21). Other (frequently) used terms are (nano)disks, loops, tires or barrels.[76, 226]

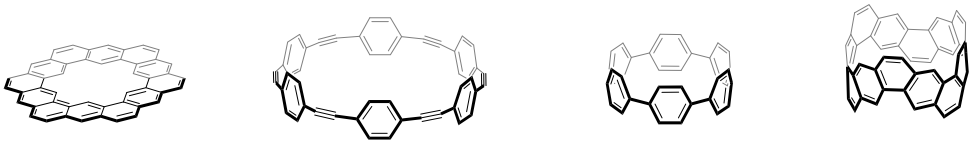

202 *[12]circulene* *"Kekulene", nanoring*

203 *[6]cyclo-para-phenylene-acetylene* *[CPPA]*

204 *[6]cyclo-para-phenylene* *[CPP]*

205 *nanobelt,* fragment of (6,6)cabonanotube

Figure 21. Chemical structures of different nanohoops. All nanohoops **202**,[231] **203**,[232] **204**[233] and **205**[234] are synthetic accessible.

In the context of nanohoops as host structures, the group of von Delius devised the cyclo-*para*-phenylene based host **206** (Figure 22a).[235] The structure contains two opposing nickel porphyrin units, which strongly alter the optoelectronic properties of the resulting nanohoop due to the exert of strain energy onto the porphyrin moieties. Nanohoop **206** revealed strong complexation capabilities for C_{60}- and C_{70}-fullerenes with binding constants $>10^7$ M^{-1} (toluene, 298 K) for 1:1 inclusion complexes (Figure 22b). UV–vis absorption spectroscopy showed the emergence of

charge-transfer bands upon addition of fullerene guests. The involvement of a charge-transfer interaction in the complex formation between electron-rich host and electron-deficient guest was further indicated by DFT calculations, which showed a location of the frontier orbitals on the respective complexation partner (Figure 22c). The obtained association parameters for fullerenes are about 100-fold higher compared to those of [10]CPP, which is similar in size to **206** but without the two porphyrin panels. Furthermore, π-extended nanohoop **207** offered a five-times higher binding affinity for C_{70}, however, no improvement for C_{60}. This unexpected result for C_{60} could be attributed to an additional deformation of the ring caused by the π-extension, which cancels the increased binding strength due to the increased π-contact area. In the case of C_{70}⊂**207** the enlarged van der Waals surface of C_{70} predominated and led to stronger binding.

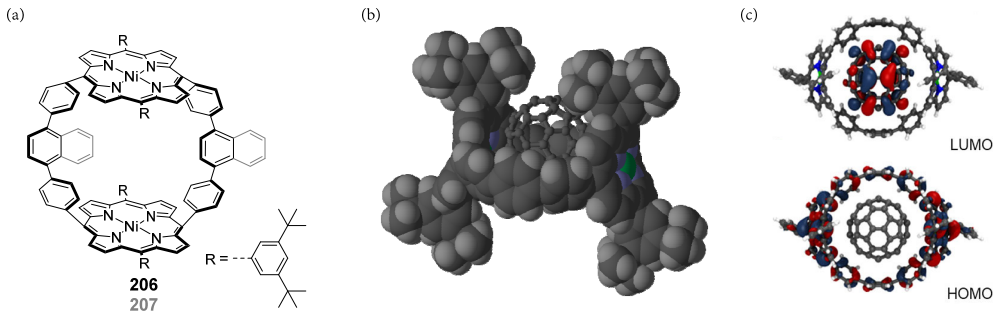

Figure 22. (a) Chemical structures of nanohoops **206** and **207**. (b) Solid-state structure of inclusion complex C_{60}⊂**206** (generated from CCDC deposition number: 1909920). (c) Representation of the calculated frontier orbitals from inclusion complex C_{60}⊂**206**. (c) is reprinted and adapted with permission from ref. [235]. Copyright 2019 American Chemical Society.

Nuckolls and coworkers reported another dye-based nanohoop (**208**), yet with an electron-accepting PBI chromophore (Figure 23a–b).[236-237] Furthermore, bithiophene donor moieties were incorporated into the scaffold to obtain a radial and alternating donor–acceptor arrangement. Hereby, not only an intramolecular charge-transfer but also at room-temperature interconverting diastereomers could be observed. More interestingly, **208** could be utilized in the complexation of fullerene-adduct $PC_{61}BM$ (Figure 23c).[238] Among others, a electrochemical titration experiment gained insights into the host–guest complexation. Thereby, a strong charge-transfer interaction between the donor moieties of **208** and $PC_{61}BM$ could be revealed by anodic shifts of the oxidation potentials of the thiophene units and cathodic shifts of the reduction potentials of the acceptor guest $PC_{61}BM$. The evidenced intermolecular electronic communication within the supramolecular assembly $PC_{61}BM$⊂**208** could be utilized in organic field-effect transistors. A more than five-fold enhancement in electron mobility of complex $PC_{61}BM$⊂**208** compared to parent **208** could be observed, which was attributed to the strong electronic interaction between guest and host.

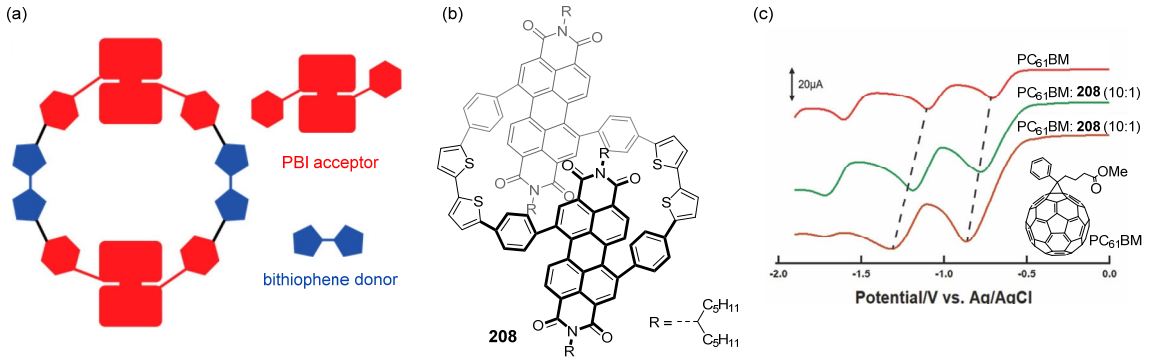

Figure 23. (a) Design strategy for the donor–acceptor nanohoop **208** by the group of Nuckolls. (b) Chemical structure of **208** (only the *meso*-form is depicted). (c) Traces of electrochemical titration experiment of **208** and $PC_{61}BM$ highlighting the cathodic shift of the $PC_{61}BM$ reduction potentials. (a) is reprinted and adapted with permission from ref. [236]. Copyright 2015 American Chemical Society. (c) is reprinted and adapted with permission from ref. [238]. Copyright 2020 Wiley-VCH Verlag GmbH & Co. KGaA.

In contrast to dye containing nanohoops **206**–**208**,[235-236, 238] the group of Stępień reported the hybrid nanohoop host **209** (Figure 24a).[239] Thereby, a calix[4]arene, itself a well-known host-structure,[189, 240] is incorporated in a cyclo-*para*-phenylene scaffold to give **209**. The obtained nanohoop could be utilized as a solid-state receptor for the adsorption of various vapors and gases. More interestingly, the electron-rich scaffold was capable in the complexation of electron-deficient guest molecules (**210**–**213**) in solution (Figure 24b). Not only the partial quenching of the emission of **209** upon titration with guests, but also the emergence of a bathochromically shifted band (observed in solution or solid-state) could be observed. These findings were attributed to charge-transfer interactions, which were further substantiated with the help of DFT calculations (Figure 24c). Correspondingly, the frontier orbitals were either located on the electron-deficient guest (LUMO) or the electron-rich host (HOMO) and the observed charge-transfer character could be confirmed by calculated charge-transfer transitions.

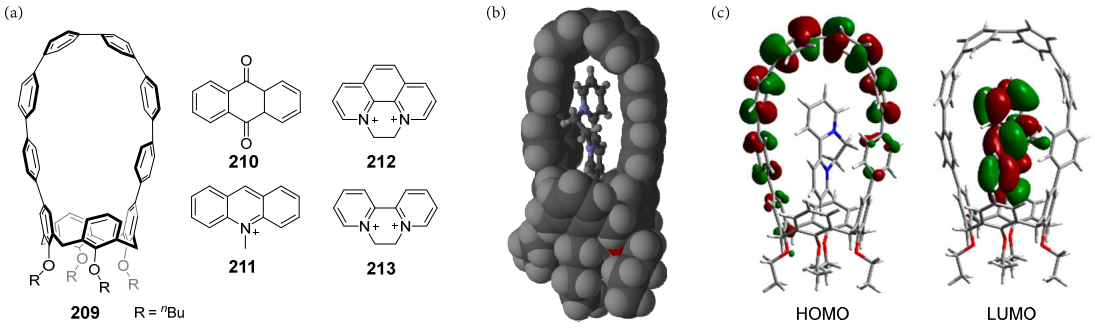

Figure 24. (a) Chemical structure of host **209** and the guests **210**–**213** (counterions are not depicted). (b) Solid-state structure of inclusion complex **213**⊂**209** (generated from CCDC deposition number: 2016791; counterions omitted for clarity). (c) Representation of the frontier orbitals from **213**⊂**209**. (c) is reprinted and adapted with permission from ref. [239]. Copyright 2020 American Chemical Society.

Gaeta and coworkers reported also a composite host from a cyclo-*para*-phenylene and a calix[4]arene, however, both were bridged *via* etherification with the hydroxyl groups at the lower rim of the calixarene.[241] The resulting nanohoop was used for the recognition of cations.

2.3.5. Tweezers and Clips

Molecular tweezers and clips have in contrast to cyclophanes principally only one bridging unit between two (aromatic) panels/pincers.[73-74, 242] Therefore, suitable guests can easily enter the constructed cavity, however, the rather open system often affords only weak binding due to smaller contact surfaces. The employed spacer units range from flexible to rigid. While latter one prevent intramolecular (self-)aggregation and offers a preorganization of the two panels. More pliable spacers can lead to a better substrate encapsulation as well as a better adaptability towards different guest topographies.[73-74] Typically, (concave–convex) π–π, C–H and/or hydrogen bond interactions are mainly contributing to the complex formation with tweezers and clips as host structures, while charge-transfer interactions often play a subordinate role.[243-244] Klärner and Kahlert defined the difference between a tweezer and clip depending on the nature of the pincers.[73-74] Following this definition, curved or bended pincers correspond to tweezers, while more straight arms lead to molecular clips (Figure 25). The transition from tweezers to clips is smooth, not strict and both are often used as synonyms, although, the term tweezer is more widespread. Another rarely used term is (molecular) cleft.[73-74]

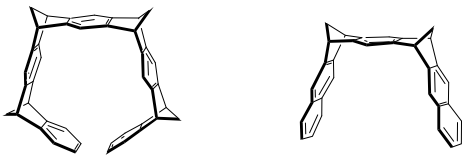

214 *tweezer* **215** *clip*

Figure 25. Comparison of a molecular tweezer (**214**) and clip (**215**) defined by Klärner and Kahlert.[73]

Fullerenes are frequently applied target-substrates for molecular tweezers due to their good shape complementary, which results in an enormous number of different reports on new fullerene hosts with various (outstanding) characteristics,[242-243, 245] for instance high binding strength[246-247] or selectivity on distinct fullerene substrates.[248-249] For such purposes, well-applied strategies are the use of pincer arms with curved scaffolds[243, 250] to facilitate concave–convex π–π-interactions and/or with a pronounced electron-donating character[251-252], which can support the complexation with additional charge-transfer interactions.

In the context of fullerene recognition, the group of Shinokubo reported the synthesis of the nitrogen containing bowl **216** (Figure 26a).[253] The Nozaki group independently reported a similar structure

at the same time.[254] However, only Shinokubo groups showed the complexation with C_{60} in solution and the solid-state (Figure 26b), while supportive charge-transfer interactions could be revealed. This finding is a result of the increased electron-donating character of **216** through the nitrogen-embedding and the strong electron-accepting character of C_{60}. Furthermore, the same group used the aza-bowl for the construction of buckybowl tweezers **217** and **218** (Figure 26c).[249] Both receptors exhibited extremely strong binding to C_{60} and C_{70} with binding constants up to 10^8 M^{-1} (toluene). Optical absorption and fluorescence as well as electrochemical titration experiments disclosed a strong intermolecular charge-transfer interaction due to the formation of a charge-transfer band, emission quenching and shift of respective redox potentials from host and guest. Further prove of through-space charge-transfer interaction was obtained by DFT calculations. These observations could be again rationalized by the pronounced electron-donating character of the hosts due to the incorporation of nitrogen-atoms into the scaffold of the bowl-shaped pincers. Furthermore, a preference for the encapsulation of C_{60} over C_{70} for tweezer **218** and *vice versa* for **217** could be disclosed.

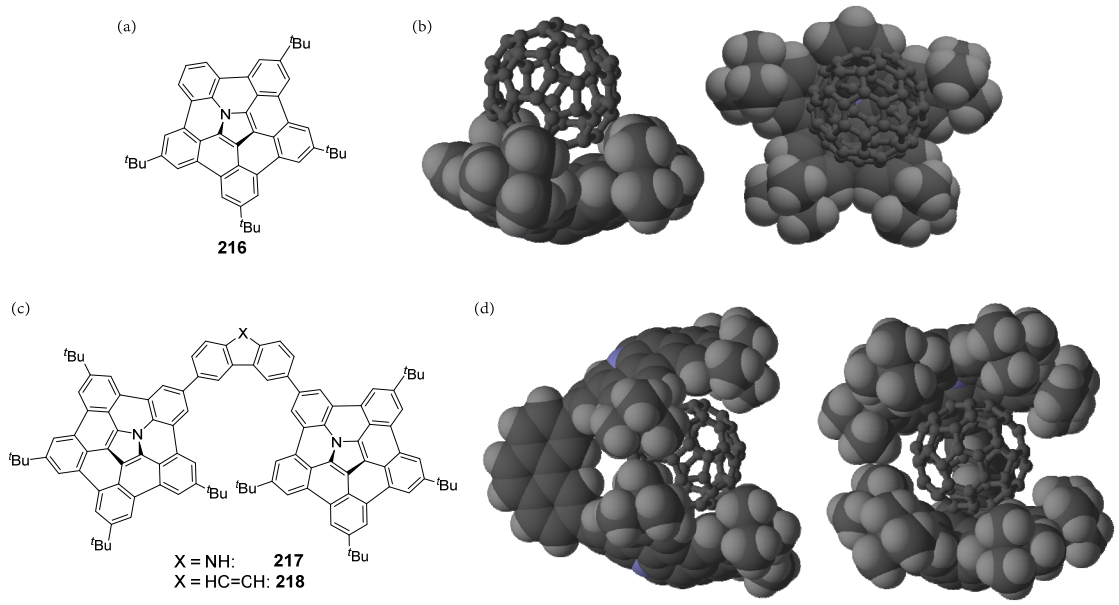

Figure 26. (a,c) Chemical structures of aza-bowl **216** and tweezers **217** and **218**. (b,d) Solid-state structure of inclusion complexes C_{60}⊂**216** (generated from CCDC deposition number: 1406873) and C_{60}⊂**218** (generated from CCDC deposition number: 1554383).

Thakur *et al.* devised with the structures **219**–**221** tweezers with a significantly smaller cavity (Figure 27a).[255] Instead of bowl-shaped pincer-arms, planar PAHs are linked to a modified terphenyl-spacer unit to create a suitable cavity for guest encapsulation. The calculated distance between the two aromatic pincers is with ~7 Å ideal for small planar substrates. UV–vis absorption spectroscopy titration experiments with highly electron-deficient guest 2,3-dichloro-5,6-dicyano-1,4-benzochinone (DDQ) revealed an efficient formation of inclusion complexes, which could be confirmed by crystallographic analysis (Figure 27b). Furthermore, the emergence of a charge-

transfer band disclosed the involvement of intermolecular donor–acceptor interactions. The obtained binding strength for tweezers **219**–**221** could be directly related to the donor-strength of the corresponding aromatic linkers. Thereby, a stronger donor (pyrene > naphthalene > benzene) led to higher association constants. However, in the investigated cases the donor strength correlates also with the surface area, which typically also influences the binding strength.

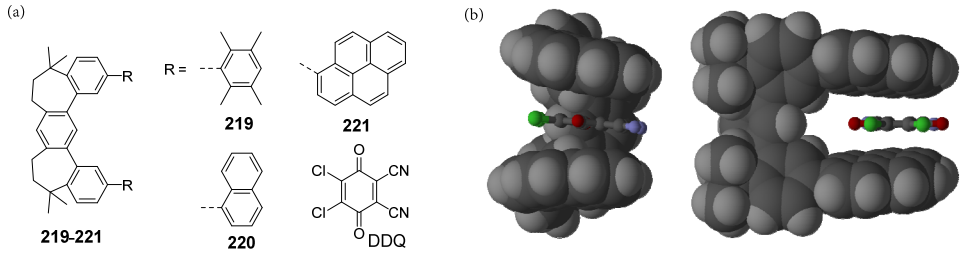

Figure 27. (a) Chemical structures of tweezers **219**–**221** and guest DDQ. (b) Solid-state structure of inclusion complex DDQ⊂**221** (generated from CCDC deposition number: 1836164).

Chapter 3

Tetrachlorinated Polycyclic Aromatic Dicarboximides: New Electron-Poor π-Scaffolds and NIR Emitters by Palladium-Catalyzed Annulation Reaction

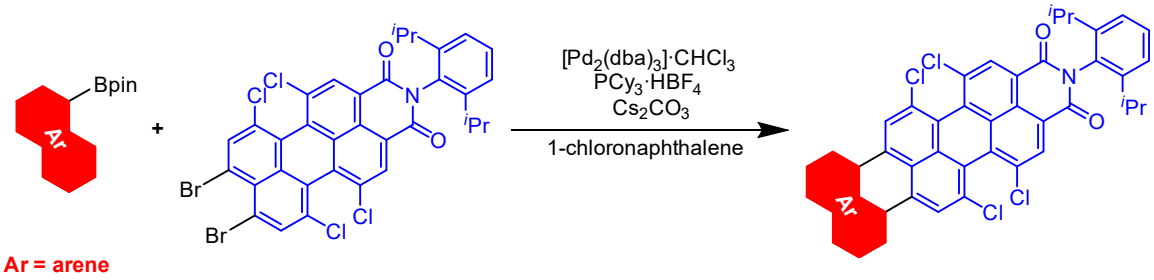

This chapter and the corresponding supporting information (*10.1. Supporting Information Chapter 3*) has been published:

M. Mahl, K. Shoyama, J. Rühe, V. Grande, F. Würthner, *Chem. Eur. J.* **2018**, *24*, 9409–9416.

Abstract:[i] Herein we report a palladium-catalyzed annulation reaction consisting of a Suzuki–Miyaura cross-coupling and a C−H arylation cascade for the synthesis of tetrachlorinated polycyclic aromatic dicarboximides (PADIs). This convergent synthetic route afforded a broad series of hitherto unknown electron-deficient PADIs under optimized reaction conditions by coupling of a dibromo-tetrachloro-perylene dicarboximide with different polycyclic aromatic hydrocarbon

[i] Synthesis using other reaction conditions and properties of compound **224d** have been described in: J. Rühe, Bachelor Thesis, Julius-Maximilians-Universität Würzburg, **2017**.

(PAH) boronic acid pinacol esters in up to 89 % yields. The new PADI compounds show broad absorption in the visible range and some of them emit in the near-infrared (NIR) region. Cyclic and square wave voltammetric studies revealed that these tetrachlorinated PADIs are more electron-deficient than a non-chlorinated reference compound and they possess lower lying frontier orbitals. Thus, the newly synthesized electron-poor PADIs are potential n-type semiconductors. Moreover, these chlorinated PADIs are interesting building blocks for the construction of large π-extended arrays by metal-mediated coupling reactions.

3.1. Introduction

The chemistry of polycyclic aromatic hydrocarbons (PAHs) and nanographenes is an increasingly growing research field due to their unique properties, such as broad absorption and emission in the visible range, adjustable frontier orbitals, rigid structure, and high thermal and mechanic stability, which enable their various applications in materials science.[78, 80, 257-264] An important aspect in regard to the synthesis of PAHs and nanographenes is the introduction of electron-withdrawing functionalities to fine-tune their desired optical and electronic properties and to increase the photochemical stability. For example, whilst perylene and other PAHs are prone to photooxidation, the respective dicarboximides afford color pigments and fluorescent dyes of outstanding stability.[1, 15, 82] The synthesis of electron-deficient PAHs bearing electron-withdrawing dicarboximide functionalities has been, however, accomplished mainly by tedious sequential multi-step reactions.[55, 91, 114, 117, 265-269] Only recently, we have introduced a convergent synthetic route to polycyclic aromatic dicarboximides (PADIs) based on palladium (Pd)-catalyzed C−C coupling cascade reaction.[53, 58-59, 270] One extensively investigated class of small PADIs is perylene dicarboximides,[29] and their higher rylene homologues.[19-20] Rylene dicarboximides have been shown to be highly promising as n-type semiconductors for application in various (opto)electronic devices,[271-274] and their core-halogenated derivatives are versatile building blocks for the synthesis of oligomeric and hybrid rylenes with interesting electronic properties.[20-21, 103, 105, 275]

We have recently reported that Pd-catalyzed annulation of naphthalene dicarboximide moieties to planar and bowl-shaped PAH substrates involving a Suzuki–Miyaura cross-coupling and C−H arylation cascade reaction afforded various PADIs,[53, 58-59, 270] including a novel C_{64} nanographene.[58] This approach has also been successfully applied for the synthesis of terrylene dicarboximides and esters, the latter compounds have been subsequently converted to dicarboximides by conventional imidization reaction.[276] Very recently, we have shown that under optimized reaction conditions this method can be applied for the synthesis of heteroatom-doped PADIs.[277] Encouraged by our recent results, we wanted to explore further scope of this Pd-catalyzed convergent method for the synthesis of more electron-poor PADIs and thought that annulation of core-chlorinated perylene dicarboximides, which have not been used in this reaction before, to polycyclic aromatic substrates would lead to a new type of electron-deficient PADIs with significantly enlarged π-scaffolds. Here we report, indeed, under optimized reaction conditions Pd-catalyzed C−C coupling cascade reaction of dibromo-tetrachloro-perylene dicarboximide **223** with different polycyclic aromatic boron esters **222a**–**g** afforded a broad series of tetrachlorinated PADIs **224a**–**g** (Table 2), emphasizing on the general scope of this method for the synthesis of PADIs. The new compounds exhibit strong absorption in the visible range and some of them show emission in the near-infrared (NIR) region. Cyclic and square wave voltammetry confirmed the desired electron-poor character of the PADIs.

3.2. Results and Discussion

3.2.1. Synthesis

We have first investigated the Pd-catalyzed C–C coupling reaction of dibromo-functionalized tetrachloro-perylene dicarboximide **223** with naphthalene boronic acid pinacol ester **222a** as a model substrate towards ring-annulated PADI **224a** to optimize the reaction conditions (Table 1). Our initial attempts using previously reported annulation conditions gave the product **224a** only in 2% isolated yield (entry 1).[270] Screening of reaction conditions revealed that the annulation reaction proceeded effectively in 1-chloronaphthalene as solvent with $[Pd_2(dba)_3]\cdot CHCl_3$ as Pd^0 source, $PCy_3\cdot HBF_4$ as ligand, and Cs_2CO_3 as base with a substrate concentration of 0.01 M at 160 °C for 20 h to afford the annulated product **224a** in a high yield of 78% (entry 6).

Table 1. Optimization of Pd-catalyzed annulation reaction for the synthesis of **224a** as a model compound.[a]

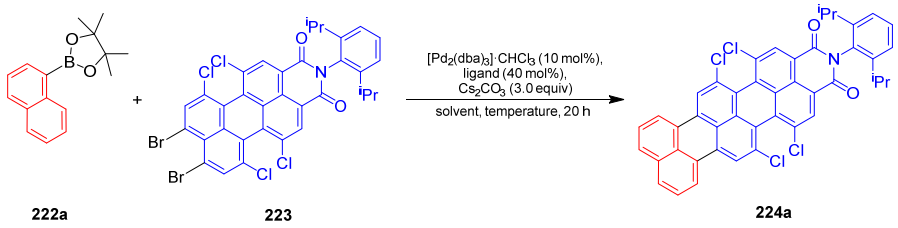

222a **223** **224a**

entry	solvent	ligand	*c* / M	*T* / °C	yield / %[b]
1	*o*-DCB	P(*o*-tolyl)$_3$	0.03	160	2
2	1-chlnaph	P(*o*-tolyl)$_3$	0.03	160	14
3	1-chlnaph	SPhos	0.03	160	12
4	1-chlnaph	$PCy_3\cdot HBF_4$	0.03	160	67
5	1-chlnaph	$PCy_3\cdot HBF_4$	0.1	160	22
6	1-chlnaph	$PCy_3\cdot HBF_4$	0.01	160	78
7	1-chlnaph	$PCy_3\cdot HBF_4$	0.01	120	5
8	1-chlnaph	$PCy_3\cdot HBF_4$	0.01	200	19

[a]Reaction conditions: **222a** (1.0 equiv), **223** (1.1 equiv), $[Pd_2(dba)_3]\cdot CHCl_3$ (10 mol%), ligand (40 mol%), Cs_2CO_3 (3.0 equiv). [b]Isolated yield. *o*-DCB: *o*-dichlorobenzene, 1-chlnaph: 1-chloronaphthalene, P(*o*-tolyl): tri(*o*-tolyl)phosphine, SPhos: 2-dicyclohexylphosphino-2′,6′-dimethoxybiphenyl, PCy_3: tri(cyclohexyl)phosphine, dba: dibenzylideneacetone.

We have examined several key parameters of this reaction that are summarized in Table 1. Solvent plays a key role in this annulation reaction. A seven-fold increase (from 2 to 14 %) in yield was observed when 1-chloronaphthalene, instead of *o*-dichlorobenzene, was used as a solvent (entries 1 and 2). After optimization of phosphine ligand, the yield could be improved to 67% using

$PCy_3 \cdot HBF_4$ as a ligand (entries 2–4). Screening reactions have also revealed that the concentration has a crucial effect on the reaction outcome since higher concentrations led to more two-fold Suzuki–Miyaura cross-coupling side product, while under dilution the intramolecular direct C–H arylation was promoted and the second intermolecular Suzuki–Miyaura cross-coupling was suppressed (entries 4–6). Noteworthy, this competing reaction has already been a problem in our previous work.[270] When the substrate concentration was increased form 0.03 M to 0.1 M the yield of **224a** was drastically decreased from 67% to 22% (entries 4 and 5). A lower concentration of 0.01 M afforded so far the best yield of 78% (entry 6). Variation of the reaction temperature from 160 °C did not improve the product yield. At a lower temperature of 120 °C the yield was dramatically decreased from 78% to 5% (entry 7), while a higher temperature of 200 °C led to a yield of 19% (entry 8). The use of $[Pd(dba)_2]$, instead of $[Pd_2(dba)_3] \cdot CHCl_3$, as Pd^0 source or Pd^{II} catalysts $[Pd(OAc)_2]$ and $[PdCl_2(MeCN)_2]$ did not improve the reaction (Table A1, *10.1. Supporting Information Chapter 3*). Moreover, other bases than Cs_2CO_3 like KO^{t}Bu or K_2CO_3 either did not lead to a conversion or gave the product **224a** in lower yields (Table A1). In any conducted reaction the potential C–C cross-coupling side reaction of substrate **222a** with the chlorine substituents of **223** was not observed, underlining the high tolerance of this Pd-catalyzed C–C coupling reaction for chlorinated coupling components. Such selectivity of bromo over chloro halides in Suzuki–Miyaura cross-coupling reactions is generally known.[278]

By using the optimized reaction conditions (Table 1, entry 6), we have then explored the substrate scope of this method. A broad variety of polycyclic aromatic boronic esters **222a**–**g** could be coupled with dibromo-tetrachloro-perylene dicarboximide **223** to afford the PADIs **224a**–**g** (Table 2). For example, the reaction of anthracene, phenanthrene and pyrene boronic pinacol esters **222b**, **222c** and **222d** with **223** gave the corresponding annulated products **224b**, **224c** and **224d** in 66, 89 and 80% yield, respectively. Noteworthy that the use of the regioisomeric anthracene boronic pinacol ester **222b′** led to a drastic decrease in yield (29%) of **224b**. This observation is in accordance with our previously proposed mechanistic rationale for the annulation reaction of naphthalene dicarboximides with different PAH derivatives, where we assume that the direct C−H arylation, which follows the Suzuki–Miyaura cross-coupling in this cascade reaction, proceeds through a Heck-type mechanism and thus prefers C−C bonds with a pronounced olefinic character.[53, 277] Accordingly, the difference in the yields of **224b** for the regioisomers **222b** and **222b′** are reflected by the aromaticity/bond order in anthracene as in regioisomer **222b** the C–H arylation takes place at 1-position with higher bond order, while in **222b′** at 9-position having a lower bond order.[277, 279]

Table 2. Substrate scope of palladium-catalyzed annulation reaction for the synthesis of tetrachlorinated polycyclic aromatic dicarboximides.[a]

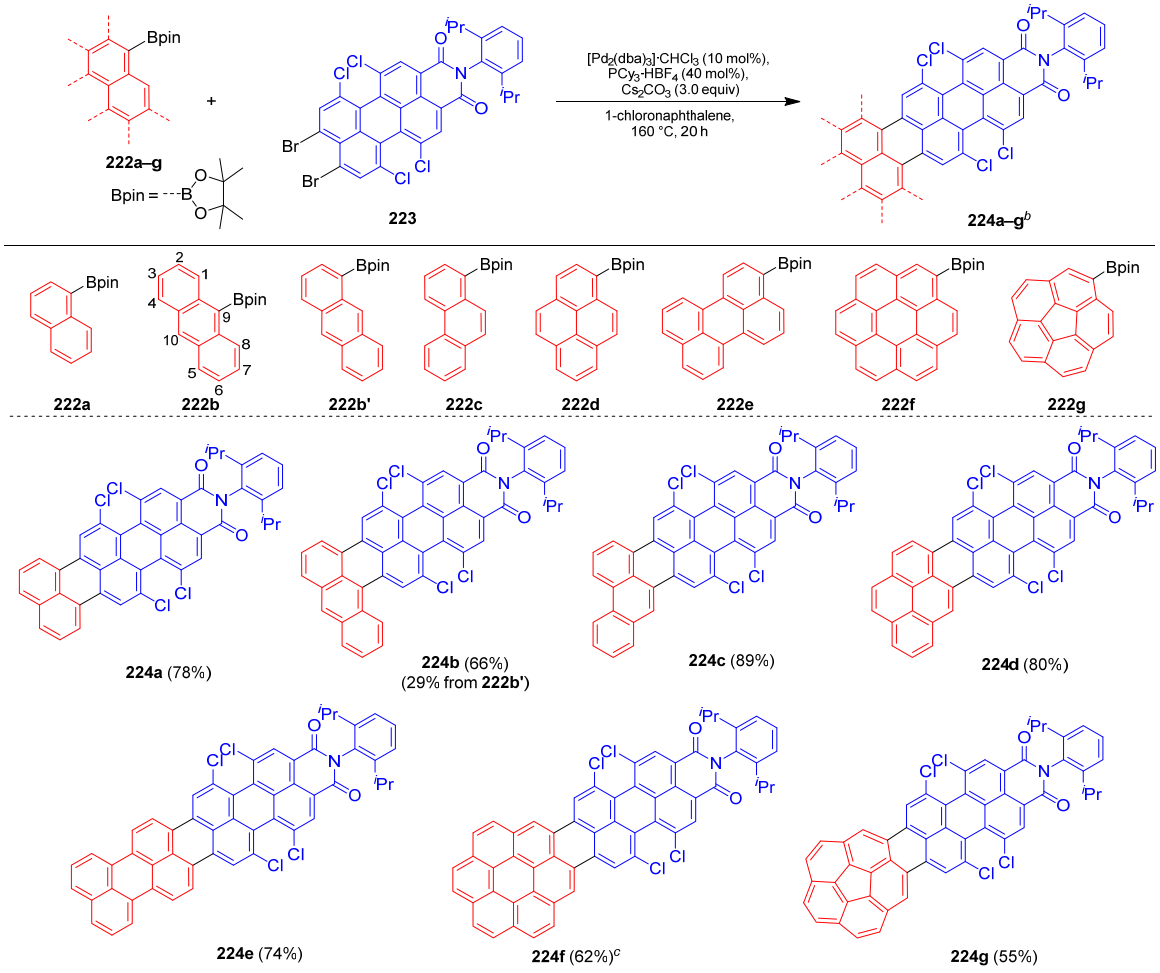

[a]Reaction conditions: boronic acid pinacol ester **222a–g** (1.0 equiv), **223** (1.1 equiv), $[Pd_2(dba)_3]\cdot CHCl_3$ (10 mol%), $PCy_3\cdot HBF_4$ (40 mol%), Cs_2CO_3 (3.0 equiv), *c*(**222a–g**) = 0.01 M, 160 °C, 20 h; PCy_3: tri(cyclohexyl)phosphine, dba: dibenzylideneacetone. [b]Isolated yields are indicated under the respective structure. [c]Reaction temperature: 200 °C.

Larger π-extended tetrachlorinated PADIs were also obtained by this Pd-catalyzed C–C coupling cascade reaction. For instance, perylene boronic ester **222e** afforded the quaterrylene dicarboximide derivative **224e** in 74% yield while coronene boronic ester **222f** gave the corresponding annulated product **224f** in 62% yield, however, a higher reaction temperature (200 °C) was required for the latter substrate due to low solubility. More appreciably, this synthetic approach could also be applied to bowl-shaped corannulene **222g** to give **224g** in 55% yield. These results demonstrate a broad substrate scope of this synthetic strategy. The newly synthesized PADIs were properly characterized by ^{1}H and ^{13}C NMR spectroscopy and high-resolution mass spectrometry. The detailed synthetic procedures and characterization data of the compounds are presented in the

Experimental Section[ii] and the NMR and MS spectra are shown in the *10.1. Supporting Information Chapter 3*.

3.2.2. Optical Properties

The optical properties of tetrachlorinated PADIs **224a–g** were investigated by UV–vis absorption and fluorescence spectroscopy in dichloromethane solutions at room temperature (Figure 28, Table 3). These PADIs show strong absorbance in the visible range with high molar extinction coefficients. The absorption spectra of these compounds do not possess any vibronic fine structure and are dominated by a broad S_0–S_1 transition band with maxima located between 614 nm (ε = 50400 $M^{-1}cm^{-1}$) for **224g** and 736 nm (ε = 73100 $M^{-1}cm^{-1}$) for **224e** (Figure 28a). The absorption maximum of the tetrachlorinated PADI **224a** is slightly bathochromically shifted to 623 nm compared with that of its non-chlorinated analogoue terrylene dicarboximide (**TMI**, 617 nm), whereas the absorptivity is decreased (**TMI**: ε = 54700 $M^{-1}cm^{-1}$, **224a**: ε = 48500 $M^{-1}cm^{-1}$). The absorption maximum of the perylene annulated PADI **224e** is 113 nm redshifted with significantly increased molar absorbance (**224e**: ε = 73100 $M^{-1}cm^{-1}$) compared to the naphthalene-fused derivative **224a**. This relationship of longitudinal π-extension and absorption properties is in accordance with that reported for rylene dyes.[19-20] A similar trend was also observed for our recently published *pseudo*-rylene dicarboximides.[59] The measured absorption spectra of the newly synthesized tetrachlorinated PADIs are in good agreement with the respective TD-DFT calculated spectra (Figure A1).

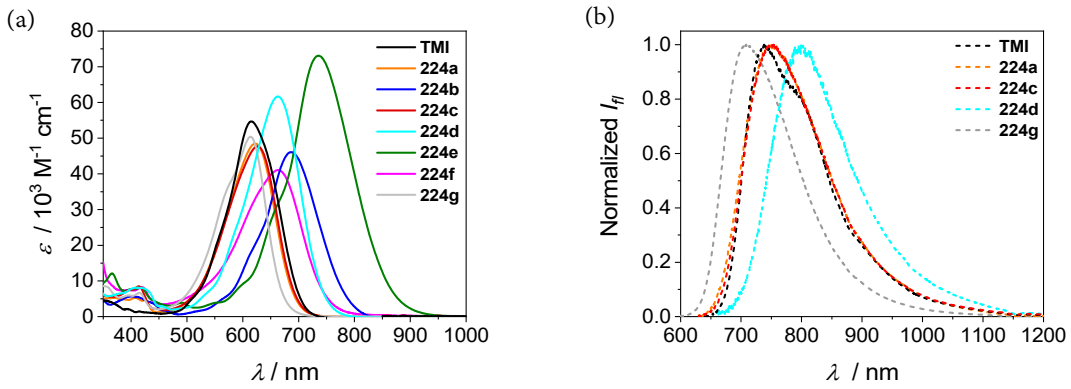

Figure 28. (a) UV–vis absorption spectra of **224a–g** and reference terrylene monoimide without chlorine atoms (**TMI**) and (b) emission spectra of **224a** (λ_{ex} = 620 nm), **224c** (λ_{ex} = 620 nm), **224d** (λ_{ex} = 600 nm), **224g** (λ_{ex} = 590 nm) and **TMI** (λ_{ex} = 630 nm) measured in CH_2Cl_2 ($c \sim 1 \cdot 10^{-6}$ M) at room temperature.

[ii] The *Experimental Section* has been moved to *10.1. Supporting Information Chapter 3*.

The observed broad and intense absorption bands of the PADIs can be explained by a charge-transfer character as revealed by TD-DFT calculated charge density differences, which describe the change of static charge distribution upon excitation expressed by a charge transfer length (Δr) parameter that provides a qualitative trend (Figure A3). In these PADIs the tetrachlorinated-perylene dicarboximide moiety acts as electron-accepting and the annulated polycyclic aromatic hydrocarbon functions as electron-donating part. Beside the charge-transfer character, the non-planarity of these molecules, implied by the significant torsion of the two neighbored chlorinated naphthalene units, may also have an effect on the structureless broad absorption spectra of these PADIs (Figure A4 and Table A3).[13]

PADIs **224a**, **224c**, **224d** and **224g** show weak to moderate emission up to in the NIR region, while **224b**, **224e** and **224f** are non-fluorescent. The emission spectra of the former compounds reveal a mirror image relationship to their respective absorption spectra with large Stokes shifts (**224a**: 2860 cm^{-1}, **224c**: 2690 cm^{-1}, **224d**: 2610 cm^{-1} and **224g**: 2180 cm^{-1}) and emission maxima ranging from 709 nm for **224g** to 801 nm for **224d**. Furthermore, these donor–acceptor systems show multiexponential lifetime decays (Figure A2 and Table A2) and relatively low fluorescent quantum yields of 2.8% (**224d**), 6.8% (**224a**), 10.6% (**224c**) and 31% (**224g**) which might be attributed to the pronounced charge-transfer character in the excited states and twisted molecular geometries.[280] The higher quantum yield for the corannulene derivative **224g** appears to be a general trend for such bowl-shaped PADIs since high quantum yields were also observed for naphthalene dicarboximide annulated corannulene.[270]

3.2.3. Redox Properties

The PADIs **224a–g**, except **224f** because of its poor solubility, were investigated by cyclic and square wave voltammetry to explore their electronic character. The measurements were performed in dichloromethane at room temperature using tetrabutylammonium hexafluorophosphate as electrolyte and the ferrocenium/ferrocene (Fc^+/Fc) redox couple as internal standard. The voltammograms are displayed in Figure 29 and Figure A5 and the electronic properties are summarized in Table 3. All measured compounds showed two reversible reduction and at least one reversible oxidation processes with well separated potentials, except the anthracene-annulated PADI **224b** for which two irreversible reduction potentials were observed. The first oxidation potentials of the PADIs range from 0.42 V (**224e**) to 0.90 V (**224g**), while the second oxidation potentials were observed between 0.88 V (**224e**) and 1.25 V (**224g**). Although the first oxidation potentials within this series of compounds differ considerably (E_{ox1} = 0.42 V for **224e** and for **224g** 0.90 V), the differences for the first reduction potentials are rather small (E_{red1} = –0.93 V (**224b**) to –1.05 V (**224a**)). The reduction potentials of these compounds are comparable to those of a

tetrachloro-perylene bis(dicarboximide) (−0.87, −1.22 V),[281] however, slightly less negative than of a fullerene-fused naphthalene dicarboximide (–1.09, –1.50 V).[92]

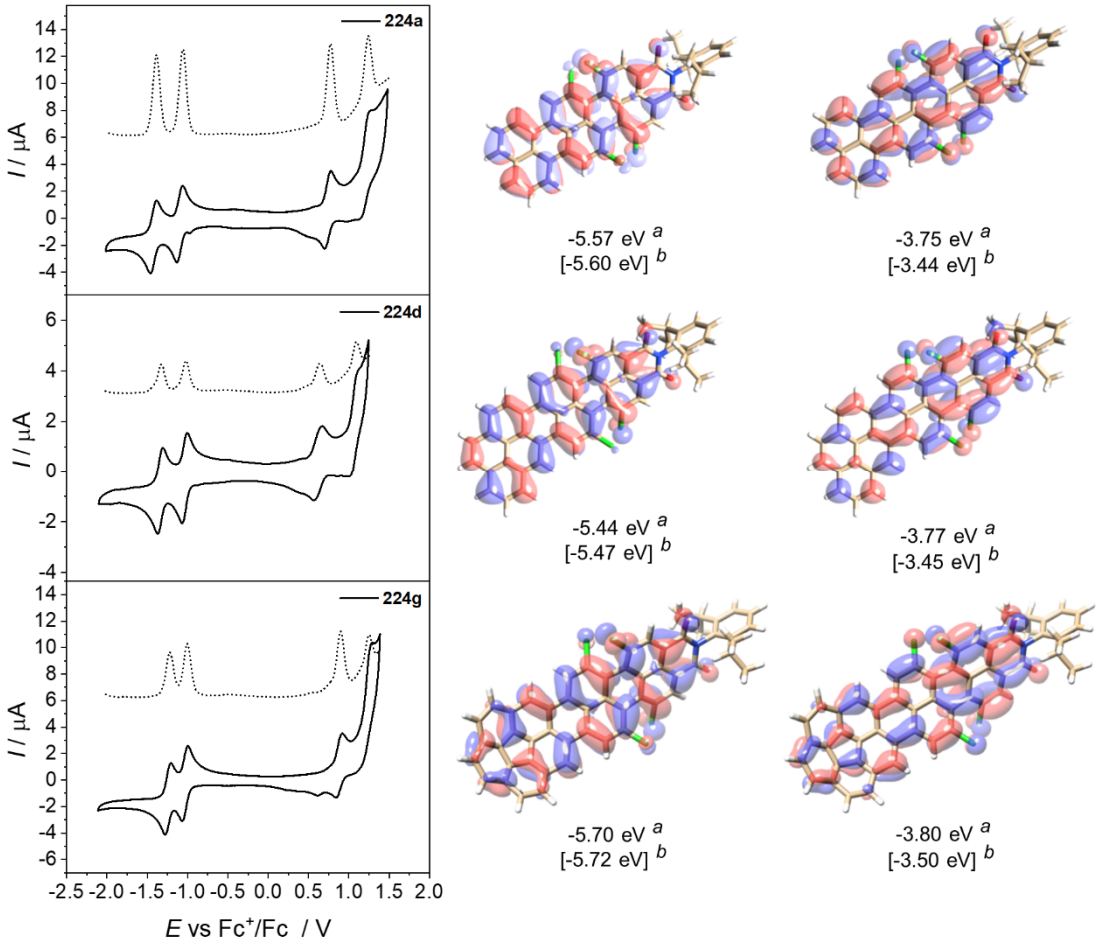

Figure 29. Cyclic voltammetry (solid lines) and square wave voltammetry (dashed lines) traces and calculated HOMO (left) and LUMO (right) levels of a selection of compounds **224a** (top), **224d** (middle) and **224g** (bottom) by DFT (B3LYP/def2-SVP). CV measurements were performed in dichloromethane ($c \sim 2 \cdot 10^{-5}$ M) at room temperature and tetrabutylammonium hexafluorophosphate (0.1 M) as electrolyte (scan rate: 100 mVs^{-1}). [a]Calculated according to literature known procedure using the experimentally determined redox potentials ($E_{LUMO} = -[E\,(M/M^-) + 4.8\ eV]$ and $E_{HOMO} = -[E\,(M/M^+) + 4.8\ eV]$) and the energy level of Fc^+/Fc with respect to the vacuum level (–4.8 eV).[282] [b]DFT calculated values (B3LYP/def2-SVP).

By comparing the first reduction potentials of chlorinated PADIs with those of the non-chlorinated reference **TMI** an increased electron-accepting character of the former is obvious. Therefore, the introduction of electron-withdrawing chlorine substituents at the aromatic core of PADIs is a suitable way to increase the electron-deficient character of this class of compounds. A similar behavior was observed for edge chlorinated nanographenes.[283] Considering the energy level of Fc^+/Fc with respect to the vacuum level (–4.8 eV),[282] we have estimated the HOMO and LUMO energy levels of the present PADIs from redox potentials (Table 3). The experimentally determined values are in good agreement with those obtained by DFT calculations (Figure 29 and Figure A6). The LUMO energy levels range from –3.75 eV (**224a**) to –3.87 eV (**224b**) and the HOMO energy

levels are located between –5.22 eV (**224e**) and –5.70 eV (**224g**). Thus, LUMO energy levels are comparable to the reported value for a terrylene bis(dicarboximide) (–3.65 eV),[42] nanographene bearing four dicarboximide groups (–3.81 eV),[58] or the fullerene derivative $PC_{60}BM$ (–3.91 eV).[284] Accordingly, the LUMO energy levels of the PADIs are in the range of n-type semiconductors.[271, 285]

Table 3. Summary of the optical and redox properties of compounds **224a–g** and reference **TMI**.

	λ_{abs} / nm[a]	λ_{em} / nm	Stokes shift / cm^{-1}	Φ_{fl} / %[b]	E_{ox1}	E_{ox2}	E_{red1}	E_{red2}	E_{HOMO}	E_{LUMO}	E_{gap}
					/ V[c]					/ eV[d]	
TMI	617	738	2660	6.5 ± 0.2	0.49	1.03	–1.25	–1.62	–5.29	–3.55	1.74
224a	623	758	2860	6.8 ± 0.3	0.77	1.24	–1.05	–1.38	–5.57	–3.75	1.82
224b	687	-[e]	-[e]	-[e]	0.58	1.01	–0.93[f]	–1.82[f]	–5.38	–3.87	1.51
224c	627	754	2690	10.6 ± 0.4	0.78	-	–1.01	–1.32	–5.58	–3.79	1.79
224d	663	801	2610	2.8 ± 0.2	0.64	1.09	–1.03	–1.33	–5.44	–3.77	1.67
224e	736	-[e]	-[e]	-[e]	0.42	0.88	–1.00	–1.31	–5.22	–3.80	1.42
224f	663	-[e]	-[e]	-[e]	-[g]	-[g]	-[g]	-[g]	[–5.50][h]	[–3.42][h]	[2.08]
224g	614	709	2180	31.2 ± 1.1	0.90	1.25	–1.00	–1.22	–5.70	–3.80	1.90

[a]Spectra were measured in dichloromethane ($c \sim 1 \cdot 10^{-6}$ M) at room temperature. [b]Fluorescence quantum yields were determined using the dilution method ($A < 0.05$) and oxazine 1 as reference. [c]Half-wave potentials were determined by cyclic or square wave voltammetry measured in DCM (0.1 M TBAHFP) vs. Fc^+/Fc. [d]Calculated according to literature known procedure using the experimentally determined redox potentials ($E_{LUMO} = -[E\ (M/M^-) + 4.8\ eV]$ and $E_{HOMO} = -[E\ (M/M^+) + 4.8\ eV]$) and the energy level of Fc^+/Fc with respect to the vacuum level (–4.8 eV).[282] [e]No emission observed. [f]Reduction is irreversible, thus peak potential is given. [g]Solubility for measurement too low. [h]DFT calculated values (B3LYP/def2-SVP). **TMI**: *N*-(2,6-diisopropylphenyl)terrylene-3,4-dicarboximide.

Our studies have shown that the Pd-catalyzed cascade C−C coupling reaction is a versatile method for the synthesis of electron-poor polycyclic aromatic dicarboximides with broad substrate scope. Multiple electron-withdrawing chlorine atoms could be introduced by this convergent synthetic approach affording novel PADIs with promising optical and electronic properties for potential application as (opto)electronic materials.

3.3. Conclusion

In summary, we have reported the synthesis of a series of new tetrachlorinated polycyclic aromatic dicarboximides (PADIs) by palladium-catalyzed annulation of a bay-tetrachloro-substituted perylene dicarboximide with a variety of polycyclic aromatic hydrocarbons involving a cascade Suzuki–Miyaura cross-coupling and direct C−H arylation reaction. The optimized reaction conditions allowed the annulation of a multiple chlorine atoms containing perylene dicarboximide

to different planar and curved PAHs affording the desired electron-poor PADIs in good to high yields. The obtained PADI derivatives show strong absorbance in the visible range and some of them exhibit emission in the NIR region with quantum yields up to 31 %. Furthermore, cyclic and square wave voltammetry confirmed an increased electron-deficient character of these chlorinated PADIs. The introduction of chlorine atoms to PADIs also leads to lower lying frontier orbitals and thus the compounds possess high potential for application in (opto)electronic devices. Moreover, these chlorinated PADIs are interesting building blocks for further functionalization and synthesis of π-extended arrays by metal-mediated C−C coupling reactions. We are currently exploring such possibilities.

Chapter 4

Aryloxy- and Aryl-Substituted Polycyclic Aromatic Dicarboximides as (Chiral) NIR Absorber and Emitter

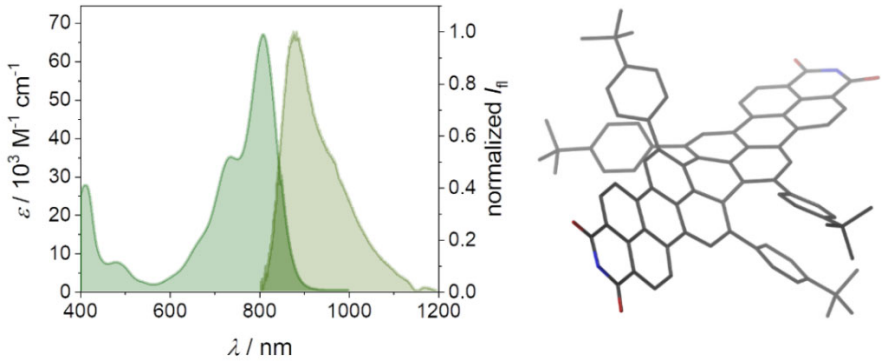

Parts of this chapter and the corresponding supporting information (*10.2. Supporting Information Chapter 4*) were submitted for publication:

M. Mahl, H. Reichelt, A. Rausch, B. Mahlmeister, K. Shoyama, M. Stolte, F. Würthner, *submitted for publication*.

Abstract:[iii] A versatile synthetic approach towards novel near-infrared (NIR) absorbing and emitting polycyclic aromatic dicarboximides (PADIs) is presented that afforded diverse and universal building blocks a variety of tetraaryloxy- and tetraaryl-substituted π-extended mono- and bisdicarboximides. UV–vis absorption and fluorescence spectroscopy revealed systematic modulation of the respective chromophoric properties and thus disclosed structure–property relationships. Emission maxima up to 884 nm for an aryl-substituted quaterrylene bisdicarboximide could be observed, which is 100 nm bathochromically shifted compared to its chlorine-substituted

[iii] The crystallographic measurements and analysis were conducted by Dr. Kazutaka Shoyama.

counterpart. Further, fluorescence quantum yields up to 20% for a bowl-shaped derivative could be obtained. In addition, the introduction of adjacent aryl substituents at the PADI-scaffold lead to inherent chiral NIR dyes as disclosed by time-dependent circular dichroism (CD) spectroscopy. Therefore, the novel NIR chromophores are promising candidates in terms of possible circularly polarized luminescence applications as well as other (related) NIR applications.

4.1. Introduction

The chemistry of dyes has sustained tremendous attention and exceptional developments since the first synthesis of a dye in the 19th century are noted unitl today.[2, 14] While early dyes and pigments were applied as colouring agents or vat dyes, modern organic synthesis paved the way to precisely designed artificial as well as modulated natural chromophores with tailor-made (optical) properties for various high-technology applications.[1, 12-13] In this regard, with dye classes like BODIPYs,[157] porphyrins,[142] phthalocyanines,[143-144] azo dyes,[139] rylene dicarboximides,[15] polymethine dyes,[153, 286] squaraines[155] and many more, a multitude of organic chromophores with different characteristics are available.[2, 12] An ambitious research field deals with the shift of the absorption and emission from the visible light spectrum to the near-infrared (NIR) region. Such corresponding NIR dyes are highly desired for their potential implementation in various applications, like photodetectors,[287] security inks,[288] NIR organic-light emitting diodes[48] or organic photovoltaics.[46, 289] Further, the "tissue-penetrating window" lays in the NIR range, allowing their use for (bio)imaging applications[136], such as cancer imaging or in surgeries,[4-5] or as photosensitizer in photodynamic therapy.[4]

However, the design of NIR dyes with customized properties faces challenges such as low dye stability and weak to none emission. Both of these problems can be attributed to a decreased energy gap, which leads to easy (photo-)oxidation caused by a high HOMO level and promotes non-emissive relaxations pathways.[290-292] In this context, higher rylene dicarboximide homologs have shown to be promising candidates for the development of new NIR absorbers due to lower HOMO levels compared to other NIR dyes, however, often with a reduced or fully quenched fluorescence.[15, 24, 39-40] Their extended aromatic surfaces as well as their strong electron-deficient dicarboximide functional groups push the absorption bathochromically into the NIR.[19, 24] Furthermore, additional substituents can be used to modify their absorption and emission properties.[15] For this purpose, we recently introduced novel tetrachlorinated polycyclic aromatic dicarboximides (PADIs), which offered an absorbance and emission in the NIR spectral range (*Chapter 3*[256]). These dyes combine, similar to rylene dicarboximides, an extended aromatic surface with electron-withdrawing dicarboximide functional groups for an absorption in the NIR region, while, however, these dyes offer a significant emission in the NIR. Encouraged by these highly intrigue findings, we were interested in further modifying the optical characteristics of these PADIs. In this regard, we aimed the substitution of the attached chlorines with aryloxy as well as aryl groups to further bathochromically shift the absorbance and fluorescence into the NIR. Such substitution pattern and their effect to alter the optical properties is well-known from perylene bisdicarboximide (PBI) dye chemistry.[15-16, 293-294] Further, the introduction of aryl substituents in spatial proximity can induce an inherent chirality due to steric constraints.[61]

Herein, we present a versatile synthetic strategy towards such new aryloxy- and aryl-substituted PADIs. Key reaction steps include a Hunsdiecker-like reaction and a palladium-catalyzed annulation reaction, which gave access to mono- and bisdicarboximide containing π-scaffolds. UV–vis absorption and fluorescence spectroscopy revealed systematic substituent-dependent properties of these new NIR chromophores. Further, time-dependent circularly dichroism (CD) spectroscopy gave insights into the stability of tetraaryl-substituted PADIs against racemization, which could be rationalized with crystallographic analysis. Therefore, the tetraarylated PADIs combine NIR chromophoric properties with an inherent chirality to yield stable atropo-enantiomeric NIR dyes.

4.2. Results and Discussion

4.2.1. Synthesis

At first, we aimed for a direct chloride substitution in the tetrachlorinated PADI **224a** (Table 2) with aryloxy and aryl groups towards compounds **225a** and **226a**, respectively. In this regard, we applied for the introduction of aryloxy substituents frequently used reaction conditions known from the chemistry of PBIs (Table A4, *10.2. Supporting Information Chapter 4*).[86-87] However, the combination of phenol with various bases including K_2CO_3 and Cs_2CO_3 and in different solvents such as DMF or NMP yielded no product or only traces. Mass spectrometry revealed a complex reaction mixture due to the detection of a broad variety of incompletely substituted side products and partial dechlorinated intermediates. Also, increased equivalents of phenol, prolonged reaction times or other reagents such as CsF in THF could not overcome these problems. Therefore, we applied *para-tert*-butyl substituted phenol to increase the nucleophilicity of the hydroxyl group and, indeed, we could isolate the desired product **225a**. However, the yield was unsatisfactorily low in 1.4% and various side-products such as incomplete substituted ones made purification extremely tedious and time-consuming (Scheme 7). For the introduction of aryl groups we used established Suzuki–Miyaura conditions for the reaction of tetrachlorinated towards tetraaryl-substituted PBIs with catalyst $Pd(PPh_3)_4$ in a toluene/EtOH/H_2O-mixture and *para-tert*-butyl phenyl boronic acid.[61, 294] Similar to the introduction of aryloxy substituents, the purification was cumbersome and the yield insufficient in 6%, which can be, again, attributed to incomplete substitution patterns (Scheme 7).

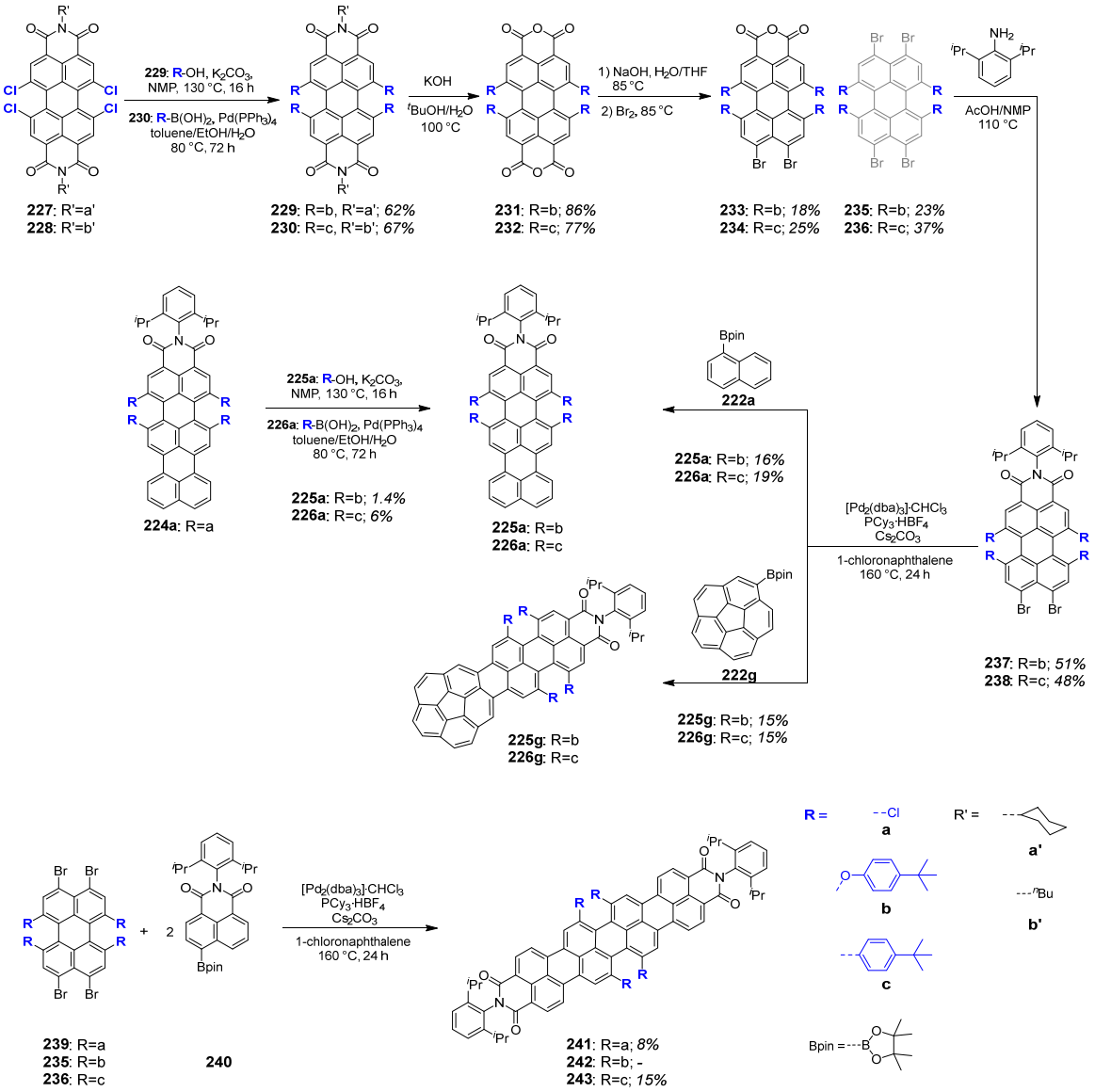

Scheme 7. Synthetic routes towards novel tetraaryloxy- and tetraaryl-substituted PADIs.

To improve the yields and ease the purification, we conceived a more straightforward synthetic strategy towards both target compounds **225a** and **226a** based on well-known PBI chemistry[86-87, 295] and our recently established annulation reaction (Scheme 7).[53, 58, 277] In this regard, above-mentioned reaction conditions applied to tetrachlorinated PBIs gave aryloxy- and aryl-substituted PBIs in good yields of 62% (**229**[296]) and 67% (**230**), respectivly. Subsequent basic saponification reactions resulted in the respective bisanhydrides **231**[296] and **232**. Hunsdiecker-like reaction conditions could brominate one out of two acid anhydride moieties to give **233** and **234** in 18% and 25% yield, respectively. These rather low yields could be attributed to the two-sided bromination, which gave side-products **235** (23%) and **236** (37%), as well as re-isolated starting materials. Imidization reactions followed by palladium-catalyzed [3+3] annulation reactions as developed by our group[53, 58, 277] with naphthalene boronic acid ester **222a** gave the desired products. Hereby, the

yields in the last step are still rather low in 16% (**225a**) and 19% (**226a**). However, easier purification of the final products as well as the synthesis of versatile building blocks **237** and **238** justified the multi-step sequence. In this regard, we chose corannulene boronic acid ester **222g** as a second substrate for the annulation reaction due to the high fluorescence quantum yield (31%, CH_2Cl_2) of tetrachlorinated analogue **224g** (Table 3). Both bowl-shaped compounds, **225g** and **226g**, could be isolated in a yield of 15%. Furthermore, we applied undesired side products of the Hunsdiecker reaction **235** and **236** in two-fold annulation reactions with naphthalene dicarboximide boronic acid ester **240**. However, only for **236** the desired quaterrylene bisdicarboximide **243** was observed and isolated (15%). In addition, we used the literature-known tetrachloro counterpart (**239**)[295] with similar reaction conditions to obtain the tetrachloro-substituted reference **241**. All compounds were fully characterized by NMR spectroscopy and mass spectrometry (*10.2. Supporting Information Chapter 4*).

4.2.2. Crystallographic Analysis

To gain insights into the structural features of the new compounds, we attempted to grow single crystals for X-ray diffraction. And indeed, a suitable crystal of quaterrylene bisdicarboximide **243** could be obtained by slow diffusion of ethanol in a chloroform solution of **243** (Figure 30a–b,e and Figure A28). The molecule crystallizes in the monoclinic space group $P2_1/c$. The adjacent aryl groups cause due to spatial proximity a strong distortion of the quaterrylene scaffold, which results in a chiral π-scaffold with an estimated twist angle of ~35°. The distance between two neighbouring aryl substituents is in the range of 3.1–3.5 Å and therefore involves π–π-interactions with each other. Similar structural features could be obtained for the crystal structure of monoanhydride **234** (Figure 30c–d and Figure A27) and are in accordance with comparable tetraaryl-substituted peropyrenes.[297-298] Further, the quaterrylene substructure of **243** is slightly bent, which might be due to packing effects in the solid-state. The racemic mixture of bisdicarboximide **243** arrange into dimeric packing motifs of *P*- and *M*-atropo-enantiomers without close π–π-interactions of the respective rylene scaffolds. The crystallographic analysis not only unambiguously confirmed the structures of **234** and **243**, but also gives a perception of the high constrain due to the sterically crowded *bay*-positions, which should result in the formation of stable enantiomers (*vide infra*).[60-61]

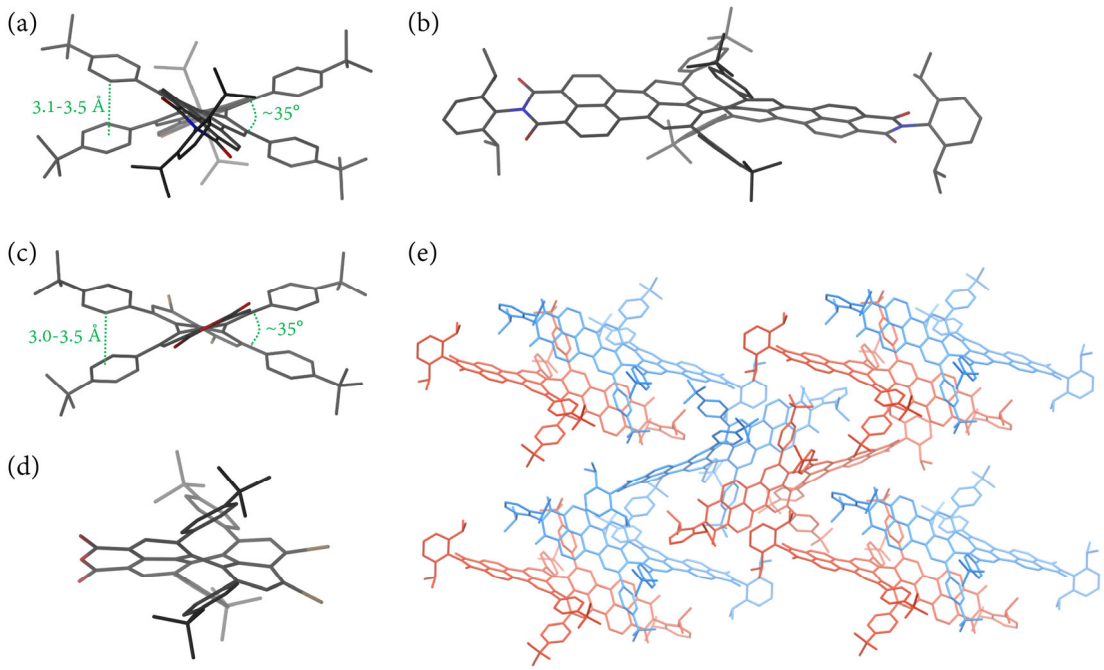

Figure 30. Molecular structures of **234** and **243** as obtained by single crystal X-ray diffraction (hydrogens are omitted for clarity). (a) Front and (b) side view of *M*-enantiomer of **243**. (c) Top and (d) side view of *P*-enantiomer of **234**. (e) Dimeric packing arrangement of a racemic mixture of **243** (red: *P*-enantiomer; blue: *M*-enantiomer).

4.2.3. Optical Properties

The optical properties of the obtained aryloxy- and aryl-substituted PADIs were investigated by UV–vis absorption and fluorescence spectroscopy in dichloromethane solutions (Figure 31 and Table 4). The substitution of the chlorine atoms in **224a** with aryloxy groups caused a modest and expected bathochromic shift in the UV–vis spectrum (**224a**: λ_{abs} = 623 nm; **225a**: λ_{abs} = 637 nm), while the extinction coefficient decreased from 48500 $M^{-1}cm^{-1}$ (**224a**) to 23900 $M^{-1}cm^{-1}$ (**225a**). These features are also present in the comparison of corannulene annulated compounds **224g** and **225g** (**224g**: λ_{abs} = 614 nm (50400 $M^{-1}cm^{-1}$); **225g**: λ_{abs} = 642 nm (23900 $M^{-1}cm^{-1}$)). The expected redshift due to the substitution with aryloxy groups is similar to the literature-known bathochromic shift from a tetrachloro-PBI compared to a tetraphenoxy-PBI.[16] According to literature, an even greater redshift is caused by the introduction of aryl substituents at the PBI-scaffold.[61, 293-294] This trend was also evident for the synthesized compounds **226a** and **226g**, whose absorption maxima of 679 nm (**226a**) and 682 nm (**226g**) are clearly redshifted compared to their aryloxy counterparts **225a** and **225g**. The absorption maxima of the quaterrylene bisdicarboximides **241** and **243** are 711 nm (**241**) and 811 nm (**243**), respectively, which is an even more pronounced redshift towards the NIR region with high extinction coefficients (**241**: 68600 $M^{-1}cm^{-1}$; **243**: 67000 $M^{-1}cm^{-1}$). This large bathochromic shift can be attributed to the longitudinal, linear expanded π-surface as known for the rylene bisdicarboximide series and the second electron-withdrawing dicarboximide unit.[15,

[19] Furthermore, both bisdicarboximides have a pronounced vibronic fine-structure compared to the rather structureless absorption bands of the monodicarboximides. This observation is consisting with rylene mono- and bisdicarboximide homologs and is a consequence of the second dicarboximide group.[15, 299]

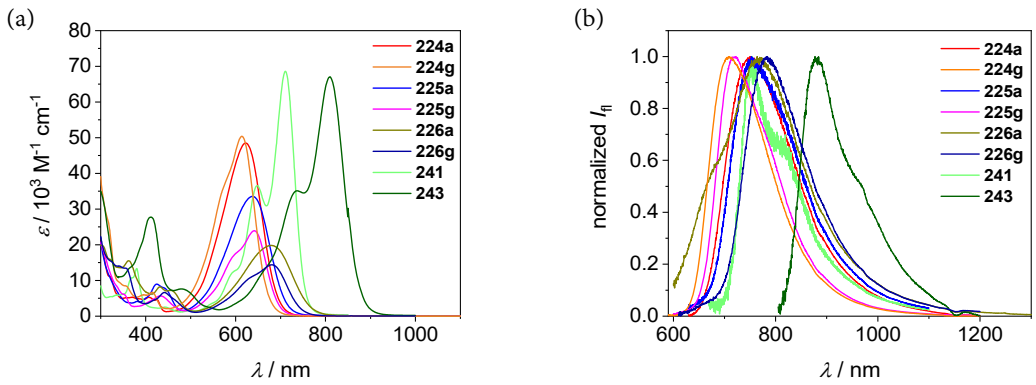

Figure 31. (a) UV–vis absorption and (b) fluorescence spectra of **224a** (λ_{ex} = 620 nm), **224g** (λ_{ex} = 590 nm), **225a** (λ_{ex} = 620 nm), **225g** (λ_{ex} = 590 nm), **226a** (λ_{ex} = 590 nm), **226g** (λ_{ex} = 600 nm), **241** (λ_{ex} = 650 nm) and **243** (λ_{ex} = 790 nm) in dichloromethane solutions at room temperature.

When comparing the emission properties of the aryloxy-substituted compounds **225a** and **225g** with emission maxima of 757 nm and 720 nm, respectively, with respect to the chlorine-substituted compounds (**224a**: λ_{em} = 758 nm, **224g**: λ_{em} = 709 nm), no or only small bathochromic shifts occur (Figure 31b and Table 4). In addition, the fluorescence quantum yields are in both cases reduced (**224a**: 6.8%; **224g**: 31%; **225a**: 4.6%; **225g**: 20%), making these compounds less interesting as NIR chromophores. In contrast, the introduction of aryl groups significantly shifted the emission maxima with 768 nm for **226a** and 786 nm for **226g** into the NIR region. Whilst for **226a** only a fluorescence quantum yield of 1.4% is obtained, **226g** exhibits a higher fluorescence quantum yield of 4.8%. The fluorescence of the quaterrylene bisdicarboximide **243** with an emission maximum of 884 nm is from all compounds the farthest in the NIR region and for such a small energy gap the quantum yield of 1.3% is quite remarkable.[42] For comparison, the absorption and emission maxima of a *tert*-butyl-substituted quaterrylene are located at 659 nm and 678 nm, respectively.[300] Whilst the emission maximum is more than >200 nm blueshifted compared to **243**, the fluorescence quantum yield of quaterrylene is with 5% only moderately better. Other quaterrylene bisdicarboximides typically show an absorption at shorter wavelengths compared to **243**, while mostly only weak or no emission has been observed.[25, 39-40]

Table 4. Summary of the optical properties of **224a** (λ_{ex} = 620 nm), **224g** (λ_{ex} = 590 nm), **225a** (λ_{ex} = 620 nm), **225g** (λ_{ex} = 590 nm), **226a** (λ_{ex} = 590 nm), **226g** (λ_{ex} = 600 nm), **241** (λ_{ex} = 650 nm) and **243** (λ_{ex} = 790 nm) measured in CH_2Cl_2 (c ~ $1 \cdot 10^{-5}$ – $1 \cdot 10^{-6}$ M) at room temperature.

	λ_{abs} / nm (ε / $M^{-1}cm^{-1}$)	λ_{em} / nm	Stokes shift / cm^{-1}	Φ_{fl} / %[a]	τ / ns
224a	623 (48500)	758	2860	6.8 ± 0.3	0.61 ± 0.004 (91.5%) 4.37 ± 0.077 (8.5%)
225a	637 (33600)	757	2420	4.6 ± 0.2	0.51 ± 0.003 (98.2%) 6.38 ± 0.47 (1.8%)
226a	679 (19800)	768	1700	1.4 ± 0.1	0.43 ± 0.022 (18.2%) 2.59 ± 0.075 (44.9%) 7.03 ± 0.133 (36.9%)
224g	614 (50400)	709	2180	31.2 ± 1.1	1.91 ± 0.007 (96.9%) 4.75 ± 0.335 (3.1%)
225g	642 (23900)	720	1690	20 ± 0.4	1.68 ± 0.009 (96.3%) 5.53 ± 0.411 (3.7%)
226g	682 (14300)	786	1940	4.8 ± 0.1	0.62 ± 0.002 (90.2%) 5.38 ± 0.06 (9.8%)
241	711 (68600)	754	800	< 1	0.22 ± 0.002 (99.1%) 2.28 ± 0.24 (0.9%)
243	811 (67000)	884	1020	1.3 ± 0.1	0.22 ± 0.006 (66.3%) 0.98 ± 0.031 (30.2%) 4.21 ± 0.365 (3.5%)

[a]Fluorescence quantum yields were determined using the relative method and oxazine 1 or IR125 as a reference.

4.2.4. Chiroptical Properties

As known from perylene bisdicarboximides, a four-fold substitution at the *bay* positions with aryl groups affords inherent chiral π-scaffolds, where two atropo-enantiomers are formed (Figure 32a).[61] In this regard, the separation of PADI **243** enantiomers by recycling chiral-HPLC in *n*-hexane/dichloromethane-mixture (v/v 2/1) could be achieved to give the two atropo-enantionmers (Figure 32b). The chiroptical properties of the separated enantiomers were investigated by circular dichroism (CD) spectroscopy (Figure 32c). The first eluted fraction shows a positive signal for the lowest energy transition and following the assignment for core-twisted chiral PBIs[60, 301] the first fraction can be tentatively assigned as (*P*)-**243**. The second fraction shows a mirror image relation and can thus be assigned as (*M*)-configuration of **243**. This provisional stereochemical assignment is verified by TD-DFT calculations (Figure A30). Both enantiomers exhibit strong Cotton effects for the lowest energy absorption band in the NIR region with $\Delta\varepsilon$ = 29 $M^{-1}cm^{-1}$ ((*P*)-**243**) and $\Delta\varepsilon$ = – 27 $M^{-1}cm^{-1}$ ((*M*)-**243**), which result in a dissymmetry factor g_{abs} = ($\Delta\varepsilon/\varepsilon$) of $4.3 \cdot 10^{-4}$. Since the interlocked structure of the tetraaryl-substituted central perylene unit should lead to high racemization barriers,[60-61] we investigated the racemization process for (*P*)-**243** by time-dependent CD spectroscopy. Elevated temperatures of 125 °C (1,1,2,2-tetrachloroethane) were necessary to

enable racemization on a reasonable time scale (Figure 32d, for details see *10.2. Supporting Information Chapter 4*). The subsequent evaluation revealed a racemization constant k_{rac} of $1.449 \cdot 10^{-5}$ s^{-1} and with this a half-life time of $t_{1/2}$ = 80 min at 125 °C can be estimated. Moreover, with a statistical transmission coefficient of $\kappa = 0.5$[60] a high free energy barrier of $\Delta G^{\#}_{398\,K}$ = 125 kJ/mol could be determined for the racemization. This value exceeds those measured for tetrabromo-PBI (118 kJ/mol),[60] tetrathioether-substituted PBI (119 kJ/mol)[302] as well as tetraaryl-substituted peropyrene (121 kJ/mol).[297] This high barrier can be rationalized by the crystallographic analysis of **234** and **243**, which disclosed the high steric constraint between the interlocked neighbouring aryl groups (Figure 30).

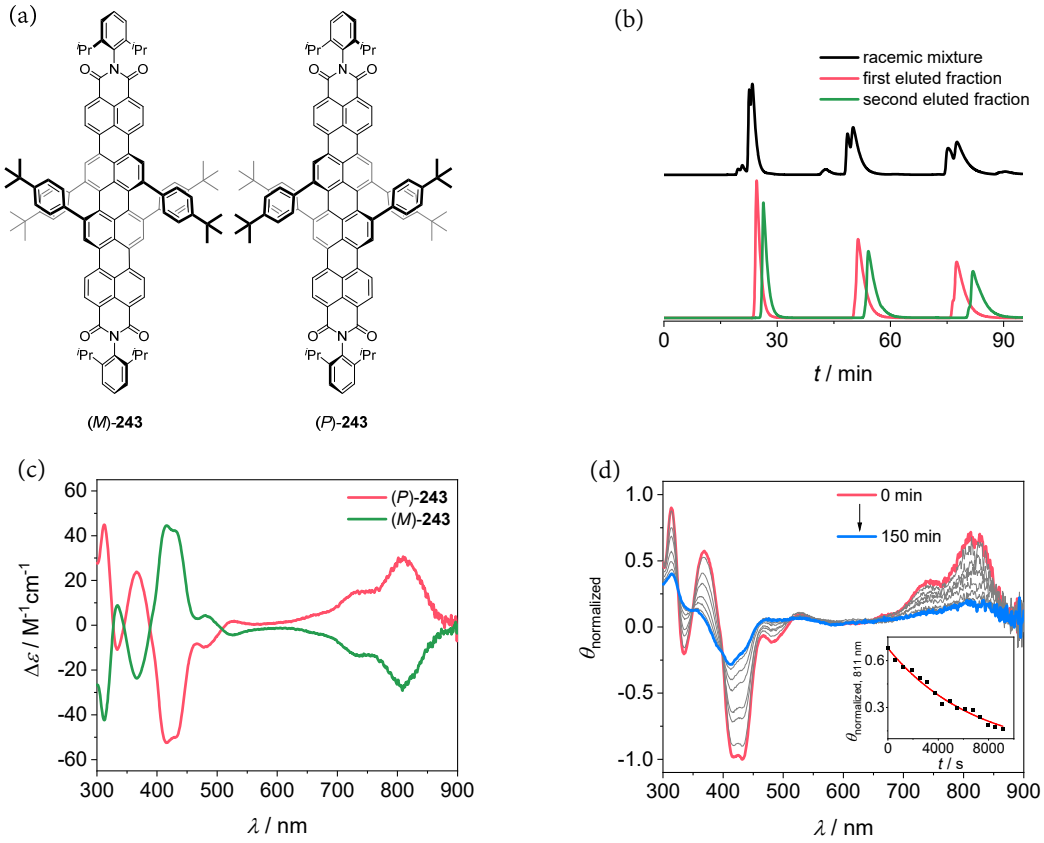

Figure 32. (a) Atropo-enantiomers of **243**. (b) HPLC traces of racemic **243** using an *n*-hexane/dichloromethane mixture (2/1) as eluent. (c) CD spectra of both enantiomers in dichloromethane at 293 K. (d) Time-dependent CD spectra of *(P)*-**243** in 1,1,2,2-tetrachloroethane at 398 K. Inset: exponential decay fit of the CD signal at 811 nm.

Therefore, the synthesized tetraaryl-substituted PADIs are not only interesting as novel NIR chromophores, but also as inherent chiral compounds with high racemization barriers, making them also promising candidates in terms of circularly polarized luminescence phenomena.

4.3. Conclusion

In summary, a straightforward synthetic route towards novel tetraaryl- and tetraaryloxy-substituted PADIs has been devised. The synthetic strategy involves a Hunsdiecker-like reaction as well as a palladium-catalyzed cascade reaction as key steps where the former one yields versatile di- and tetra-brominated building blocks. The synthetic approach gives access to mono- as well as bisdicarboximides, while also the introduction of an additional curvature, due to annulation towards bowl-shaped substrate corannulene, is feasible. The aryloxy and aryl substituents (strongly) alter the optical properties compared to their chlorinated counterparts. The absorption and emission maxima are in most cases bathochromically shifted into the NIR region. The emission shift is most pronounced for a tetraaryl-substituted quaterrylene bisdicarboximide with a 100 nm shift compared to the chlorine-substituted analogue. In addition, exemplary separation of atropo-enantiomers of a tetraaryl-substituted PADI disclosed the high racemization barrier of such inherent chiral compounds, which was supported by single crystal X-ray analysis. Therefore, the synthesized tetra-aryl PADI molecules combine NIR absorbing and emitting features with a stable chirality center, which makes such molecules highly interesting in terms of circularly polarized luminescence phenomena in the NIR range.[303-305] Further, the implementation of such dyes in organic photovoltaic devices might be a promising research field.[306-307]

Chapter 5

Palladium-Catalyzed [3+2] Annulation of Naphthalimide Acceptors and Thiophene Donors

This chapter and the corresponding supporting information (*10.3. Supporting Information Chapter 5*) has been published:

K. Shoyama,* M. Mahl,* M. A. Niyas, M. Ebert, V. Kachler, C. Keck, F. Würthner, *J. Org. Chem.* **2020**, *85*, 142–149.

* Equal contribution authors.

Abstract:[iv] Donor–acceptor (D–A) dyes constitute one of the fundamental structural motifs of functional organic materials. In most cases, the donor and acceptor moieties are connected by a single bond, which could potentially be replaced by a fused aromatic ring to enhance the rigidity and conjugation of the dye moieties. However, there is still a lack of synthetic methodologies for such fused D–A systems. Here we report the synthesis of D–A and A–D–A dyes that possess fully annulated donor and acceptor moieties based on palladium (Pd)-catalyzed [3+2] annulation reaction between bromo-chloro-naphthalene dicarboximide and thiophene- and indole-based boronic esters. Thus, a series of fused D–A and A–D–A conjugated dyes were synthesized in good to high yields by a cascade of Pd-catalyzed Suzuki–Miyaura cross-coupling and direct arylation reactions. The newly synthesized fused D–A and A–D–A dyes with one or two naphthalimide units fused to five-

[iv] Synthesis of compound **244e** has been described in: M. Ebert, Bachelor Thesis, Julius-Maximilians-Universität Würzburg, **2017**.

membered electron-rich heterocyles were systematically investigated by ultraviolet–visible spectroscopy, cyclic and square wave voltammetry, and density functional theory calculations. These dyes possess desirable optical and electrochemical properties for application as organic electronic materials as they show absorption up to the near-infrared region, undergo up to 4-fold reduction processes, and have low-lying LUMO energy levels down to −3.62 eV.

5.1. Introduction

Conjugated organic molecules comprising linked donor and acceptor moieties, often named as donor–acceptor (D–A) dyes, have become major synthetic targets in recent years due to their suitable molecular properties for organic semiconductor materials.[9, 110, 309-310] Their optical properties are of particular interest as represented in early synthetic efforts toward applications in nonlinear optics,[311] and later in solar cells.[312-313] As the application of organic materials in solar cells has become increasingly more attractive in the past decade, the structural design principles for such chromophores have diverged to achieve suitable absorption wavelengths and optimal processability. As such, not only simple D–A systems but also D–A copolymers,[314] D–A–D or A–D–A small molecules,[315-318] and D–A–A systems[319] have been synthesized.

Despite such structural versatility, the connectivity of the donor and acceptor moieties in such multisubunit dyes is in most cases limited to a single bond, and only a few examples are known for donor–acceptor dyes whose donor and acceptor moieties are connected by at least two chemical bonds.[51, 320-321] This uniformity of the connection motif is surprising considering the recent development in the synthetic method for extended π-systems by cyclization or annulation reactions.[20, 57, 264] Such π-extension would potentially realize better conjugation between donor and acceptor moieties and allow stronger interaction between two moieties as well as planarity that would be beneficial for material stability, proper organization in bulk material, and processability.

We have recently developed a synthetic methodology for annulating electron-deficient naphthalene and perylene dicarboximide building blocks to various aryl boronic esters via [3+3] annulation reaction.[53, 58, 95, 270, 277] In this method, palladium (Pd) catalysis was employed to construct two C–C bonds by a cascade of Suzuki–Miyaura cross-coupling and direct arylation reactions to form one additional benzene ring. In one of our previous works, we observed that upon variation of the reaction conditions [3+2] annulation with the formation of a five-membered ring is possible.[53] Thus, we conjectured that this method could be extended to synthesize fully conjugated donor–acceptor molecules using very common thiophene-based donor moieties.

Here we report the synthesis of fused D–A and A–D–A conjugated dyes comprising an electron-deficient naphthalene dicarboximide subunit and electron-rich heteroles based on thiophene and indole as donor subunits by Pd-catalyzed [3+2] annulation reaction of bromo-chloro-naphthalene dicarboximide and thiophene or pyrrole boronic esters. Our optimized reaction conditions yielded the desired synthetic targets in moderate to high yields. Systematic investigations of the optical and electrochemical properties of these fused D–A and A–D–A dyes were conducted. These investigations reveal a correlation between the electronic nature of donor moieties and the charge

transfer (CT) characteristic of the dye molecules, which resulted in different absorption properties. This was also supported by theoretical calculations using density functional theory (DFT).

5.2. Results and Discussion

5.2.1. Synthesis

For the synthesis of fused donor–acceptor dyes, 4-bromo-5-chloro-naphthalene dicarboximide **245**[270] and benzothiophene-2-boronic acid (pinacol)ester **244a** were used in a model reaction to optimize the reaction conditions (Table A8, *10.3. Supporting Information Chapter 5*). The highest isolated yield of 86% was obtained when boronic ester **244a** (1.0 equiv) and dihalide **245** (1.1 equiv) were reacted using $[Pd_2(dba)_3 \cdot CHCl_3]$ as the Pd^0 source, P(*m*-tolyl)$_3$ as the ligand, Cs_2CO_3 as the base, and 1-chloronaphthalene as the solvent at 90 °C for 2 h, followed by addition of Bu_4NCl and further reaction at 160 °C for 16 h. We used this two-step approach to conduct Suzuki–Miyaura cross-coupling in the first step at a lower temperature and direct arylation in the second step at a higher temperature. This stepwise approach was shown to be effective to prevent 2-fold Suzuki–Miyaura cross-coupling between **244a** and **245**.[270] Notably, the use of dibromo-naphthalene dicarboximide instead of bromo-chloro-naphthalene dicarboximide **245** resulted in 2-fold Suzuki–Miyaura coupling. Analogous to our previous work,[270] the use of Bu_4NCl as an additive for the direct arylation step was effective for the annulation reaction. The reason might be that the direct arylation step includes a Heck-type mechanism[322] due to the high double bond character of the C_2–C_3 bond of thiophene and pyrrole moieties. The use of other phosphine ligands such as $PCy_3 \cdot HBF_4$, P(*o*-tolyl)$_3$, SPhos, and P(1-Ad)$_2$Bu, which were applied in previous annulation reactions, leads to lower yields of 23–74% (Table A8).

With these optimized reaction conditions in hand, we explored the substrate scope of this Pd-catalyzed [3+2] annulation reaction (Table 5). For a nitrogen analogue of **244a**, the [3+2] annulation reaction using 1-methyl-indol-2-boronic ester (**244b**) afforded the corresponding coupling product **246b** in a high yield of 86%. Using thiophene mono- and diboronic esters **244c** and **244d** as coupling components, the corresponding annulated products **246c** and **246d** could be synthesized in yields of 62% and 63%, respectively. For the reaction of **245** with thiophene monoboronic ester **244c**, a shorter reaction time of 2 h in the second step was used to prevent undesired oxidative homocoupling of the product **246c**.[323-324] For the 2-fold annulation reaction with diboronic ester **244d**, double amounts of dihalide **245**, catalyst, ligand, base, and additive were applied at a higher reaction temperature of 120 °C in the first step.

Table 5. Substrate scope of Pd-catalyzed [3+2] annulation for the synthesis of **246a**–**h**.[a]

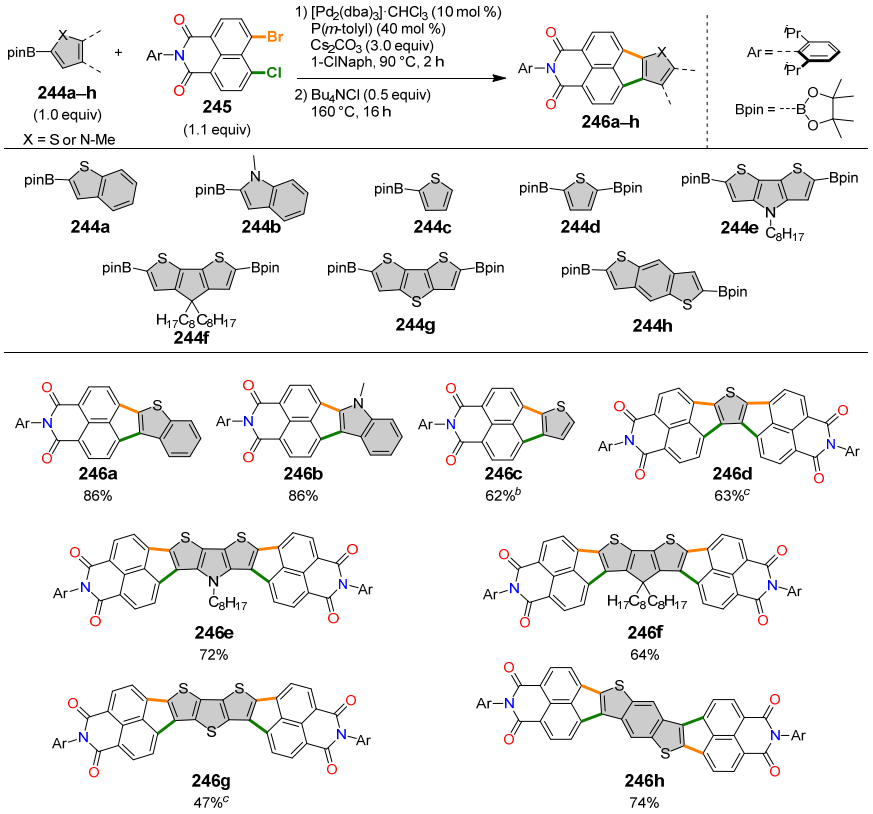

[a]Reaction conditions: **244** (1.0 equiv), **245** (1.1 equiv), $[Pd_2(dba)_3]\cdot CHCl_3$ (10 mol %), P(*m*-tolyl)$_3$ (40 mol %), Cs_2CO_3 (3.0 equiv), Bu_4NCl (0.5 equiv), 1-chloronaphthalene [*c*(**244**) = 0.02–0.03 M] as a solvent. For 2-fold annulated products **246d**–**h**, the amounts of **245**, catalyst, ligand, base, and Bu_4NCl were doubled. [b]The reaction time in the second step was decreased to 2 h. [c]The reaction temperature in the first step was increased to 120 °C. P(*m*-tolyl): tri-*m*-tolylphosphine; dba: dibenzylideneacetone; 1-ClNaph: 1-chloronaphthalene.

To explore the scope of this synthetic method, more extended, electron-rich donor structures were employed, which are part of already applied D–A dyes in the field of organic semiconductor materials.[110, 318] Therefore, we applied the diboronic acid bis(pinacol)esters of dithienopyrrole (**244e**), cyclopentadithiophene (**244f**), and dithienothiophene (**244g**) in this stepwise annulation procedure. Indeed, the respective C_2 symmetric A–D–A dyes could be obtaind in good to moderate yields of 72% (**246e**), 64% (**246f**), and 47% (**246g**). Furthermore, the use of **244h**, in which the outer thiophene units are oppositely oriented, gave the desired centrosymmetric product **246h** in 74% yield. This broad substrate scope shows the versatility of this method for the synthesis of fused D–A and A–D–A chromophores. The new fused D–A and A–D–A dyes are properly characterized by NMR spectroscopy and high-resolution mass spectrometry (details in the *10.3. Supporting Information Chapter 5*[v]).

[v] The *Experimental Section* has been moved to *10.3. Supporting Information Chapter 5*.

5.2.2. Optical Properties

The optical properties of the new annulated D–A and A–D–A dyes **246a**–**h** were investigated by UV–vis absorption spectroscopy in dichloromethane solutions at room temperature (Figure 33 and Table 6). All three monoannulated D–A compounds **246a**–**c** show a broad, weak, and featureless absorption band between 400 and 700 nm (Figure 33a), which can be attributed to an enhanced CT character between the electron-deficient naphthalene dicarboximide groups and the electron-rich heterocycles (*vide infra*). Among these three D–A dyes, the indole derivative **246b** has slightly red-shifted absorption compared to those of benzothiophene and thiophene annulated compounds **246a** and **246c**. The absorption spectra of these compounds are not dominated by their S_0–S_1 transition but by higher-energy absorption bands below 500 nm. Their longest wavelength absorption maxima are located at 418 nm (**246a**, 15500 $M^{-1}cm^{-1}$), 419 nm (**246b**, 13700 $M^{-1}cm^{-1}$), and 404 nm (**246c**, 19800 $M^{-1}cm^{-1}$). It is interesting to note that, in contrast to [3+2] annulated product **246a**, the regioisomeric [3+3] annulated compound phenaleno[1,2,3-*cd*][1]benzothiophene-8,9-dicarboximide reported previously shows a more pronounced vibronic fine structure with an absorption maximum at 497 nm (29500 $M^{-1}cm^{-1}$).[277] A similar trend was observed for [3+2] and [3+3] annulation products of naphthalene dicarboximides and polycyclic aromatic hydrocarbons, which is explained by an increased CT character of the [3+2] annulation products in comparison to [3+3] annulation ones.[53] Due to such CT characteristics, these D–A dyes **246a**–**c** are non-emissive.

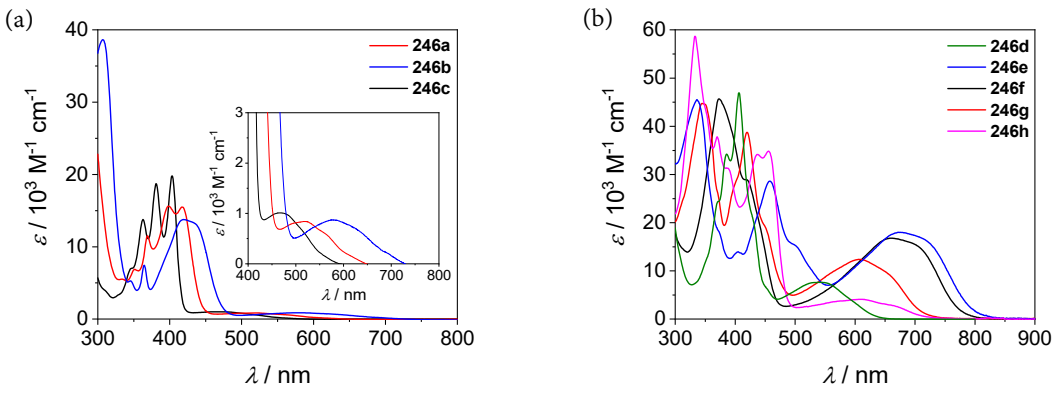

Figure 33. UV–vis absorption spectra of (a) **246a**–**c** and (b) **246d**–**h** in dichloromethane ($c \sim 10^{-5}$ M) at room temperature. The inset in panel (a) shows magnified CT bands of **246a**–**c**.

Compared to monoannulated compounds **246a**–**c**, the 2-fold annulation products **246d**–**h** have higher extinction coefficients for the CT absorption band. Furthermore, π-extended dyes **246e**–**h** even show absorption over the whole visible range while **246e** and **246f** extend into the near-infrared (NIR) region. Similar to the 1-fold annulated compounds, A–D–A dyes are non-emissive. Moreover, all 2-fold-annulated dyes display a broad and structureless absorption band at longer wavelengths. Thereby, the absorbance for **246d** (543 nm, 7600 $M^{-1}cm^{-1}$) and **246h** (608 nm, 4100 $M^{-1}cm^{-1}$) is rather low compared to that of the more red-shifted compounds **246e** (675 nm, 18000

$M^{-1}cm^{-1}$) and **246f** (661 nm, 16800 $M^{-1}cm^{-1}$). Therefore, the optical properties of such fused A–D–A dyes can be tuned by their respective donor/acceptor strength analogous to common A–D–A systems.[325-326]

Table 6. Summary of the optical and redox properties of compounds **246a**–**h**.

	λ_{abs} / nm (ε / $M^{-1}cm^{-1}$)	E_{ox1}	E_{ox2}	E_{red1}	E_{red2}	E_{red3}	E_{red4}	E_{HOMO}	E_{LUMO}
		/ V[a]						/ eV[b]	
246a	418 (15500)	1.17		−1.22	−1.64			−5.97	−3.58
246b	419 (13700)	1.00	1.13	−1.42	−1.88			−5.80	−3.38
246c	404 (19800)	1.28		−1.31	−1.76			−6.08	−3.49
246d	543 (7600)	1.17		−1.16	−1.35	−1.80	−2.20	−5.97	−3.64
246e	675 (18000)	0.55	1.17	−1.21	−1.31	−1.71	−1.92	−5.35	−3.59
246f	661 (16800)	0.62	1.21	−1.23	−1.34	−1.77	−1.98	−5.42	−3.57
246g	606 (12400)	0.82	1.32	−1.19	−1.26	−1.66	−1.84	−5.62	−3.61
246h	608 (4100)	0.84	1.24	−1.18	−1.24	−1.64	−1.80	−5.64	−3.62

[a]Half-wave potentials were determined by cyclic or square wave voltammetry measured in dichloromethane (0.1 M TBAHFP) vs Fc^+/Fc. [b]Calculated using the equations $E_{LUMO} = -[E(M/M^-) + 4.8\ eV]$ and $E_{HOMO} = -[E(M/M^+) + 4.8\ eV]$, assuming that the energy level of Fc^+/Fc with respect to the vacuum level is −4.8 eV.[327]

5.2.3. Electrochemical Properties

The introduction of electron-deficient naphthalene dicarboximide groups into a π-scaffold leads to lowering of LUMO energy levels.[58] Such conjugated molecules exhibit multiple reduction processes, and their electronic properties are of interest for their potential application as n-type semiconductor materials. Therefore, we performed cyclic and square wave voltammetry of **246a**–**h** in dichloromethane solutions with tetrabutylammonium hexafluorophosphate (TBAHFP) as the supporting electrolyte at room temperature using ferrocenium/ferrocene (Fc^+/Fc) coupling as an internal standard. The voltammograms are displayed in Figure A60, and the redox properties are summarized in Table 6 and Figure 34.

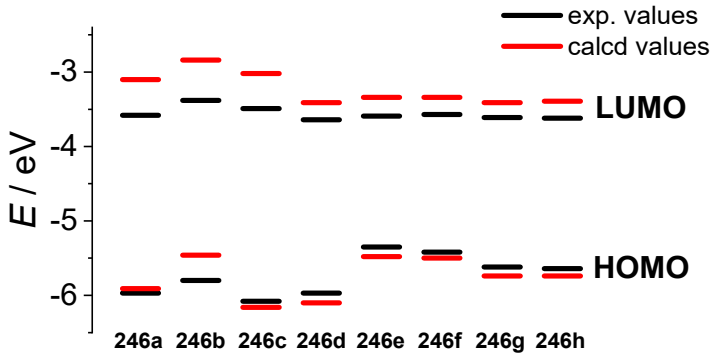

Figure 34. Graphical representation of experimental (black) and calculated (red) HOMO and LUMO energy levels. Experimental values were calculated using the Fc^+/Fc redox couple as reference (−4.8 eV with respect to vacuum).[327]

The 1-fold annulated compounds **246a**–**c** each show two reductions and either one or two oxidations. Their first oxidation processes occur between 1.00 V (**246b**) and 1.28 V (**246c**), among which the one for **246a** (1.17 V) is reversible. The two reversible reduction potentials are in all cases well resolved and range between −1.22 V (**246a**) and −1.42 V (**246b**) for the first reduction process (Figure A60). The first reduction potential for **246a** is higher than that of the regioisomeric [3+3] annulation product phenaleno[1,2,3-*cd*][1]benzothiophene-8,9-dicarboximide (−1.48 V)[277] and a naphthalene annulated product benzo[*j*]fluoranthene-3,4-dicarboximide (−1.31 V).[53] An additional fused naphthalene dicarboximide group significantly increases the reduction potentials as exemplified by the first two reduction potentials of 2-fold annulated thiophene **246d** (E_{red1} = −1.16 V, and E_{red2} = −1.35 V). These are more positive than the corresponding reduction processes of 1-fold annulated thiophene **246c** (E_{red1} = −1.31 V, and E_{red2} = −1.76 V). Two-fold fused dyes **246e**–**h** show four reversible reduction processes and two oxidation potentials. For the latter, the first oxidation potentials differ considerably with values between 0.55 V (**246e**) and 0.84 V (**246h**). In contrast, the difference for the first reduction potentials, which are in all cases close to the second reduction processes, is small [−1.18 V (**246h**) to −1.23 V (**246f**)]. The first reduction potential of the naphthalene dicarboximide-annulated dithienopyrrole A–D–A dye **246e** (E_{red1} = −1.21 V) is significantly higher than those of the corresponding benzothiadiazole-substituted (−1.86 V)[317] and indandione-substituted (−1.52 V)[325] dyes but lower than that of the 3-(dicyanomethylene)-1-indanone-substitued dye (−0.96 V).[325] These electrochemical data indicate that the fused naphthalene dicarboximide unit is a suitable acceptor group for D–A and A–D–A dyes.

5.2.4. Theoretical Calculations

To gain more insights into the electronic and optical properties of the newly synthesized D–A and A–D–A dyes, time-dependent density functional theory [TD-DFT, B3LYP/6-31G(d)] calculations

were performed. The graphical representation of the frontier molecular orbitals (Figure A61) shows a stronger localization of the HOMO wave functions on the electron-rich donors and the LUMOs on the electron-deficient naphthalene dicarboximide unit for the monoannulated compounds. In contrast, the HOMOs and LUMOs of the 2-fold annulated dyes are distributed over donor as well as acceptor moieties. This agrees well with substituted D–A chromophores, which often show a localization of the HOMO wave functions at the electron-rich donor unit and the LUMOs at the electron-deficient acceptor unit and thereby indicate the possibility of CT upon excitation.[317, 328] The computed charge density differences, which describe the change in the static charge distribution upon excitation, reveal a pronounced CT character for the D–A dyes (Figure A62). The CT character can be quantitatively expressed by the charge transfer distance parameter D_{CT},[329] which describes the calculated spatial separation between the barycenters of electron density depletion (donors) and addition (acceptors) regions upon excitation (Figure A62). For the monoannulated systems, the CT length (D_{CT}) is comparable for **246a** (D_{CT} = 2.42 Å) and **246b** (D_{CT} = 2.35 Å) while it is significantly shorter for **246c** (D_{CT} = 1.75 Å). The decrease in D_{CT} for **246c** might be due to smaller size of its donor moiety.

For the 2-fold annulated chromophores, D_{CT} is not a suitable parameter for characterizing CT because of the symmetry and possible multidirectional CT in the A–D–A architecture. Therefore, we computed $\Delta\sigma_{CT}$,[330] which is a measure of the difference between the spread of positive and negative density regions upon excitation (Figure 35). The calculated $\Delta\sigma_{CT}$ supports the experimentally observed absorption behavior for compounds **246e**–**h** with comparable size and symmetry. Within this series, an increased level of CT character leads to weaker and broader absorption in the low-energy region (Figure 33b). The $\Delta\sigma_{CT}$ and extinction coefficient (ε) for **246e** ($\Delta\sigma_{CT}$ = 1.27 Å; ε = 18000 $M^{-1}cm^{-1}$) and **246f** ($\Delta\sigma_{CT}$ = 1.26 Å; ε = 16800 $M^{-1}cm^{-1}$) are rather similar, while more pronounced CT for **246g** ($\Delta\sigma_{CT}$ = 1.36 Å; ε = 12400 $M^{-1}cm^{-1}$) and **246h** ($\Delta\sigma_{CT}$ = 1.64 Å; ε = 4100 $M^{-1}cm^{-1}$) causes a decrease in the extinction coefficient. The bathochromic shift of CT absorption bands corresponds to the strength of electron donors as revealed by the separate frontier molecular orbital calculations of electron donor and naphthalene dicarboximide electron acceptor units. D–A dye **246b** with a higher HOMO energy level shows the most red-shifted band among the monoannulated dyes, while 2-fold annulated dyes **246d**–**h** show a clear red-shift in stronger electron donors [$\lambda_{\mathbf{246e}} > \lambda_{\mathbf{246f}} > \lambda_{\mathbf{246h}} > \lambda_{\mathbf{246g}} > \lambda_{\mathbf{246d}}$ (Figure A63, Figure A64 and Table 6)]. Accordingly, the band gap (Figure 34 and Table 6) of these dyes also corresponds to the strength of electron donor moieties (Figure A63 and Figure A64). For instance, the dithienoindole derivative **246e** has a higher HOMO energy level in comparison to that of the dithienocyclopentadiene derivative **246f** and hence a narrower band gap.

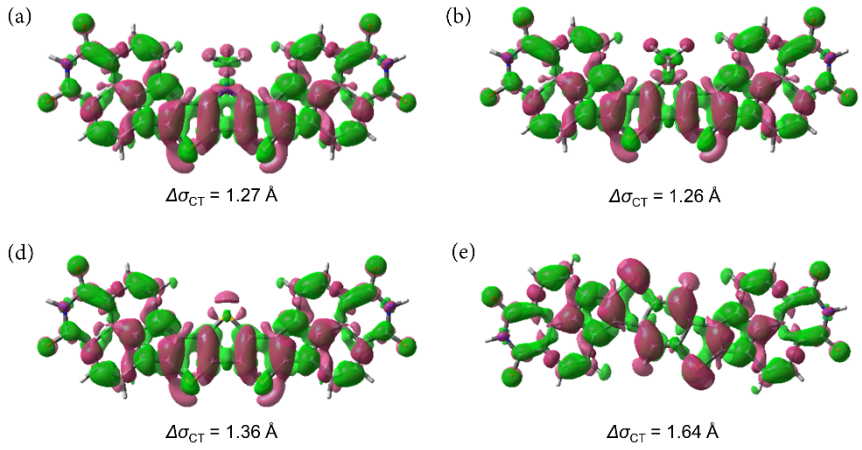

Figure 35. Charge density differences for the S_0–S_1 transition and the respective $\Delta\sigma_{CT}$ for (a) **246e**, (b) **246f**, (c) **246g**, and (d) **246h** calculated by TD-DFT [B3LYP/6-31G(d), isovalue of 0.0004 a.u.]. Red (positive) and green (negative) regions represent decreases and increases in electron density, respectively, upon excitation. For the sake of simplicity, the 2,6-diisopropylphenyl groups were replaced by hydrogens and octyl groups by methyl groups.

Correlation of experimental observation to the calculated charge transfer parameters provides a better depiction regarding the scope of the fused dye systems synthesized by [3+2] annulation reactions. D_{CT} and $\Delta\sigma_{CT}$ give a quantitative measure of CT lengths in D–A and A–D–A dyes, respectively. The experimental charge transfer nature of the synthesized chromophores and the computed distribution of electron density difference upon excitation together provide a way to tune the CT character.

5.3. Conclusion

We have developed a synthetic method for fused D–A and A–D–A dyes. This was achieved by [3+2] 1- and 2-fold annulation, respectively, of naphthalene dicarboximide with various heteroles by palladium catalysis. The new dyes constitute fully annulated donor–acceptor systems and have promising optical and electrochemical properties for potential application as organic semiconductors in photovoltaics. Their LUMO energy levels are similar to each other and lie between −3.62 and −3.38 eV, contrary to their HOMO energy levels that vary between −6.08 and −5.35 eV depending on the nature of the donor moiety. The lowering of LUMO energy levels is stronger than in the cases in which benzothiadiazole, an archetypical electron-withdrawing group for donor–acceptor dyes, is used as the acceptor moiety, demonstrating that annulated naphthalene dicarboximide is a stronger acceptor moiety. The absorption of the dyes can be tuned by using different donor moieties and extended to the NIR range up to 800 nm. These properties of present D–A and A–D–A dyes should be of potential interest as organic materials for field-effect transistors and organic solar cells.

Chapter 6

Base-Assisted Imidization: A Synthetic Method for the Introduction of Bulky Imide Substituents to Control Packing and Optical Properties of Naphthalene and Perylene Imides

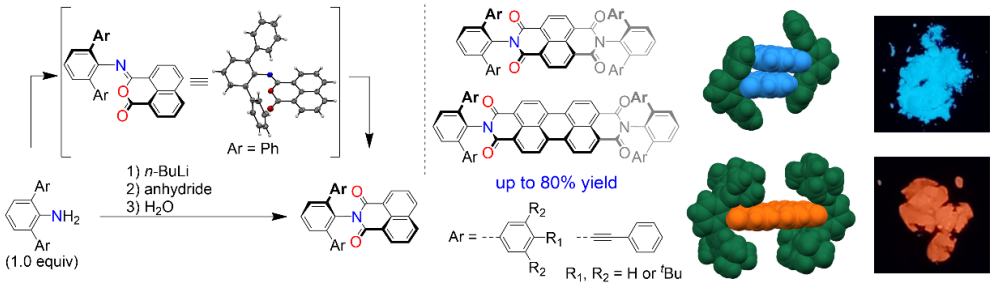

This chapter and the corresponding supporting information (*10.4. Supporting Information Chapter 6*) has been published:

M. Mahl, K. Shoyama, D. Schmidt, A.-M. Krause, F. Würthner, *Angew. Chem. Int. Ed.* **2020**, *59*, 13401–13405; *Angew. Chem.* **2020**, *132*, 13503–13507.

Abstract:[vi] We report the direct imidization of naphthalene and perylene dicarboxylic anhydrides/esters with bulky *ortho*,*ortho*-diaryl- and *ortho*,*ortho*-dialkynylaniline derivatives. This imidization method uses *n*-butyllithium as a strong base to increase the reactivity of bulky amine derivatives, proceeds under mild reaction conditions, requires only stoichiometric amounts of

[vi] Parts of these results have been described in: M. Mahl, Master Thesis, Julius-Maximilians-Universität Würzburg, **2016**.

reactants and gives straightforward access to new sterically crowded rylene dicarboximides. Mechanistic investigations suggest an isoimide as intermediary product, which was converted to the corresponding imide upon addition of an aqueous base. Single-crystal X-ray diffraction analyses reveal dimeric packing motifs for monoimides, while two-side shielded bisimides crystallize in isolated molecules without close π–π-interactions. Spectroscopic investigations disclose the influence of the bulky substituents on the optical properties in the solid state.

6.1. Introduction

Rylene dicarboximides are a subject of intense research for materials scientists owing to their high absorptivities and extraordinary stability.[15, 17-18, 29, 50, 133, 332-333] Originating from this research, rylene dicarboximides are applied as color pigments[332] and fluorescence dyes[15] in market products and investigated heavily for applications in organic electronics and photovoltaics.[18, 333] Due to their strong tendency to aggregate through the π-surface, introduction of bulky substituents to inhibit intermolecular interactions is indispensable for the investigation of their intrinsic molecular properties. In early studies, this was achieved by the introduction of long and branched alkyl chains[130] or aryl substituents such as 2,6-diisopropylphenyl or 2,5-di-*tert*-butylphenyl groups[82, 334] at the imide positions of perylene bis(dicarboximides) (PBIs). Furthermore, by introducing much bulkier aryl groups, such chromophores can crystallize in an isolated packing arrangement, allowing their use as solid-state emitters.[35-36] For PBIs bulky substituents can be introduced either at the bay-positions,[23, 33] *ortho*-positions[34, 335] or the imide-positions.[31-32, 35-36] The last is ideal for preserving the original properties of perylene dyes[35] and allows the introduction of additional substituents at the rylene scaffold to tune the optical and the electronic characteristics.[86] The *N*-substituents of rylene dicarboximides are often introduced by imidization of corresponding rylene dicarboxylic acid anhydride and an excess of amine, typically in the presence of zinc(II) salts, in solvents with high-boiling points at elevated temperatures up to 180 °C.[82] However, such direct introduction of large substituents is hampered by the low reactivity of the amine substrate as already seen in the imidization using 2,4,6-triphenylaniline and perylene bisanhydride, in which even under extremely harsh reaction conditions did not yield the desired product but only decomposition of the anhydride.[31]

Herein, we report the direct synthesis of naphthalene and perylene (dicarboximides) with sterically demanding *ortho*,*ortho*-diarylphenyl or *ortho*,*ortho*-dialkynylphenyl imide groups. Direct imidization was achieved by using stoichiometric amounts of amine and *n*-butyllithium (*n*-BuLi) as a strong base to deprotonate the bulky amine substrate. Crystallographic analyses disclosed the impact of sterically demanding imide-substituents on the packing motifs and elucidated solid-state structure–property relationships.

6.2. Results and Discussion

6.2.1. Synthesis

The reaction of 2,6-bis(3,5-di-*tert*-butylphenyl)aniline (**247d**) as sterically demanding amine and naphthalene-1,8-dicarboxylic anhydride (**248**) was used as a model reaction (Table 7 and Table A9,

10.4. Supporting Information Chapter 6). In the initial investigation, we used lithium diisopropyl amide (LDA) as a base to deprotonate the amine. Thus, as the first step **247d** (1.0 equiv) and LDA (2.0 equiv) were reacted in THF at −78 °C. Subsequently, the mixture was allowed to warm up to room temperature, followed by the addition of **248** (1.0 equiv) and refluxed for 18 h. This one-pot reaction yielded the desired product **252d** only in 2% yield (entry 1). We found that isoimide was formed under comparable conditions and addition of aqueous base was required to convert the isoimide into the corresponding imide (see below). Therefore, with addition of water (5.0 equiv) after 6 h in the second step **252d** was obtained in 42% yield (entry 2).

Table 7. Optimization of the reaction conditions for **252d**.[a]

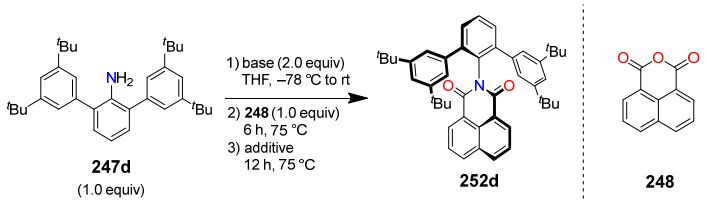

entry	base	additive (equiv)	yield / %[b]
1	LDA	-	2
2	LDA	H_2O (5.0)	42
3	LDA	H_2O (1.0)	18
4	LDA	H_2O (100)	40
5[c]	LDA	H_2O (5.0)	39
6[d]	LDA	H_2O (5.0)	18
7[e]	LDA	H_2O (5.0)	11
8[e]	LDA	-	13
9	P4-*t*-Bu	H_2O (5.0)	63
10	*n*-BuLi	H_2O (5.0)	80
11	*sec*-BuLi	H_2O (5.0)	44
12	*tert*-BuLi	H_2O (5.0)	51

[a]Reaction conditions: **247d** (0.1 mmol), base (2.0 equiv), **248** (1.0 equiv), *c*(**247d**) = 0.07 M. [b]Isolated yields. [c]Addition of water after 12 h of heating. Reaction time 36 h for the third step. [d]Addition of water after 1 h. [e]Use of naphthalene-1,8-dicarboxylic acid dimethyl ester instead of **248**. LDA=lithium diisopropylamide, BuLi = butyllithium, THF = tetrahydrofuran.

In the pursuit of higher product yields, we investigated the amount of water (entries 2–4) as well as the point of addition (entries 5 and 6). Neither a higher loading of water nor longer reaction time before the addition of water lead to significant improvement. The use of the more soluble naphthalene-1,8-dicarboxylic acid dimethyl ester instead of **248** lead with and without the addition of water to decreased but similar yields of 11% and 13%, respectively (entries 7 and 8). These results hint at the formation of isoimide when using the dicarboxylic anhydride **248**, which is

improbable when applying the corresponding methyl ester. Next, we tested different strong bases including superbases[336] and combinations of two bases (entries 9–12, and Table A9). The bulky Schwesinger-base[337] P4-*t*-Bu improved the yield to 63% (entry 9). Moreover, the use of various isomeric butyllithium bases also improved the yield compared to LDA (entrie 10–12). The best yield of 80% was obtained when *n*-BuLi was used as the base (entry 10).

As known from literature, steric restrictions or electronic effects can lead to formation of isoimides instead of imides. These isoimides suffer from low stability and their isolation was scarce.[338-339] Such isoimides can be transformed easily through a rearrangement into the corresponding imides with aqueous acid or base.[338, 340] Therefore, we hypothesized that during the applied reaction conditions, unstable isoimide was formed due to the high steric demand of the 2,6-substituents, which rearranged through the addition of water into the corresponding imide. While in the conducted reactions during the optimization as well as in the substrate scope, no isoimide intermediates were observed, we were able to isolate isoimide **256a** under slightly modified reaction conditions with LDA (1.0 equiv) and no addition of water (Scheme 8). The isoimide structure could be unambiguously confirmed by crystallographic analysis. Isoimide **256a** could be quantitatively transformed under basic conditions in THF (*tert*-BuOK$_{aq}$) into the corresponding imide **252a**. These results support our reaction pathway rationale for the imide formation via an isoimide intermediate when the respective anhydride is used as starting material.

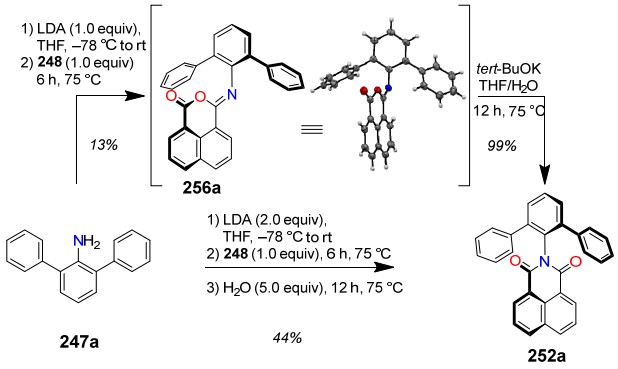

Scheme 8. Reaction pathways towards **252a**.

Using the optimized reaction conditions, we examined the substrate scope of this imidization (Table 8). Sterically demanding aryl amines **247a**–**c** were used for the imidization reaction with naphthalene dicarboxylic anhydride **248**. The respective products **252a**–**c** could be isolated in comparable yields to **252d** for **252a** (71%) and **252c** (65%), but a reduced yield for **252b** (34%). In all reactions most of the remaining amines could be recovered. Furthermore, we tested the more challenging substrate naphthalene bisanhydride **249**. The expected low reactivity due to the close proximity of the bulky substituents in the desired products was reflected in the reaction yields. While **253a** could be isolated in a good yield of 49%, the yields for bulkier substituents in **253b**–**d**

decreased to 24–36%. To our disappointment, the imidization with perylene mono and bisanhydrides afforded only starting material or traces of products, which may be due to their lower solubility. This could be overcome by the use of corresponding perylene methyl esters[341] **250** and **251** (Table A10) with an increased reaction temperature of 90 °C (pressure-stable Schlenk-tube) and a longer reaction time of 72 h without the need of water addition. With these modifications new perylene mono(dicarboximides) **254a**–**d** were obtained in moderate yields of 23–42%. Two-fold imidization of perylene tetramethyl ester with **247a**–**d** yielded the respective products in 12–21%. All dicarboximides were fully characterized by ^{1}H and ^{13}C NMR spectroscopy as well as high-resolution mass spectrometry (*10.4. Supporting Information Chapter 6*).

Table 8. Substrate scope of the *n*-butyllithium-mediated imidization reaction (details in *10.4. Supporting Information Chapter 6*).

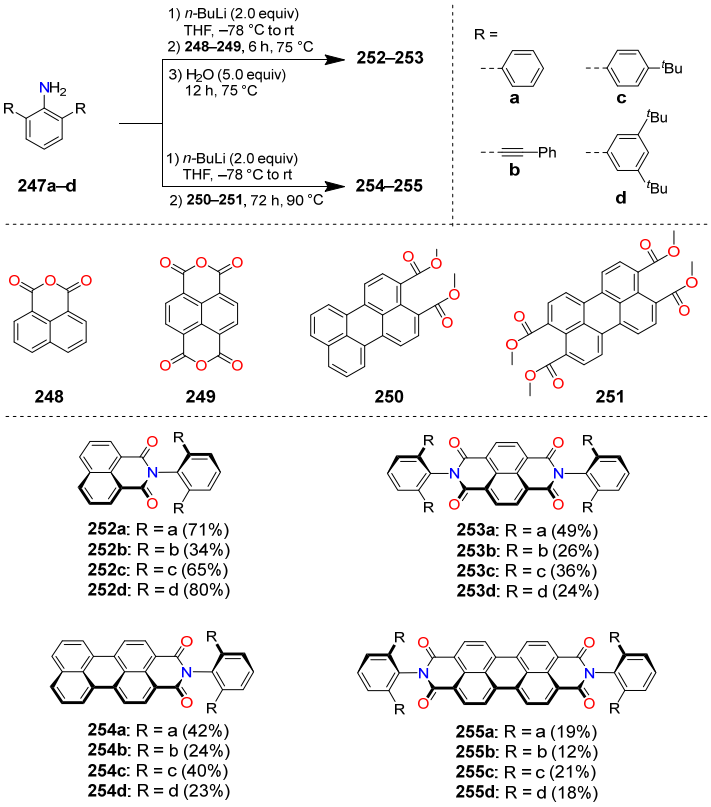

6.2.2. Crystallographic Analysis[vii]

X-ray crystallography was used to elucidate the influence of bulky imide substituents on the solid-state packing. Single crystals suitable for X-ray diffraction were grown by slow diffusion of methanol or *n*-hexane into dichloromethane or chloroform solutions and were obtained for **252a**–**d**, **254a**, **254d**, **255b** and **255d** (Figure 36, Figure 37, and the *10.4. Supporting Information Chapter 6*). For the mono(dicarboximides) dimer packing motifs are observed. Within the series of naphthalene mono(dicarboximides) **252a**–**d** the naphthalene units are more displaced and hence had decreased π–π-contact with increasing bulkiness of the imide substituent (Figure 36). As we will show later, this variation in packing arrangement has a pronounced impact on the optical properties in the solid-state.[342]

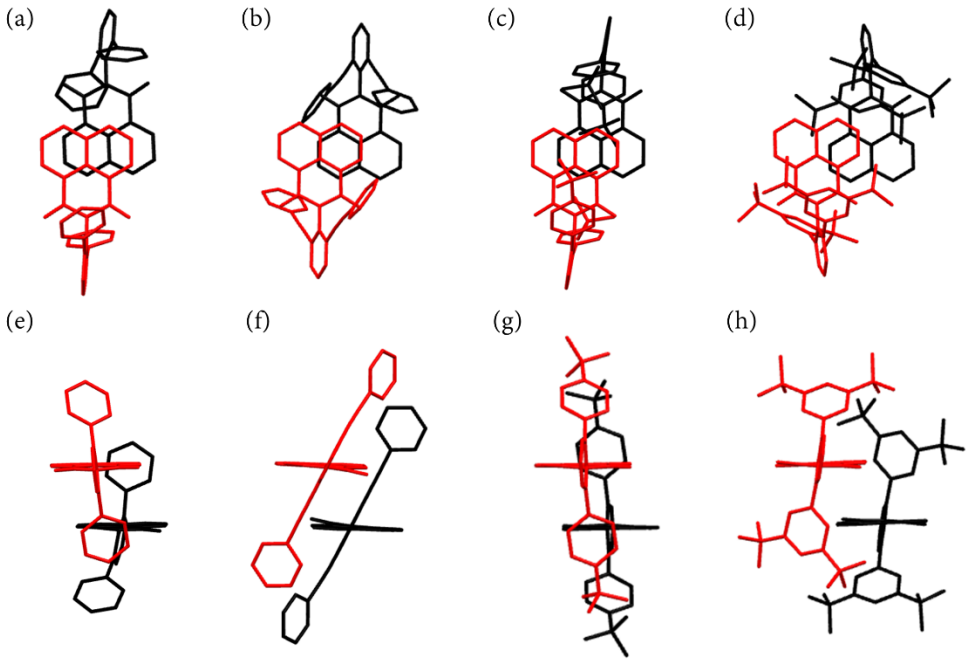

Figure 36. Crystal structures of (a,e) **252a**, (b,f) **252b**, (c,g) **252c**, (d,h) **252d** as obtained by single-crystal X-ray diffraction analysis.

As shown in Figure 37a,b similar packing motifs are observed for perylene monoimide **254d**, however, with a much larger π–π-contact surface due to the enlarged perylene π-scaffold. In contrast, the crystal structures of perylene bis(dicarboximides) **255b** and **255d** show no direct π–π-contact for the perylene cores (Figure 37c,d and Figure A98), which can be attributed to bilateral shielding with large substituents and is in accordance with the results of Wong and co-workers.[35]

[vii] Supplementary crystallographic data is provided free of charge *via* the joint Cambridge Crystallographic Data Centre and FIZ Karlsruhe: www.ccdc.cam.uk/structures. CCDC Deposition Numbers: 1988196 (**252a**), 1988190 (**252b**), 1988198 (**252c**), 1988197 (**252d**), 1988191 (**254a**), 1988194 (**254d**), 1988192 (**255b**), 1988195 (**255d**) and 1988193 (**256a**).

Therefore, bulky imide-substituents are a suitable tool to effectively control and prevent close π–π-interactions.

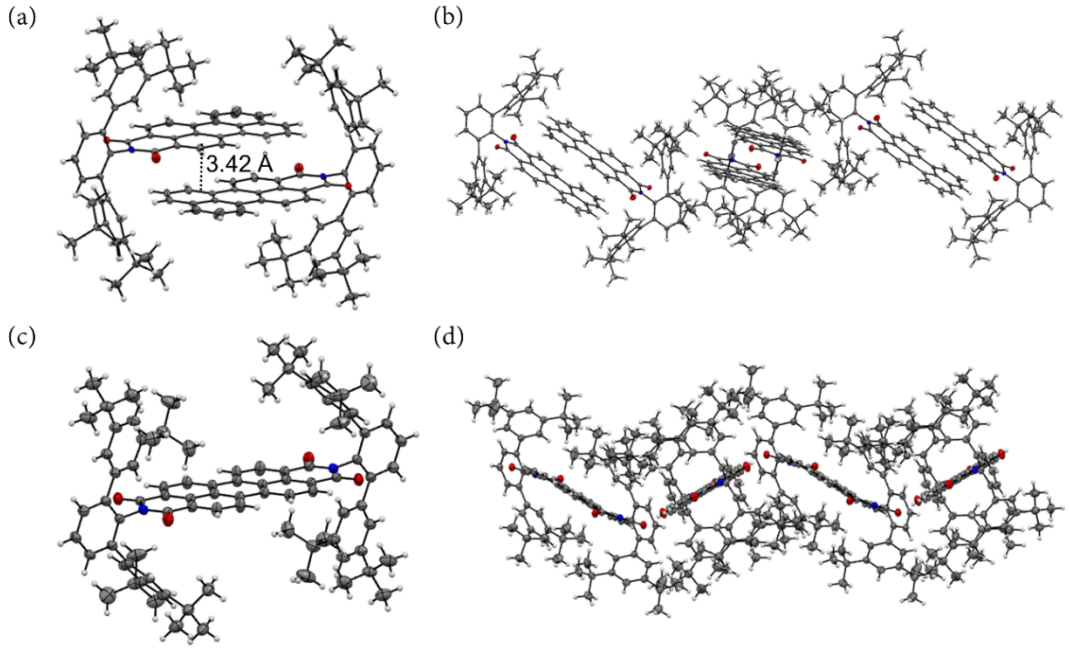

Figure 37. Crystal structures of (a,b) **254d** and (c,d) **255d**. ORTEP drawing at 50 % probability for thermal ellipsoids.

6.2.3. Optical Properties

The UV–vis absorption and fluorescence emission spectra of the imides **252**–**255** in chloroform solution show the characteristic vibronic patterns of the monomeric dyes (Figure A101–Figure A104, Table A20–Table A23).[15, 333] While perylene imides **254** and **255** are highly fluorescent with quantum yields close to unity, naphthalene imides **252** and **253** show negligible fluorescence in solution (Φ_{fl} <0.5%), which is due to deactivation through close triplet states.[343-344]

Pronounced effects of the bulky *N*-substituents were observed in the solid-state optical properties. The absorption spectra of spin-coated thin-films of the imides largely resemble their respective solution spectra (Figure A105 and Figure A106, Table A24). The vibronic structure becomes sharper with increased bulkiness of the substituents. This suggests a more effective shielding of the rylene cores and less intermolecular couplings.[345] While naphthalene bis(dicarboximides) **253** are non-emissive in the solid-state, the respective mono(dicarboximides) **252** show solid-state luminescence (Figure 38) with remarkably high quantum yields up to 18% (**252a**) (Table 9). Interestingly, the observed emission spectra are highly dependent on the nature of the imide substituent. While **252a** and **252c** show a rather broad and structureless emission with a pronounced Stokes shift and a cyan hue, **252d** with the most steric demanding imide substituent shows a sharp

emission profile centered at 405 nm, resulting in a dark-blue fluorescence. The luminescence color of **252b** is orange due to two emission bands at 415 and 582 nm. We attribute the pronounced Stokes shift observed for **252a** and **252c** to a relaxation into excimers which originate from the "preformed"[346] dimers in the solid-state (Figure 36). It is known that such "excimerization" is supported by nearly parallel alignments[347-348] and a significant π–π-contact surface as found in the crystals of these dyes (Figure 36a,c).[349] It is interesting to note that this relaxation process of photoexcited **252a**,**c** into excimers affords an increase of the fluorescence quantum yield by a factor greater than 30 for **252a** compared to the monomeric state in solution. Similar observations were made for naphthalene dicarboximide-based systems.[350-351] This formation of excimers is further supported by strongly increased fluorescence lifetimes up to 30.5 ns (**252a**) in the solid state (Table A26) compared to monomeric naphthalene monodicarboximides in solution reported in the literature (typically <0.5 ns).[344, 348]

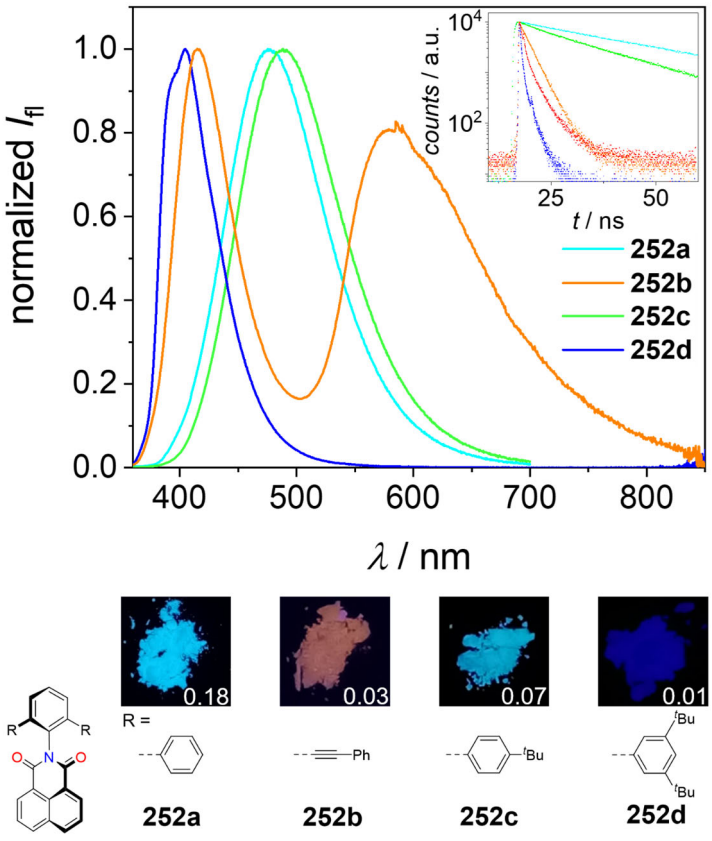

Figure 38. Solid-state (powder) fluorescence spectra of **252a**–**d** (λ_{ex} = 300 nm). Inset: Excerpts of lifetime-decays of **252a** (cyano), **252b** (orange: λ_{det} = 416 nm; red: λ_{det} = 578 nm), **252c** (green) and **252d** (blue). Values in photographs are respective effective Φ_{fl}.

In contrast, the structured luminescence of **252d** at shorter wavelengths and with short lifetimes can be attributed to an emission from a monomeric species, which is attributed to the rather small overlap of the naphthalimide moieties in the solid state (Figure 36d). To elucidate the origin of the more complicated dual emission of **252b**, we performed additional excitation-dependent

fluorescence and excitation spectroscopy (Figure A108). These studies revealed two independent radiative processes (Table A26). We assume that the fluorescence located at longer wavelengths (around 582 nm) originates from an intramolecular charge-transfer state (CT). Indeed, a weak CT band is already observed in the UV–vis spectra of **252b** for dissolved dye monomers in solution as well as in the solid state (Figure A101 and Figure A105b). Accordingly, these absorption and fluorescence bands are attributed to the interaction between electron-rich phenyleneethynylene imide substituents and electron-poor naphthalene dicarboximide moiety. An excitation in the CT-region substantially deactivates the first emission maxima attributable to the locally excited state of the naphthalene imide, supporting this assumption (Figure A108b).

Table 9. Comparison of fluorescence maxima and fluorescence quantum yields in chloroform solution and bulk powder samples of **252** and **255**.

	$\lambda_{em,\,max}$ ($CHCl_3$) / nm	$\lambda_{em,\,max}$ (powder) / nm	Φ_{fl} ($CHCl_3$) / %[a]	Φ_{fl} (powder) / %[b]
252a	-	478	< 0.5	18
252b	-	415, 582	< 0.5	3
252c	-	490	< 0.5	7
252d	-	405	< 0.5	1
255a	535, 577, 627	670	95 ± 2	5
255b	534, 576, 624	653	96 ± 1	3
255c	534, 577, 626	670	97 ± 1	5
255d	533, 577, 625	585, 640	93 ± 2	17

[a]Fluorescence quantum yields were determined using the relative method (A<0.05) and *N*,*N*′-bis(2,6-diisopropylphenyl)perylene-3,4:9,10-bis(dicarboximide) (Φ_{fl} ($CHCl_3$) = 1.00) as reference. [b]Effective fluorescence quantum yields of bulk powder samples were determined using an integration sphere and represent the lower limit of the intrinsic fluorescence quantum yields due to reabsorption effects.

Intense solid-state fluorescence was also observed for perylene bis(dicarboximides) **255** (Table 9) with quantum yields ranging between 3% (**255b**) and 17% (**255d**). We note that these solid-state fluorescence spectra are likely affected by reabsorption losses, in particular for the (0,0) fluorescence band, which is known for dyes with small Stokes shifts and strong absorbance. Therefore, the obtained effective fluorescence quantum yields represent the lower limit of the intrinsic quantum yields.[33] The strongest fluorescent PBI **255d** exhibits also the most pronounced vibronic progression in its solid-state fluorescence spectrum (Figure A107). This can be ascribed to emission from isolated monomer-like species due to the largest steric demand of the imide substituent, thereby impeding any π–π-contact between the perylene bisimide π-scaffolds of neighbouring dyes (Figure 37). In contrast, perylene mono(dicarboximides) **254** are either non-emissive (**254a** and **254b**) or only weakly fluorescent (quantum yields of 1% and 2% for **254c** and **254d**, respectively) in the solid state (Table A24). This can be attributed to an insufficient shielding

of the extended π-surfaces (Figure 37, Figure A96b and Figure A97b) whose contact area is quite extended and enables relaxation pathways into excimers[352] or other non-emissive excited states.[353]

6.3. Conclusion

In summary, we described for the first time a direct one-pot synthetic method for naphthalene and perylene dicarboximides bearing bulky imide substituents. With the use of *n*-BuLi as a strong base the low reactivity of the bulky amine substrates could be overcome. When dicarboxylic anhydrides are applied as the starting material, we propose a reaction pathway *via* an isoimide–imide rearrangement induced by the addition of water. This hypothesis is supported by the isolation of an isoimide and its subsequent transformation to the respective imide. In comparison to the typically quite harsh conditions for imidizations, the reaction proceeds under mild conditions and only stoichiometric amounts of starting materials are needed. A broad substrate scope showed the versatility of the new method. The new imide molecules reveal highly *N*-substituent-dependent emission properties in the solid-state, which originates from subtle differences in the packing arrangement as revealed by crystallographic analyses. This demonstrates the utility of sterically demanding imide substituents to control the solid-state properties of this class of rylene imide dyes. The application of these and other sterically demanding imide substituents for solid-state emitters,[33, 35] in solar light concentrators[36, 334] and in photonic devices[23, 354] is expected. We further expect that our new method might be applicable for the functionalization with larger dendrons for solubilization of theses dyes in water,[133] for example, through click-chemistry of alkyne-containing moieties.

Chapter 7

A Capped Nanographene as Supramolecular Host for the Complexation of Large Polyaromatics

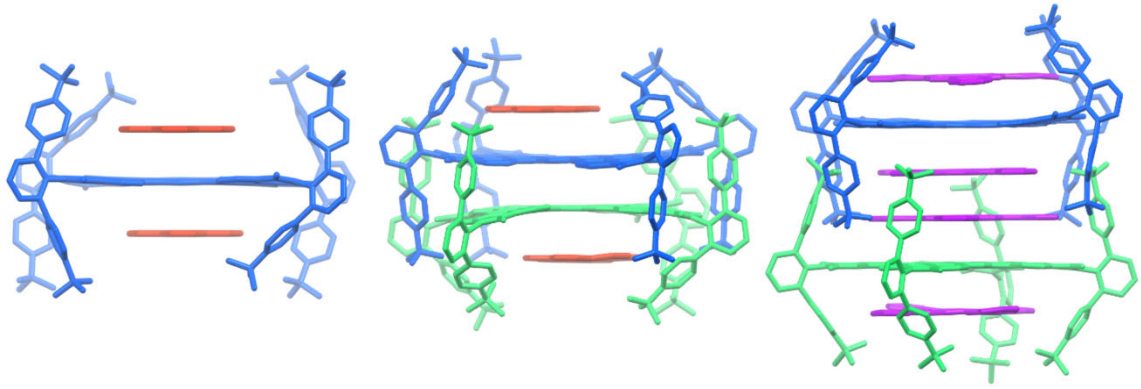

Abstract:[viii,ix] The non-covalent interaction of host and guest molecules in supramolecular chemistry leads to fascinating and stunning complex structures, which are not only interesting in terms of intermolecular interactions, recognition and assembly but also for the construction of (extended) supramolecules based on small units. Thereby, available host designs are rather limited e.g. macrocycles, tweezers or cage compounds and there is a lack of new design principles of host structures. Here, we devised a novel, ditopic host structure based on an extended nanographene, which is equipped with four bulky imide substituents at the periphery to build up two molecular cavities. These allow the binding of smaller and enlarged polyaromatics up to the size of poorly soluble ovalene, hexabenzocoronene and pristine phthalocyanine in solution. The complexations could be followed by optical and NMR spectroscopy as well as isothermal titration calorimetry and are supported by DFT calculations. Furthermore, crystallographic analysis disclosed highly interesting molecular arrangements in the solid-state.

[viii] The following group members contributed to this chapter: Dr. Kazutaka Shoyama and Ana-Maria Krause conducted the crystallographic measurements and analysis. Niyas Mundakkamattathil Abdul Salam performed the theoretical calculations and grew two of the co-crystals for crystallographic analysis.
[ix] Synthesis of compound **259** using other reaction conditions has been described in: M. Mahl, Master Thesis, Julius-Maximilians-Universität Würzburg, **2016**.

7.1. Introduction

The concept of host–guest chemistry is a cornerstone in chemistry and biology due to the importance for molecular recognition, (enzymatic) catalysis and self-organization of matter and therefore is continuously aspiring towards new developments.[62, 66] Moreover, the weak intermolecular interactions between host and guest can lead to superior optical, electronic as well as material properties, which urge the application in (supramolecular) material science.[68, 171-172, 355-356] For these purposes, supramolecular chemists have developed precisely and thoroughly designed host systems for the uptake of various guest molecules (Figure 39a–c).[64, 357] Such host structures include the initial works from Pedersen[358] with his famous crown ethers for cation recognition, Crams[359] carcerands for the permeant guest encapsulation or the highly selective cryptands from Lehn.[206] In the last decades, tailor-made and more complex host-systems were developed for the precise complexation of several guest molecules, like molecular tweezer/clips[73-74, 242] and more recently nanohoops,[76] which are both ideal for the encapsulation of spherical aromatic guests e.g. fullerenes. In contrast, the complexation of planar polycyclic aromatic hydrocarbons (PAHs) typically relies on cyclophanes and macrocycles[71, 185] or molecular cage structures[75, 183] as host frameworks. These systems often have an intricate design principle and suffer from linear multi-step synthesis. Furthermore, these scaffolds often have a rather rigid structure for the construction of a suitable cavity and to facilitate strong binding, which limits the size of guest molecules.[71] Therefore, the recognition of small polycyclic aromatic hydrocarbons (PAHs) up to the size of coronene is well-studied due to suitable binding sites as well as sufficient solubility of these guests. However, the encapsulation of larger polyaromatics like hexabenzocoronene or even pigments e.g. phthalocyanines are scarce due to insufficient solubility of such compounds as well as often rather small host cavities.[360-361] The association with such enlarged guests often requires additional solubilizing groups at the guest peripheries,[196, 361] the interplay of an undefined number of host molecules[360, 362-364] or is only achieved in stoichiometric ratios[360, 365-367] of host and guest, while the latter two prohibits the possibility of detailed host–guest studies.

In contrast to such defined host structures, extended π-scaffolds like carbon nanotubes[368] or graphene sheets[369-370] can also be utilized as hosts for the non-covalent assembly with (enlarged) guest molecules. Hereby, the interactions with the guests can be used to tune and modify the properties of the blank carbon allotropes, while these lead only to rather weak association due to the lack of strong binding of the guest molecules. In addition, guests need often to be equipped with anchoring groups[371-372] like pyrenes. Therefore, the complexation event is hard to localize and the number of interacting guest molecules is difficult to determine. On the other hand, the use of graphene cut-outs – nanographenes – is well-established for the defined complexation in the solid-state. Thereby, the complex formation is often driven by dispersion forces due to the extended π-surface of the host structures as well as donor–acceptor interactions and such complexes can be

utilized in supramolecular organic materials.[174, 373-374] However, these systems are rarely used for the complexation in solution, which might be due to weak binding affinities and/or solubility issues.[181-182]

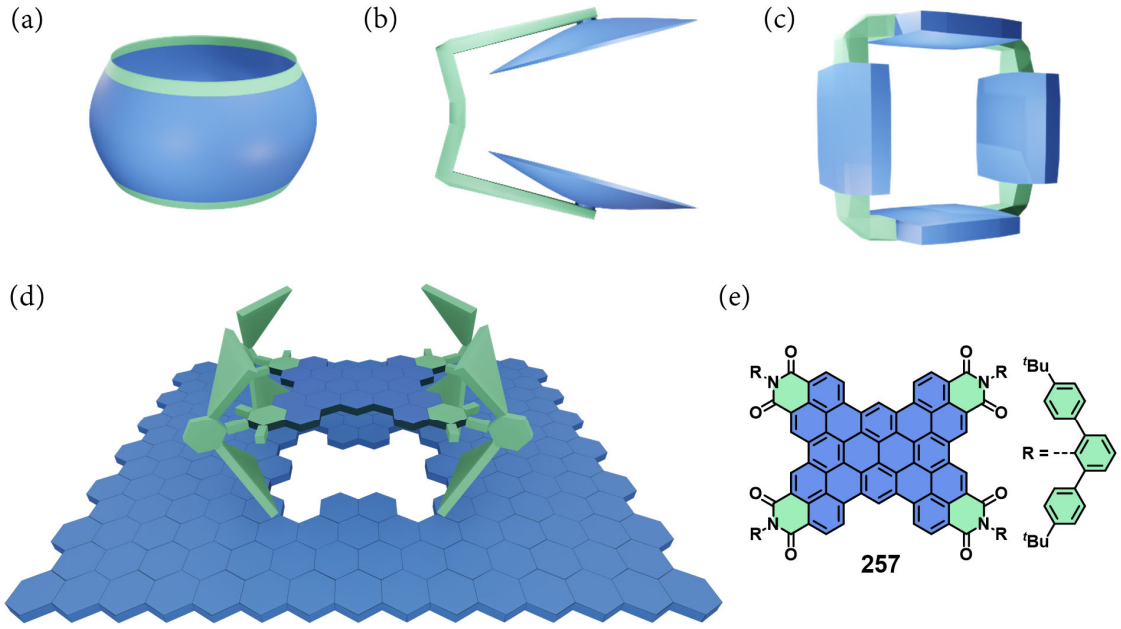

Figure 39. Schematic representation of commonly used host structures and nanographene **257**. Graphical representation of (a) nanohoop, (b) tweezer and (c) macrocyclic host structures. (d) Design-principle and (e) chemical structure of nanographene host **257**.

Here we use a flexible and electron-poor nanographene host (**257**), which combines the aspects of defined molecular cavities and an extended π-surface for the binding of PAH guest molecules (Figure 39d,e). For this purpose, we used our recently developed electron-poor nanographene[58] scaffold, consisting of 64 sp^2-hybridized carbon atoms and equipped with four imide groups at the periphery, as initial point for the design of a new ditopic host platform. Therefore, we introduced bulky substituents in the imide positions, which should not only provide a good solubility due to prevention of close π–π-interactions,[35, 331] but also for the construction of two, one above and one below the π-surface, molecular cavities. These voids should be capable in the complexation of aromatic guests in solution, while the imide substituents additionally stabilize and support the binding with supplementary intermolecular interactions.

The desired nanographene host **257** could be synthesized in a convergent strategy and subsequently the complexation capabilities with various PAHs were investigated. The enlarged aromatic surface of **257** allowed the association with a broad variety of PAHs, including smaller and larger ones. Hereby, the virtually insoluble ovalene as well as hexabenzocoronene are solubilized upon complexation. This effect allowed also the investigation of the pigment phthalocyanine (*Pigment Blue 16*) as guest and lead – due to perfect shape complementary – to high association constants.

Detailed investigations disclose the composition of the involved intermolecular interactions, gave insights into the cooperativity of the stepwise binding events. In addition, crystallographic analysis confirmed not only the expected inclusion of two guest molecules by the nanographene host, but was also used to indirectly isolate the 1:1 intermediate complex as 2:2 supramolecule.

7.2. Results and Discussion

7.2.1. Synthesis

The nanographene **257** was synthesized in a straightforward palladium-catalyzed annulation cascade reaction starting from pyrene tetraboronic ester **260** and dibromo-functionalized naphthalene dicarboximide **259** (Figure 40a). The required dicarboximide **259** could be synthesized in 38% yield by using our recently introduced *n*-butyllithium mediated method for the direct imidization with sterically demanding *ortho*,*ortho*-substituted aniline derivatives.[331] Notably, a dehalogenation of the naphthalene scaffold was not observed. The obtained naphthalene imide was then subjected to the reaction with **260** under optimized annulation reaction conditions[277] in a one-pot reaction to yield the desired nanographene in a high yield of 22%. Hereby, the catalyst loading was reduced 2.5 times compared to the initial reaction conditions reported by the Seifert *et al*.[58] The synthesized nanographene was fully characterized by NMR spectroscopy and mass spectrometry (*10.5. Supporting Information Chapter 7*).

The extended structure of **257** was confirmed by single crystal X-ray analysis (Figure 40b–d and Figure A176). Hereby, three crystallographic independent molecules with strongly different degrees of distortion of the π-scaffolds could be resolved. These are reflected not only in the expected planar geometry but also in rather unusual "s-shaped" and curved structures. These different structures disclose the flexibility of the enlarged nanographene scaffold, which should be beneficial for the capturing of guest molecules. Furthermore, the individual nanographene surfaces have no direct π-contact verifying the concept of bulky imide substituents[35, 331] to prevent close π–π-interactions. Absorption and fluorescence spectroscopy in chloroform solutions revealed a high tinctorial strength (ε = 163400 $M^{-1}cm^{-1}$ (λ_{abs} = 585 nm), ε = 319900 $M^{-1}cm^{-1}$ (λ_{abs} = 490 nm)) and strong emission (Φ_{fl} = 0.68 (λ_{em} = 604 nm)) of **257**, which are comparable to the nanographene with the much smaller diisopropylphenyl imide substituents[58] and disclose the expected negligible influence of the imide substituents, similar as known for rylene bisdicarboximides[16, 87] (Figure A165a and Table A27, *10.5. Supporting Information Chapter 7*). Furthermore, cyclic and differential pulse voltammetry revealed five reduction processes, showcasing the strong electron-deficient character of **257** (Figure A165b and Table A28).

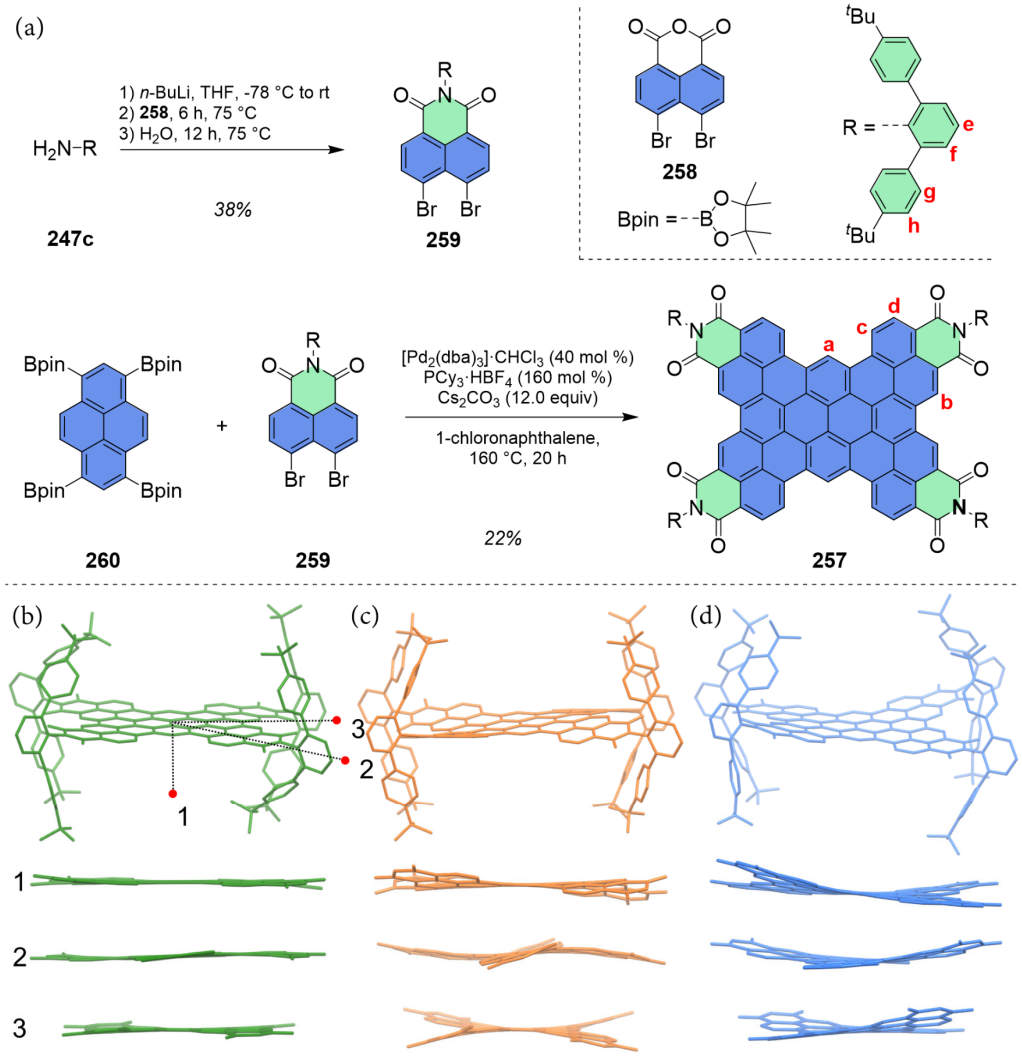

Figure 40. Synthesis and molecular structure as obtained from single crystal diffraction of **257**. (a) Synthetic route towards nanographene **257**. (b-d) The three crystallographic independent structures of **257** as obtained by single crystal X-ray diffraction (top) and three different views on the nanographene core without the imide substituents (bottom). Hydrogens are omitted for clarity.

7.2.2. Host–Guest Studies

We were then interest in the complexation capabilities of **257**. For this purpose, we used for our initial studies the frequently[193, 219, 375-376] applied PAH coronene as a model substrate. Due to the strong and distinct absorbance of **257** in solution (Figure A165a), we utilized UV–vis absorption spectroscopy and constant host titration experiments for following the binding event (c(**257**) = $6.0 \cdot 10^{-6}$ M, 295 K, details *10.5. Supporting Information Chapter 7*). Notably, our study is performed in chloroform, which is the best solvent for aromatic molecules and therefore should lead to the smallest binding constants compared to other solvents.[131] The addition of coronene induced significant changes in the absorption spectrum of **257** (Figure 41b). Thereby, a

bathochromically shifted band is observed, which can be attributed to a charge-transfer transition originating from the rather electron-rich coronene as donor and electron-deficient **257** as acceptor. By applying global-fit analysis with a 1:2-binding model[377-378] of host to guest (*vide infra*), the obtained data could give the corresponding binding constants K_1 and K_2 (Table 10). The values obtained, $K_1 = (2.73 \pm 0.01) \cdot 10^5$ M^{-1} and $K_2 = (6.14 \pm 0.04) \cdot 10^4$ M^{-1}, are remarkable high, since other host systems typically use rigid cyclic structures for an efficient encapsulation, which rely on interactions with both π-surfaces of the guest by the macrocyclic effect.[170]

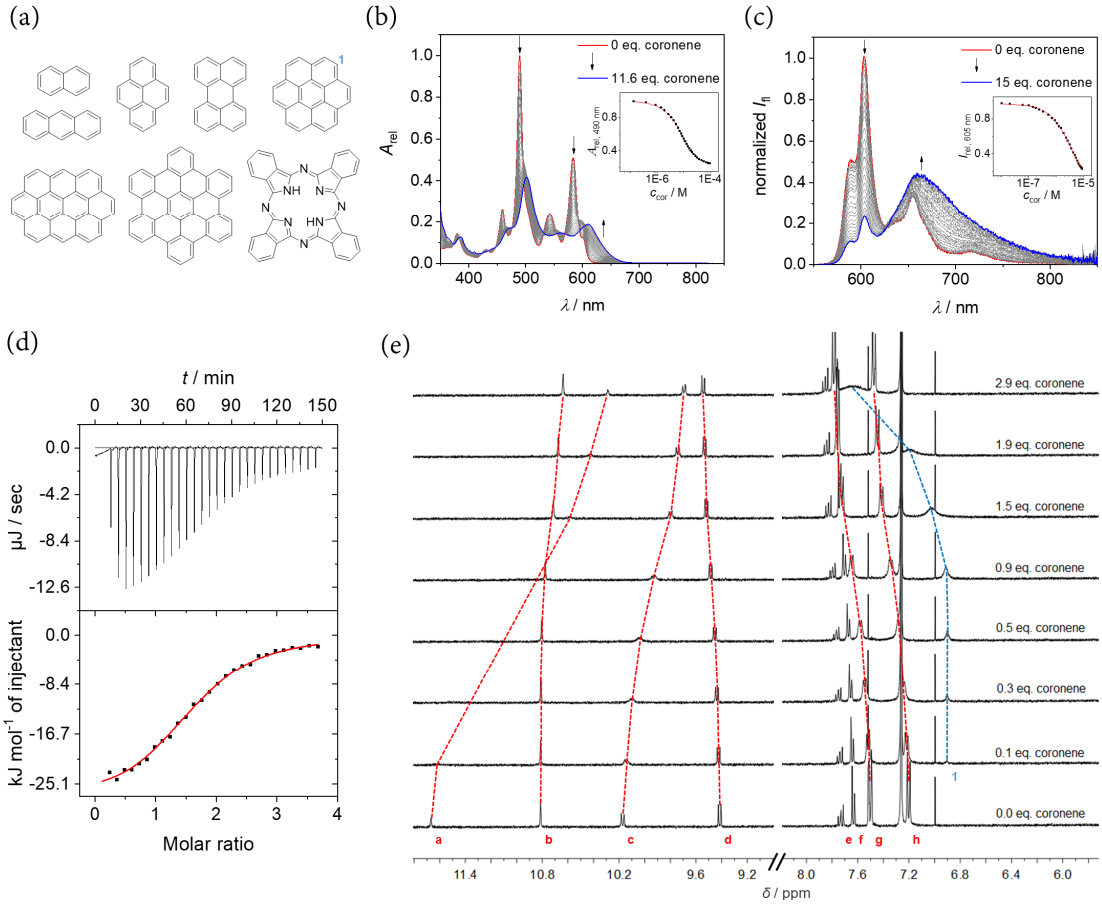

Figure 41. Applied guest molecules and exemplary complexation experiments of host **257**. (a) Structures of guest molecules naphthalene, anthracene, pyrene, perylene, coronene, ovalene, hexabenzocoronene and phthalocyanine. (b) UV–vis absorption ($CHCl_3$, c(**257**) = $6.0 \cdot 10^{-6}$ M, 295 K), (c) fluorescence ($CHCl_3$, c(**257**) = $6.0 \cdot 10^{-7}$ M, 295 K), (d) isothermal titration calorimetry ($CHCl_3$, c(**257**) = $7.0 \cdot 10^{-4}$ M, 298 K) and ^{1}H NMR ($CDCl_3$, c(**257**) = $1.0 \cdot 10^{-4}$ M, 295 K) titration experiment of host **257** with coronene (assignment of protons for **257** see Figure 40a and for coronene Figure 41a).

Next, the strong emission of host **257** (Φ_{fl} ($CHCl_3$) = 0.68) allowed us the investigations of the complex formation *via* fluorescence titration experiments (Figure 41c), for which we used more diluted conditions to prevent reabsorption effects ($CHCl_3$, c(**257**) = $6.0 \cdot 10^{-7}$ M, 295 K). The titration with coronene diminished the main emission band located at λ_{max} = 604 nm of **257**, while a new redshifted and broad band rises. We attribute this band to an exciplex-like emission, which is known to have in some cases a pronounced charge-transfer character.[379-380] This assumption is

supported by a characteristic prolonged lifetime[346, 352] (**257**: τ = 12.0 ns; complex: **257** with coronene τ = 17.3 ns, Figure A170c and Table A32). In addition, detailed temperature-dependent fluorescence studies of a mixture of **257** and coronene further disclosed the involvement of two contrary processes due to opposing temperature response (Figure A171). While the intensity of the band at 604 nm (free host) rises at elevated temperature and hints to a static quenching[346] through complex formation of photo-excited **257** (classical exiplex), the intensity of the band at 677 nm is reduced at higher temperatures and therefore indicates an emission from the pre-assembled complex between **257** and coronene in the ground state. In addition to these findings, the determined binding constants of the fluorescence titration experiments are with $K_1 = (2.92 \pm 0.01)\cdot10^5\ M^{-1}$ and $K_2 = (7.09 \pm 0.14)\cdot10^4\ M^{-1}$ in accordance with the values obtained by the UV–vis experiment, thereby demonstrating the reliability of the chosen techniques (Table 10 and Table A31).

To gain further insights, we conducted a ^{1}H NMR titration experiment ($CDCl_3$, c(**257**) = $1.0\cdot10^{-4}$ M, 295 K) with coronene, in which due to fast exchange averaged signals for **257**, coronene and the complex are observed (Figure 41e and Figure A172). The complexation lead to distinct shifts of most of the signals of **257**, while the single coronene signal is strongly affected by an upfield shift due to shielding effects. The proton signals of the nanographene core (protons: *a–d*; assignment: Figure 40a) are much more shifted upon complexation than the protons of the imide substituents (protons: *e–h*) indicating main interactions derived from the π-surfaces of host and guest. The obtained binding constants ($K_1 = (3.07 \pm 0.72)\cdot10^5\ M^{-1}$ and $K_2 = (4.31 \pm 0.03)\cdot10^4\ M^{-1}$) match those from UV–vis and fluorescence experiments (Table A29 and Figure A173).

For clarification of the stoichiometry, we used low temperature ^{1}H NMR spectroscopy (CD_2Cl_2, 194 K) to reach the slow exchange region and obtain the signals for complexed and free coronene (Figure A174). Their integral-ratio gave direct access to the stoichiometry of host and guest. Indeed, the conducted experiment confirmed the 1:2 stoichiometry, which corroborates the applied 1:2 binding model. In addition, a DOSY measurement confirmed the size of the 1:2 complexes and excluded larger assembled structures in solution (Figure A175). Further, a low temperature ^{1}H NMR titration experiment gave insights into the binding event (Figure 42). Upon addition of coronene a stepwise binding to the nanographene can be observed. First, a 1:1 host–guest complex with reduced symmetry is formed which can be easily seen by a splitting of the signals from the *tert*-butyl groups of **257**. Second, upon further addition of coronene the signals of the 1:1 complex vanished and a 1:2 supramolecule with higher symmetry is formed. The complexation was completed after addition of two equivalents of coronene and further coronene led to no changes. This experiment additionally reflect the (slight) negative cooperativity for the guest coronene due to the favourable formation of a 1:1 complex over the 1:2 complex in the presence of less than two equivalents coronene.

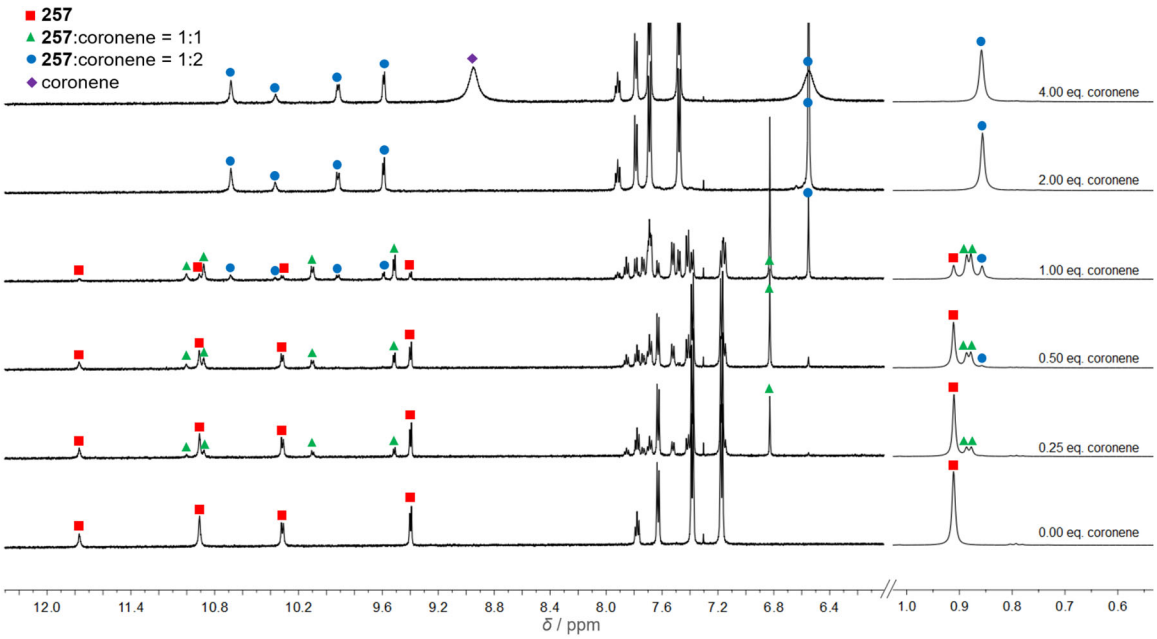

Figure 42. Low-temperature ^{1}H NMR titration experiment. Excerpts of ^{1}H NMR (600 MHz, CD_2Cl_2, 194 K) titration experiment of **257** and coronene (c(**257**) = $1.0 \cdot 10^{-4}$ M) showing the stepwise binding pathway towards 1:2 complex over an intermediate 1:1 complex (signals between 7.1–7.9 ppm are not assigned for clarity).

The thermodynamic parameters of the host–guest assembly were assessed with an isothermal titration calorimetry experiment (Figure 41d, $CHCl_3$, c(**257**) = $7.0 \cdot 10^{-4}$ M, 298 K). Hereby, not only the 1:2 stoichiometry was validated but also the received binding affinities with K_1 = (3.60 ± 0.35)$\cdot 10^5$ M^{-1} and K_2 = (3.94 ±0.26)$\cdot 10^4$ M^{-1} reflect the values from the other techniques (Table A29). For both, 1:1 as well as 1:2 complex formation, a mainly enthalpy-driven complexation event was disclosed (ΔH_1 = –27.67 kJ mol^{-1}, ΔH_2 = –19.75 kJ mol^{-1}), while additionally the entropy supports the bindings with favourable values ($-\Delta S_1 T$ = –5.93 kJ mol^{-1}, $-\Delta S_2 T$ = –6.48 kJ mol^{-1}). The latter points at the importance of desolvation effects[170] of the extended host and guest molecules upon complex formation, i.e. the gain of entropy by liberation of solvent molecules bound to the π-surfaces surpasses the loss of entropy by the association of the three π-scaffolds in the 1:2 complex.

We used X-ray crystallography to elucidate the association between nanographene and coronene in the solid-state. Therefore, single crystals of **257** and coronene suitable for X-ray diffraction were grown by slow diffusion of *n*-hexane into a chloroform solution of **257** and coronene in a 1:6 ratio (Figure 43a–c and Figure A177). The crystallographic analysis unambiguously confirmed the intercalation of the guests in the molecular cavities of **257**. Furthermore, the 1:2 stoichiometry obtained by the experiments in solution could be confirmed also in the solid-state structure. Thereby, one coronene molecule is located on top and another below the nearly planar nanographene surface, while both are slightly displaced to each other. The coronene molecules are

parallel enclosed at a characteristic π-distances of 3.2–3.4 Å from the nanographene core. The imide substituents of the latter one show only negligible stabilization of the complex with a few [CH···HC]-interactions, revealing a rather weak influence of the imide substituents on the binding strength. The 1:2 complex arrange into slightly slipped cofacial columnar stacks. Such packing motifs might allow the future application of such donor–acceptor systems in co-crystal transistors.[381] An obtained second polymorph of 1:2 complex disclosed slightly different arrangement of coronenes and a packing into isolated dimers of 1:2 complexes (Figure A178).

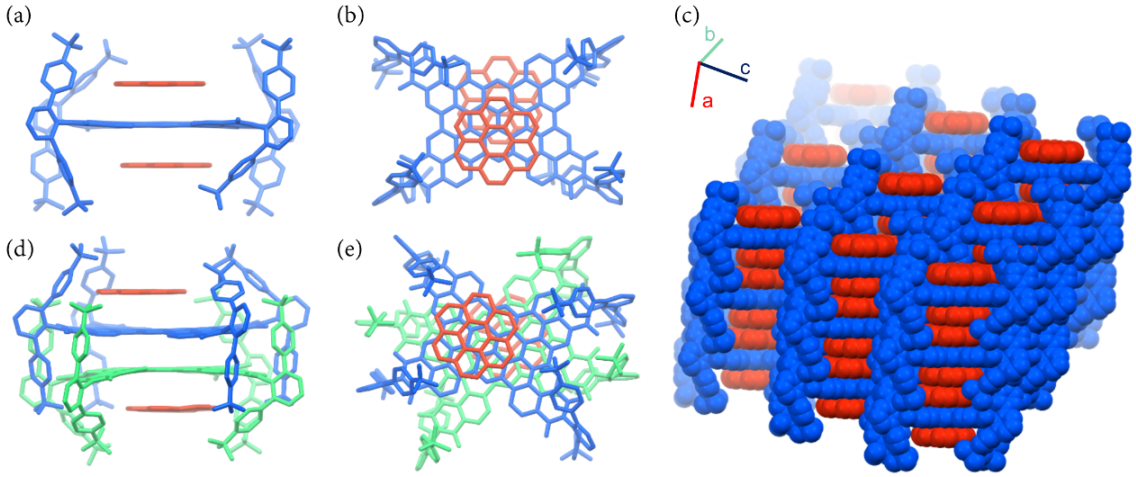

Figure 43. Molecular structures of 1:2 and 2:2 complexes from nanographene **257** and coronene. (a) Side view, (b) top view and (c) packing arrangement of an obtained solid-state structure for a 1:2 complex of **257** and coronene. (d) Side view and (e) top view of obtained solid-state structure of a 2:2 complex of **257** and coronene. (Coronene: orange; nanographene: blue and green; hydrogens are omitted for clarity.)

Further, we were interested in the solid-state structure of the intermediate 1:1 complexes. Therefore, we used a reduced 1:1 ratio of **257** and coronene for crystallization. To our delight, crystallographic analysis of obtained co-crystals revealed an unexpected 2:2 structure (Figure 43d–e and Figure A179). Despite their bulky imide substituents, two nanographenes arrange by a slight rotation (~45°) close to each other. The close proximity lead to a distortion of the enlarged π-systems of **257**, while the imide substituents point in opposite direction of neighbouring nanographenes. The solid-state complex is stabilized not only due to extended π-contacts but also due to intermolecular [CH···π]-interactions of nanographene core protons and imide substituents. The two cavities on top and below the non-covalent nanographene dimer are filled with one coronene, respectively. We assume the obtained 2:2 suprastructure as a result of the dimerization during crystallization of intermediate 1:1 complex. Therefore, in-depth crystallization experiments with different host–guest ratios and various concentrations gained further insights into the formation of these solid-state structures (details *10.5. Supporting Information Chapter 7*, Table A38–Table A42). Host–guest ratios of ≤1:2, independent from the applied concentrations, yielded exclusively one of the two 1:2 crystal structures. In contrast, a reduced ratio gave either 2:2 or 1:2 crystals, while higher

concentrations supported the formation of 2:2 crystals. These results support our assumption of the formation of the 2:2 structure from the intermediate 1:1 complex due to crystal packing effects.[382]

Due to the strong binding with coronene, we were interested in the complexation capabilities of host **257** towards other smaller and larger PAHs. Therefore, we additionally applied naphthalene, anthracene, pyrene, perylene, ovalene and hexabenzocoronene in UV–vis titration experiments. While the smallest guest naphthalene lead only to minor changes, the other PAHs induced comparable changes to coronene (Figure A166 and Figure A167). Noteworthy, also the very poorly soluble PAHs ovalene and hexabenzocoronene could be investigated due to their solubilisation upon complexation. These studies represent, best to our knowledge, the first example for the defined complexation of parent ovalene and hexabenzocoronene. The encapsulation of such PAHs are only known for the interplay of multiple host and guest molecules leading to undefined host–guest ratios, which excluded detailed supramolecular investigations.[363-364] The obtained data was evaluated with a 1:2 binding model to receive the corresponding binding constants K_1 and K_2 (Table 10). While for small naphthalene with $K_1 = (10.27 \pm 0.03)\ M^{-1}$ and $K_2 = (3.03 \pm 0.01)\ M^{-1}$ only negligible binding affinities could be obtained, the largest PAH (hexabenzocoronene) showed the highest binding constants of $K_1 = (8.05 \pm 0.04) \cdot 10^5\ M^{-1}$ and $K_2 = (1.61 \pm 0.01) \cdot 10^5\ M^{-1}$ among the series of PAHs. It should be noted that for the smaller guest molecules other binding modes with multiple (>2) guest-molecules can not be excluded.

Table 10. Association parameters of host **257** and various guests.

	UV–vis[a]		fluorescence[b]			
	K_1 / M^{-1}	K_2 / M^{-1}	K_1 / M^{-1}	K_2 / M^{-1}	ΔG_1 (295 K)[c] / kJ mol^{-1}	ΔG_2 (295 K)[c] / kJ mol^{-1}
naphthalene	10.27 ± 0.03	3.03 ± 0.01	-[d]	-[d]	–5.71	–2.72
anthracene	$(1.62 \pm 0.01) \cdot 10^2$	$(4.24 \pm 0.01) \cdot 10$	$(1.06 \pm 0.01) \cdot 10^2$	$(7.79 \pm 0.17) \cdot 10$	–12.0	–10.0
pyrene	$(5.36 \pm 0.04) \cdot 10^2$	$(2.10 \pm 0.02) \cdot 10^2$	$(9.47 \pm 0.04) \cdot 10^2$	$(2.14 \pm 0.04) \cdot 10^2$	–16.2	–13.1
perylene[e]	$(1.20 \pm 0.01) \cdot 10^4$	$(3.38 \pm 0.01) \cdot 10^3$	$(1.51 \pm 0.01) \cdot 10^4$	$(3.09 \pm 0.12) \cdot 10^3$	–23.3	–19.8
coronene	$(2.73 \pm 0.01) \cdot 10^5$	$(6.14 \pm 0.03) \cdot 10^4$	$(2.92 \pm 0.01) \cdot 10^5$	$(7.09 \pm 0.14) \cdot 10^4$	–30.8	–27.2
ovalene[e,f]	$(6.81 \pm 0.17) \cdot 10^5$	$(3.03 \pm 0.02) \cdot 10^4$	$(1.01 \pm 0.02) \cdot 10^6$	$(1.63 \pm 0.01) \cdot 10^5$	–33.5	–28.1
hexabenzocoronene[e,f]	$(8.05 \pm 0.04) \cdot 10^5$	$(1.61 \pm 0.01) \cdot 10^5$	$(1.11 \pm 0.02) \cdot 10^6$	$(6.08 \pm 0.09) \cdot 10^5$	–33.8	–31.5
phthalocyanine[g]	-[h]	-[h]	$(9.24 \pm 0.07) \cdot 10^6$	$(5.09 \pm 0.04) \cdot 10^6$	–39.3	–37.9

[a]Association constants $K_{1/2}$ determined using global-fit-analysis (fitting range: λ = 480–520 nm) with the program *bindfit*[377] for a 1:2 binding model (chloroform, 295 K, c(**257**) = $6.0 \cdot 10^{-6}$ M). [b]Association constants $K_{1/2}$ determined using global-fit-analysis (fitting range: λ = 580-620 nm) with the program *bindfit*[377] for a 1:2 binding model (chloroform, 295 K, c(**257**) = $6.0 \cdot 10^{-7}$ M). [c]Gibbs free energies ΔG^0(295 K) calculated from $K_{1/2}$ (from average values of K_1 and K_2 of UV–vis and fluorescence titration experiments) according to $\Delta G^0 = -RT\ln(K_{1/2})$. [d]Not determined due to negligible changes upon addition of guest. [e]Fitting range UV–vis: λ = 580–620 nm. [f]Use of lower concentrations: UV–vis: c(**257**) = $1.0 \cdot 10^{-6}$ M; Fluorescence: c(**257**) = $1.0 \cdot 10^{-7}$ M. [g]Use of lower concentrations: c(**257**) = $6.0 \cdot 10^{-8}$ M. [h]Only determined with fluorescence titration experiment.

The determined binding constants by UV–vis spectroscopy were verified with respective fluorescence titration experiments (Figure A168 and Figure A169). Upon addition the PAHs the emission of **257** diminished again, except for naphthalene due to poor binding affinities (no changes). Furthermore, for all substrates (except perylene and ovalene) a new bathochromic structureless band rises, which we could again assign to exciplex emissions based on lifetime measurements (Figure A170 and Table A32).

A detailed comparison of the calculated binding affinities with the spatial extension of the investigated PAHs revealed a systematic relationship between them. This is best illustrated by comparing the respective Gibbs free energies with the number of π-electrons of the guest substrates (Figure 44a). Thereby, a linear dependency between both is disclosed, indicating dispersion interactions as main driving force for the complexation. Such observations are in accordance with other studies concerning the number of π-electrons in host–guest structures.[193, 200, 219] However, when considering the size of coronene (π-electrons: 24), ovalene (π-electrons: 32) and hexabenzocoronene (π-electrons: 42) no linear dependency anymore of the corresponding Gibbs free energy with the size of the π-surfaces can be observed. The Gibbs free energy reaches a plateau for the large guests, which can be attributed to increased repulsion forces due to the restricted available space provided by **257**. Further, an incomplete overlap with the host surface seem to limit the π-contact and might explain the departure from the linear trend.

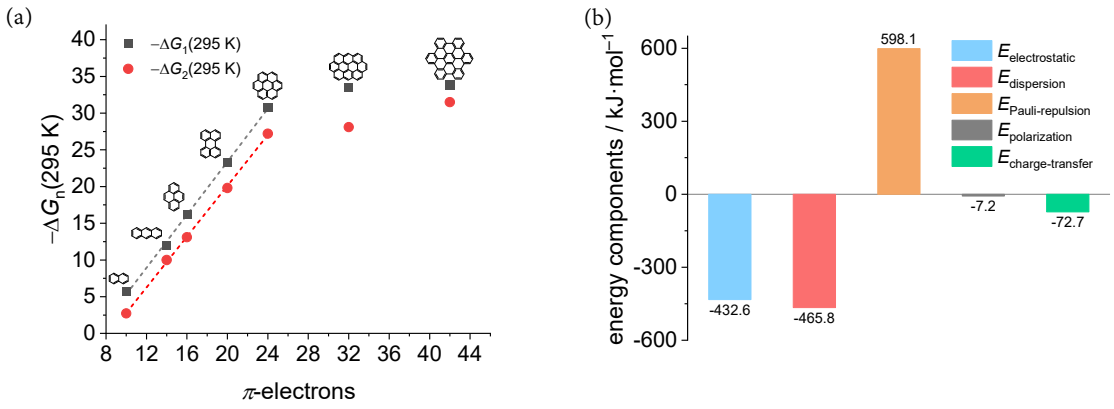

Figure 44. (a) Average Gibbs free energies according to UV–vis and fluorescence titration experiments with the number of π-electrons of the guest molecules. (b) Contribution of various factors to total interaction energy from ALMO-EDA calculation based on the 1:2 crystal structure of nanographene **257** and coronene (detailes *10.5 Supporting Information Chapter 7*).

To further probe the stabilizing interactions of the host–guest assemblies, we performed on basis of the obtained 1:2 crystal structure of nanographene and coronene an energy decomposition analyses (EDA) based on Head-Gordon's absolutely localized molecular orbital (ALMO) approach (Figure 44b).[383] As expected, the main driving force for the complexation are dispersion interactions, which is in accordance with the linear dependency of Gibbs free energy and spatial extension of the

aromatic guests. In addition, to some extend charge-transfer interactions between rather electron-rich coronene and electron-deficient **257** support the binding events, which is similar to other electron-poor dicarboximide-based host structures.[72]

Encouraged by the high binding affinities for PAHs as well as solubilisation of poorly soluble guests (ovalene and hexabenzocoronene) upon complexation, we were interested in the encapsulation capabilities of **257** for pristine phthalocyanine (*Pigment Blue 16*), which is an insoluble pigment. Indeed, through the addition of phthalocyanine powder to a solution of **257** over time a colour change from red to purple can be observed and a respective fluorescence titration experiment (Figure A169d) gave high association constants ($K_1 = (9.24 \pm 0.04) \cdot 10^6\ M^{-1}$ and $K_2 = (5.09 \pm 0.04) \cdot 10^6\ M^{-1}$). These can be explained by the perfect shape complementary of **257** and phthalocyanine as well as additional strong donor–acceptor interactions between rather electron-rich phthalocyanine, a well-known p-type organic semiconductor,[143, 384] and electron-deficient nanographene tetraimide **257**. Unambiguous proof of an intercalation of two phthalocyanines could be obtained crystallographic analysis (Figure 45 and Figure A180).

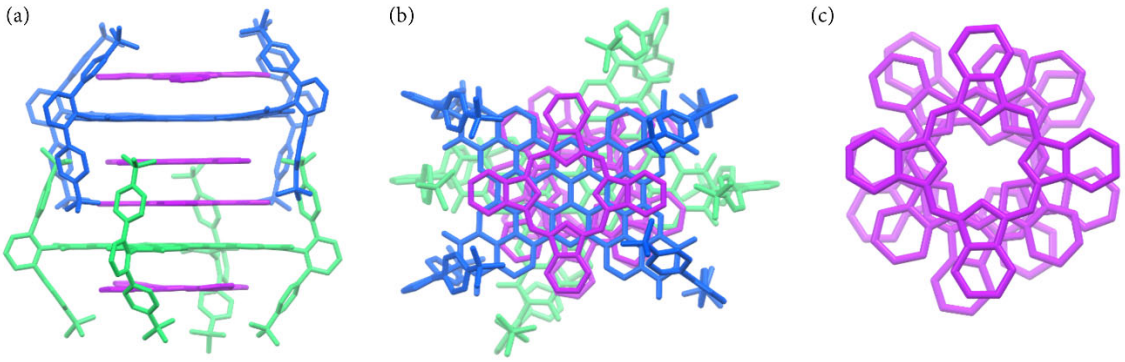

Figure 45. Molecular structures of dimeric 1:2 complex from nanographene **257** and phthalocyanine. (a) Side view and (b) top view of obtained solid-state structure for a dimeric 1:2 complex of **257** and phthalocyanine. (c) Top view of dimeric 1:2 complex with omission of the nanographenes. (Coronene: purple; nanographene: blue and green; hydrogens are omitted for clarity.)

An enormously large unit cell consisting of 48 molecules and a volume of 83127 $Å^3$ was revealed. The 1:2 complexes arrange into defined, finite dimeric structures yielding hexameric stacks consisting of two nanographenes and four phthalocyanines. These complexation capabilities are especially interesting in terms of possible application like influencing of dye/pigment properties upon inclusion,[385] fluorescence upconversion due to complexation of phthalocyanine-based photosensitizer[367, 386] or the construction of defined and alternating donor–acceptor moieties in supramolecular structures.[174]

7.3. Conclusion

In summary, we devised a unique ditopic, flexible host structure for the supramolecular complexation of various PAHs. An easy and convergent synthetic strategy yielded an enlarged electron-deficient nanographene, which is enwrapped by bulky substituents to provide two π-surfaces as recognition sites for PAHs. This design allows the uptake of various PAHs, ranging from small naphthalene to extended and sparingly soluble guests like ovalene and hexabenzocoronene up to the phthalocyanine *Pigment Blue 16*, with high binding constant (up to 10^6 M^{-1} in $CHCl_3$). Detailed studies reveal dispersion forces due to the extended nanographene surface as main driving force, which is supported by additional charge-transfer interactions from the strongly electron-poor character of **257**. Single crystal X-ray crystallography unambiguously confirmed the binding of two coronene guest molecules inside the two host cavities yielding donor–acceptor–donor arrangements. Furthermore, we assume our isolation of an unexpected 2:2 crystal structure as a result of the intermediate 1:1 complex. We are convinced that our approach with a defined nanographene as host structure enable new perspectives for supramolecular complexation chemistry and facilitates the understanding of intermolecular interactions as well as stimulate towards new supramolecular materials. Furthermore, our rational host-design might act as platform for the encapsulation of small supramolecular assemblies[387] or can be applied for the catalysis[388] for organic reactions.

Chapter 8

Summary and Conclusion

Modern organic synthetic chemistry paved the way towards highly diverse functional organic dyes with tailor-made properties. In addition to their early use as vat dyes and pigments, modern organic dyes continuously emerge in various high-tech applications such as their utilization in organic electronics or their biomedical usage. Therefore, these dyes are not only interesting in terms of their optical characteristics, but also for instance due to their electronic properties, intra- and intermolecular interactions or interactions with external stimuli. In this regard, rational control of these characteristics by precise and careful molecular design is indispensable to obtain dyes with the desired properties. In this context, polycyclic aromatic dicarboximides (PADIs), like rylene dicarboximides, have shown to be a promising dye class due to the simple modification/manipulation of their properties by structural adjustments (*Chapter 2.1*). However, synthetic strategies to access extended PADIs are still often tedious and cumbersome. An intriguing and highly relevant dye research field deals with organic chromophores with an absorption or emission in the near-infrared (NIR) region (*Chapter 2.2*). These dyes have not only shown to be important for efficient light-harvesting in organic photovoltaics, but also their use in bioimaging or photodynamic therapy are of great importance due to their absorption of tissue-penetrating NIR light. Dyes are beyond that important building blocks in fundamental research fields such as supramolecular chemistry. For instance, dye-based host structures are important building blocks for the construction of non-covalently bonded organic donor–acceptor complexes (*Chapter 2.3*). Such supramolecular structures contribute not only to the fundamental understanding of intermolecular interactions, but are also used, for example, in optoelectronic devices, sensors and supramolecular catalysis. The general aim of this thesis was the development of synthetic methodologies towards novel polycyclic aromatic dicarboximides, which can be utilized as NIR dyes, electron-deficient scaffolds, solid-state emitters or host structure for charge-transfer complexes.

In this regard, first a series of tetrachlorinated PADIs with an extended aromatic surface, which should function as electron-deficient NIR dyes, was devised (*Chapter 3*). For this purpose, the conditions of a palladium-catalysed [3+3] annulation reaction were optimized using a dibromo-tetrachloroperylene monodicarboximide (**223**) and naphthalene boronic acid ester (**222a**) as model

reaction. Subsequently, the optimized reaction conditions could be utilized with other PAH boronic acid esters to demonstrate a broad substrate scope with yields up to 89% (Figure 46a).

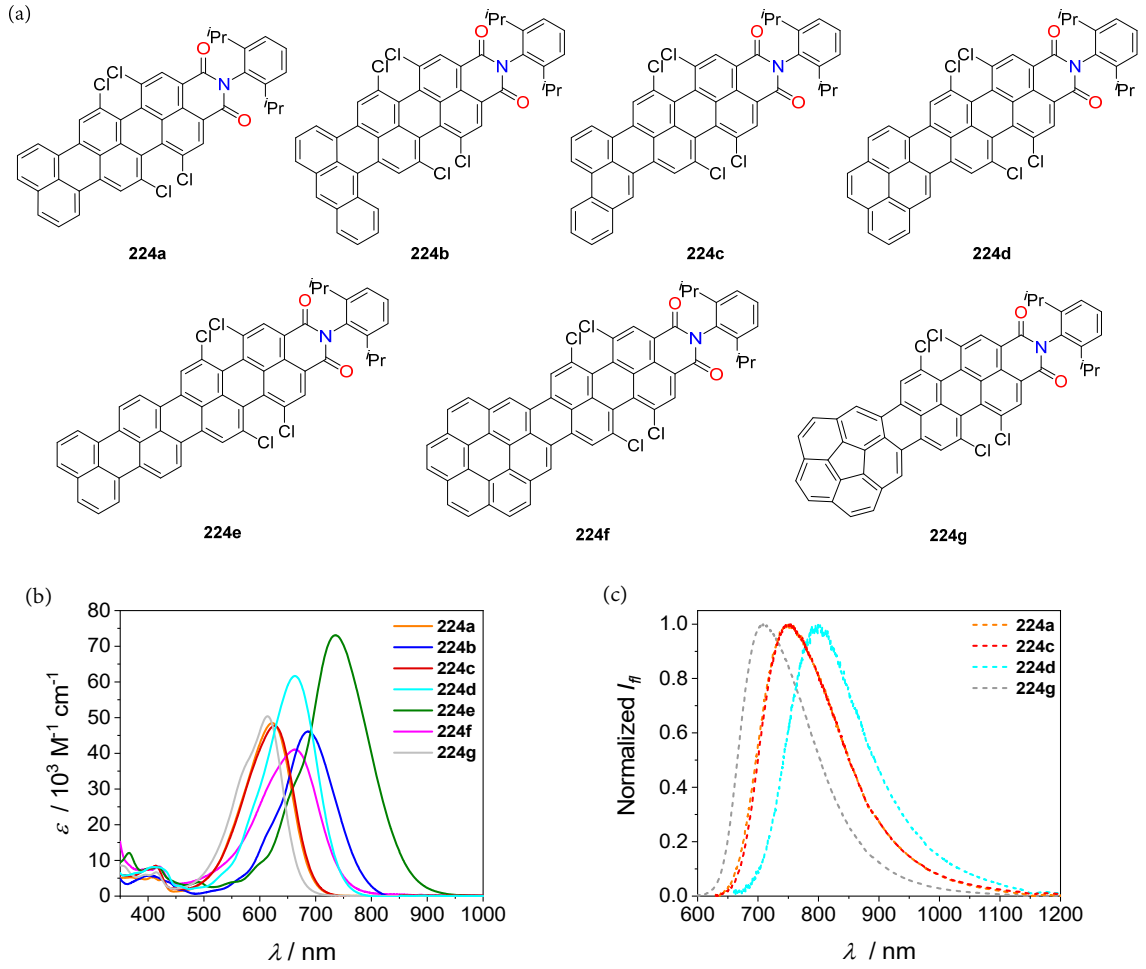

Figure 46. (a) Chemical structures of synthesized tetrachlorinated PADIs **224a–g**. (b) UV–vis absorption and (c) fluorescence spectra of **224a–g** (CH_2Cl_2, room temperature, $c \sim 10^{-6}$–10^{-7} M, **224a**: λ_{ex} = 620 nm, **224c**: λ_{ex} = 620 nm, **224d**: λ_{ex} = 600 nm, **224g**: λ_{ex} = 590 nm, compounds **224b**,**e**,**f** are non-emissive).

The analysis of the optical properties by UV–vis absorption and fluorescence spectroscopy using their dichloromethane solutions revealed highly interesting features. For instance, all compounds exhibited a strong and broad absorbance in or close to the NIR region with maxima up to 736 nm (**224e**, Figure 46b). The observed absorption spectra could be evaluated with the help of DFT calculations, which revealed a pronounced charge-transfer character for the synthesized PADIs. This is a consequence of the interaction of rather electron-rich PAH moieties with the electron-deficient tetrachloroperylene dicarboximide unit. More interestingly, some of these dyes are emissive, while the fluorescence maxima are all located in the NIR ranging from 709 nm (**224g**) to 801 nm (**224d**) (Figure 46c). Moreover, high fluorescence quantum yields up to 31% (**224g**) could be obtained. In addition, electrochemical analysis with cyclic and square wave voltammetry measurements revealed a pronounced electron-deficient character of these compounds, which is induced by the electron-withdrawing dicarboximide group. A direct comparison of tetrachlorinated

PADI **224a** with its non-chlorinated counterpart (**TMI**) revealed the influence of the attached chloro substituents. These cause not only a bathochromic shift of the absorption and emission maximum, but also a lowering of the LUMO levels. Thus, the devised synthetic strategy with a [3+3] annulation reaction yielded a broad variety of π-extended PADIs in good yields, which are not only interesting in terms of their NIR absorbing and emitting properties, but also due to their pronounced electron-deficient character. These features make them promising candidates as NIR dye as well as n-type semiconductors for (opto)electronic materials and their pronounced NIR absorption might be useful for an efficient light-harvesting in organic solar cells.

In the following *Chapter 4*, the optical properties of the PADIs **224a** and **224g** were modulated by replacing the chloro substituents with aryloxy or aryl groups (Figure 47a). These substitution patterns were aimed to redshift the absorption and emission similar to substituent effects known for PBIs. For this purpose, a multi-step synthesis, including the [3+3] annulation reaction of *Chapter 3*, was employed to give the desired target compounds **225a**,**g** and **226a**,**g**. In addition, the applied synthetic route opened up the possibility for the synthesis of tetraaryl-substituted quaterrylene bisdicarboximide **243**. UV–vis absorption and fluorescence spectroscopic studies of their dichloromethane solutions disclosed the influence of the introduced aryloxy and aryl substituents. First, the introduction of *tert*-butylphenoxy groups led only to minor or moderate bathochromic shifts in the absorption spectra of **225a** (637 nm) and **225g** (642 nm) compared to its chlorinated counterparts **224a** (623 nm) and **224g** (614 nm), respectively. A similar and negligible effect was observed for their emission maxima, however, with decreased quantum yields. In contrast, the aryl substituents caused pronounced redshifts in the absorption spectra of **226a** (679 nm) and **226g** (682 nm), which were also present in their fluorescence spectra due to emission maxima up to 786 nm (**226g**). Similar to the aryloxy-substituted PADIs, their fluorescence quantum yields were lower. More interestingly, quaterrylene bisdicarboximide **243** offered with absorption and fluorescence maxima of 811 nm and 884 nm, respectively, pronounced optical features in the NIR region (Figure 47b). The fluorescence quantum yield of 1.3% is highly interesting for this emission range. Moreover, the chiroptical properties of tetraaryl-substituted compounds were exemplarily disclosed with model substrate **243**. Time-dependent circular dichroism spectroscopy showed the high racemization barriers ($\Delta G^{\#}_{398\,K}$ = 125 kJ/mol) of the isolated atropo-enantiomers. This is a consequence of the spatial proximity of the adjacent aryl groups, which could be manifested with crystallographic analysis of the tetraaryl-substituted quaterrylene bisdicarboximide **243** (Figure 47c). Overall, the developed versatile synthetic approach gives access to aryloxy- and aryl-substituted PADIs. The devised PADIs offer systematically tailored optical features compared to its chlorinated counterparts and reveal with this substituent-dependent properties. Further, the room-temperature stable atropo-enantiomers of tetraaryl-substituted PADIs are promising materials for circularly polarized luminescence phenomena in the NIR range.

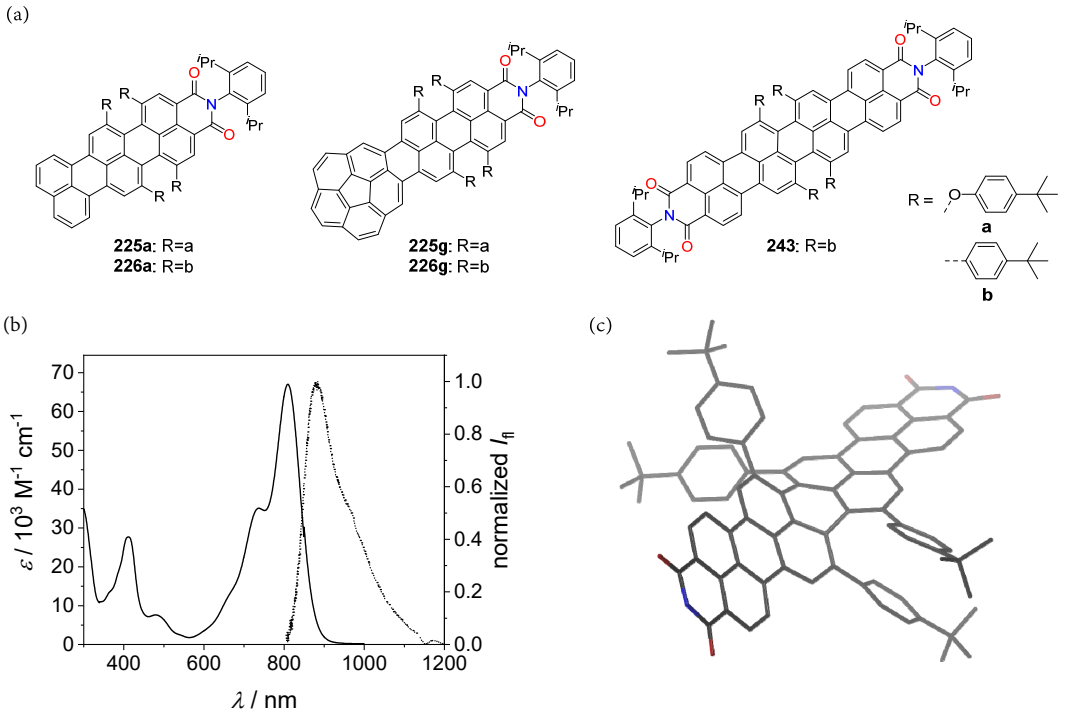

Figure 47. (a) Chemical structures of final compounds from *Chapter 4*. (b) UV–vis absorption (solid line) and fluorescence (dotted line) spectrum of **243** (CH_2Cl_2, room temperature, $c \sim 10^{-6}$–10^{-7} M, λ_{ex} = 790 nm). (c) Molecular structure of **243** (depiction of *M*-enantiomer) obtained from single crystal X-ray diffraction analysis (hydrogens and dicarboximide substituents are omitted for clarity).

In *Chapter 5*, dyes with a broad visible light absorption up to the NIR region was targeted by a pronounced intramolecular charge-transfer. Therefore, donor–acceptor structures based on PADIs were designed. Donor and acceptor should be connected through annulation of both moieties to enhance rigidity and conjugation. This approach is rather unusual, because donor and acceptor units are commonly linked only by one bond. In this regard, we used electron-rich thiophene or pyrrol containing units as donors and naphthalene dicarboximide units as acceptors. A devised palladium catalysed [3+2] annulation on the basis of our research on annulation reactions (e.g. *Chapter 3*) was used to fuse donor and acceptor units and access a broad variety of acceptor–donor (**246a**–**c**) and acceptor–donor–acceptor (**246d**–**h**) structures (Figure 48a). Absorption spectroscopy and electrochemical investigations were applied to elucidate the properties of these novel structures. All compounds exhibited a broad and structureless absorption for the lowest energy transition with maxima up to 675 nm (**246e**), which tailed for some in the NIR range (up to 800 nm, Figure 48b,c). Further, the acceptor–donor(–acceptor) PADIs offered comparable low-lying LUMO levels ranging from –3.49 eV (**246c**) to –3.64 eV (**246d**), but highly diverse HOMO levels between –5.35 eV (**246e**) and –6.08 eV (**246c**).

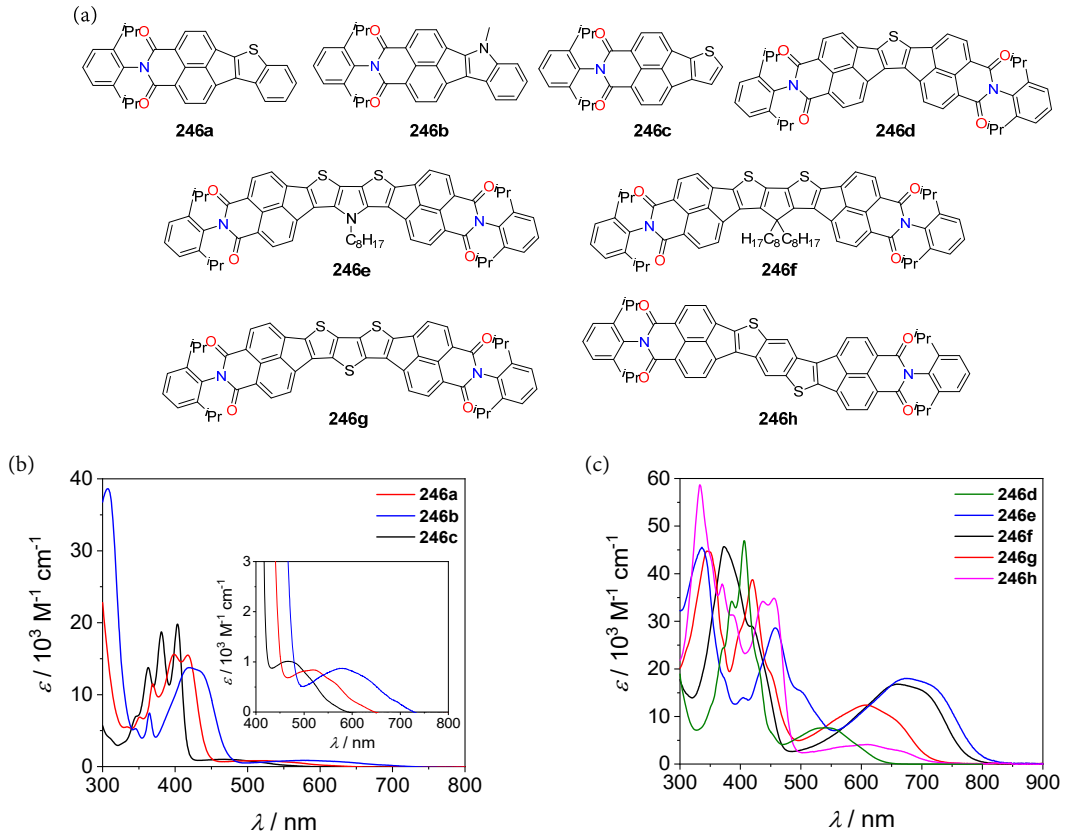

Figure 48. (a) Chemical structures of synthesized acceptor–donor and acceptor–donor–acceptor PADIs **246a**–**h**. UV–vis absorption spectra of (a) **246a**–**c** and (b) **246d**–**h** (CH_2Cl_2, room temperature, $c \sim 10^{-5}$ M). The inset in panel (b) shows magnified charge-transfer bands of **246a**–**c**.

Detailed evaluation of the optical and electronic properties and the use of DFT calculations revealed a high dependence of these characteristics on the donor-strength as well as the number of acceptor units. For instance, an increased donor strength correlated directly with a pronounced redshift of the absorption maximum. This is a result of an increased charge-transfer character, which was revealed by computing D_{CT} (for mono-fold annulated products) and $\Delta\sigma_{CT}$ (for two-fold annulated products). The increased charge-transfer character led also to broader and weaker absorbance. Furthermore, the strong difference of the HOMO energy levels are directly linked to the strength of the donor moieties. Comparison of mono- and two-fold annulated thiophenes **246c** and **246d** disclosed the impact of a second acceptor unit. This second acceptor moiety led due to its electron withdrawing character not only to a redshift of the absorbance, but also to a lowering of the LUMO level. In summary of this chapter, a conceived [3+2] annulation reaction gave simple and fast access to novel fused acceptor–donor(–acceptor) dyes with tuneable optical and electronic properties, low-lying LUMO levels and absorbance up to the NIR region. Therefore, derivatives of such small chromophores might be useful for the implementation in organic transistors or photovoltaic devices. In addition, the small molecular weights make these dyes interesting in terms of vacuum deposition processing methods.

Chapter 6 focused on the optical properties of dicarboximide containing compounds in the solid-state. The aim of this chapter was the development of a direct imidization of rylene anhydrides with bulky amines to obtain easy sterically enwrapped rylene dicarboximides with enhanced fluorescence properties in the solid-state. In this regard, a new imidization protocol, which uses stoichiometric amounts of reactants and mild reaction conditions, was devised (Figure 49a). For this purpose, the anilines were deprotonated with *n*-butyllithium to overcome the low reactivity of the sterically crowded amine starting materials. This base-assisted conditions yielded a broad variety of naphthalene and perylene mono- as well as bisdicarboximides (Figure 49b). Hereby, either the respective anhydride or ester were used as starting materials, whereby only the former one required the addition of water. The crucial role of this water addition was revealed by the isolation of an isoimide intermediate (**256a**, Figure 49a), which was subsequently converted under aqueous basic conditions to the respective dicarboximide. This suggests a reaction pathway *via* an isoimide-imide rearrangement. The sterically enwrapped rylene dicarboximides exhibit highly interesting optical properties in the solid-state. Thus, perylene bisdicarboximides **255a**–**d** offer an enhanced emission in the solid-state. This is most pronounced for PBI **255d** with an effective fluorescence quantum yield of 18%, which has the bulkiest *N*-substituent (Figure 49d). We attributed this to packing motifs without close interchromphoric interactions as revealed by crystallographic analysis. These prevented the complete fluorescence quenching in the solid-state. In contrast, naphthalene monodicarboximides **252a**–**d**, which are non-emissive in solution, showed highly diverse emission features in the solid-state and effective fluorescence quantum yields up to 17% (**252a**, Figure 49c). The diverse solid-state fluorescence could be traced to different packing motifs for **252a**–**d**, which were caused by the different steric demand of the *N*-substituents. This resulted in monomer- or excimer-like emission behaviour. Therefore, these investigations disclosed the importance of the *N*-substituents on the optical properties of rylene dicarboximides in the solid-state, which is contrary to their negligible influence on monomeric species in solution. Therefore, the rational control of packing motifs by a careful and precise design of the *N*-substituent is indispensable to obtain the desired optical properties in the solid-state. To summarize this part, a one-pot base-assisted imidization reaction with bulky amine derivatives was devised, which gave straightforward access to new sterically crowded rylene dicarboximides. Optical spectroscopy as well as crystallographic analyses revealed structure–property relationships in the solid-state and therefore highlights the importance of a sophisticated molecular design. The conceived reaction might stimulate further developments for new solid-state emitter based on dicarboximides and therefore additionally contribute to fundamental insights into the research field of crystal engineering.

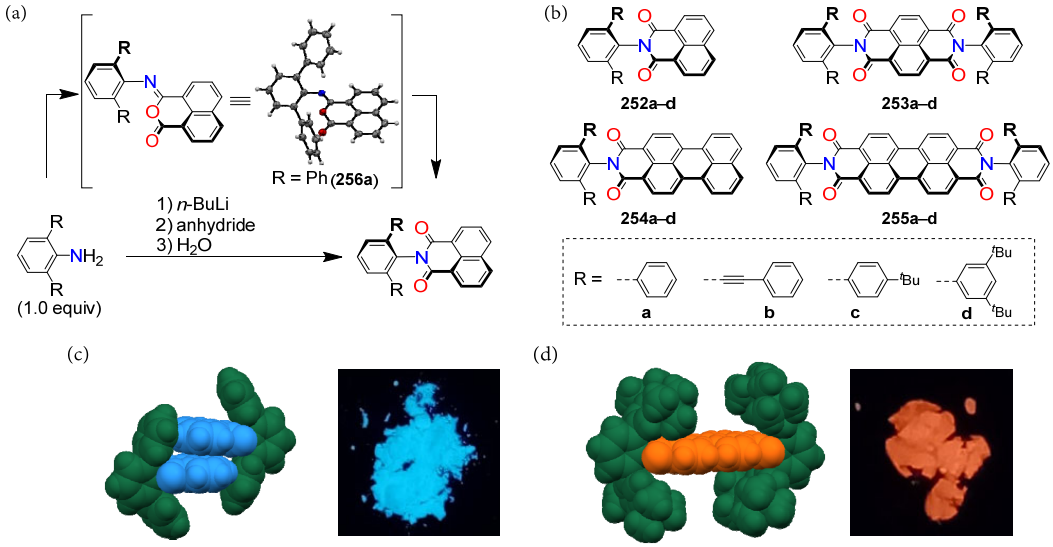

Figure 49. (a) Exemplary depiction of the developed base-assisted imidization reaction with bulky amine derivatives for naphthalene monodicarboximides and single crystal structure of isolated isoimide intermediate **256a**. (b) Substrate scope of the devised imidization reaction. (c) Dimeric packing motif of **252a** as found in the single crystal and photograph of powder from **252a** under UV-light irradiation. (c) Molecular structure of **255d** as found in the single crystal and photograph of powder from **255d** under UV-light irradiation.

In the final *Chapter 7*, an electron-deficient tetrakisdicarboximide nanographene was introduced as novel host-structure for supramolecular host–guest chemistry. For this purpose, based on the imidization method developed in *Chapter 6*, four bulky dicarboximide substituents were used to build-up two extended π-scffolds for the binding of electron-rich guests (Figure 50a). The desired nanographene **257** was synthesized in a straightforward reaction sequence, including a four-fold [3+3] annulation reaction in the final step. Ditopic host **257** showed the non-covalent binding of various electron-rich PAHs in chloroform solutions – from small naphthalene to larger coronene (Figure 50b). In addition, the solubilisation upon complexation allowed the investigation of barely soluble ovalene, hexabenzocoronene and phthalocyanine as guest molecules, whereby high binding constants up to 10^6 M^{-1} were obtained ($CHCl_3$, 295 K). Hereby, the strong and distinct optical properties of **257** enabled following the complexation events by UV–vis absorption and fluorescence spectroscopy. Detailed investigations with ^{1}H NMR spectroscopy and isothermal titration calorimetry gave additional insights into the binding processes. For instance, low temperature ^{1}H NMR measurements confirmed not only a 1:2 host:guest ratio (guest: coronene), but also gave systematic insights into the step-wise complex formation. Moreover, the involved interaction forces were deconvoluted with the help of DFT calculations. This theoretical analysis revealed the expected contribution of a charge-transfer interaction to the binding event, which arise from the interplay of electron-poor host and the electron-rich guests. This was additionally witnessed by bathochromically shifted and broad absorption bands in the UV–vis titration experiments. Most importantly, structural disclosure of the host–guest arrangement in the solid-state were gained by crystallographic analysis. The obtained co-crystal for the guests coronene and phthalocyanine supported the applied 1:2 stoichiometry of host and guest in solution (Figure 50c,d).

Furthermore, an unexpected 2:2 crystal structure (guest: coronene) was found as a result of the dimerization of the intermediate 1:1 complex (Figure 50e). Overall, the devised ditopic nanographene host offers new perspectives for supramolecular chemistry with its rather large and electron-deficient cavities. Further, the unique molecular design of the host with its bulky dicarboximide substituents might be useful in the construction of donor–acceptor stacks with a defined size, which is typically achieved by folding or templating approaches.

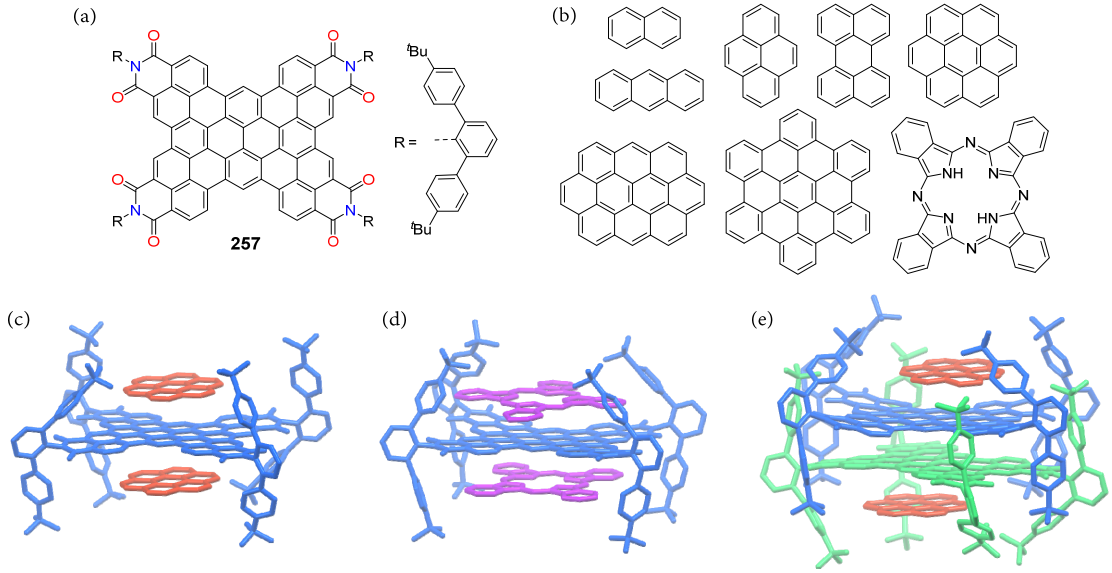

Figure 50. Chemical structures (a) of nanographene tetrakisdicarboximide host **257** and (b) of the studied guest molecules. Crystal structure of 1:2 complexes with (c) coronene (orange) and (d) phthalocyanine (purple) with the nanographene host (blue). (e) Crystal structure of 2:2 complex from coronene (orange) and nanographene (blue and green). (Hydrogens in the crystal structures are omitted for clarity.)

In conclusion, the present thesis introduced different synthetic strategies towards a variety of polycyclic aromatic dicarboximides. This included tetrachlorinated, tetraaryloxy- and tetraaryl-substituted dicarboximides, fused acceptor–donor(–acceptor) structures as well as sterically shielded rylene and nanographene dicarboximides. The resulting dyes exhibit highly interesting and diverse properties. For instance, some of the fused and substituted PADIs offer strong absorption of visible and NIR light, NIR emission and low-lying LUMO levels. On the contrary, intriguing optical features in the solid-state characterize the rylene dicarboximides with their bulky *N*-substituents, while the devised sterically enwrapped nanographene host offered remarkable complexation capabilities in solution. The valuable disclosure of structure–property relationships might pave the way for new electron-deficient PADIs with precisely adjustable properties in solution and the solid-state. Furthermore, such chromophores might find applications in organic (opto)electronic devices or as NIR dyes. Additionally, the contribution with a new electron-deficient host design might stimulate the field of supramolecular host–guest chemistry concerning charge-transfer interactions, complexation of enlarged guest molecules or supramolecular catalysis.

Chapter 9

Zusammenfassung und Fazit

Die moderne organische Synthesechemie ebnete den Weg zu sehr unterschiedlichen funktionalen organischen Farbstoffen mit maßgeschneiderten Eigenschaften. Zusätzlich zu ihren früheren Verwendungen als Küpenfarbstoffe und Pigmente, dringen moderne organische Farbstoffe kontinuierlich in verschiedene hochtechnologische Anwendungen vor, wie zum Beispiel deren Verwendung in der organischen Elektronik oder deren biomedizinischer Einsatz. Deshalb sind diese Farbstoffe nicht mehr nur in Bezug auf ihre optischen Charakteristika interessant, sondern zum Beispiel auch hinsichtlich ihrer elektronischen Eigenschaften, intra- und intermolekularen Wechselwirkungen oder Wechselwirkungen mit externen Reizen. Diesbezüglich ist die rationale Kontrolle dieser Charakteristika durch ein präzises und sorgfältiges molekulares Design unverzichtbar, um Farbstoffe mit den gewünschten Eigenschaften zu erhalten. In diesem Zusammenhang haben polyzyklische aromatische Dicarboximide (PADIs) wie die Rylendicarboximide gezeigt, dass sie durch die Modifizierung ihrer Eigenschaften durch (einfache) Strukturanpassungen eine vielversprechende Farbstoffklasse sind (*Kapitel 2.1*). Jedoch sind synthetische Strategien für die Zugänglichkeit von ausgedehnten PADIs oft noch mühsam und umständlich. Ein faszinierender und hoch relevanter Farbstoff-Forschungsbereich beschäftigt sich mit organischen Chromophoren, welche eine Absorption oder Emission im nahen Infrarot (NIR)-Bereich haben (*Kapitel 2.2*). Diese Farbstoffe haben gezeigt, dass sie nicht nur für eine effiziente Sammlung von Licht in der organischen Photovoltaik wichtig sind, sondern auch ihr Einsatz in der biologischen Bildgebung oder photodynamischen Therapie sind durch ihre Absorption von Gewebe-durchdringendem NIR-Licht von großer Bedeutung. Farbstoffe sind darüber hinaus auch in fundamentalen Forschungsbereichen wie der supramolekularen Chemie wichtige Bausteine. Beispielsweise sind Farbstoff-basierte Wirts-Strukturen wichtige Bausteine zum Aufbau nicht-kovalent gebundener organischer Donor–Akzeptor Komplexe (*Kapitel 2.3*). Solche supramolekularen Strukturen tragen nicht nur zum grundlegendem Verständnis von intermolekularen Wechselwirkungen bei, sondern finden beispielsweise auch Anwendung in optoelektronischen Bauteilen, Sensoren und der supramolekularen Katalyse. Das allgemeine Ziel dieser Arbeit war die Entwicklung von synthetischen Methoden für neue polyzyklische aromatische Dicarboximide, welche als NIR-Farbstoffe, elektronenarme Strukturen, Festkörper-Emitter oder Wirt-Struktur für Ladungstransfer-Komplexe eingesetzt werden können.

In diesem Zusammenhang wurde zuerst eine Serie an tetrachlorierten PADIs mit einer ausgedehnten aromatischen Oberfläche, welche als elektronenarme NIR-Farbstoffe fungieren sollen, konzipiert (*Kapitel 3*). Aus diesem Grund wurden die Bedingungen einer Palladium-katalysierten [3+3] Anellierungsreaktion anhand der Modellreaktion aus Dibrom-tetrachlor-perylenmonodicarboximide (**223**) und Naphthalinboronsäureester (**222a**) optimiert. Anschließend konnten die optimierten Reaktionsbedingungen auf andere PAH (*polyzyklische aromatische Kohlenwasserstoffe*) -Boronsäureester angewandt werden, wodurch ein breiter Substratbereich mit Ausbeuten bis zu 89% demonstriert werden konnte (Abbildung 1a).

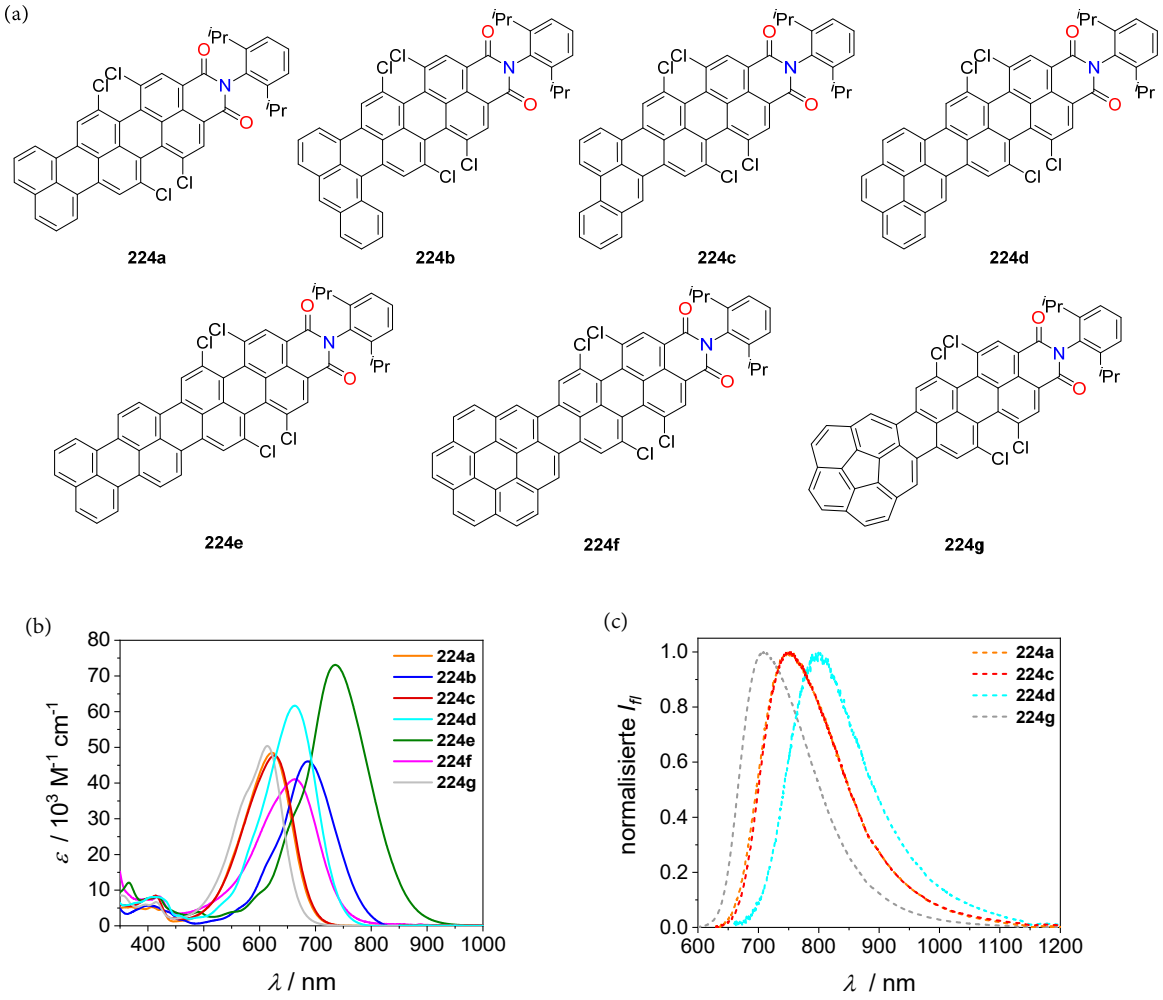

Abbildung 1. (a) Chemische Strukturen der synthetisierten tetrachlorierten PADIs **224a**–**g**. (b) UV–vis Absorptions- und (c) Fluoreszenzspektren von **224a**–**g** (CH_2Cl_2, Raumtemperatur, $c \sim 10^{-6}$–10^{-7} M, **224a**: $\lambda_{ex} = 620$ nm, **224c**: $\lambda_{ex} = 620$ nm, **224d**: $\lambda_{ex} = 600$ nm, **224g**: $\lambda_{ex} = 590$ nm, Verbindungen **224b**,**e**,**f** emittieren nicht).

Die Analyse der optischen Eigenschaften durch UV–vis Absorptions- und Fluoreszenzspektroskopie ihrer Dichlormethan-Lösungen legte hochinteressante Eigenschaften offen. Zum Beispiel zeigten alle Verbindungen eine starke und breite Absorbanz im oder nahe dem NIR-Bereich mit Maxima bis zu 736 nm (**224e**, Abbildung 1b). Die beobachteten

Absorptionsspektren konnten mit der Hilfe von DFT-Berechnungen ausgewertet werden, welche einen ausgeprägten Ladungstransfer-Charakter der synthetisierten PADIs offenlegten. Dies ist eine Folge der Wechselwirkung der eher elektronen-reichen PAH-Teile mit der elektronenarmen tetrachlorierten Perylendicarboximid-Einheit. Noch interessanter ist, dass einige der Farbstoffe emittierend sind, wobei die Fluoreszenzmaxima zwischen 709 nm (**224g**) und 801 nm (**224d**) alle im NIR liegen. Außerdem konnten Fluoreszenzquantenausbeuten bis zu 31% (**224g**) erhalten werden. Zusätzlich zeigte die elektrochemische Analyse mittels Cyclo- und Square Wave Voltammetrie den ausgeprägten elektronenarmen Charakter dieser Verbindungen auf, welcher durch die elektronenziehende Dicarboximid-Gruppe induziert ist. Ein direkter Vergleich des tetrachlorierten PADI **224a** mit dem nicht-chlorierten Gegenstück (**TMI**) offenbarte den Einfluss der angebrachten Chlorsubstituenten. Diese verursachen nicht nur eine bathochrome Verschiebung des Absorptions- und Emissionsmaximums, sondern auch in einer Verringerung der LUMO-Niveaus. Daher liefert die konzipierte synthetische Strategie mit einer [3+3] Anellierungsreaktion eine breite Palette an π-ausgedehnten PADIs in guten Ausbeuten, welche nicht nur in Bezug auf ihre NIR-absorbierenden und -emittierenden Eigenschaften interessant sind, sondern auch durch ihren ausgeprägten elektronenarmen Charakter. Diese Eigenschaften machen sie zu vielversprechenden Kandidaten als NIR-Farbstoffe wie auch n-Halbleiter für (opto)elektronische Materialen und ihre ausgeprägte NIR-Absorption könnte für eine effiziente Lichtsammlung in organischen Solarzellen nützlich sein.

Im folgenden *Kapitel 4* wurden die optischen Eigenschaften der PADIs **224a** und **224g** durch den Austausch der Chlorsubstituenten mit Aryloxy- oder Aryl-Gruppen verändert (Abbildung 2a). Diese Substitutionsmuster zielten auf eine Rotverschiebung der Absorption und Emission, ähnlich zu den bekannten Substituenteneffekten bei PBIs, ab. Aus diesem Grund wurde eine mehrstufige Synthese, inklusive der [3+3] Anellierungsreaktion aus *Kapitel 3*, eingesetzt, um die gewünschten Zielverbindungen **225a**,**g** und **226a**,**g** zu erhalten. Zusätzlich eröffnete die angewandte Syntheseroute die Möglichkeit zur Synthese des Tetraaryl-substituierten Quaterrylenbisdicarboximids **243**. UV–vis absorptions- und fluoreszenzspektroskopische Untersuchungen der Dichlormethan-Lösungen legten den Einfluss der eingeführten Aryloxy- und Arylsubstituenten offen. Zuerst führt die Einführung von *tert*-Butylphenoxy-Gruppen im Vergleich zu ihren chlorierten Gegenstücken **224a** (623 nm) und **224g** (614 nm) jeweils nur zu kleinen oder moderaten bathochromen Verschiebungen in den Absorptionsspektren von **225a** (637 nm) und **225g** (642 nm). Ein vergleichbarer und vernachlässigbarer Effekt konnte für ihre Emissionsmaximas erhalten werden, jedoch mit verringerten Fluoreszenzquantenausbeuten. Im Gegensatz dazu verursachten die Arylsubstituenten ausgeprägte Rotverschiebungen in den Absorptionsspektren von **226a** (679 nm) und **226g** (682 nm), welche mit Emissionsmaxima bis zu 786 nm (**226g**) auch in ihren Fluoreszenzspektren zu erkennen waren. Ähnlich zu den Aryloxy-

substituierten PADIs, waren ihre Fluoreszenzquantenausbeuten verringert. Noch interessanter ist das Quaterrylenbisdicarboximid **243**, welches mit einem Absorptions- und Fluoreszenzmaximum von 811 nm beziehungsweise 884 nm ausgeprägte optische Eigenschaften im NIR-Bereich zeigte (Abbildung 2b). Die Fluoreszenzquantenausbeute ist mit 1.3% für diesen Emissionsbereich hochinteressant. Darüber hinaus wurden die chiroptischen Eigenschaften der Tetraaryl-substituierten Verbindung exemplarisch an dem Modellsubstrat **243** offengelegt. Zeitabhängige Circulardichroismus-Spektroskopie zeigte die hohe Racemisierungsbarrieren ($\Delta G^{\#}_{398\,K}$ = 125 kJ/mol) der isolierten Atropenantiomere. Dies ist eine Folge der räumlichen Nähe der benachbarten Aryl-Gruppen, was mittels kristallographischer Analyse des Tetraaryl-substituierten Quaterrylenbisdicarboximids offenkundig wurde (Abbildung 2c). Insgesamt liefert der entwickelte vielseitige synthetische Ansatz Zugang zu Aryloxy- und Aryl-substituierten PADIs. Die konzipierten PADIs haben im Vergleich zu ihren chlorierten Gegenstücken systematisch angepasste optische Eigenschaften und zeigen damit Substituenten-abhängige Eigenschaften. Außerdem sind die bei Raumtemperatur stabilen Atropenantiomere der Tetraaryl-substituierten PADIs vielversprechende Kandidaten für circularpolarisierte Lumineszenzphänomene im NIR-Bereich.

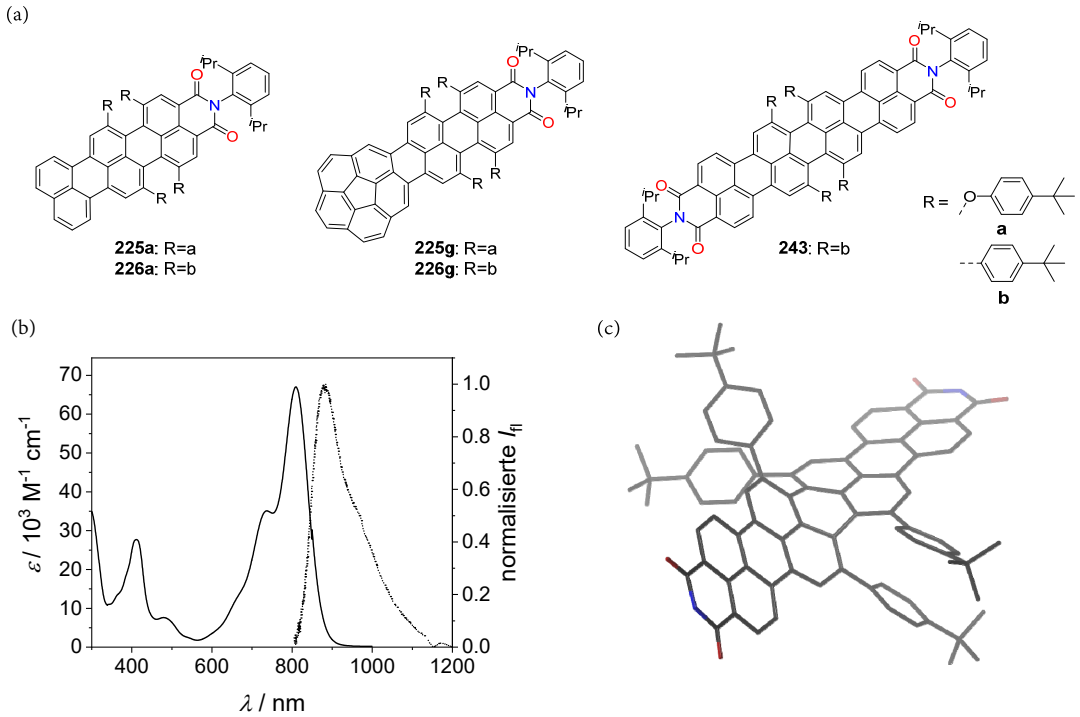

Abbildung 2. (a) Chemische Strukturen der Zielverbindungen aus *Kapitel 4*. (b) UV–vis Absorptions- (durchgehende Linie) und Fluoreszenzspektrum (gepunktete Linie) von **243** (CH_2Cl_2, Raumtemperatur, $c \sim 10^{-6}$–10^{-7} M, λ_{ex} = 790 nm). (c) Molekulare Struktur von **243** (Darstellung des *M*-Enantiomers) aus der Röntgen-Einkristallstrukturanalyse (Wasserstoffatome und Dicarboximidsubstituenten sind aus Gründen der Übersichtlichkeit ausgeblendet).

Kapitel 5 hatte Farbstoffe mit einer breiten Absorption des sichtbaren Lichts bis in den NIR-Bereich durch einen ausgeprägten intramolekularen Ladungstransfer zum Ziel. Hierfür wurden Donor–

Akzeptor-Strukturen auf der Basis von PADIs konzipiert. Donor und Akzeptor sollten mittels Anellierung miteinander verbunden werden, um die Rigidität und Konjugation zu erhöhen. Dieser Ansatz ist eher ungewöhnlich, weil Donor- und Akzeptor-Einheiten normalerweise nur mittels einer Bindung verknüpft sind. In diesem Zusammenhang benutzten wir elektronenreiche Thiophen- oder Pyrrol-haltige Einheiten als Donoren und Naphthalindicarboximid-Einheiten als Akzeptoren. Eine Palladium-katalysierte [3+2] Anellierung auf der Basis unserer Forschung zu Anellierungsreaktionen (zum Beispiel *Kapitel 3*) wurde eingesetzt, um Donor- und Akzeptor-Einheiten zu fusionieren und lieferte Zugang zu einer breiten Vielfalt an Akzeptor–Donor (**246a–c**) und Akzeptor–Donor–Akzeptor (**246d–h**) Strukturen (Abbildung 3a). Absorptionsspektroskopie und elektrochemische Untersuchungen wurden eingesetzt, um die Eigenschaften dieser neuen Strukturen aufzuklären. Alle Verbindungen weisten eine breite und strukturlose Absorption für den niedrigenergetischsten Übergang mit Maxima bis zu 675 nm (**246e**) auf, welche für einige bis in den NIR-Bereich ausliefen (bis zu 800 nm, Abbildung 3b,c). Außerdem zeigten die Akzeptor–Donor(–Akzeptor) PADIs vergleichbar niedrigliegende LUMO-Niveaus von –3.49 eV (**246c**) bis –3.64 eV (**246d**), aber höchst unterschiedliche HOMO-Niveaus zwischen –5.35 eV (**246e**) und –6.08 eV (**246c**).

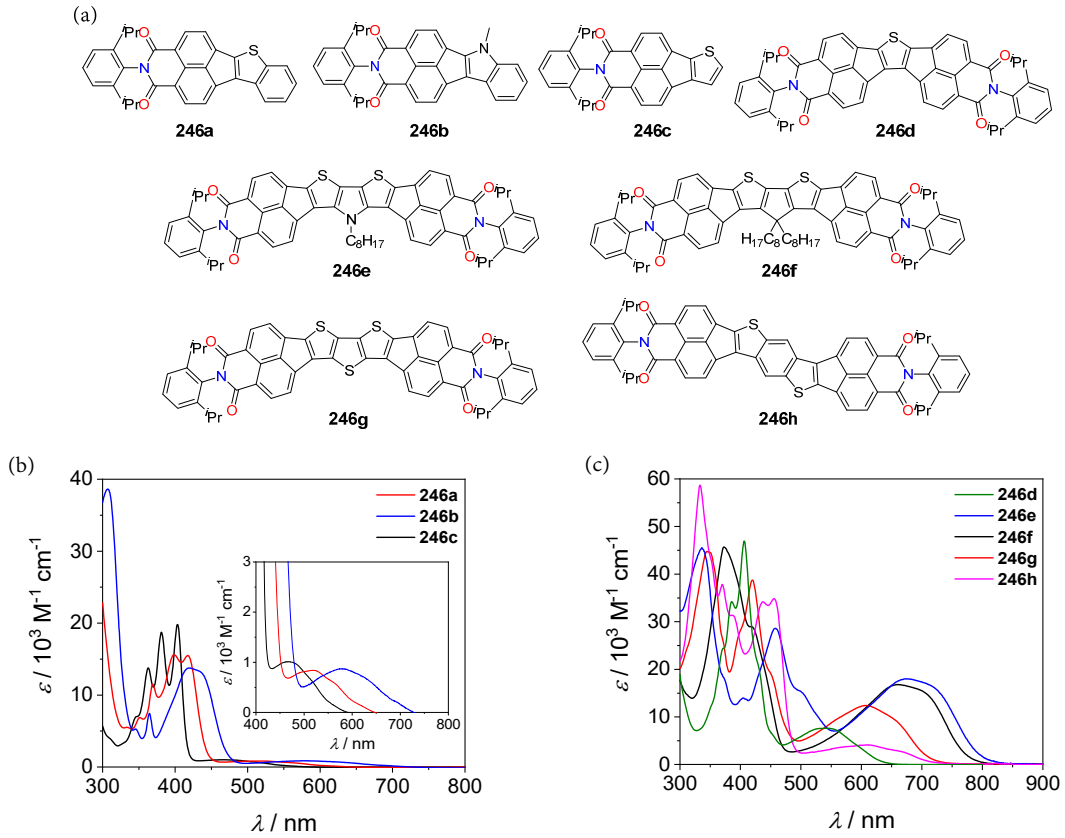

Abbildung 3. (a) Chemische Strukturen der synthetisierten Akzeptor–Donor und Akzeptor–Donor–Akzeptor PADIs **246a–h**. UV–vis Absorptionsspektren von (a) **246a–c** und (b) **246d–h** (CH_2Cl_2, Raumtemperatur, $c \sim 10^{-5}$ M). Der Einsatz in Feld (b) zeigt die vergrößerten Ladungstransferbanden von **246a–c**.

Eine detaillierte Auswertung der optischen und elektronischen Eigenschaften und der Einsatz von DFT-Berechnungen legte die hohe Abhängigkeit dieser Charakteristika bezüglich der Donorstärke wie auch der Anzahl der Akzeptoreinheiten offen. Zum Beispiel korreliert eine erhöhte Donorstärke direkt mit einer ausgeprägten Rotverschiebung des Absorptionsmaximums. Dies ist eine Folge eines erhöhten Ladungstransfer-Charakters, welcher durch die Berechnung von D_{CT} (für einfach anellierte Produkte) und $\Delta\sigma_{CT}$ (für zweifach anellierte Produkte) aufgedeckt wurde. Der erhöhte Ladungstransfer-Charakter führte auch zu einer breiteren und schwächeren Absorbanz. Des Weiteren ist der starke Unterschied zwischen den HOMO-Energieniveaus direkt mit der Stärke der Donoreinheiten verknüpft. Ein Vergleich zwischen ein- und zweifach anellierten Thiophenen **246c** und **246d** offenbarte den Einfluss der zweiten Akzeptoreinheit. Dieser zweite Akzeptorteil führte durch seinen elektronen-ziehenden Charakter nicht nur zu einer Rotverschiebung der Absorption, sondern auch zu einer Herabsenkungen des LUMO-Niveaus. Das Kapitel lieferte zusammenfassend mit der konzipierten [3+2] Anellierungsreaktion einfachen und schnellen Zugang zu neuartigen fusionierten Akzeptor–Donor(–Akzeptor)-Farbstoffen mit abstimmbaren optischen und elektronischen Eigenschaften, niedrigliegende LUMO-Niveaus und einer Absorbanz bis in den NIR-Bereich. Deshalb könnten Derivate dieser kleinen Chromophore nützlich für die Implementierung in organischen Transistoren oder photovoltaischen Bauteilen sein. Zusätzlich machen die geringen Molekulargewichte diese Farbstoffe für Vakuumabscheidungs-basierte Prozessierungsmethoden interessant.

Kapitel 6 fokussierte auf die optischen Eigenschaften von Dicarboximid-enthaltenen Verbindungen im Festkörper. Das Ziel dieses Kapitels war die Entwicklung einer direkten Imidisierung von Rylenanhydriden mit voluminösen Aminen, um einfach sterisch eingehüllte Rylendicarboximide mit verbesserten Fluoreszenzeigenschaften im Festkörper zu erhalten. Diesbezüglich wurde ein neues Imidisierungsprotokoll, welches stöchiometrische Mengen an Reaktanten und milden Reaktionsbedingungen verwendet, entworfen (Abbildung 4a). Hierzu wurden die Aniline mit *n*-Butyllithium deprotoniert, um die geringe Reaktivität der sterisch anspruchsvollen Amin-Edukte zu überwinden. Diese Basen-unterstützten Bedingungen lieferten eine breite Vielfalt an Naphthalin- und Perylen- mono- und bisdicarboximiden (Abbildung 4b). Dabei wurde entweder das zugehörige Anhydrid oder der Ester als Edukte eingesetzt, wobei nur Erstgenannter die Zugabe von Wasser erforderte. Die zentrale Rolle dieser Wasserzugabe wurde mit der Isolierung eines Isoimid-Intermediates aufgeklärt (**256a**, Abbildung 4a), welches anschließend unter wässrig-basischen Bedingungen in das zugehörige Dicarboximid überführt wurde. Dies deutet auf einen Reaktionsweg über eine Isoimid-Imid-Umlagerung hin. Die sterisch eingehüllten Rylendicarboximide weisen hochinteressante optische Eigenschaften im Festkörper auf. Dementsprechend zeigen die Perylenbisdicarboximide **255a**–**d** eine verstärkte Emission im Festkörper. Dies ist am stärksten für PBI **255d**, welches den voluminösesten *N*-Substituenten besitzt, mit einer effektiven

Fluoreszenzquantenausbeute von 18% ausgeprägt (Abbildung 4d). Wir schrieben dies den Packungsmuster ohne nahe interchromophore Wechselwirkungen zu, welche durch kristallographische Analyse aufgedeckt wurden. Diese verhinderten die komplette Fluoreszenzlöschung im Festkörper. Demgegenüber zeigten die Naphthalinmonodicarboximide **252a**–**d**, welche nicht emittierend in Lösung sind, höchst unterschiedliche Emissionseigenschaften im Festkörper und effektive Fluoreszenquantenausbeuten bis zu 17% (**252a**, Abbildung 4c). Die unterschiedliche Festkörperfluoreszenz wurde auf verschiedene Packungsmuster für **252a**–**d** zurückgeführt, welche durch die unterschiedlichen sterischen Ansprüche der *N*-Substituenten verursacht wurden. Dies führte zu Monomer- oder Excimer-artigem Emissionsverhalten. Deshalb legten diese Untersuchungen die Wichtigkeit der *N*-Substituenten für die optischen Eigenschaften von Rylendicarboximiden im Festkörper offen, was gegensätzlich zu ihrem vernachlässigbaren Einfluss auf die monomeren Spezies in Lösung ist. Demnach ist die rationale Kontrolle der Packungsmuster durch sorgfältiges und präzises Design der *N*-Substituenten unabdingbar, um die gewünschten optischen Eigenschaften im Festkörper zu erhalten. Zusammenfassend wurde in diesem Teil eine Eintopf Basen-unterstützte Imidisierungsreaktion mit voluminösen Amin-Derivaten entwickelt, welche einen unkomplizierten Zugang zu neuen sterisch-überladenen Rylendicarboximiden lieferte. Optische Spektroskopie wie auch kristallographische Analysen legten Struktur–Eigenschaftsbeziehungen im Festkörper offen und unterstreichen damit die Wichtigkeit eines ausgefeilten Moleküldesigns. Die konzipierte Reaktion könnte weitere Entwicklungen für neue Festkörper-Emitter auf der Basis von Dicarboximiden anregen und deshalb zusätzlich zum fundamentalen Verständnis des Forschungsfeldes des Kristall-Ingenieurwesens beitragen.

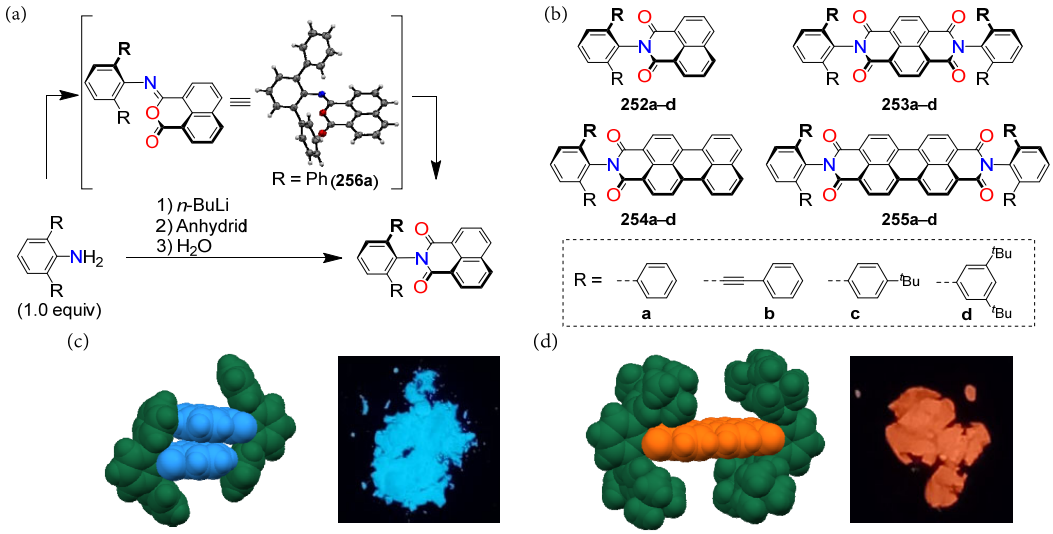

Abbildung 4. (a) Exemplarische Darstellung der entwickelten Basen-unterstützten Imidisierungsreaktion mit voluminösen Amin-Derivaten für Naphthalinmonodicarboximide und Einkristallstruktur des isolierten Isoimid-Intermediates **256a**. (b) Substratumfang der entworfenen Imidisierungsreaktion. (c) Dimeres Packungsmuster von **252a** wie es im Einkristall gefunden wurde und Foto des Pulvers von **252a** unter UV-Lichtbestrahlung. (c) Molekulare Struktur von **255d** wie sie im Einkristall gefunden wurde und Foto des Pulvers von **255d** unter UV-Lichtbestrahlung.

Im letzten *Kapitel 7* wurde ein elektronenarmes Tetrakisdicarboximid-Nanographen als neuartige Wirt-Struktur für die supramolekulare Wirt–Gast Chemie vorgestellt. Aus diesem Grund wurden, auf der Basis der in *Kapitel 6* entwickelten Imidisierungsmethode, vier voluminöse Dicarboximidsubstituenten für den Aufbau von zwei erweiterten π-Gerüsten für die Bindung von elektronenreichen Gästen verwendet (Abbildung 5a). Das gewünschte Nanographen **257** wurde in einer einfachen Reaktionsfolge, inklusive einer vierfachen [3+3] Anellierungsreaktion im letzten Schritt, synthetisiert. Der ditopische Wirt **257** zeigte die nicht-kovalente Bindung von verschiedenen elektronenreichen PAHs in Chloroform-Lösungen – von kleinem Naphthalin bis zu größerem Coronen (Abbildung 5b). Zusätzlich ermöglichte die Solubilisierung durch die Komplexierung auch die Untersuchung von kaum löslichen Ovalen, Hexabenzocoronen und Phthalocyanin, wobei hohe Bindungskonstanten bis zu 10^6 M^{-1} erhalten wurden ($CHCl_3$, 295 K). Hierbei ermöglichten die starken und klaren optischen Eigenschaften von **257** die Verfolgung der Komplexierungsereignisse mittels UV–vis Absorptions- und Fluoreszenzspektroskopie. Detaillierte Untersuchungen mit ^{1}H NMR-Spektroskopie und der isothermen Titrationskalorimetrie lieferten zusätzliche Erkenntnisse über die Bindungsprozesse. Zum Beispiel bestätigten Tieftemperatur ^{1}H NMR-Messungen nicht nur das 1:2 Wirt:Gast Verhältnis (Gast: Coronen), sondern gaben auch systematische Einblicke in die schrittweise Komplexbildung. Darüber hinaus wurden die beteiligten Wechselwirkungskräfte mit der Hilfe von DFT-Berechnungen aufgeschlüsselt. Diese theoretische Analyse deckte die erwartete Beteiligung einer Ladungstransfer-Wechselwirkung bei der Komplexbildung auf, welche von dem Zusammenspiel aus elektronenarmen Wirt und elektronenreichen Gästen hervorgeht. Dies war zusätzlich durch bathochrom verschobene und breite Absorptionsbanden in den UV–vis Titrationsexperimenten zu beobachten. Am wichtigsten waren die gewonnen Einblicke durch die strukturelle Offenlegung der Wirt–Gast-Anordnung im Festkörper mittels kristallographischer Analyse. Die erhaltenen Co-Kristalle für die Gäste Coronen und Phthalocyanin unterstützten die verwendete 1:2 Stöchiometrie von Wirt und Gast in Lösung (Abbildung 5c,d). Des Weiteren wurde eine unerwartete 2:2 Kristallstruktur (Gast: Coronen) als Ergebnis einer Dimerisierung des intermediären 1:1 Komplex gefunden (Abbildung 5e). Insgesamt bietet der konzipierte ditopische Nanographen-Wirt mit seinen eher größeren und elektronenarmen Kavitäten neue Perspektiven für die supramolekulare Chemie. Zusätzlich könnte das einzigartige Moleküldesign des Wirts mit seinen voluminösen Dicarboximidsubstituenten nützlich für den Aufbau von Donor–Akzeptor-Stapeln von definierter Größe sein, was gewöhnlich mittels Faltungs- oder Templat-Ansätzen erzielt wird.

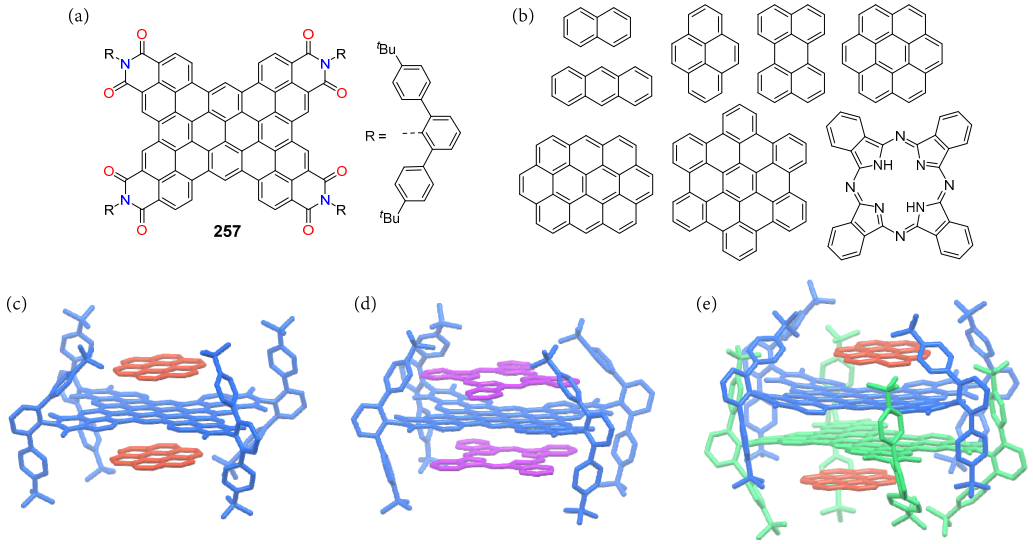

Abbildung 5. Chemische Strukturen (a) des Tetrakisdicarboximid-Nanographen-Wirts **257** und (b) der untersuchten Gastmoleküle. Kristallstrukturen der 1:2 Komplexe mit (c) Coronen (orange) und (d) Phthalocyanin (lila) mit dem Nanographen-Wirt (blau). (e) Kristallstruktur des 2:2 Komplexes von Coronen (orange) und Nanographen (blau und grün). (Wasserstoffatome sind aus Gründen der Übersichtlichkeit ausgeblendet.)

Zusammenfassend stellte die vorliegende Arbeit verschiedene Synthesestrategien für eine Vielfalt an polyzyklischen aromatischen Dicarboximiden vor. Dies beinhaltete tetrachlorierte, tetraryloxy- und tetraaryl-substituierte Dicarboximide, fusionierte Akzeptor–Donor(–Akzeptor)-Strukturen wie auch sterisch abgeschirmte Rylen- und Nanographen-Dicarboximide. Die resultierenden Farbstoffe zeigen hochinteressante und vielfältige Eigenschaften. Zum Beispiel bieten einige der fusionierten und substituierten PADIs eine starke Absorption von sichtbaren und NIR-Licht, NIR-Emission und niedrigliegende LUMO-Niveaus. Im Gegensatz dazu sind die Rylendicarboximide mit ihren voluminösen *N*-Substituenten durch faszinierende optische Eigenschaften im Festkörper charakterisiert, wohingegen der konzipierte sterisch eingehüllte Nanographen-Wirt bemerkenswerte Komplexierungs-Fähigkeiten in Lösung zeigte. Die wertvolle Offenlegung von Struktur–Eigenschaftsbeziehungen könnte den Weg zu neuen elektronenarmen PADIs mit präzise einstellbaren Eigenschaften in Lösung und im Festkörper ebnen. Des Weiteren könnten solche Chromophore Anwendungen in organischen (opto)elektrischen Bauteilen oder als NIR-Farbstoffe finden. Zusätzlich könnte der Beitrag mit dem neuen elektronenarmen Wirt-Design das Feld der supramolekularen Wirt–Gast Chemie bezüglich Ladungstransfer-Wechselwirkungen, Komplexierungen von vergrößerten Gästen oder der supramolekularen Katalyse fördern.

Chapter 10

Supporting Information

10.1. Supporting Information Chapter 3[x]

General Information

Unless otherwise stated, all chemicals, reagents and solvents were purchased from commercial suppliers and used after appropriate purification. Column chromatography was performed on silica gel (particle size 0.040–0.063 mm) with freshly distilled solvents. Size exclusion chromatography was performed with Bio-Beads SX-3 using HPLC grade solvents (dichloromethane/methanol 9:1) as eluent. ^{1}H and ^{13}C NMR spectra were recorded on a Bruker Avance HD III 400 or Bruker Avance HD III 600 spectrometer. The ^{13}C NMR spectra are broad band proton decoupled. Chemical shifts (δ) are listed in parts per million (ppm) and are reported relative to tetramethylsilane and referenced internally to residual proton solvent resonances or natural abundance carbon resonances. The coupling constants (J) are quoted in Hertz (Hz). MALDI-TOF mass spectra were acquired on a Bruker Daltonics autoflex II LRF mass spectrometer. ESI-TOF and APCI-TOF measurements were carried out on a Bruker Daltonics micOTOF focus mass spectrometer. Melting points were measured on an *Olympus* BX41 polarisation microscope with a temperature regulator TP84 from *Linkam Scientific*. The reported values are uncorrected.

UV–vis absorption and emission spectroscopy

All measurements were carried out using spectroscopic grade solvents. UV/Vis absorption spectra were recorded on a Jasco V-770-ST spectrometer. Fluorescence steady-state and lifetime measurements were recorded on a FLS980 Edinburgh Instrument fluorescence spectrometer. The quantum yields were determined by using the dilution method (A < 0.05)[380] and oxazine 1 (Φ_{fl} = 15% in ethanol) as a reference.[159] The lifetime measurements were performed using a pulsed laser diode (λ_{ex} = 505 nm; λ_{det} = 750 nm) and determined with the recording of the instrumental response function (IRF).

[x] This Supporting Information has been published. For the sake of harmonization of all *Supporting Information Chapters*, some modifications were made.
Adapted and reproduced with permission from reference: M. Mahl, K. Shoyama, J. Rühe, V. Grande, F. Würthner, *Chem. Eur. J.* **2018**, *24*, 9409–9416. Copyright 2018 Wiley-VCH Verlag GmbH & Co. KGaA.

Cyclic and square wave voltammetry

Cyclic and square wave voltammetry measurements were conducted on a standard commercial electrochemical analyzer (EC epsilon, BAS instruments, UK) with a three-electrode single-compartment cell. A Pt disc electrode was used as a working electrode, a platinum wire as a counter electrode and an Ag/AgCl reference electrode using ferrocenium/ferrocene (Fc^+/Fc) as an internal standard for the calibration of the potential. The measurements were carried out under an argon atmosphere in dichloromethane and tetrabutylammonium hexafluorophosphate (TBAHFP; recrystallized from ethanol/water and dried under vacuum) was added as supporting electrolyte.

Synthesis

The boronic acid pinacol esters **222a**,[53] **222b′**,[389] **222c**,[53] **222d**,[53] **222f**[390] and **222g**[270] and $[Pd_2(dba)_3]\cdot CHCl_3$[391] were synthesized according to the literature procedures. Boronic ester **222e** was purchased from commercial supplier.

Dibromo-tetrachloro-perylene dicarboximide 223[392]

A mixture of 2.00 g (3.24 mmol, 1.0 equiv) 9,10-dibromo-1,6,7,12-tetrachloro-3,4-perylenedicarboxilyc acid anhydride[393] and 1.15 g (1.22 ml, 6.48 mmol, 2.0 equiv) 2,6-diisopropyl aniline in 16 mL acetic acid and 32 mL *N*-methyl-2-pyrrolidone was heated to 110 °C for 60 h. After cooling down to room temperature, the reaction mixture was poured into 500 mL water, filtrated and successively washed with water and methanol and the crude product was dissolved in dichloromethane from the residue. Subsequently, the solvent was removed under reduced pressure to obtain the crude product, which was further purified by column chromatography (gradient of *n*-hexane/dichloromethane 10:1 to 4:1) to yield 1.13 g (1.45 mmol, 45%) of **223** as a red solid. M.p.: > 350 °C. ^{1}H NMR (CD_2Cl_2, 400 MHz, 298 K): δ/ppm = 8.65 (*s*, 2H), 8.21 (*s*, 2H), 7.52 (*t*, *J* = 7.7Hz, 1H), 7.36 (*d*, *J* = 7.7 Hz, 2H), 2.73 (*sep*, *J* = 6.8 Hz, 2H), 1.14 (*dd*, *J* = 6.8 Hz, *J* = 5.1 Hz, 12H). ^{13}C NMR ($CDCl_3$, 101 MHz, 298 K): δ/ppm = 162.7, 145.6, 137.2, 135.5, 135.0, 133.8, 133.2, 133.2, 131.6, 130.2, 129.9, 129.9, 125.4, 124.2, 123.6, 122.7, 121.9, 29.3, 24.1. MS (MALDI-TOF, positive mode, DCTB/chloroform): 776.864 $[M]^+$. HRMS (ESI-TOF, positive mode, acetonitrile/chloroform): calcd for $C_{34}H_{21}Br_2Cl_4NO_2Na$: 795.8591; found: 795.8585 $[M+Na]^+$.

General procedure for the synthesis of tetrachlorinated polycyclic aromatic dicarboximides 224a–g

A Schlenk-tube was charged with the respective aryl boronic pinacol ester **222a–g** (1.0 equiv), **223** (1.1 equiv), tris(dibenzylideneacetone)dipalladium(0)-chloroform adduct $[Pd_2(dba)_3]\cdot CHCl_3$ (10 mol %), tricyclohexylphosphine tetrafluoroborate $PCy_3\cdot HBF_4$ (40 mol %), Cs_2CO_3 (3.0 equiv) and 1-chloronaphthalene (2.6-6.6 mL) as a solvent under an inert atmosphere at room temperature and heated to 160 °C for 20 h. After cooling down to room temperature, the reaction mixture was filtrated with *n*-hexane over a pad of silica gel to remove 1-chloronaphthalene and the crude product was eluated with dichloromethane. Subsequently, the solvent was removed under reduced pressure to obtain the respective crude product, which was further purified by column chromatography (silica gel), followed by size exclusion chromatography and precipitation.

Tetrachlorinated polycyclic aromatic dicarboximide 224a

According to the general procedure, the reaction of 10.0 mg (39.4 µmol, 1.0 equiv) **222a**, 33.6 mg (43.3 µmol, 1.1 equiv) **223**, 4.1 mg (3.94 µmol, 10 mol %) $[Pd_2(dba)_3]\cdot CHCl_3$, 5.8 mg (15.8 µmol, 40 mol %) $PCy_3\cdot HBF_4$ and 38.5 mg Cs_2CO_3 (118.2 µmol, 3.0 equiv) in 3.9 mL 1-chloronaphthalene afforded **224a**. The crude product was purified by column chromatography (gradient of dichloromethane/*n*-hexane 1:5 to 2:1), followed by size exclusion chromatography and precipitation from dichloromethane/methanol. The isolated solid was washed with *n*-hexane and methanol. The product was dried under high vacuum to give 22.8 mg (30.7 µmol, 78%) of compound **224a** as a dark-blue solid. M.p.: > 350 °C. ^{1}H NMR (CD_2Cl_2, 400 MHz, 298 K): δ/ppm = 8.68 (*s*, 2H), 8.39–8.42 (*m*, 4H), 7.92 (*d*, J = 8.1 Hz, 2H), 7.65 (*t*, J = 8.1 Hz, 2H), 7.53 (*t*, J = 7.8 Hz, 1H), 7.37 (*d*, J = 7.8 Hz, 2H), 2.76 (*sep*, J = 6.3 Hz, 2H), 1.56 (*t*, J = 6.3 Hz, 12H). ^{13}C NMR (CD_2Cl_2, 101 MHz, 298 K): δ/ppm = 163.4, 146.5, 136.7, 136.7, 134.4, 134.3, 133.2, 133.1, 133.0, 131.3, 131.0, 130.0, 128.5, 128.5, 127.5, 127.4, 124.2, 124.1, 123.4, 123.4, 121.3, 29.5, 24.1. UV–vis (CH_2Cl_2): λ_{max} / nm (ε / $M^{-1}cm^{-1}$) = 623 (85200). Fluorescence (CH_2Cl_2, λ_{ex} = 620 nm): λ_{max} / nm (Φ_{fl} / %) = 758 (6.8 ± 0.3). CV (CH_2Cl_2): E_{ox1} = 0.77 V, E_{ox2} = 1.24 V, E_{red1} = –1.05 V, E_{red2} = –1.38 V. MS (MALDI-TOF, negative mode, DCTB in chloroform): 743.065 $[M]^-$. HRMS (ESI-TOF, positive mode, acetonitrile/chloroform): calcd for $C_{44}H_{27}Cl_4NO_2Na$: 764.0688; found: 764.0688 $[M+Na]^+$.

Tetrachlorinated polycyclic aromatic dicarboximide 224b

According to the general procedure, the reaction of 7.9 mg (26.0 µmol, 1.0 equiv) **222b**, 22.2 mg (28.6 µmol, 1.1 equiv) **223**, 2.7 mg (2.60 µmol, 10 mol %) $[Pd_2(dba)_3]\cdot CHCl_3$, 3.8 mg (10.4 µmol, 40 mol %) $PCy_3\cdot HBF_4$ and 25.5 mg Cs_2CO_3 (77.9 µmol, 3.0 equiv) in 2.6 mL 1-chloronaphthalene afforded **224b**. The crude product was purified by column chromatography (gradient of dichloromethane/*n*-hexane 1:7 to 1:1), followed by size exclusion chromatography and precipitation from dichloromethane/methanol. The isolated solid was washed with *n*-hexane and methanol. The product was dried under high vacuum to give 13.6 mg (17.1 µmol, 66%) of compound **224b** as a dark-blue solid. M.p.: > 350 °C. ^{1}H NMR (CD_2Cl_2, 400 MHz, 298 K): δ/ppm = 8.97 (*d*, *J* = 8.7 Hz, 1H), 8.67 (*s*, 1H), 8.65 (*s*, 1H), 8.52–8.53 (*d*, *J* = 3.4 Hz, 2H), 8.45–8.50 (*m*, 2H), 8.14 (*d*, *J* = 8.3 Hz, 1H), 8.10 (*d*, *J* = 8.3 Hz, 1H), 7.68–7.74 (*m*, 4H), 7.59 (*t*, *J* = 8.1 Hz, 1H), 7.47 (*t*, *J* = 8.1 Hz, 1H), 7.32 (*d*, *J* = 8.1 Hz, 2H), 2.72 (*qui*, *J* = 6.9 Hz, 2H), 1.10 (*t*, *J* = 6.9 Hz, 12H). ^{13}C NMR (CD_2Cl_2, 101 MHz, 298 K): δ/ppm = 163.4, 163.3, 146.4, 146.4, 136.2, 136.2, 133.8, 133.2, 133.1, 133.1, 133.0, 132.8, 131.5, 131.3, 131.2, 131.1, 131.0, 130.7, 130.1, 130.0, 129.9, 129.5, 128.8, 126.9, 126.8, 126.5, 126.4, 125.8, 125.6, 124.7, 124.6, 124.5, 123.6, 123.1, 122.4, 121.2, 121.1, 29.5, 24.0. UV–vis (CH_2Cl_2): λ_{max} / nm (ε / $M^{-1}cm^{-1}$) = 687 (82400). CV (CH_2Cl_2): E_{ox1} = 0.58 V, E_{ox2} = 1.01 V, E_{red1} = –0.93 V, E_{red2} = –1.82 V. MS (MALDI-TOF, negative mode, DCTB in chloroform): 793.073 $[M]^-$. HRMS (ESI-TOF, negative mode, acetonitrile/chloroform): calcd for $C_{48}H_{29}Cl_4NO_2Na$: 818.0850; found: 818.0845 $[M+Na]^+$.

Tetrachlorinated polycyclic aromatic dicarboximide 224c

According to the general procedure, the reaction of 10.0 mg (32.9 µmol, 1.0 equiv) **222c**, 28.1 mg (36.2 µmol, 1.1 equiv) **223**, 3.4 mg (3.29 µmol, 10 mol %) $[Pd_2(dba)_3]\cdot CHCl_3$, 4.8 mg (13.2 µmol, 40 mol %) $PCy_3\cdot HBF_4$ and 32.1 mg Cs_2CO_3 (98.6 µmol, 3.0 equiv) in 3.3 mL 1-chloronaphthalene afforded **224c**.The crude product was purified by column chromatography (gradient of dichloromethane/*n*-hexane 1:7 to 1:1), followed by size exclusion chromatography and precipitation from dichloromethane/methanol. The isolated solid was washed with *n*-hexane and methanol. The product was dried under high vacuum to give 23.2 mg (29.2 µmol, 89%) of compound **224c** as a dark-blue solid. M.p.: 311–312 °C. ^{1}H NMR (CD_2Cl_2, 400 MHz, 298 K): δ/ppm = 8.72 (*d*, *J* = 7.7 Hz, 1H), 8.58–8.66 (*m*, 4H), 8.49 (*s*, 1H), 8.44 (*d*, *J* = 8.7 Hz, 1H), 8.37 (*s*, 1H), 7.97 (*d*, *J* = 6.7 Hz, 1H), 7.77 (*t*, *J* = 7.7 Hz, 1H), 7.60–7.72 (*m*, 2H), 7.46 (*t*, *J* = 7.7 Hz, 1H), 7.30 (*d*, *J* = 7.7 Hz, 2H), 2.69 (*qui*, *J* = 6.7 Hz, 2H), 1.09 (*t*, *J* = 6.7 Hz, 12H). ^{13}C NMR (CD_2Cl_2, 101 MHz, 298 K): δ/ppm = 163.3, 146.4, 146.4, 136.7, 136.4, 134.3, 134.0, 133.2, 133.2, 133.1, 132.9, 132.9, 131.8, 131.2, 131.2, 131.1, 131.0, 129.9, 129.9, 128.9, 128.3, 128.0, 127.6,

126.0, 125.7, 125.3, 124.5, 124.5, 123.7, 123.4, 123.3, 123.2, 123.1, 123.1, 121.2, 29.5, 24.1, 24.1. UV–vis (CH_2Cl_2): λ_{max} / nm (ε / $M^{-1}cm^{-1}$) = 627 (87000). Fluorescence (CH_2Cl_2, λ_{ex} = 620 nm): λ_{max} / nm (Φ_{fl} / %) = 754 (10.6 ± 0.4). CV (CH_2Cl_2): E_{ox1} = 0.78 V, E_{red1} = –1.01 V, E_{red2} = –1.32 V. MS (MALDI-TOF, negative mode, DCTB in chloroform): 793.112 $[M]^-$. HRMS (ESI-TOF, positive mode, acetonitrile/chloroform): calcd for $C_{48}H_{29}Cl_4NO_2Na$: 818.0850; found: 818.0845 $[M+Na]^+$.

Tetrachlorinated polycyclic aromatic dicarboximide 224d

According to the general procedure, the reaction of 10.0 mg (30.8 µmol, 1.0 equiv) **222d**, 26.4mg (33.9 µmol, 1.1 equiv) **223**, 3.2 mg (3.08 µmol, 10 mol %) $[Pd_2(dba)_3]\cdot CHCl_3$, 4.5 mg (12.3 µmol, 40 mol %) $PCy_3\cdot HBF_4$ and 30.1 mg Cs_2CO_3 (92.4 µmol, 3.0 equiv) in 3.1 mL 1-chloronaphthalene afforded **224d**. The crude product was purified by column chromatography (gradient of dichloromethane/*n*-hexane 1:4 to 2:1), followed by size exclusion chromatography and precipitation from dichloromethane/methanol. The isolated solid was washed with *n*-hexane and methanol. The product was dried under high vacuum to give 20.2 mg (24.6 µmol, 80%) of compound **224d** as a dark-blue solid. M.p.: > 350 °C. ^{1}H NMR (CD_2Cl_2, 400 MHz, 298 K): δ/ppm = 8.73 (*s*, 1H), 8.72 (*s*, 1H), 7.86–7.93 (*m*, 2H), 7.67–7.82 (*m*, 6H), 7.53–7.60 (*m*, 3H), 7.41 (*d*, *J* = 7.8 Hz, 2H), 2.75–2.86 (*m*, 4H), 1.17–1.23 (*m*, 12H). ^{13}C NMR (CD_2Cl_2, 101 MHz, 345 K): δ/ppm = 163.0, 146.0, 137.1, 136.5, 134.7, 134.4, 134.2, 133.1, 133.1, 133.0, 133.0, 133.0, 131.7, 131.3, 131.2, 131.0, 130.8, 130.7, 129.7, 129.0, 128.9, 128.3, 128.3, 128.0, 127.9, 127.0, 126.0, 125.7, 125.6, 125.2, 125.1, 124.3, 124.1, 123.6, 123.2, 122.5, 121.4, 121.3, 29.5, 24.3. UV–vis (CH_2Cl_2): λ_{max} / nm (ε / $M^{-1}cm^{-1}$) = 663 (108400). Fluorescence (CH_2Cl_2, λ_{ex} = 600 nm): λ_{max} / nm (Φ_{fl} / %) = 801 (2.8 ± 0.2). CV (CH_2Cl_2): E_{ox1} = 0.64 V, E_{ox2} = 1.09 V, E_{red1} = –1.03 V, E_{red2} = –1.33 V. MS (MALDI-TOF, negative mode, DCTB in chloroform): 817.170 $[M]^-$. HRMS (APCI-TOF, positive mode, acetonitrile/chloroform): calcd for $C_{50}H_{30}Cl_4NO_2$: 816.1031; found: 816.1025 $[M+H]^+$.

Tetrachlorinated polycyclic aromatic dicarboximide 224e

According to the general procedure, the reaction of 25.0 mg (66.1 µmol, 1.0 equiv) **222e**, 56.5 mg (72.73 µmol, 1.1 equiv) **223**, 6.8 mg (6.61 µmol, 10 mol %) $[Pd_2(dba)_3]\cdot CHCl_3$, 9.7 mg (26.4 µmol, 40 mol %) $PCy_3\cdot HBF_4$ and 64.6 mg Cs_2CO_3 (198.3 µmol, 3.0 equiv) in 6.6 mL 1-chloronaphthalene afforded **224e**. The crude product was purified by column chromatography (gradient of dichloromethane/*n*-hexane 1:2 to 10:1), followed by size exclusion chromatography and precipitation from dichloromethane/methanol. The isolated solid was washed with *n*-hexane and methanol. The product was dried under high vacuum to give 42.3 mg (48.8 µmol, 74%) of

compound **224e** as a dark-green solid. M.p.: > 350 °C. ^{1}H NMR ($C_2D_2Cl_4$, 600 MHz, 385 K): δ/ppm = 8.73 (*s*, 2H), 8.37–8.49 (*m*, 8H), 7.87 (*d*, *J* = 6.7 Hz, 1H), 7.64 (*t*, *J* = 6.7 Hz, 1H), 7.53 (*t*, *J* = 7.8 Hz, 1H), 7.39 (*d*, *J* = 7.8 Hz, 2H), 2.85 (*sep*, *J* = 6.7 Hz, 2H), 1.27 (*t*, *J* = 6.7 Hz, 12H). Solubility is too low for recording ^{13}C NMR. UV–vis (CH_2Cl_2): λ_{max} / nm (ε / $M^{-1}cm^{-1}$) = 736 (128500). CV (CH_2Cl_2): E_{ox1} = 0.42 V, E_{ox2} = 0.88 V, E_{red1} = –1.00 V, E_{red2} = –1.31 V. MS (MALDI-TOF, negative mode, DCTB in chloroform): 867.040 $[M]^-$. HRMS (ESI-TOF, positive mode, acetonitrile/chloroform): calcd for $C_{54}H_{31}Cl_4NO_2Na$: 888.1007; found: 888.1001 $[M+Na]^+$.

Tetrachlorinated polycyclic aromatic dicarboximide 224f

According to the general procedure, the reaction of 10.0 mg (23.5 µmol, 1.0 equiv) **222f**, 20.1 mg (25.9 µmol, 1.1 equiv) **223**, 2.4 mg (2.35 µmol, 10 mol %) $[Pd_2(dba)_3]\cdot CHCl_3$, 3.5 mg (9.38 µmol, 40 mol %) $PCy_3\cdot HBF_4$ and 22.9 mg Cs_2CO_3 (70.4 µmol, 3.0 equiv) in 2.4 mL 1-chloronaphthalene at a reaction temperature of 200 °C afforded **224f**. The crude product was purified by column chromatography (gradient of dichloromethane/*n*-hexane 1:5 to 2:1), followed by size exclusion chromatography and precipitation from dichloromethane/methanol. The isolated solid was washed with *n*-hexane and methanol. The product was dried under high vacuum to give 13.3 mg (14.5 µmol, 62%) of compound **224f** as a dark-blue solid. M.p.: > 350 °C. ^{1}H NMR ($C_2D_2Cl_4$, 600 MHz, 385 K): δ/ppm = 9.40 (*s*, 2H), 8.75–8.88 (*m*, 12H), 7.55 (*t*, *J* = 7.8 Hz, 1H), 7.41 (*d*, *J* = 7.8 Hz, 2H), 2.89 (*qui*, *J* = 6.9 Hz, 2H), 1.30 (*t*, *J* = 7.8 Hz, 12H). Solubility is too low for recording ^{13}C NMR. UV–vis (CH_2Cl_2): λ_{max} / nm (ε / $M^{-1}cm^{-1}$) = 663 (72200). MS (MALDI-TOF, negative mode, DCTB in chloroform): 914.882 $[M]^-$. HRMS (ESI-TOF, positive mode, acetonitrile/chloroform): calcd for $C_{58}H_{31}Cl_4NO_2Na$: 936.1007; found: 936.1001 $[M+Na]^+$.

Tetrachlorinated polycyclic aromatic dicarboximide 224g

According to the general procedure, the reaction of 10.0 mg (26.6 µmol, 1.0 equiv) **222g**, 22.7 mg (29.3 µmol, 1.1 equiv) **223**, 2.8 mg (2.66 µmol, 10 mol %) $[Pd_2(dba)_3]\cdot CHCl_3$, 3.9 mg (10.6 µmol, 40 mol %) $PCy_3\cdot HBF_4$ and 26.0 mg Cs_2CO_3 (79.7 µmol, 3.0 equiv) in 2.7 mL 1-chloronaphthalene afforded **224g**. The crude product was purified by column chromatography (gradient of dichloromethane/*n*-hexane 1:5 to 2:1), followed by size exclusion chromatography and precipitation from dichloromethane/methanol. The isolated solid was washed with *n*-hexane and methanol. The product was dried under high vacuum to give 12.7 mg (14.7 µmol, 55%) of compound **224g** as a blue solid. M.p.: > 350 °C. ^{1}H NMR ($C_2D_2Cl_4$, 400 MHz, 350 K): δ/ppm = 8.68 (*s*, 2H), 8.47 (*s*, 2H), 8.31 (*s*, 2H), 7.82 (*qua*, *J* = 8.0 Hz, 8H), 7.75 (*s*, 2H), 7.49 (*t*, *J* = 8.0 Hz,

1H), 7.34 (*d*, *J* = 8.0 Hz, 2H), 2.76 (*qui*, *J* = 6.6 Hz, 2H), 1.20 (*t*, *J* = 6.6 Hz, 12H). ^{13}C NMR (CD_2Cl_2, 101 MHz, 298 K): δ/ppm = 162.5, 145.6, 136.9, 136.6, 136.1, 135.6, 134.2, 134.0, 133.0, 132.7, 132.5, 131.5, 131.4, 130.9, 130.6, 130.3, 129.3, 128.1, 127.6, 127.5, 124.4, 124.1, 123.8, 123.8, 123.6, 121.4, 120.2, 29.1, 23.9. UV–vis (CH_2Cl_2): λ_{max} / nm (ε / $M^{-1}cm^{-1}$) = 614 (88300). Fluorescence (CH_2Cl_2, λ_{ex} = 590 nm): λ_{max} / nm (Φ_{fl} / %) = 709 (31.2 ± 1.1). CV (CH_2Cl_2): E_{ox1} = 0.90 V, E_{ox2} = 1.25 V, E_{red1} = –1.00 V, E_{red2} = –1.22 V. MS (MALDI-TOF, negative mode, DCTB in chloroform): 865.017 $[M]^-$. HRMS (ESI-TOF, positive mode, acetonitrile/chloroform): calcd for $C_{54}H_{29}Cl_4NO_2Na$: 886.0850; found: 886.0853 $[M+Na]^+$.

Optimization

Table A1. Optimization of reaction conditions for the synthesis of **224a**.[a]

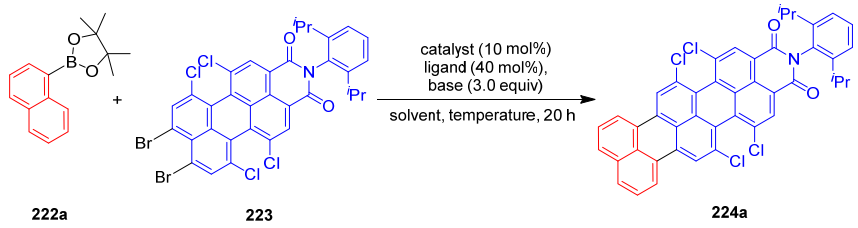

222a **223** **224a**

entry	solvent	catalyst	ligand	base	*c* / M	*T* / °C	yield / %
1	*o*-DCB	$[Pd_2(dba)_3]\cdot CHCl_3$	P(*o*-tolyl)$_3$	Cs_2CO_3	0.03	160	2
2	1-chlnaph	$[Pd_2(dba)_3]\cdot CHCl_3$	P(*o*-tolyl)$_3$	Cs_2CO_3	0.03	160	14
3	1-chlnaph	$[Pd_2(dba)_3]\cdot CHCl_3$	SPhos	Cs_2CO_3	0.03	160	12
4	1-chlnaph	$[Pd_2(dba)_3]\cdot CHCl_3$	$PCy_3\cdot HBF_4$	Cs_2CO_3	0.03	160	67
5	1-chlnaph	$[Pd_2(dba)_3]\cdot CHCl_3$	$PCy_3\cdot HBF_4$	Cs_2CO_3	0.1	160	22
6	1-chlnaph	$[Pd_2(dba)_3]\cdot CHCl_3$	$PCy_3\cdot HBF_4$	Cs_2CO_3	0.01	160	78
7	1-chlnaph	$[Pd_2(dba)_3]\cdot CHCl_3$	$PCy_3\cdot HBF_4$	Cs_2CO_3	0.01	120	5
8	1-chlnaph	$[Pd_2(dba)_3]\cdot CHCl_3$	$PCy_3\cdot HBF_4$	Cs_2CO_3	0.01	200	19
9[b]	1-chlnaph	$Pd(OAc)_2$	$PCy_3\cdot HBF_4$	Cs_2CO_3	0.01	160	37
10[b]	1-chlnaph	$Pd(dba)_2$	$PCy_3\cdot HBF_4$	Cs_2CO_3	0.01	160	59
11[b]	1-chlnaph	$PdCl_2(MeCN)$	$PCy_3\cdot HBF_4$	Cs_2CO_3	0.01	160	36
12	1-chlnaph	$[Pd_2(dba)_3]\cdot CHCl_3$	$PCy_3\cdot HBF_4$	KO^{t}BU	0.01	160	34
13	1-chlnaph	$[Pd_2(dba)_3]\cdot CHCl_3$	$PCy_3\cdot HBF_4$	K_2CO_3	0.01	160	-
14[c]	1-chlnaph	$[Pd_2(dba)_3]\cdot CHCl_3$	$PCy_3\cdot HBF_4$	Cs_2CO_3	0.01	160	29

[a]Reaction conditions: **222a** (1.0 equiv), **223** (1.1 equiv), catalyst (10 mol%), ligand (40 mol%), base (3.0 equiv). *o*-DCB: *o*-dichlorobenzene, 1-chlnaph: 1-chloronaphthalene, P(*o*-tolyl): tri(*o*-tolyl)phosphine, SPhos: 2-dicyclohexylphosphino-2′,6′-dimethoxybiphenyl, PCy_3: tri(cyclohexyl)phosphine, dba: dibenzylideneacetone. [b]Catalyst loading: 20 mol %. [c]1.5 equiv of base instead of 3.0 equiv.

Optical Properties

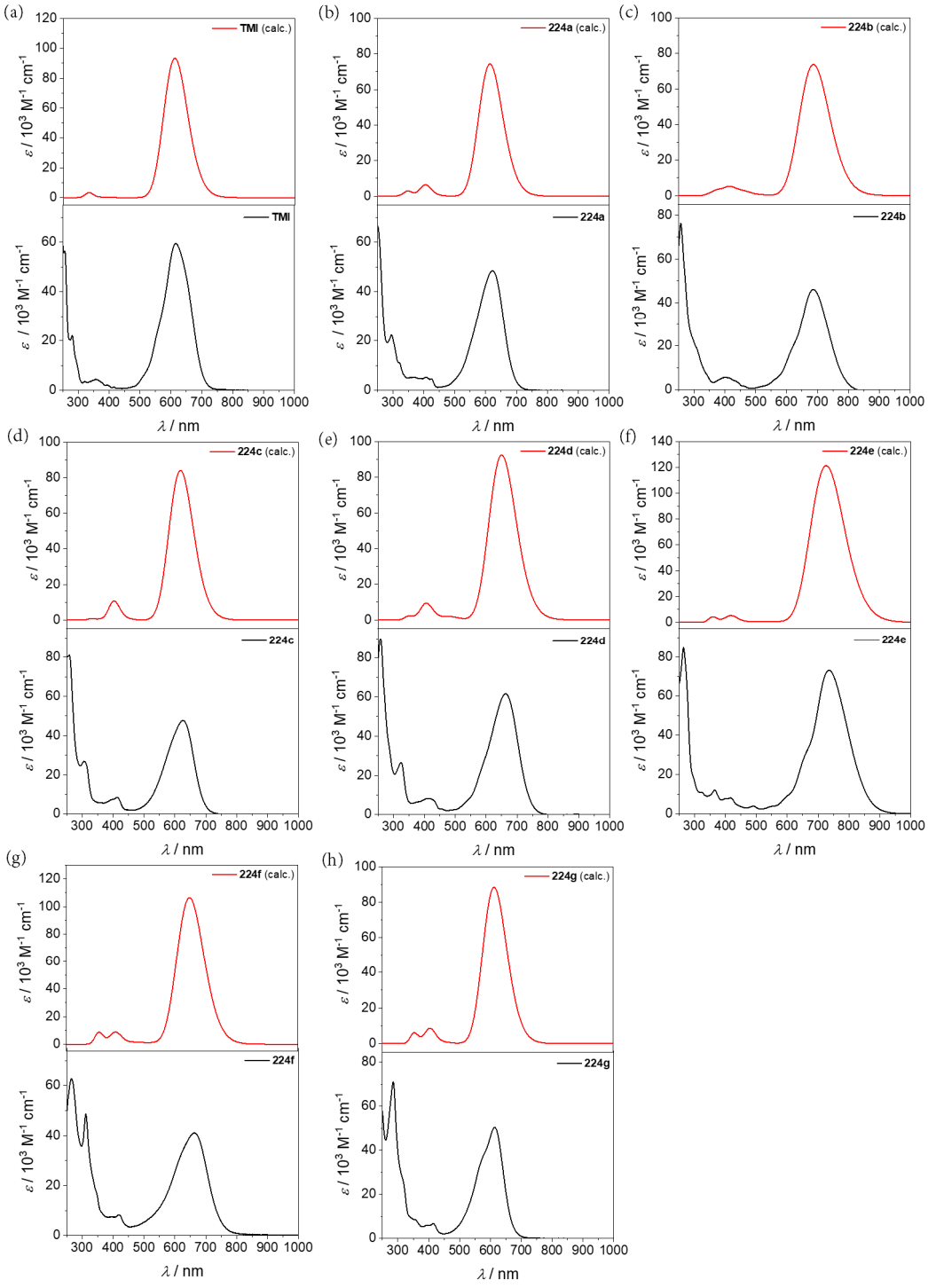

Figure A1. Comparison of calculated (top) and measured (bottom) UV–vis spectra of compounds (a) **TMI**, (b) **224a**, (c) **224b**, (d) **224c**, (e) **224d**, (f) **224e**, (g) **224f** and (h) **224g**. Spectra were calculated using B3LYP/def2-SVP (half-width 0.15 eV).

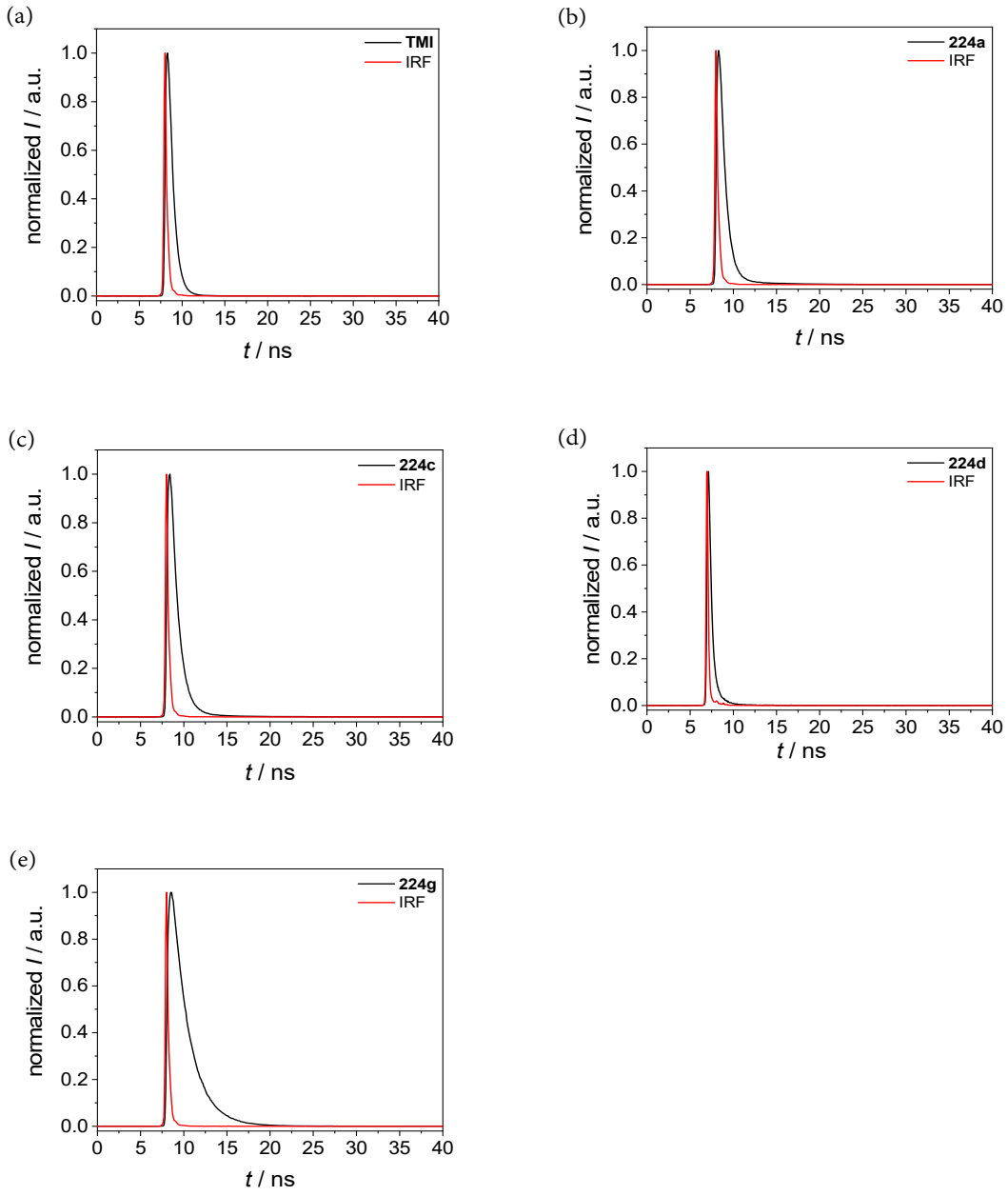

Figure A2. Time-resolved fluorescence decay of (a) **TMI**, (b) **224a**, (c) **224c**, (d) **224d** and (e) **224g** (IRF = instrumental response function; λ_{ex} = 505 nm; λ_{det} = 750 nm).

Table A2. Determined fluorescence lifetimes for **TMI**, **224a**, **224c**, **224d** and **224g** (λ_{ex} = 505 nm; λ_{det} = 750 nm).

	TMI	**224a**	**224c**	**224d**	**224g**
τ / ns	0.53 ± 0.002 (99%) 3.44 ± 0.199 (1%)	0.61 ± 0.004 (91.5%) 4.37 ± 0.077 (8.5%)	0.80 ± 0.005 (94.1%) 4.32 ± 0.069 (5.9%)	0.29 ± 0.002 (95%) 2.33 ± 0.070 (5%)	1.91 ± 0.007 (96.9%) 4.75 ± 0.335 (3.1%)

Theoretical Calculations

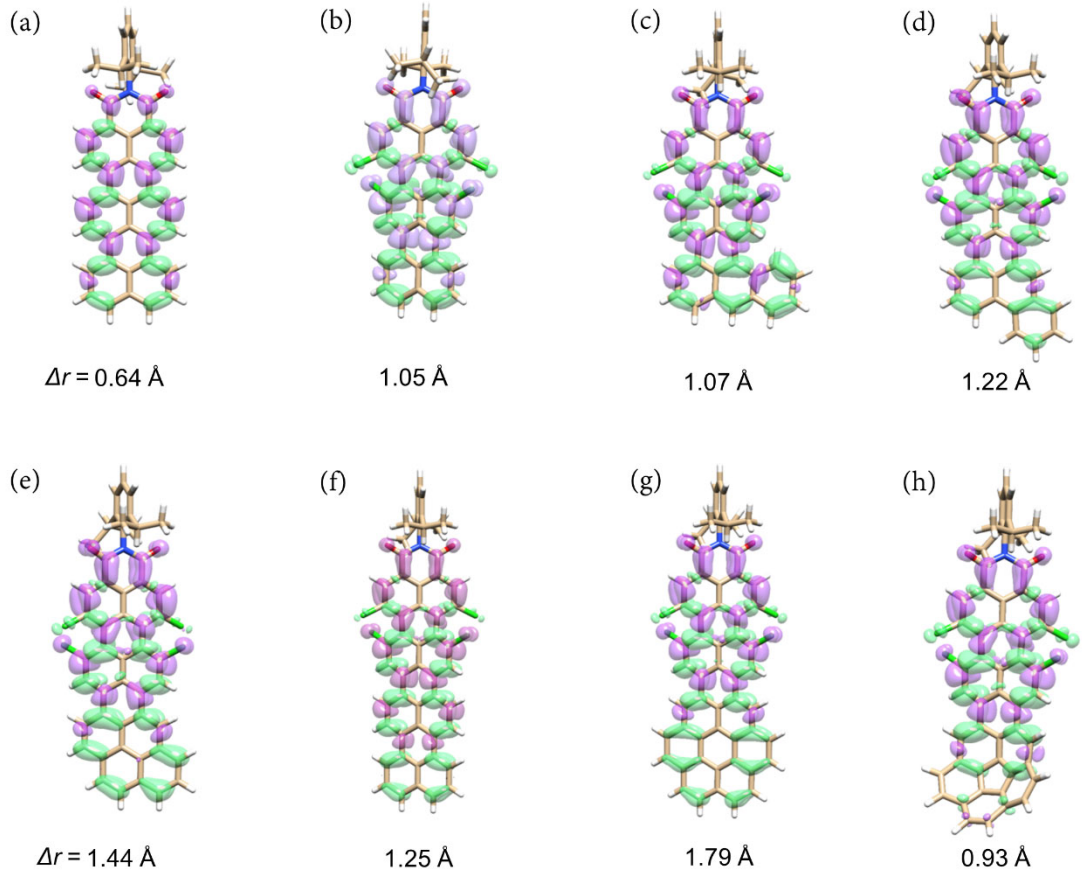

Figure A3. Calculated charge density differences for the S_0–S_1 transition by TD-DFT (B3LYP/def2-SVP, isovalue = 0.0004 a. u.): Green (positive) and purple (negative) regions represent an increase or decrease in electron density due to the excitation. (a) **TMI**, (b) **224a**, (c) **224b**, (d) **224c**, (e) **224d**, (f) **224e**, (g) **224f** and (h) **224g** and their respective charge transfer length parameter Δr (calculated by using MultiWfn program[394]).

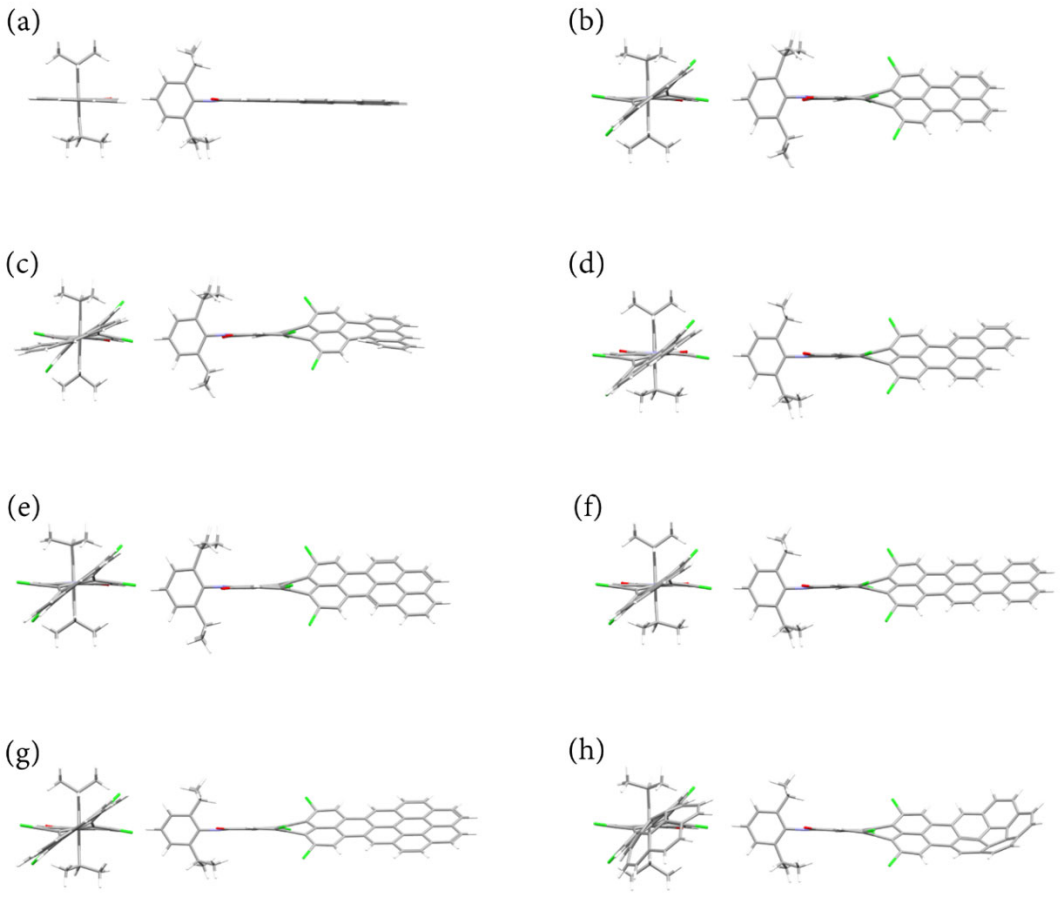

Figure A4. Optimized geometries (left: side view; right: front view) of (a) reference **TMI**, (b) **224a**, (c) **224b**, (d) **224c**, (e) **224d**, (f) **224e**, (g) **224f** and (h) **224g** calculated using B3LYP/def2-SVP.

Table A3. Calculated twist angle of the two chlorinated naphthalene subunits in PADIs **224a**–**g** from the optimized geometries.[a]

	TMI	**224a**	**224b**	**224c**	**224d**	**224e**	**224f**	**224g**
Twist angle / °	0	39	35	39	39	38	38	39

[a]DFT calculations using B3LYP/def2-SVP.

Electronic Properties

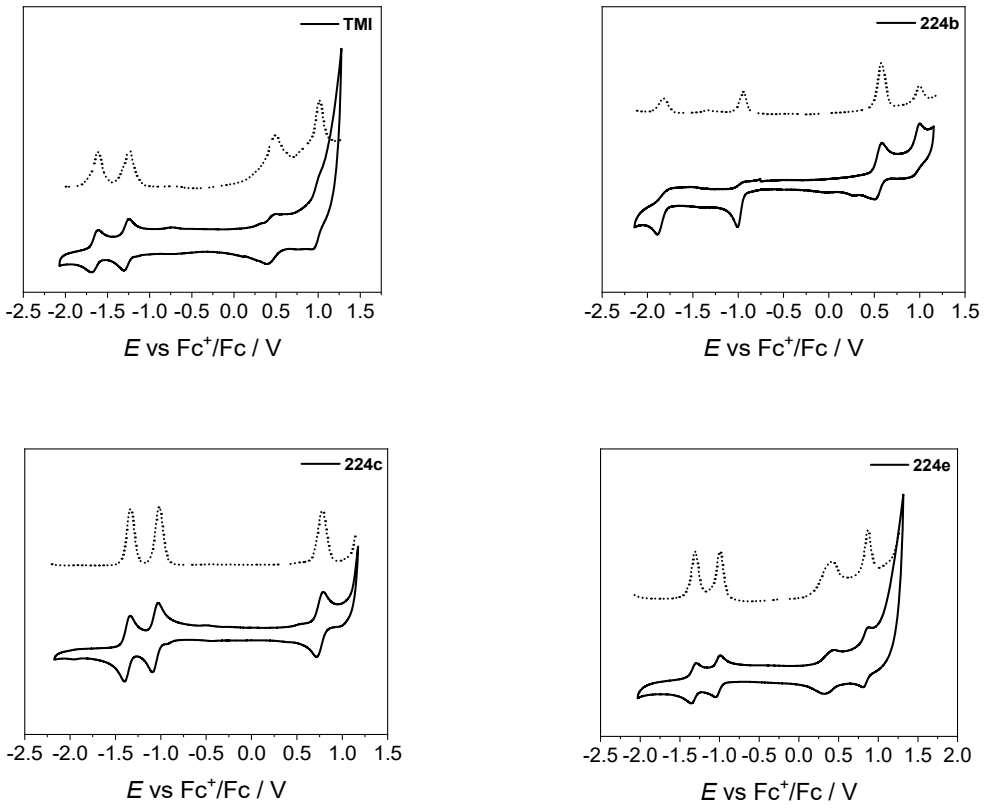

Figure A5. Cyclic voltammetry (solid line) and square wave voltammetry (dashed line) traces of **TMI**, **224b**, **224c** and **224e**. Measurements were performed using dichlormethane solutions ($c \sim 2 \cdot 10^{-5}$ M) at room temperature using tetrabutylammonium hexafluorophosphate (0.1 M) as electrolyte (scan rate 100 mVs^{-1}).

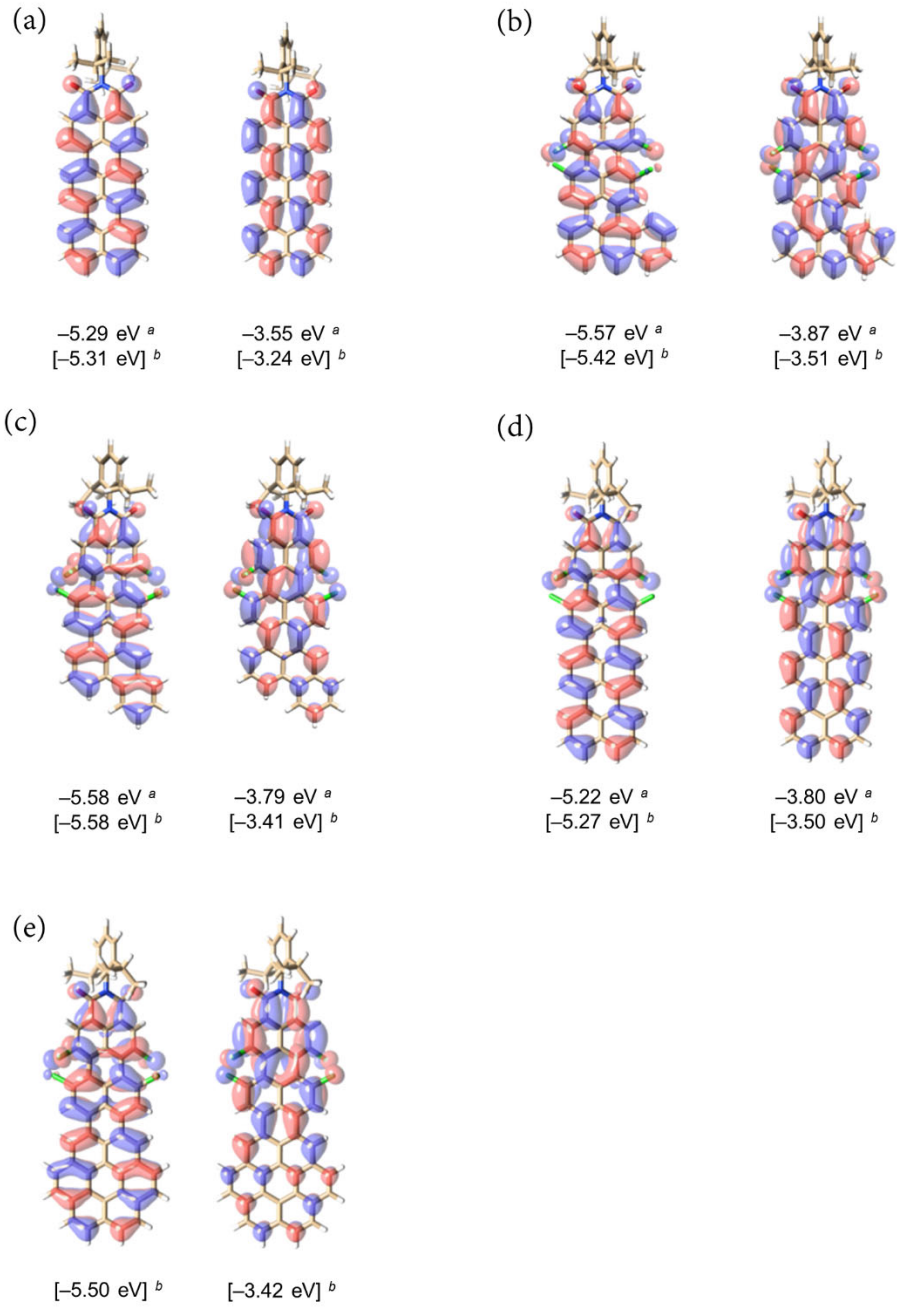

Figure A6. Calculated shapes and energies of frontier orbitals (HOMO left; LUMO right) using B3LYP/def2-SVP: (a) **TMI**, (b) **224b**, (c) **224c**, (d) **224e** and (e) **224f**. [a]Calculated according to $E_{LUMO} = -[E(M^{-}/M) + 4.8\ eV]$ and $E_{HOMO} = -[E(M^{+}/M) + 4.8\ eV]$ using the experimentally determined redox potentials and the energy level of ferrocenium/ferrocene (Fc^{+}/Fc) with respect to the vacuum level (–4.8 eV). [b]DFT calculations by using B3LYP/def2-SVP.

NMR Spectroscopy

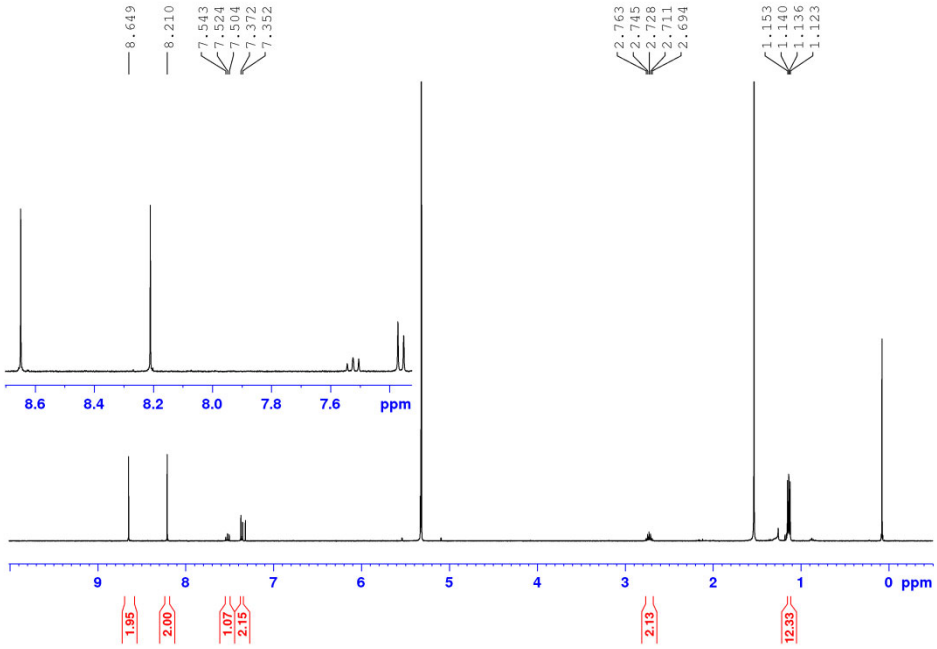

Figure A7. ^{1}H NMR (400 MHz, 298 K) spectrum of **223** in CD_2Cl_2, contains residual water peak at 1.52.

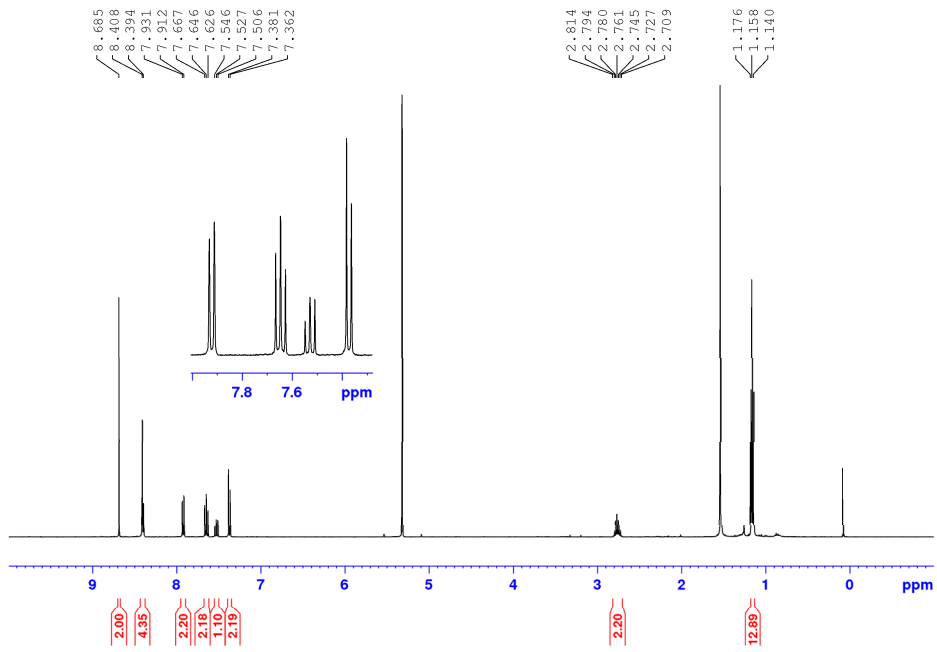

Figure A8. ^{1}H NMR (400 MHz, 298 K) spectrum of **224a** in CD_2Cl_2, contains residual water peak at 1.52.

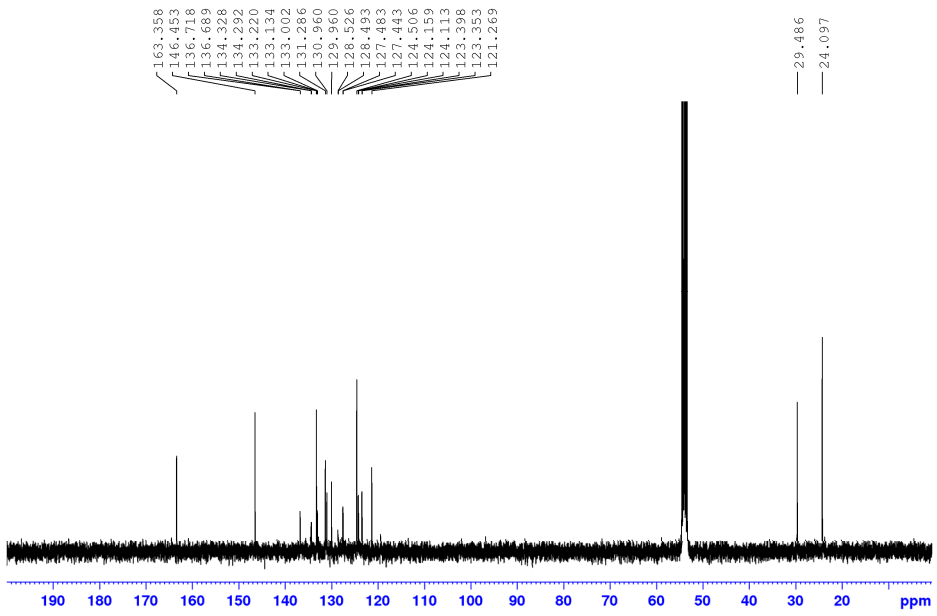

Figure A9. ^{13}C NMR (101 MHz, 298 K) spectrum of **224a** in CD_2Cl_2.

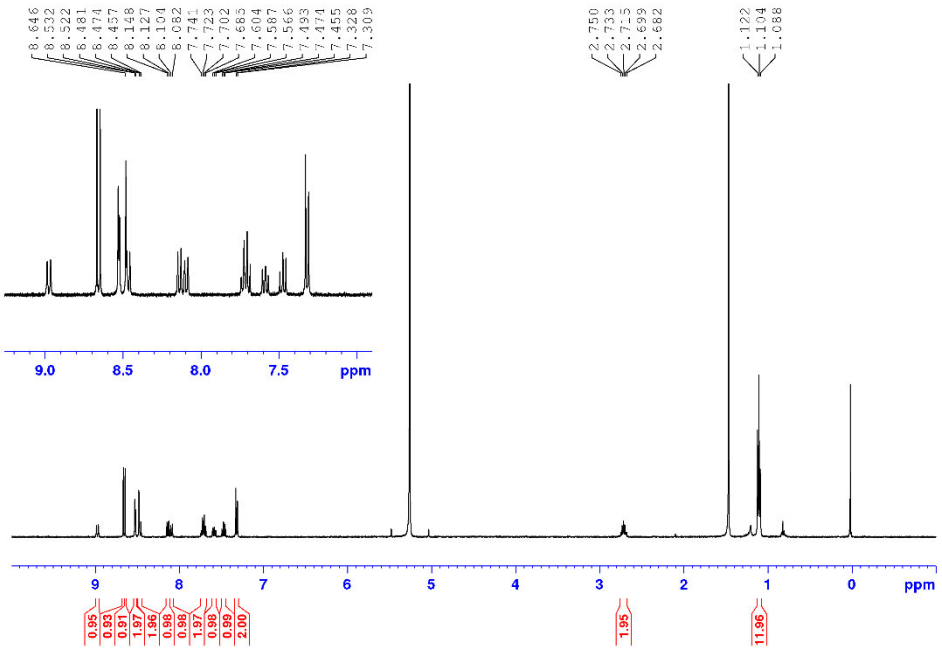

Figure A10. ^{1}H NMR (400 MHz, 298 K) spectrum of **224b** in CD_2Cl_2, contains residual water peak at 1.52.

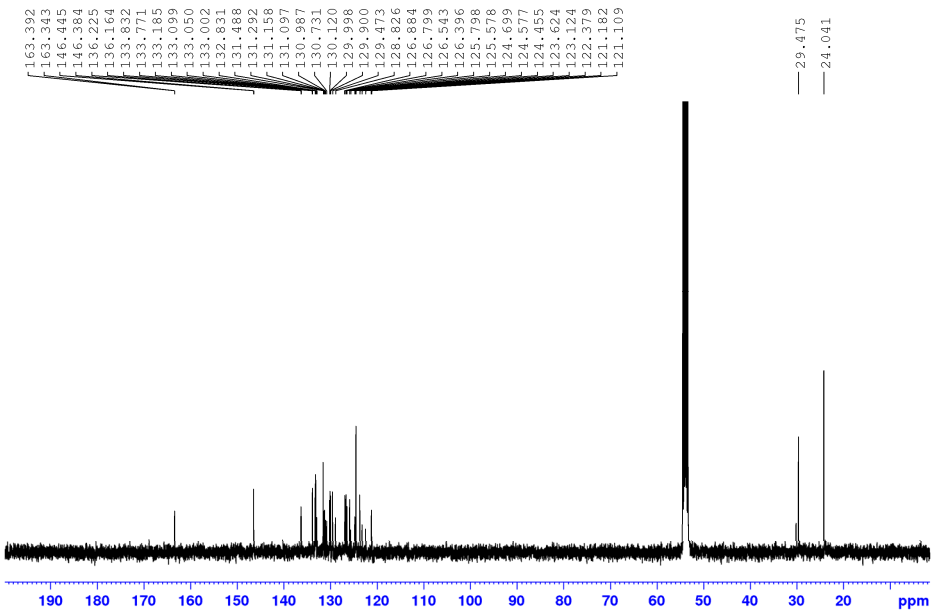

Figure A11. ^{13}C NMR (101 MHz, 298 K) spectrum of **224b** in CD_2Cl_2.

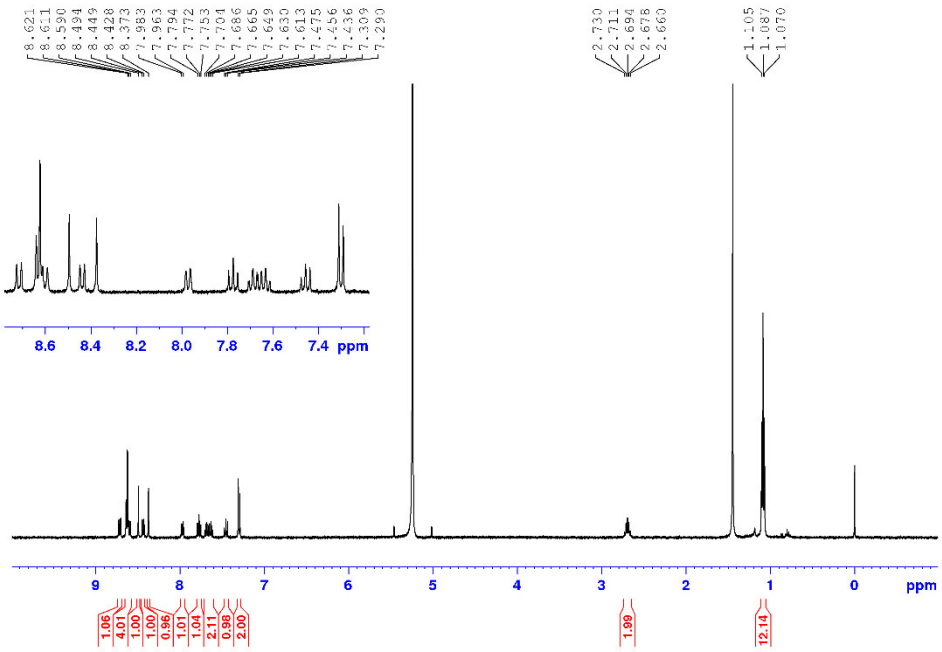

Figure A12. ^{1}H NMR (400 MHz, 298 K) spectrum of **224c** in CD_2Cl_2, contains residual water peak at 1.52.

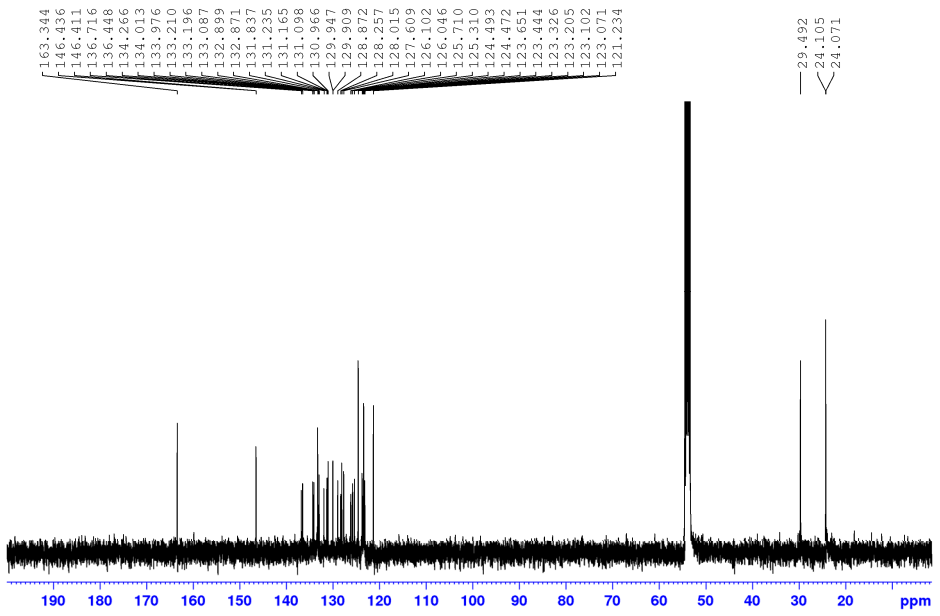

Figure A13. ^{13}C NMR (101 MHz, 298 K) spectrum of **224c** in CD_2Cl_2.

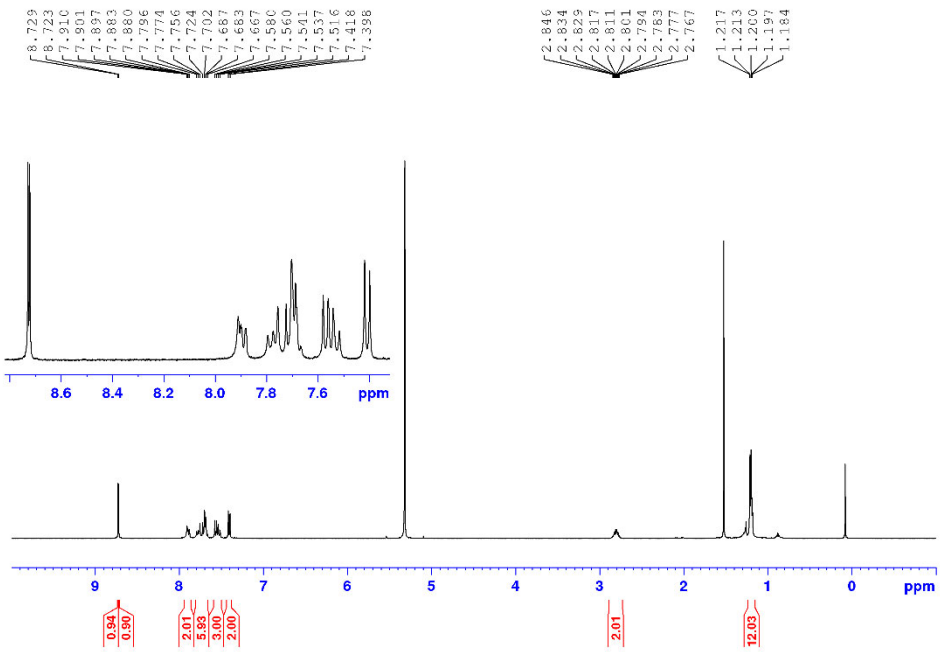

Figure A14. ^{1}H NMR (400 MHz, 298 K) spectrum of **224d** in CD_2Cl_2, contains residual water peak at 1.52.

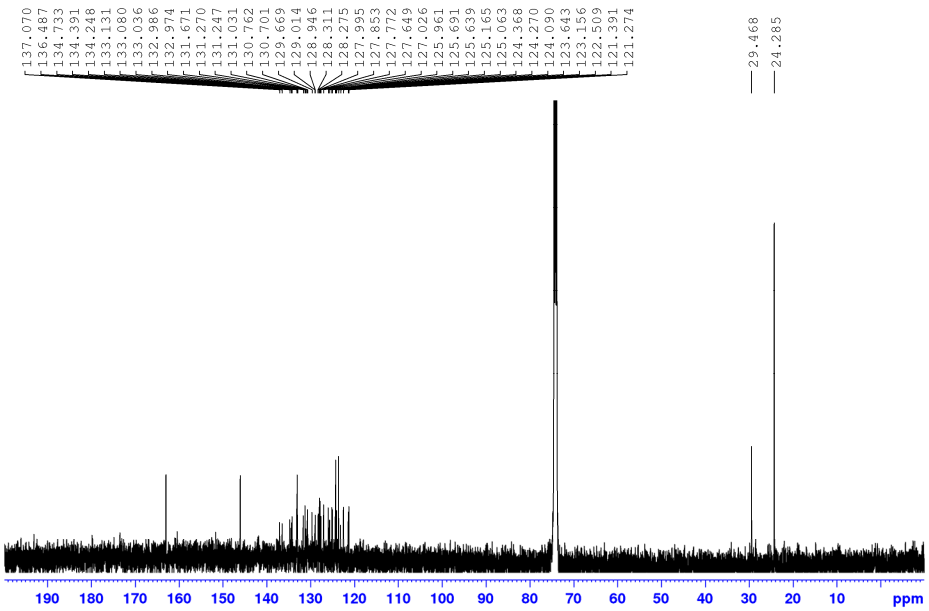

Figure A15. ^{13}C NMR (101 MHz, 345 K) spectrum of **224d** in $C_2D_2Cl_4$.

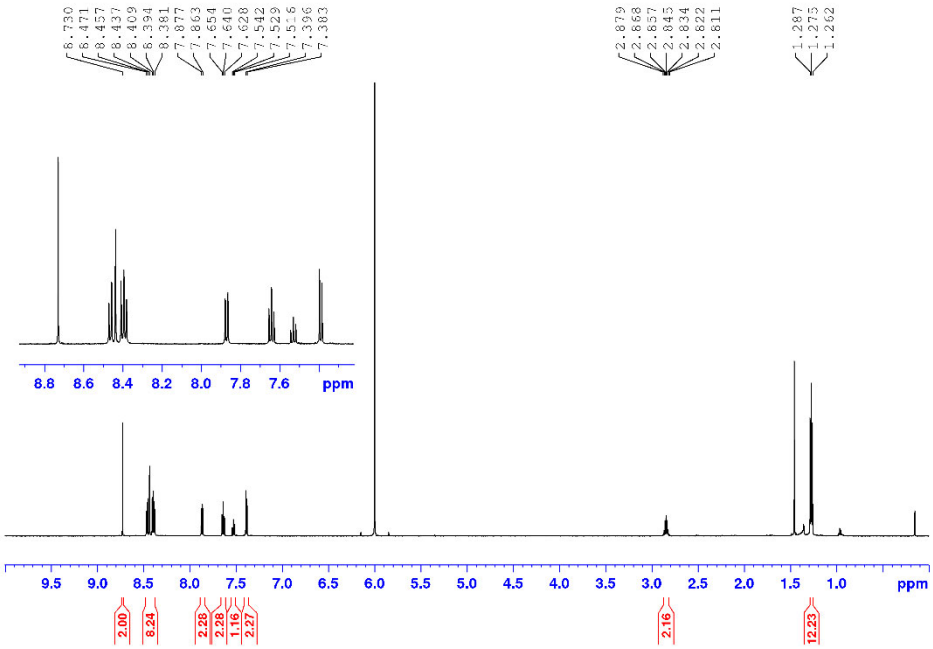

Figure A16. ^{1}H NMR (600 MHz, 385 K) spectrum of **224e** in $C_2D_2Cl_4$, contains residual water peak at 1.44.

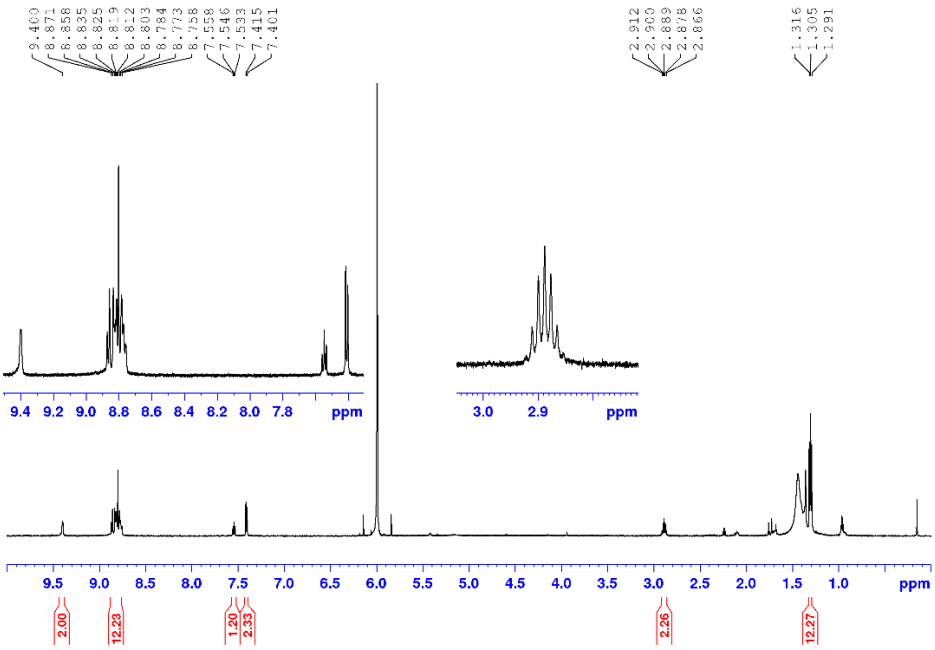

Figure A17. ^{1}H NMR (600 MHz, 385 K) spectrum of **224f** in $C_2D_2Cl_4$, contains solvent impurities in the aliphatic region (hexane).

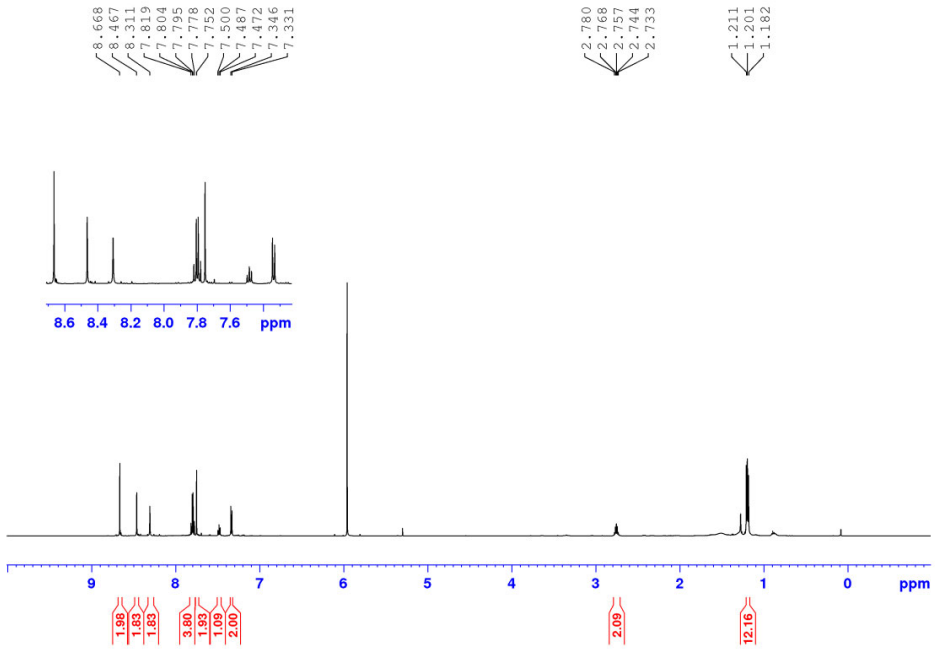

Figure A18. ^{1}H NMR (600 MHz, 350 K) spectrum of **224g** in $C_2D_2Cl_4$.

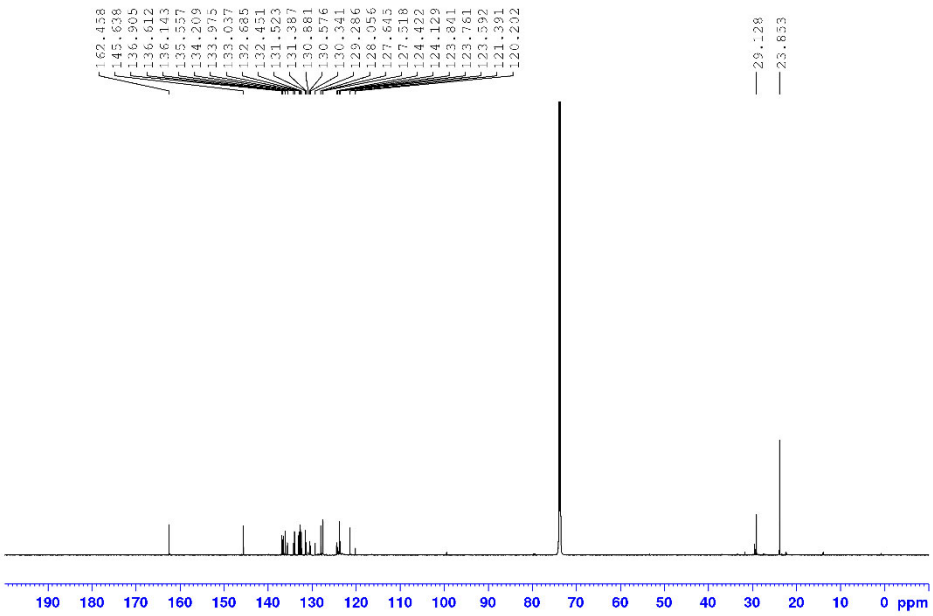

Figure A19. ^{13}C NMR (151 MHz, 350 K) spectrum of **224g** in $C_2D_2Cl_4$.

Mass Spectrometry

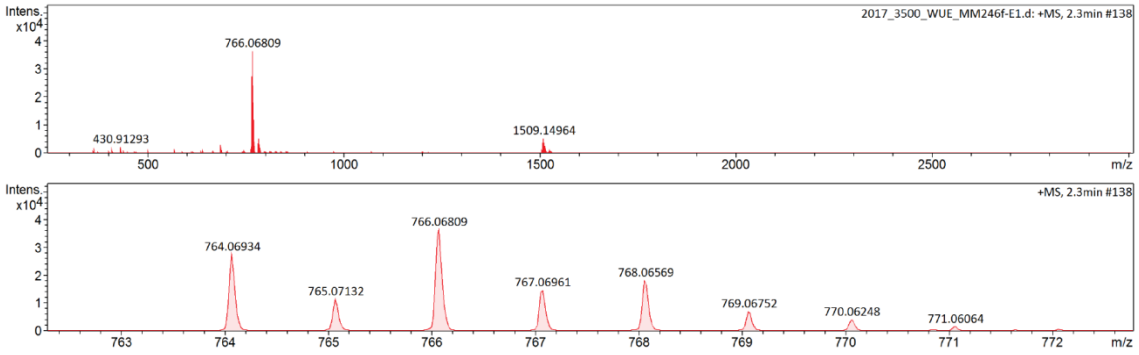

Figure A20. HRMS (ESI-TOF, positive mode, acetonitrile/chloroform) of **224a** $[M+Na]^+$.

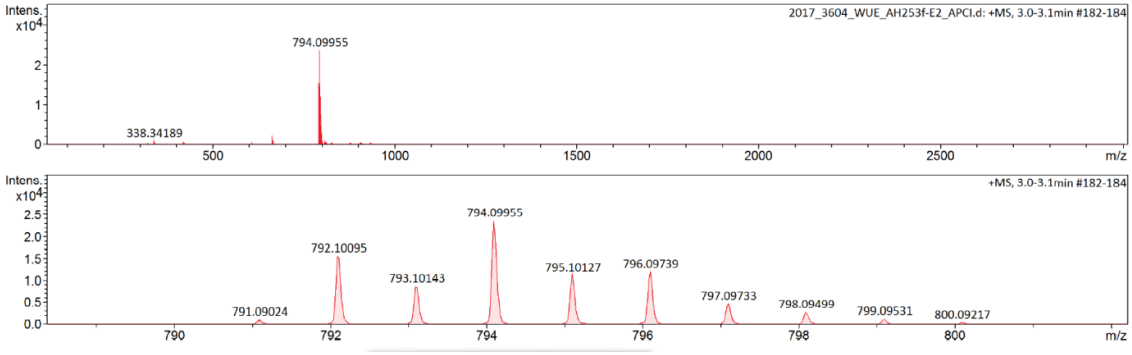

Figure A21. HRMS (APCI-TOF, positive mode, acetonitrile/chloroform) of **224b** $[M]^+$.

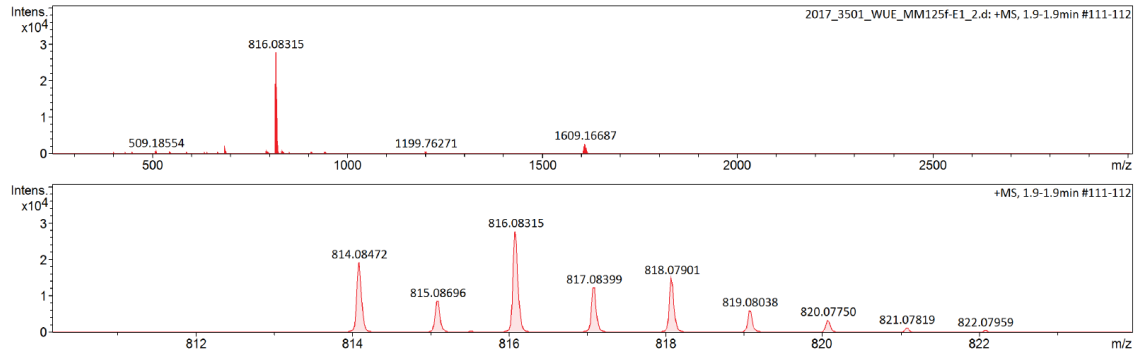

Figure A22. HRMS (ESI-TOF, positive mode, acetonitrile/chloroform) of **224c** $[M+Na]^+$.

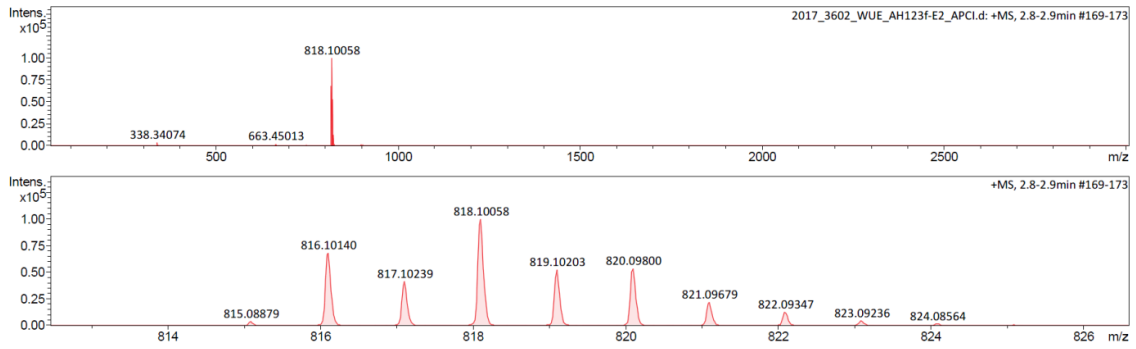

Figure A23. HRMS (APCI-TOF, positive mode, acetonitrile/chloroform) of **224d** $[M]^+$.

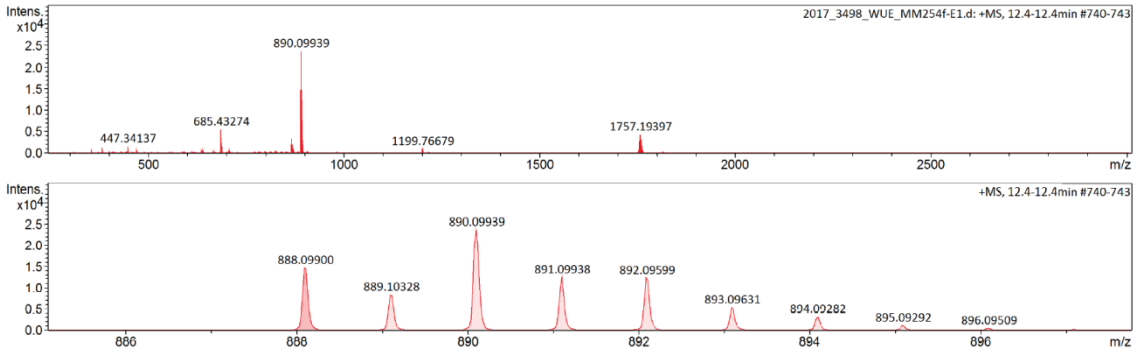

Figure A24. HRMS (ESI-TOF, positive mode, acetonitrile/chloroform) of **224e** $[M+Na]^+$.

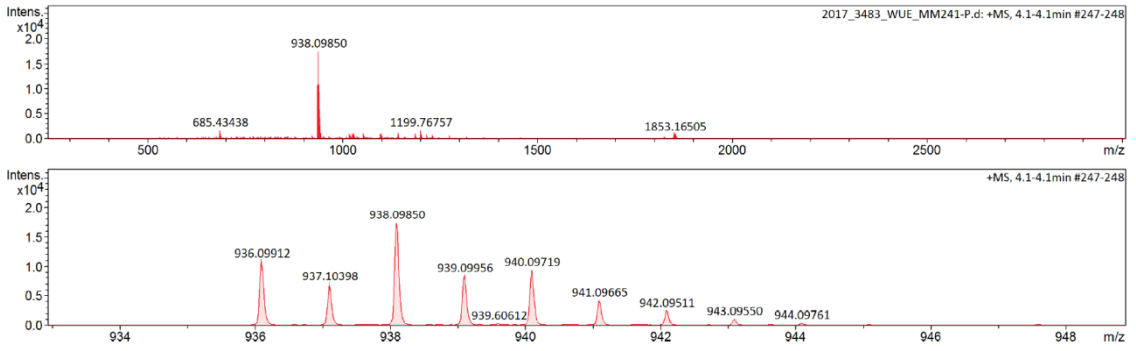

Figure A25. HRMS (ESI-TOF, positive mode, acetonitrile/chloroform) of **224f** $[M+Na]^+$.

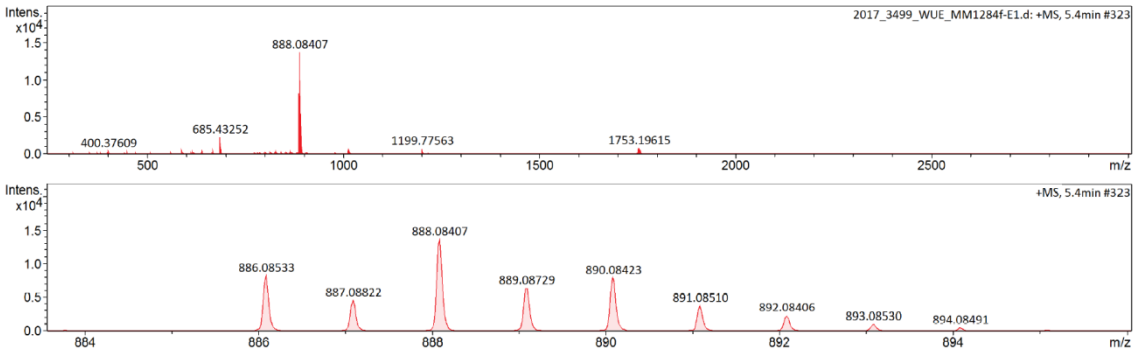

Figure A26. HRMS (ESI-TOF, positive mode, acetonitrile/chloroform) of **224g** $[M+Na]^+$.

10.2. Supporting Information Chapter 4[xi]

General Methods

Unless otherwise noted, all chemicals, reagents and solvents were purchased from commercial suppliers and used after appropriate purification. Column chromatography was performed on silica gel (particle size 0.040–0.063 mm) with freshly distilled solvents. ^{1}H and ^{13}C NMR spectra were recorded on a Bruker Avance HD III 400 or Bruker Avance HD III 600 spectrometer. The ^{13}C NMR spectra are broad band proton decoupled. Chemical shifts (δ) are listed in parts per million (ppm) and are reported relative to tetramethylsilane and referenced internally to residual proton solvent resonances or natural abundance carbon resonances. The coupling constants (J) are quoted in Hertz (Hz). MALDI-TOF mass spectra were acquired on a Bruker Daltonics autoflex II LRF mass spectrometer. ESI-TOF and APCI-TOF measurements were carried out on a Bruker Daltonics micOTOF focus mass spectrometer. Melting points were measured on an *Olympus* BX41 polarisation microscope with the temperature regulator TP84 from *Linkam Scientific*. The reported values are uncorrected.

Gel permeation chromatography (GPC)

Gel permeation chromatography was performed on a Prominence CBM GPC-device with recycling-mode from *Shimadzu*. Ethanol-stabilized chloroform (HPLC grade) was used as a solvent.

High-performance liquid chromatography (HPLC)

Semipreparative HPLC was carried out on a JAI LC-9105 HPLC-device from *Japan Analytical Industries*, while HPLC grade solvents were used. Semipreparative ($Ø$ = 20 mm) Reprosil 100 Chiral-NR chiral columns from *Trentec* were used.

UV–vis absorption, emission and circular dichroism spectroscopy

All measurements were carried out using spectroscopic grade solvents. UV–vis absorption spectra were recorded on a Jasco V670 or V-770-ST spectrometer. Fluorescence steady-state and lifetime measurements were recorded on a FLS980 Edinburgh Instrument fluorescence spectrometer. The quantum yields were determined by using the relative method and oxazine 1 (Φ_{fl} = 15% in ethanol; used for **225a**, **225g**, **226a**, **226g** and **241**) or IR125 (Φ_{fl} = 23% in DMSO, used for **243**) as a reference. The lifetime measurements were performed using pulsed laser diodes and determined

[xi] Parts of this Supporting Information were submitted for publication:
M. Mahl, H. Reichelt, A. Rausch, B. Mahlmeister, K. Shoyama, M. Stolte, F. Würthner, *submitted for publication*.

with the recording of the instrumental response function (IRF). Circular dichroism spectra were recorded on a *Jasco* CPL-300/J-1500 hybrid spectrometer.

Crystallographic Analysis

Suitable single crystals for X-ray crystallography were measured on a Bruker D8 Quest Diffractometer with a PhotonII detector using Cu K_α radiation. The structures were solved using direct methods, expanded with Fourier techniques and refined using the SHELX software package.[395] All non-hydrogen atoms were refined anisotropically. Hydrogen atoms were assigned idealized positions and were included in calculation of structure factors.

Synthesis

The compounds **222g**,[270] **227**,[296] **228**,[294] **229**,[296] **231**,[296] **239**,[295] **240**[396] and $[Pd_2(dba)_3]\cdot CHCl_3$[391] were synthesized according to the literature procedures.

Tetraaryl-substituted perylene bisdicarboximide 230

A Schlenk-tube was charged with 2.50 g (3.90 mmol, 1.0 equiv) **228**,[294] 13.9 g (78.1 mmol, 20.0 equiv) *para-tert*-butylphenylboronic acid, 1.35 g (1.17 mmol, 30 mol %) tetrakis(triphenylphosphine)palladium(0) $[Pd(PPh_3)_4]$, 5.67 g (41.0 mmol, 10.5 equiv) K_2CO_3 under an inert atmosphere. Subsequently, 125 mL toluene, 25 mL ethanol and 63 mL water was added (all solvents were degassed prior to use). The reaction mixture was cooled to –78 °C and evacuated and backfilled with nitrogen three times. Subsequently, the reaction mixture was heated to 80 °C for four days. After cooling down to room temperature, the reaction mixture was extracted with dichloromethane, the combined organic phases were dried over $MgSO_4$ and the solvent was removed under reduced pressure. The crude product was purified by column chromatography (gradient of dichloromethane/cyclohexane 1:2 to 1:1). The product was dried under high vacuum to give 2.71 g (2.63 mmol, 67%) of compound **230** as a green solid. M.p.: 287 °C. ^{1}H NMR (CD_2Cl_2, 400 MHz, 298 K): δ/ppm = 8.42 (*s*, 4H), 7.17–6.98 (*br*, 8H), 6.79–6.46 (*br*, 8H), 4.20 (*t*, J = 7.90 Hz, 4H), 1.80–1.71 (*m*, 4H), 1.52–1.45 (*m*, 4H), 1.37 (*s*, 36H), 1.02 (*t*, J = 7.4, 6H). ^{13}C NMR (CD_2Cl_2, 151 MHz, 298 K): δ/ppm = 164.0, 150.8, 142.1, 138.2, 133.7, 132.3, 131.9, 128.5, 126.3, 122.6, 40.6, 34.8, 31.4, 30.7, 20.8, 14.1. MS (MALDI-TOF, positive mode, DCTB in chloroform): 1030.57 $[M]^+$. HRMS (ESI-TOF, positive mode, acetonitrile/chloroform): calcd for $C_{74}H_{74}N_2O_4Na$: 1053.5546; found: 1053.5557 $[M+Na]^+$.

Tetraaryl-substituted perylene bisanhydride 232

Under an inert atmosphere 1.00 g (970 µmol, 1.0 equiv) **230** was suspended in 50 mL *tert*-butanol. Subsequently, 5.0 mL water and 54.4 g (970 mmol, 1000 equiv) KOH was added and the mixture was heated to 95 °C for 16 h. After cooling down to room temperature, the reaction mixture was poured into 500 mL cold 10% aq. HCl and the resulting precipitate was collected and washed with water. The residue was dissolved in dichloromethane and washed water, dried over $MgSO_4$ and the solvent was removed under reduced pressure. The crude product was purified by column chromatography (gradient of cyclohexane/dichloromethane 1:1 to 1:4; due to decomposition on the column, this step should be done fast) to give 689 mg (748 µmol, 77%) of **232** as a dark-green solid. M.p.: >350 °C. ^{1}H NMR (CD_2Cl_2, 400 MHz, 298 K): δ/ppm = 8.28 (*s*, 4H), 7.21–7.01 (*br*, 8H), 6.78–6.43 (*m*, 8H), 1.37 (*s*, 36H). ^{13}C NMR (CD_2Cl_2, 101 MHz, 298 K): δ/ppm = 160.7, 151.6, 143.0, 137.3, 135.8, 133.4, 132.4, 128.5, 128.4, 125.5, 118.8, 34.9, 31.3. MS (MALDI-TOF, negative mode, DCTB in chloroform): 920.45 $[M]^-$. HRMS (ESI-TOF, positive mode, acetonitrile/chloroform): calcd for $C_{64}H_{56}O_6Na$: 943.3975; found: 943.3949 $[M+Na]^+$.

Tetraaryloxy-substituted dibromoperylene monoanhydride 233 and tetraaryloxy-substituted tetrabromoperylene 235

To a suspension of 500.0 mg (507 µmol, 1.0 equiv) **231**[296] in 50 mL water an aqueous 1 M NaOH-solution (30.5 mL, 30.5 mmol, 60.0 equiv) was added and the mixture heated to 85 °C. Subsequently, THF was added carefully in small portions until a clear solution appeared (ca. 50 mL) and the reaction mixture was further heated to 85 °C for 20 min. Afterwards, 207 µL (406 mmol, 649 mg, 40.0 equiv, 3.12 g/mL) bromine was added in one portion and the mixture was heated to 85 °C for 20 h. After cooling down to room temperature, an excess of saturated aq. $Na_2S_2O_3$ was added and the reaction mixture was poured into 400 mL water and filtered. The precipitation was dissolved in dichloromethane and dried over $MgSO_4$. The crude product was purified by column chromatography (gradient of dichloromethane/cyclohexane 1:1 to 1:0) to yield **233** (95.7 mg, 89.2 µmol, 18%, orange/red solid) and **235** (133 mg, 114.5 µmol, 23%, yellow solid). Characterization data of **233**: M.p.: 290 °C (decomposition). ^{1}H NMR (CD_2Cl_2, 400 MHz, 298 K): δ/ppm = 8.08 (*s*, 2H), 7.59 (*s*, 2H), 7.31–7.23 (*m*, 8H), 6.86–6.81 (*m*, 4H), 6.80–6.75 (*m*, 4H), 1.30 (*s*, 18H), 1.28 (*s*, 18H). ^{13}C NMR (CD_2Cl_2, 151 MHz, 298 K): δ/ppm = 160.7, 155.6, 154.4, 153.4, 153.1, 148.0, 147.7, 137.7, 133.4, 127.1, 127.0, 125.6, 123.5, 123.0, 122.2, 122.1, 121.3, 119.6, 119.4, 116.9, 115.1, 34.7, 34.6, 31.6, 27.3. MS (MALDI-TOF, negative mode, DCTB in chloroform): 1072.32 $[M]^-$. HRMS (ESI-TOF, positive mode, acetonitrile/chloroform): calcd for $C_{62}H_{56}Br_4O_7$: 1070.2393; found: 1070.2393 $[M]^+$. Characterization data of **235**: M.p.: 117 °C. ^{1}H NMR (CD_2Cl_2, 400 MHz, 298 K): δ/ppm = 7.49 (*s*, 4H), 7.26–7.22 (*m*, 8H), 6.78–6.73 (*m*, 8H),

1.28 (*s*, 36H). ^{13}C NMR (CD_2Cl_2, 151 MHz, 298 K): δ/ppm = 153.6, 153.2, 147.3, 126.8, 125.9, 119.6, 119.3, 116.2, 34.6, 31.6. MS (MALDI-TOF, positive mode, DCTB in chloroform): 1160.11 $[M]^+$. HRMS (APCI-TOF, positive mode): calcd for $C_{60}H_{45}Br_4O_4$: 1156.0912; found: 1156.0907 $[M]^+$.

Tetraaryl-substituted dibromoperylene monoanhydride 234 and tetraaryl-substituted tetrabromoperylene 236

To a suspension of 250.0 mg (271 µmol, 1.0 equiv) **232** in 25 mL water an aqueous 1M NaOH-solution (1.63 mL, 1.63 mmol, 6.0 equiv) was added and the mixture heated to 85 °C. Subsequently, THF was added carefully in small portions until a clear solution appeared (ca. 25 mL) and the reaction mixture was further heated to 85 °C for 20 min. Afterwards, 556.1 µL (10.9 mmol, 1.73 g, 40.0 equiv, 3.12 g/mL) bromine was added in one portion and the mixture was heated to 85 °C for 16 h. After cooling down to room temperature, the reaction mixture was poured into 100 mL 10% aq. HCl, filtered and washed with water. The precipitation was dissolved in dichloromethane, washed with water and dried over $MgSO_4$. The crude product was purified by column chromatography (dichloromethane/cyclohexane 2:3) to yield **234** (68.7 mg, 68.1 µmol, 25%, bluish green solid) and **236** (111.2 mg, 101 µmol, 37%, red solid). Characterization data of **234**: M.p.: >350 °C. ^{1}H NMR (CD_2Cl_2, 400 MHz, 298 K): δ/ppm = 8.21 (*s*, 2H), 7.72 (*s*, 2H), 7.12–7.01 (*m*, 8H), 6.70–6.30 (*br*, 8H), 1.37 (*s*, 18H), 1.35 (*s*, 18H). ^{13}C NMR (CD_2Cl_2, 101 MHz, 298 K): δ/ppm = 161.2, 151.1, 150.8, 142.8, 140.9, 138.7, 137.5, 137.2, 137.1, 135.5, 135.2, 132.3, 128.7, 128.2, 127.9, 126.6, 122.3, 117.0, 34.8, 34.8, 31.4, 31.4. MS (MALDI-TOF, positive mode, DCTB in chloroform): 1008.32 $[M]^+$. HRMS (ESI-TOF, positive mode, acetonitrile/chloroform): calcd for $C_{62}H_{56}Br_2O_3Na$: 1029.2494; found: 1029.2488 $[M+Na]^+$. Characterization data of **236**: M.p.: 272 °C. ^{1}H NMR (CD_2Cl_2, 400 MHz, 298 K): δ/ppm = 7.63 (*s*, 4H), 7.06–7.01 (*m*, 8H), 6.49–6.36 (*br*, 8H), 1.35 (*s*, 36H). ^{13}C NMR (CD_2Cl_2, 101 MHz, 298 K): δ/ppm = 150.3, 140.8, 138.1, 137.6, 137.3, 128.6, 128.0, 127.2, 126.1, 119.5, 34.8, 31.4. MS (MALDI-TOF, positive mode, DCTB in chloroform): 1096.17 $[M]^+$. HRMS (APCI-TOF, positive mode): calcd for $C_{60}H_{45}Br_4$: 1092.1116; found: 1092.1110 $[M]^+$.

Tetraaryloxy-substituted dibromoperylene monodicarboximide 237

A mixture of 25.0 mg (23.3 µmol, 1.0 equiv) **233** and 41.3 mg (44.0 µl, 233 µmol, 10.0 equiv) 2,6-diisopropyl aniline in 0.25 mL acetic acid and 0.50 mL *N*-methyl-2-pyrrolidone was heated to 110 °C for 24 h. After cooling down to room temperature, the reaction mixture was poured into water, extracted with dichloromethane, the combined organic phases dried over $MgSO_4$ and the

solvent removed under reduced pressure. The crude product was further purified by column chromatography (gradient of cyclohexane/dichloromethane 3:2 to 0:1) to yield 14.5 mg (11.8 µmol, 51%) of compound **237** as a red solid. M.p.: 166–170 °C. ^{1}H NMR (CD_2Cl_2, 400 MHz, 298 K): δ/ppm = 8.11 (*s*, 2H), 7.60 (*s*, 2H), 7.45 (*t*, *J* = 7.7 Hz, 1H), 7.32–7.23 (*m*, 10H), 6.88–6.78 (*m*, 8H), 2.99 (*sep*, J = 6.9 Hz, 2H), 1.31 (*s*, 18H), 1.28 (*s*, 18H), 1.11–1.05 (m, 12H). ^{13}C NMR (CD_2Cl_2, 101 MHz, 298 K): δ/ppm = 164.0, 155.1, 154.4, 153.7, 153.3, 147.8, 147.4, 146.4, 137.5, 133.5, 131.7, 129.6, 127.0, 127.0, 125.7, 124.3, 122.3, 122.1, 121.5, 121.4, 1209, 120.6, 119.5, 119.3, 115.6, 34.7. 34.6 31.6, 31.6, 29.4, 24.1. MS (MALDI-TOF, positive mode, DCTB in chloroform): 1231.37 $[M]^+$. HRMS (ESI-TOF, positive mode, acetonitrile/chloroform): calcd for $C_{68}H_{64}Cl_4N_2O_4Na$: 1252.3702; found: 1252.3697 $[M+Na]^+$.

Tetraaryl-substituted dibromoperylene monodicarboximide 238

A mixture of 25.0 mg (24.8 µmol, 1.0 equiv) **234** and 43.9 mg (46.7 µl, 247.8 µmol, 10.0 equiv) 2,6-diisopropyl aniline in 0.25 mL acetic acid and 0.5 mL *N*-methyl-2-pyrrolidone was heated to 110 °C for 24 h. After cooling down to room temperature, the reaction mixture was poured into water, extracted with dichloromethane, the combined organic phases dried over $MgSO_4$ and the solvent removed under reduced pressure. The crude product was further purified by column chromatography (cyclohexane/dichloromethane 1:1) to yield 14.0 mg (12.0 µmol, 48%) of compound **238** as a dark-purple solid. M.p.: 286–290 °C. ^{1}H NMR (CD_2Cl_2, 400 MHz, 298 K): δ/ppm = 8.25 (*s*, 2H), 7.71 (*s*, 2H), 7.51 (*t*, *J* = 7.8 Hz, 1H), 7.36 (*d*, *J* = 7.8 Hz, 2H), 7.11–7.05 (*m*, 8H), 6.80–6.30 (*m*, 8H), 2.86 (*sep*, J = 6.9 Hz, 2H), 1.36 (*s*, 36H), 1.22 (d, *J* = 6.9 Hz, 6H), 1.13 (d, *J* = 6.9 Hz, 6H). ^{13}C NMR (CD_2Cl_2, 101 MHz, 298 K): δ/ppm = 164.6, 150.8, 150.5, 146.6, 142.6, 140.9, 138.9, 138.2, 137.6, 137.2, 134.0, 133.7, 132.4, 132.1, 129.7, 128.6, 128.4, 127.9, 127.2, 126.7, 124.4, 121.7, 121.0, 34.8, 34.8, 31.4, 31.4, 24.2, 24.1. MS (MALDI-TOF, negative mode, DCTB in chloroform): 1167.45 $[M]^-$. HRMS (ESI-TOF, positive mode, acetonitrile/chloroform): calcd for $C_{74}H_{73}Br_2NO_2Na$: 1188.3906; found: 1188.3874 $[M+Na]^+$.

Tetraaryloxy-substituted polycyclic aromatic dicarboximide 225a

Starting from **224a**

A Schlenk-tube was charged with 50.0 mg (67.3 µmol, 1.0 equiv) **224a**, 202 mg (1.34 mmol, 20.0 equiv) *para-tert*-butyl phenol and 186 mg (1.34 mµmol, 20.0 equiv) potassium carbonate and 5.0 mL dry DMF as a solvent under an inert atmosphere at room temperature and heated to 130 °C for 16 h. After cooling down to room temperature, the reaction mixture was poured into water,

extracted with dichloromethane, the combined organic phases dried over $MgSO_4$ and the solvent removed under reduced pressure. The crude product was purified by preparative thin layer chromatography (dichloromethane/cyclohexane 2:3), followed by GPC. The product was dried under high vacuum to give 1.3 mg (1.08 µmol, 2%) of compound **225a** as a dark-blue solid.

Starting from **237**

A Schlenk-tube was charged with 1.5 mg (4.72 µmol, 1.0 equiv) **222a**, 8.0 mg (5.19 µmol, 1.1 equiv) **237**, 0.5 mg (0.472 µmol, 10 mol %) tris(dibenzylideneacetone)dipalladium(0)-chloroform adduct $[Pd_2(dba)_3]\cdot CHCl_3$, 0.7 mg (1.89 µmol, 40 mol %) tricyclohexylphosphine tetrafluoroborate $PCy_3\cdot HBF_4$, 4.62 mg (14.2 µmol, 3.0 equiv) Cs_2CO_3 and 0.15 mL 1-chloronaphthalene as a solvent under an inert atmosphere at room temperature and heated to 160 °C for 16 h. After cooling down to room temperature, the reaction mixture was filtrated with cyclohexane over a pad of silca-gel to remove 1-chloronaphthalene and the crude product was eluted with dichloromethane. The crude product was purified by preparative thin layer chromatography (dichloromethane/cyclohexane 2:3), followed by GPC. The product was dried under high vacuum to give 1.1 mg (0.918 µmol, 19%) of compound **225a** as a dark-blue solid.

M.p.: >350 °C. ^{1}H NMR (CD_2Cl_2, 400 MHz, 298 K): δ/ppm = 8.13 (*s*, 2H), 8.04 (*d*, *J* = 7.7Hz, 2H), 7.98 (*s*, 2H), 7.80 (*d*, *J* = 7.7 Hz, 2H), 7.49 (*t*, *J* = 7.7 Hz, 2H), 7.45 (*t*, *J* = 7.7 Hz, 1H), 7.33–7.26 (*m*, 8H), 6.96–6.90 (*m*, 4H), 6.89–6.84 (*m*, 4H), 2.71 (*qui*, *J* = 6.8 Hz, 2H), 1.33 (*s*, 18H), 1.29 (*s*, 18H), 1.08 (*d*, *J* = 6.8 Hz, 12H). ^{13}C NMR (CD_2Cl_2, 151 MHz, 298 K): δ/ppm = 164.1, 157.2, 154.1, 154.1, 154.0, 147.2, 147.0, 146.4, 135.5, 134.7, 134.0, 133.7, 132.0, 130.0, 129.8, 129.5, 128.1, 127.2, 126.9, 126.9, 124.3, 123.3, 122.9, 121.2, 120.8, 120.6, 120.6, 119.3, 119.3, 115.9, 111.52, 34.6, 34.5, 34.6, 31.6, 34.6, 29.3, 24.0. UV–vis (CH_2Cl_2): λ_{max} / nm (ε / $M^{-1}cm^{-1}$) = 637 (33600). Fluorescence (CH_2Cl_2, λ_{ex} = 620 nm): λ_{max} / nm (Φ_{fl} / %) = 757 (4.6 ± 0.2). MS (MALDI-TOF, negative mode, DCTB in chloroform): 1197.60 $[M]^-$. HRMS (ESI-TOF, positive mode, acetonitrile/chloroform): calcd for $C_{84}H_{79}NO_6$: 1220.5805; found: 1220.5750 $[M+Na]^+$.

Tetraaryloxy-substituted polycyclic aromatic dicarboximide 225g

A Schlenk-tube was charged with 2.8 mg (7.44 µmol, 1.0 equiv) **222g**, 10.1 mg (8.19 µmol, 1.1 equiv) **237**, 0.8 mg (0.744 µmol, 10 mol %) tris(dibenzylideneacetone)dipalladium(0)-chloroform adduct $[Pd_2(dba)_3]\cdot CHCl_3$, 1.1 mg (2.98 µmol, 40 mol %) tricyclohexylphosphine tetrafluoroborate $PCy_3\cdot HBF_4$, 7.27 mg (22.3 µmol, 3.0 equiv) Cs_2CO_3 and 0.22 mL 1-chloronaphthalene as a solvent under an inert atmosphere at room temperature and heated to 160 °C for 20 h. After cooling down to room temperature, the reaction mixture was filtrated with

cyclohexane over a pad of silca-gel to remove 1-chloronaphthalene and the crude product was eluted with dichloromethane. The crude product was purified by preparative thin layer chromatography (dichloromethane/cyclohexane 8:2 to 9:1), followed by GPC. The product was dried under high vacuum to give 1.5 mg (1.14 µmol, 15%) of compound **225g** as a dark-blue solid. M.p.: 118–121 °C. ^{1}H NMR (CD_2Cl_2, 400 MHz, 298 K): δ/ppm = 8.17–8.03 (*m*, 6H), 8.17–8.03 (*m*, 6H), 7.82–7.74 (*m*, 6H), 8.17–8.03 (*m*, 6H), 7.45 (*t*, J = 8.7 Hz, 1H), 7.38–7.26 (*m*, 10H), 7.02–6.93 (*m*, 4H), 6.88–6.83 (*m*, 4H), 2.76–2.67 (*br*, 2H), 1.36 (*s*, 18H), 1.29 (*s*, 18H), 1.13–1.06 (*br*, 18H). ^{13}C NMR (CD_2Cl_2, 151 MHz, 298 K): δ/ppm = 164.1, 154.1, 153.9, 14.3, 147.2, 146.5, 137.7, 136.9, 136.2, 136.0, 133.7, 133.0, 132.0, 131.9, 131.1,129.6, 128.5, 128.3, 128.1, 127.8, 127.0, 127.0, 124.3, 123.0 ,121.2, 121.1, 121.0, 120.6, 119.4, 119.3, 116.6, 34.7, 34.6, 31.7, 31.6, 24.1, 23.1. UV–vis (CH_2Cl_2): λ_{max} / nm (ε / $M^{-1}cm^{-1}$) = 642 (23900). Fluorescence (CH_2Cl_2, λ_{ex} = 590 nm): λ_{max} / nm (Φ_{fl} / %) = 720 (20 ± 0.4). MS (MALDI-TOF, negative mode, DCTB in chloroform): 1320.61 $[M]^-$. HRMS (ESI-TOF, positive mode, acetonitrile/chloroform): calcd for $C_{94}H_{81}NO_6K$: 1358.5701; found: 1358.5725 $[M+K]^+$.

Tetraaryl-substituted polycyclic aromatic dicarboximide 226a

Starting from **224a**

A Schlenk-tube was charged with 25.0 mg (33.6 µmol, 1.0 equiv) **224a**, 120 mg (672 µmol, 20.0 equiv) *para-tert*-buylphenylboronic acid, 11.7 mg (10.1 µmol, 30 mol %) tetrakis(triphenylphosphine)palladium(0) $[Pd(PPh_3)_4]$, 45.3 mg (328 µmol, 9.75 equiv) K_2CO_3 under an inert atmosphere. Subsequently, 2.5 mL toluene, 0.5 mL ethanol and 1.25 mL water was added (all solvents were degassed prior to use). The reaction mixture was cooled to –78 °C and evacuated and backfilled with nitrogen three times. Subsequently, the reaction mixture was heated to 80 °C for 16 h. After cooling down to room temperature, the reaction mixture was extracted with dichloromethane, the combined organic phases were dried over $MgSO_4$ and the solvent was removed under reduced pressure. The crude product was purified by column chromatography (dichloromethane/cyclohexane 1:1), followed by GPC. The product was dried under high vacuum to give 2.4 mg (2.12 µmol, 6%) of compound **226a** as a dark-green solid.

Starting from **238**

A Schlenk-tube was charged with 3.9 mg (15.4 µmol, 1.0 equiv) **222a**, 19.7 mg (16.9 µmol, 1.1 equiv) **238**, 1.6 mg (1.57 µmol, 10 mol %) tris(dibenzylideneacetone)dipalladium(0)-chloroform adduct $[Pd_2(dba)_3]\cdot CHCl_3$, 2.3 mg (6.14 µmol, 40 mol %) tricyclohexylphosphine tetrafluoroborate $PCy_3\cdot HBF_4$, 15.0 mg (46.0 µmol, 3.0 equiv) Cs_2CO_3 and 0.47 mL 1-

chloronaphthalene as a solvent under an inert atmosphere at room temperature and heated to 160 °C for 16 h. After cooling down to room temperature, the reaction mixture was filtrated with cyclohexane over a pad of silca-gel to remove 1-chloronaphthalene and the crude product was eluted with dichloromethane. The crude product was purified by column chromatography (gradient of dichloromethane/cyclohexane 1:1 to 1:0), followed by GPC. The product was dried under high vacuum to give 3.3 mg (2.91 µmol, 19%) of compound **226a** as a dark-green solid.

M.p.: >350 °C. ^{1}H NMR (CD_2Cl_2, 400 MHz, 298 K): δ/ppm = 8.40 (*d*, J = 7.9 Hz, 2H), 8.26 (*s*, 2H), 8.09 (*s*, 2H), 7.87 (*d*, J = 7.9 Hz, 2H), 7.62 (*t*, J = 7.9 Hz, 2H), 7.51 (*t*, J = 7.9 Hz, 1H), 7.37 (*d*, J = 7.9 Hz, 2H), 7.22–6.50 (*m*, 16H), 2.87 (*sep*, J = 6.9 Hz, 2H), 1.41 (*s*, 18H), 1.36 (*s*, 18H), 1.23 (*d*, J = 6.9 Hz, 6H), 1.12 (*d*, J = 6.9 Hz, 6H). ^{13}C NMR (CD_2Cl_2, 101 MHz, 298 K): *δ*/ppm = 164.8, 150.3, 150.0, 146.7, 143.4, 140.3, 139.7, 139.2, 134.9, 134.4, 134.2, 133.9, 133.2, 132.5, 132.3, 130.6, 129.6, 129.6, 128.6, 128.2, 128.2, 127.3, 127.1, 126.6, 126.6, 124.9, 124., 4, 122.5, 120.2, 34.8, 34.8, 31.5, 31.4, 30.1, 29.4, 24.3, 24.1. UV–vis (CH_2Cl_2): λ_{max} / nm (ε / $M^{-1}cm^{-1}$) = 679 (19800). Fluorescence (CH_2Cl_2, λ_{ex} = 590 nm): λ_{max} / nm (Φ_{fl} / %) = 768 (1.4 ± 0.1). MS (MALDI-TOF, positive mode, DCTB in chloroform): 1133.61 $[M]^+$. HRMS (ESI-TOF, positive mode, acetonitrile/chloroform): calcd for $C_{84}H_{79}NO_2K$: 1172.5748; found: 1172.5747 $[M+K]^+$.

Tetraaryl-substituted polycyclic aromatic dicarboximide 226g

A Schlenk-tube was charged with 6.0 mg (16.0 µmol, 1.0 equiv) **222g**, 20.5 mg (17.6 µmol, 1.1 equiv) **238**, 1.7 mg (1.60 µmol, 10 mol %) tris(dibenzylideneacetone)dipalladium(0)-chloroform adduct $[Pd_2(dba)_3]\cdot CHCl_3$, 2.4 mg (6.38 µmol, 40 mol %) tricyclohexylphosphine tetrafluoroborate $PCy_3\cdot HBF_4$, 16.0 mg (47.8 µmol, 3.0 equiv) Cs_2CO_3 and 0.48 mL 1-chloronaphthalene as a solvent under an inert atmosphere at room temperature and heated to 160 °C for 16 h. After cooling down to room temperature, the reaction mixture was filtrated with cyclohexane over a pad of silca-gel to remove 1-chloronaphthalene and the crude product was eluted with dichloromethane/cyclohexane 1:1-mixture. The crude product was purified by GPC, followed by preparative thin layer chromatography (dichloromethane/cyclohexane 2:3). The product was dried under high vacuum to give 3.0 mg (2.39 µmol, 15%) of compound **226g** as a green solid. M.p.: >350 °C. ^{1}H NMR (CD_2Cl_2, 400 MHz, 298 K): *δ*/ppm = 8.43 (*s*, 2H), 8.32–8.20 (*m*, 4H), 7.99–7.81 (*m*, 6H), 7.51 (*t*, *J* = 7.8 Hz, 1H), 7.37 (*d*, *J* = 7.8 Hz, 2H), 7.42–6.59 (*m*, 162.89 (*qui*, *J* = 6.9 Hz, 2H), 1.42 (*s*, 18H), 1.29–1.20 (*m*, 24H), 1.17–1.10 (*m*, 6H). ^{13}C NMR (CD_2Cl_2, 101 MHz, 298 K): *δ*/ppm = 164.7, 150.5, 146.7, 140.7, 139.0, 136.8, 136.4, 134.7, 134.1, 133.6, 132.3, 132.1, 129.6, 1287, 128.3, 128.1, 127.7, 124.4, 120.6, 34.9, 31.5, 30.1, 29.4, 24.3, 24.1. UV–vis (CH_2Cl_2): λ_{max} / nm (ε / $M^{-1}cm^{-1}$) = 682 (14300). Fluorescence (CH_2Cl_2, λ_{ex} = 600 nm): λ_{max} /

nm (Φ_{fl} / %) = 786 (4.8 ± 0.1). MS (MALDI-TOF, positive mode, DCTB in chloroform): 1256.64 $[M]^+$. HRMS (ESI-TOF, positive mode, acetonitrile/chloroform): calcd for $C_{94}H_{81}NO_2Na$: 1278.6165; found: 1278.6130 $[M+Na]^+$.

Tetrachloro-substituted polycyclic aromatic dicarboximide 241

A Schlenk-tube was charged with 10.0 mg (14.2 µmol, 1.0 equiv) **239**, 15.1 mg (31.2 µmol, 2.2 equiv) **240**, 2.9 mg (2.83 µmol, 20 mol %) tris(dibenzylideneacetone)dipalladium(0)-chloroform adduct $[Pd_2(dba)_3]\cdot CHCl_3$, 4.2 mg (11.3 µmol, 80 mol %) tricyclohexylphosphine tetrafluoroborate $PCy_3\cdot HBF_4$, 27.7 mg (85.0 µmol, 6.0 equiv) Cs_2CO_3 and 0.47 mL 1-chloronaphthalene as a solvent under an inert atmosphere at room temperature and heated to 160 °C for 20 h. After cooling down to room temperature, the reaction mixture was filtrated with cyclohexane over a pad of silca-gel to remove 1-chloronaphthalene and the crude product was eluted with dichloromethane. The crude product was purified by column chromatography (gradient of dichloromethane/cyclohexane 1:5 to 1:0), followed by size exclusion chromatography and precipitation from dichloromethane/methanol. The isolated solid was washed with methanol and further purified by GPC. The product was dried under high vacuum to give 1.2 mg (1.09 µmol, 8%) of compound **241** as a dark-green solid. M.p.: 250 °C (decomposition). ^{1}H NMR (CD_2Cl_2, 400 MHz, 298 K): δ/ppm = 8.77 (*d*, *J* = 8.0 Hz, 4H), 8.71–8.67 (*m*, 8H), 7.53 (*t*, *J* = 7.8 Hz, 2H), 7.38 (*d*, *J* = 7.8 Hz, 4H), 2.78 (*qui*, *J* = 6.8 Hz, 4H), 1.16 (*dd*, *J* = 1.0 Hz, *J* = 6.8 Hz, 24H). ^{13}C NMR (CD_2Cl_2, 151 MHz, 298 K): δ/ppm = 164.1, 146.5, 135.3, 135.3, 134.4, 132.3, 131.6, 130.8, 130.6, 129.8, 129.9, 129.9, 126.3, 124.5, 123.7, 122.9, 122.9, 30.1, 24.1. UV–vis (CH_2Cl_2): λ_{max} / nm (ε / $M^{-1}cm^{-1}$) = 711 (68600). Fluorescence (CH_2Cl_2, λ_{ex} = 650 nm): λ_{max} / nm (Φ_{fl} / %) = 754 (< 1). MS (MALDI-TOF, negative mode, DCTB in chloroform): 1096.23 $[M]^-$. HRMS (ESI-TOF, positive mode, acetonitrile/chloroform): calcd for $C_{68}H_{64}Cl_4N_2O_4$: 1117.2109; found: 1117.2055 $[M+Na]^+$.

Tetraaryl-substituted polycyclic aromatic dicarboximide 243

A Schlenk-tube was charged with 15.0 mg (13.5 µmol, 1.0 equiv) **236**, 14.4 mg (29.7 µmol, 2.2 equiv) **240**, 2.8 mg (2.70 µmol, 20 mol %) tris(dibenzylideneacetone)dipalladium(0)-chloroform adduct $[Pd_2(dba)_3]\cdot CHCl_3$, 4.0 mg (10.8 µmol, 80 mol %) tricyclohexylphosphine tetrafluoroborate $PCy_3\cdot HBF_4$, 26.4 mg (81.0 µmol, 6.0 equiv) Cs_2CO_3 and 0.40 mL 1-chloronaphthalene as a solvent under an inert atmosphere at room temperature and heated to 160 °C for 20 h. After cooling down to room temperature, the reaction mixture was filtrated with cyclohexane over a pad of silca-gel to remove 1-chloronaphthalene and the crude product was eluted with dichloromethane. The crude product was purified by column chromatography (gradient

of dichloromethane/cyclohexane 1:1 to 1:0), followed by GPC and preparative thin layer chromatography (dichloromethane/*n*-hexane 2:1). The product was dried under high vacuum to give 3.5 mg (2.35 µmol, 18%) of compound **243** as a light-green solid. M.p.: >350 °C. ^{1}H NMR (CD_2Cl_2, 400 MHz, 298 K): δ/ppm = 8.70 (*d*, *J* = 8.2 Hz, 4H), 8.63 (*d*, *J* = 8.2 Hz, 4H), 8.35 (*s*, 4H), 7.52 (*t*, *J* = 7.8 Hz, 2H), 7.37 (*d*, *J* = 7.8 Hz, 4H), 7.22–7.07 (*br*, 8H), 6.92–6.60 (*br*, 8H), 2.78 (*qui*, *J* = 6.8 Hz, 4H), 1.41 (*s*, 36H), 1.18–1.14 (*m*, 24H). ^{13}C NMR (CD_2Cl_2, 151 MHz, 298 K): δ/ppm = 164.4, 150.5, 146.6, 142.2, 139.4, 137.3, 133.8, 132.1, 131.1, 130.3, 129.7, 129.1, 128.5, 127.6, 127.0, 125.7, 124.4, 121.4, 121.4, 34.8, 31.5, 30.1, 24.1. UV–vis (CH_2Cl_2): λ_{max} / nm (ε / $M^{-1}cm^{-1}$) = 811 (67000). Fluorescence (CH_2Cl_2, λ_{ex} = 790 nm): λ_{max} / nm (Φ_{fl} / %) = 884 (1.3 ± 0.1). MS (MALDI-TOF, positive mode, DCTB in chloroform): 1487.76 $[M]^+$. HRMS (ESI-TOF, positive mode, acetonitrile/chloroform): calcd for $C_{108}H_{98}N_2O_4$: 1486.7527; found: 1486.7517 $[M]^+$.

Optimization

Table A4. Applied reaction conditions for the introduction of phenoxy substituents towards **225a′**.[a]

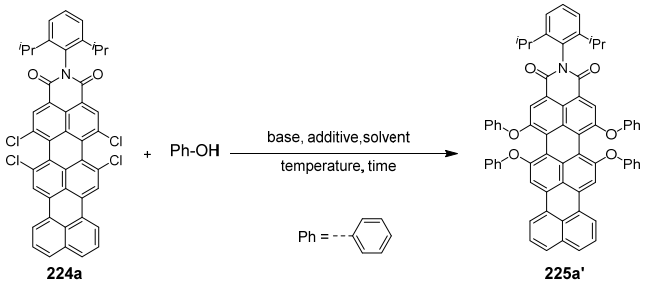

entry	base	solvent	*T* / °C	*t* / h	additive	yield	note
1	K_2CO_3	DMF	100	20	-	-	incomplete substitution
2	K_2CO_3	DMF	130	20	-	traces	product observed; yield too low for isolation
3	Cs_2CO_3	DMF	100	20	-	-	decomposition
4	Cs_2CO_3	DMF	130	20	-	-	decomposition
5	K_2CO_3	NMP	100	20	-	-	incomplete substitution
6	K_2CO_3	NMP	130	20	-	traces	product observed; yield too low for isolation
7	Cs_2CO_3	NMP	100	20	-	-	decomposition
8	Cs_2CO_3	NMP	130	20	-	-	decomposition
9[b]	K_2CO_3	NMP	130	20	-	-	decomposition
10	K_3PO_4	NMP	130	20	-	-	decomposition
11[c]	K_2CO_3	NMP	130	20	-	-	incomplete substitution and dechlorination
12[d]	K_2CO_3	NMP	130	20	-	-	incomplete substitution and dechlorination
13	K_2CO_3	DMF	130	72	-	traces	extended reaction time
14[e]	K_2CO_3	DMF	130	20	-	traces	doubled equiv base and phenol
15	K_2CO_3	DMF	115	20	-	traces	lower temperature
16[f]	K_2CO_3	DMF	130	20	-	traces	half concentration
17[g]	K_2CO_3	DMF	130	20	-	traces	two-fold concentration
18[h]	K_2CO_3	DMF	130	20	$^nBu_4NBF_4$	traces	addition of phasetransfer-catalyst
19[i]	CsF	THF	70	20	18-crown-6	-	only starting material and partial decomposition
20[i]	KF	THF	70	20	18-crown-6	-	only starting material

[a]Reaction conditions: 1.0 equiv **224a**, 10.0 equiv phenol; 10.0 equiv base, 1.0 mL solvent (*c*(**224a**) = 0.013 M). [b]Sodium phenolat instead of phenol. [c]Phenol: 5.0 equiv; base: 5.0 equiv. [d]Phenol: 8.0 equiv; base: 4.0 equiv. [e]Phenol: 20.0 equiv; base: 20.0 equiv. [f]2.0 mL solvent (*c*(**224a**) = 0.007 M. [g]0.5 mL solvent (c(**224a**) = 0.026 M). [h]Adapted from ref.[302] for the introduction of alkylthioethers. [i]Adapted from ref.[397] for the substitution for a tetrachloro-PBI. DMF: *N*,*N*-dimethylformamide, NMP: 1-methylpyrrolidin-2-one.

Crystallographic Analysis

Single crystals of **234** suitable for X-ray diffraction could be grown by slow evaporation of a dichloromethane solution containing a racemic mixture of **234**. Single crystals of **243** suitable for X-ray diffraction could be grown by slow diffusion of ethanol into a chloroform solution of a racemic mixture of **243**.

Table A5. Crystal data and structure refinement for **234**.

Empirical formula	($C_{62}H_{56}Br_2O_3$)
Formula weight	1008.88
Temperature	100(2) K
Wavelength	1.54178 Å
Crystal system, space group	Monoclinic, $P2_1/c$
Unit cell dimensions	a = 20.1055(15) Å
	b = 26.7587(19) Å
	c = 10.2202(8) Å
	α = 90 °
	β = 103.474(4) °
	γ = 90 °
Volume	5347.1(7) $Å^3$
Z	4
Calculated density	1.253 Mg/m^3
Absorption coefficient	2.253 mm^{-1}
F(000)	2088
Crystal size	0.510 × 0.060 × 0.060 mm
Theta range for data collection	2.260 to 79.103 °
Limiting indices	$-25 \leq h \leq 25$, $-34 \leq k \leq 28$, $-12 \leq l \leq 13$
Reflections collected / unique	118040 / 11518 [R_{int} = 0.0555]
Completeness	100.0%
Absorption correction	Semi-empirical from equivalents
Max. and min. transmission	0.7542 and 0.5411
Refinement method	Full-matrix least-squares on F^2
Data / restraints / parameters	11518 / 170 / 802
Goodness-of-fit	1.082
Final R indices [$I > 2\sigma(I)$]	R_1 = 0.0560, wR_2 = 0.1063
R indices (all data)	R_1 = 0.0709, wR_2 = 0.1176
Largest diff. peak and hole	1.478 and –1.195 $e \cdot Å^{-3}$

Table A6. Crystal data and structure refinement for **243**.

Empirical formula	$(C_{108}H_{98}N_2O_4)$, 0.283·$(CHCl_3)$, 0.717·(C_2H_6O)
Formula weight	1554.70
Temperature	100(2) K
Wavelength	1.54178 Å
Crystal system, space group	Monoclinic, $P2_1/c$
Unit cell dimensions	a = 18.4815(14) Å
	b = 18.4586(12) Å
	c = 30.406(2) Å
	α = 90 °
	β = 101.598(5) °
	γ = 90 °
Volume	10161.0(13) Å^3
Z	4
Calculated density	1.016 Mg/m^3
Absorption coefficient	0.669 mm^{-1}
F(000)	3308.2
Crystal size	0.360 × 0.280 × 0.010 mm
Theta range for data collection	2.440 to 68.497 °
Limiting indices	–22 <= h <= 22, –22 <= k <= 22, –36 <=l <= 36
Reflections collected / unique	75812 / 18563 [R_{int} = 0.1428]
Completeness	99.6%
Absorption correction	Semi-empirical from equivalents
Max. and min. transmission	0.7531 and 0.5300
Refinement method	Full-matrix least-squares on F^2
Data / restraints / parameters	18563 / 231 / 1220
Goodness-of-fit	1.178
Final R indices [$I > 2\sigma(I)$]	R_1 = 0.1162, wR_2 = 0.2697
R indices (all data)	R_1 = 0.1994, wR_2 = 0.3297
Largest diff. peak and hole	0.381 and –0.279 e·Å^{-3}

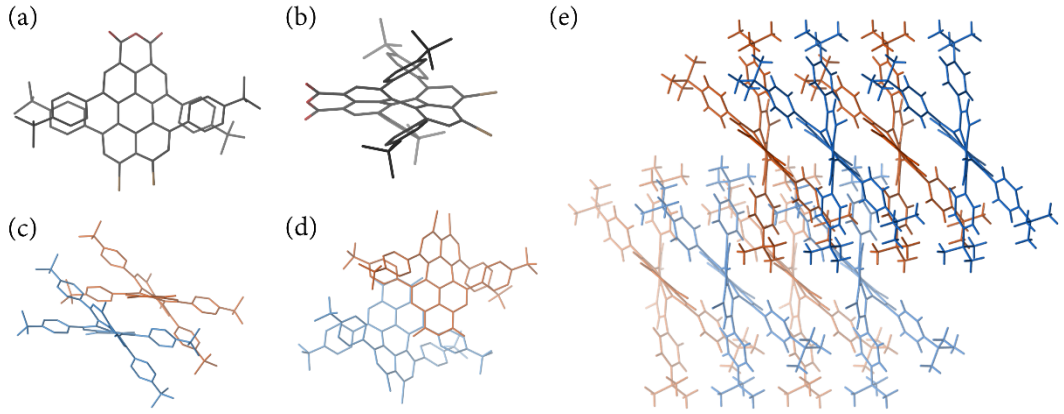

Figure A27. Molecular structure of racemic **234** as obtained by single crystal X-ray diffraction. (a) Front and (b) top view of *M*-enantiomer of **234**. (c,d) Dimeric packing motif of *P*- and *M*-enantiomer of **234** (blue: *M*-enantiomer; red: *P*-enantiomer). (e) Packing arrangement of racemic mixture of **234** (blue: *M*-enantiomer; red: *P*-enantiomer).

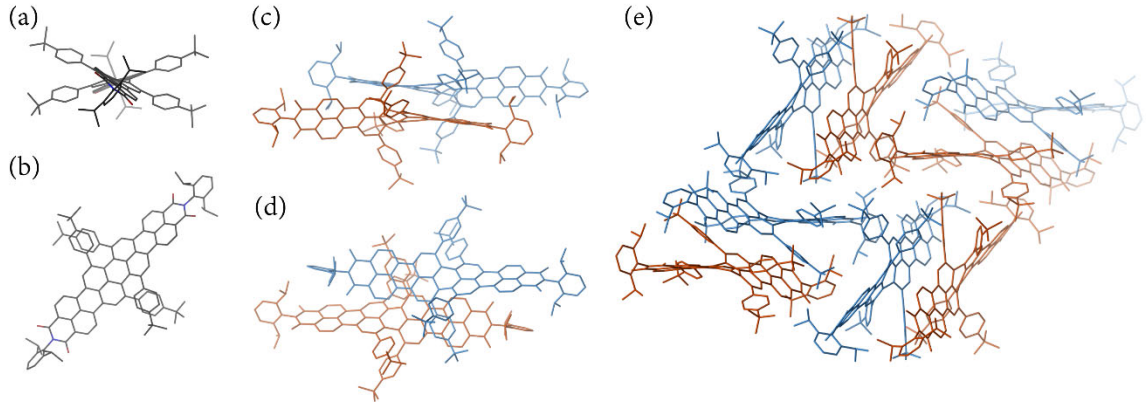

Figure A28. Molecular structure of racemic **243** as obtained by single crystal X-ray diffraction. (a) Front and (b) top view of *M*-enantiomer of **243**. (c,d) Dimeric packing motif of *P*- and *M*-enantiomer of **243** (blue: *M*-enantiomer; red: *P*-enantiomer). (e) Packing arrangement of racemic mixture of **243** (blue: *M*-enantiomer; red: *P*-enantiomer).

Theoretical Calculations

Theoretical calculations of electronic circular dichroism spectra of **243** enantiomers were calculated with the program Gaussian 09 using B3LYP/6-31G(d,p). For calculations, the *N*-substituents and *tert*-butyl groups were both replaced by methyl groups.

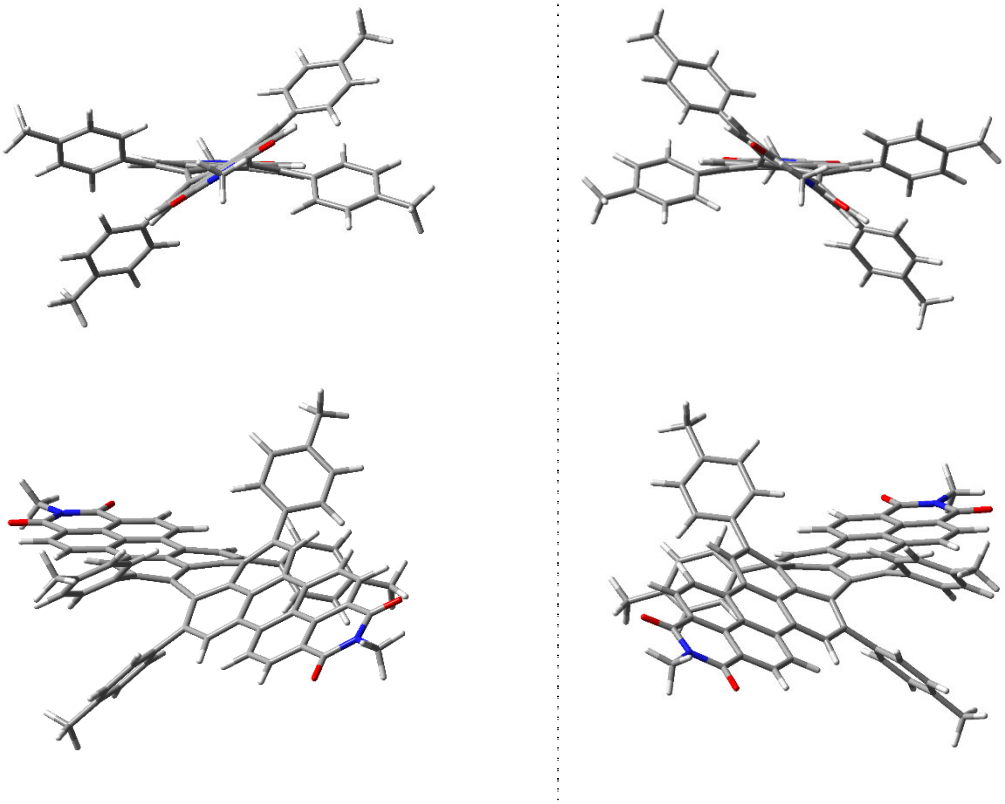

Figure A29. Calculated geometries of simplified (*P*)-**243** (left) and (*M*)-**243** (right) using B3LYP/6-31G(d,p).

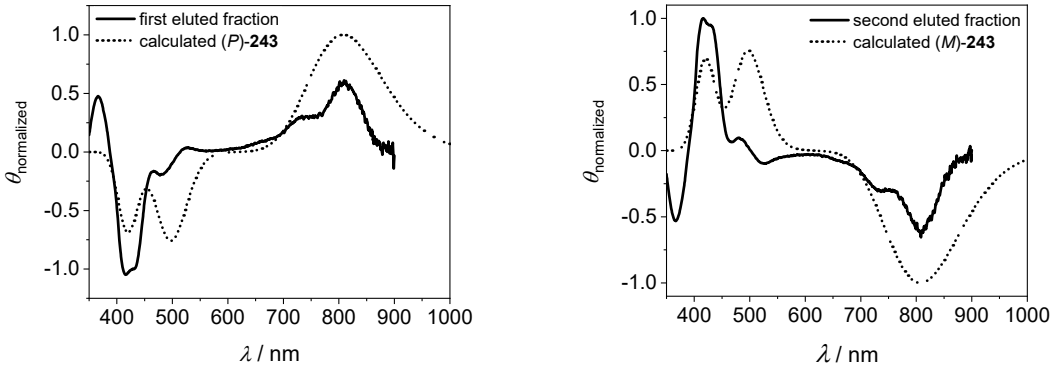

Figure A30. Calculated CD spectra of (*P*)-**243** and (*M*)-**243** using B3LYP/6-31G(d,p) and measured CD spectra for the first and second eluted fractions.

Chiroptical Properties

The rate constant k_{rac}, half-life $t_{1/2}$ and free enthalpy for the activation of the racemization $\Delta G^{\#}$ are determined according to a literature procedure.[60] Time-dependent CD spectroscopy with (*P*)-**243** in 1,1,2,2-tetrachloroethane at 398 K was applied. The racemization process can be described by first order kinetic and therefore an exponential decay function can be used (equation 1). For this purpose, the obtained CD signals were fitted at 431 nm and 811 nm (equation 1) to obtain the respective k_{rac} (Figure A31).

$$A = A_0 \cdot e^{(-k_{rac}t)} \tag{1}$$

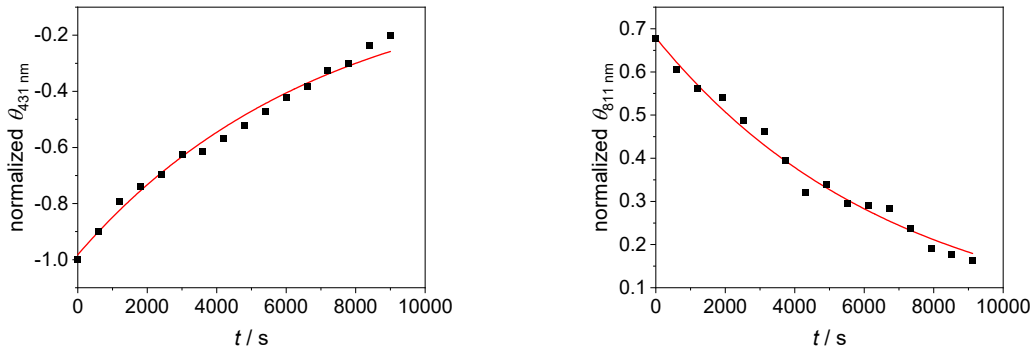

Figure A31. Exponential decay of the CD signal at 431 nm (left) and 811 nm (right) of (*P*)-**243** in 1,1,2,2-tetrachloroethane at 398 K.

The corresponding half-life was determined according to equation 2:

$$t_{1/2} = \frac{\ln(2)}{k_{rac}} \tag{2}$$

The free enthalpy for the activation of the racemization $\Delta G^{\#}$ was determined by the Eyring equation (equation 3). Thereby, R represents the gas constant, h the Planck constant and k_B the Boltzmann constant. The transmission coefficient κ is set to 0.5.[60] The obtained data for both fitted wavelengths are summarized in Table A7.

$$\Delta G^{\#} = -RT \cdot \ln\left(\frac{hk_{rac}}{\kappa T k_B}\right) \tag{3}$$

Table A7. Summary of the obtained data for the racemization process of (*P*)-**243** in 1,1,2,2-tetrachloroethane at 398 K.

fitted wavelength	k_{rac} / s^{-1}	$t_{1/2}$ / min	$\Delta G^{\#}_{398\ K}$ / kJ·mol^{-1}
431nm	$1.434 \cdot 10^{-4}$	81	125.4
811 nm	$1.464 \cdot 10^{-4}$	79	125.4
average values	$1.449 \cdot 10^{-4}$	80	125.4

NMR Spectroscopy

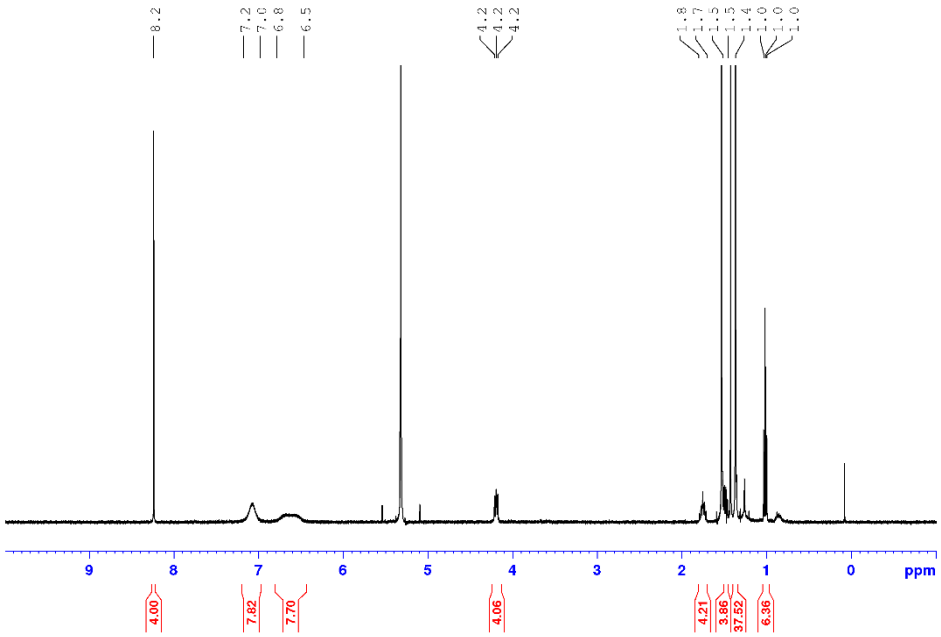

Figure A32. ^{1}H NMR (400 MHz) spectrum of **230** in CD_2Cl_2 at room temperature.

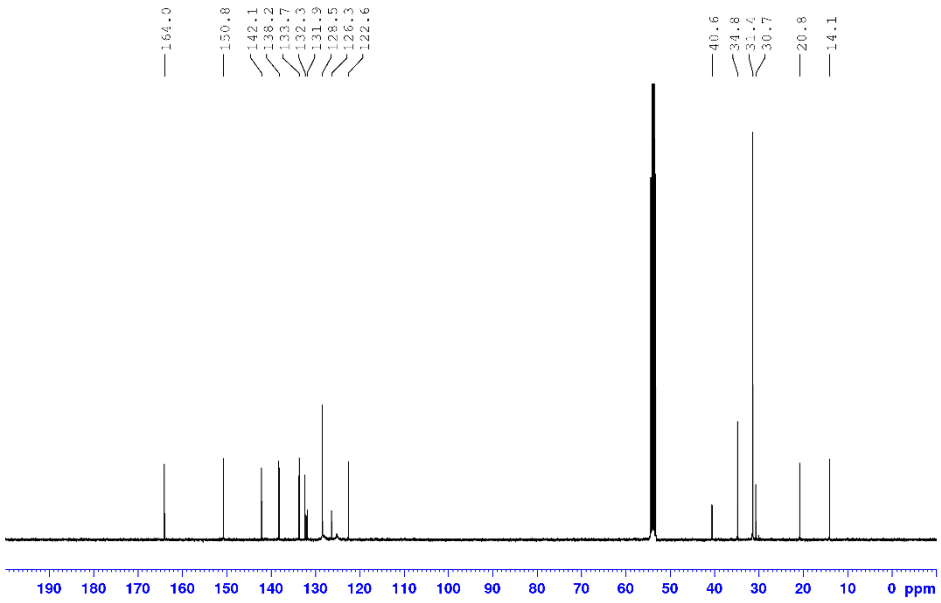

Figure A33. ^{13}C NMR (101 MHz) spectrum of **230** in CD_2Cl_2 at room temperature.

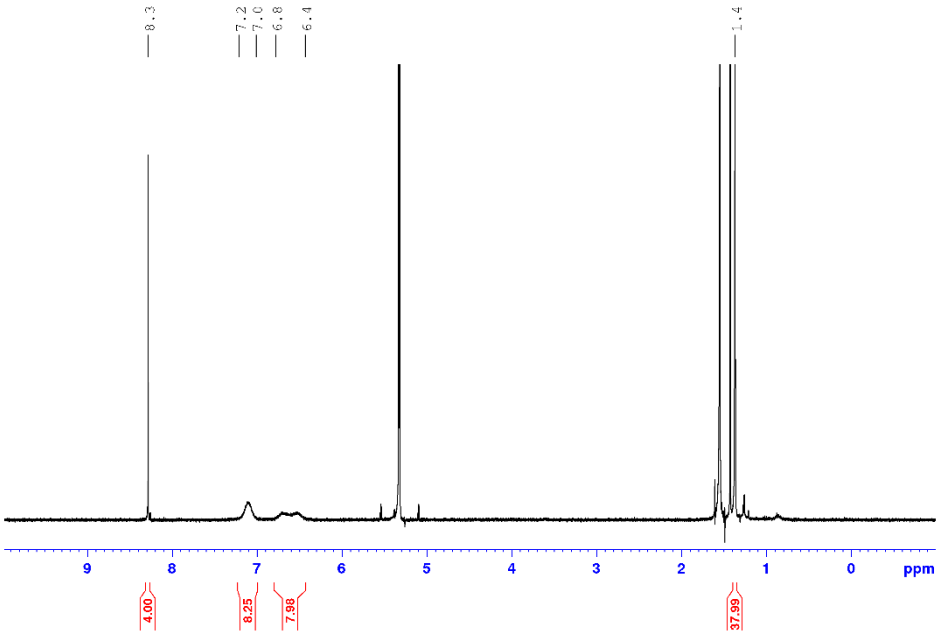

Figure A34. ^{1}H NMR (400 MHz) spectrum of **232** in CD_2Cl_2 at room temperature.

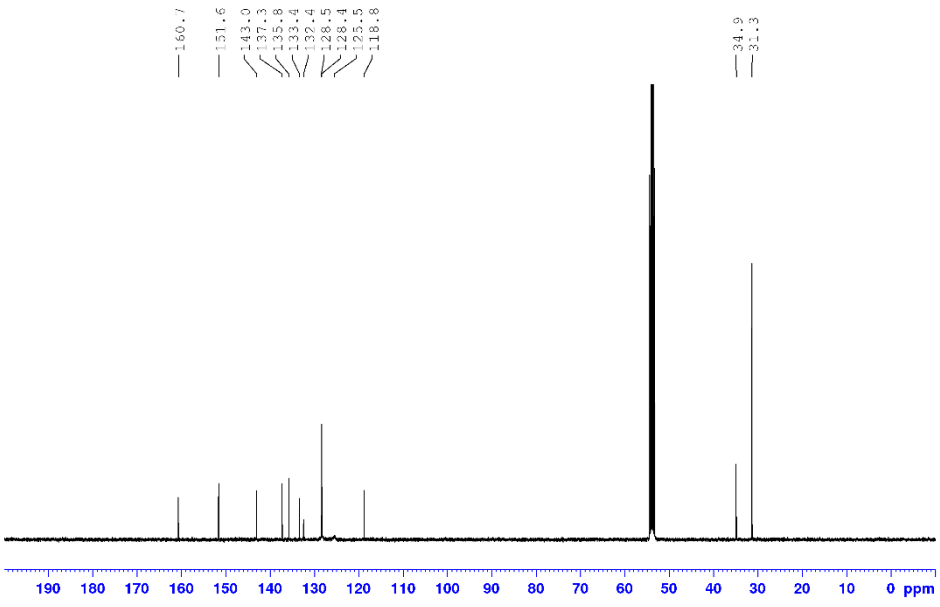

Figure A35. ^{13}C NMR (101 MHz) spectrum of **232** in CD_2Cl_2 at room temperature.

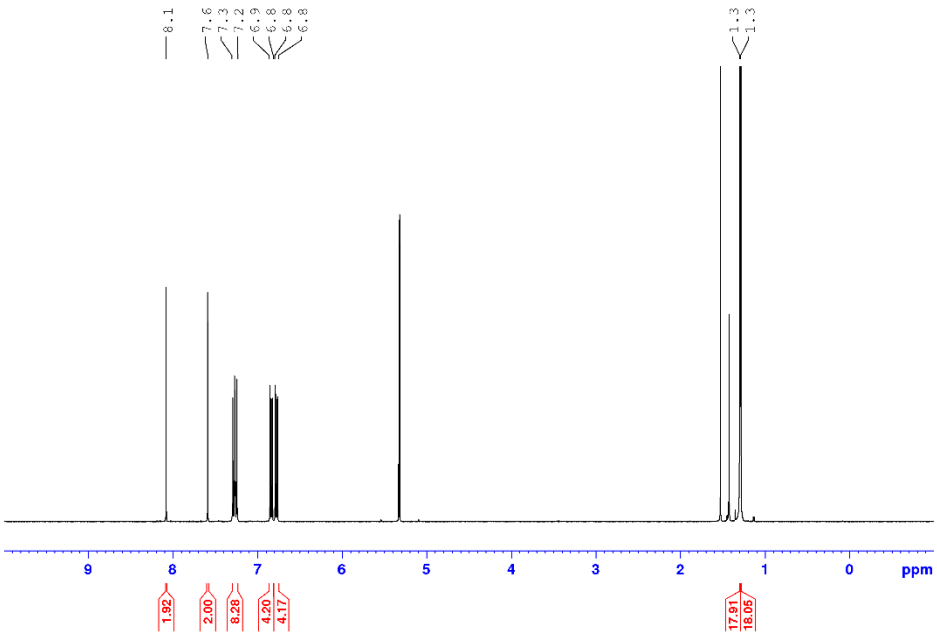

Figure A36. ^{1}H NMR (400 MHz) spectrum of **233** in CD_2Cl_2 at room temperature.

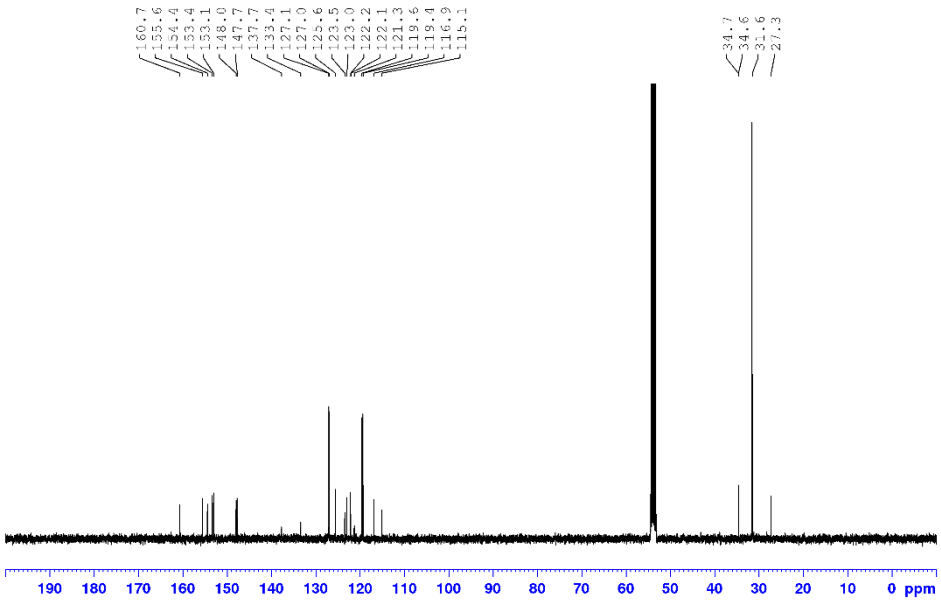

Figure A37. ^{13}C NMR (101 MHz) spectrum of **233** in CD_2Cl_2 at room temperature.

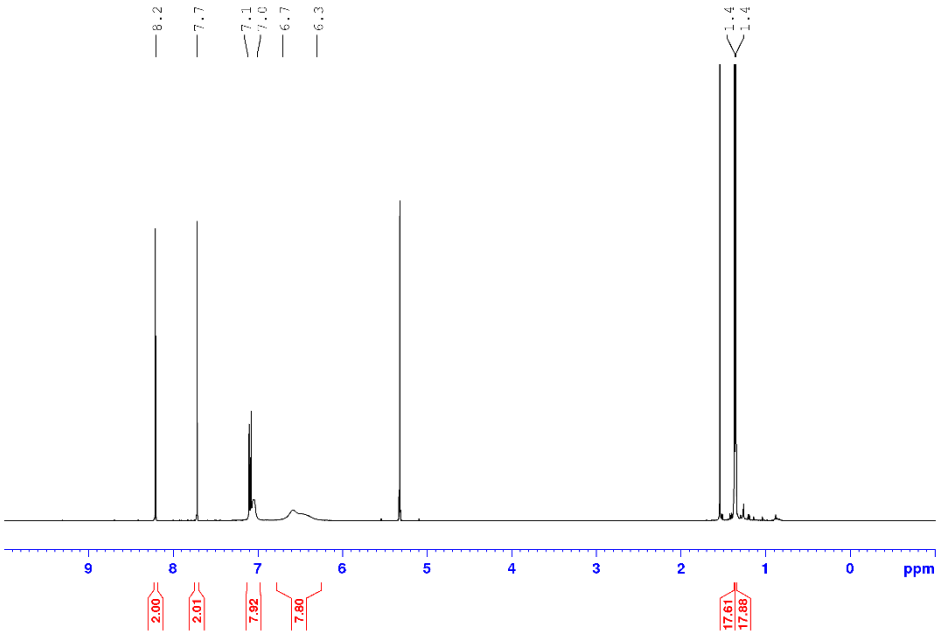

Figure A38. ^{1}H NMR (400 MHz) spectrum of **234** in CD_2Cl_2 at room temperature.

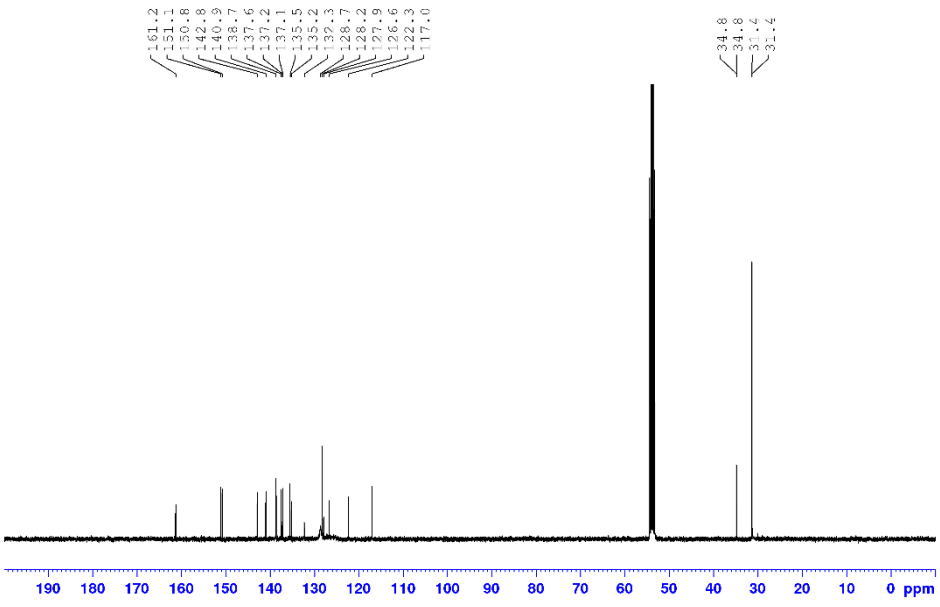

Figure A39. ^{13}C NMR (101 MHz) spectrum of **234** in CD_2Cl_2 at room temperature.

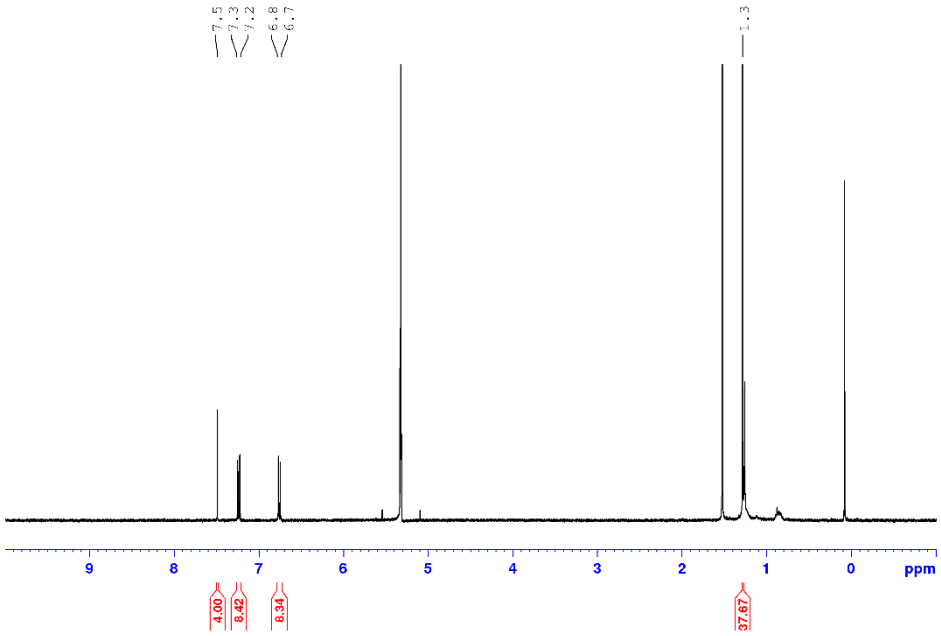

Figure A40. ^{1}H NMR (400 MHz) spectrum of **235** in CD_2Cl_2 at room temperature.

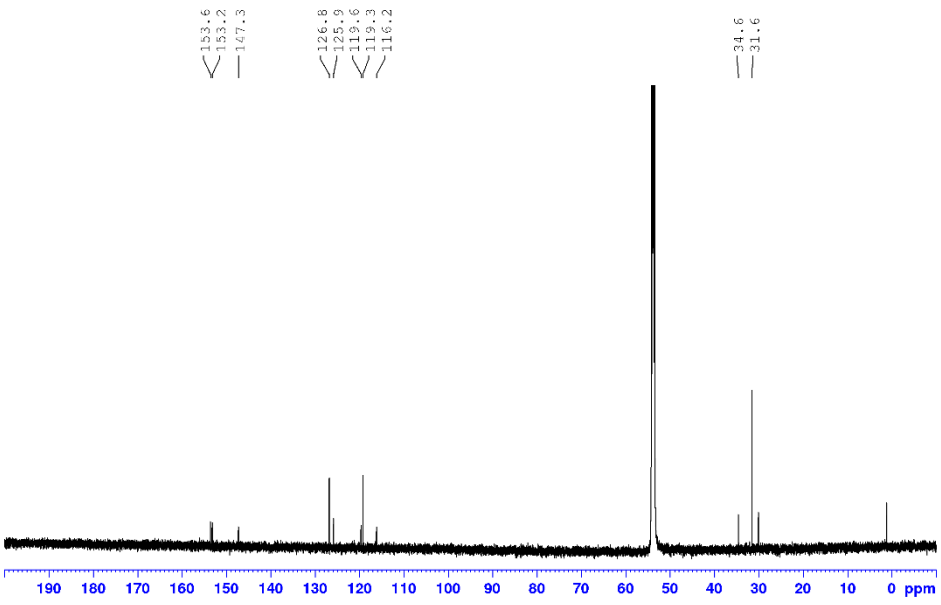

Figure A41. ^{13}C NMR (151 MHz) spectrum of **235** in CD_2Cl_2 at room temperature.

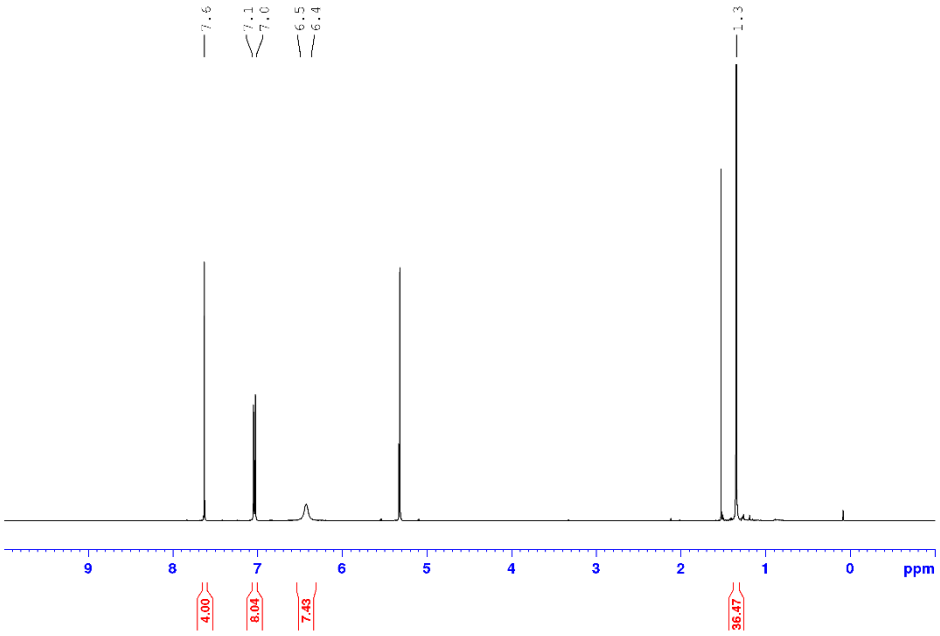

Figure A42. ^{1}H NMR (400 MHz) spectrum of **236** in CD_2Cl_2 at room temperature.

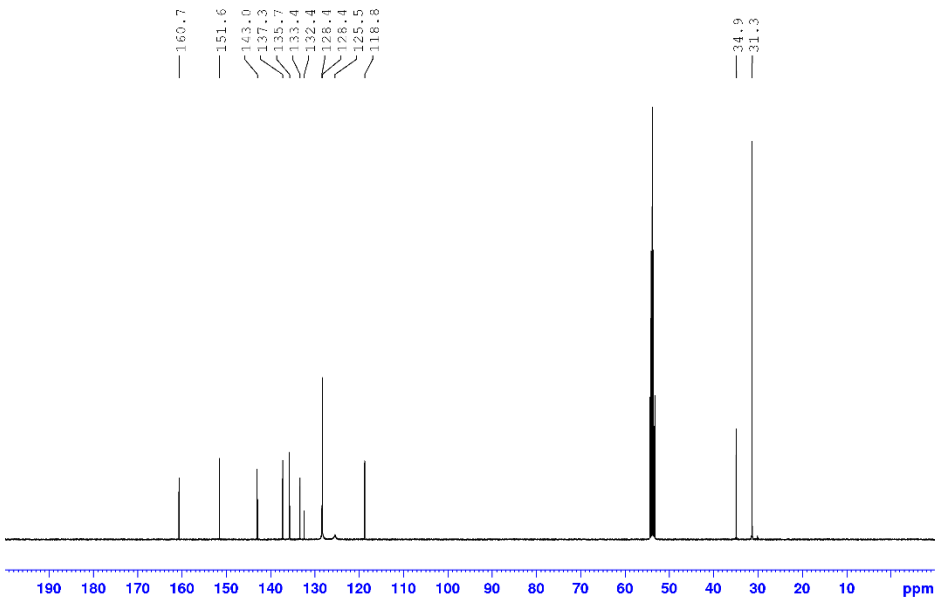

Figure A43. ^{13}C NMR (101 MHz) spectrum of **236** in CD_2Cl_2 at room temperature.

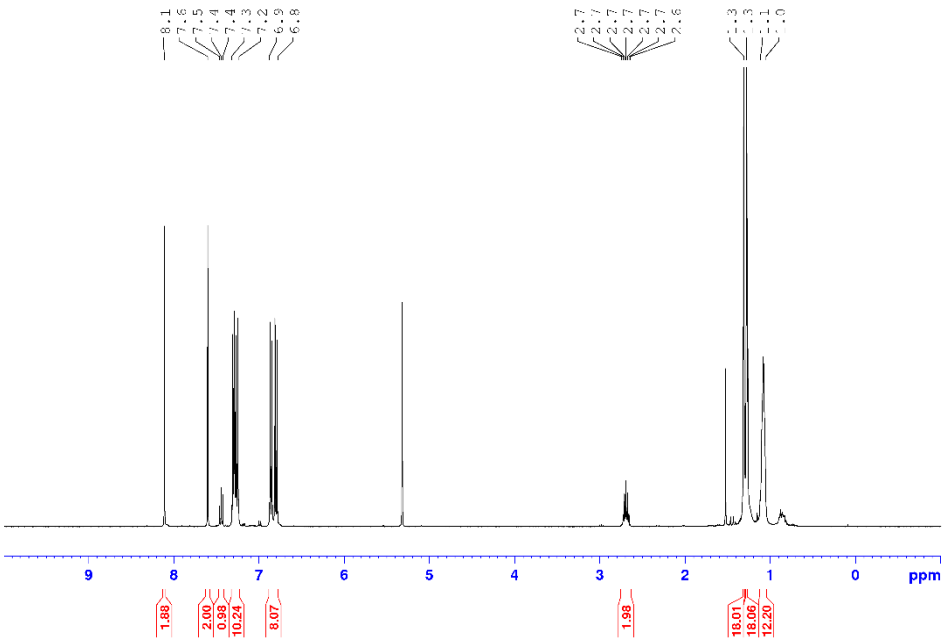

Figure A44. ^{1}H NMR (400 MHz) spectrum of **237** in CD_2Cl_2 at room temperature (contains solvent impurities in the aliphatic region).

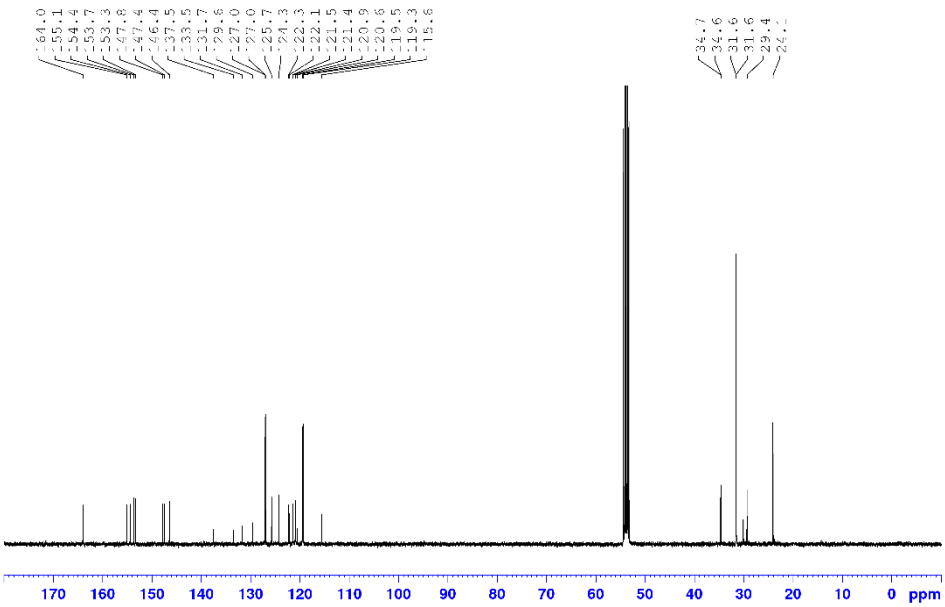

Figure A45. ^{13}C NMR (101 MHz) spectrum of **237** in CD_2Cl_2 at room temperature (contains solvent impurities in the aliphatic region).

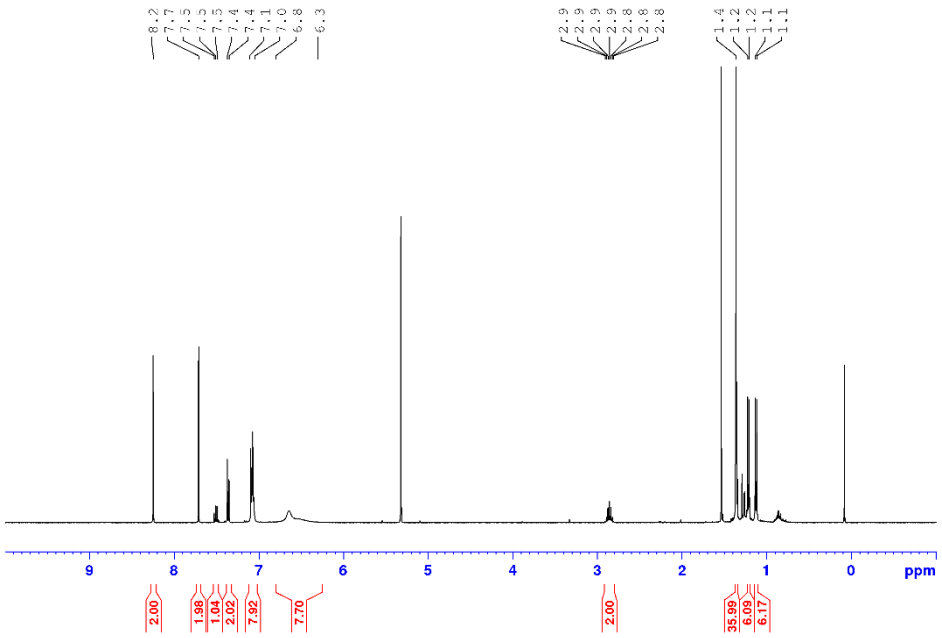

Figure A 46. ^{1}H NMR (400 MHz) spectrum of **238** in CD_2Cl_2 at room temperature.

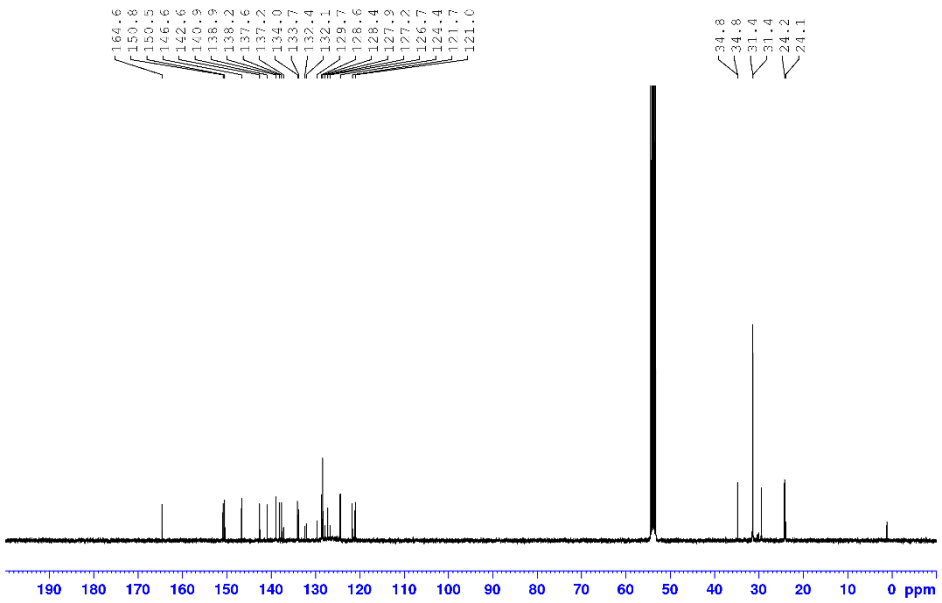

Figure A 47. ^{13}C NMR (101 MHz) spectrum of **238** in CD_2Cl_2 at room temperature.

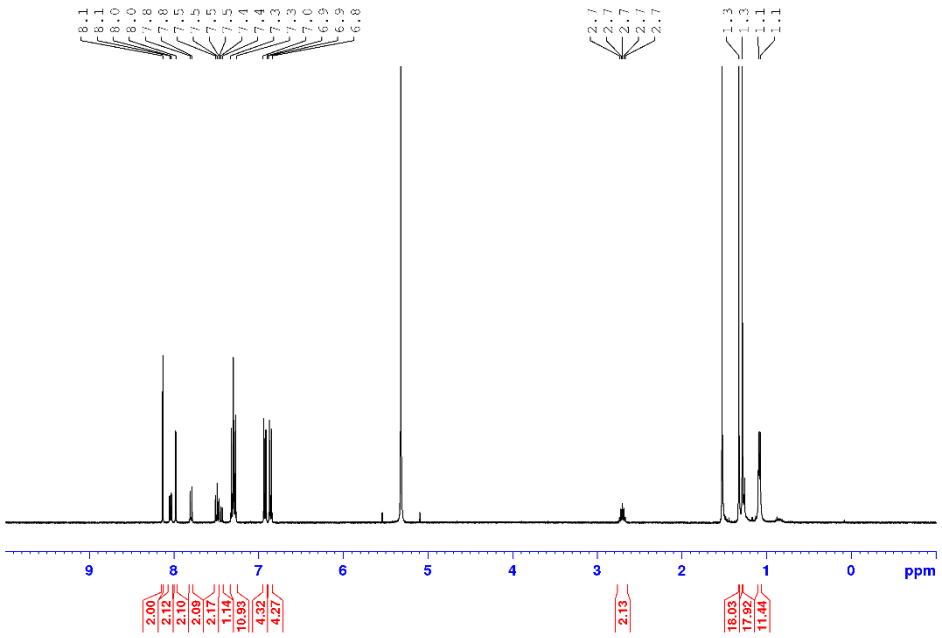

Figure A48. ^{1}H NMR (400 MHz) spectrum of **225a** in CD_2Cl_2 at room temperature.

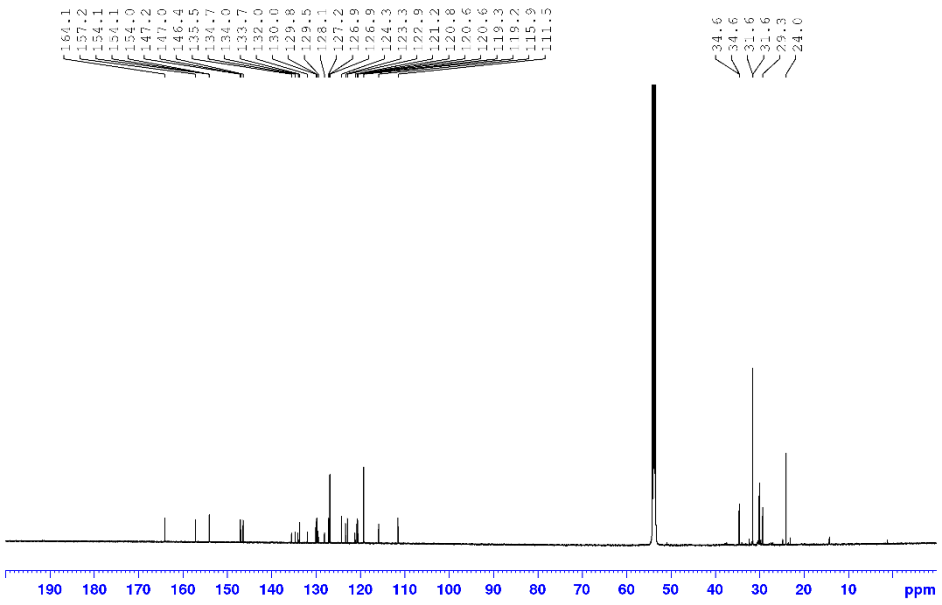

Figure A49. ^{13}C NMR (151 MHz) spectrum of **225a** in CD_2Cl_2 at room temperature.

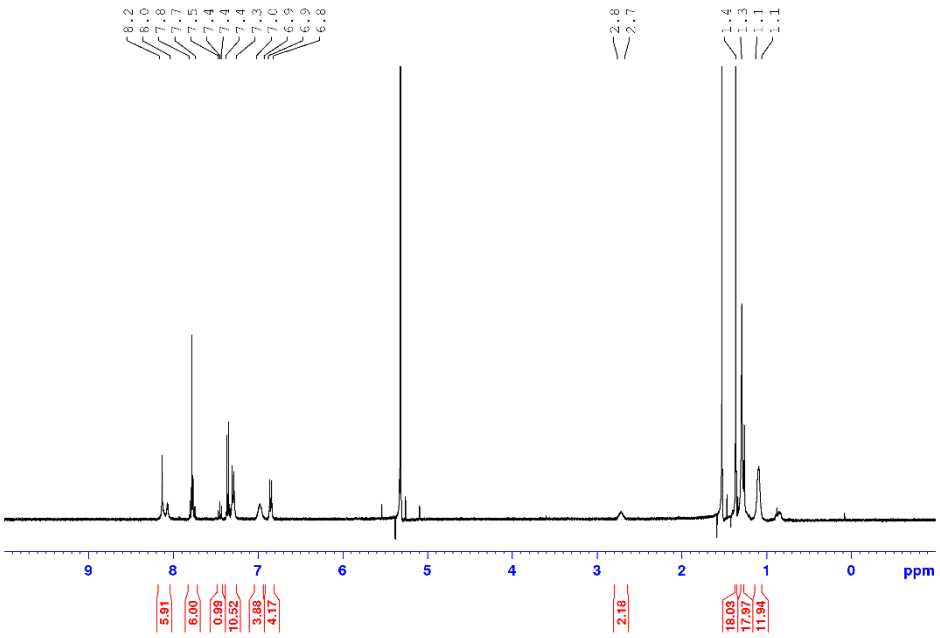

Figure A50. ^{1}H NMR (400 MHz) spectrum of **225g** in CD_2Cl_2 at room temperature (contains solvent impurities in the aliphatic region).

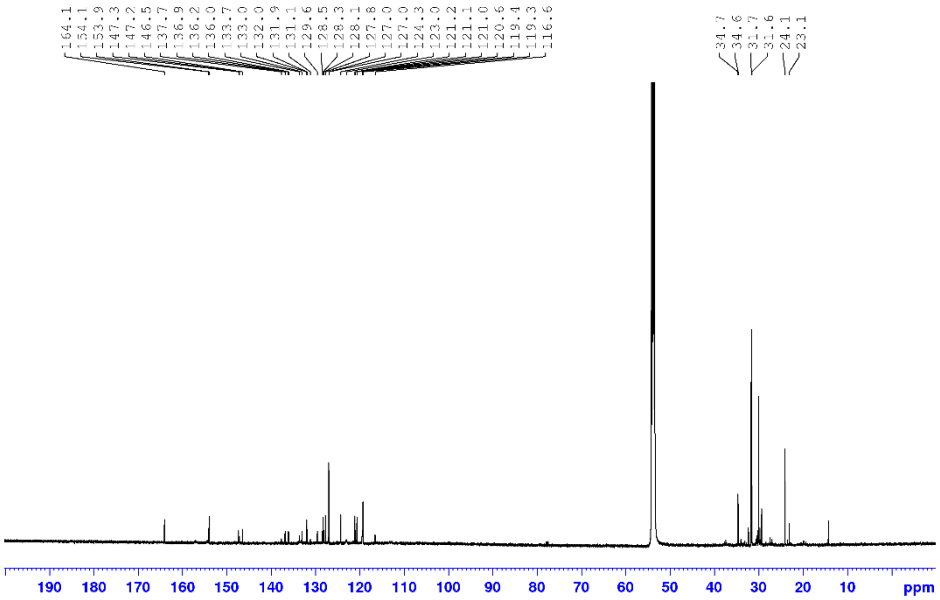

Figure A51. ^{13}C NMR (151 MHz) spectrum of **225g** in CD_2Cl_2 at room temperature (contains solvent impurities in the aliphatic region).

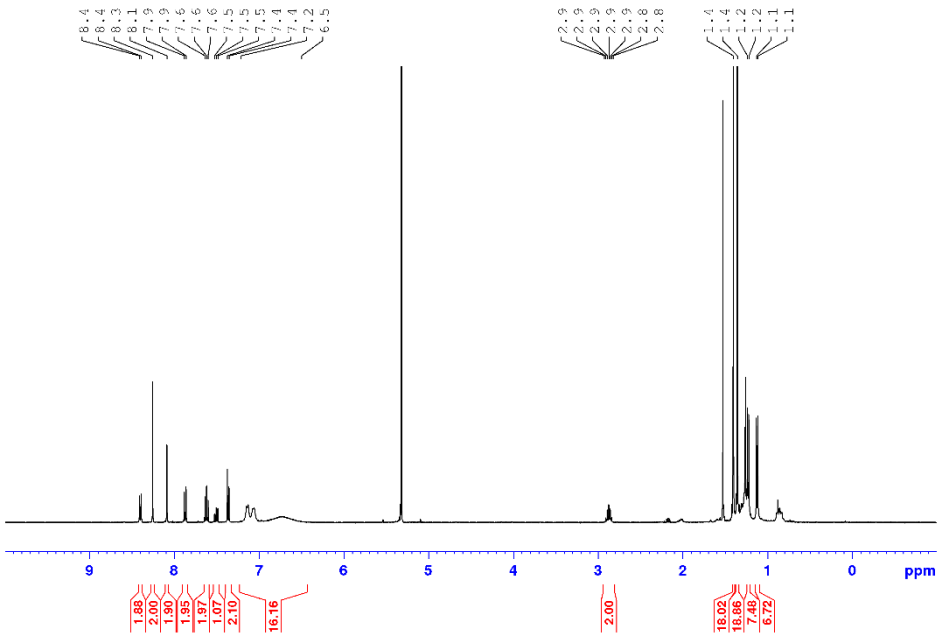

Figure A52. ^{1}H NMR (400 MHz) spectrum of **226a** in CD_2Cl_2 at room temperature.

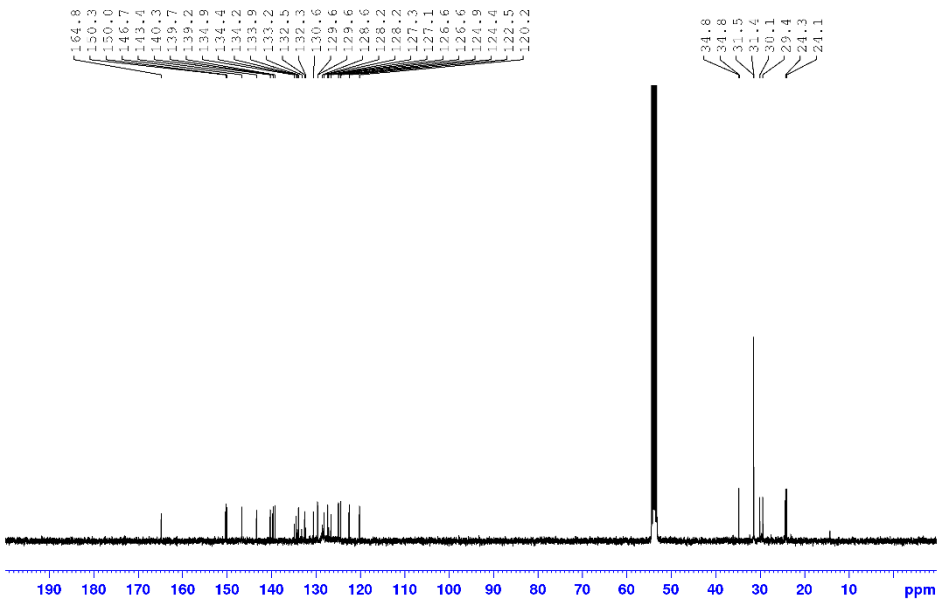

Figure A53. ^{13}C NMR (101 MHz) spectrum of **226a** in CD_2Cl_2 at room temperature.

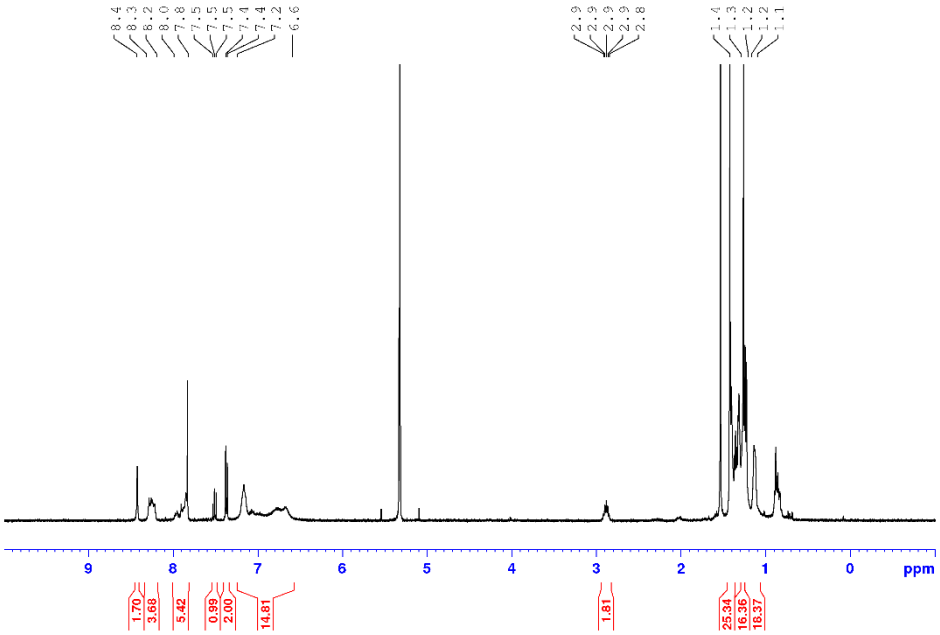

Figure A54. ^{1}H NMR (400 MHz) spectrum of **226g** in CD_2Cl_2 at room temperature.

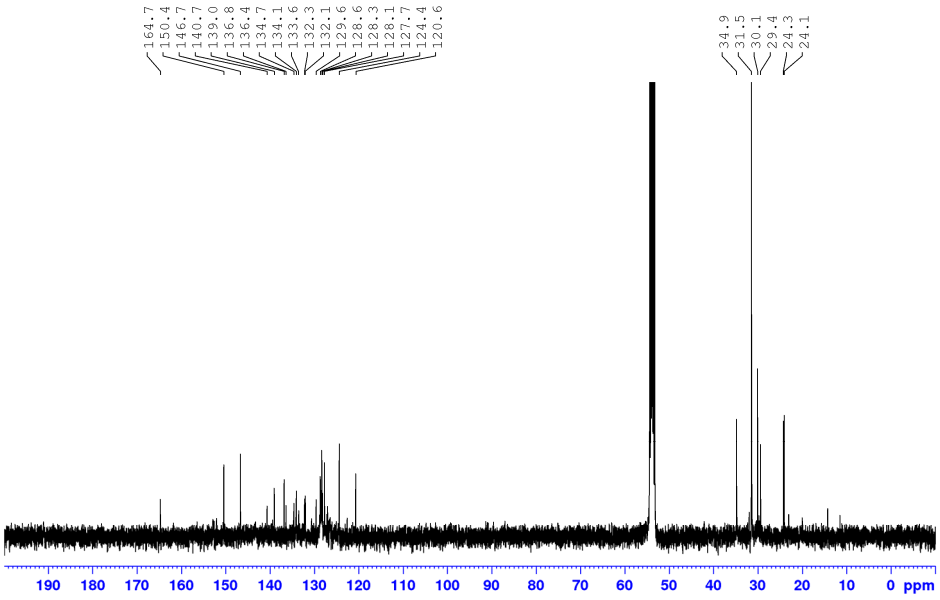

Figure A55. ^{13}C NMR (101 MHz) spectrum of **226g** in CD_2Cl_2 at room temperature.

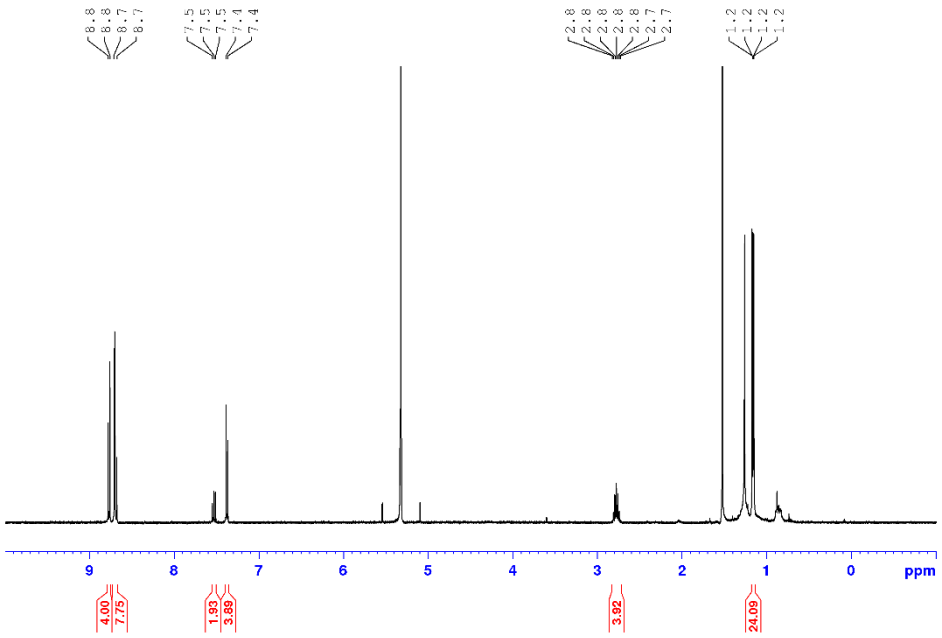

Figure A56. ^{1}H NMR (400 MHz) spectrum of **241** in CD_2Cl_2 at room temperature (contains solvent impurities in the aliphatic region).

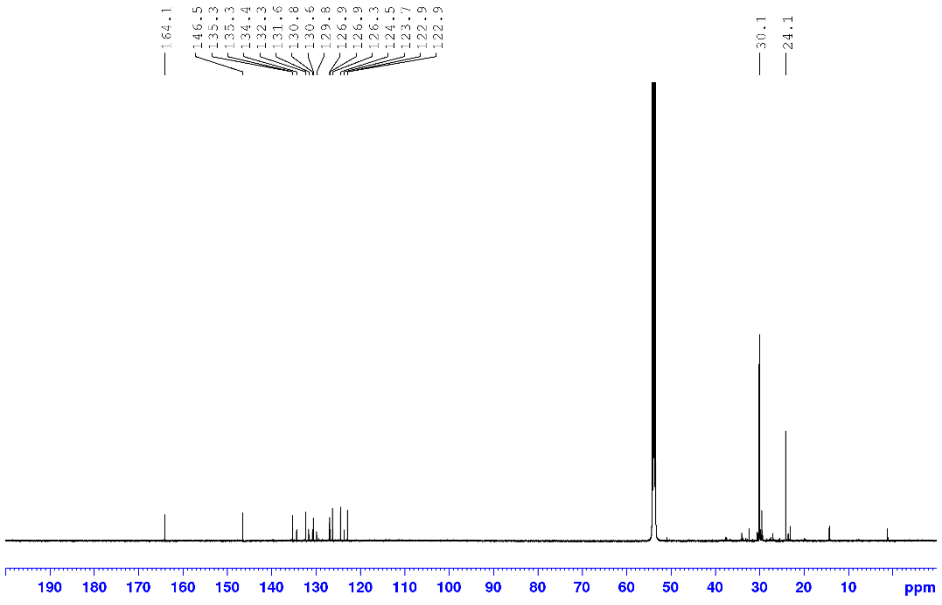

Figure A57. ^{13}C NMR (151 MHz) spectrum of **241** in CD_2Cl_2 at room temperature (contains solvent impurities in the aliphatic region).

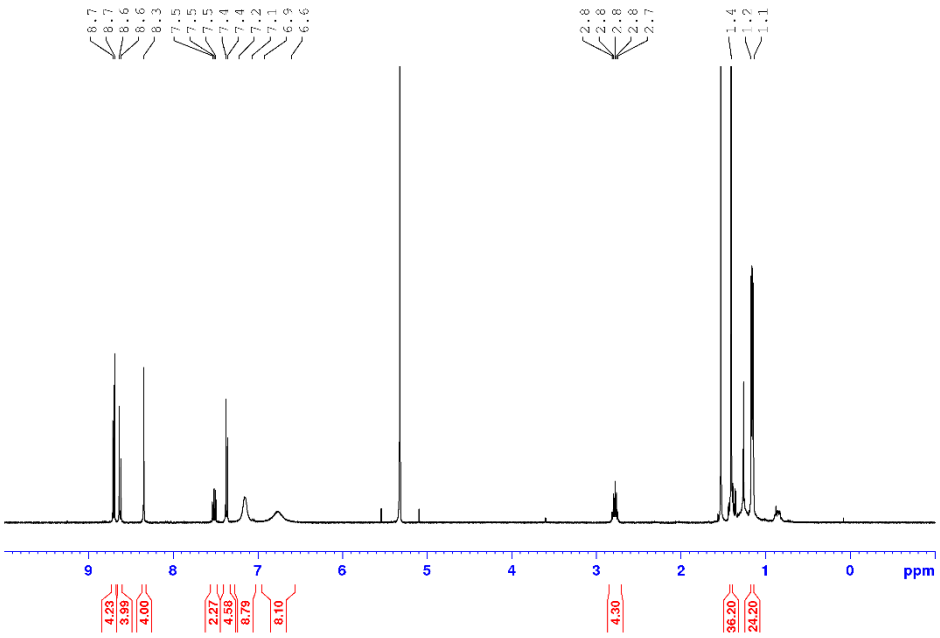

Figure A58. ^{1}H NMR (400 MHz) spectrum of **243** in CD_2Cl_2 at room temperature (contains solvent impurities in the aliphatic region).

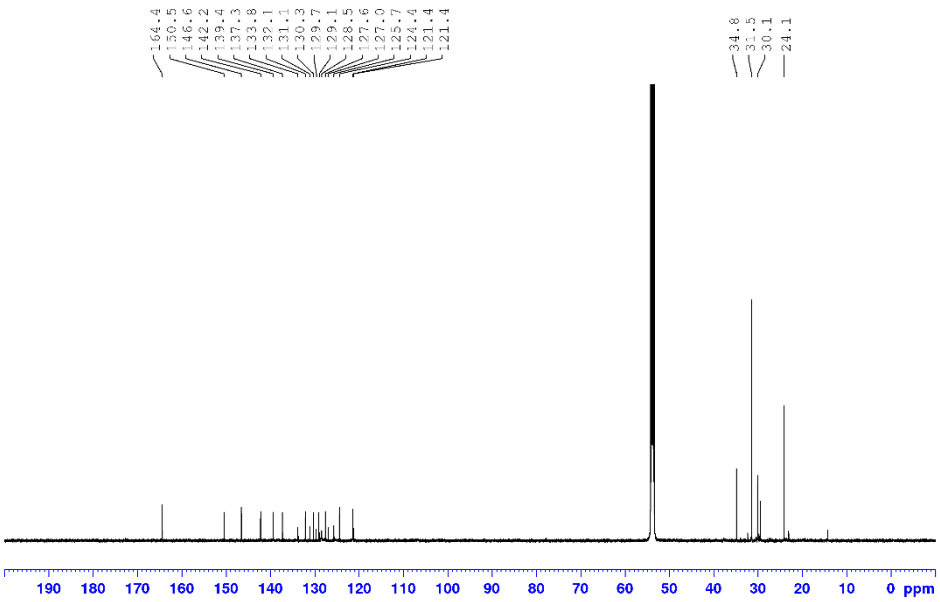

Figure A59. ^{13}C NMR (151 MHz) spectrum of **243** in CD_2Cl_2 at room temperature (contains solvent impurities in the aliphatic region).

10.3. Supporting Information Chapter 5[xii]

General Methods

All reactions were carried out by standard Schlenk techniques in dry reaction vessels under a nitrogen or an argon atmosphere. For reactions that require heating, an oil bath was used as the heat source. Flash silica gel column chromatography was performed on silica gel (particle size of 0.040–0.063 mm) with freshly distilled solvents. Size exclusion chromatography was performed with S-X3 Bio-Beads with HPLC grade solvents (9/1 dichloromethane/methanol). ^{1}H NMR and ^{13}C NMR spectra were recorded on a Bruker Avance III HD 400 spectrometer at 298 K. Chemical shift data are reported in parts per million (ppm, δ scale) downfield from tetramethylsilane and referenced internally to the residual proton (for proton NMR) in the solvent ($CDCl_3$, δ 7.26; CD_2Cl_2, δ 5.32) or to the carbon resonance ($CDCl_3$, δ 77.16; CD_2Cl_2, δ 53.84). The coupling constants are listed in Hertz. MALDI-TOF measurements were carried out on a Bruker Daltonics ultrafleXtreme mass spectrometer. High-resolution ESI-TOF spectra were acquired on a Bruker Daltonics microTOF focus spectrometer. Melting points were measured with an Olympus BX41 polarization microscope connected to a TP84 Linkam scientific temperature regulator. UV–vis absorption spectra are recorded on a JASCO V-770 or V-670 spectrometer. Cyclic voltammetry (CV) and square wave voltammetry (SWV) were conducted on an EC epsilon standard electrochemical analyzer. A Pt disc electrode was used as the working electrode, a platinum wire as the counter electrode, and a Ag/AgCl reference electrode using the ferrocenium/ferrocene (Fc^+/Fc) redox couple as the internal standard. The measurements were conducted in dichloromethane solutions (0.1 M) and tetrabutylammonium hexafluorophosphate as an electrolyte with a scan rate of 100 mV/s at room temperature. Boronic esters **244a**–**d** and **244h** were purchased from commercial sources. *N*-(2,6-Diisopropylphenyl)-4-bromo-5-chloronaphthalene-1,8-dicarboximide **245**,[270] **244f**,[398] and $[Pd_2(dba)_3]\cdot CHCl_3$[391] were synthesized according to literature procedures.

Computational Methods

Ground state structure optimization and frontier molecular orbital analyses were performed using DFT with Gaussian 09[399] at the B3LYP/6-31G(d) level of theory. Excited state calculations were performed using TD-DFT at the B3LYP/6-31G(d) level of theory. Multiwfn[394] was used to calculate the electron density difference D_{CT} and $\Delta\sigma_{CT}$ upon excitation. The $\Delta\sigma_{CT}$ was originally used for centrosymmetric molecules, and because the spread of positive and negative density

[xii] This Supporting Information has been published. For the sake of harmonization of all *Supporting Information Chapters*, some modifications were made.
Adapted and reproduced with permission from reference: K. Shoyama,* M. Mahl,* M. A. Niyas, M. Ebert, V. Kachler, C. Keck, F. Würthner, *J. Org. Chem.* **2020**, *85*, 142–149. Copyright 2020 American Chemical Society.

regions is multidirectional in **246d**–**h** due to the A–D–A architecture, we have used this parameter to rationalize the CT character in this work.

Synthesis

2,6-Bis(4,4,5,5-tetramethyl-1,3,2-dioxaborolan-2-yl)-4-octyl-4*H*-dithieno[3,2-*b*:2′,3′-*d*]pyrrole (244e)

A solution of 4-*n*-octyl-4*H*-dithieno[3,2-*b*:2′,3′-*d*]pyrrole (421 mg, 1.44 mmol, 1.0 equiv) in THF (40 mL) was cooled to −78 °C, and butyllithium (2.61 mL, 2.5 M in hexane, 6.53 mmol, 4.5 equiv) was added dropwise. The reaction mixture was stirred at −78 °C for 1 h and then at room temperature for additional 1 h. Subsequently, the mixture was again cooled to −78 °C, and 2-isopropoxy-4,4,5,5-tetramethyl-1,3,2-dioxaborolane (2.31 mL, 13.5 mmol, 9.4 equiv) was added. The reaction mixture was allowed to warm to room temperature and stirred overnight. Subsequently, water (50 mL) and brine (50 mL) were added to the reaction mixture, and the resulting mixture was extracted with dichloromethane. The combined organic layers were washed with brine and water and dried over magnesium sulfate, and the solvent was removed under reduced pressure. The crude product was purified by column chromatography (dichloromethane) to give **244e** as a light-gray solid. Yield: 395 mg (51%). M.p: 179–180 °C. ^{1}H NMR (400 MHz, $CDCl_3$): δ/ppm = 7.51 (*s*, 2H), 4.16 (*t*, *J* = 7.2 Hz, 2H), 1.90–1.80 (*m*, 2H), 1.37 (*s*, 24H), 1.31–1.20 (*m*, 10H), 0.87 (*t*, *J* = 7.2 Hz, 3H). ^{13}C NMR (101 MHz, $CDCl_3$): δ/ppm = 148.5, 121.3, 119.9, 84.3, 47.6, 31.9, 30.5, 29.4, 29.3, 27.2, 24.9, 24.7, 22.7, 14.3. MS (MALDI-TOF, positive mode, DCTB in chloroform): 543.3 $[M]^+$. HRMS (ESI-TOF, positive mode, acetonitrile/chloroform): calcd for $C_{28}H_{43}B_2NO_4S_2$: 543.2820; found, 543.2814 $[M]^+$.

2,6-Bis(4,4,5,5-tetramethyl-1,3,2-dioxaborolan-2-yl)dithieno[3,2-*b*;2′,3′-*d*]thiophene (244g)

Synthesis of this compound was reported in the literature using an Ir catalyst.[400] We have used an alternative method to synthesize this compound by lithiation.

A solution of dithieno[3,2-*b*;2′,3′-*d*]thiophene (356 mg, 1.81 mmol, 1.0 equiv) in THF (18 mL) was cooled to −78 °C. Butyllithium (1.67 mL, 2.5 M in hexane, 4.18 mmol, 2.3 equiv) was added dropwise to the mixture. The reaction mixture was stirred at −78 °C for 1 h and then at room temperature for an additional 1 h. Subsequently, the mixture was again cooled to −78 °C, and 2-isopropoxy-4,4,5,5-tetramethyl-1,3,2-dioxaborolane (1.48 mL, 7.24 mmol, 4.0 equiv) was added.

The reaction mixture was allowed to warm to room temperature and stirred overnight. The reaction was quenched by addition of water (20 mL) and brine (20 mL), and the resulting mixture was extracted with dichloromethane. The combined organic layers were washed with brine and water, dried over magnesium sulfate, and filtered. The filtrate was concentrated under reduced pressure. The crude product was purified by column chromatography (gradient of 10:1:0 to 0:99:1 *n*-hexane/dichloromethane/methanol) to give **244g** as a light-gray solid. Yield: 174 mg (21%). ^{1}H NMR (400 MHz, $CDCl_3$): δ/ppm = 7.76 (*s*, 2H), 1.36 (*s*, 24H).

General Procedure for the [3+2] Annulation Reaction of Arylboronic Acid (Pinacol)ester (244a–h) and 4-Bromo-5-chloronaphthalene-1,8-dicarboximide (245)

A Schlenk tube was charged with the respective aryl boronic pinacol ester **244** (1.0 equiv), 4-bromo-5-chloro-naphthalene 1,8-dicarboximide (**245**) (1.1 equiv), tris(dibenzylideneacetone)-dipalladium(0)-chloroform adduct (10 mol %), P(*m*-tolyl)$_3$ (40 mol %), Cs_2CO_3 (3.0 equiv), and 1-chloronaphthalene as a solvent under an inert atmosphere at room temperature and heated to 90 °C for 2 h. Subsequently, tetrabutylammonium chloride (0.5 equiv) was added, and the reaction mixture heated to 160 °C for 16 h. After cooling to room temperature, the reaction mixture was filtered with *n*-hexane over a pad of silica gel to remove 1-chloronaphthalene, and the crude product was eluted with dichloromethane. Subsequently, the solvent was removed under reduced pressure to obtain the respective annulated crude product, which was further purified by column chromatography followed by precipitation. For 2-fold annulated products **246d**–**h**, the amounts of **245**, $[Pd_2(dba)_3]\cdot CHCl_3$, P(*m*-tolyl)$_3$, Cs_2CO_3, and Bu_4NCl were doubled.

***N*-(2,6-Diisopropylphenyl)acenaphthyleno[1,2-*b*][1]benzothiophene-3,4-dicarboximide (246a)**

According to the general procedure, the reaction of **244a** (10.0 mg, 38.4 µmol, 1.0 equiv), **245** (19.9 mg, 42.3 µmol, 1.1 equiv), $[Pd_2(dba)_3]\cdot CHCl_3$, (4.0 mg, 3.84 µmol, 10 mol %), P(*m*-tolyl)$_3$ (4.7 mg, 15.4 µmol, 40 mol %), Cs_2CO_3 (37.6 mg, 115 µmol, 3.0 equiv), and Bu_4NCl (5.4 mg, 19.2 µmol, 0.5 equiv) in 1.2 mL of 1-chloronaphthalene afforded **246a**. The crude product was purified by column chromatography (gradient of 1:5 to 1:1 dichloromethane/*n*-hexane) and subsequent precipitation from dichloromethane/methanol. The isolated solid was washed with methanol and dried under high vacuum to give **246a** as an orange-red solid. Yield: 16.2 mg (86%). M.p: >350 °C. ^{1}H NMR (400 MHz, $CDCl_3$): δ/ppm = 8.45 (*d*, *J* = 7.2 Hz, 1H), 8.43 (*d*, *J* = 7.3 Hz, 1H), 8.15–8.12 (*m*, 1H), 8.00 (*d*, *J* = 7.2 Hz, 1H), 7.90 (*dt*, *J* = 0.8, 8.1 Hz, 1H), 7.85 (*d*, *J* = 7.2 Hz, 1H), 7.55–7.50

(*m*, 1H), 7.48 (*t*, *J* = 7.7 Hz, 1H), 7.44–7.39 (*m*, 1H), 7.33 (*d*, *J* = 7.7 Hz, 2 H), 2.82 (*sep*, *J* = 6.8 Hz, 2 H), 1.18 (*dd*, *J* = 0.9, 6.8 Hz, 12 H). ^{13}C NMR (101 MHz, $CDCl_3$): δ/ppm = 163.9, 163.8, 146.0, 144.6, 144.2, 141.2, 139.4, 139.0, 133.1, 132.9, 132.6, 131.0, 129.6, 126.1, 125.5, 124.9, 124.5, 124.1, 122.9, 122.7, 122.5, 121.80, 121.79, 29.2, 24.2. UV–vis (CH_2Cl_2): λ_{max} / nm (ε / $M^{-1}cm^{-1}$) = 418 (15500). CV (CH_2Cl_2): E_{ox1} = 1.17 V, E_{red1} = −1.22 V, E_{red2} = −1.64 V. MS (MALDI-TOF, positive mode, DCTB in chloroform): 487.1 $[M]^+$. HRMS (ESI-TOF, positive mode, acetonitrile/chloroform): calcd for $C_{32}H_{25}NO_2SNa$: 510.1498; found, 510.1506 $[M+Na]^+$.

N-(2,6-Diisopropylphenyl)acenaphthyleno[1,2-*b*]-1-methyl-1*H*-indole-3,4-dicarboximide (246b)

According to the general procedure, the reaction of **244b** (10.0 mg, 38.9 µmol, 1.0 equiv), **245** (20.1 mg, 42.8 µmol, 1.1 equiv), $[Pd_2(dba)_3]\cdot CHCl_3$ (4.0 mg, 3.89 µmol, 10 mol %), P(*m*-tolyl)$_3$ (4.7 mg, 15.6 µmol, 40 mol %), Cs_2CO_3 (38.0 mg, 117 µmol, 3.0 equiv), and Bu_4NCl (5.48 mg, 19.4 µmol, 0.5 equiv) in 1.2 mL of 1-chloronaphthalene afforded **246b**. The crude product was purified by column chromatography (gradient of 1:2 to 2:1 dichloromethane/*n*-hexane) and precipitation from dichloromethane/methanol. The isolated solid was washed with *n*-hexane and methanol. The product was dried under high vacuum to give **246b** as a green solid. Yield: 16.2 mg (86%). M.p: >350 °C. ^{1}H NMR (400 MHz, $CDCl_3$): δ/ppm = 8.33–8.27 (*m*, 2H), 7.78 (*d*, *J* = 7.2 Hz, 1H), 7.76–7.73 (*m*, 1H), 7.69 (*d*, *J* = 7.2 Hz, 1H), 7.47 (*t*, *J* = 7.6 Hz, 1H), 7.38–7.35 (*m*, 1H), 7.31 (*d*, *J* = 7.6 Hz, 2H), 7.27–7.19 (*m*, 2H), 4.02 (*s*, 3H), 2.82 (*sep*, *J* = 7.0 Hz, 2H), 1.12 (*d*, *J* = 7.0 Hz, 12H). ^{13}C NMR (101 MHz, $CDCl_3$): δ/ppm = 164.31, 164.25, 146.9, 146.7, 143.3, 140.5, 135.5, 133.9, 132.9, 132.04, 131.96, 129.5, 125.5, 124.2, 123.45, 123.39, 123.1, 122.5, 121.25, 121.19, 120.8, 120.2, 120.1, 111.4, 32.3, 29.3, 24.1. UV–vis (CH_2Cl_2): λ_{max} / nm (ε / $M^{-1}cm^{-1}$) = 419 (13700). CV (CH_2Cl_2): E_{ox1} = 1.00 V, E_{ox2} = 1.13 V, E_{red1} = −1.42 V, E_{red2} = −1.88 V. MS (MALDI-TOF, positive mode, DCTB in chloroform): 484.2 $[M]^+$. HRMS (ESI-TOF, positive mode, acetonitrile/chloroform): calcd for $C_{33}H_{28}N_2O_2Na$: 507.2048; found, 507.2030 $[M+Na]^+$.

N-(2,6-Diisopropylphenyl)acenaphthyleno[1,2-*b*]thiophene-3,4-dicarboximide (246c)

According to the general procedure, the reaction of **244c** (10.0 mg, 47.6 µmol, 1.0 equiv), **245** (24.6 mg, 52.4 µmol, 1.1 equiv), $[Pd_2(dba)_3]\cdot CHCl_3$ (4.9 mg, 4.76 µmol, 10 mol %), P(*m*-tolyl)$_3$ (5.8 mg, 19.0 µmol, 40 mol %), Cs_2CO_3 (46.5 mg, 143 µmol, 3.0 equiv), and Bu_4NCl (6.6 mg, 23.8 µmol, 0.5 equiv) in 1.4 mL of 1-chloronaphthalene afforded **246c**. The reaction time after the addition of NBu_4Cl was 2 h. The crude product was purified by column chromatography (gradient of 0:1 to 1:1

dichloromethane/*n*-hexane) and precipitation from dichloromethane/methanol. The isolated solid was washed with cold methanol. The product was dried under high vacuum to give **246c** as an orange solid. Yield: 12.9 mg (62%). M.p: 322–324 °C. ^{1}H NMR (400 MHz, $CDCl_3$): δ/ppm = 8.43–8.41 (*m*, 2H), 7.79 (*d*, *J* = 7.2 Hz, 1H), 7.76 (*d*, *J* = 7.3 Hz, 1H), 7.49–7.44 (*m*, 2H), 7.39 (*d*, *J* = 4.9 Hz, 1H), 7.32 (*d*, *J* = 7.8 Hz, 2H), 2.80 (*sep*, *J* = 6.8 Hz, 2H), 1.16 (*d*, *J* = 6.8 Hz, 12H). ^{13}C NMR (101 MHz, $CDCl_3$): δ/ppm = 164.0, 163.9 147.7, 146.0, 143.4, 139.3, 138.8, 133.2, 132.9, 132.8, 131.7, 131.1, 129.6, 125.4, 124.0, 122.0, 121.8, 121.7, 121.3, 121.2, 29.2, 24.2. UV–vis (CH_2Cl_2): λ_{max} / nm (ε / $M^{-1}cm^{-1}$) = 404 (19800). CV (CH_2Cl_2): E_{ox1} = 1.28 V, E_{red1} = −1.31 V, E_{red2} = −1.76 V. MS (MALDI-TOF, positive mode, DCTB in chloroform): 437.1 $[M]^+$. HRMS (ESI-TOF, positive mode, acetonitrile/chloroform): calcd for $C_{28}H_{23}NO_2SNa$: 460.1342; found, 460.1332 $[M+Na]^+$.

N,*N*′-Bis(2,6-diisopropylphenyl)diacenaphthyleno[1,2-*b*:1′,2′-*d*]thiophene-3,4:10,11-bis(dicarboximide) (246d)

According to the general procedure, the reaction of **244d** (10.0 mg, 29.8 µmol, 1.0 equiv), **245** (30.8 mg, 65.5 µmol, 2.2 equiv), $[Pd_2(dba)_3]\cdot CHCl_3$ (6.2 mg, 5.95 µmol, 20 mol %), P(*m*-tolyl)$_3$ (7.2 mg, 23.8 µmol, 80 mol %), Cs_2CO_3 (58.2 mg, 179 µmol, 6.0 equiv), and Bu_4NCl (8.3 mg, 29.8 µmol, 1.0 equiv) in 1-chloronaphthalene (0.9 mL) afforded **246d**. The reaction temperature in the first step was increased to 120 °C. The crude product was purified by column chromatography (gradient of 1:1 to 5:1 dichloromethane/*n*-hexane) and precipitation from dichloromethane/methanol. The isolated solid was successively washed with methanol and *n*-hexane and dried under high vacuum to give **246d** as an orange-red solid. Yield: 14.2 mg (63%). M.p: >350 °C. ^{1}H NMR (400 MHz, $CDCl_3$): δ/ppm = 8.59 (*d*, *J* = 7.2 Hz, 2H), 8.51 (*d*, *J* = 7.3 Hz, 2H), 8.13 (*d*, *J* = 7.2 Hz, 2H), 7.89 (*d*, *J* = 7.3 Hz, 2H), 7.49 (*t*, *J* = 7.8 Hz, 2H), 7.34 (*d*, *J* = 7.8 Hz, 4H), 2.81 (*sep*, *J* = 6.9 Hz, 4H), 1.18 (*d*, *J* = 6.9 Hz, 24H). ^{13}C NMR (101 MHz, $CDCl_3$): δ/ppm = 163.75, 163.68, 148.5, 146.0, 140.5, 138.8, 137.5, 133.14, 133.07, 132.8, 130.9, 129.7, 125.5, 124.1, 123.4, 122.8, 122.5, 121.7, 29.4, 24.2. UV–vis (CH_2Cl_2): λ_{max} / nm (ε / $M^{-1}cm^{-1}$) = 543 (7600). CV (CH_2Cl_2): E_{ox1} = 1.17 V, E_{red1} = −1.16 V, E_{red2} = −1.35 V, E_{red3} = −1.80 V, E_{red4} = −2.20 V. MS (MALDI-TOF, positive mode, DCTB in chloroform): 790.3 $[M]^+$. HRMS (ESI-TOF, positive mode, acetonitrile/chloroform): calcd for $C_{52}H_{42}N_2O_4SNa$: 813.2758; found, 813.2760 $[M+Na]^+$.

N,*N*′-Bis(2,6-diisopropylphenyl)-15-octyl-15*H*-bis(acenaphthyleno[1,2–4,5]thieno)[3,2-*b*:2′,3′-*d*]pyrrol-3,4:11,12-bis(dicarboximide) (246e)

According to the general procedure, the reaction of **244e** (10.0 mg, 19.2 µmol, 1.0 equiv), **245** (19.9 mg, 42.3 µmol, 2.2 equiv), $[Pd_2(dba)_3]\cdot CHCl_3$ (4.0 mg, 3.85 µmol, 20 mol %), P(*m*-tolyl)$_3$ (4.7 mg,

15.4 µmol, 80 mol %), Cs_2CO_3 (37.6 mg, 115 µmol, 6.0 equiv), and Bu_4NCl (5.3 mg, 19.2 µmol, 1.0 equiv) in 1-chloronaphthalene (0.6 mL) afforded **246e**. The crude product was purified by column chromatography (gradient of 1:1 to 7:1 dichloromethane/*n*-hexane) and precipitation from dichloromethane/methanol. The isolated solid was washed with *n*-hexane and methanol and dried under high vacuum to give **246e** as a brown-green solid. Yield: 13.9 mg (72%). M.p: >350 °C. ^{1}H NMR (400 MHz, $CDCl_3$): δ/ppm = 8.47 (*d*, *J* = 7.3 Hz, 2H), 8.41 (*d*, *J* = 7.3 Hz, 2H), 7.82 (*d*, *J* = 7.3 Hz, 2H), 7.73 (*d*, *J* = 7.3 Hz, 2H), 7.48 (*d*, *J* = 7.7 Hz, 2H), 7.33 (*d*, *J* = 7.7 Hz, 4H), 4.88 (*t*, *J* = 7.8 Hz, 2H), 2.81 (*sep*, *J* = 6.8 Hz, 4H), 2.20–2.10 (*m*, 2H), 1.39–1.21 (*m*, 8H), 1.17 (*d*, *J* = 6.8 Hz, 24H), 0.90–0.76 (*m*, 5H). The ^{13}C NMR spectrum was not measured due to poor solubility. UV–vis (CH_2Cl_2): λ_{max} / nm (ε / $M^{-1}cm^{-1}$) = 675 (18000). CV (CH_2Cl_2): E_{ox1} = 0.55 V, E_{ox2} = 1.17 V, E_{red1} = −1.21 V, E_{red2} = −1.31 V, E_{red3} = −1.71 V, E_{red4} = −1.92 V. MS (MALDI-TOF, negative mode, DCTB in chloroform): 997.423 $[M]^-$. HRMS (ESI-TOF, positive mode, acetonitrile/chloroform): calcd for $C_{64}H_{59}N_3O_4S_2Na$: 1020.3845; found, 1020.3839 $[M+Na]^+$.

N,*N*′-Bis(2,6-diisopropylphenyl)-15,15-dioctyl-15*H*-diacenaphthyleno[1,2-*d*:1′,2′-*d*′]cyclopenta[2,1-*b*:3,4-*b*′]dithiophene-3,4:11,12-bis(dicarboximide) (246f)

According to the general procedure, the reaction of **244f** (29.2 mg, 44.6 µmol, 1.0 equiv), **245** (46.2 mg, 98.1 µmol, 2.2 equiv), $[Pd_2(dba)_3]\cdot CHCl_3$ (9.2 mg, 8.92 µmol, 20 mol %), P(*m*-tolyl)$_3$ (10.9 mg, 35.7 µmol, 80 mol %), Cs_2CO_3 (78.3 mg, 268 µmol, 6.0 equiv), and Bu_4NCl (6.2 mg, 4.46 µmol, 1.0 equiv) in 1-chloronaphthalene (1.5 mL) afforded **246f**. The crude product was purified by column chromatography (gradient of 2:1 to 3:1 dichloromethane/*n*-hexane), followed by size exclusion chromatography and precipitation from dichloromethane/methanol. The isolated solid was washed with methanol and dried under high vacuum to give **246f** as a green solid. Yield: 31.4 mg (64%). M.p: 166–168 °C. ^{1}H NMR (400 MHz, $CDCl_3$): δ/ppm = 8.52 (*d*, *J* = 7.3 Hz, 2H), 8.44 (*d*, *J* = 7.3 Hz, 2H), 7.87 (*d*, *J* = 7.3 Hz, 2H), 7.76 (*d*, *J* = 7.3 Hz, 2H), 7.48 (*t*, *J* = 7.7 Hz, 2H), 7.32 (*d*, *J* = 7.7 Hz, 4H), 2.80 (*sep*, *J* = 6.9 Hz, 4H), 2.51–2.42 (*m*, 4H), 1.16 (*dd*, *J* = 1.2, 6.9 Hz, 24H), 1.11–0.92 (*m*, 24H), 0.68 (*t*, *J* = 7.0 Hz, 6H). ^{13}C NMR (101 MHz, $CDCl_3$): δ/ppm = 163.9, 163.8, 151.9, 146.0, 144.4, 143.3, 141.2, 139.7, 138.1, 133.4, 133.2, 132.6, 131.1, 129.6, 125.4, 124.1, 123.0, 122.4, 121.4, 120.6, 54.8, 38.2, 31.8, 29.7, 29.3, 29.13, 29.08, 24.5, 24.1, 22.6, 14.1. UV–vis (CH_2Cl_2): λ_{max} / nm (ε / $M^{-1}cm^{-1}$) = 661 (16800). CV (CH_2Cl_2): E_{ox1} = 0.62 V, E_{ox2} = 1.21 V, E_{red1} = −1.23 V, E_{red2} = −1.34 V, E_{red3} = −1.77 V, E_{red4} = −1.98 V. MS (MALDI-TOF, negative mode, DCTB in chloroform): 1108.5 $[M]^-$. HRMS (ESI-TOF, positive mode, acetonitrile/chloroform): calcd for $C_{73}H_{76}N_2O_4S_2Na$: 1131.5144; found, 1131.5139 $[M+Na]^+$.

_N_,_N′_-Bis(2,6-diisopropylphenyl)-bis(acenaphthyleno[1,2:4,5]thieno)[3,2-_b_:2′,3′-_d_]thiophene-3,4:11,12-bis(dicarboximide) (246g)

According to the general procedure, the reaction of **244g** (10.0 mg, 22.3 µmol, 1.0 equiv), **245** (23.1 mg, 49.1 µmol, 2.2 equiv), $[Pd_2(dba)_3]\cdot CHCl_3$ (4.6 mg, 4.46 µmol, 20 mol %), P(*m*-tolyl)$_3$ (5.5 mg, 17.9 µmol, 80 mol %), Cs_2CO_3 (44.4 mg, 133 µmol, 6.0 equiv), and Bu_4NCl (6.2 mg, 4.46 µmol, 1.0 equiv) in 1-chloronaphthalene (0.75 mL) afforded **246g**. The reaction temperature in the first step was increased to 120 °C. The crude product was purified by column chromatography (gradient of 1:1 to 2:1 dichloromethane/*n*-hexane), followed by precipitation from dichloromethane/methanol. The isolated solid was washed with methanol and dried under high vacuum to give **246g** as a green solid. Yield: 9.5 mg (47%). M.p: >350 °C. ^{1}H NMR (400 MHz, $CDCl_3$): δ/ppm = 8.51 (*d*, *J* = 7.5 Hz, 2H), 8.47 (*d*, *J* = 7.5 Hz, 2H), 7.92 (*d*, *J* = 7.5 Hz, 2H), 7.84 (*d*, *J* = 7.5 Hz, 2H), 7.49 (*t*, *J* = 7.9 Hz, 2H), 7.34 (*d*, *J* = 7.9 Hz, 4H), 2.81 (*sep*, *J* = 7.0 Hz, 4H), 1.17 (*d*, *J* = 7.0 Hz, 24H). ^{13}C NMR (101 MHz, $CDCl_3$): δ/ppm = 163.8, 163.7, 146.0, 144.1, 139.4, 139.0, 137.3, 137.2, 135.5, 133.2, 132.73, 132.69, 131.0, 129.7, 125.3, 124.1, 122.6, 122.5, 122.4, 121.8, 29.3, 24.2. UV–vis (CH_2Cl_2): λ_{max} / nm (ε / $M^{-1}cm^{-1}$) = 606 (12400). CV (CH_2Cl_2): E_{ox1} = 0.82 V, E_{ox2} = 1.32 V, E_{red1} = −1.19 V, E_{red2} = −1.26 V, E_{red3} = −1.66 V, E_{red4} = −1.84 V. MS (MALDI-TOF, negative mode, DCTB in chloroform): 902.2 $[M]^-$. HRMS (ESI-TOF, positive mode, acetonitrile/chloroform): calcd for $C_{56}H_{43}N_2O_4S_3$: 903.2384; found, 903.2380 $[M+H]^+$.

_N_,_N′_-Bis(2,6-diisopropylphenyl)-diacenaphthyleno[1,2-_d_:1′,2′-_d′_]benzo[1,2-_b_:4,5-_b′_]dithiophene-3,4:11,12-bis(dicarboximide) (246h)

According to the general procedure, the reaction of **244h** (40.0 mg, 90.5 µmol, 1.0 equiv), **245** (93.6 mg, 199 µmol, 2.2 equiv), $[Pd_2(dba)_3]\cdot CHCl_3$ (18.7 mg, 8.92 µmol, 20 mol %), P(*m*-tolyl)$_3$ (22.0 mg, 72.4 µmol, 80 mol %), Cs_2CO_3 (177 mg, 543 µmol, 6.0 equiv), and Bu_4NCl (25.2 mg, 90.6 µmol, 1.0 equiv) in 1-chloronaphthalene (4.5 mL) afforded **246h**. The crude product was purified by column chromatography (gradient of 2:1 to 4:1 dichloromethane/*n*-hexane) and precipitation from dichloromethane/methanol. The isolated solid was washed with *n*-hexane and methanol and dried under high vacuum to give **246h** as a brown solid. Yield: 60.0 mg (74%). M.p: >350 °C. ^{1}H NMR (400 MHz, $CDCl_3$): δ/ppm = 8.62 (*s*, 2H), 8.52 (*d*, *J* = 7.2 Hz, 2H), 8.45 (*d*, *J* = 7.2 Hz, 2H), 8.13 (*d*, *J* = 7.2 Hz, 2H), 7.88 (*d*, *J* = 7.2 Hz, 2H), 7.49 (*t*, *J* = 7.7 Hz, 2H), 7.35 (*d*, *J* = 7.7 Hz, 4H), 2.83 (*sep*, *J* = 6.8 Hz, 4H), 1.19 (*dd*, *J* = 2.3, 6.8 Hz, 24H). ^{13}C NMR (101 MHz, $CDCl_3$): δ/ppm = 163.8, 163.7, 146.0, 145.6, 144.3, 140.0, 139.0, 138.8, 133.1, 133.0, 132.7, 131.01, 130.96, 129.7, 125.0, 124.1, 123.3, 123.2, 122.13, 122.09, 117.6, 29.3, 24.2. UV–vis (CH_2Cl_2): λ_{max} / nm (ε / $M^{-1}cm^{-1}$) = 608 (4100). CV (CH_2Cl_2): E_{ox1} = 0.84 V, E_{ox2} = 1.24 V, E_{red1} = −1.18 V, E_{red2} = −1.24 V, E_{red3} = −1.64 V, E_{red4} = −1.80 V. MS (MALDI-TOF, negative mode, DCTB in chloroform):

896.4 $[M]^-$. HRMS (ESI-TOF, positive mode, acetonitrile/chloroform): calcd for $C_{58}H_{44}N_2O_4S_2Na$: 919.2640; found, 919.2634 $[M+Na]^+$.

Optimization

Table A8. Screening of the ligand for the annulation reaction for the model compound **246a**.[a]

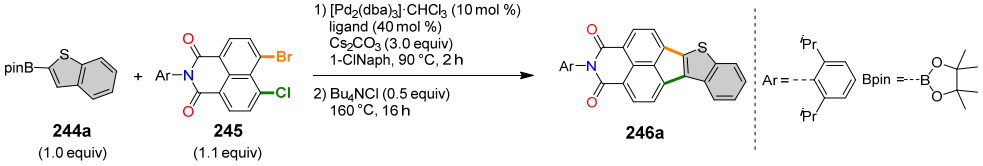

entry	ligand	yield / %[b]
1	$PCy_3 \cdot HBF_4$	74
2	P(*m*-tolyl)$_3$	86
3	P(*o*-tolyl)$_3$	23
4	SPhos	32
5	P(Ad)$_2$Bu	48

[a]Reaction conditions: **244a** (1.0 equiv), **245** (1.1 equiv), $[Pd_2(dba)_3]\cdot CHCl_3$ (10 mol %), ligand (40 mol %), Cs_2CO_3 (3.0 equiv). [b]Isolated yield. PCy_3: tri(cyclohexyl)phosphine, P(*m*-tolyl): tri(*m*-tolyl)phosphine, P(*o*-tolyl): tri(*o*-tolyl)phosphine, SPhos: 2-dicyclohexylphosphino-2′,6′-dimethoxybiphenyl, P(Ad)$_2$Bu: di(1-adamantyl)-n-butylphosphine, dba: dibenzylideneacetone.

Electronic Investigations

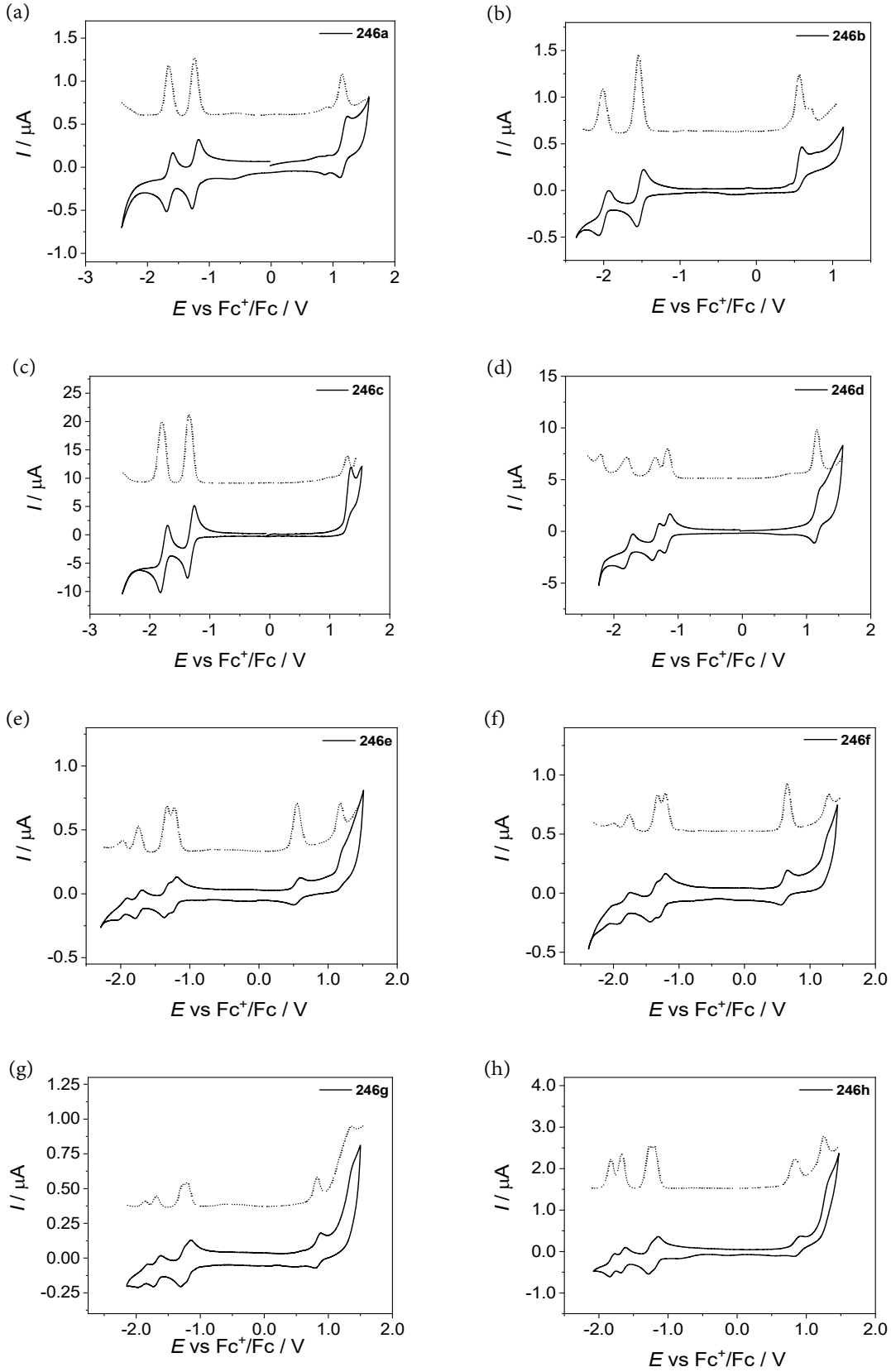

Figure A60. Cyclic (solid line) and square (dashed line) voltammetry traces of (a) **246a**, (b) **246b**, (c) **246c**, (d) **246d**, (e) **246e**, (f) **246f**, (g) **246g** and (h) and **246h** in dichloromethane solutions (c ~ 10^{-5} M) with TBAHFP (0.1 M) as a supporting electrolyte at room temperature (scan rate 100 mV s^{-1}).

Theoretical Calculations

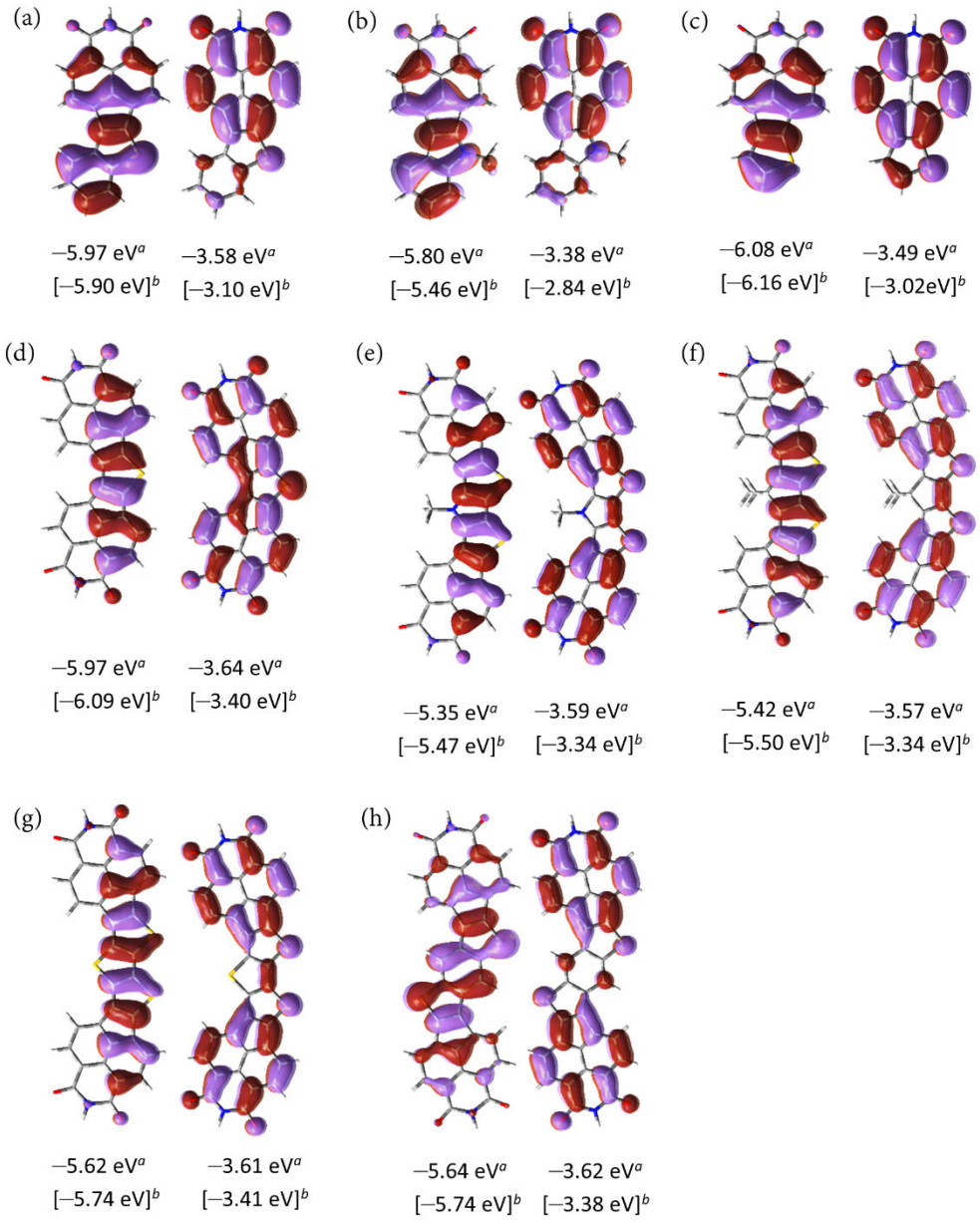

Figure A61. Calculated orbitals and energies of HOMO (left) and LUMO (right) of compounds (a) **246a**, (b) **246b**, (c) **246c**, (d) **246d**, (e) **246e**, (f) **246f**, (g) **246g** and (h) and **246h** by DFT calculations (B3LYP/6-31G(d) / isoval: 0.02 a.u.). The 2,6-diisopropylphenyl groups were replaced by hydrogens and octyl groups by methyl groups for simplicity. [a] Experimentally determined energy levels using Fc^{+}/Fc redox couple with respect to the vacuum (–4.8 eV). [b] Calculated energies by DFT (B3LYP/6-31G(d)).

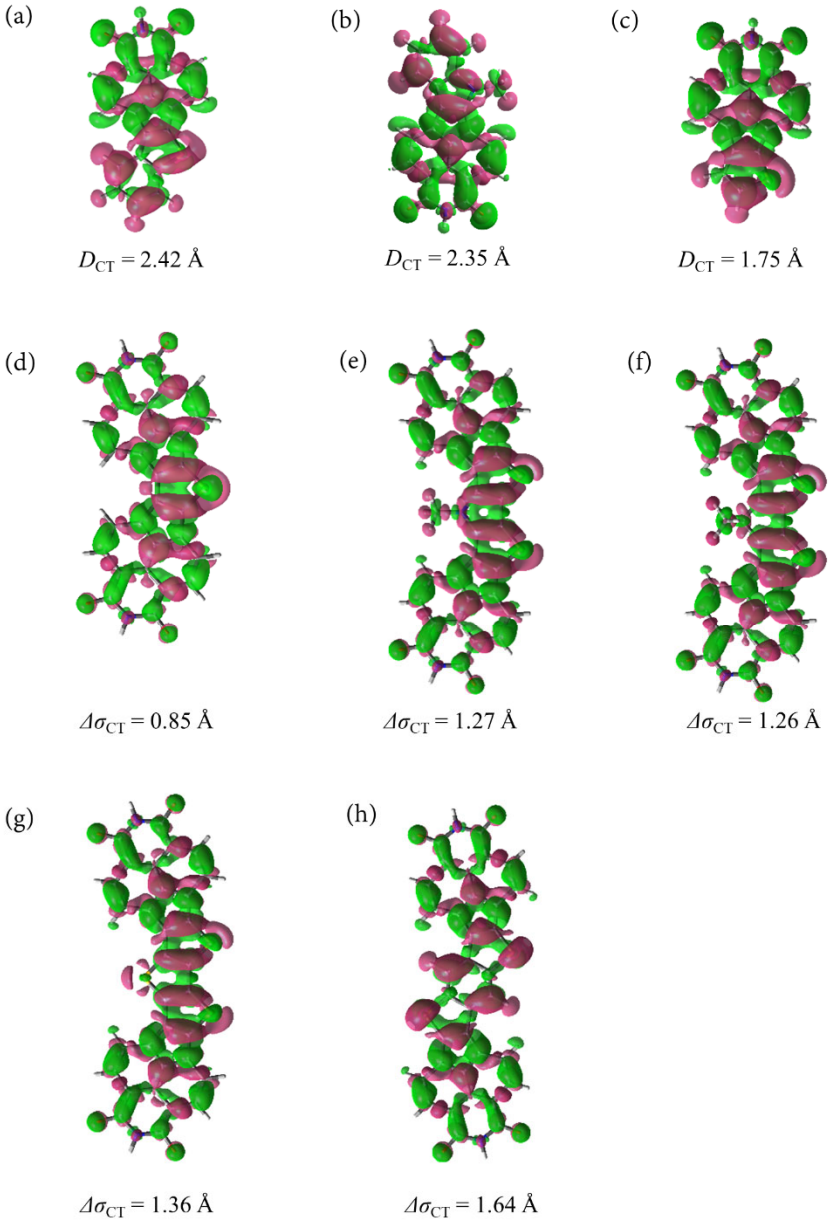

Figure A62. Charge density differences for S_0–S_1 transition and the respective $D_{CT}/\Delta\sigma_{CT}$ for (a) **246a**, (b) **246b**, (c) **246c**, (d) **246d**, (e) **246e**, (f) **246f**, (g) **246g** and (h) and **246h** calculated by TD-DFT (B3LYP/6-31G(d) / isoval: 0.0004 a.u.). Red (positive) and green (negative) regions represent increase or decrease of electron density upon excitation. The 2,6-diisopropylphenyl groups were replaced by hydrogens and octyl groups by methyl groups for simplicity.

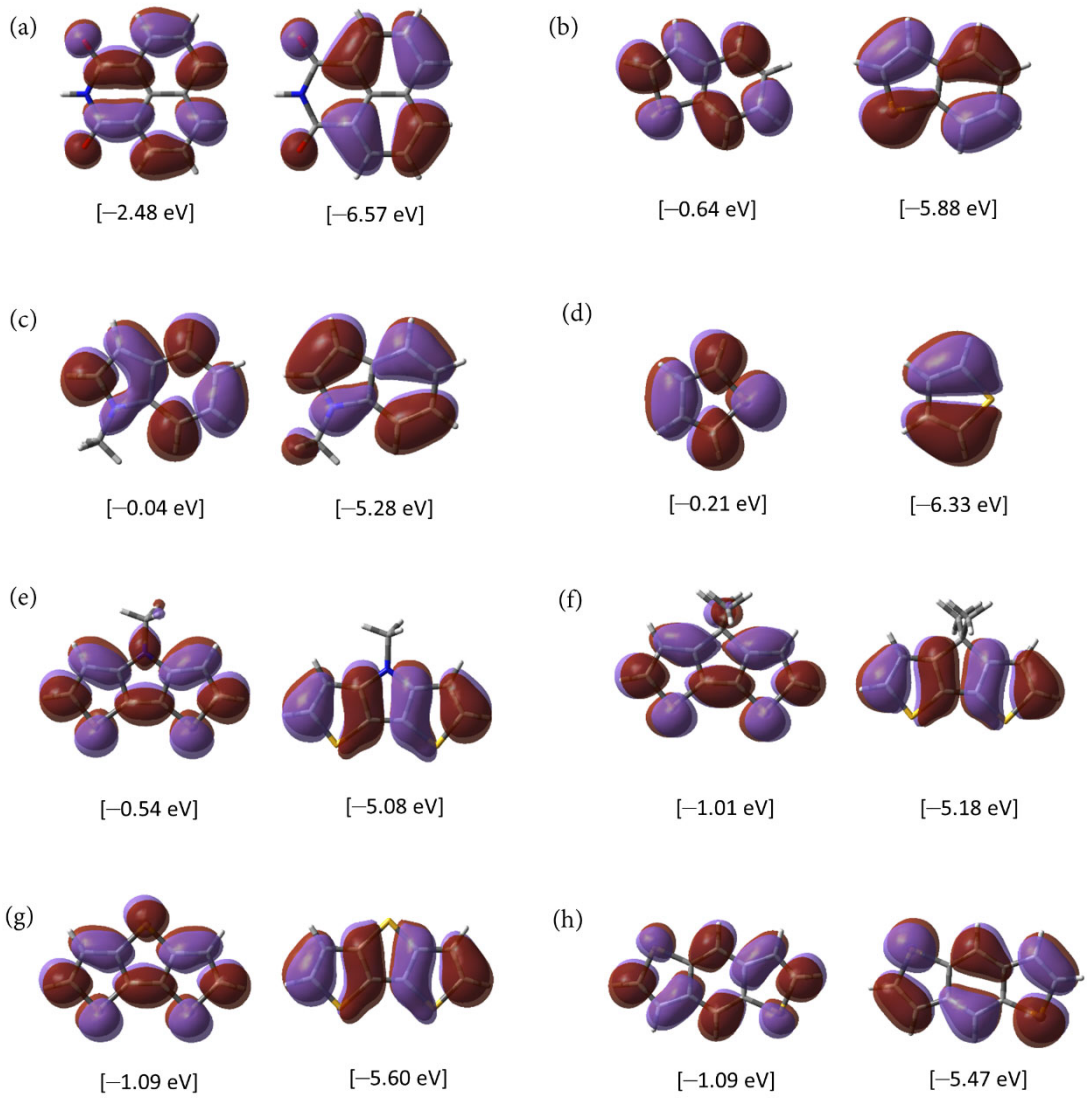

Figure A63. Calculated shapes and energies of LUMO (left) and HOMO (right) of (a) naphthalene dicarboximide acceptor, and the respective donors of (b) **246a**, (c) **246b**, (d) **246c** and **246d**, (e) **246e**, (f) **246f**, (g) **246g**, and (h) **246h** by DFT calculations (B3LYP/6-31G(d) / isoval: 0.02 a.u.). The 2,6-diisopropylphenyl groups were replaced by hydrogens and octyl groups by methyl groups for simplicity.

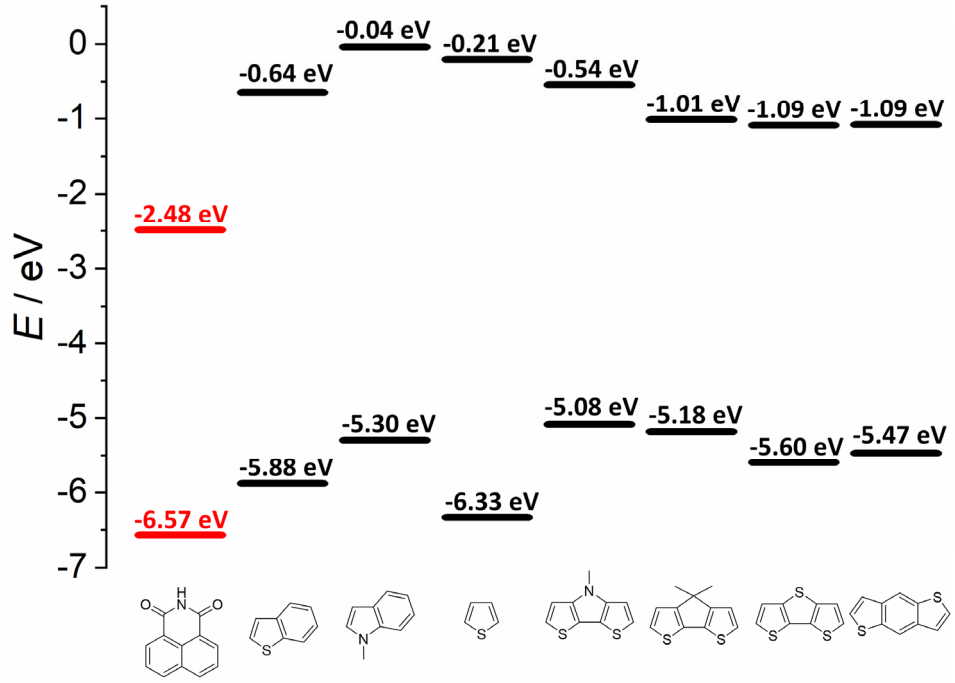

Figure A64. Calculated energy levels of LUMO (top) and HOMO (bottom) of naphthalene dicarboximide acceptor and the respective donors of **246a**–**h** by DFT calculations (B3LYP/6-31G(d)). The 2,6-diisopropylphenyl group was replaced by hydrogen and octyl groups by methyl groups.

NMR Spectroscopy

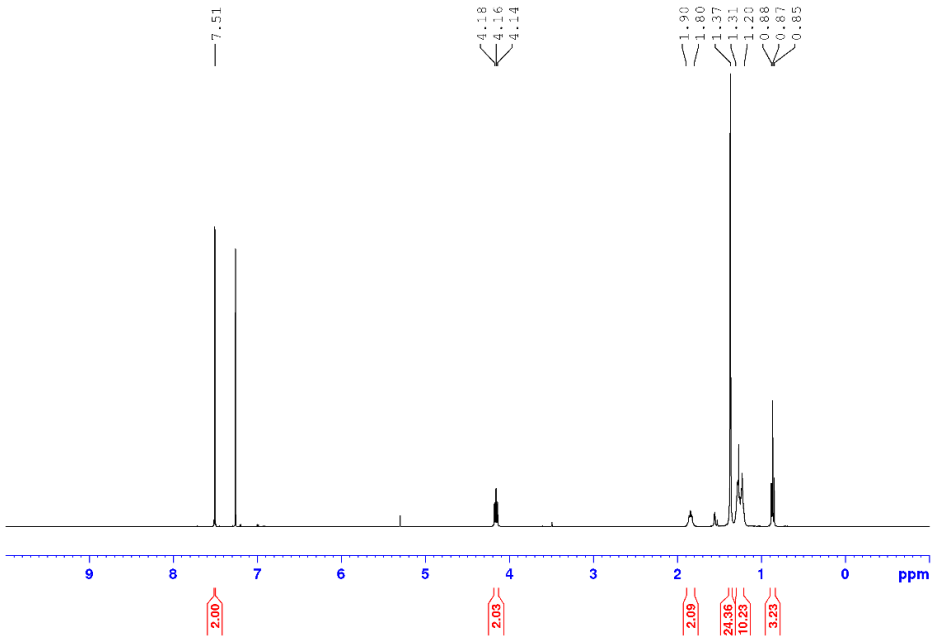

Figure A65. ^{1}H NMR (400 MHz) spectrum of **244e** in $CDCl_3$ at room temperature.

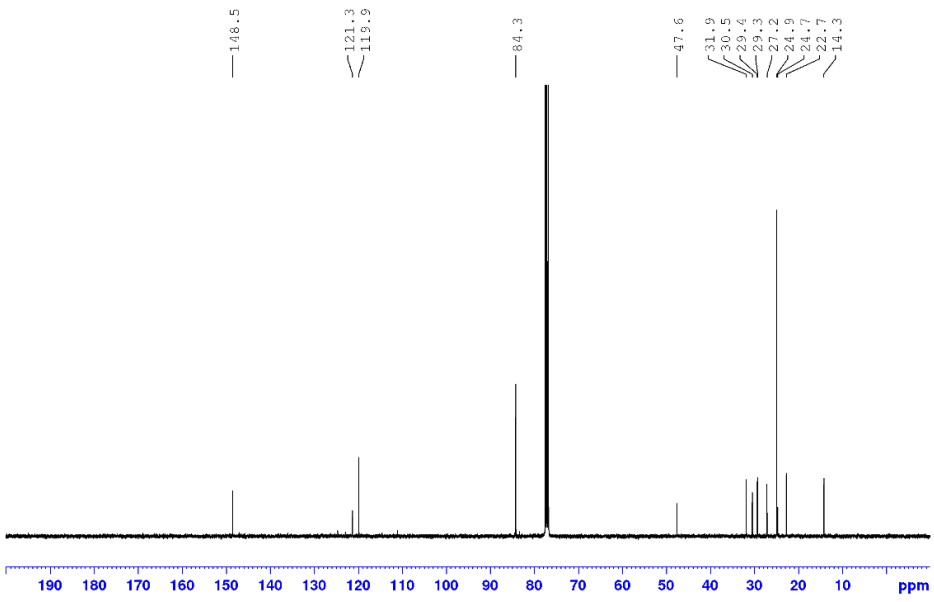

Figure A66. ^{13}C NMR (101 MHz) spectrum of **244e** in $CDCl_3$ at room temperature.

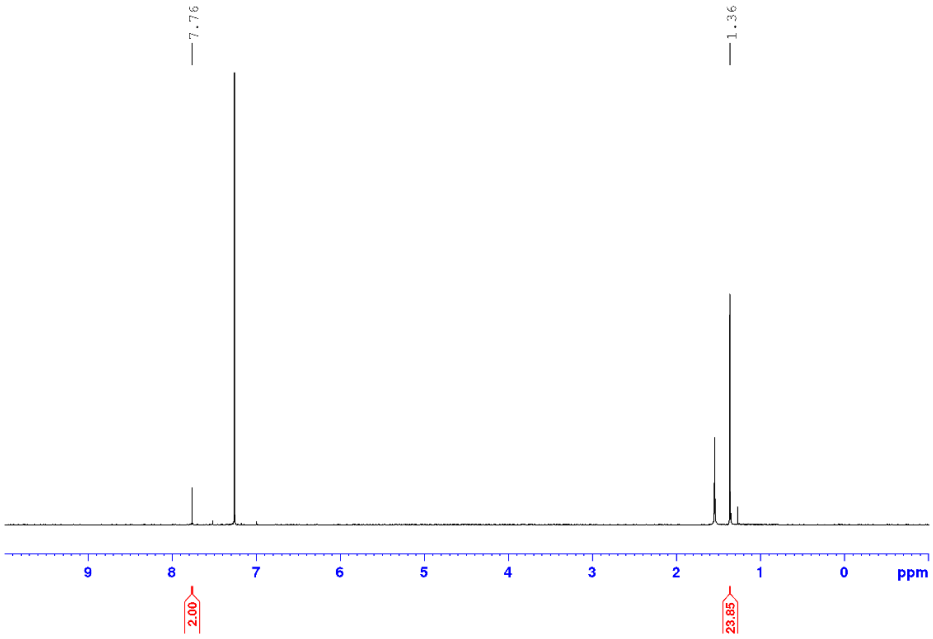

Figure A67. ^{1}H NMR (400 MHz) spectrum of **244g** in $CDCl_3$ at room temperature.

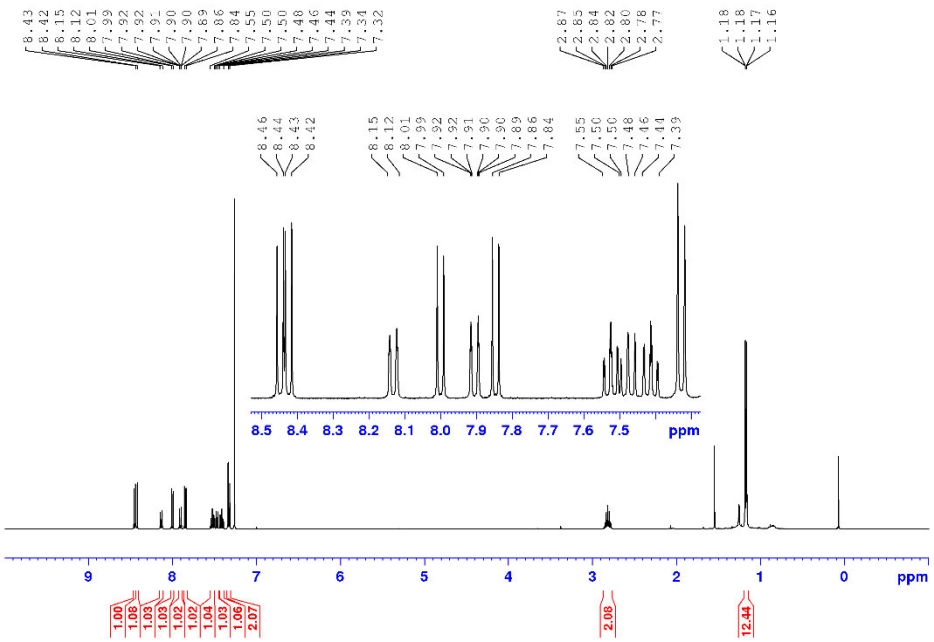

Figure A68. ^{1}H NMR (400 MHz) spectrum of **246a** in $CDCl_3$ at room temperature.

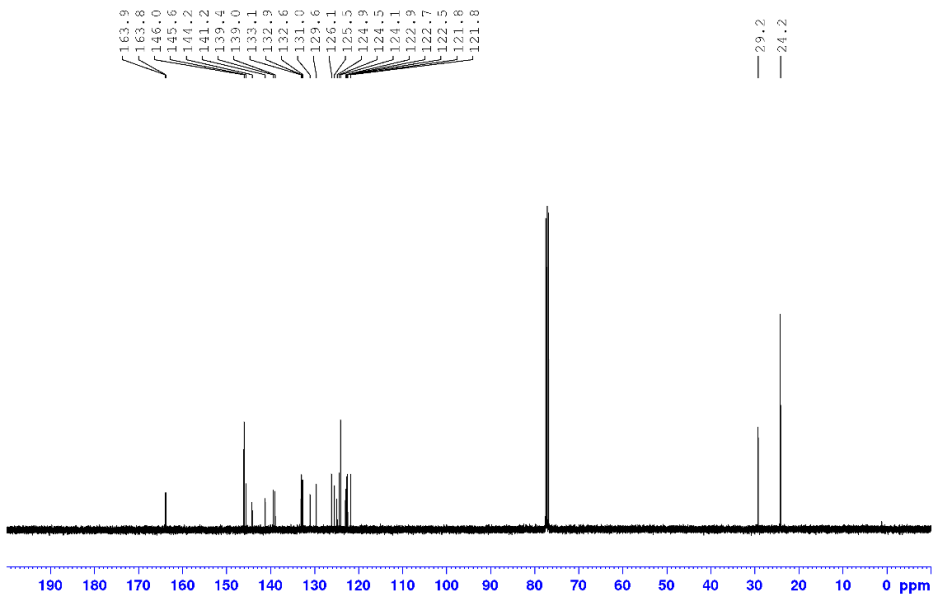

Figure A69. ^{13}C NMR (101 MHz) spectrum of **246a** in $CDCl_3$ at room temperature.

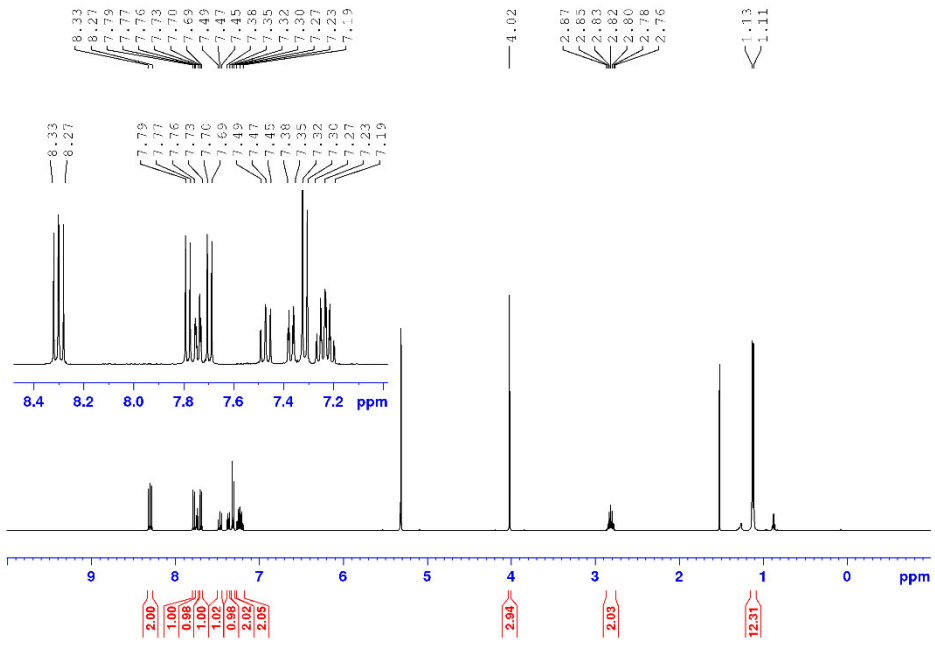

Figure A70. ^{1}H NMR (400 MHz) spectrum of **246b** in CD_2Cl_2 at room temperature.

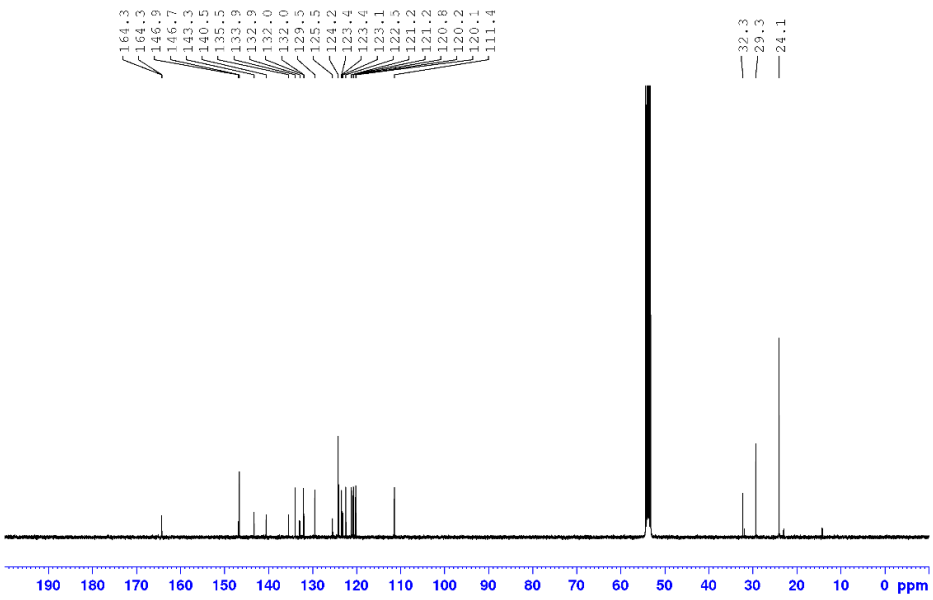

Figure A71. ^{13}C NMR (101MHz) spectrum of **246b** in CD_2Cl_2 at room temperature.

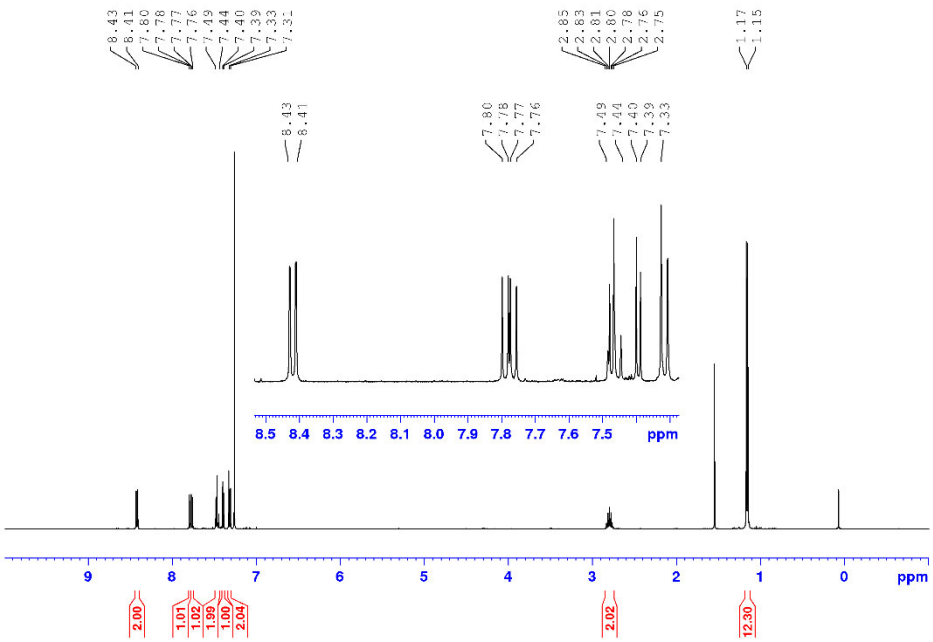

Figure A72. ^{1}H NMR (400 MHz) spectrum of **246c** in $CDCl_3$ at room temperature.

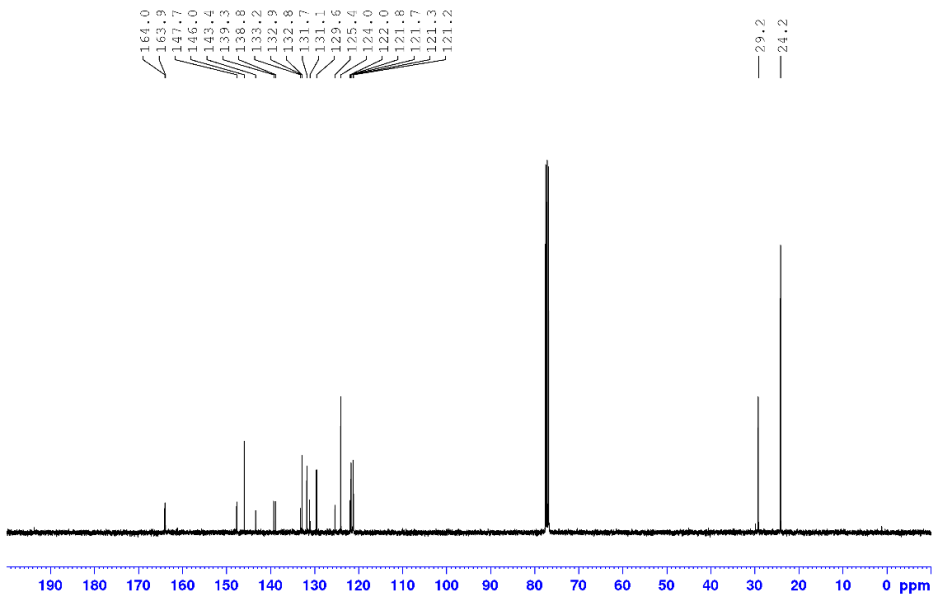

Figure A73. ^{13}C NMR (101 MHz) spectrum of **246c** in $CDCl_3$ at room temperature.

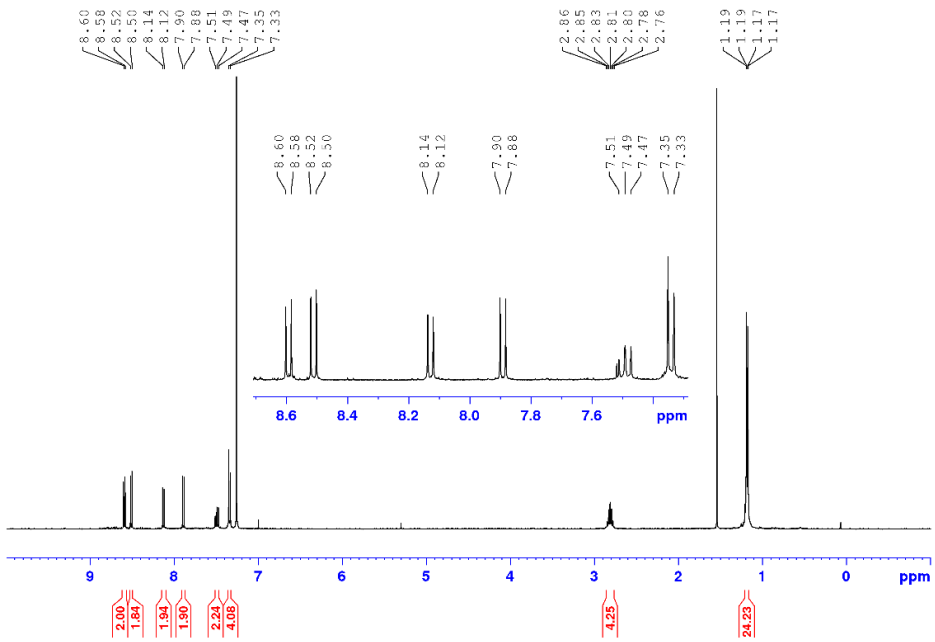

Figure A74. ^{1}H NMR (400 MHz) spectrum of **246d** in $CDCl_3$ at room temperature.

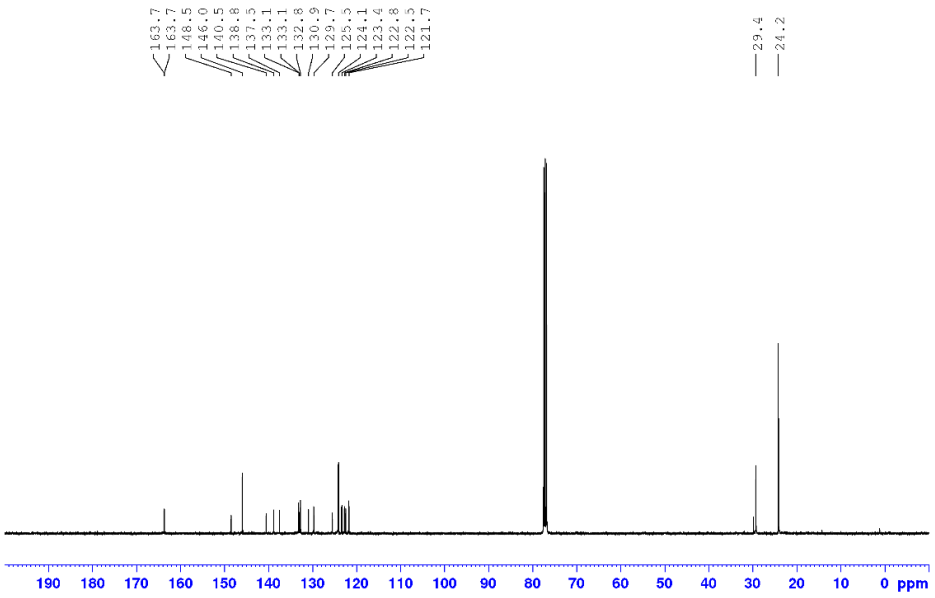

Figure A75. ^{13}C NMR (101 MHz) spectrum of **246d** in $CDCl_3$ at room temperature.

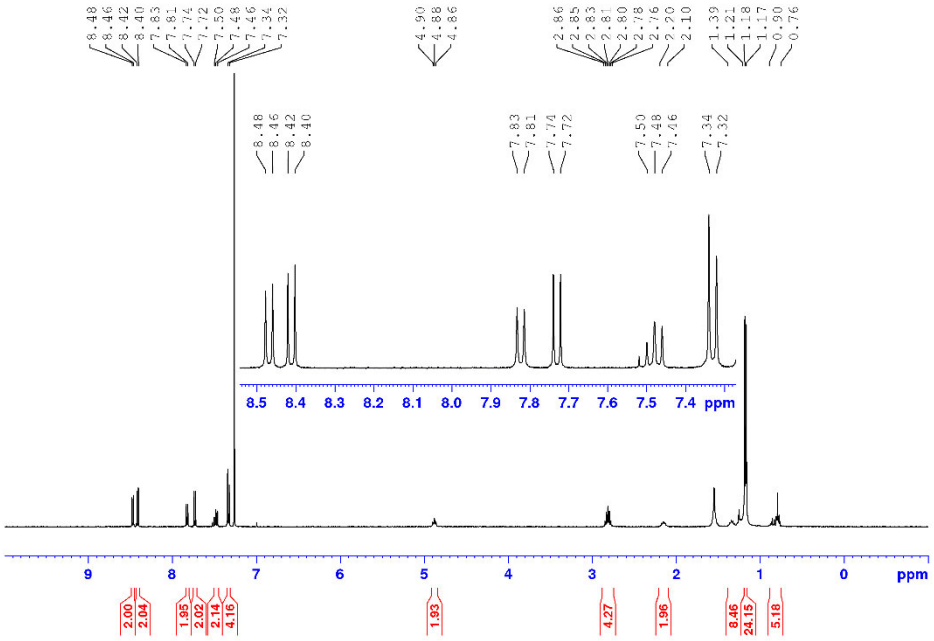

Figure A76. ^{1}H NMR (400 MHz) spectrum of **246e** in $CDCl_3$ at room temperature.

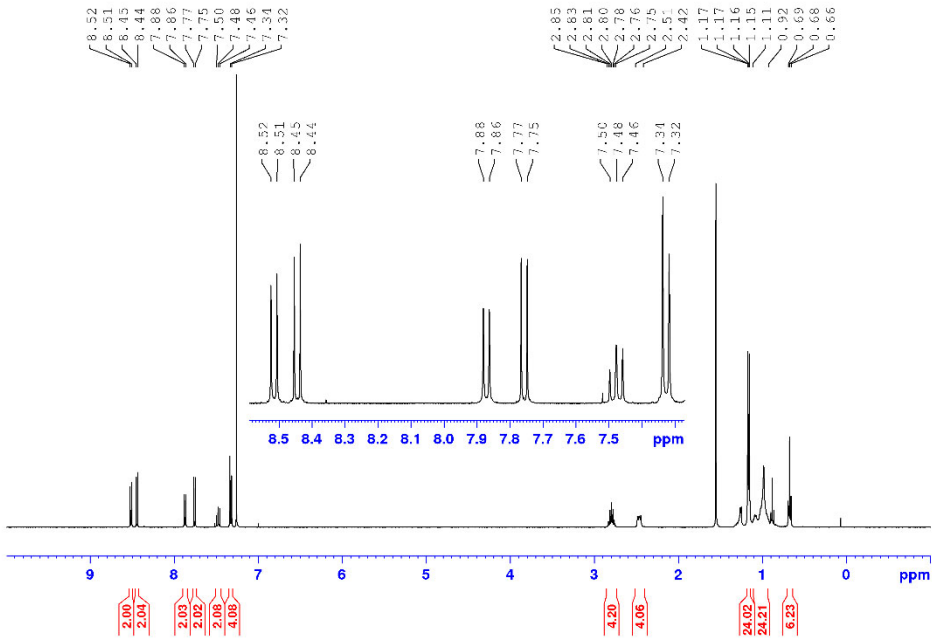

Figure A77. ^{1}H NMR (400 MHz) spectrum of **246f** in $CDCl_3$ at room temperature.

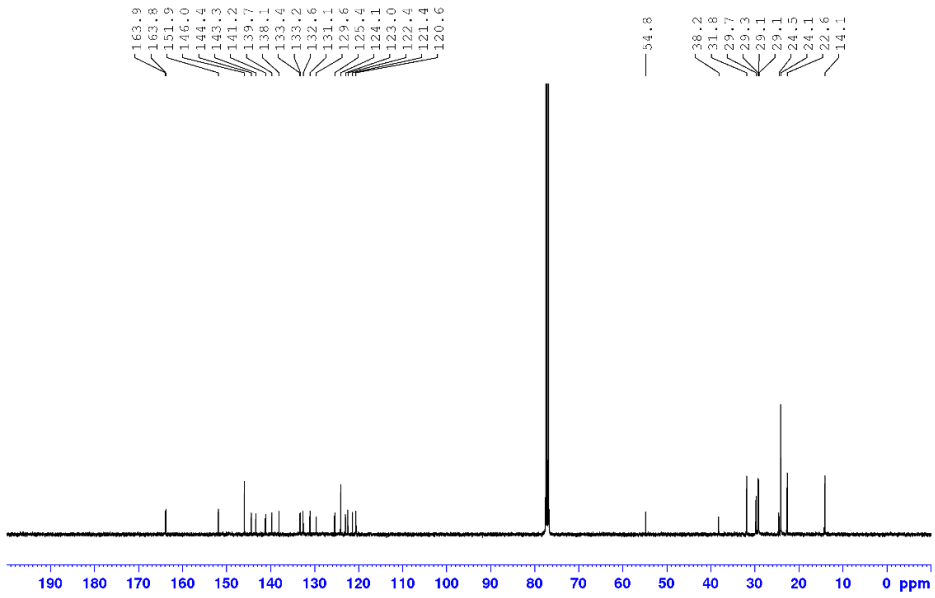

Figure A78. ^{13}C NMR (101MHz) spectrum of **246f** in $CDCl_3$ at room temperature.

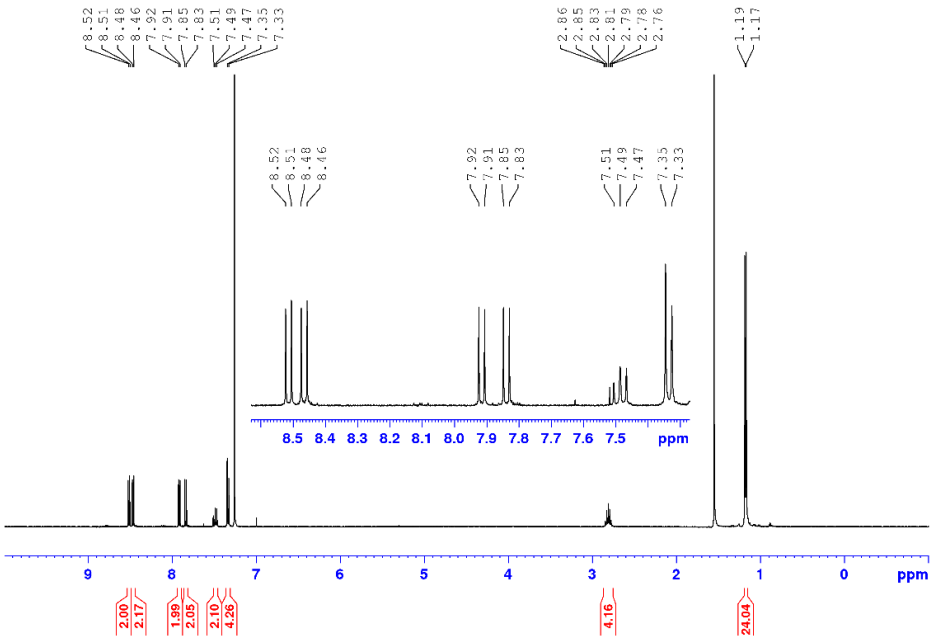

Figure A79. ^{1}H NMR (400 MHz) spectrum of **246g** in $CDCl_3$ at room temperature.

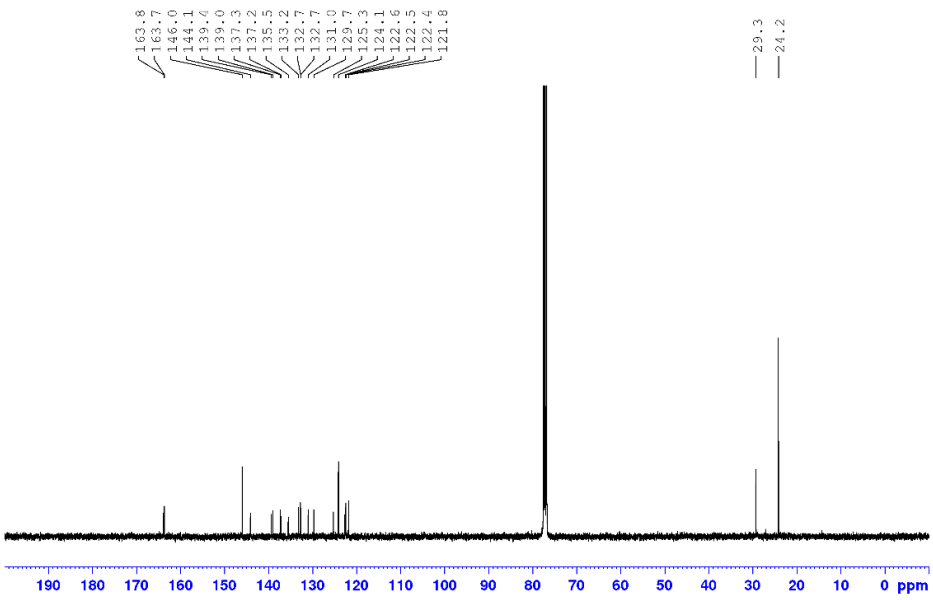

Figure A80. ^{13}C NMR (101 MHz) spectrum of **246g** in $CDCl_3$ at room temperature.

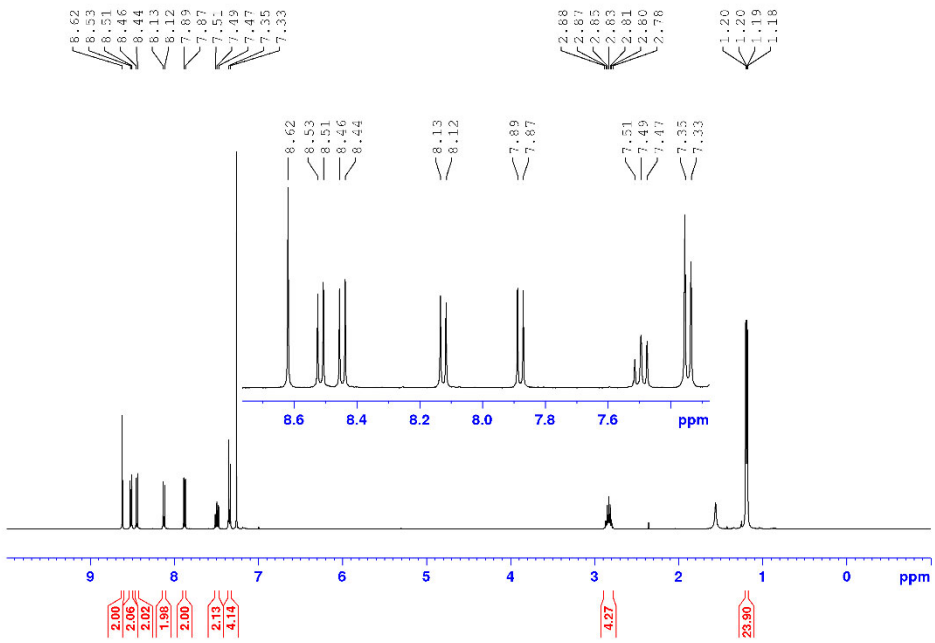

Figure A 81. ^{1}H NMR (400 MHz) spectrum of **246h** in $CDCl_3$ at room temperature.

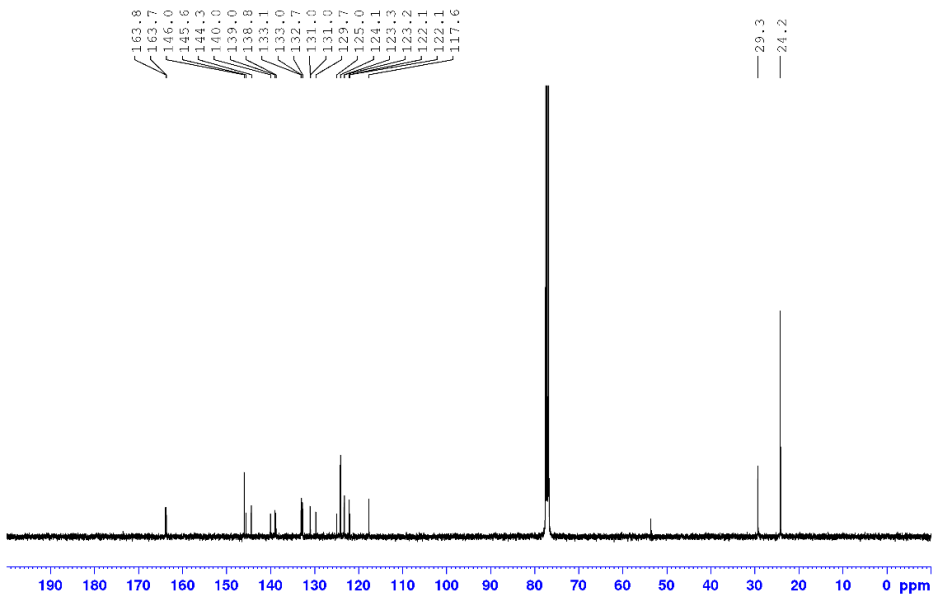

Figure A82. ^{13}C NMR (101 MHz) spectrum of **246h** in $CDCl_3$ at room temperature.

Mass Spectrometry

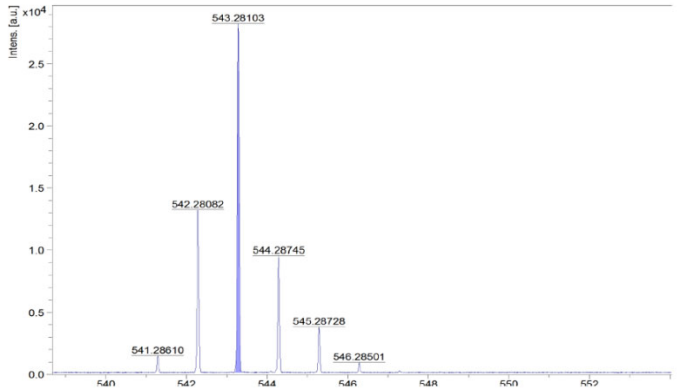

Formula	Mass	Error	mSigma	DblEq	N rule	Electron Configuration
C 28 H 43 B 2 N O 4 S 2	543.2814	0.7041	11.5436	9.00	ok	odd

Figure A83. HRMS (MALDI-TOF, positive mode, DCTB in chloroform) of **244e** $[M]^+$.

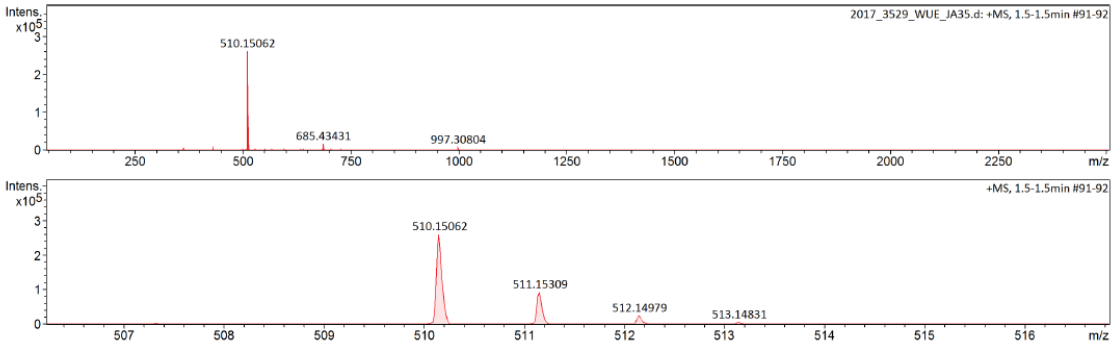

Meas. m/z	#	Ion Formula	m/z	err [ppm]	mSigma	# mSigma	Score	rdb	e⁻ Conf	N-Rule
510.15062	1	C32H25NNaO2S	510.14982	-1.56	11.4	1	100.00	20.5	even	ok

Figure A84. HRMS (ESI-TOF, positive mode, acetonitrile/chloroform) of **246a** $[M+Na]^+$.

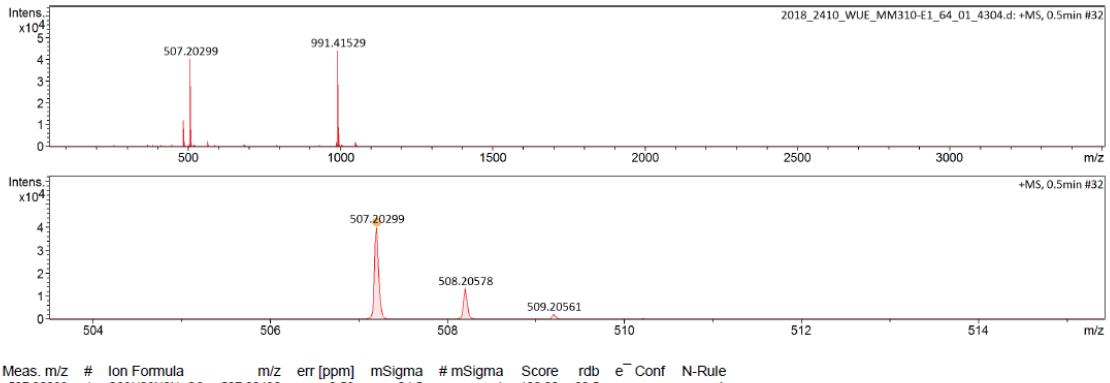

Meas. m/z	#	Ion Formula	m/z	err [ppm]	mSigma	# mSigma	Score	rdb	e⁻ Conf	N-Rule
507.20299	1	C33H28N2NaO2	507.20430	2.58	24.5	1	100.00	20.5	even	ok

Figure A 85. HRMS (ESI-TOF, positive mode, acetonitrile/chloroform) of **246b** $[M+Na]^+$.

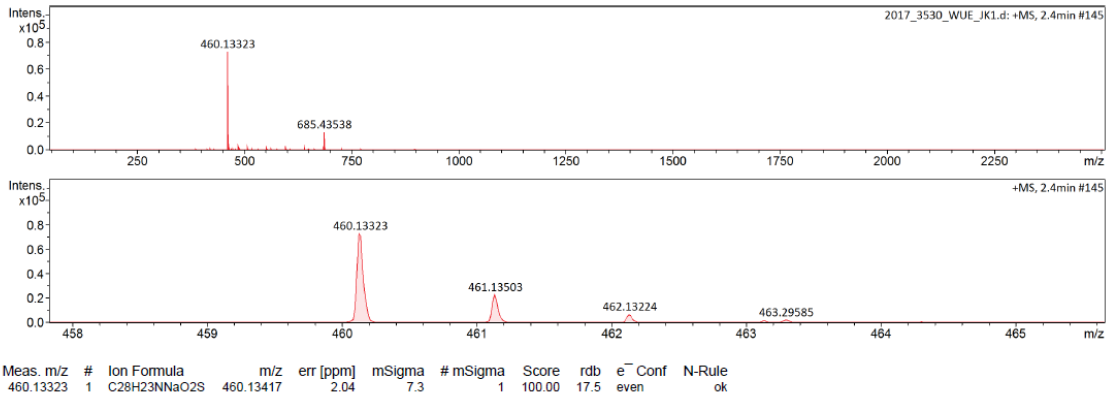

Figure A86. HRMS (ESI-TOF, positive mode, acetonitrile/chloroform) of **246c** $[M+Na]^+$.

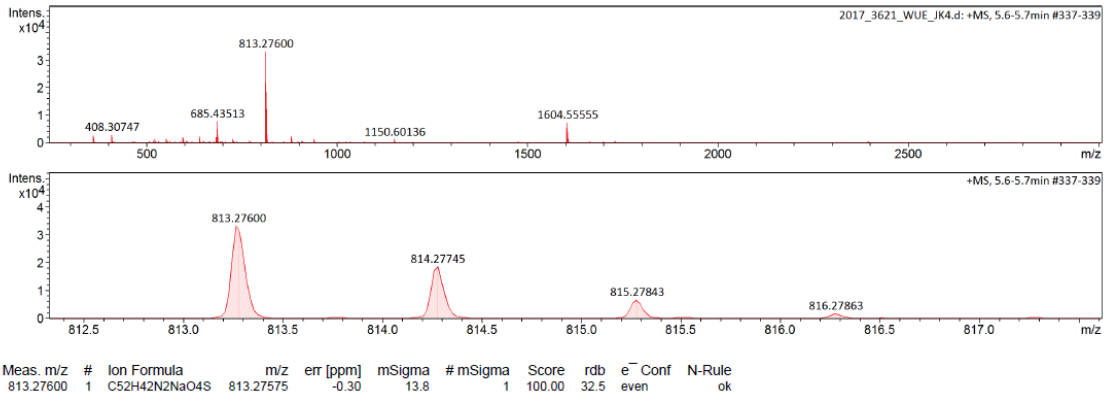

Figure A87. HRMS (ESI-TOF, positive mode, acetonitrile/chloroform) of **246d** $[M+Na]^+$.

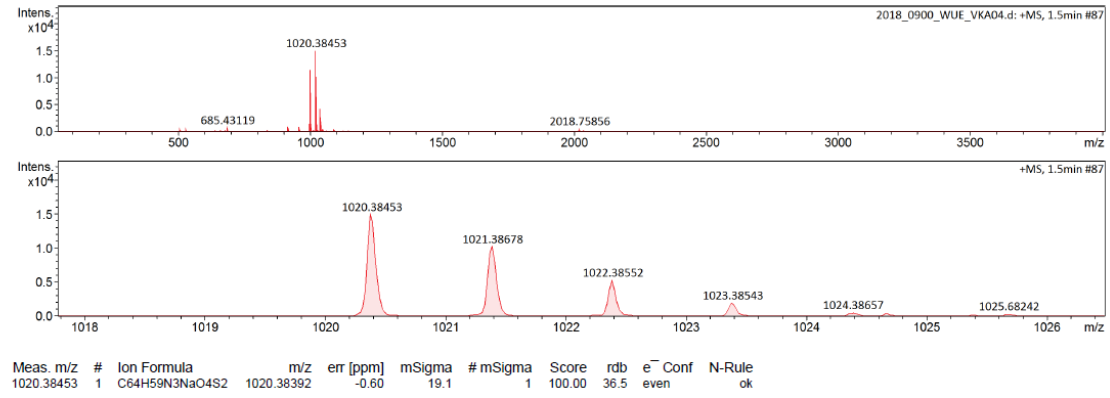

Figure A88. HRMS (ESI-TOF, positive mode, acetonitrile/chloroform) of **246e** $[M+Na]^+$.

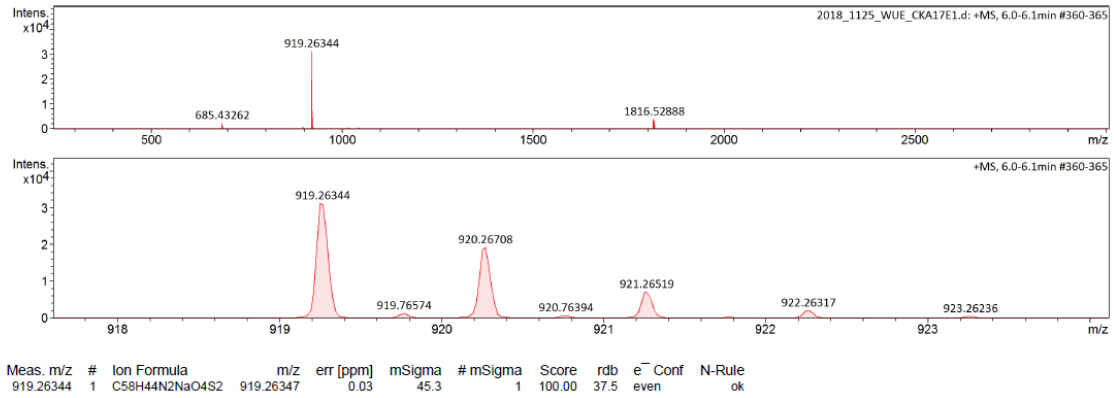

Figure A89. HRMS (ESI-TOF, positive mode, acetonitrile/chloroform) of **246f** $[M+Na]^+$.

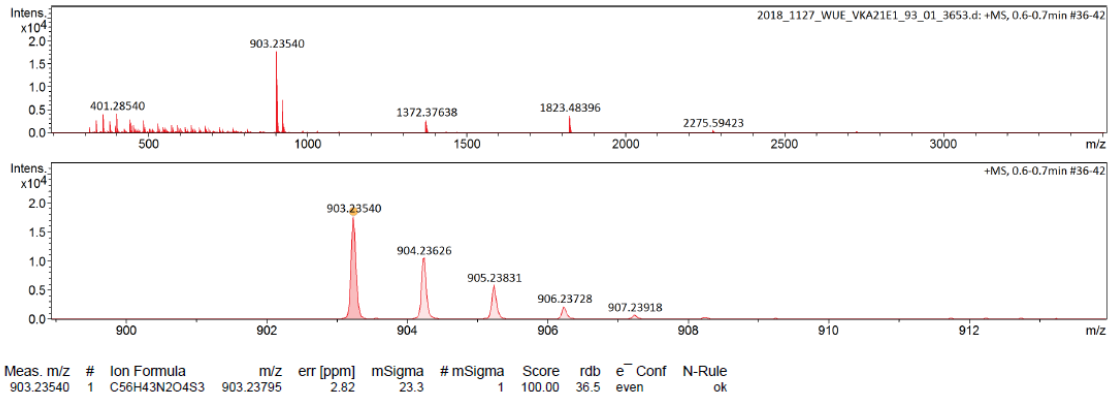

Figure A90. HRMS (ESI-TOF, positive mode, acetonitrile/chloroform) of **246g** $[M+H]^+$.

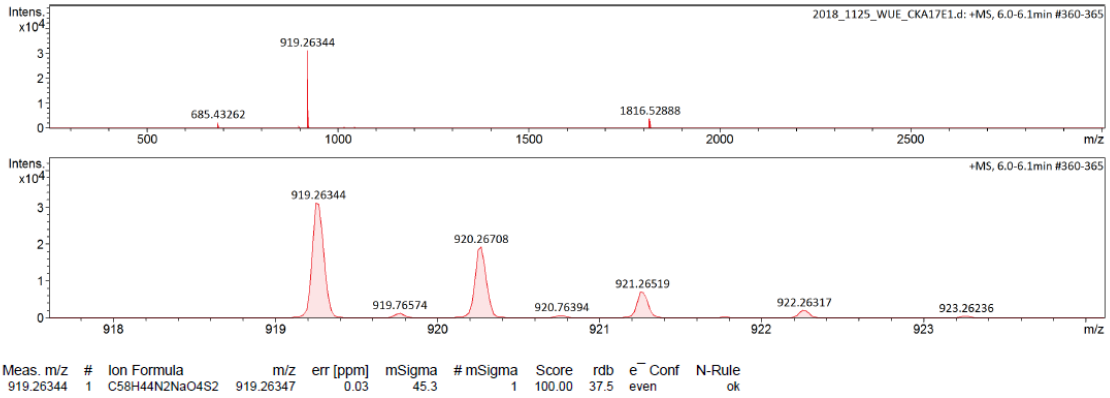

Figure A 91. HRMS (ESI-TOF, positive mode, acetonitrile/chloroform) of **246h** $[M+Na]^+$.

Cartesian Coordinates of the Ground State Optimized Structures

246a
Total energy of the optimized structure: -1371.00209620 a.u.
Number of imaginary frequencies: 0

C	5.02982600	1.92282500	-0.00021800
C	3.83535600	-0.58200600	-0.00000800
C	3.01764000	0.58339000	0.00010700
C	5.81940900	0.75889500	-0.00011800
S	2.88033800	-2.07245300	0.00036500
C	1.41262500	-1.14252400	0.00005100
C	1.62745300	0.23049500	-0.00006200
C	-0.63528600	-0.15822400	-0.00001000
C	-1.57619600	2.41702500	-0.00011100
C	-0.16963400	2.19656900	0.00003300
C	0.31439300	0.89867600	-0.00011900
C	-2.00739500	0.03243000	0.00008800
C	-2.48734600	1.37020700	-0.00006200
C	-0.02024800	-1.43975800	-0.00016400
C	-0.83810700	-2.55781600	-0.00028700
C	-2.24939700	-2.38146700	-0.00045400
C	-2.83518100	-1.12225900	0.00015300
C	-4.30492000	-0.92960800	-0.00000100
N	-4.71701600	0.41147500	0.00019200
C	-3.95231400	1.58880500	0.00005900
O	-4.49540900	2.68165200	0.00013100
O	-5.12600900	-1.83248700	-0.00002000
C	5.22944500	-0.50099600	0.00000000
C	3.64451800	1.84405300	-0.00009400
H	5.51202400	2.89619300	-0.00035700
H	6.90232700	0.84246300	-0.00000500
H	-1.96140400	3.43205700	0.00020900
H	0.49450600	3.05580600	0.00024600
H	-0.43024500	-3.56461600	-0.00014400
H	-2.90079800	-3.24986100	-0.00084600
H	5.83934200	-1.39968100	0.00020300
H	3.04381800	2.74892300	-0.00016300
H	-5.72235400	0.55204500	0.00010300

246b
Total energy of the optimized structure: -1067.47601998 a.u.
Number of imaginary frequencies: 0

C	-5.15648100	-1.89216300	0.00719400
C	-3.67299900	0.44935700	-0.00625700
C	-3.00080000	-0.81619100	-0.00071300
C	-5.79840300	-0.63722600	0.00736600
N	-2.72311500	1.46947000	-0.02179300
C	-1.48477400	0.87931400	-0.00711000
C	-1.60424200	-0.51250500	-0.00109300
C	0.62040600	0.04223000	-0.00517700
C	1.73829800	-2.46463700	-0.00113000
C	0.32040000	-2.34369400	-0.00079300
C	-0.25741600	-1.08449500	-0.00298200
C	2.00208600	-0.05606900	-0.00272700
C	2.57611100	-1.35862200	-0.00176000
C	-0.07768000	1.28524800	-0.00398500
C	0.66990100	2.45278700	0.00495800
C	2.08860100	2.36860000	0.00506200
C	2.75337100	1.15020800	0.00054000
C	4.23279200	1.05814300	0.00239500
N	4.73484500	-0.24974500	0.00116500
C	4.04944000	-1.47725800	-0.00016400
O	4.66973200	-2.52896900	0.00003800
O	4.98919700	2.01695900	0.00491400
H	5.74715800	-0.32337700	0.00254500
C	-5.06772500	0.54610800	0.00257000
C	-3.77162000	-1.99145900	0.00354900
C	-3.01456700	2.89011600	0.00479900
H	-5.75879800	-2.79626300	0.01181600
H	-6.88367200	-0.59218700	0.01457400
H	2.19311100	-3.45062300	0.00018600
H	-0.28390100	-3.24619500	0.00161200
H	0.20607100	3.43472700	0.01734700
H	2.68266800	3.27719400	0.01051200
H	-5.57022300	1.50891900	0.01111100
H	-3.28884400	-2.96465200	0.00599500
H	-3.87506100	3.10258700	-0.63581900
H	-3.23383600	3.23949100	1.02124800
H	-2.15641700	3.44163300	-0.38361400

246c
Total energy of the optimized structure: -1217.35089904 a.u.
Number of imaginary frequencies: 0

C	4.71418300	0.55488400	-0.00001200
C	3.71573200	1.49682400	-0.00001200
S	4.10121000	-1.07937600	0.00000400
C	2.47540200	-0.49847400	0.00001000
C	2.42722100	0.89803200	-0.00000100
C	0.27880500	0.08514200	0.00000200
C	-1.13039600	2.43974800	-0.00000800
C	0.29231900	2.48750800	-0.00001100
C	1.00872900	1.30311700	-0.00000500
C	-1.10576600	0.01514100	0.00000100
C	-1.82721700	1.23919600	0.00000200
C	1.12463800	-1.05978800	0.00001100
C	0.52855700	-2.31026000	0.00001900
C	-0.89093300	-2.40048700	0.00001200
C	-1.70305400	-1.27400200	-0.00000100
C	-3.18230900	-1.36062000	-0.00003100
N	-3.83869700	-0.11988100	-0.00000400
C	-3.30811100	1.17934600	0.00002700
O	-4.04571700	2.15166200	0.00002100
O	-3.82070800	-2.40085000	-0.00002500
H	-4.85257900	-0.17020800	-0.00000400
H	5.78358400	0.71847400	-0.00001300
H	3.90851000	2.56382900	-0.00002100
H	-1.70033200	3.36377300	-0.00000500
H	0.78773700	3.45435100	-0.00001500
H	1.11675500	-3.22349100	0.00002800
H	-1.36755500	-3.37588200	0.00000900

246d
Total energy of the optimized structure: -1881.69879686 a.u.
Number of imaginary frequencies: 0

C	1.22960900	-1.70402700	-0.00009100
C	0.70687700	-0.39735100	-0.00003900
S	0.00000000	-2.92655400	-0.00012200
C	-1.22961000	-1.70402700	-0.00011000
C	-0.70687700	-0.39735100	-0.00003400
C	-3.00181200	-0.28678200	-0.00004200
C	-3.35565200	2.43479900	0.00003400
C	-2.03306800	1.91079800	-0.00002900
C	-1.84678300	0.53856300	-0.00007500
C	-4.29988600	0.20188400	0.00001400
C	-4.47303700	1.61150300	0.00002500
C	-2.68681300	-1.67518000	-0.00007000
C	-3.73451200	-2.58355200	-0.00003400
C	-5.06989700	-2.09843900	0.00001100
C	-5.36293400	-0.74051200	0.00003700
C	-6.75345800	-0.22912600	0.00011000
N	-6.86036700	1.17045300	0.00008700
C	-5.85541200	2.14869100	0.00001000
O	-6.13983300	3.33500400	-0.00006400
O	-7.75282700	-0.92904800	0.00020800
C	3.00181100	-0.28678300	0.00000000
C	3.35565200	2.43479900	-0.00006600
C	2.03306800	1.91079800	-0.00010000
C	1.84678300	0.53856200	-0.00008500
C	4.29988600	0.20188400	0.00001100
C	4.47303700	1.61150200	-0.00005800
C	2.68681200	-1.67518100	-0.00002000
C	3.73451200	-2.58355200	0.00002400
C	5.06989700	-2.09843900	0.00005000
C	5.36293400	-0.74051300	0.00006100
C	6.75345800	-0.22912600	0.00011000
N	6.86036700	1.17045300	0.00006300
C	5.85541200	2.14869100	-0.00004800
O	6.13983300	3.33500300	-0.00005100
O	7.75282700	-0.92904700	0.00024900
H	-3.50982800	3.50935500	0.00020100

H	-1.19573800	2.60225100	0.00008200
H	-3.56097800	-3.65578600	-0.00005800
H	-5.89764600	-2.80076200	0.00005000
H	3.50982800	3.50935500	0.00000600
H	1.19573800	2.60225100	-0.00006000
H	3.56097800	-3.65578600	0.00004000
H	5.89764600	-2.80076200	0.00007900
H	-7.81021900	1.52896300	0.00008100
H	7.81021900	1.52896200	0.00016700

246e
Total energy of the optimized structure: -2526.96602887 a.u.
Number of imaginary frequencies: 0

C	0.70309600	-1.89949400	0.00223400
C	-0.70309800	-1.89950600	0.00258700
C	-1.11766500	-0.54850500	0.04221100
N	0.00000000	0.26950600	0.08204800
C	1.11766000	-0.54850200	0.04204500
S	-2.04828300	-3.01100200	-0.01576900
C	-3.15270900	-1.66281900	0.01949900
C	-2.52930700	-0.40402900	0.03851400
C	2.52930400	-0.40402300	0.03879900
C	3.15270700	-1.66281200	0.01986100
S	2.04829100	-3.01099900	-0.01565300
C	-4.81011600	-0.11177000	0.01530600
C	4.81011300	-0.11176500	0.01541500
C	4.59908500	-1.51960100	0.00922200
C	-4.96328400	2.62618400	-0.01391100
C	-3.68355200	2.00593900	0.00269400
C	-3.59362600	0.62257900	0.02530200
C	-6.06812200	0.47120500	-0.00288600
C	-6.13842300	1.88941000	-0.01410200
C	-4.59908600	-1.51960700	0.00896000
C	-5.71258100	-2.34756300	-0.00853900
C	-7.00754700	-1.76501900	-0.01969000
C	-7.19964200	-0.38899300	-0.01823000
C	-8.54686200	0.22336600	-0.03640400
N	-8.55054200	1.62808200	-0.04061200
C	-7.47625500	2.52824600	-0.03311100
O	-7.67063300	3.73313900	-0.04207300
O	-9.59671900	-0.39891900	-0.04757700
C	4.96328000	2.62618400	-0.01423000
C	3.68354700	2.00594300	0.00254500
C	3.59362000	0.62258500	0.02535300
C	6.06811900	0.47120800	-0.00285600
C	6.13842000	1.88941200	-0.01433800
C	5.71257800	-2.34756200	-0.00816200
C	7.00754400	-1.76502000	-0.01939100
C	7.19963700	-0.38899300	-0.01808800
C	8.54685900	0.22336400	-0.03629000
N	8.55053900	1.62807800	-0.04075700
C	7.47625100	2.52824400	-0.03348900
O	7.67063000	3.73313500	-0.04270200
O	9.59671600	-0.39892400	-0.04730000
H	-5.03611800	3.70922000	-0.02936400
H	-2.80367100	2.64087800	-0.01277100
H	-5.61854400	-3.42966700	-0.01525700
H	-7.88496500	-2.40419100	-0.03285500
H	5.03611000	3.70921900	-0.02979800
H	2.80366700	2.64088200	-0.01291800
H	5.61853700	-3.42966600	-0.01479300
H	7.88496300	-2.40419300	-0.03243600
H	9.47135600	2.05522000	-0.05398000
H	-9.47135800	2.05522600	-0.05384300
C	0.00003200	1.71468800	0.21827400
H	0.88127400	2.02193500	0.78397200
H	0.00013600	2.22021700	-0.75517100
H	-0.88130300	2.02197700	0.78380000

246f
Total energy of the optimized structure: -2550.24151128 a.u.
Number of imaginary frequencies: 0

C	-0.71716100	-1.75031400	-0.00006600
C	0.71716100	-1.75031400	0.00008100
C	1.17521000	-0.43325400	0.00012100
C	0.00000000	0.54455100	0.00000800
C	-1.17521000	0.43325400	-0.00011000
S	1.99282600	-2.93255100	-0.00005100
C	3.17019800	-1.65252100	-0.00011600
C	2.58471100	-0.37192800	0.00002500
C	-2.58471100	-0.37192800	-0.00002100
C	-3.17019800	-1.65252000	0.00011900
S	-1.99282600	-2.93255100	0.00006600
C	4.87429900	-0.15400700	0.00002000
C	-4.87429900	-0.15400600	-0.00003500
C	-4.62074200	-1.55682700	0.00000000
C	5.10375700	2.58098900	0.00004700
C	3.80653800	1.99692500	0.00001900
C	3.68333600	0.61721700	0.00000200
C	6.14863900	0.39321300	-0.00000300
C	6.25712200	1.80923500	-0.00000600
C	4.62074200	-1.55682800	-0.00000800
C	5.71124100	-2.41534700	-0.00000600
C	7.02217800	-1.86923200	-0.00001000
C	7.25466000	-0.49916500	-0.00003700
C	8.61880600	0.07446400	0.00000400
N	8.66167500	1.47852700	-0.00004600
C	7.61347900	2.40928100	-0.00005200
O	7.84296000	3.60788200	-0.00006400
O	9.65084300	-0.57709700	0.00013900
C	-5.10375800	2.58098900	-0.00005800
C	-3.80653900	1.99692600	-0.00002100
C	-3.68333600	0.61721800	-0.00000400
C	-6.14863900	0.39321300	-0.00001900
C	-6.25712300	1.80923500	-0.00001000
C	-5.71124100	-2.41534700	-0.00000300
C	-7.02217800	-1.86923200	-0.00000900
C	-7.25465900	-0.49916500	0.00000900
C	-8.61880600	0.07446300	-0.00005500
N	-8.66167500	1.47852600	0.00003600
C	-7.61348000	2.40928100	0.00003900
O	-7.84296100	3.60788200	0.00010100
O	-9.65084200	-0.57709800	-0.00010100
C	-0.00015200	1.42097100	1.27304400
C	0.00015300	1.42097700	-1.27302400
H	5.20922700	3.66143800	0.00016900
H	2.93810100	2.64932400	0.00012900
H	5.58777100	-3.49451200	-0.00002600
H	7.88096500	-2.53340000	-0.00001300
H	-5.20922800	3.66143800	-0.00019100
H	-2.93810200	2.64932500	-0.00013400
H	-5.58777100	-3.49451200	0.00002300
H	-7.88096500	-2.53340000	-0.00001200
H	-0.88652900	2.06407700	1.29941400
H	0.88619600	2.06411300	1.29960600
H	-0.00023800	0.80229400	2.17541100
H	0.00023800	0.80230300	-2.17539400
H	-0.88619400	2.06412000	-1.29958400
H	0.88653100	2.06408200	-1.29939200
H	9.59423100	1.87963100	0.00003800
H	-9.59423200	1.87963100	-0.00001200

246g
Total energy of the optimized structure: -2830.49955624 a.u.
Number of imaginary frequencies: 0

C	-0.70808000	-1.52086100	0.00014200
C	0.70808000	-1.52086000	0.00007800
C	1.24561700	-0.22553100	0.00009800
S	0.00000000	1.01435000	0.00017600
C	-1.24561600	-0.22553100	0.00013000
S	1.95225400	-2.75244800	0.00000000
C	3.18018300	-1.51811700	-0.00004600
C	2.65889700	-0.21738300	0.00005200
C	-2.65889700	-0.21738300	0.00013800
C	-3.18018400	-1.51811800	0.00013900
S	-1.95225300	-2.75244900	0.00016400
C	4.94663700	-0.09055200	0.00005900
C	-4.94663800	-0.09055300	0.00005800
C	-4.63758400	-1.48072900	0.00016800
C	5.27996800	2.63419100	0.00027000
C	3.96007700	2.10164300	0.00020300
C	3.78777500	0.72798700	0.00009300
C	6.24021000	0.40691200	0.00006100
C	6.40286100	1.81822700	0.00015300
C	4.63758400	-1.48072800	-0.00013200
C	5.69137500	-2.38222000	-0.00034300
C	7.02404000	-1.88837500	-0.00035600
C	7.30946100	-0.52883700	-0.00011500
C	8.69621600	-0.00808000	-0.00018600
N	8.79325400	1.39239300	-0.00011700
C	7.78184500	2.36418800	0.00006800

O	8.05911700	3.55224000	0.00009700
O	9.70076200	-0.70069500	-0.00029600
C	-5.27996900	2.63419000	-0.00014400
C	-3.96007700	2.10164300	-0.00004100
C	-3.78777600	0.72798600	0.00009700
C	-6.24021000	0.40691100	-0.00003300
C	-6.40286100	1.81822600	-0.00008500
C	-5.69137700	-2.38222000	0.00019700
C	-7.02404100	-1.88837500	0.00011900
C	-7.30946200	-0.52883600	-0.00001100
C	-8.69621600	-0.00807900	-0.00015800
N	-8.79325300	1.39239300	-0.00024300
C	-7.78184500	2.36418800	-0.00014000
O	-8.05911600	3.55224000	-0.00017500
O	-9.70076300	-0.70069300	-0.00025000
H	5.42699300	3.70971300	0.00047200
H	3.11561600	2.78503500	0.00029800
H	5.52526200	-3.45563300	-0.00043800
H	7.85577600	-2.58598900	-0.00052600
H	-5.42699300	3.70971200	-0.00041300
H	-3.11561600	2.78503400	-0.00028000
H	-5.52526400	-3.45563300	0.00023000
H	-7.85577800	-2.58598900	0.00012600
H	-9.74061500	1.75735500	-0.00043800
H	9.74061600	1.75735600	-0.00016600

246h
Total energy of the optimized structure: -2509.75310203 a.u.
Number of imaginary frequencies: 0

C	0.71201400	1.18290800	0.00000300
C	-0.71201400	-1.18291100	-0.00000500
C	-1.41030300	0.06904300	0.00000900
C	1.41030300	-0.06904400	0.00000300
S	-1.82076600	-2.56539700	-0.00008900
C	-3.18344200	-1.48323200	-0.00005000
C	-2.82808200	-0.14011700	0.00000900
C	2.82808100	0.14011500	-0.00000400
C	3.18344100	1.48323200	-0.00006200
S	1.82076700	2.56539600	-0.00009000
C	-5.11768300	-0.29361900	0.00002600
C	5.11768200	0.29361800	0.00003100
C	4.63797700	1.63140000	-0.00004300
C	-5.79140200	2.36414500	0.00008600
C	-4.41445700	2.00133200	0.00007500
C	-4.06559900	0.66074400	0.00004100
C	-6.46346700	0.03616900	0.00002400
C	-6.80396900	1.41558400	0.00007500
C	-4.63797800	-1.63140000	-0.00003900
C	-5.56578900	-2.66028800	-0.00012800
C	-6.95153100	-2.34042700	-0.00012200
C	-7.40467800	-1.02762300	-0.00003300
C	-8.84756900	-0.68592400	-0.00001900
N	-9.12093700	0.69013600	0.00006700
C	-8.23983500	1.78285400	0.00009700
O	-8.66688600	2.92567100	0.00017600
O	-9.75519100	-1.50124100	-0.00004600
H	-10.10669600	0.93291300	0.00009200
C	5.79140300	-2.36414500	0.00009000
C	4.41445800	-2.00133300	0.00007200
C	4.06559900	-0.66074400	0.00003600
C	6.46346700	-0.03616800	0.00003300
C	6.80397000	-1.41558300	0.00008300
C	5.56578700	2.66028800	-0.00013600
C	6.95153000	2.34042800	-0.00012100
C	7.40467800	1.02762400	-0.00002500
C	8.84756800	0.68592600	-0.00000600
N	9.12093700	-0.69013400	0.00006800
C	8.23983600	-1.78285200	0.00010600
O	8.66688800	-2.92566900	0.00016500
O	9.75519000	1.50124300	-0.00005000
H	10.10669700	-0.93291100	0.00007900
C	0.67309900	-1.26310300	-0.00004100
C	-0.67309900	1.26310100	-0.00002600
H	-6.07063100	3.41324200	0.00011600
H	-3.66726400	2.78946500	0.00008900
H	-5.26280300	-3.70341900	-0.00019600
H	-7.68792300	-3.13795600	-0.00017500
H	6.07063200	-3.41324200	0.00011400
H	3.66726600	-2.78946600	0.00007600
H	5.26280100	3.70341800	-0.00021700
H	7.68792200	3.13795600	-0.00018300
H	1.17822100	-2.22389000	-0.00004200
H	-1.17822100	2.22388900	-0.00001800

Coordinates of the donor and acceptor computed fragments

Naphthalene dicarboximide (acceptor fragment)
Total energy of the optimized structure: -666.75139655 a.u.
Number of imaginary frequencies: 0

C	1.85567100	-0.00000500	0.00000000
C	0.42798900	2.43396900	0.00000300
C	1.83819000	2.43626900	0.00000100
C	2.53662700	1.24637000	-0.00000200
C	0.42659800	-0.00000100	0.00001400
C	-0.26995400	1.23958900	0.00001300
C	2.53662000	-1.24638200	-0.00001000
C	1.83817800	-2.43627800	-0.00001200
C	0.42797600	-2.43397100	-0.00000200
C	-0.26996000	-1.23958700	0.00002000
C	-1.75347700	-1.25773700	0.00005500
N	-2.35918900	0.00000600	0.00001500
C	-1.75346900	1.25774500	0.00000600
O	-2.43018700	2.27450700	-0.00003300
O	-2.43019800	-2.27449600	-0.00003400
H	-3.37419300	0.00001000	-0.00001900
H	-0.13435100	3.36256200	0.00000200
H	2.37303900	3.38168500	-0.00000400
H	3.62416000	1.24874700	-0.00001000
H	3.62415200	-1.24876400	-0.00002200
H	2.37302400	-3.38169600	-0.00002200
H	-0.13437100	-3.36256100	0.00000100

a (Donor fragment of 246a)
Total energy of the optimized structure: -706.65362209 a.u.
Number of imaginary frequencies: 0

C	-0.06204400	-0.55403800	0.00000000
C	0.11118100	0.85297400	0.00000000
C	-1.15031800	1.54994400	0.00000000
C	-2.21876900	0.71269700	0.00000000
S	-1.76768800	-0.98050900	0.00000000
C	1.02973500	-1.42821200	0.00000000
C	2.31022500	-0.88615800	0.00000000
C	2.50293900	0.50772300	0.00000000
C	1.41863000	1.37383800	0.00000000
H	-1.23675800	2.63146900	-0.00000100
H	-3.26790400	0.97850000	0.00000000
H	0.88234800	-2.50443300	0.00000000
H	3.17167800	-1.54823500	-0.00000100
H	3.51296800	0.90807400	0.00000000
H	1.57119700	2.45014800	0.00000000

b (Donor fragment of 246b)
Total energy of the optimized structure: -403.12893007 a.u.
Number of imaginary frequencies: 0

C	-0.15160400	-0.33255700	-0.00002900
C	0.38910200	0.98530700	-0.00002000
C	-0.72653300	1.88883800	0.00000400
C	-1.86052300	1.12082600	0.00001200
N	-1.52996900	-0.22400300	-0.00000800
C	-2.46025400	-1.33282200	0.00001900
C	0.66002800	-1.47310800	-0.00001600
C	2.03732500	-1.28132300	0.00000400
C	2.59449700	0.01402900	0.00001600
C	1.78565300	1.14349100	0.00000600
H	-0.69053300	2.96962800	0.00000200
H	-2.90127200	1.41685700	-0.00003000
H	-2.32789200	-1.95927700	-0.89043400
H	-2.32773100	-1.95936000	0.89038200
H	-3.48015100	-0.94189600	0.00013200
H	0.23479700	-2.47301500	-0.00003300
H	2.69592300	-2.14570400	0.00001700
H	3.67536600	0.12680300	0.00003600
H	2.22513400	2.13791100	0.00000400

c and d (Donor fragment of 246c and 246d)
Total energy of the optimized structure: -553.00262846 a.u.
Number of imaginary frequencies: 0

C	-0.01160300	-1.24363200	0.00000000
C	-1.27269200	-0.71482300	0.00000000
C	-1.27267900	0.71484300	0.00000000
C	-0.01157800	1.24362500	-0.00000100
S	1.19972700	-0.00000700	0.00000000
H	0.28064400	-2.28507700	0.00000000
H	-2.17283300	-1.32025100	-0.00000300
H	-2.17280900	1.32028800	0.00000200
H	0.28068100	2.28506700	0.00000300

e (Donor fragment of 246e)
Total energy of the optimized structure: -1198.26858565 a.u.
Number of imaginary frequencies: 0

C	-0.58177800	0.00204100	0.70773900
C	-0.58177800	0.00204100	-0.70773900
C	0.75999500	-0.01629600	-1.11423400
N	1.58392600	-0.04420800	0.00000000
C	0.75999500	-0.01629600	1.11423400
S	-1.64484000	0.00904200	-2.08591300
C	-0.26583500	-0.00301700	-3.17357000
C	0.94047900	-0.01539700	-2.52749200
C	0.94047900	-0.01539700	2.52749200
C	-0.26583500	-0.00301700	3.17357000
S	-1.64484000	0.00904200	2.08591300
C	3.02924100	0.04629100	0.00000000
H	-0.44102300	0.00236700	-4.24081600
H	1.89420000	-0.02006800	-3.04301800
H	1.89420000	-0.02006800	3.04301800
H	-0.44102300	0.00236700	4.24081600
H	3.42632800	-0.45868300	-0.88488700
H	3.37861900	1.08714600	0.00000000
H	3.42632800	-0.45868300	0.88488700

f (Donor fragment of 246f)
Total energy of the optimized structure: -1221.54217585 a.u.
Number of imaginary frequencies: 0

C	-0.72204100	-0.68903400	0.00000300
C	0.72204100	-0.68903300	-0.00000300
C	1.17435100	0.61772900	-0.00000500
C	0.00000000	1.59741600	0.00000000
C	-1.17435100	0.61772900	0.00000500
S	2.02182200	-1.83213100	0.00000100
C	3.18841000	-0.52831300	0.00000000
C	2.59251100	0.70833100	-0.00000300
C	-2.59251100	0.70833100	0.00000400
C	-3.18841000	-0.52831400	0.00000100
S	-2.02182100	-1.83213100	-0.00000100
C	0.00000700	2.48024700	1.26743400
C	-0.00000700	2.48024600	-1.26743400
H	4.24428600	-0.76303100	-0.00000200
H	3.15879500	1.63396800	-0.00000400
H	-3.15879500	1.63396800	0.00000600
H	-4.24428600	-0.76303100	0.00000300
H	0.88626200	3.12524400	1.28835500
H	-0.88624900	3.12524200	1.28836800
H	0.00001400	1.86666500	2.17352200
H	-0.88626200	3.12524300	-1.28835600
H	0.88624900	3.12524100	-1.28836900
H	-0.00001500	1.86666400	-2.17352300

g (Donor fragment of 246g)
Total energy of the optimized structure: -1501.80204187 a.u.
Number of imaginary frequencies: 0

C	-0.71101300	-0.38014300	0.00000300
C	0.71101400	-0.38014500	-0.00000500
C	1.24585100	0.90538400	-0.00000600
S	0.00000200	2.14856500	0.00000000
C	-1.24585000	0.90538500	0.00000500
S	1.97477900	-1.57840200	0.00000200
C	3.19638400	-0.32414400	0.00000200
C	2.67023000	0.93760400	-0.00000200
C	-2.67022900	0.93760600	0.00000200
C	-3.19638300	-0.32414200	-0.00000100
S	-1.97478200	-1.57840000	-0.00000200
H	4.24076300	-0.60574200	0.00000200
H	3.27145500	1.83941900	-0.00000400
H	-3.27145400	1.83942100	0.00000400
H	-4.24076200	-0.60573800	0.00000000

h (Donor fragment of 246h)
Total energy of the optimized structure: -1181.05680475 a.u.
Number of imaginary frequencies: 0

C	-1.10576200	-0.87101900	0.00000000
C	-1.26738200	0.54708200	0.00000100
C	-0.18458400	1.41798200	-0.00000100
C	1.10576100	0.87101900	-0.00000100
C	1.26738200	-0.54708200	-0.00000100
C	0.18458400	-1.41798100	-0.00000100
C	2.37543400	1.55412300	0.00000000
C	3.43578400	0.70847800	0.00000200
S	2.97510900	-0.98401500	0.00000100
C	-2.37543400	-1.55412300	0.00000000
C	-3.43578400	-0.70847800	-0.00000100
S	-2.97510900	0.98401500	0.00000100
H	-0.32544800	2.49527700	-0.00000300
H	0.32544800	-2.49527700	-0.00000300
H	2.47087900	2.63484700	-0.00000100
H	4.48675800	0.96705300	0.00000000
H	-2.47087900	-2.63484700	0.00000000
H	-4.48675800	-0.96705300	0.00000200

10.4. Supporting Information Chapter 6[xiii]

General Methods

Unless otherwise stated, all chemicals, reagents and solvents were purchased from commercial suppliers and used without further purification. Column chromatography was performed on silica gel (particle size 0.040–0.063 mm) and freshly distilled solvents. ^{1}H and ^{13}C NMR spectra were recorded on a Bruker Avance HD III 400 spectrometer and ^{13}C NMR spectra are broad band proton decoupled. Chemical shift (δ) data are listed in parts per million (ppm), are reported relative to tetramethylsilane and referenced internally to residual proton solvent resonances or natural abundance carbon resonances. Coupling constants (J) are reported in Hertz (Hz). MALDI-TOF measurements were carried out on a Bruker Daltonics autoflex II LRF or Bruker Daltonics ultrafleXtreme mass spectrometer. ESI-TOF spectra were acquired on a Bruker Daltonics micOTOF focus mass spectrometer. EI mass spectra were measured on a Finnigan MAT90. Melting points were measured on an Olympus BX41 polarization microscope and are uncorrected. All spectroscopic measurements were carried out using spectroscopic grade solvents. Thin-films samples were prepared by spin-coating 10^{-2} – 10^{-3} M chloroform solutions (due to low solubility: $1.2 \cdot 10^{-4}$ M for **254a**) onto quartz substrates (50 µL, 3000 rpm, 30 s). Subsequently, the quartz substrates were annealed for 5 min at 130 °C on a precision hot plate from Harry Gestigkeit PZ28-2. UV–vis absorption spectra in solution were recorded on a Jasco V670 or Jasco V-770-ST spectrometer. For solid-state UV–vis measurements a Perkin-Elmar 950 with an including integration sphere was used. Fluorescence measurements were conducted on an Edinburgh Instruments FLS980 fluorescence spectrometer. Solid-state fluorescence spectra were recorded with a front face sample holder. The fluorescence quantum yields in solution were determined by using the dilution method (A < 0.05) and *N,N`*-bis[2,6-diisopropylphenyl]perylene-3,4:9,10-bis(dicarboximide) (Φ_{fl} = 100% in chloroform) as a reference. Solid-state fluorescence quanatum yields were measured by using a Hamamatsu Photonics C9920-02 integration sphere. Single crystals suitable for X-ray diffraction were measured on a Bruker D8 Quest Diffractometer with a PhotonII detector using Cu K_α radiation. The structures were solved using direct methods, expanded with Fourier techniques and refined using the SHELX software package.[395] All non-hydrogen atoms were refined anisotropically and hydrogen atoms were assigned idealized positions and were included in calculation of structures factors.

Compounds **247a**,[401] **247c**,[402] **247d**,[403] and **251-Bu**[404] were synthesized according to literature.

[xiii] This Supporting Information has been published. For the sake of harmonization of all *Supporting Information Chapters*, some modifications were made.

Optimization

Table A9. Additional optimization for the reaction conditions for **252d**.[a]

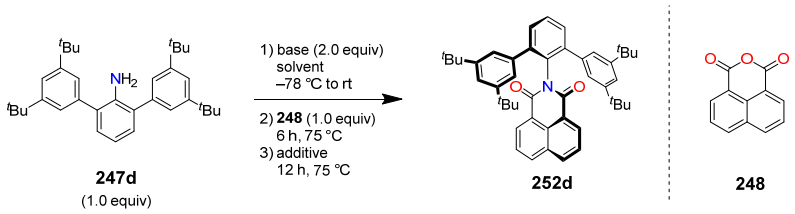

entry	base	solvent	additive (equiv)	yield / %[b]
1	LDA	THF	EtOH (5.0)	-
2	LDA	THF	10% HCl_{aq} (5.0)	42
3[c]	LDA	toluene	H_2O (5.0)	12
4[d]	LDA	DME	H_2O (5.0)	9
5[e]	LDA	diglyme	H_2O (5.0)	14
6[e]	LDA	DGDEE	H_2O (5.0)	7
7	LiTMP	THF	H_2O (5.0)	12
8	KHMDS	THF	H_2O (5.0)	-
9[f]	NaH	THF	H_2O (5.0)	-
10	LDA/KO^{t}Bu	THF	H_2O (5.0)	24
11	LDA/P4-*t*-Bu	THF	H_2O (5.0)	38
12	*n*-BuLi/KO^{t}Bu	THF	H_2O (5.0)	-
13	*n*-BuLi/P4-*t*-Bu	THF	H_2O (5.0)	52
14	*n*-BuLi/TMEDA	THF	H_2O (5.0)	54

[a]Reaction conditions: **247d** (0.1 mmol), base/base-solution (2.0 equiv), **248** (1.0 equiv), *c*(**247d**) = 0.07 M. [b]Isolated yields. [c]Reaction temperature 120 °C. [d]Reaction temperature 100 °C. [e]Reaction temperature 160 °C. [f]Deprotonation step at 75 °C instead of –78 °C. LDA: lithium diisopropylamide; LiTMP: lithium tetramethylpiperidide; KHMDS: potassium bis(trimethylsilyl)amide; BuLi: butyllithium; TMEDA: tetramethylethylenediamine; THF: tetrahydrofuran; DME: dimethoxyethane; diglyme: bis(2-methoxyethyl) ether; DGDEE: bis(2-ethoxyethyl) ether.

Table A10. Optimization for the reaction conditions for **255d**.[a]

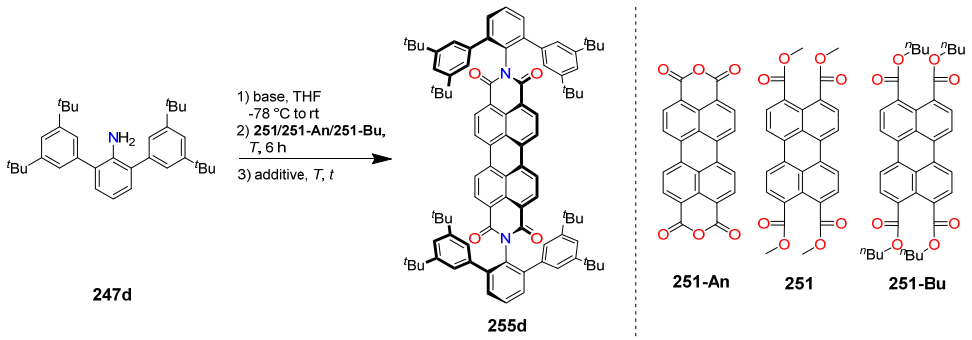

entry	starting material	base	equiv base	additive (equiv)	*T* / °C	*t* / h	yield / %[b]
1	**251-An**	LDA	4.0	H_2O (5.0)	75	24	-
2	**251-An**	*n*-BuLi	4.0	H_2O (5.0)	75	24	traces
3[c]	**251-An**	*n*-BuLi	4.0	H_2O (5.0)	75	72	-
4[d]	**251-An**	*n*-BuLi	4.0	H_2O (5.0)	75	24	-
5[e]	**251-An**	*n*-BuLi	4.0	H_2O (5.0) / $Zn(OAc)_2$ (0.3)	75	24	-
6[f]	**251-An**	*n*-BuLi	4.0	H_2O (5.0)	110	6	4
7[g]	**251-An**	*n*-BuLi	4.0	H_2O (5.0)	75	24	7
8[h]	**251-An**	*n*-BuLi	4.0	H_2O (5.0)	90	24	-
9[i]	**251-An**	*n*-BuLi	8.0	H_2O (10.0)	75	24	-
10	**251**	*n*-BuLi	4.0	-	75	24	14
11	**251-Bu**	*n*-BuLi	4.0	-	75	24	13
12[h]	**251**	*n*-BuLi	4.0	-	90	72	18
13[h]	**251-Bu**	*n*-BuLi	4.0	-	90	72	14
14[f]	**251**	*n*-BuLi	4.0	-	120	6	10
15[e, h]	**251**	*n*-BuLi	4.0	DCC (4.0)	90	72	traces
16[h, j]	**251**	*n*-BuLi	8.0	-	90	72	15

[a]Reaction conditions: **247d** (0.1 mmol), base-solution (2.0 equiv), **251**/**251-An**/**251-Bu** (0.5 equiv), 1.5 mL THF. [b]Isolated yields. [c]Addition of water after 24 h. [d]3.0 mL THF. [e]Addition of additive with **251**/**251-Bu**. [f]Use of microwave. Additive after 2 h. [g]Use of sonication bath in the first 6 hours. [h]Use of pressure resistant Schlenk-tube. [i]Two-fold equivalents of base and additive. [j]Two-fold equivalents of amine and base. LDA: lithium diisopropylamide; BuLi: butyllithium; THF: tetrahydrofuran; DCC: *N*,*N*′-dicyclohexylcarbodiimide.

Synthesis

Perylene-3,4-dicarboxylic acid dimethyl ester (250)

Synthesis of this compound is already reported in literature.[405] We used an alternative route for the synthesis of **250**.

Under nitrogen atmosphere perylene-3,4-dicarboxylic anhydride[402] (948 mg, 2.94 mmol, 1.0 equiv) was suspended in methanol (50 mL) and acetonitrile (100 mL). Subsequently, methyl iodide (2.09 g, 14.7 mmol, 5.0 equiv) was added and the reaction mixture was cooled to 0 °C and 1,8-diazabicyclo[5.4.0]undec-7-ene (DBU) (1.79 g, 11.8 mmol, 4.0 equiv) was added dropwise. The reaction mixture was allowed to warm-up to room temperature and then heated to 65 °C for 6 d. The mixture was cooled to room temperature and carefully added 10% NH_3(aq)-solution (25 mL) to destroy excess of methyl iodide. The resulting mixture was extracted with dichloromethane. The organic phases were washed with water, dried over $MgSO_4$ and concentrated under reduced pressure. The crude product was purified by silica gel column chromatography (chloroform) to yield **250** (831 mg, 2.26 mmol, 77%) as an orange solid. ^{1}H NMR (400 MHz, $CDCl_3$, 298 K): δ/ppm = 8.32 (*dd*, *J* = 0.8 Hz, *J* = 7.7 Hz, 2H), 8.27 (*d*, *J* = 8.0 Hz, 2H), 8.04 (*d*, *J* = 8.0 Hz, 2H), 7.81 (*dd*, *J* = 0.8 Hz, *J* = 8.3 Hz, 2H), 7.57 (*t*, *J* = 7.7 Hz, 2H), 3.93 (*s*, 6H).

Perylene-3,4,9,10-tetracarboxylic acid tetramethyl ester (251)

Synthesis of this compound is already reported in literature.[406] We used an alternative route for the synthesis of **251**.

Under nitrogen atmosphere perylene-3,4:9,10-tetracarboxylic dianhydride (4.00 g, 10.2 mmol, 1.0 equiv) was suspended in methanol (50 mL) and acetonitrile (100 mL). Subsequently, methyl iodide (14.5 g, 102 mmol, 10 equiv) was added and the reaction mixture was cooled to 0 °C and 1,8-diazabicyclo[5.4.0]undec-7-ene (DBU) (12.4 g, 81.6 mmol, 8.0 equiv) was added dropwise. The reaction mixture was allowed to warm-up to room temperature and then heated to 65 °C for 6 d. The mixture was cooled down to room temperature and carefully added 10% NH_3(aq)-solution (50 mL) to destroy excess of methyl iodide. The resulting mixture was extracted with dichloromethane. The organic phases were washed with water, dried over $MgSO_4$ and concentrated under reduced pressure. The crude product was purified by silica gel column chromatography (chloroform) to yield **251** (4.21 g, 8.69 mmol, 85%) as an orange solid. ^{1}H NMR (400 MHz, $CDCl_3$, 298 K): δ/ppm = 8.37 (*d*, *J* = 8.0 Hz, 4H), 8.09 (*d*, *J* = 8.0 Hz, 4H), 3.95 (*s*, 12H).

2,6-Bis(phenylethynyl)aniline (247b)

A Schlenk-tube was charged with $PdCl_2$ (136 mg, 767 µmol, 5.5 mol %), CuI (146 mg, 767 µmol, 5.5 mol %) and PPh_3 (146 mg, 1.53 mmol, 11 mol %) under an inert atmosphere and dry triethylamine (190 mL) was added. Subsequently, 2,6-dibromo aniline (3.50 g, 14.0 mmol, 1.0 equiv) and phenylacetylene (4.27 g, 41.8 mmol, 3.0 equiv) were added and the reaction mixture was stirred at 80 °C for 4 d. After the reaction mixture was cooled to room temperature, the solvent was removed under reduced pressure and the residue was dissolved in dichloromethane (75 mL). The solution was washed with water, dried over $MgSO_4$ and concentrated under reduced pressure. The crude product was purified by silica gel column chromatography (*n*-hexane/dichlormethane 10/1) to give **247b** (2.24 g, 7.62 mmol, 55%) as a light-brown solid. M.p.: 106–107 °C. ^{1}H NMR (400 MHz, $CDCl_3$, 298 K): δ/ppm = 7.51–7.57 (*m*, 4H), 7.34–7.40 (*m*, 8H), 6.69 (*t*, *J* = 7.7 Hz, 1H), 4.92 (*s*, 2H). ^{13}C NMR (101 MHz, $CDCl_3$, 298 K): δ/ppm = 149.0, 132.5, 131.6, 128.5, 128.4, 123.2, 117.4, 107.6, 95.1, 85.5. MS (EI, positive mode): 293.1 $[M]^+$. HRMS (ESI-TOF, positive mode, acetonitrile/chloroform): calcd for $C_{22}H_{15}NNa$: 316.1102; found: 316.1093 $[M+Na]^+$.

General method A

In a Schlenk-tube the respective amine **247a**–**d** (1.0 equiv) was dissolved in dry THF under a nitrogen atmosphere and cooled to –78 °C. Subsequently, 1.6 M *n*-BuLi solution in *n*-hexane (2.0 equiv) was added and the reaction mixture was stirred for 1 h at –78 °C. The solution was allowed to warm-up to room temperature and the respective anhydride **248**–**249** (1.0 equiv) was added. The mixture was heated to 75 °C for 6 h and water (5.0 equiv) was added. The reaction mixture was stirred for another 12 h at 75 °C and then cooled to room temperature. The resulting mixture was concentrated under reduced pressure. The crude product was purified by silica gel column chromatography to obtain the respective product. For two-fold imidization equivalents of amine **247a**–**d**, *n*-BuLi and water were doubled.

General method B

In a pressure-stable Schlenk-tube the respective amine **247a**–**d** (1.0 equiv) was dissolved in dry THF under a nitrogen atmosphere and cooled to –78 °C. Subsequently, 1.6 M *n*-BuLi solution (2.0 equiv) was added and the reaction mixture was stirred for 1 h at –78 °C. The solution was allowed to warm-up to room temperature and the respective ester **250**–**251** (1.0 equiv) was added. The mixture was heated to 90 °C for 72 h (caution: Schlenk-tube under pressure) and then cooled to room temperature. The resulting mixture was concentrated under reduced pressure. The crude

product was purified by silica gel column chromatography to obtain the respective product. For two-fold imidization equivalents of amine **247a**–**d** and *n*-BuLi were doubled.

N-[2,6-(Diphenyl)phenyl]naphthalene-1,8-dicarboximide (252a)

General method A: **247a** (50.0 mg, 204 µmol, 1.0 equiv), *n*-BuLi (255 µL, 1.6 M in *n*-hexane, 408 µmol, 2.0 equiv), **248** (40.4 mg, 204 µmol, 1.0 equiv), THF (2.9 mL) and water (18.3 µL, 1.02 mmol, 5.0 equiv) were used. The crude product was purified by silica gel column chromatography (gradient of cyclohexane/dichloromethane from 3/1 to 1/2) and washed with *n*-hexane and methanol. The product was dried under high vacuum to give **252a** (61.3 mg, 144 µmol, 71%) as a white solid. M.p.: 243–245 °C. ^{1}H NMR (400 MHz, $CDCl_3$, 298 K): δ/ppm = 8.39 (*dd*, *J* = 1.1 Hz, *J* = 7.4 Hz, 2H), 8.10 (*dd*, *J* = 1.1 Hz, *J* = 7.4 Hz, 2H), 7.57–7.65 (*m*, 3H), 7.47–7.49 (*m*, 2H), 7.32–7.36 (*m*, 4H), 7.10–7.16 (*m*, 4H), 7.05–7.10 (*m*, 2H). ^{13}C NMR (101 MHz, $CDCl_3$, 298 K): δ/ppm = 164.3, 141.8, 139.4, 134.1, 131.59, 131.55, 131.4, 130.3, 129.0, 128.5, 128.4, 128.0, 127.3, 126.8, 122.3. UV–vis ($CHCl_3$): λ_{max} / nm (ε / $M^{-1}cm^{-1}$) = 351 (12300). MS (MALDI-TOF, positive mode, DCTB in chloroform): 425.1 $[M]^+$. HRMS (ESI-TOF, positive mode, acetonitrile/chloroform): calcd for $C_{30}H_{19}NO_2Na$: 448.1313; found: 448.1302 $[M+Na]^+$.

N-[2,6-Bis(phenylethynyl)phenyl]naphthalene-1,8-dicarboximide (252b)

General method A: **247b** (50.0 mg, 170 µmol, 1.0 equiv), *n*-BuLi (213 µL, 1.6 M in *n*-hexane, 341 µmol, 2.0 equiv), **248** (33.8 mg, 170 µmol, 1.0 equiv), THF (2.4 mL) and water (15.3 µL, 852 µmol, 5.0 equiv) were used. The crude product was purified by silica gel column chromatography (gradient of cyclohexane/dichloromethane from 1/1 to 1/2) and washed with *n*-hexane and methanol. The product was dried under high vacuum to give **252b** (27.8 mg, 58.7 µmol, 34%) as a light-yellow solid. M.p.: 221–222 °C. ^{1}H NMR (400 MHz, $CDCl_3$, 298 K): δ/ppm = 8.74 (*dd*, *J* = 1.1 Hz, *J* = 7.3 Hz, 2H), 8.33 (*dd*, *J* = 1.1 Hz, *J* = 8.3 Hz, 2H), 7.82–7.86 (*m*, 2H), 7.74 (*d*, *J* = 7.7 Hz, 2H), 7.48–7.55 (*m*, 1H), 7.17 (*tt*, *J* = 2.3 Hz, *J* = 7.4 Hz, 2H), 7.06–7.11 (*m*, 4H; Ar-*H*), 7.00–7.04 (*m*, 4H). ^{13}C NMR (101 MHz, $CDCl_3$, 298 K): δ/ppm = 163.6, 139.4, 134.5, 132.6, 132.0, 131.8, 1316, 128.9, 128.8, 128.5, 128.2, 127.2, 124.1, 122.9, 122.7, 94.1, 85.2. UV–vis ($CHCl_3$): λ_{max} / nm (ε / $M^{-1}cm^{-1}$) = 350 (10800). MS (MALDI-TOF, positive mode, DCTB in chloroform): 473.1 $[M]^+$. HRMS (ESI-TOF, positive mode, acetonitrile/chloroform): calcd for $C_{34}H_{20}NO_2$: 474.1416; found: 474.1477 $[M+H]^+$.

_N_-[2,6-Bis(4-_tert_-butylphenyl)phenyl]naphthalene-1,8-dicarboximide (252c)

General method A: **247c** (50.0 mg, 140 µmol, 1.0 equiv), *n*-BuLi (175 µL, 1.6 M in *n*-hexane, 280 µmol, 2.0 equiv), **248** (27.7 mg, 140 µmol, 1.0 equiv), THF (2.0 mL) and water (12.6 µL, 852 µmol, 5.0 equiv) were used. The crude product was purified by silica gel column chromatography (gradient of cyclohexane/dichloromethane from 1/1 to 1/2) and washed with methanol. The product was dried under high vacuum to give **252c** (48.8 mg, 90.8 µmol, 65%) as a white solid. M.p.: 251–252 °C. ^{1}H NMR (400 MHz, CD_2Cl_2, 298 K): δ/ppm = 8.36 (*dd*, *J* = 1.2 Hz, *J* = 7.3 Hz, 2H), 8.15 (*dd*, *J* = 1.1 Hz, *J* = 8.2 Hz, 2H), 7.59–7.68 (*m*, 3H), 7.47–7.49 (*m*, 2H), 7.19–7.23 (*m*, 4H), 7.11–7.15 (*m*, 4H), 1.08 (*s*, 18H). ^{13}C NMR (101 MHz, $CDCl_3$, 298 K): δ/ppm = 164.5, 150.0, 141.7, 136.5, 133.8, 132.0, 131.5, 131.3, 130.1, 129.0, 128.4, 128.1, 126.7, 124.9, 122.5, 34.4, 31.2. UV–vis ($CHCl_3$): λ_{max} / nm (ε / $M^{-1}cm^{-1}$) = 351 (11300). MS (MALDI-TOF, positive mode, DCTB in chloroform): 537.2 $[M]^+$. HRMS (ESI-TOF, positive mode, acetonitrile/chloroform): calcd for $C_{38}H_{36}NO_2$: 538.2746; found: 538.2741 $[M+H]^+$.

_N_-[2,6-Bis(3,5-di-_tert_-butylphenyl)phenyl]naphthalene-1,8-dicarboximide (252d)

General method A: **247d** (50.0 mg, 106 µmol, 1.0 equiv), *n*-BuLi (133 µL, 1.6 M in *n*-hexane, 212 µmol, 2.0 equiv), **248** (21.1 mg, 106 µmol, 1.0 equiv), THF (1.5 mL) and water (9.6 µL, 532 µmol, 5.0 equiv) were used. The crude product was purified by silica gel column chromatography (gradient of cyclohexane/dichloromethane from 3/1 to 1/1) and washed with methanol. The product was dried under high vacuum to give **252d** (55.3 mg, 85.1 µmol, 80%) as a white solid. M.p.: 257–259 °C. ^{1}H NMR (400 MHz, $CDCl_3$, 298 K): δ/ppm = 8.33 (*dd*, *J* = 1.2 Hz, *J* = 7.3 Hz, 2H), 8.05 (*dd*, *J* = 1.1 Hz, *J* = 8.3 Hz, 2H), 7.56–7.62 (*m*, 3H), 7.51–7.54 (*m*, 2H), 7.21 (*d*, *J* = 1.9 Hz, 4H), 7.06 (*t*, *J* = 1.9 Hz, 2H), 1.04 (*s*, 36H). ^{13}C NMR (101 MHz, $CDCl_3$, 298 K): δ/ppm = 164.0, 149.8, 142.5, 138.4, 133.5, 132.2, 131.2, 130.8, 129.5, 128.8, 128.1, 126.5, 123.0, 122.6, 120.6, 34.6, 31.1. UV–vis ($CHCl_3$): λ_{max} / nm (ε / $M^{-1}cm^{-1}$) = 351 (11400). MS (MALDI-TOF, positive mode, DCTB in chloroform): 649.3 $[M]^+$. HRMS (ESI-TOF, positive mode, acetonitrile/chloroform): calcd for $C_{46}H_{52}NO_2$: 650.3998; found: 650.3994 $[M+H]^+$.

_N,N`_-Bis[2,6-(diphenyl)phenyl]naphthalene-1,4:5,8-bis(dicarboximide) (253a)

General method A: **247a** (50.0 mg, 204 µmol, 2.0 equiv), *n*-BuLi (255 µL, 1.6 M in *n*-hexane, 408 µmol, 4.0 equiv), **249** (27.3 mg, 102 µmol, 1.0 eq equiv), THF (2.9 mL) and water (18.3 µL, 1.02 mmol, 10.0 equiv) were used. The crude product was purified by silica gel column chromatography (gradient of cyclohexane/dichloromethane from 1/1 to 1/8) and washed with *n*-

hexane and methanol. The product was dried under high vacuum to give **253a** (35.9 mg, 49.7 µmol, 49%) as a white solid. M.p.: > 350 °C. ^{1}H NMR (400 MHz, CD_2Cl_2, 298 K): δ/ppm = 8.41 (*s*, 4H), 7.62–7.67 (*m*, 2H), 7.47–7.50 (*m*, 4H), 7.21–7.25 (*m*, 8H), 7.09–7.16 (*m*, 12H). ^{13}C NMR (101 MHz, CD_2Cl_2, 298 K): δ/ppm = 163.2, 142.1, 139.2, 131.2, 131.1, 130.7, 129.6, 128.5, 128.4, 127.9, 127.1, 126.4. UV–vis ($CHCl_3$): λ_{max} / nm (ε / $M^{-1}cm^{-1}$) = 381 (24000). MS (MALDI-TOF, positive mode, DCTB in chloroform): 722.1 $[M]^+$. HRMS (ESI-TOF, positive mode, acetonitrile/chloroform): calcd for $C_{50}H_{30}N_2O_4Na$: 745.2103; found: 745.2101 $[M+Na]^+$.

***N,N`*-Bis[2,6-bis(phenylethynyl)pheny] naphthalene-1,4:5,8-bis(dicarboximide) (253b)**

General method A: **247b** (50.0 mg, 170 µmol, 2.0 equiv), *n*-BuLi (213 µL, 1.6 M in *n*-hexane, 341 µmol, 4.0 equiv), **249** (22.8 mg, 85.2 µmol, 1.0 equiv), THF (2.4 mL) and water (15.3 µL, 852 µmol, 10.0 equiv) were used. The crude product was purified by silica gel column chromatography (gradient of cyclohexane/dichloromethane from 1/1 to 1/10) and washed with *n*-hexane and methanol. The product was dried under high vacuum to give **253b** (18.3 mg, 22.3 µmol, 26%) as a light yellow solid. M.p.: > 350 °C. ^{1}H NMR (400 MHz, $CDCl_3$, 298 K): δ/ppm = 8.94 (*s*, 4H), 7.75 (*d*, *J* = 7.8 Hz, 4H), 7.51–7.56 (*m*, 2H), 7.05–7.10 (*m*, 4H), 6.93–7.02 (*m*, 16H). ^{13}C NMR (101 MHz, $CDCl_3$, 298 K): δ/ppm = 162.1, 138.0, 132.9, 131.7, 131.4, 129.5, 128.8, 128.3, 127.4, 127.1, 124.0, 122.3, 94.6, 84.8. UV–vis ($CHCl_3$): λ_{max} / nm (ε / $M^{-1}cm^{-1}$) = 378 (23100). MS (MALDI-TOF, positive mode, DCTB in chloroform): 818.1 $[M]^+$. HRMS (ESI-TOF, positive mode, acetonitrile/chloroform): calcd for $C_{58}H_{30}N_2O_4Na$: 842.2103; found: 841.2094 $[M+Na]^+$.

***N,N`*-Bis[2,6-bis(4-*tert*-butylphenyl)phenyl] naphthalene-1,4:5,8-bis(dicarboximide) (253c)**

General method A: **247c** (50.0 mg, 140 µmol, 2.0 equiv), *n*-BuLi (175 µL, 1.6 M in *n*-hexane, 280 µmol, 4.0 equiv), **249** (27.7 mg, 69.9 µmol, 1.0 equiv), THF (2.0 mL) and water (12.6 µL, 852 µmol, 10.0 equiv) were used. The crude product was purified by silica gel column chromatography (gradient of cyclohexane/dichloromethane from 1/1 to 1/5) and washed with methanol. The product was dried under high vacuum to give **253c** (23.8 mg, 25.1 µmol, 36%) as a white solid. M.p.: > 350 °C. ^{1}H NMR (400 MHz, CD_2Cl_2, 298 K): δ/ppm = 8.42 (*s*, 4H), 7.60–7.65 (*m*, 2H), 7.46–7.49 (*m*, 4H), 7.09–7.17 (*m*, 16H), 1.08 (*s*, 36H). ^{13}C NMR (101 MHz, $CDCl_3$, 298 K): δ/ppm = 163.0, 150.3, 141.9, 141.6, 136.2, 131.1, 130.8, 130.3, 129.5, 128.1, 126.2, 125.0, 34.5, 31.3. UV–vis ($CHCl_3$): λ_{max} / nm (ε / $M^{-1}cm^{-1}$) = 381 (24700). MS (MALDI-TOF, positive mode, DCTB in chloroform): 946.4 $[M]^+$. HRMS (ESI-TOF, positive mode, acetonitrile/chloroform): calcd for $C_{66}H_{62}N_2O_4Na$: 969.4607; found: 969.4604 $[M+Na]^+$.

_N,N`_-Bis[2,6-bis(3,5-di-*tert*-butylphenyl)phenyl]naphthalene-1,4:5,8-bis(dicarboximide) (253d)

General method A: **247d** (50.0 mg, 106 µmol, 2.0 equiv), *n*-BuLi (133 µL, 1.6 M in *n*-hexane, 212 µmol, 4.0 equiv), **249** (14.1 mg, 53.2 µmol, 1.0 equiv), THF (1.5 mL) and water (9.6 µL, 532 µmol, 10.0 equiv) were used. The crude product was purified by silica gel column chromatography (gradient of cyclohexane/dichloromethane from 2/1 to 1/1) and washed with methanol. The product was dried under high vacuum to give **253d** (15.2 mg, 12.9 µmol, 24%) as a white solid. M.p.: > 350 °C. ^{1}H NMR (400 MHz, $CDCl_3$, 298 K): δ/ppm = 8.33 (*s*, 4H), 7.59–7.63 (*m*, 2H), 7.50–7.53 (*m*, 4H), 7.12 (*d*, *J* = 1.8 Hz, 8H), 7.04 (*d*, *J* = 1.8 Hz, 4H), 1.02 (*s*, 72H). ^{13}C NMR (101 MHz, $CDCl_3$, 298 K): δ/ppm = 162.7, 151.9, 150.1, 142.5, 138.1, 131.5, 130.4, 129.8, 126.2, 123.0, 120.7, 120.4, 34.8, 31.3. UV–vis ($CHCl_3$): λ_{max} / nm (ε / $M^{-1}cm^{-1}$) = 381 (23200). MS (MALDI-TOF, positive mode, DCTB in chloroform): 1170.7 $[M]^+$. HRMS (ESI-TOF, positive mode, acetonitrile/chloroform): calcd for $C_{82}H_{94}N_2O_4Na$: 1193.7111; found: 1193.7065 $[M+Na]^+$.

***N*-[2,6-(Diphenyl)phenyl]perylene-3,4-dicarboximide (254a)**

General method B: **247a** (50.0 mg, 204 µmol, 1.0 equiv), *n*-BuLi (255 µL, 1.6 M in *n*-hexane, 408 µmol, 2.0 equiv), **250** (75.1 mg, 204 µmol, 1.0 equiv) and THF (2.9 mL) were used. The crude product was purified by silica gel column chromatography (gradient of cyclohexane/dichloromethane from 1/1 to 1/5) and washed with *n*-hexane and methanol. The product was dried under high vacuum to give **254a** (47.6 mg, 86.6 µmol, 42%) as a red solid. M.p.: > 350 °C. ^{1}H NMR (400 MHz, $CDCl_3$, 298 K): δ/ppm = 8.38 (*d*, *J* = 8.1 Hz, 2H), 8.32 (*d*, *J* = 7.7 Hz, 2H), 8.25 (*d*, *J* = 8.1 Hz, 2H), 7.83 (*d*, *J* = 8.1 Hz, 2H), 7.53–7.63 (*m*, 3H), 7.48–7.52 (*m*, 2H), 7.36–7.40 (*m*, 4H), 7.13–7.19 (*m*, 4H), 7.06–7.11 (m, 2H). ^{13}C NMR (101 MHz, $CDCl_3$, 298 K): δ/ppm = 164.1, 141.9, 139.5, 137.4, 134.3, 131.73, 131.71, 130.1, 130.3, 130.1, 129.2, 129.0, 128.5, 128.0, 127.9, 127.4, 127.1, 126.8, 123.8, 120.5, 120.1. UV–vis ($CHCl_3$): λ_{max} / nm (ε / $M^{-1}cm^{-1}$) = 510 (29600). Fluorescence ($CHCl_3$): λ_{max} / nm (Φ_{fl} / %) = 538 nm (87±4). MS (MALDI-TOF, positive mode, DCTB in chloroform): 549.1 $[M]^+$. HRMS (ESI-TOF, positive mode, acetonitrile/chloroform): calcd for $C_{40}H_{23}NO_2Na$: 572.1626; found: 572.1604 $[M+Na]^+$.

***N*-[2,6-bis(phenylethynyl)phenyl]perylene-3,4-dicarboximide (254b)**

General method B: **247b** (50.0 mg, 170 µmol, 1.0 equiv), *n*-BuLi (213 µL, 1.6 M in *n*-hexane, 341 µmol, 2.0 equiv), **250** (62.8 mg, 170 µmol, 1.0 equiv) and THF (2.4 mL) were used. The crude product was purified by silica gel column chromatography (gradient of

cyclohexane/dichloromethane from 1/1 to 1/2) and washed with *n*-hexane and methanol. The product was dried under high vacuum to give **254b** (24.0 mg, 40.2 µmol, 24%) as a red solid. M.p.: 295–297 °C. ^{1}H NMR (400 MHz, $CDCl_3$, 298 K): δ/ppm = 8.71 (*d*, *J* = 8.1 Hz, 2H), 8.45–8.49 (*m*, 4H), 7.91–7.94 (*m*, 2H), 7.73 (*d*, *J* = 7.7 Hz, 2H), 7.65 (*t*, *J* = 7.7 Hz, 2H), 7.47–7.51 (*m*, 1H), 7.02–7.13 (*m*, 10H). ^{13}C NMR (101 MHz, $CDCl_3$, 298 K): δ/ppm = 163.4, 139.5, 137.8, 134.5, 132.6, 132.2, 131.7, 131.2, 130.6, 129.4, 128.9, 128.5, 128.2, 128.2, 127.3, 127.2, 124.12, 124.06, 122.8, 121.1, 120.5, 94.1, 85.3. UV–vis ($CHCl_3$): λ_{max} / nm (ε / $M^{-1}cm^{-1}$) = 510 (30900). Fluorescence ($CHCl_3$): λ_{max} / nm (Φ_{fl} / %) = 540 nm (86±4). MS (MALDI-TOF, positive mode, DCTB in chloroform): 597.2 $[M]^+$. HRMS (ESI-TOF, positive mode, acetonitrile/chloroform): calcd for $C_{44}H_{23}NO_2Na$: 620.1626; found: 620.1623 $[M+Na]^+$.

_N_-[2,6-bis(4-*tert*-butylphenyl)phenyl]perylene-3,4-dicarboximide (254c)

General method B: **247c** (50.0 mg, 140 µmol, 1.0 equiv), *n*-BuLi (175 µL, 1.6 M in *n*-hexane, 280 µmol, 2.0 equiv), **250** (51.5 mg, 140 µmol, 1.0 equiv) and THF (2.0 mL) were used. The crude product was purified by silica gel column chromatography (gradient of cyclohexane/dichloromethane from 2/1 to 1/1) and washed with methanol. The product was dried under high vacuum to give **254c** (37.3 mg, 56.3 µmol, 40%) as a red solid. M.p.: >350 °C. ^{1}H NMR (400 MHz, $CDCl_3$, 298 K): δ/ppm = 8.38 (*d*, *J* = 8.1 Hz, 2H), 8.34 (*d*, *J* = 7.6 Hz, 2H), 8.26 (*d*, *J* = 8.1 Hz, 2H), 7.82–7.85 (*m*, 2H), 7.54–7.60 (*m*, 3H), 7.47–7.50 (*m*, 2H), 7.28–7.32 (*m*, 4H), 7.13–7.17 (*m*, 4H), 1.08 (*s*, 18H). ^{13}C NMR (101 MHz, $CDCl_3$, 298 K): δ/ppm = 164.2, 150.0, 141.8, 137.0, 136.7, 134.1, 131.9, 131.5, 130.8, 130.3, 130.0, 129.0, 128.9, 128.2, 127.8, 126.9, 126.6, 125.0, 123.6, 120.6, 119.8, 34.5, 31.3. UV–vis ($CHCl_3$): λ_{max} / nm (ε / $M^{-1}cm^{-1}$) = 509 (31900). Fluorescence ($CHCl_3$): λ_{max} / nm (Φ_{fl} / %) = 539 nm (84±4). MS (MALDI-TOF, positive mode, DCTB in chloroform): 661.3 $[M]^+$. HRMS (ESI-TOF, positive mode, acetonitrile/chloroform): calcd for $C_{48}H_{39}NO_2Na$: 684.2878; found: 684.2839 $[M+Na]^+$.

_N_-[2,6-bis(3,5-di-*tert*-butylphenyl)phenyl]perylene-3,4-dicarboximide (254d)

General method B: **247d** (50.0 mg, 106 µmol, 1.0 equiv), *n*-BuLi (133 µL, 1.6 M in *n*-hexane, 212 µmol, 2.0 equiv), **250** (39.2 mg, 106 µmol, 1.0 equiv) and THF (1.5 mL) were used. The crude product was purified by silica gel column chromatography (gradient of cyclohexane/dichloromethane from 2/1 to 1/2) and washed with methanol. The product was dried under high vacuum to give **254d** (18.8 mg, 24.3 µmol, 23%) as a red solid. M.p.: 316–318 °C. ^{1}H NMR (400 MHz, $CDCl_3$, 298 K): δ/ppm = 8.38 (*d*, *J* = 7.8 Hz, 2H), 8.35 (*d*, *J* = 8.1 Hz, 2H), 8.28

(*d*, *J* = 8.1 Hz, 2H), 7.87 (*d*, *J* = 8.1 Hz, 2H), 7.57–7.62 (*m*, 3H), 7.52–7.55 (*m*, 2H), 7.24 (*d*, *J* = 1.9 Hz, 4H), 7.07(*t*, *J* = 1.9 Hz, 2H), 1.07 (*s*, 36H). ^{13}C NMR (101 MHz, $CDCl_3$, 298 K): δ/ppm = 163.8, 149.9, 142.7, 138.5, 136.9, 134.4, 132.5, 131.3, 130.8, 130.0, 129.6, 129.4, 128.9, 128.1, 127.1, 126.7, 123.7, 123.2, 121.1, 120.7, 120.0, 34.8, 31.3. UV–vis ($CHCl_3$): λ_{max} / nm (ε / $M^{-1}cm^{-1}$) = 508 (31500). Fluorescence ($CHCl_3$): λ_{max} / nm (Φ_{fl} / %) = 534 nm (84±4). MS (MALDI-TOF, positive mode, DCTB in chloroform): 773.4 $[M]^+$. HRMS (ESI-TOF, positive mode, acetonitrile/chloroform): calcd for $C_{56}H_{55}NO_2Na$: 796.4130; found: 796.4103 $[M+Na]^+$.

_N,N`_-Bis[2,6-(diphenyl)phenyl]perylene-3,4:9,10-bis(dicarboximide) (255a)

General method B: **247a** (50.0 mg, 204 µmol, 2.0 equiv), *n*-BuLi (255 µL, 1.6 M in *n*-hexane, 408 µmol, 4.0 equiv), **251** (49.4 mg, 102 µmol, 1.0 equiv) and THF (2.9 mL) were used. The crude product was purified by silica gel column chromatography (gradient of cyclohexane/dichloromethane from 3/1 to 1/3) and washed with *n*-hexane and methanol. The product was dried under high vacuum to give **255a** (16.5 mg, 19.5 µmol, 19%) as a red solid. M.p.: >350 °C. ^{1}H NMR (400 MHz, CD_2Cl_2, 298 K): δ/ppm = 8.37 (*d*, *J* = 8.1 Hz, 4H), 8.17–8.25 (*br*, 4H), 7.61–7.65 (*m*, 2H), 7.49–7.52 (*m*, 4H), 7.33–7.38 (*m*, 8H), 7.13–7.19 (*m*, 8H), 7.06–7.11 (*m*, 4H). ^{13}C NMR (101 MHz, $CDCl_3$, 298 K): δ/ppm = 163.4, 141.8, 139.5, 134.3, 131.4, 131.2, 130.4, 129.3, 129.2, 128.6, 128.1, 127.5, 126.1, 122.6, 122.5. UV–vis ($CHCl_3$): λ_{max} / nm (ε / $M^{-1}cm^{-1}$) = 528 (77400). Fluorescence ($CHCl_3$): λ_{max} / nm (Φ_{fl} / %) = 535 nm (95±2). MS (MALDI-TOF, positive mode, DCTB in chloroform): 846.2 $[M]^+$. HRMS (ESI-TOF, positive mode, acetonitrile/chloroform): calcd for $C_{60}H_{34}N_2O_4Na$: 869.2416; found: 869.2484 $[M+Na]^+$.

_N,N`_-Bis[2,6-di(phenylethynyl)phenyl]perylene-3,4:9,10-bis(dicarboximide) (255b)

General method B: **247b** (50.0 mg, 170 µmol, 2.0 equiv), *n*-BuLi (213 µL, 1.6 M in *n*-hexane, 341 µmol, 4.0 equiv), **251** (41.3 mg, 85.2 µmol, 1.0 equiv) and THF (2.4 mL) were used. The crude product was purified by silica gel column chromatography (gradient of cyclohexane/dichloromethane from 1/2 to 0/1) and washed with *n*-hexane and methanol. The product was dried under high vacuum to give **255b** (9.7 mg, 10.3 µmol, 12%) as a red solid. M.p.: >350 °C. ^{1}H NMR (400 MHz, $CDCl_3$, 298 K): δ/ppm = 8.84 (*d*, *J* = 8.0 Hz, 4H), 8.74 (*d*, *J* = 8.0 Hz, 4H), 7.75 (*d*, *J* = 7.9 Hz, 4H), 7.50–7.55 (*m*, 2H), 7.04–7.16 (*m*, 20H). ^{13}C NMR (101 MHz, $CDCl_3$, 298 K): δ/ppm = 162.8, 138.8, 135.3, 132.8, 132.1, 131.6, 130.1, 129.2, 128.6, 128.3, 127.0, 124.0, 123.6, 123.5, 122.6, 94.2, 85.0. UV–vis ($CHCl_3$): λ_{max} / nm (ε / $M^{-1}cm^{-1}$) = 527 (78800). Fluorescence ($CHCl_3$): λ_{max} / nm (Φ_{fl} / %) = 534 nm (96±1). MS (MALDI-TOF, positive mode,

DCTB in chloroform): 942.3 $[M]^+$. HRMS (ESI-TOF, positive mode, acetonitrile/chloroform): calcd for $C_{68}H_{34}N_2O_4Na$: 965.2416; found: 965.2419 $[M+Na]^+$.

***N,N`*-Bis[2,6-bis(4-*tert*-butylphenyl)phenyl]perylene-3,4:9,10-bis(dicarboximide) (255c)**

General method B: **247c** (50.0 mg, 140 µmol, 2.0 equiv), *n*-BuLi (175 µL, 1.6 M in *n*-hexane, 280 µmol, 4.0 equiv), **251** (33.9 mg, 69.9 µmol, 1.0 equiv) and THF (2.0 mL) were used. The crude product was purified by silica gel column chromatography (gradient of cyclohexane/dichloromethane from 1/1 to 1/5) and washed with *n*-hexane and methanol. The product was dried under high vacuum to give **255c** (15.6 mg, 14.6 µmol, 21%) as a red solid. M.p.: >350 °C. ^{1}H NMR (400 MHz, $C_2D_2Cl_4$, 373 K): δ/ppm = 8.43–8.18 (*br*, 8H, due to broad signal not all protons could be resolved), 7.51–7.56 (*m*, 2H), 7.44–7.47 (*m*, 4H), 7.23 (*d*, J = 8.3 Hz, 8H), 7.08 (*d*, J = 8.3 Hz, 8H), 1.03 (*s*, 36H). ^{13}C NMR (101 MHz, $C_2D_2Cl_4$, 373 K): δ/ppm = 163.4, 150.4, 142.1, 136.7, 132.2, 131.1, 130.2, 129.4, 128.91, 128.86, 128.6, 124.7, 123.4, 122.6, 120.6, 34.4, 31.3. UV–vis ($CHCl_3$): λ_{max} / nm (ε / $M^{-1}cm^{-1}$) = 528 (87700). Fluorescence ($CHCl_3$): λ_{max} / nm (Φ_{fl} / %) = 533 nm (97±1). MS (MALDI-TOF, positive mode, DCTB in chloroform): 1070.4 $[M]^+$. HRMS (ESI-TOF, positive mode, acetonitrile/chloroform): calcd for $C_{76}H_{66}N_2O_4Na$: 1093.4920; found: 1093.4865 $[M+Na]^+$.

***N,N`*-Bis[2,6-bis(3,5-di-*tert*-butylphenyl)phenyl]perylene-3,4:9,10-bis(dicarboximide) (255d)**

General method B: **247d** (50.0 mg, 106 µmol, 2.0 equiv), *n*-BuLi (133 µL, 1.6 M in *n*-hexane, 212 µmol, 4.0 equiv), **251** (25.8 mg, 53.2 µmol, 1.0 equiv) and THF (1.5 mL) were used. The crude product was purified by silica gel column chromatography (gradient of cyclohexane/dichloromethane from 2/1 to 1/2) and washed with methanol. The product was dried under high vacuum to give **255d** (14.1 mg, 10.8 µmol, 18%) as a red-orange solid. M.p.: >350 °C. ^{1}H NMR (400 MHz, $CDCl_3$, 298 K): δ/ppm = 8.40 (*s*, 8H), 7.59–7.64 (*m*, 2H), 7.52–7.55 (*m*, 4H), 7.20 (*d*, J = 1.9 Hz, 8H), 7.06 (*t*, J = 1.9 Hz, 4H), 1.06 (*s*, 72H). ^{13}C NMR (101 MHz, $CDCl_3$, 298 K): δ/ppm = 163.2, 149.9, 142.6, 138.4, 134.6, 132.0, 131.2, 129.7, 129.4, 129.1, 126.4, 123.2, 123.1, 122.8, 120.7, 34.8, 31.4. UV–vis ($CHCl_3$): λ_{max} / nm (ε / $M^{-1}cm^{-1}$) = 527 (91100). Fluorescence ($CHCl_3$): λ_{max} / nm (Φ_{fl} / %) = 534 nm (93±2). MS (MALDI-TOF, positive mode, DCTB in chloroform): 1294.6 $[M]^+$. HRMS (ESI-TOF, positive mode, acetonitrile/chloroform): calcd for $C_{92}H_{98}N_2O_4Na$: 1317.7424; found: 1317.7379 $[M+Na]^+$.

3-[2,6-(Diphenyl)phenyl]imino-*1H*,*3H*-Naphtho[1,8-*cd*]pyran-1-one (256a)

In a Schlenk-tube **247a** (50.0 mg, 204 µmol, 1.0 equiv) was dissolved in THF (1.5 mL) under a nitrogen atmosphere and cooled to –78 °C. Subsequently, LDA (102 µL, 2.0 M in THF/heptane/ethylbenzene, 204 µmol, 1.0 equiv) was added and the reaction mixture was stirred for 1 h at –78 °C. The solution was allowed to warm up to room temperature and **248** (40.4 mg, 204 µmol, 1.0 equiv) was added. The mixture was stirred at 75 °C for 6 h and then cooled to room temperature. The resulting mixture was concentrated under reduced pressure. The crude product was purified by silica gel column chromatography (gradient of cyclohexane/dichloromethane from 1/1 to 1/3) and washed with cold methanol. The product was dried under high vacuum to give **256a** (10.9 mg, 25.6 µmol, 13%) as a yellow solid. M.p.: 249–251 °C. ^{1}H NMR (400 MHz, $CDCl_3$, 298 K): δ/ppm = 8.48 (*dd*, *J* = 1.0 Hz, *J* = 7.4 Hz, 1H), 8.30 (*dd*, *J* = 1.2 Hz, *J* = 7.4 Hz, 1H), 8.14 (*dd*, *J* = 1.1 Hz, *J* = 8.3 Hz, 1H), 8.05 (*dd*, *J* = 1.0 Hz, *J* = 8.3 Hz, 1H), 7.61–7.67 (*m*, 2H), 7.51–7.55 (*m*, 4H), 7.39–7.42 (*m*, 2H), 7.30–7.34 (*m*, 1H), 7.19–7.25 (*m*, 4H), 7.08–7.13 (*m*, 2H). ^{13}C NMR (101 MHz, $CDCl_3$, 298 K): δ/ppm = 159.4, 146.3, 141.3, 140.6, 134.6, 133.8, 131.8, 131.7, 131.6, 129.7, 129.4, 129.3, 129.0, 127.9, 127.5, 126.7, 126.7, 124.7, 121.4, 118.7. MS (MALDI-TOF, positive mode, DCTB in chloroform): 425.1 $[M]^+$. HRMS (ESI-TOF, positive mode, acetonitrile/chloroform): calcd for $C_{30}H_{20}NO_2$: 426.1494; found: 426.1490 $[M+H]^+$.

Conversion of isoimide 256a to imide 252a

In a Schlenk-tube **256a** (10.0 mg, 23.5 µmol, 1.0 equiv) was dissolved in THF (1.0 mL) under a nitrogen atmosphere and heated to 75 °C. Subsequently, *tert*-BuOK solution (0.24 mL, 0.5 M in water, 118 µmol, 5.0 equiv) was carefully added and heated for 6 h at 75 °C. The reaction mixture was cooled to room temperature and 20 mL dichloromethane and 20 mL water was added. The mixture was extracted with dichloromethane. The combined organic layers were washed with water, dried over $MgSO_4$ and concentrated under reduced pressure. The product was dried under high vacuum to give **252a** (9.9 mg, 23.5 µmol, 99%) as a white solid. ^{1}H NMR spectrum was in accordance with product identity of one-pot procedure.

Single Crystal X-Ray Analysis

Crystals suitable for single X-ray diffraction were grown by slow evaporation of concentrated dichloromethane or chloroform solutions or slow diffusion of *n*-hexane or methanol into dichloromethane or chloroform solutions.

Table A11. Crystal data and structure refinement for **252a**.

CCDC Number	1988196
Empirical formula	$C_{30}H_{19}NO_2$, 0.237(CH_4O)
Formula weight	433.07
Temperature	100(2) K
Wavelength	1.54178 Å
Crystal system, space group	Monoclinic, $P2_1/n$
Unit cell dimensions	a = 9.4521(3) Å b = 27.4078(8) Å c = 17.1937(5) Å α = 90 ° β = 92.3620(10) ° γ = 90 °
Volume	4450.4(2) $Å^3$
Z	8
Calculated density	1.293 Mg/m^3
Absorption coefficient	0.644 mm^{-1}
F(000)	1810
Crystal size	0.520 × 0.490 × 0.470 mm
Theta range for data collection	3.036 to 72.417 °
Limiting indices	–11 <= h <= 11, –32 <= k <= 33, –21 <= l <= 21
Reflections collected / unique	93592 / 8779 [R_{int} = 0.0271]
Completeness	99.7%
Absorption correction	Semi-empirical from equivalents
Max. and min. transmission	0.7536 and 0.6771
Refinement method	Full-matrix least-squares on F^2
Data / restraints / parameters	8779 / 1 / 635
Goodness-of-fit	1.037
Final R indices [$I > 2\sigma(I)$]	R_1 = 0.0421, wR_2 = 0.1068
R indices (all data)	R_1 = 0.0441, wR_2 = 0.1085
Largest diff. peak and hole	0.526 and –0.349 e·$Å^{-3}$

Table A12. Crystal data and structure refinement for **252b**.

CCDC Number	1988190
Empirical formula	$C_{34}H_{19}NO_2$
Formula weight	473.50
Temperature	100(2) K
Wavelength	1.54178 Å
Crystal system, space group	Triclinic, $P\bar{1}$
Unit cell dimensions	a = 9.5047(4) Å
	b = 11.4030(5) Å
	c = 13.0745(5) Å
	α = 113.5620(10) °
	β = 96.4210(10) °
	γ = 106.8600(10) °
Volume	1200.43(9) Å^3
Z	2
Calculated density	1.310 Mg/m^3
Absorption coefficient	0.641 mm^{-1}
F(000)	492
Crystal size	0.580 × 0.520 × 0.520 mm
Theta range for data collection	3.819 to 72.165 °
Limiting indices	–11 <= h <= 11, –14 <= k <= 14, –16 <=l <= 16
Reflections collected / unique	20993 / 4697 [R_{int} = 0.0352]
Completeness	99.7%
Absorption correction	Semi-empirical from equivalents
Max. and min. transmission	0.7536 and 0.5996
Refinement method	Full-matrix least-squares on F^2
Data / restraints / parameters	4697 / 0 / 335
Goodness-of-fit on F^2	1.078
Final R indices [$I > 2\sigma(I)$]	R_1 = 0.0384, wR_2 = 0.0959
R indices (all data)	R_1 = 0.0417, wR_2 = 0.0983
Largest diff. peak and hole	0.270 and –0.296 e·Å^{-3}

Table A13. Crystal data and structure refinement for **252c**.

CCDC Number	1988198
Empirical formula	$C_{38}H_{35}NO_2$, 0.276(C_6H_{14})
Formula weight	561.44
Temperature	100(2) K
Wavelength	1.54178 Å
Crystal system, space group	Trigonal, $R\bar{3}$
Unit cell dimensions	a = 42.7740(12) Å
	b = 42.774(3) Å
	c = 9.467(5) Å
	a = 90 °
	β = 90 °
	γ = 120 °
Volume	15000(8) Å^3
Z	18
Calculated density	1.119 Mg/m^3
Absorption coefficient	0.525 mm^{-1}
F(000)	5396
Crystal size	0.391 × 0.244 × 0.236 mm
Theta range for data collection	3.579 to 72.359 °
Limiting indices	–52 <= h <= 50, –52 <= k <= 52, –11 <=l <= 11
Reflections collected / unique	128131 / 6597 [R_{int} = 0.0492]
Completeness	100.0%
Absorption correction	Semi-empirical from equivalents
Max. and min. transmission	0.7536 and 0.6340
Refinement method	Full-matrix least-squares on F^2
Data / restraints / parameters	6597 / 0 / 384
Goodness-of-fit	1.057
Final R indices [$I > 2\sigma(I)$]	R_1 = 0.0644, wR_2 = 0.1700
R indices (all data)	R_1 = 0.0669, wR_2 = 0.1722
Largest diff. peak and hole	0.704 and –0.357 e·Å^{-3}

Table A14. Crystal data and structure refinement for **252d**.

CCDC Number	1988197
Empirical formula	$C_{46}H_{51}NO_2$
Formula weight	649.88
Temperature	100(2) K
Wavelength	1.54178 Å
Crystal system, space group	Monoclinic, $P2_1/n$
Unit cell dimensions	a = 9.3190(6) Å
	b = 23.5604(14) Å
	c = 17.6446(11) Å
	α = 90 °
	β = 97.518(3) °
	γ = 90 °
Volume	3840.7(4) Å^3
Z	4
Calculated density	1.124 Mg/m^3
Absorption coefficient	0.516 mm^{-1}
F(000)	1400
Crystal size	0.226 × 0.110 × 0.078 mm
Theta range for data collection	3.146 to 72.674 °
Limiting indices	–11 <= h <= 11, –29 <= k <= 29, –21 <=l <= 21
Reflections collected / unique	69915 / 7613 [R_{int} = 0.0565]
Completeness	100.0%
Absorption correction	Semi-empirical from equivalents
Max. and min. transmission	0.7536 and 0.6670
Refinement method	Full-matrix least-squares on F^2
Data / restraints / parameters	7613 / 0 / 454
Goodness-of-fit	1.036
Final R indices [$I > 2\sigma(I)$]	R_1 = 0.0498, wR_2 = 0.1250
R indices (all data)	R_1 = 0.0581, wR_2 = 0.1317
Largest diff. peak and hole	0.599 and –0.284 e·Å^{-3}

Table A15. Crystal data and structure refinement for **254a**.

CCDC Number	1988191
Empirical formula	$C_{40}H_{23}NO_2$
Formula weight	549.59
Temperature	100(2) K
Wavelength	1.54178 Å
Crystal system, space group	Monoclinic, $P2_1/n$
Unit cell dimensions	a = 8.2649(8) Å
	b = 18.9881(18) Å
	c = 16.9669(16) Å
	α = 90 °
	β = 94.814(4) °
	γ = 90 °
Volume	2653.3(4) Å^3
Z	4
Calculated density	1.376 Mg/m^3
Absorption coefficient	0.662 mm^{-1}
F(000)	1144
Crystal size	0.691 × 0.328 × 0.248 mm
Theta range for data collection	3.500 to 72.820 °
Limiting indices	–10 <= h <= 10, –19 <= k <= 23, –20 <=l <= 20
Reflections collected / unique	46803 / 5254 [R_{int} = 0.0530]
Completeness	100.0%
Absorption correction	Semi-empirical from equivalents
Max. and min. transmission	0.7536 and 0.6546
Refinement method	Full-matrix least-squares on F^2
Data / restraints / parameters	5254 / 0 / 388
Goodness-of-fit	1.050
Final R indices [$I > 2\sigma(I)$]	R_1 = 0.0382, wR_2 = 0.0953
R indices (all data)	R_1 = 0.0453, wR_2 = 0.1005
Largest diff. peak and hole	0.199 and –0.252 e·Å^{-3}

Table A16. Crystal data and structure refinement for **254d**.

CCDC Number	1988194
Empirical formula	$C_{56}H_{55}NO_2$, 2($CHCl_3$)
Formula weight	1012.74
Temperature	100(2) K
Wavelength	1.54178 Å
Crystal system, space group	Monoclinic, $P2_1/c$
Unit cell dimensions	a = 12.3323(3) Å
	b = 16.5743(4) Å
	c = 25.3982(6) Å
	α = 90 °
	β = 92.2790(10) °
	γ = 90 °
Volume	5187.3(2) Å ^{3}
Z	4
Calculated density	1.297 Mg/m^3
Absorption coefficient	3.352 mm^{-1}
F(000)	2120
Crystal size	0.485 × 0.358 × 0.142 mm
Theta range for data collection	3.185 to 72.222 °
Limiting indices	–15 <= h <= 15, –19 <= k <= 20, –31 <=l <= 31
Reflections collected / unique	69426 / 10235 [R_{int} = 0.0438]
Completeness	100.0%
Absorption correction	Semi-empirical from equivalents
Max. and min. transmission	0.7536 and 0.4999
Refinement method	Full-matrix least-squares on F^2
Data / restraints / parameters	10235 / 24 / 673
Goodness-of-fit	1.027
Final R indices [$I > 2\sigma(I)$]	R_1 = 0.0499, wR_2 = 0.1324
R indices (all data)	R_1 = 0.0574, wR_2 = 0.1378
Largest diff. peak and hole	0.530 and –0.889 e·Å $^{-3}$

Table A17. Crystal data and structure refinement for **255b**.

CCDC Number	1988192
Empirical formula	$C_{68}H_{34}N_2O_4$, 2(C_7H_8)
Formula weight	1127.24
Temperature	173(2) K
Wavelength	1.54178 Å
Crystal system, space group	Triclinic, $P\bar{1}$
Unit cell dimensions	a = 9.8083(3) Å
	b = 10.9966(3) Å
	c = 13.7096(4) Å
	α = 95.4630(10) °
	β = 96.3940(10) °
	γ = 91.7980(10) °
Volume	1461.50(7) Å^3
Z	1
Calculated density	1.281 Mg/m^3
Absorption coefficient	0.614 mm^{-1}
F(000)	588
Crystal size	0.271 × 0.133 × 0.068 mm
Theta range for data collection	3.260 to 72.215 °
Limiting indices	–12 <= h <= 12, –13 <= k <= 12, –16 <=l <= 16
Reflections collected / unique	28837 / 5734 [R_{int} = 0.0448]
Completeness	99.8%
Absorption correction	Semi-empirical from equivalents
Max. and min. transmission	0.7536 and 0.6827
Refinement method	Full-matrix least-squares on F^2
Data / restraints / parameters	5734 / 1 / 393
Goodness-of-fit	1.031
Final R indices [$I > 2\sigma(I)$]	R_1 = 0.0401, wR_2 = 0.1064
R indices (all data)	R_1 = 0.0495, wR_2 = 0.1130
Largest diff. peak and hole	0.186 and –0.208 e·Å^{-3}

Table A18. Crystal data and structure refinement for **255d**.

CCDC Number	1988195
Empirical formula	$C_{92}H_{98}N_2O_4$, (CH_2Cl_2), (CH_4O)
Formula weight	1412.69
Temperature	100(2) K
Wavelength	1.54178 Å
Crystal system, space group	Triclinic, $P\bar{1}$
Unit cell dimensions	a = 16.5016(7) Å
	b = 17.4206(8) Å
	c = 17.6995(9) Å
	α = 99.922(3) °
	β = 112.305(3) °
	γ = 112.149(2) °
Volume	4053.9(3) Å^3
Z	2
Calculated density	1.157 Mg/m^3
Absorption coefficient	1.128 mm^{-1}
F(000)	1512
Crystal size	0.122 × 0.074 × 0.059 mm
Theta range for data collection	2.902 to 72.314 °
Limiting indices	–20 <= h <= 20, –21 <= k <= 21, –17 <= l <= 21
Reflections collected / unique	80522 / 15965 [R_{int} = 0.0475]
Completeness	99.9%
Absorption correction	Semi-empirical from equivalents
Max. and min. transmission	0.7536 and 0.5884
Refinement method	Full-matrix least-squares on F^2
Data / restraints / parameters	15965 / 1 / 975
Goodness-of-fit	1.027
Final R indices [$I > 2\sigma(I)$]	R_1 = 0.0695, wR_2 = 0.1940
R indices (all data)	R_1 = 0.0855, wR_2 = 0.2117
Largest diff. peak and hole	0.922 and –1.101 e·Å^{-3}

Table A19. Crystal data and structure refinement for **256a**.

CCDC Number	1988193
Empirical formula	$C_{30}H_{19}NO_2$
Formula weight	425.46
Temperature	100(2) K
Wavelength	1.54178 Å
Crystal system, space group	Orthorhombic, *Pbca*
Unit cell dimensions	a = 7.5150(7) Å
	b = 18.211(2) Å
	c = 31.154(3) Å
	α = 90 °
	β = 90 °
	γ = 90 °
Volume	4263.5(7) Å^3
Z	8
Calculated density	1.326 Mg/m^3
Absorption coefficient	0.655 mm^{-1}
F(000)	1776
Crystal size	0.202 × 0.088 × 0.024 mm
Theta range for data collection	2.837 to 72.481 °
Limiting indices	–8 <= h <= 9, –22 <= k <= 22, –37 <=l <= 26
Reflections collected / unique	26331 / 4217 [R_{int} = 0.0628]
Completeness	99.9%
Absorption correction	Semi-empirical from equivalents
Max. and min. transmission	0.7536 and 0.6494
Refinement method	Full-matrix least-squares on F^2
Data / restraints / parameters	4217 / 0 / 298
Goodness-of-fit	1.031
Final R indices [$I > 2\sigma(I)$]	R_1 = 0.0437, wR_2 = 0.1059
R indices (all data)	R_1 = 0.0585, wR_2 = 0.1164
Largest diff. peak and hole	0.186 and –0.205 e·Å^{-3}

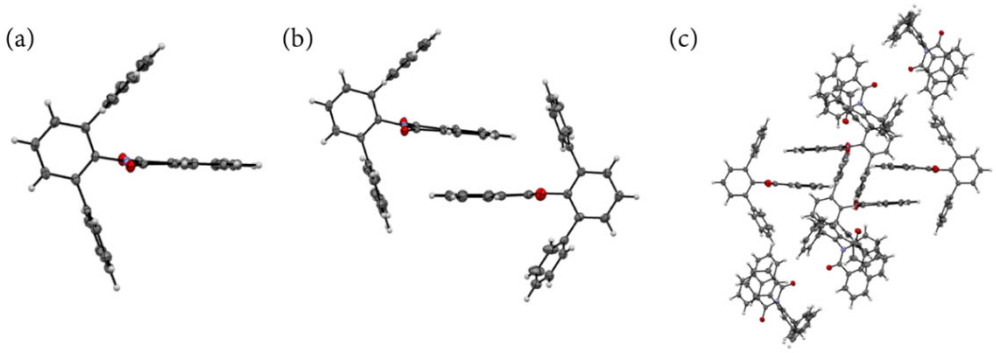

Figure A92. Molecular structure of **252a** in the solid-state. (a) Side view on the imide substituent, (b) dimeric fashion motif and (c) packing arrangement in the solid-state (methanol molecules were omitted for clarity).

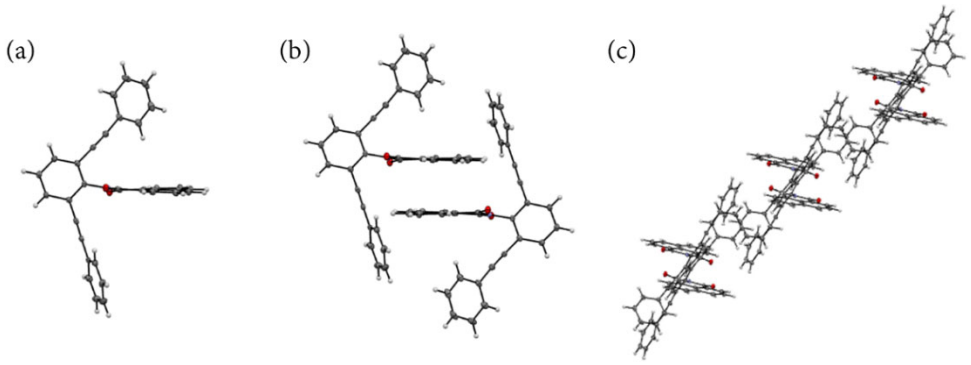

Figure A93. Molecular structure of **252b** in the solid-state. (a) Side view on the imide substituent, (b) dimeric fashion motif and (c) packing arrangement in the solid-state.

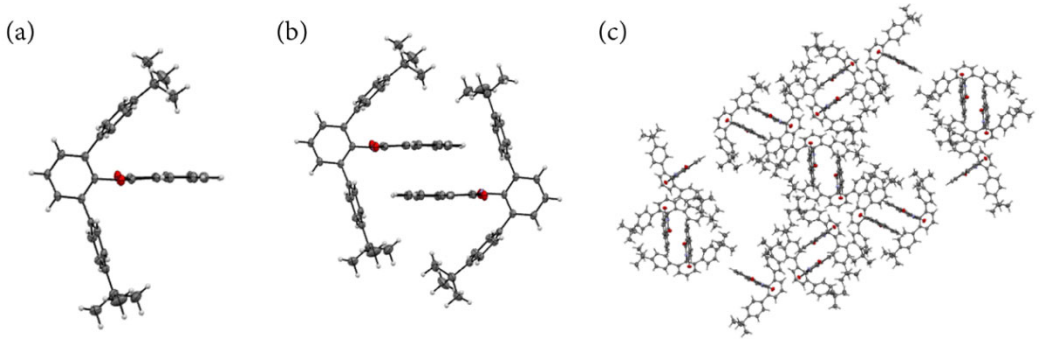

Figure A94. Molecular structure of **252c** in the solid-state. (a) Side view on the imide substituent, (b) dimeric fashion motif and (c) packing arrangement in the solid-state (*n*-hexane molecules were omitted for clarity).

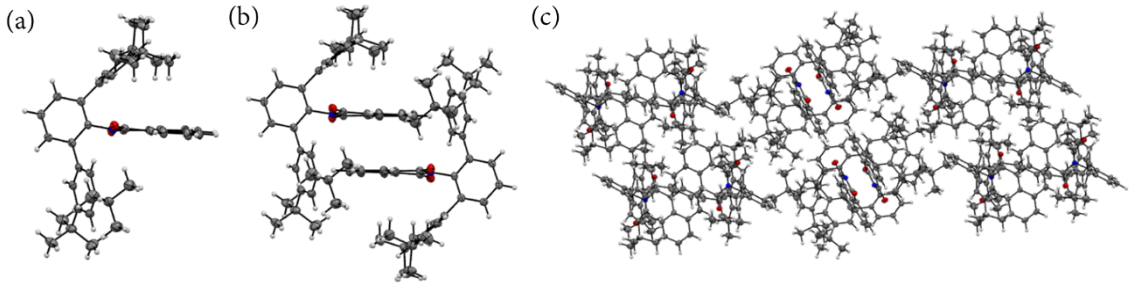

Figure A95. Molecular structure of **252d** in the solid-state. (a) Side view on the imide substituent, (b) dimeric fashion motif and (c) packing arrangement in the solid-state.

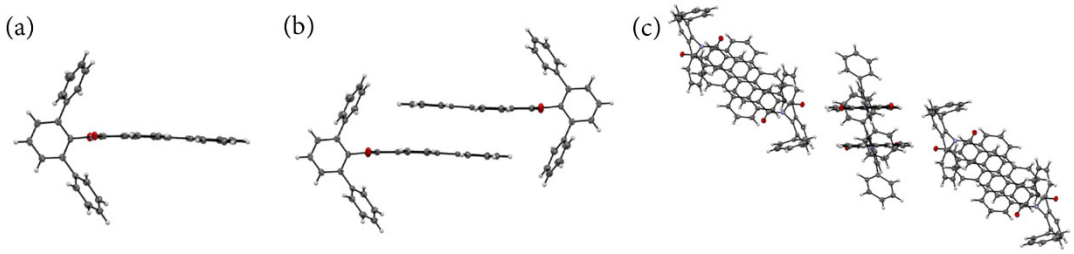

Figure A96. Molecular structure of **254a** in the solid-state. (a) Side view on the imide substituent, (b) dimeric fashion motif and (c) packing arrangement in the solid-state.

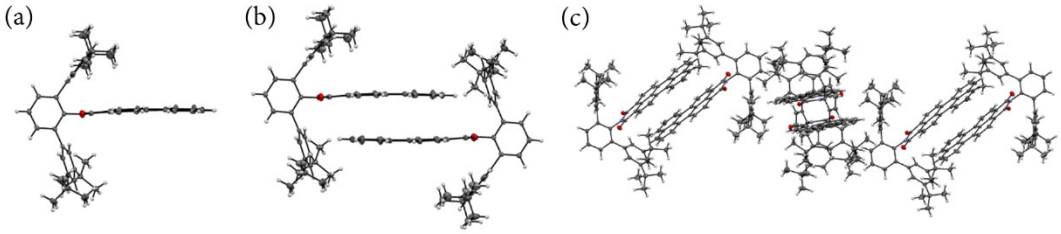

Figure A97. Molecular structure of **254d** in the solid-state. (a) Side view on the imide substituent, (b) dimeric fashion motif and (c) packing arrangement in the solid-state (chloroform molecules were omitted for clarity).

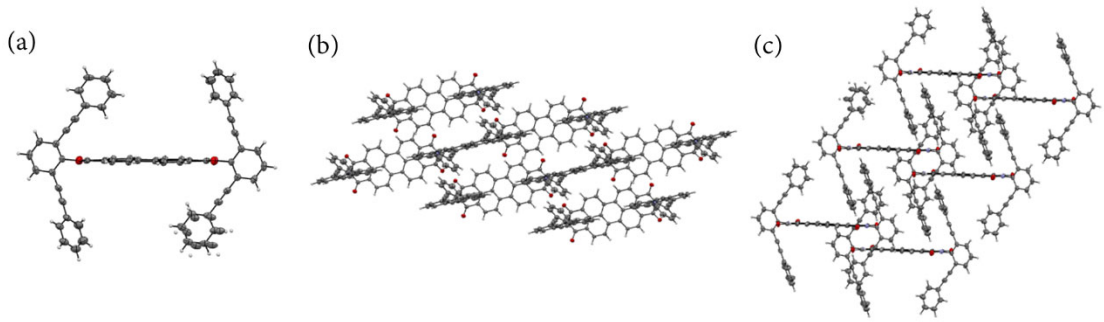

Figure A98. Molecular structure of **255b** in the solid-state. (a) Side view on the imide substituent, (b) and (c) packing arrangement in the solid-state (toluene molecules were omitted for clarity).

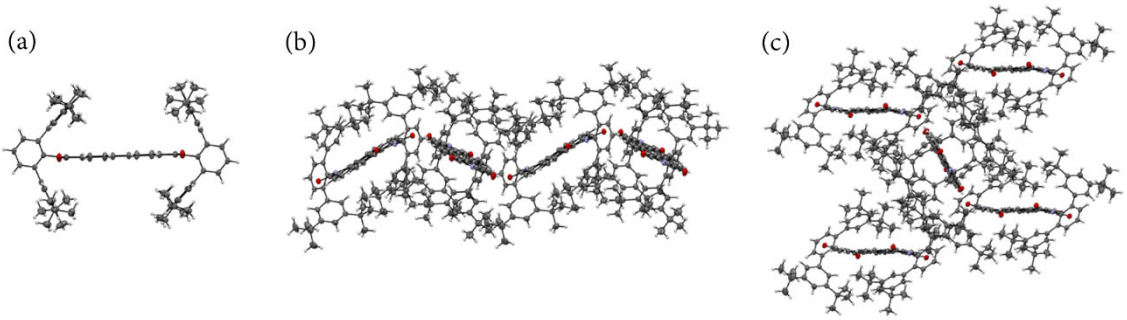

Figure A99. Molecular structure of **255d** in the solid-state. (a) Side view on the imide substituent, (b) and (c) packing arrangement in the solid-state (dichloromethane and methanol molecules were omitted for clarity).

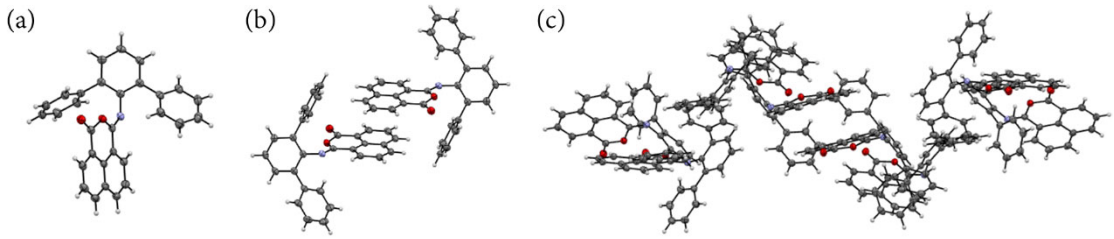

Figure A 100. Molecular structure of **256a** in the solid-state. (a) Side view, (b) dimeric fashion motif and (c) packing arrangement in the solid-state.

Optical Properties in Solution

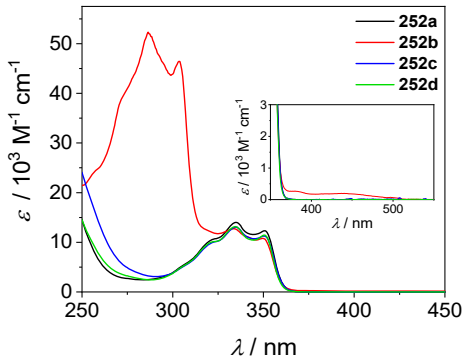

Figure A101. UV–vis spectra of **252a**–**d** in chloroform solutions at room temperature ($c \sim 10^{-5}$ M). Inset: Magnified region between 350–550 nm.

Table A20. UV–vis absorption properties of naphthalene monoimides **252a**–**d** in chloroform solutions at room temperature.

	λ_{abs} / nm (ε / M^{-1} cm^{-1})
252a	351 (12300)
252b	350 (10800)
252c	351 (11300)
252d	351 (11400)

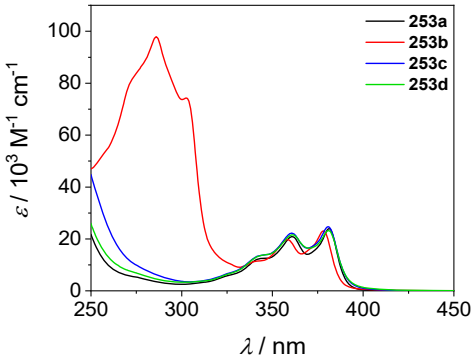

Figure A102. UV–vis spectra of **253a**–**d** in chloroform solutions at room temperature ($c \sim 10^{-5}$ M).

Table A21. UV–vis absorption properties of naphthalene bisimides **253a**–**d** in chloroform solutions at room temperature.

	λ_{abs} / nm (ε / M^{-1} cm^{-1})
253a	381 (24000)
253b	378 (23100)
253c	381 (24700)
253d	381 (23200)

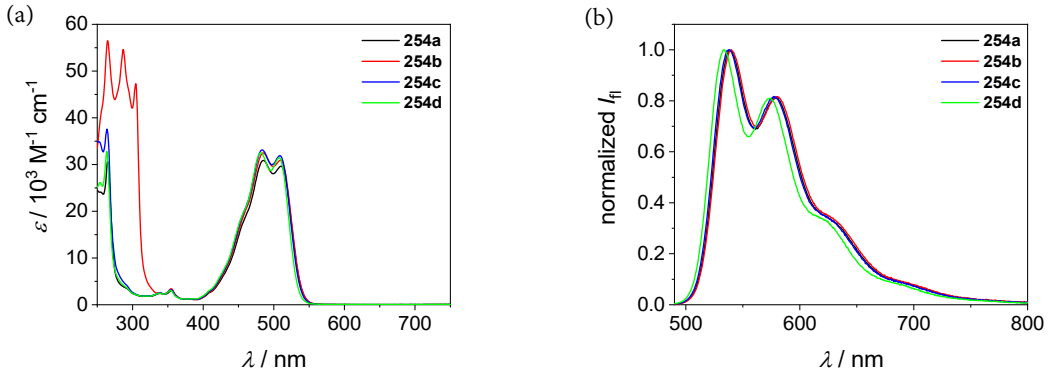

Figure A103. (a) UV–vis and (b) fluorescence spectra of **254a**–**d** in chloroform solutions at room temperature ($c \sim 10^{-5}$–10^{-7}M).

Table A22. Optical properties of perylene monoimides **254a**–**d** in chloroform solutions at room temperature.

	λ_{abs} / nm (ε / M^{-1} cm^{-1})	λ_{em} / nm	Stokes shift / cm^{-1}	Φ_{fl} / %[a]	τ / ns[b]
254a	510 (29600)	538	1020	87 ± 4	5.0
254b	510 (30900)	540	1090	86 ± 4	5.2
254c	509 (31900)	539	1090	84 ± 4	5.0
254d	508 (31500)	534	960	84 ± 4	4.8

[a]Fluorescence quantum yields were determined using the relative method (A < 0.05) and *N*,*N*′-bis(2,6-diisopropylphenyl)perylene-3,4:9,10-bis(dicarboximide) (Φ_{fl} ($CHCl_3$) = 1.00) as reference. [b]Excitation wavelength: λ_{ex} = 506 nm; detection wavelength: λ_{det} = 537 nm.

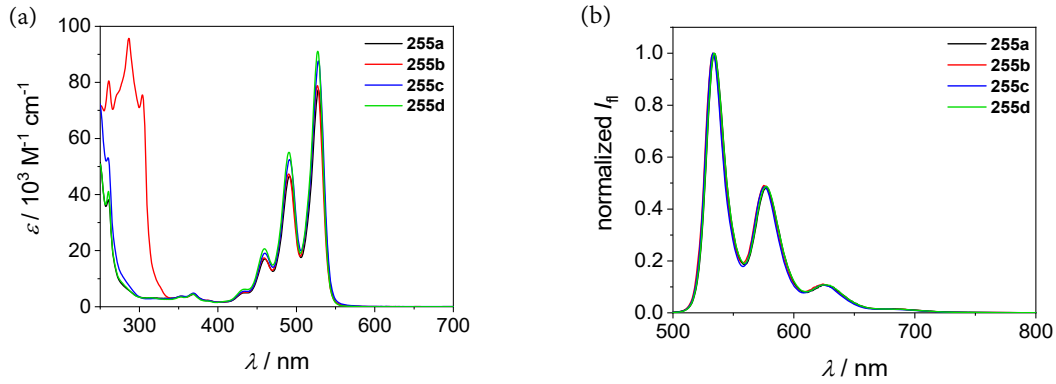

Figure A104. (a) UV–vis and (b) fluorescence spectra of **255a**–**d** in chloroform solutions at room temperature ($c \sim 10^{-5}$–10^{-7}M).

Table A23. Optical properties of perylene bisimides **255a**–**d** in chloroform solutions at room temperature.

	λ_{abs} / nm (ε / M^{-1} cm^{-1})	λ_{em} / nm	Stokes shift / cm^{-1}	Φ_{fl} / %[a]	τ / ns[b]
255a	528 (77400)	535	250	95 ± 2	3.8
255b	527 (78800)	534	250	96 ± 1	3.7
255c	528 (87700)	533	180	97 ± 1	3.8
255d	527 (91100)	534	250	93 ± 2	3.8

[a]Fluorescence quantum yields were determined using the relative method ($A < 0.05$) and *N*,*N*′-bis(2,6-diisopropylphenyl)perylene-3,4:9,10-bis(dicarboximide) (Φ_{fl} ($CHCl_3$) = 1.00) as reference. [b]Excitation wavelength: λ_{ex} = 506 nm; detection wavelength: λ_{det} = 537 nm.

Optical Properties in the Solid-state

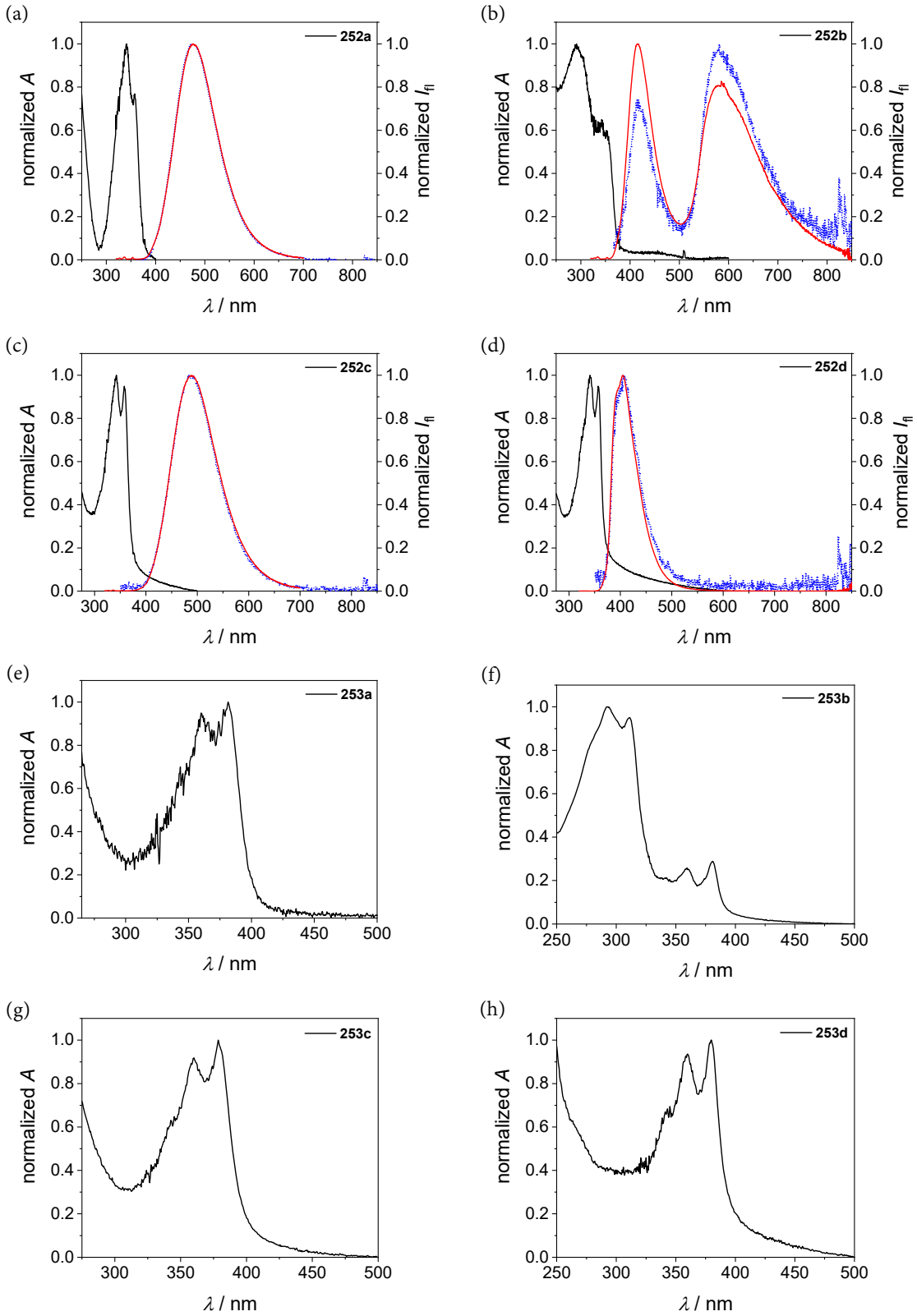

Figure A105. UV–vis absorption (black solid line; spin-coated films) and fluorescence (dotted lines, red: measurement with front face setup (λ_{ex} = 320 nm), blue: measurement with integrations sphere (λ_{ex} = 325 nm); powder samples) spectra of (a) **252a**, (b) **252b**, (a) **252c**, (b) **252d**, (c) **253a**, (d) **253b**, (e) **253c** and (f) **253d** (no fluorescence spectra for non-emissive compounds **253a–d**).

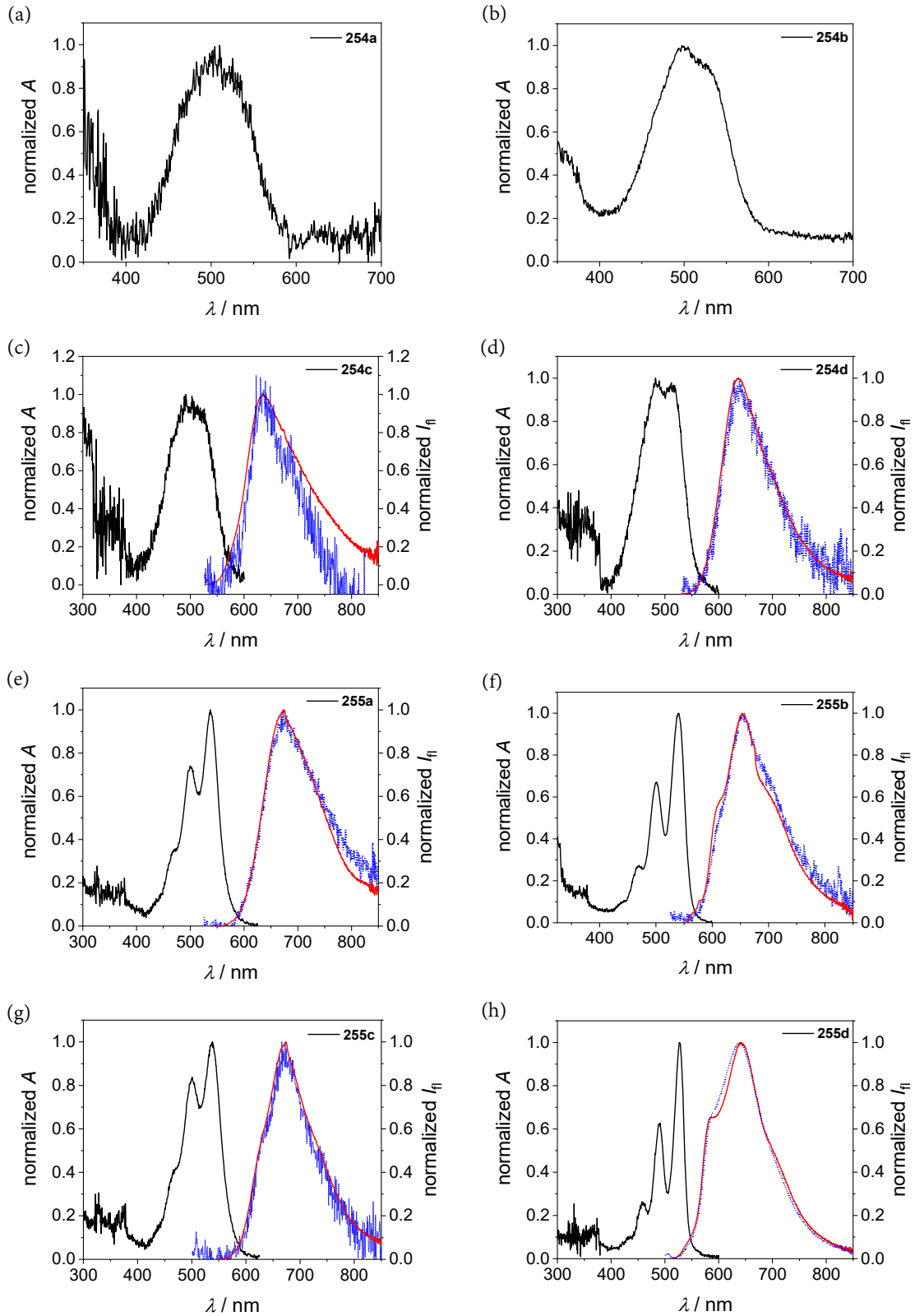

Figure A106. UV–vis absorption (black solid line; spin-coated films) and fluorescence (red solid lines: measurement in front face setup (**254**: λ_{ex} = 470 nm, **255**: λ_{ex} = 490 nm), blue dotted lines: measurement with integrations sphere (λ_{ex} = 490 nm); powder samples) spectra of (a) **254a**, (b) **254b**, (a) **254c**, (b) **254d**, (c) **255a**, (d) **255b**, (e) **255c** and (f) **255d** (no fluorescence spectra for non-emissive compounds **254a**–**b**).

Table A24. Comparison of optical properties from **252**–**255** in the solid-state.

	λ_{abs} / nm[a]	λ_{em} / nm[b]	Φ_{fl} / %[c]
252a	357, 343	478	18
252b	[d]	415, 582	3
252c	358, 343	490	7
252d	357, 341	405	1
253a	382, 360	-	<0.5
253b	381, 360, 311, 293	-	<0.5
253c	379, 360	-	<0.5
253d	380, 360	-	<0.5
254a	[d]	-	<0.5
254b	[d]	-	<0.5
254c	[d]	634	1
254d	512, 487	636	2
255a	539, 501	670	5
255b	540, 501, 469	653	3
255c	537, 501	670	5
255d	528, 489, 458	585, 640	17

[a]Absorption properties from spin-coated thin-films. [b]Fluorescence properties from bulk powder samples, which might be affected by reabsorption effects. [c]Effective fluorescence quantum yields of bulk powder samples were determined using an integration sphere. Represent the lower limit of the intrinsic fluorescence quantum yields due to reabsorption effects. [d]Precise determination not possible due to weak resolution of absorption spectra (low solubility of substrate).

Table A25. Comparison of fluorescence quantum yields from **252**–**255** in chloroform solution and bulk powder.

	Φ_{fl} ($CHCl_3$) / %[a]	Φ_{fl} (powder) / %[b]
252a	<0.5	18
252b	<0.5	3
252c	<0.5	7
252d	<0.5	1
253a	<0.5	<0.5
253b	<0.5	<0.5
253c	<0.5	<0.5
253d	<0.5	<0.5
254a	87 ± 4	<0.5
254b	86 ± 4	<0.5
254c	84 ± 4	1
254d	84 ± 4	2
255a	95 ± 2	5
255b	96 ± 1	3
255c	97 ± 1	5
255d	93 ± 2	17

[a]Fluorescence quantum yields were determined using the relative method (A < 0.05) and *N*,*N*'-bis(2,6-diisopropylphenyl)perylene-3,4:9,10-bis(dicarboximide) (Φ_{fl} ($CHCl_3$) = 1.00). [b]Fluorescence quantum yields of bulk powder samples were determined using an integration sphere.

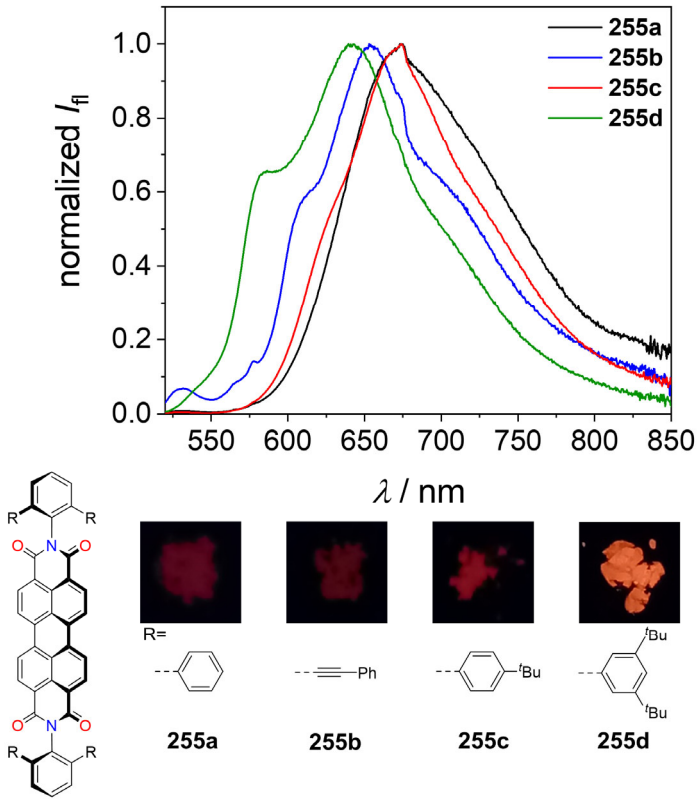

Figure A107. Solid-state (powder) fluorescence spectra of **255a–d** (top) and photographs of powder samples from **255a–d** under UV–light irradiation.

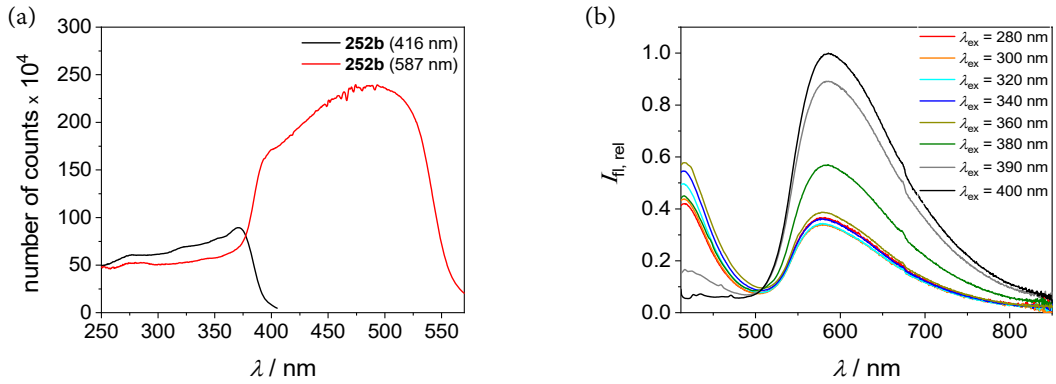

Figure A108. (a) Excitation spectra of **252b** (black line: λ_{rec} = 416 nm; red line: λ_{rec} = 587 nm). (b) Relative excitation-dependent fluorescence spectra from powder sample of **252b**.

Table A26. Determined fluorescence lifetime decays of **252a–d** (λ_{ex} = 378 nm) in powder samples.

	λ_{det} / nm	τ / ns
252a	477	τ_1 = 12.97 ± 0.64 (5.4%) τ_2 = 30.45 ± 0.07 (94.6%)
252b	416	τ_1 = 2.57 ± 0.01
	578	τ_1 = 1.00 ± 0.04 (38.0%) τ_2 = 3.39 ± 0.09 (62.0%)
252c	489	τ_1 = 6.33 ± 0.22 (7.3%) τ_2 = 18.84 ± 0.04 (92.7%)
252d	405	τ_1 = 0.32 ± 0.002 (60.5%) τ_2 = 1.90 ± 0.01 (39.5%)

NMR Spectroscopy

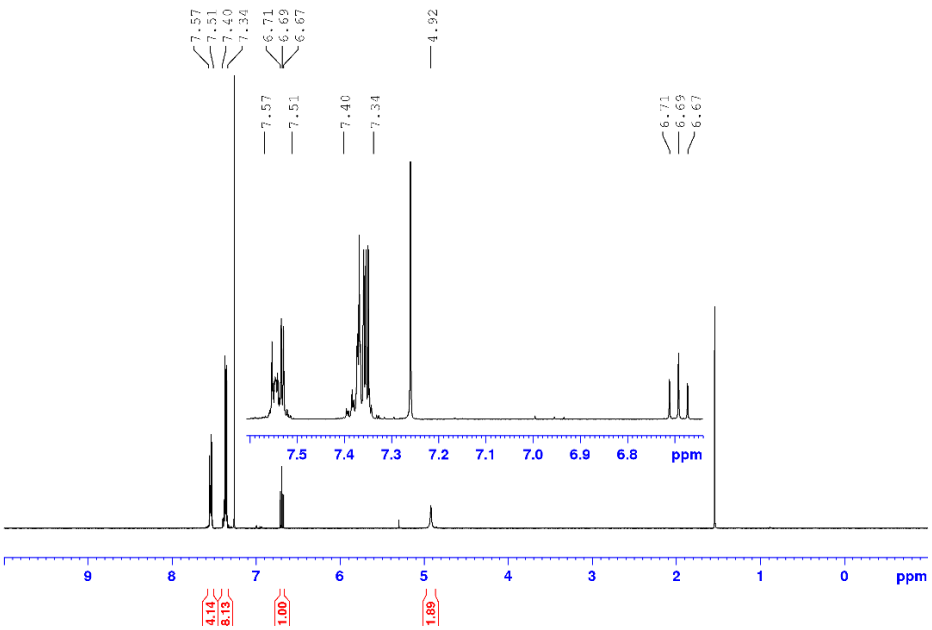

Figure A109. ^{1}H NMR (400 MHz) of **247b** in $CDCl_3$ at room temperature.

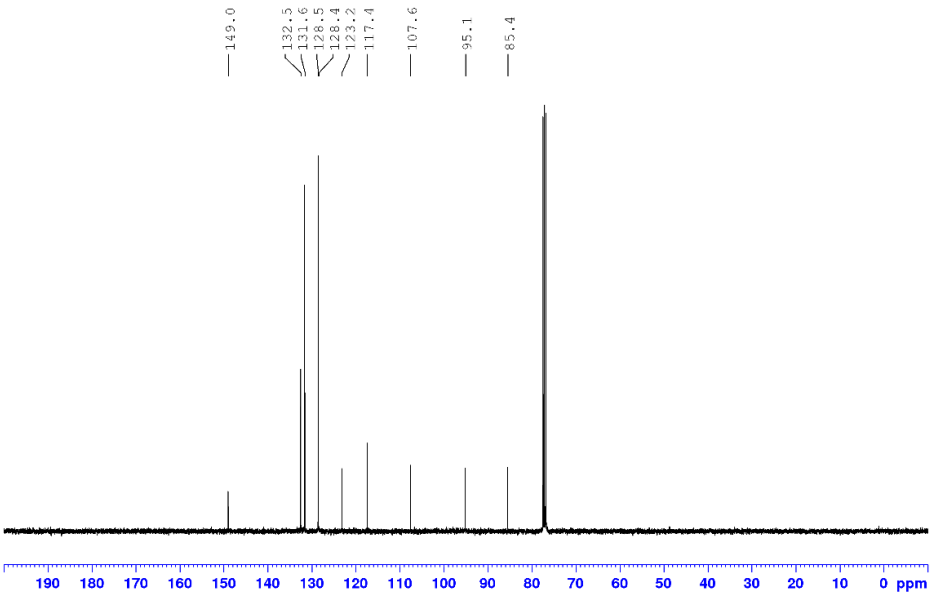

Figure A110. ^{13}C NMR (101 MHz) of **247b** in $CDCl_3$ at room temperature.

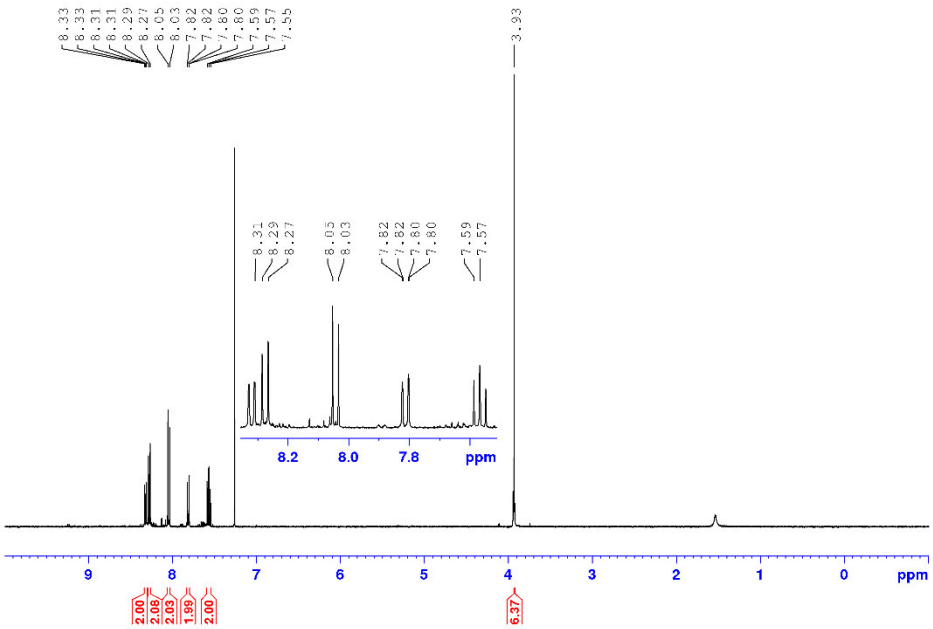

Figure A111. ^{1}H NMR (400 MHz) of **250** in $CDCl_3$ at room temperature.

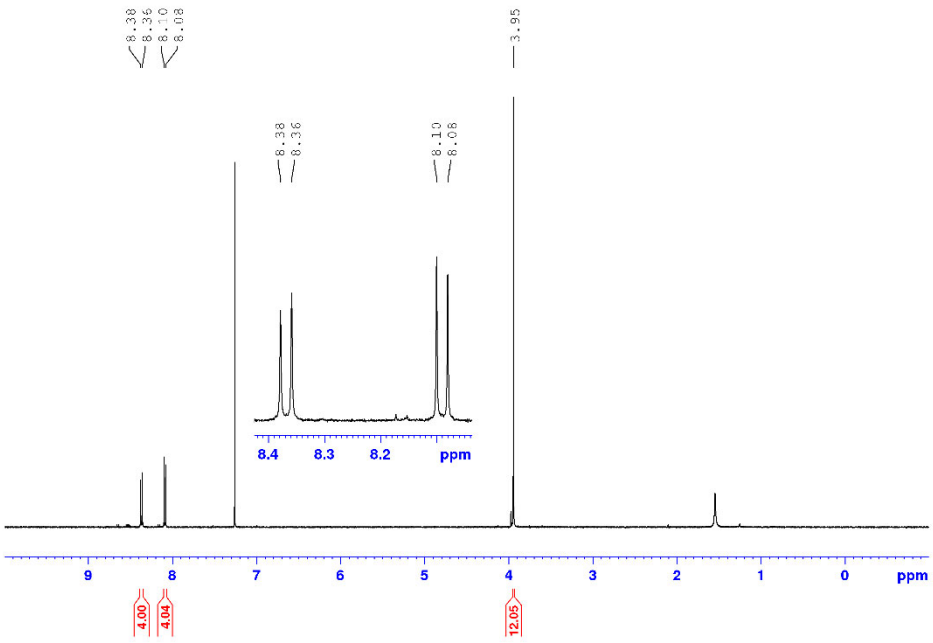

Figure A112. ^{1}H NMR (400 MHz) of **251** in $CDCl_3$ at room temperature.

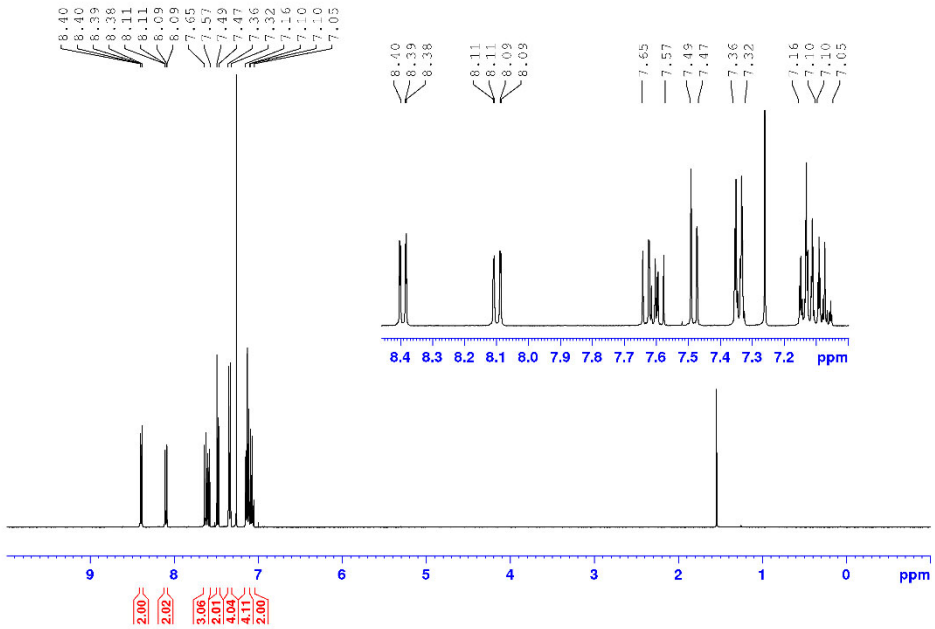

Figure A113. ^{1}H NMR (400 MHz) of **252a** in $CDCl_3$ at room temperature.

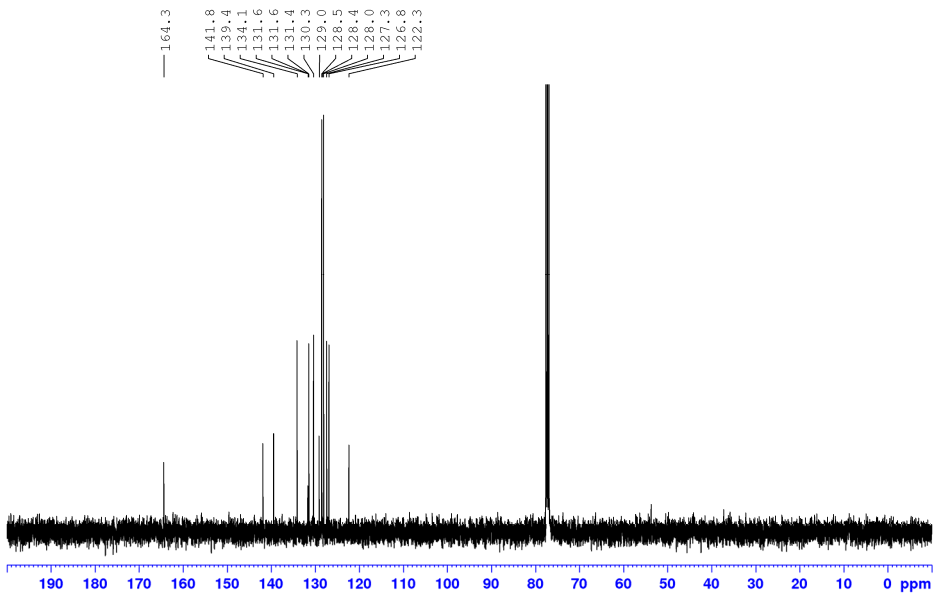

Figure A114. ^{13}C NMR (101 MHz) of **252a** in $CDCl_3$ at room temperature.

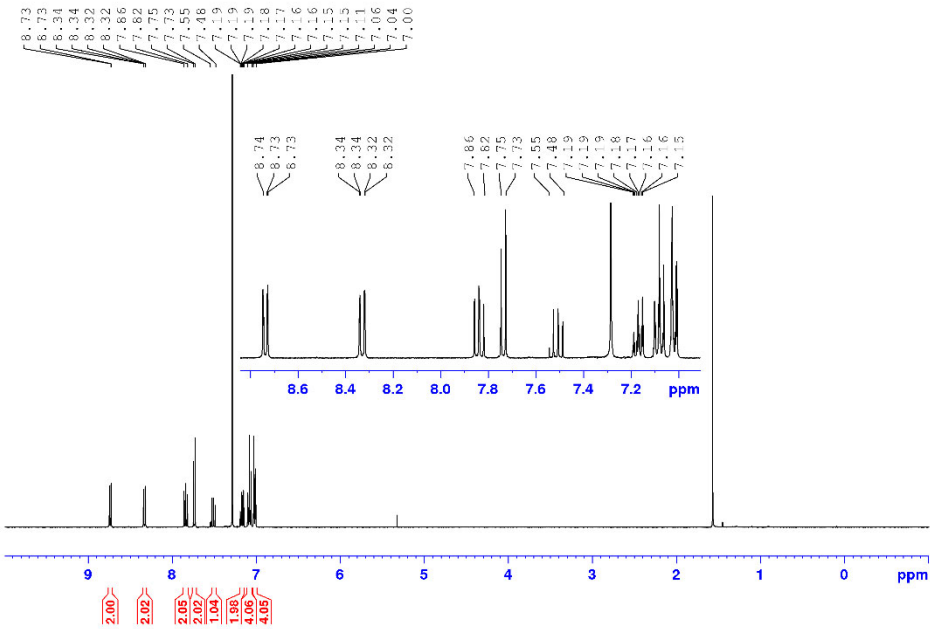

Figure A115. ^{1}H NMR (400 MHz) of **252b** in $CDCl_3$ at room temperature.

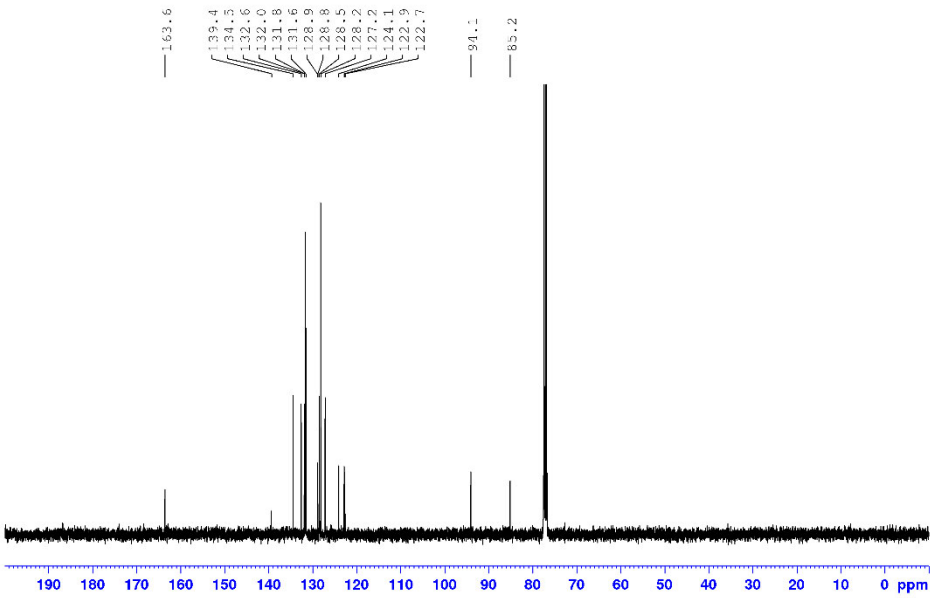

Figure A116. ^{13}C NMR (101 MHz) of **252b** in $CDCl_3$ at room temperature.

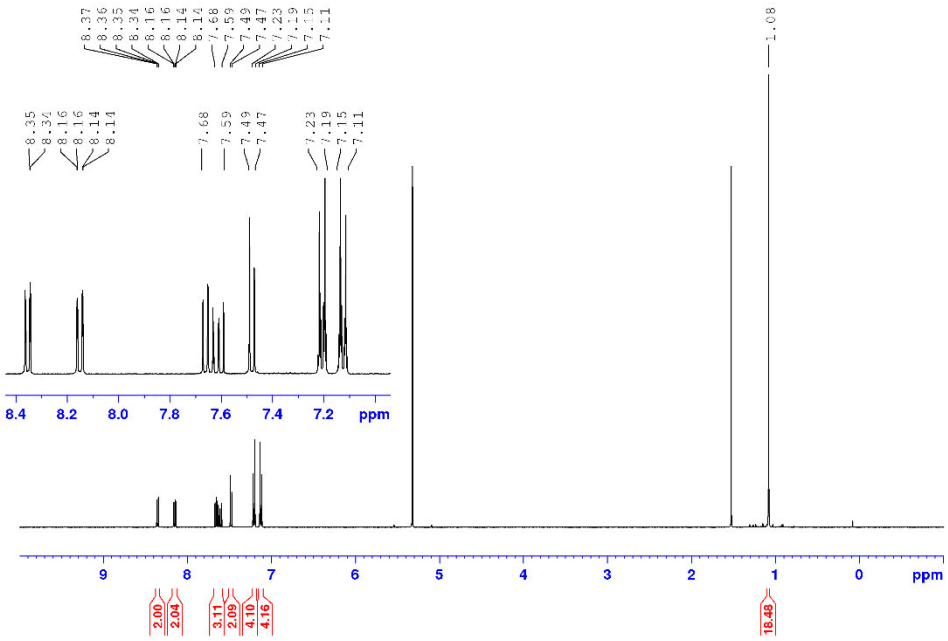

Figure A117. ^{1}H NMR (400 MHz) of **252c** in CD_2Cl_2 at room temperature.

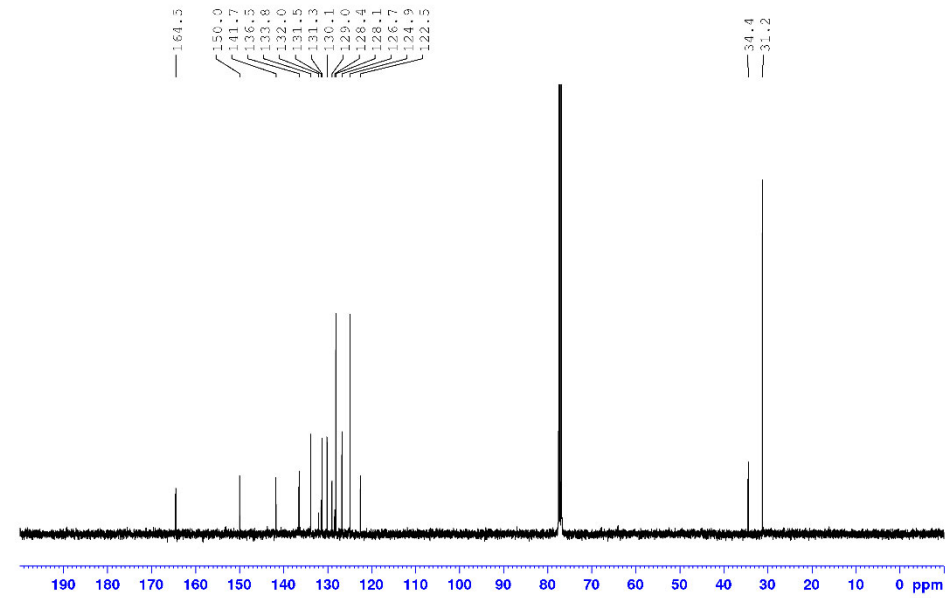

Figure A118. ^{13}C NMR (101 MHz) of **252c** in $CDCl_3$ at room temperature.

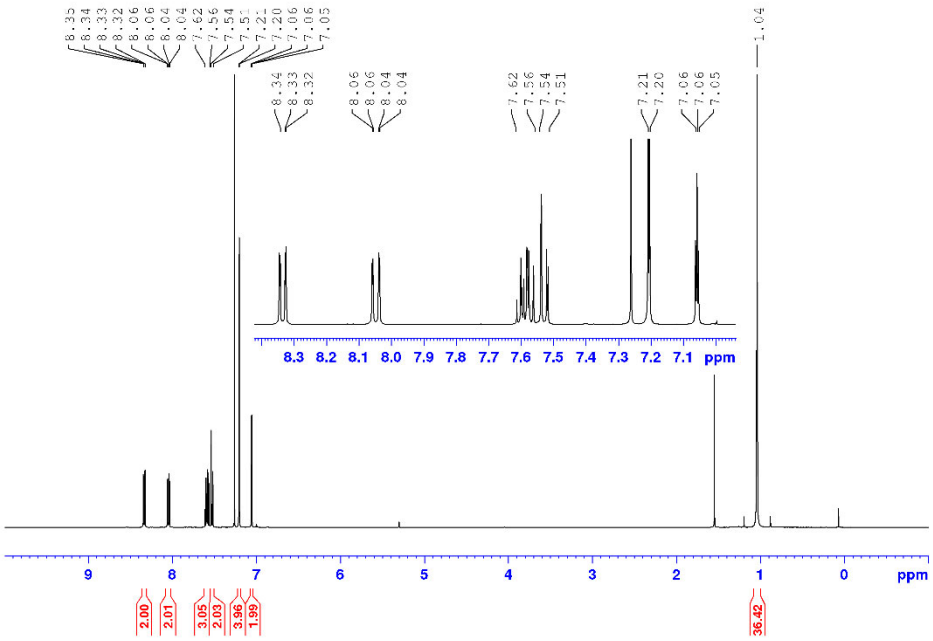

Figure A119. ^{1}H NMR (400 MHz) of **252d** in $CDCl_3$ at room temperature.

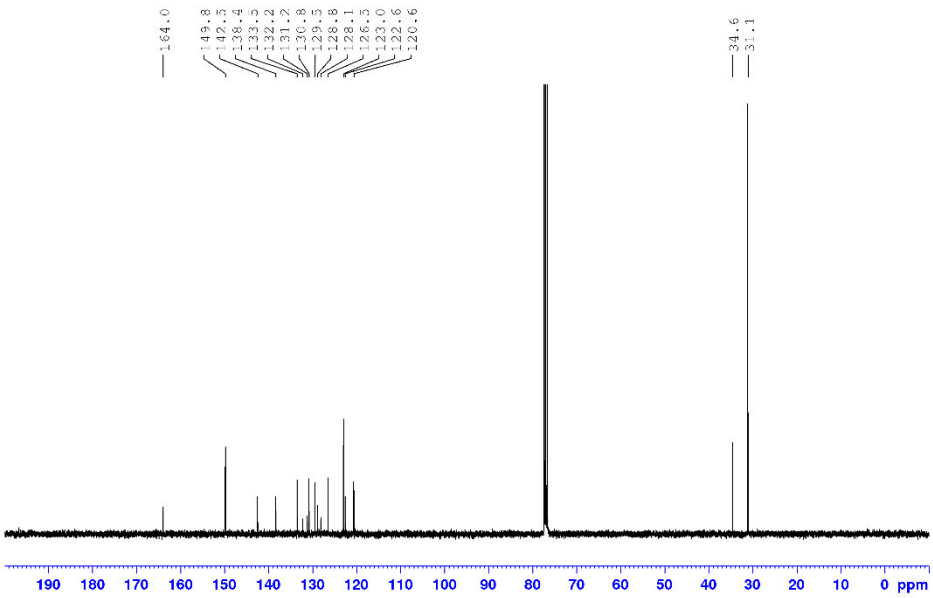

Figure A120. ^{13}C NMR (101 MHz) of **252d** in $CDCl_3$ at room temperature.

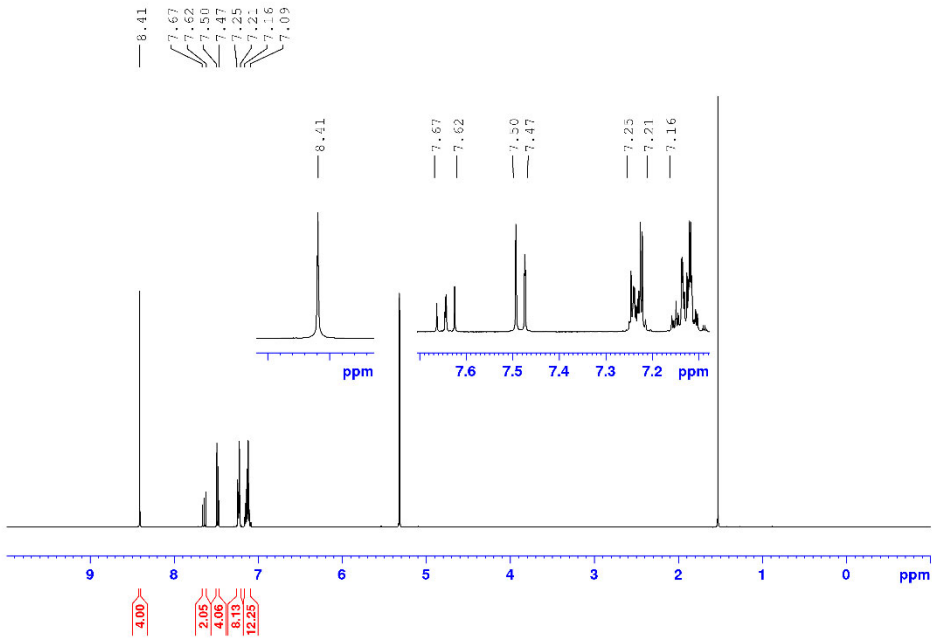

Figure A121. ^{1}H NMR (400 MHz) of **253a** in CD_2Cl_2 at room temperature.

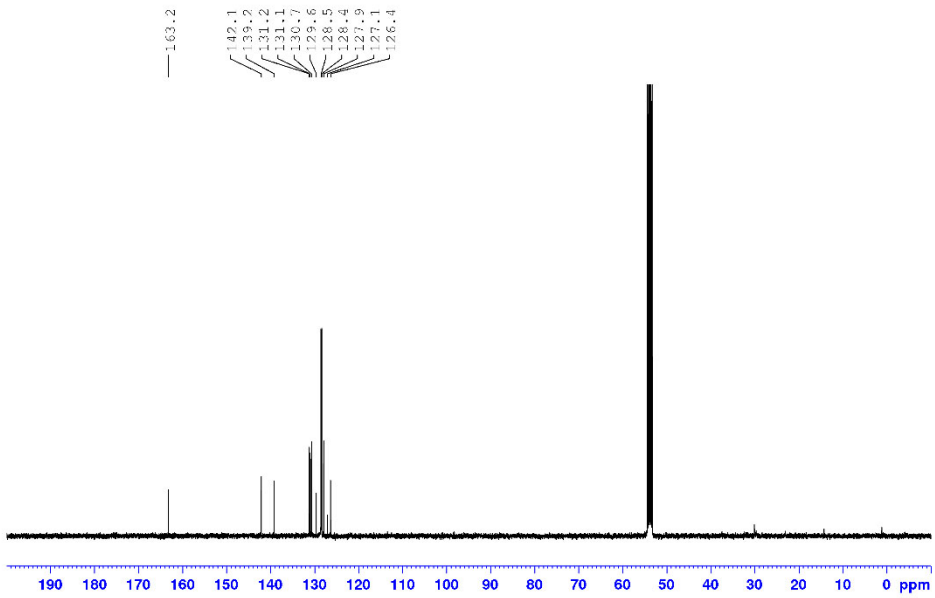

Figure A122. ^{13}C NMR (101 MHz) of **253a** in CD_2Cl_2 at room temperature.

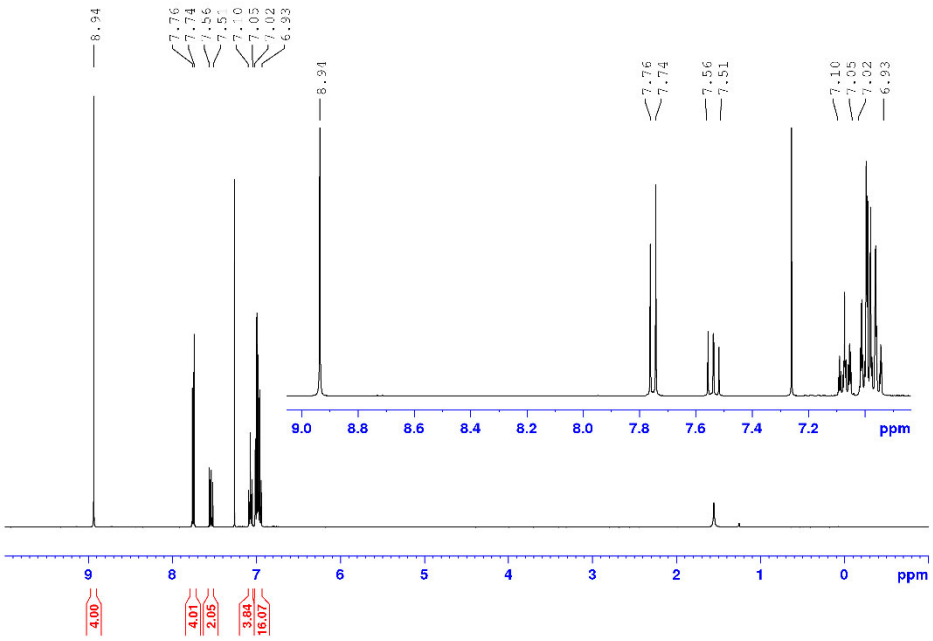

Figure A123. ^{1}H NMR (400 MHz) of **253b** in $CDCl_3$ at room temperature.

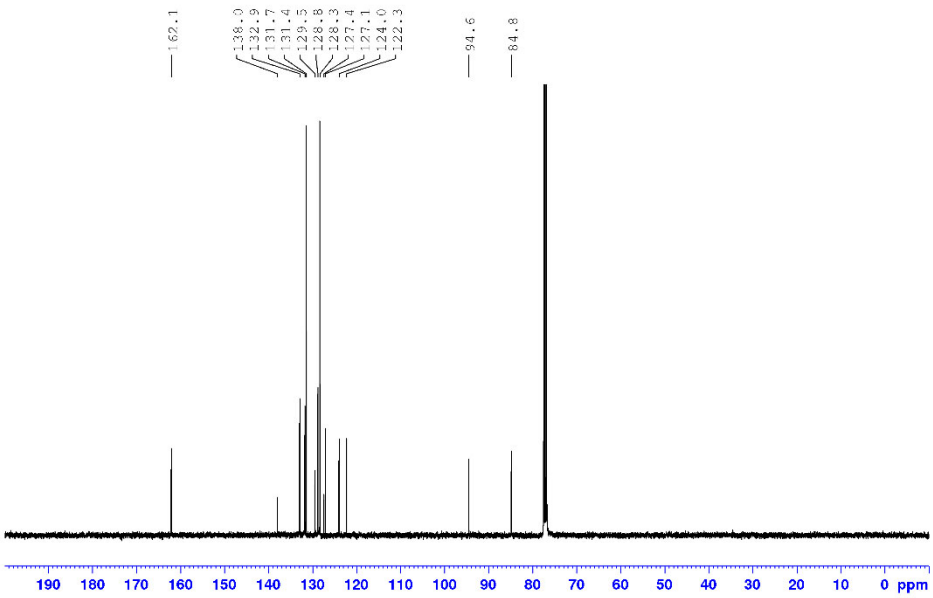

Figure A124. ^{13}C NMR (101 MHz) of **253b** in $CDCl_3$ at room temperature.

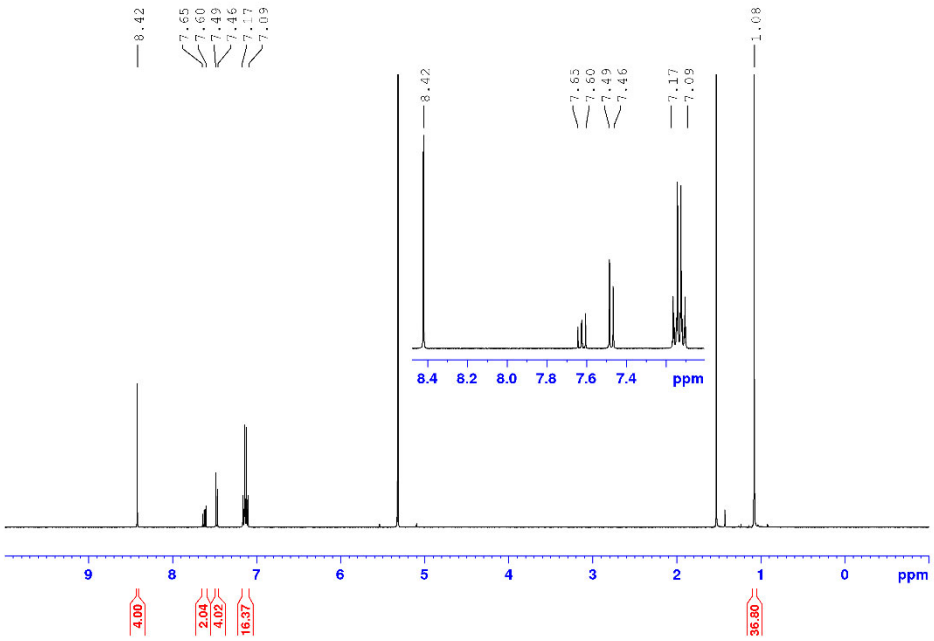

Figure A125. ^{1}H NMR (400 MHz) of **253c** in CD_2Cl_2 at room temperature.

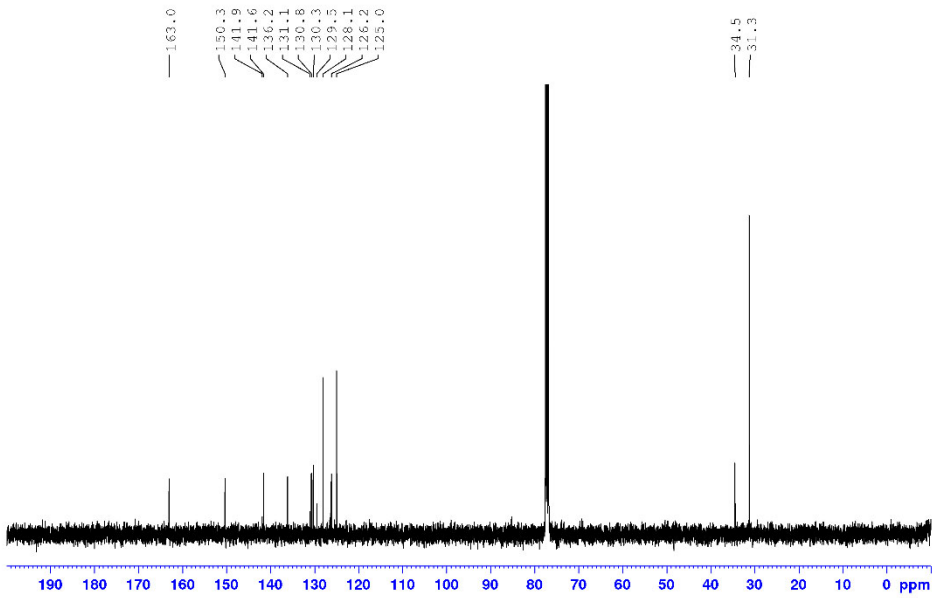

Figure A126. ^{13}C NMR (101 MHz) of **253c** in $CDCl_3$ at room temperature.

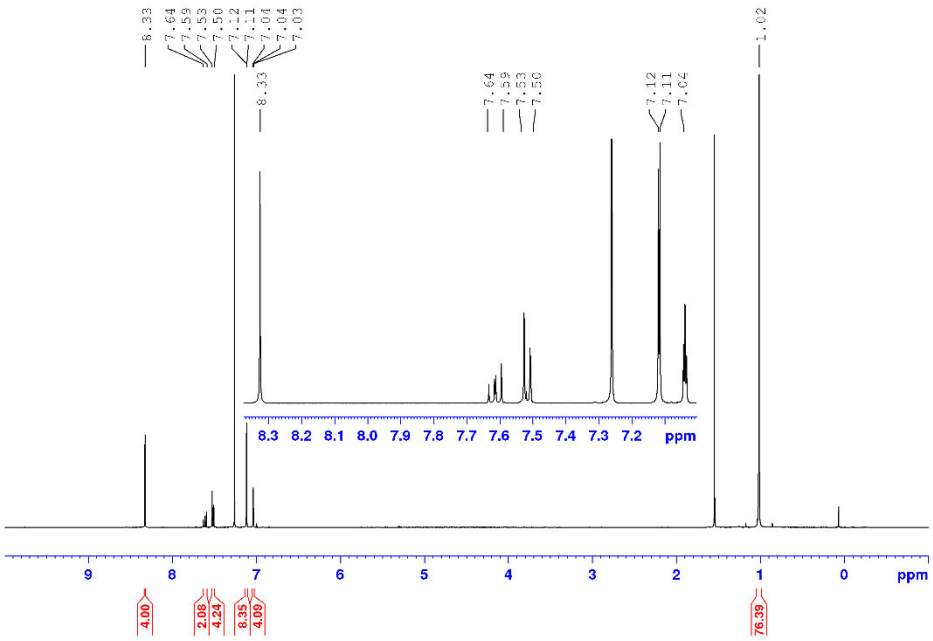

Figure A127. ^{1}H NMR (400 MHz) of **253d** in $CDCl_3$ at room temperature.

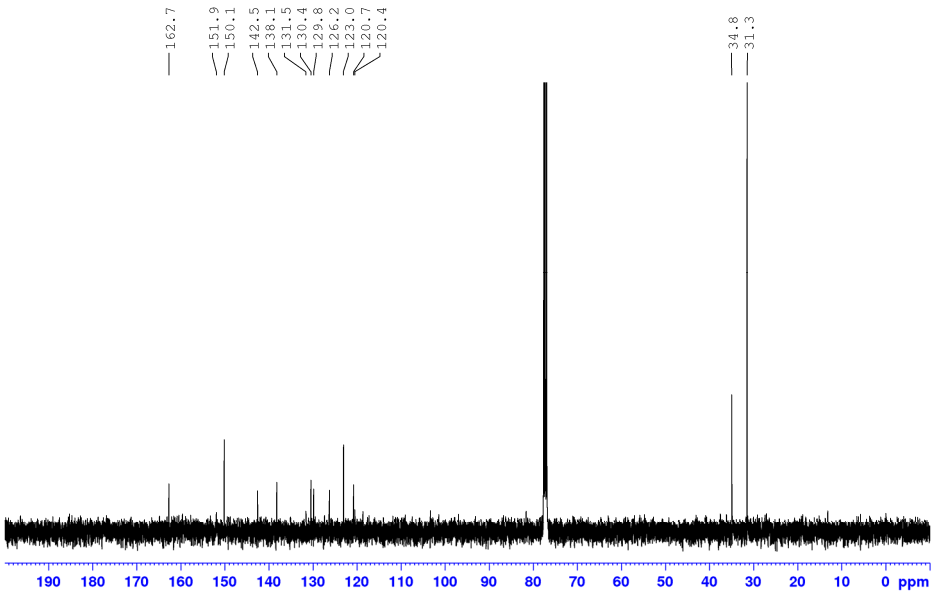

Figure A128. ^{13}C NMR (101 MHz) of **253d** in $CDCl_3$ at room temperature.

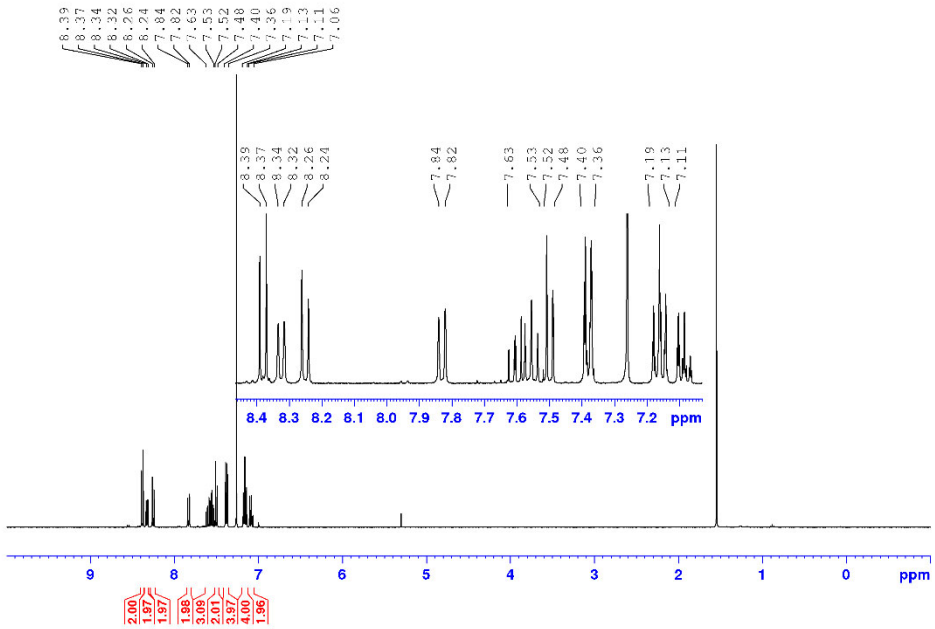

Figure A129. ^{1}H NMR (400 MHz) of **254a** in $CDCl_3$ at room temperature.

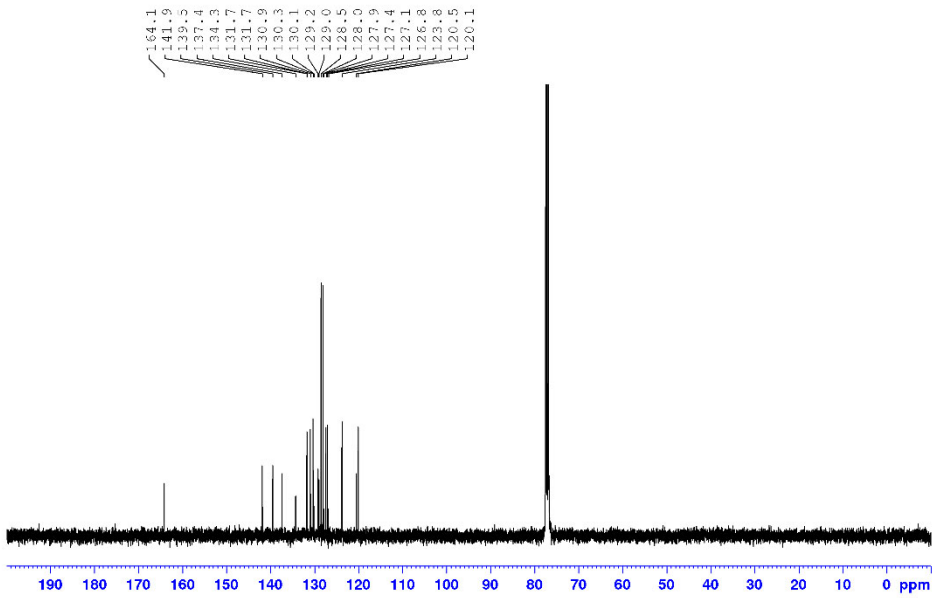

Figure A130. ^{13}C NMR (101 MHz) of **254a** in $CDCl_3$ at room temperature.

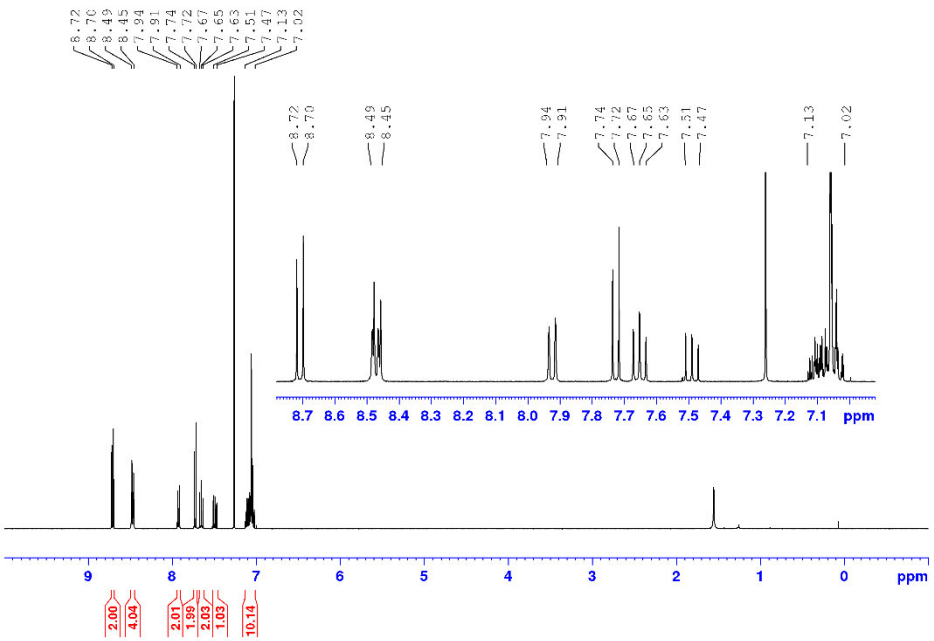

Figure A131. ^{1}H NMR (400 MHz) of **254b** in $CDCl_3$ at room temperature.

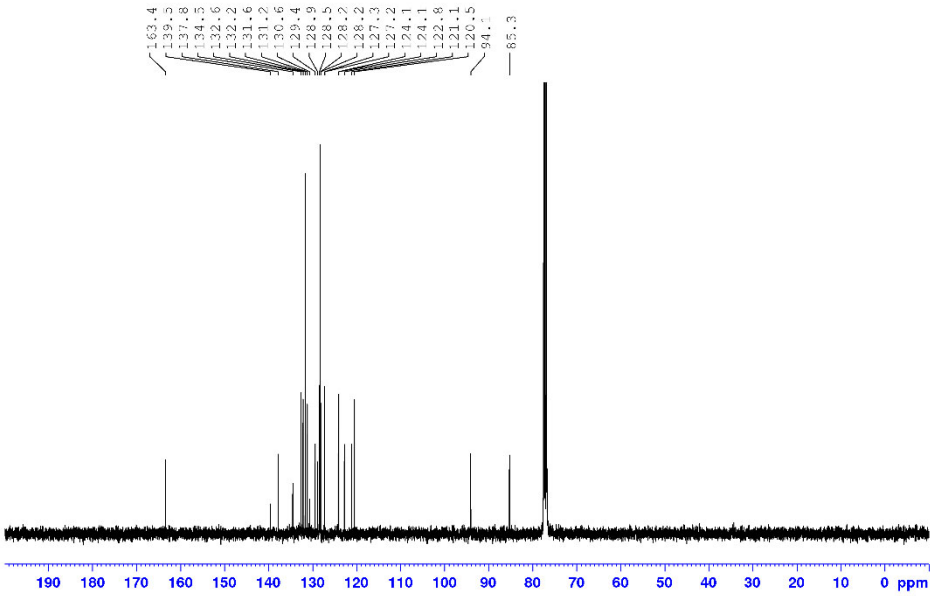

Figure A132. ^{13}C NMR (101 MHz) of **254b** in $CDCl_3$ at room temperature.

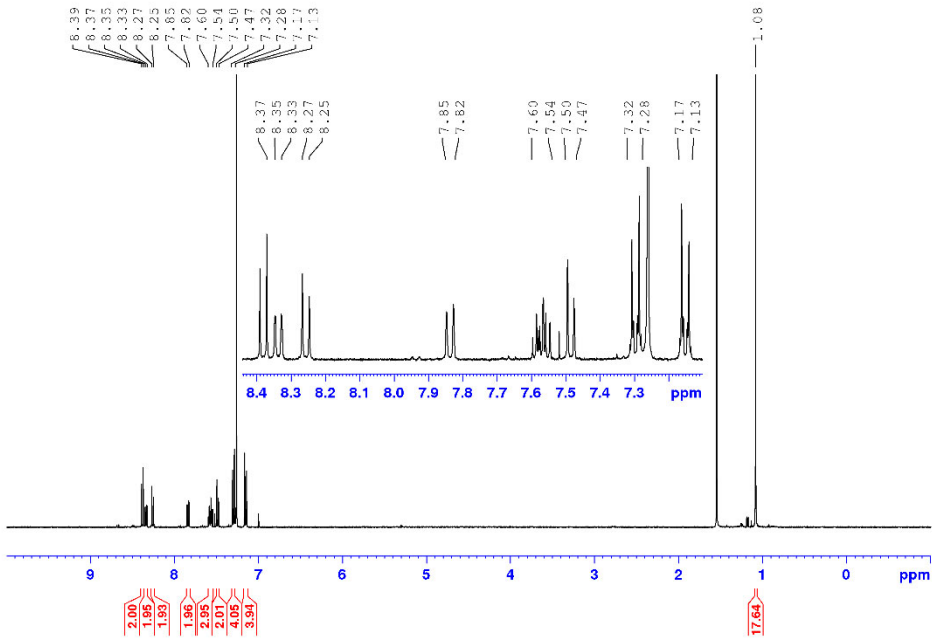

Figure A133. ^{1}H NMR (400 MHz) of **254c** in $CDCl_3$ at room temperature.

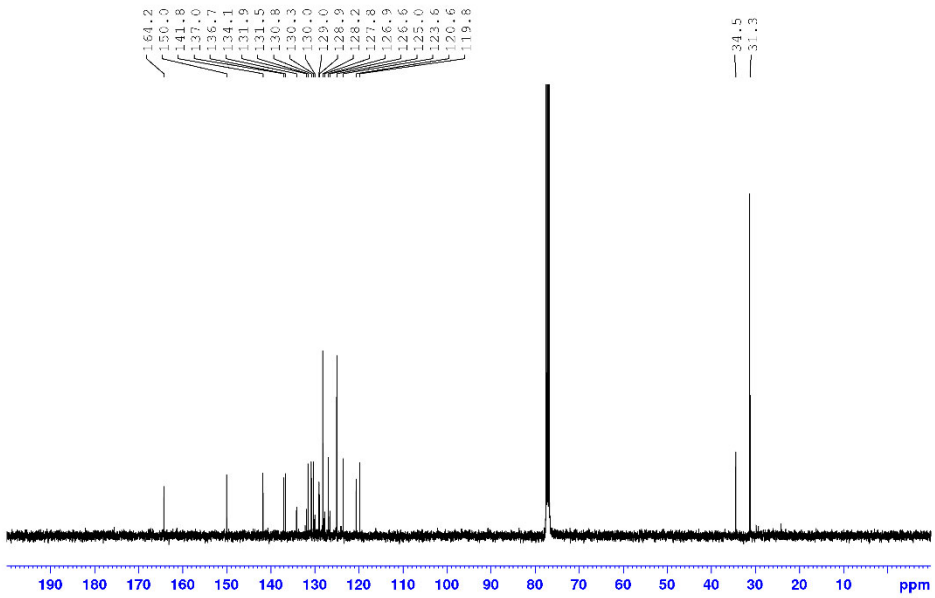

Figure A134. ^{13}C NMR (101 MHz) of **254c** in $CDCl_3$ at room temperature.

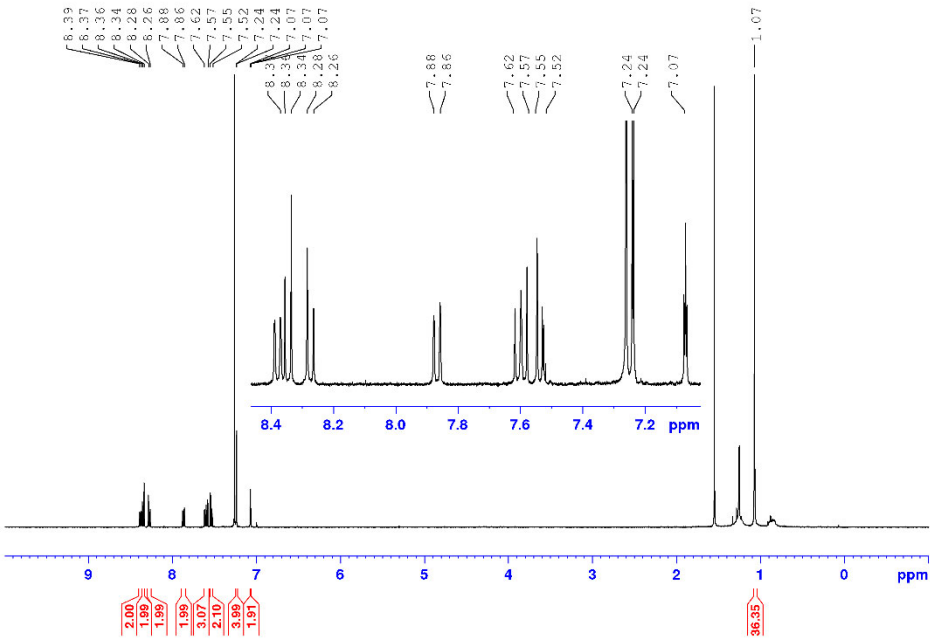

Figure A135. ^{1}H NMR (400 MHz) of **254d** in $CDCl_3$ at room temperature.

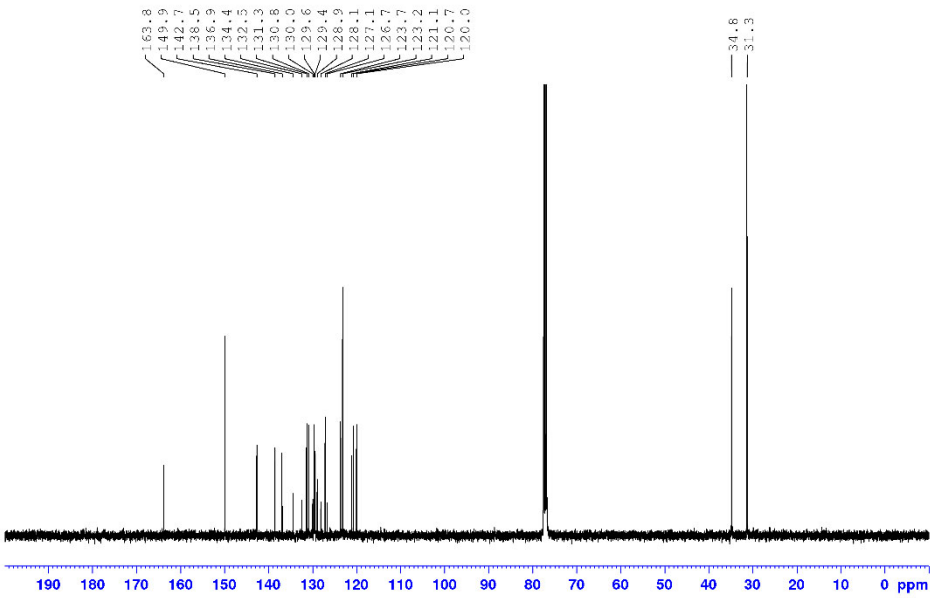

Figure A136. ^{13}C NMR (101 MHz) of **254d** in $CDCl_3$ at room temperature.

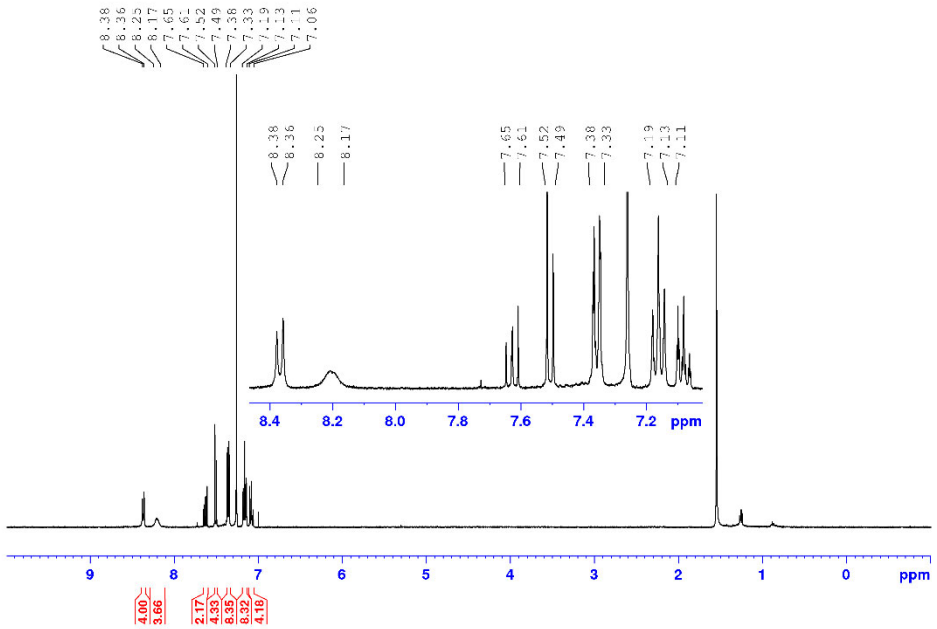

Figure A137. ^{1}H NMR (400 MHz) of **255a** in $CDCl_3$ at room temperature.

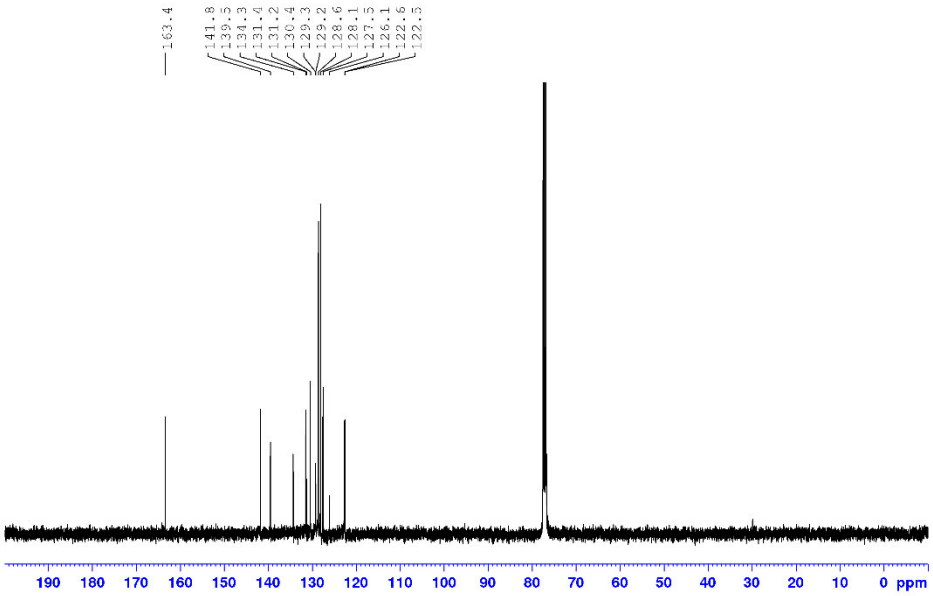

Figure A138. ^{13}C NMR (101 MHz) of **255a** in $CDCl_3$ at room temperature.

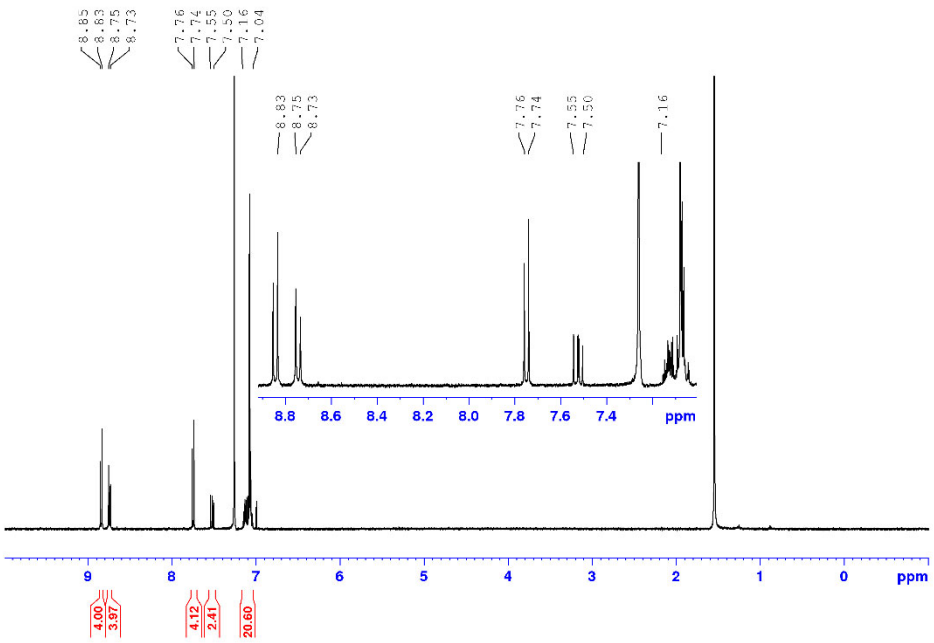

Figure A139. ^{1}H NMR (400 MHz) of **255b** in $CDCl_3$ at room temperature.

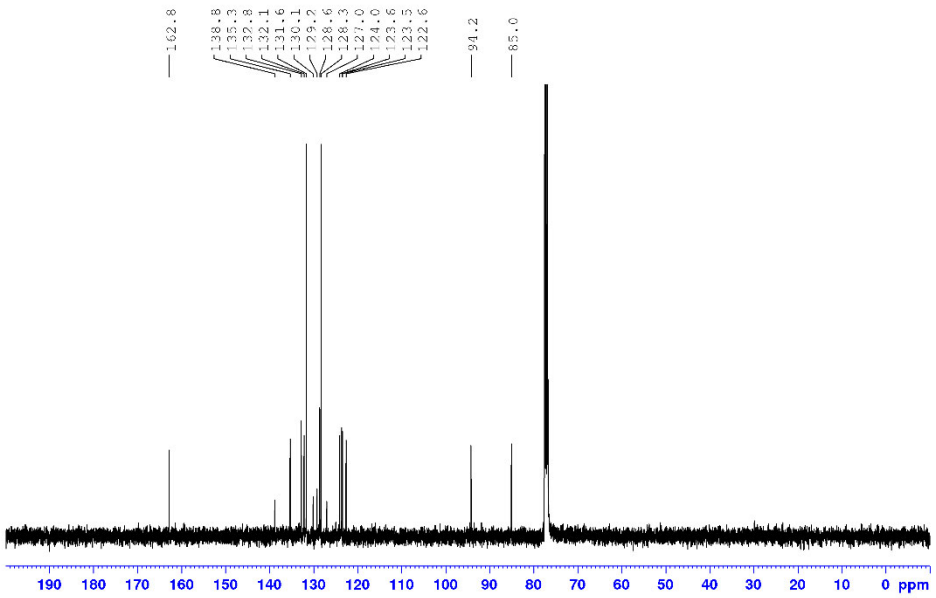

Figure A140. ^{13}C NMR (101 MHz) of **255b** in $CDCl_3$ at room temperature.

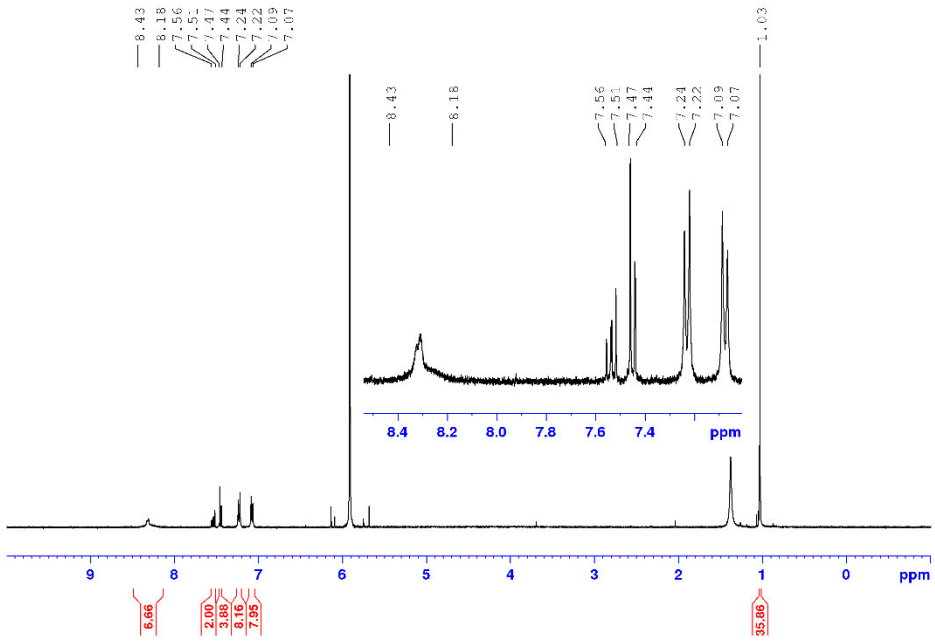

Figure A141. ^{1}H NMR (400 MHz) of **255c** in $C_2D_2Cl_4$ at 373 K.

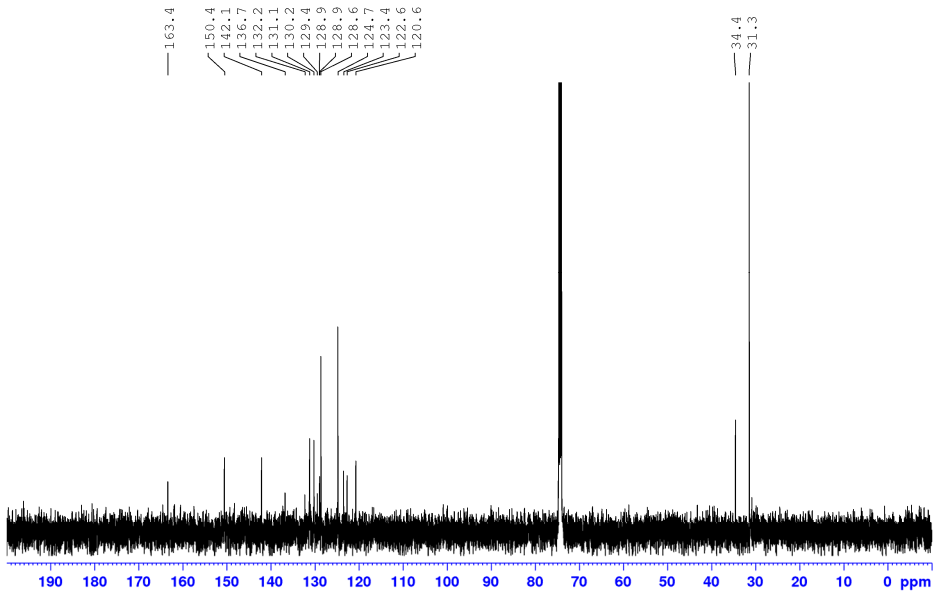

Figure A142. ^{13}C NMR (101 MHz) of **255c** in $C_2D_2Cl_4$ at 373 K.

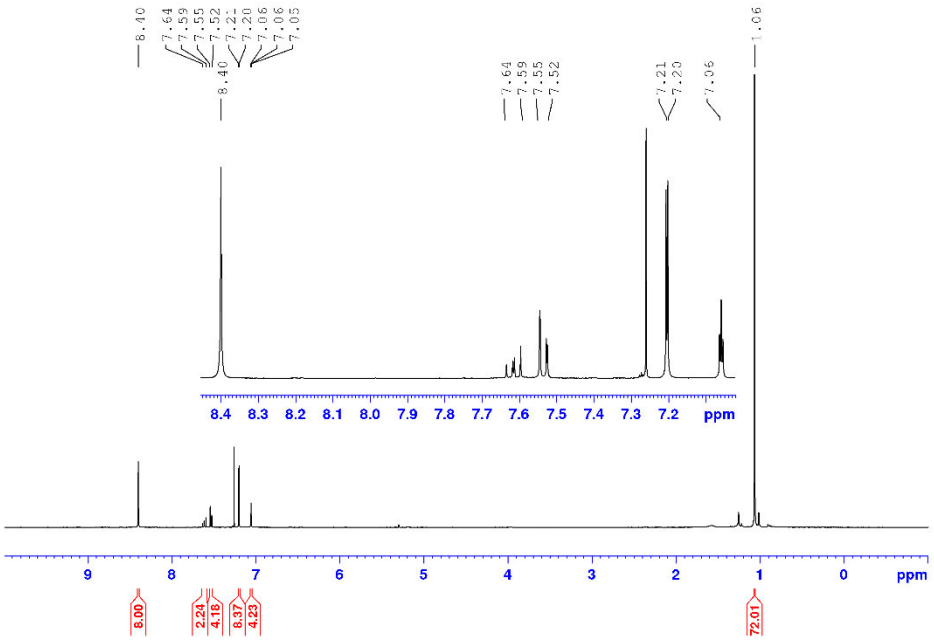

Figure A143. ^{1}H NMR (400 MHz) of **255d** in $CDCl_3$ at room temperature.

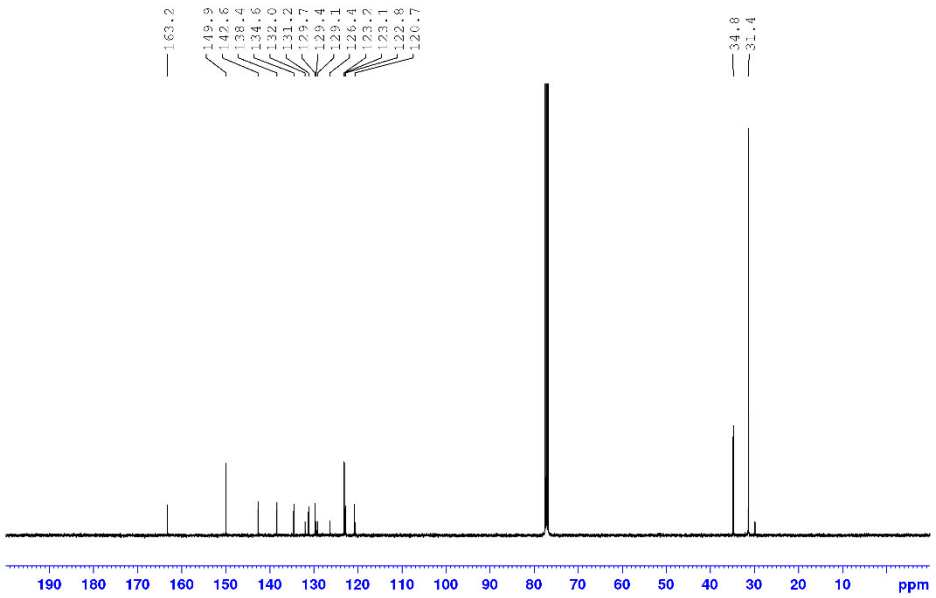

Figure A144. ^{13}C NMR (101 MHz) of **255d** in $CDCl_3$ at room temperature.

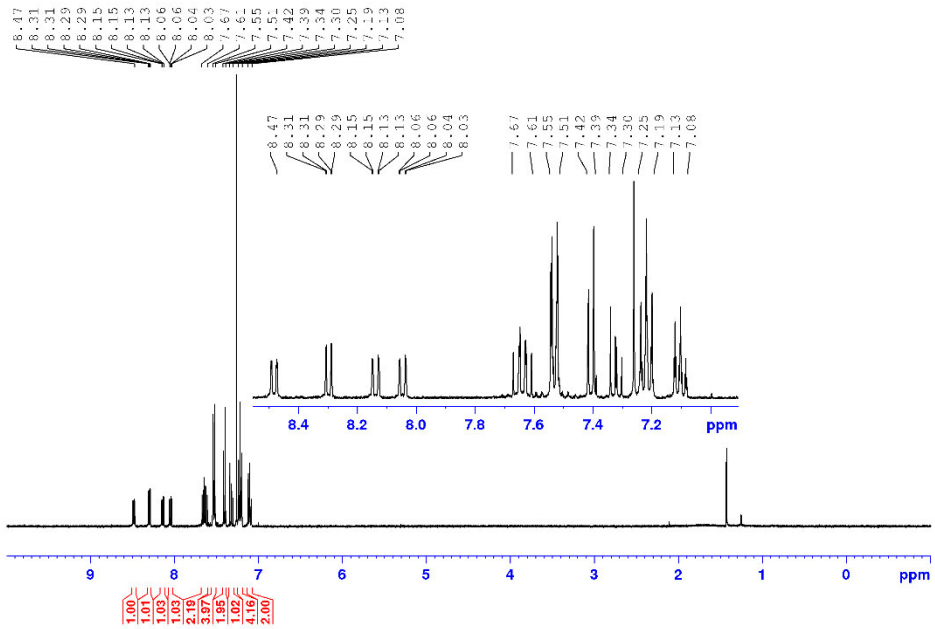

Figure A145. ^{1}H NMR (400 MHz) of **256a** in $CDCl_3$ at room temperature.

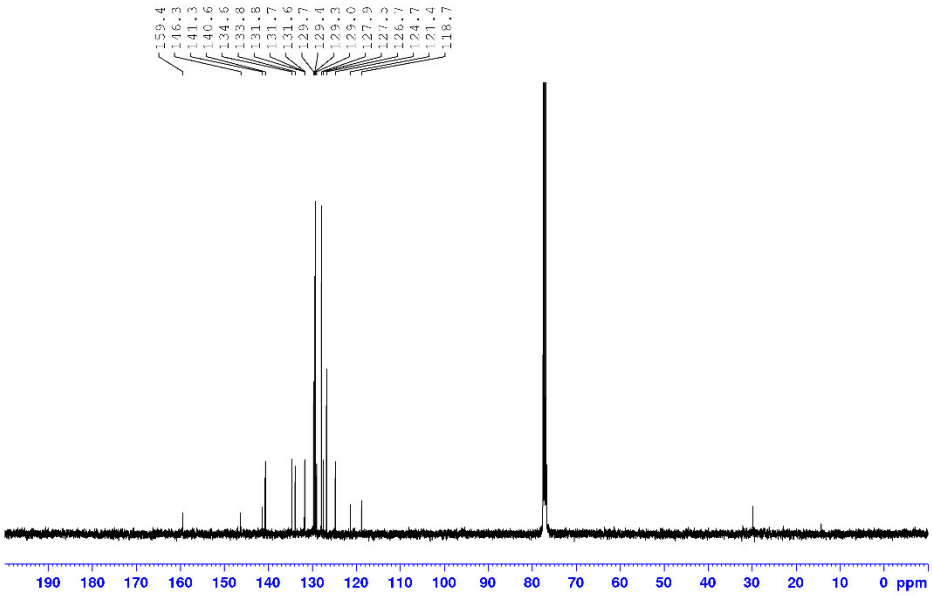

Figure A146. ^{13}C NMR (101 MHz) of **256a** in $CDCl_3$ at room temperature.

Mass Spectrometry

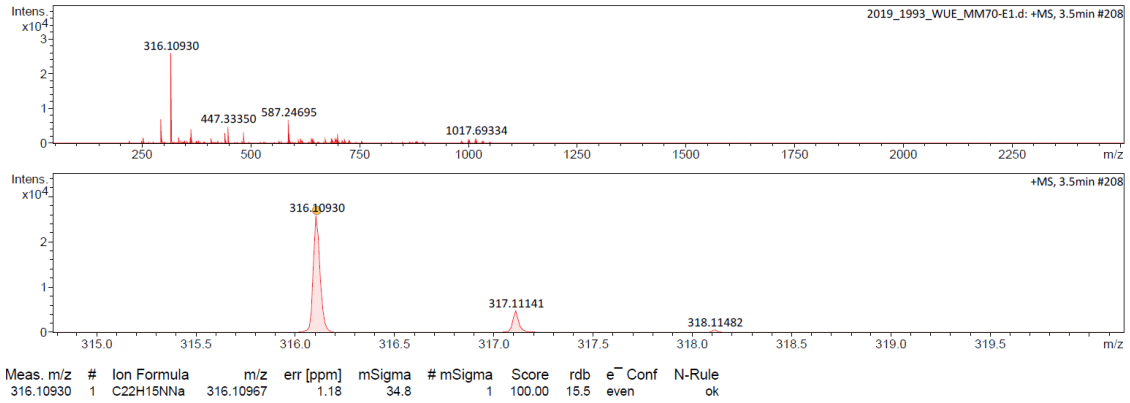

Figure A147. HRMS (ESI-TOF, positive mode, acetonitrile/chloroform) spectrum of **247b**.

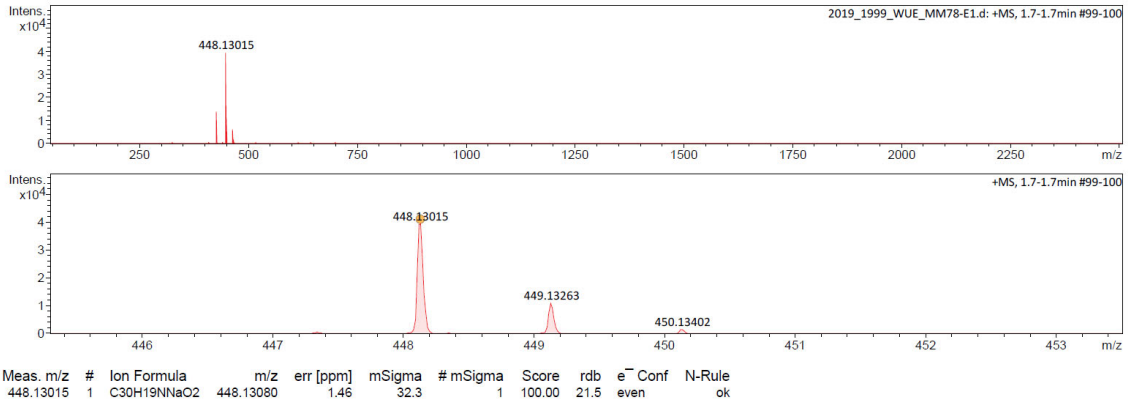

Figure A148. HRMS (ESI-TOF, positive mode, acetonitrile/chloroform) spectrum of **252a**.

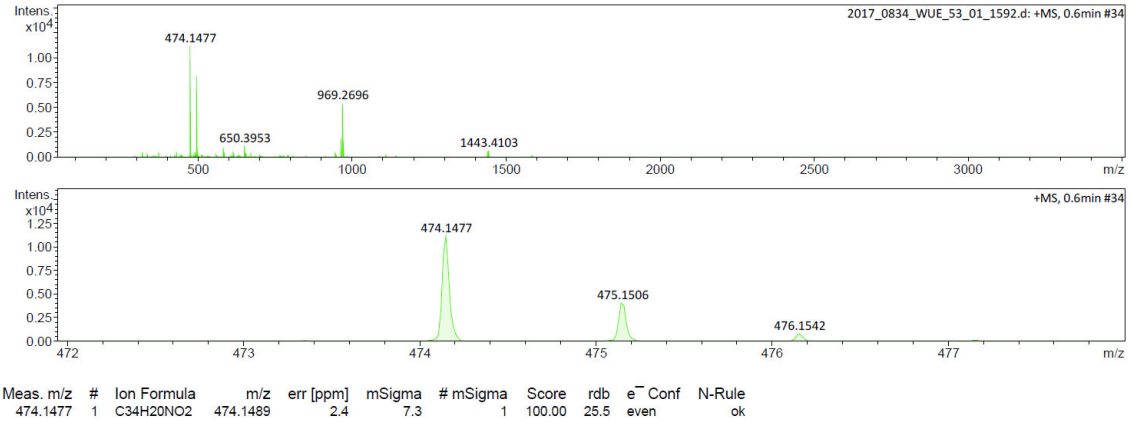

Figure A149. HRMS (ESI-TOF, positive mode, acetonitrile/chloroform) spectrum of **252b**.

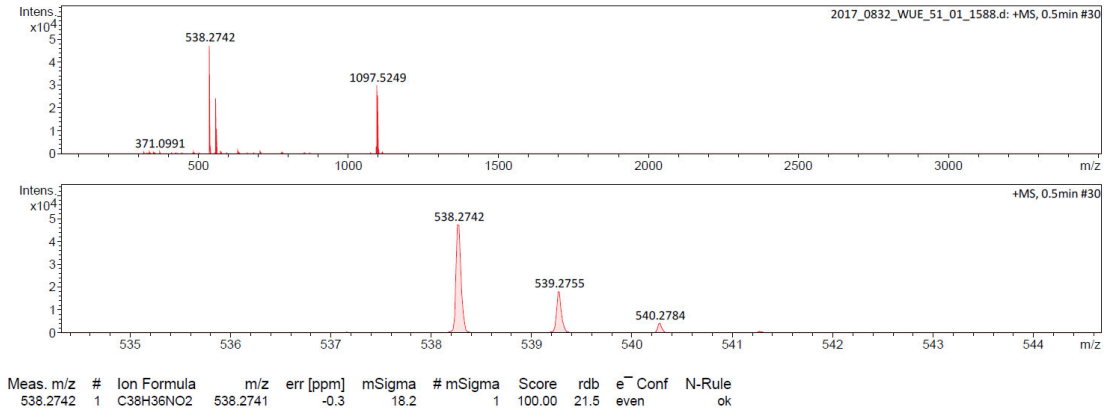

Meas. m/z	#	Ion Formula	m/z	err [ppm]	mSigma	# mSigma	Score	rdb	e⁻ Conf	N-Rule
538.2742	1	C38H36NO2	538.2741	-0.3	18.2	1	100.00	21.5	even	ok

Figure A150. HRMS (ESI-TOF, positive mode, acetonitrile/chloroform) spectrum of **252c**.

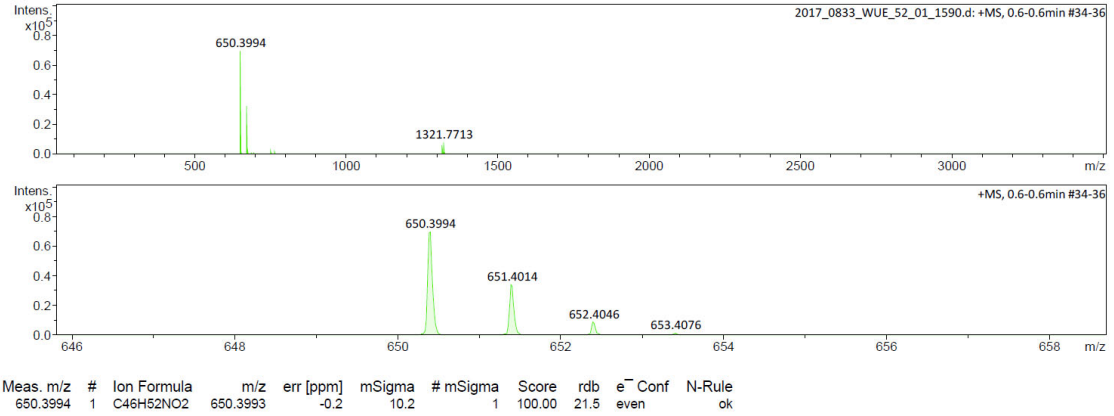

Meas. m/z	#	Ion Formula	m/z	err [ppm]	mSigma	# mSigma	Score	rdb	e⁻ Conf	N-Rule
650.3994	1	C46H52NO2	650.3993	-0.2	10.2	1	100.00	21.5	even	ok

Figure A151. HRMS (ESI-TOF, positive mode, acetonitrile/chloroform) spectrum of **252d**.

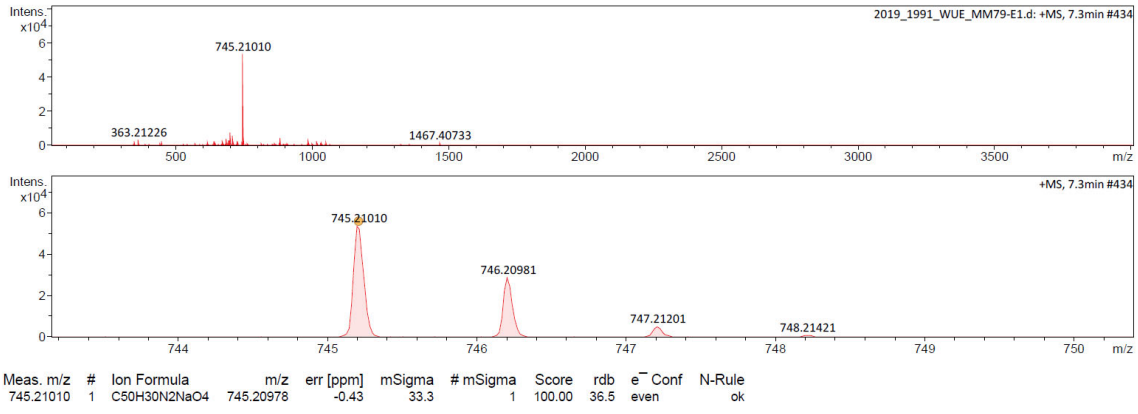

Meas. m/z	#	Ion Formula	m/z	err [ppm]	mSigma	# mSigma	Score	rdb	e⁻ Conf	N-Rule
745.21010	1	C50H30N2NaO4	745.20978	-0.43	33.3	1	100.00	36.5	even	ok

Figure A152. HRMS (ESI-TOF, positive mode, acetonitrile/chloroform) spectrum of **253a**.

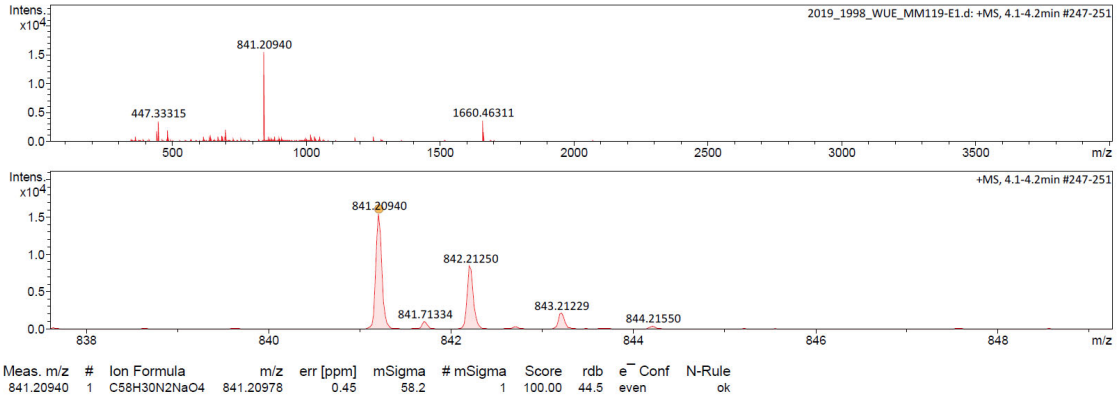

Meas. m/z	#	Ion Formula	m/z	err [ppm]	mSigma	# mSigma	Score	rdb	e⁻ Conf	N-Rule
841.20940	1	C58H30N2NaO4	841.20978	0.45	58.2	1	100.00	44.5	even	ok

Figure A153. HRMS (ESI-TOF, positive mode, acetonitrile/chloroform) spectrum of **253b**.

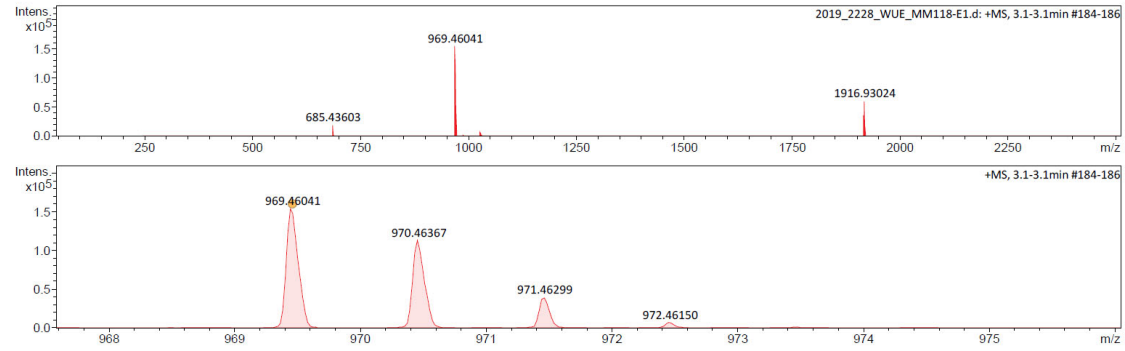

Meas. m/z	#	Ion Formula	m/z	err [ppm]	mSigma	# mSigma	Score	rdb	e⁻ Conf	N-Rule
969.46041	1	C66H62N2NaO4	969.46018	-0.24	14.1	1	100.00	36.5	even	ok

Figure A154. HRMS (ESI-TOF, positive mode, acetonitrile/chloroform) spectrum of **253c**.

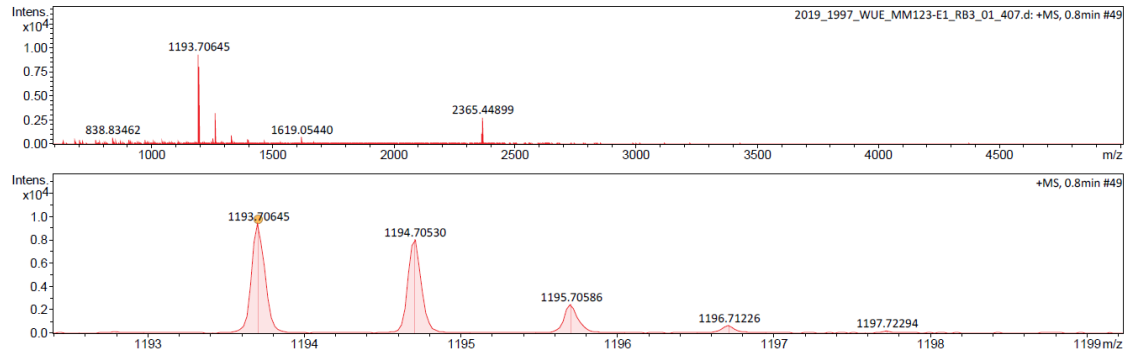

Meas. m/z	#	Ion Formula	m/z	err [ppm]	mSigma	# mSigma	Score	rdb	e⁻ Conf	N-Rule
1193.70645	1	C82H94N2NaO4	1193.71058	3.46	74.8	1	100.00	36.5	even	ok

Figure A 155. HRMS (ESI-TOF, positive mode, acetonitrile/chloroform) spectrum of **253d**.

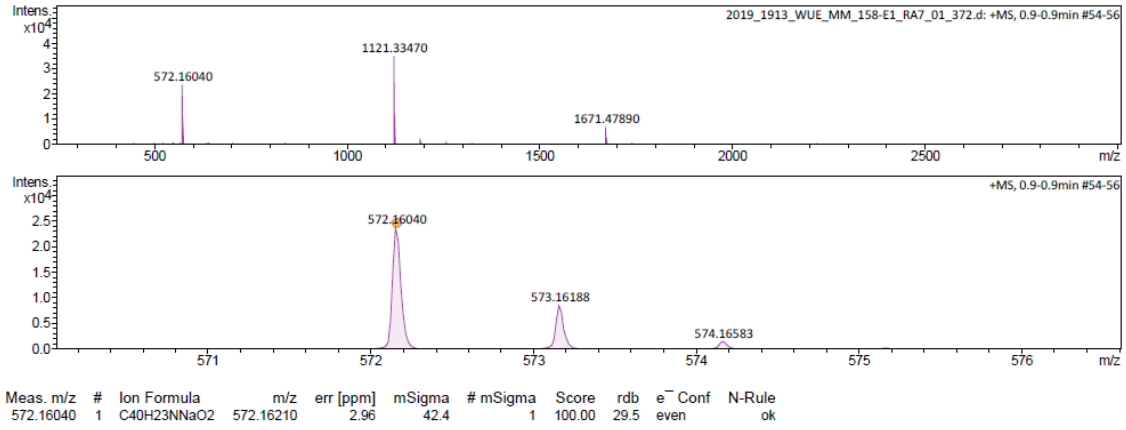

Figure A156. HRMS (ESI-TOF, positive mode, acetonitrile/chloroform) spectrum of **254a**.

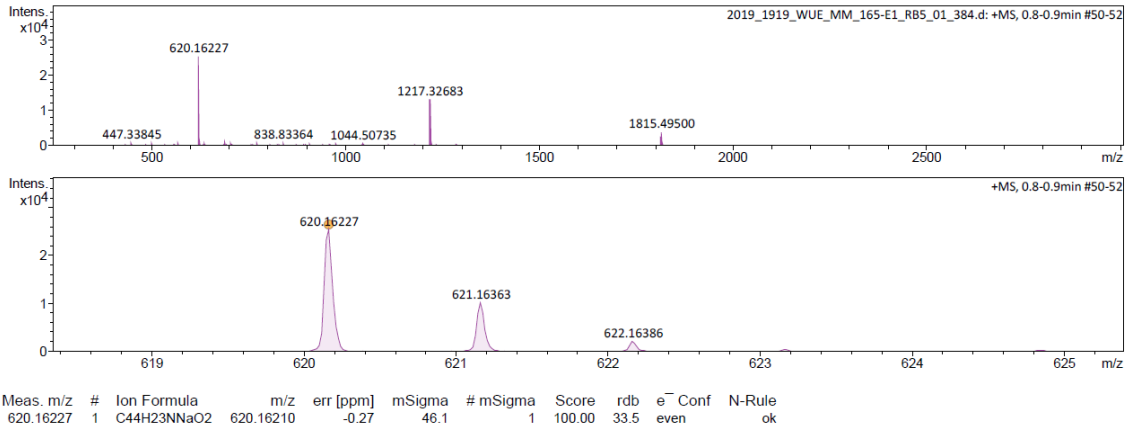

Figure A157. HRMS (ESI-TOF, positive mode, acetonitrile/chloroform) spectrum of **254b**.

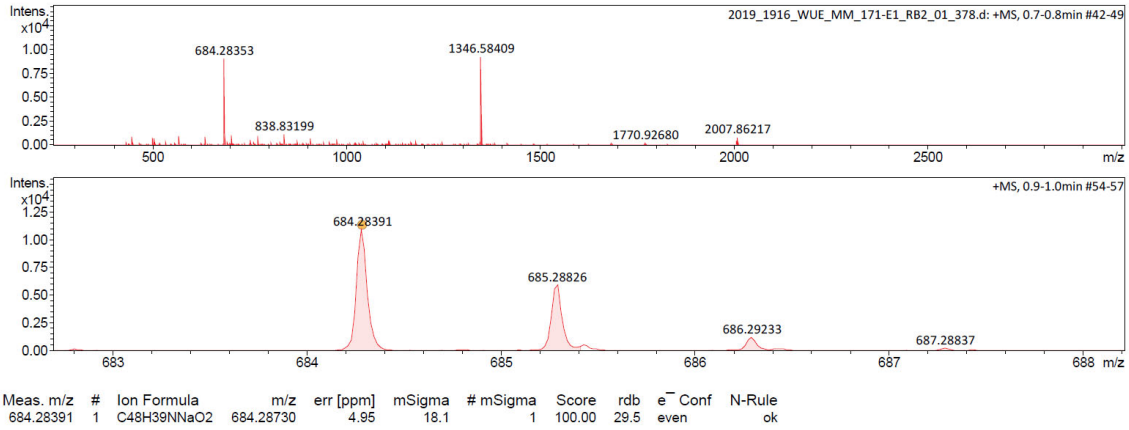

Figure A158. HRMS (ESI-TOF, positive mode, acetonitrile/chloroform) spectrum of **254c**.

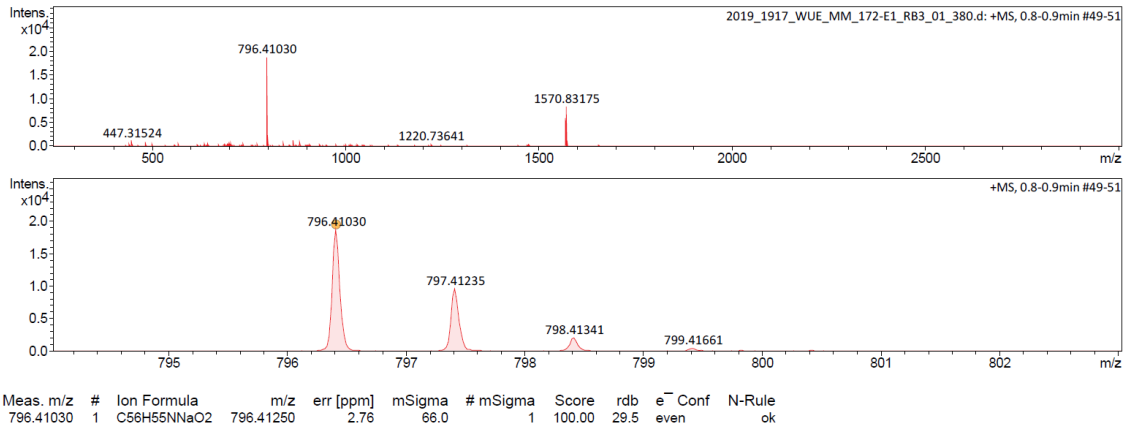

Figure A159. HRMS (ESI-TOF, positive mode, acetonitrile/chloroform) spectrum of **254d**.

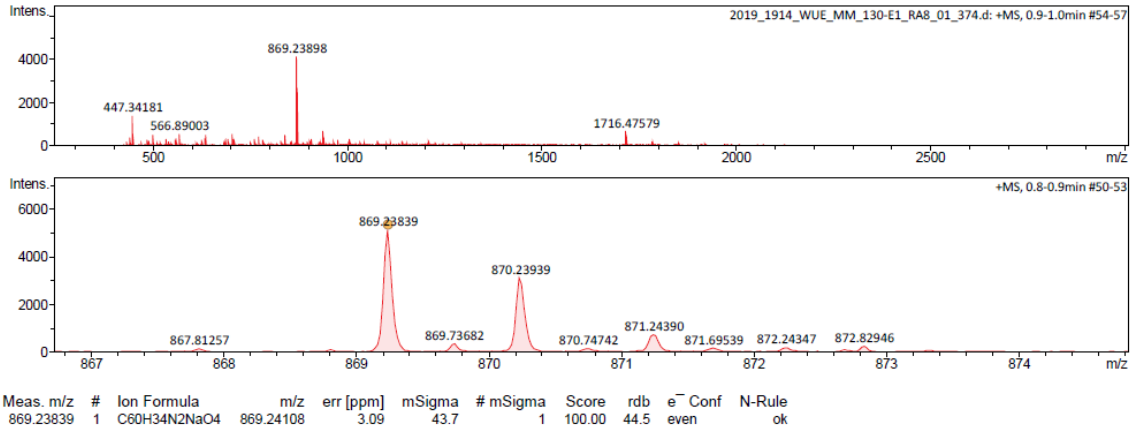

Figure A160. HRMS (ESI-TOF, positive mode, acetonitrile/chloroform) spectrum of **255a**.

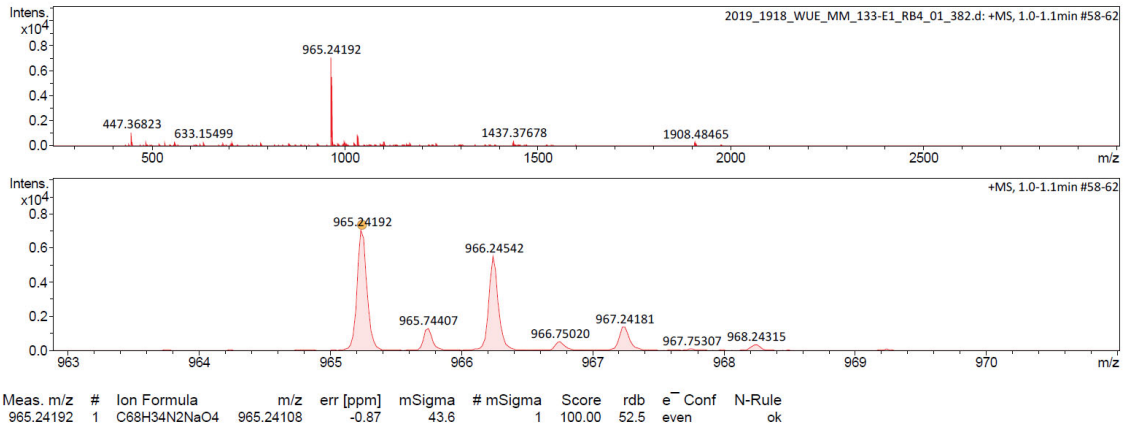

Figure A161. HRMS (ESI-TOF, positive mode, acetonitrile/chloroform) spectrum of **255b**.

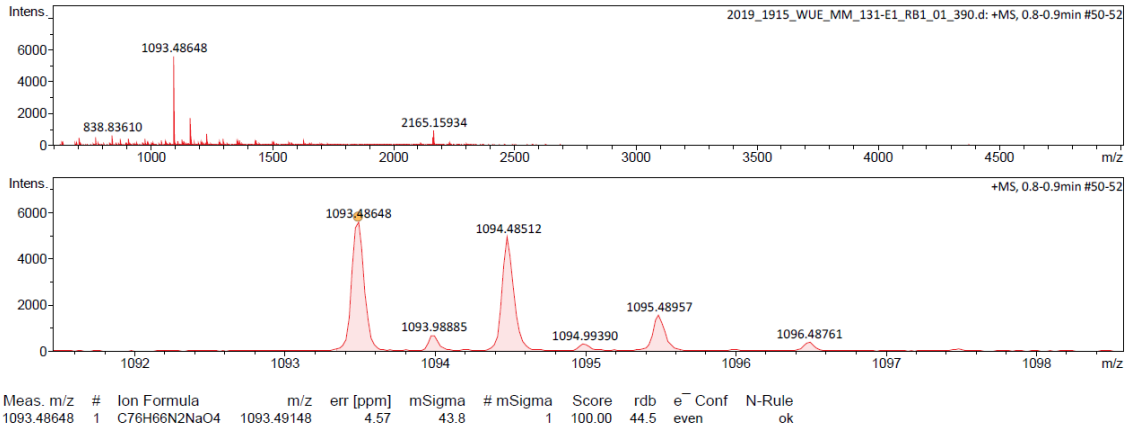

Figure A162. HRMS (ESI-TOF, positive mode, acetonitrile/chloroform) spectrum of **255c**.

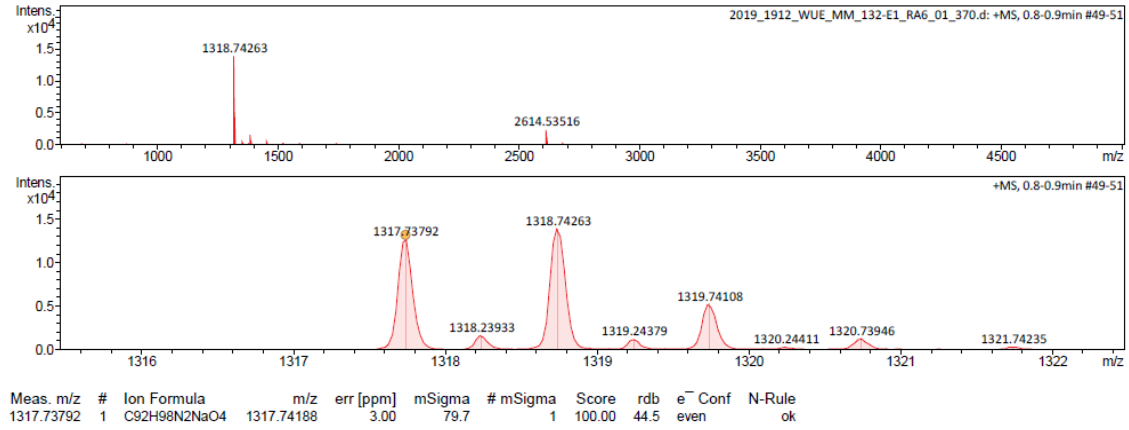

Figure A163. HRMS (ESI-TOF, positive mode, acetonitrile/chloroform) spectrum of **255d**.

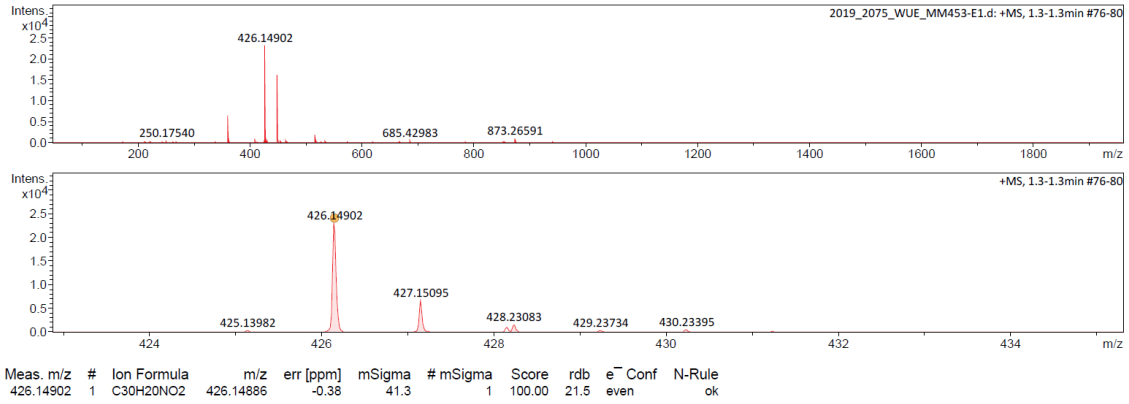

Figure A164. HRMS (ESI-TOF, positive mode, acetonitrile/chloroform) spectrum of **256a**.

10.5. Supporting Information Chapter 7

General Methods

All commercial chemicals and reagents, unless otherwise stated, were used without further purification. All air or moisture sensitive reactions were carried out under a nitrogen atmosphere by standard Schlenk techniques. Column chromatography was performed on silica gel (particle size 0.040–0.063 mm) with freshly distilled solvents as eluents. Size exclusion chromatography was conducted with SX-3 BioBeads and HPLC grade solvents (dichloromethane/methanol 9/1). Recycling gel permeations chromatography (GPC) was performed on a Shimadzu Prominence CBM and HPLC grade chloroform as solvent. Melting points were acquired with an Olympus BX41 polarization microscope and are uncorrected. ^{1}H and ^{13}C NMR spectroscopy was performed with a Bruker Avance III HD 400 MHz or Bruker Avance III HD 600 MHz spectrometer. ^{13}C NMR spectra are broad band proton decoupled. The chemical shifts (δ) are reported in parts per million (ppm), reported relative to tetramethylsilane and referenced internally to the residual proton solvent resonances (CD_2Cl_2: 5.32; $CDCl_3$: 7.26) or natural abundance carbon resonances ($CDCl_3$: 77.16). The coupling constants (J) are listed in Hertz (Hz). MALDI-TOF mass spectrometry was performed with a Bruker Daltonics autoflex II LRF or Burker Daltonics ultrafleXtreme mass spectrometer. ESI-TOF mass spectra were recorded on a Bruker Daltonics microOTOF focus spectrometer. Cyclic and differential pulse voltammetry experiments were conducted on a Bas Cellstand C3 from Bas Epsilon using a Pt disc electrode as working electrode, a Pt wire electrode as counter electrode and an Ag^+/Ag reference electrode. Measurements were performed under an Ar atmosphere, with tetrabutylammonium hexafluorophosphate ($c \sim 0.1$ M) as supporting electrolyte and dichloromethane as solvent. The ferrocenium/ferrocene (Fc^+/Fc) redox couple was used as internal reference for the determination of the redox potentials. UV–vis absorption and fluorescence measurements were conducted with spectroscopic grade solvents. UV–vis absorption spectroscopy were recorded with a Jasco V-770-ST spectrometer. Fluorescence spectroscopy was performed with a FLS980 Edinburgh fluorescent instrument. For lifetime measurements a pulsed laser diode (λ_{ex}= 505 nm) was used. Fluorescence quantum yields were determined with the relative method (A < 0.05) and using *N,N′*-bis[2,6-diisopropylphenyl]perylene-3,4:9,10-bis(dicarboximide) (Φ_{fl} = 100% in chloroform) as reference. Isothermal titration calorimetry experiments were conducted with a MicroCal VP-iTC calorimeter from GE Healthcare. Single crystal X-ray crystallography were performed on a Bruker D8 Quest Diffractometer with a PhotonII detector using Cu K_α radiation. The structures were solved using direct methods, expanded with Fourier techniques and refined using the SHELX software package.[395] Hydrogen atoms were assigned idealized positions and were included in calculation of structure factors. All non-hydrogen atoms were refined anisotropically.

The refinement in nearly all solved structures showed additional heavily disordered solvent molecules. Their respective electron-density was removed using the SQUEEZE[407] routine as implemented in the PLATON software.[408]

The catalyst tris(dibenzylideneacetone)dipalladium(0)-chloroform adduct $[Pd_2(dba)_3]\cdot CHCl_3$,[391] **247c**,[402] **258**,[409] **260**,[410] ovalene[411] and hexabenzocoronene[412] were synthesized according to the literature. All applied guests were either recrystallized or sublimed before used.

Synthesis

***N*-(2,6-Bis-(4-*tert*-butylphenyl)phenyl)-4,5-dibromo-1,8-naphthalene imide (259)**

The amine **247c** (50.0 mg, 140 µmol, 1.0 equiv) was dissolved in dry THF (2.0 mL) under a nitrogen atmosphere and cooled to –78 °C. Subsequently, an *n*-BuLi solution (175 µL, 1.6 M in *n*-hexane, 280 µmol, 2.0 equiv) was added and the reaction mixture was stirred for 1 hour at –78 °C. The solution was allowed to warm-up to room temperature and anhydride **258** (49.8 mg, 140 µmol, 1.0 equiv) was added. The mixture was heated to 75 °C for 6 hours and water (12.6 µL, 852 µmol, 5.0 equiv) was added carefully. The reaction mixture was stirred for another 12 hours at 75 °C and then cooled to room temperature. The solvent was removed under reduced pressure and the crude product was purified by column chromatography (gradient of cyclohexane/dichloromethane from 2/1 to 1/1) and washed with *n*-hexane and methanol. The product was dried under high vacuum to give **259** (36.8 mg, 52.9 µmol, 38%) as a white solid. M.p.: 220–221 °C. ^{1}H NMR (400 MHz, $CDCl_3$, 298 K): δ/ppm = 8.19 (d, J = 8.0 Hz, 2 H), 8.09 (d, J = 8.0 Hz, 2 H), 7.55–7.60 (m, 1 H), 7.45–7.48 (m, 2 H), 7.19–7.23 (m, 4 H), 7.11–7.15 (m, 4 H), 1.12 (s, 18 H). ^{13}C NMR (101 MHz, $CDCl_3$, 298 K): δ/ppm = 163.5, 150.2, 141.6, 136.2, 136.0, 131.6, 131.4, 131.1, 130.2, 129.3, 128.2, 128.0, 127.7, 125.0, 122.9, 34.5, 31.3. MS (MALDI-TOF, positive mode, DCTB in chloroform): 695.1 $[M]^+$. HRMS (ESI-TOF, positive mode, acetonitrile/chloroform): calcd for $C_{38}H_{33}Br_2NO_2Na$: 716.0776; found: 716.0778 $[M+Na]^+$.

Nanographene 257

A Schlenk-tube was charged with **260** (10.0 mg, 14.1 µmol, 1.0 equiv), **259** (44.5 mg, 62.0 µmol, 4.4 equiv.), tris(dibenzylideneacetone)dipalladium(0)-chloroform adduct $[Pd_2(dba)_3]\cdot CHCl_3$ (5.8 mg, 5.64 µmol, 40 mol%), $PCy_3\cdot HBF_4$ (8.3 mg, 22.6 µmol, 160 mol%) and Cs_2CO_3 (55.1 mg, 169.2 µmol, 12.0 equiv) under a nitrogen atmosphere. Subsequently, 1-chloronaphthalene (0.71 mL) was added and the mixture was heated to 160 °C for 3 days. The reaction mixture was

cooled down to room temperature, and the mixture was filtrated over a pad of silica gel to remove 1-chloronaphthalene and the product was eluted with dichloromethane. The crude product was purified by column chromatography (cyclohexane/dichloromethane from 1:1 to 0:1), size exclusion chromatography (SX3), recycling GPC and precipitation from dichloromethane/methanol. The precipitate was washed with methanol and *n*-hexane to obtain **257** (7.3 mg, 3.13 µmol, 22%) as a dark-purple solid. M.p.: > 350°C. ^{1}H NMR (400 MHz, $CDCl_3$, 298 K): δ/ppm = 11.67 (*s*, 2 H). 10.81 (*s*, 4 H), 10.17 (*d*, *J* = 8.5 Hz, 4 H), 9.42 (*d*, *J* = 8.5 Hz, 4 H), 7.70–7.75 (*m*, 4), 7.61–7.64 (*m*, 8H), 7.48–7.52 (*m*, 16 H), 7.18–7.22 (*m*, 16 H), 0.95 (*s*, 72 H). ^{13}C-NMR (101 MHz, $CDCl_3$, 298 K): δ/ppm = 164.7, 164.6, 150.2, 142.9, 136.6, 134.6, 131.6, 130.7, 130.6, 130.5, 129.9, 129.5, 129.2, 128.2, 127.8, 126.7, 125.2, 124.7, 124.5, 124.0, 123.3, 122.9, 121.6, 119.9, 34.4, 31.1. HRMS (MALDI-TOF, negative mode, DCTB in chloroform): calcd for $C_{168}H_{130}N_4O_8$: 2330.9889, found: 2330.9937 $[M]^-$. UV–vis ($CHCl_3$): λ_{max} / nm (ε / $M^{-1}cm^{-1}$) = 585 (163400), 490 (319900). Fluorescence ($CHCl_3$): $\lambda_{em,\,max}$ / nm (Φ_{fl} / %): 604 nm (68±2). CV (CH_2Cl_2): E_{ox1} = 1.02 V, E_{red1} = –1.04 V, E_{red2} = –1.22 V, E_{red3} = –1.61 V, E_{red4} = –1.70 V, E_{red5} = –2.14 V.

Optical and Electronic Properties

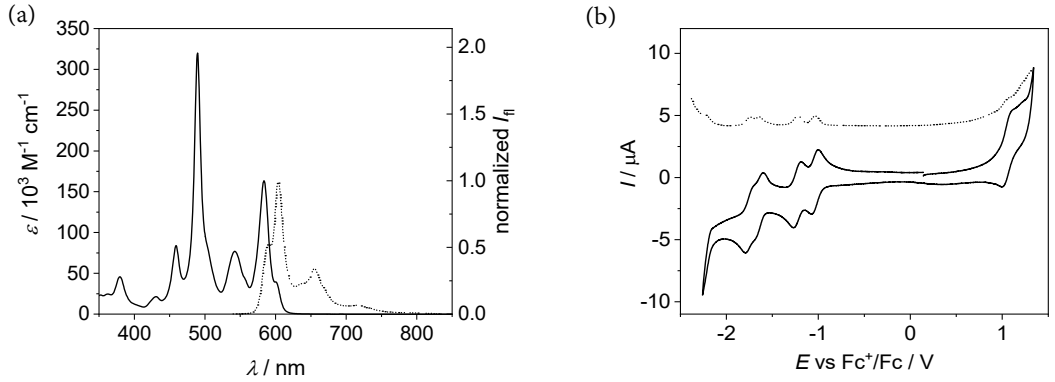

Figure A165. (a) UV–vis absorption (solid, $c \sim 10^{-6}$ M) and normalized fluorescence (dashed, λ_{ex} = 530 nm, $c \sim 10^{-7}$ M) spectra of **257** in chloroform solutions at room temperature. (b) Cyclic (solid) and differential pulse (dashed) voltammograms of **257** in dichloromethane solutions using tetrabutylammonium hexafluorophosphate as supporting electrolyte at room temperature (scan rate: 100 mV/s).

Table A27. Summary of the optical properties of **257** in chloroform solution at room temperature.[a]

	λ_{abs} /nm (ε / M^{-1} cm^{-1})	λ_{em} / nm [b]	Φ_{fl} / %[c]	τ / ns[d]
257	585 (163400) 490 (319900)	604	68 ± 2	12.00 ± 0.01

[a]Measurements were conducted in chloroform solutions at room temperature (UV–vis: $c \sim 10^{-6}$ M; fluorescence: $c \sim 10^{-7}$ M). [b]Excitation wavelength: λ_{ex} = 530 nm. [c]Determined using the relative method ($A < 0.05$) and *N*,*N*′-bis[2,6-diisopropylphenyl]perylene-3,4:9,10-bis(dicarboximide) (Φ_{fl} ($CHCl_3$) = 100%). [d]Excitation wavelength: λ_{ex} = 505 nm; detection wavelength: λ_{ex} = 605 nm.

Table A28. Summary of the redox properties of **257**.[a]

	E_{red1} / V	E_{red2} / V	E_{red3} / V	E_{red4} / V	E_{red5} / V	E_{ox1} / V
257	–1.04	–1.22	–1.61	–1.70	–2.14	1.02

[a]Measurements conducted in dichloromethane solution using tetrabutylammonium hexafluorophosphate as supporting electrolyte ($c \sim$ 0.1 M) at room temperature and using the Fc^+/Fc redox-couple as reference.

Complexation Studies

UV–vis absorption and fluorescence titration experiments were conducted by applying the constant host routine in chloroform solutions. For this purpose, a solution of host (c(**257**) = 10^{-6}–10^{-8} M, $CHCl_3$) and a defined excess of guest was titrated to a pure host solution with the same concentration. For poorly soluble guests ovalene, hexabenzocoronene and phthalocyanine the stock solutions were stirred for 24 hours to dissolve the guest molecules and equilibrate the respective solutions. Further, each titration point was equilibrated for another 24 hours (in these cases separated solutions for each titration point). The obtained data was fitted globally (UV–vis: λ = 480–520 nm; fluorescence: λ = 580–620 nm) with a 1:2 binding model by a non-linear regression method using the program *bindfit* from P. Thordason *et al.*, which is avialable free of charge.[377-378] The ^{1}H NMR titration data was treated analogously (selected signals; see Figure A173). The used solvent for ITC measurement was degassed and the solutions were stirred with 307 rpm at 25 °C while the guest was titrated with 10 µL injections. Data obtained from isothermal titration calorimetry was evaluated by using the included software package of the MicroCal iTC.

Table A29. Comparison of obtained association constants and thermodynamic parameters of **257** as host and coronene as guest in chloroform.

	K_1 / 10^5·M^{-1}	K_2 / 10^4·M^{-1}	ΔG_1(295 K)[a] / kJ·mol^{-1}	ΔG_2(295 K)[a] / kJ·mol^{-1}	ΔH_1 / kJ·mol^{-1}	ΔH_2 / kJ·mol^{-1}	ΔS_1T / kJ·mol^{-1}	ΔS_2T / kJ·mol^{-1}
UV–vis[b]	(2.73 ± 0.01)	(6.14 ± 0.03)	–30.7	–27.0				
Fluores-cence[c]	(2.92 ± 0.01)	(7.09 ± 0.14)	–31.2	–27.7				
^{1}H NMR[d]	(3.07 ± 0.72)	(4.31 ± 0.03)	–31.3	–26.4				
ITC[e]	(3.60 ± 0.35)	(3.94 ±0.26)	–31.7	–26.2	–27.67	–19.75	5.93	6.48

[a]Gibbs free energies for UV–vis, fluorescence and ^{1}H NMR data calculated from $K_{1/2}$ according to $\Delta G_{1/2}$=−RTln($K_{1/2}$). [b]Association constants $K_{1/2}$ determined using global-fit analysis (fitting range: λ = 480–520 nm) with the program *bindfit*[377] for a 1:2 binding model (chloroform, 295 K, c(**257**) = 6.0·10^{-6} M). [c]Association constants $K_{1/2}$ determined using global-fit analysis (fitting range: λ = 580–620 nm) with the program *bindfit*[377] for a 1:2 binding model (chloroform, 295 K, c(**257**) = 6.0·10^{-7} M). [d]Association constants $K_{1/2}$ determined for four different signals with the program *bindfit*[377] for a 1:2 binding model (deuterated-chloroform, 295 K, c(**257**) = 1.0·10^{-4} M). [e]Measurement and reported values at 298 K, association constants $K_{1/2}$ were determined with the program MicroCal iTC for a 1:2 binding model (chloroform, c(**257**) = 7.0·10^{-5} M, 298 K).

UV–vis spectroscopy

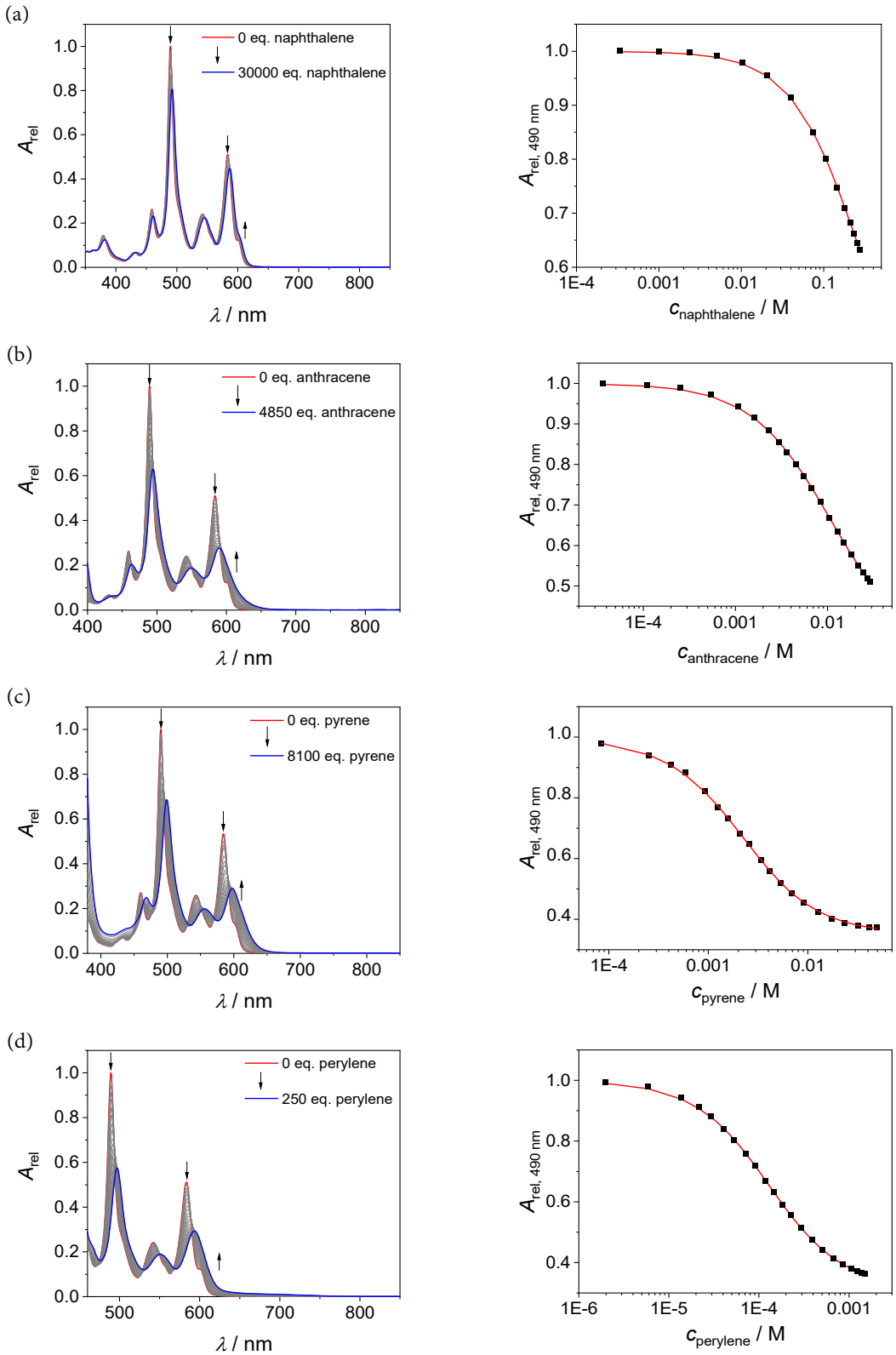

Figure A166. Left: Normalized UV–vis titration experiments of nanographene **257** in chloroform solutions (c(**257**) = 6.0·10^{-6} M, 295 K) with (a) naphthalene, (b) anthracene, (c) pyrene and (d) perylene as guests. Right: Respective plots of UV–vis titration experiment at a certain wavelength for a 1:2 binding model.

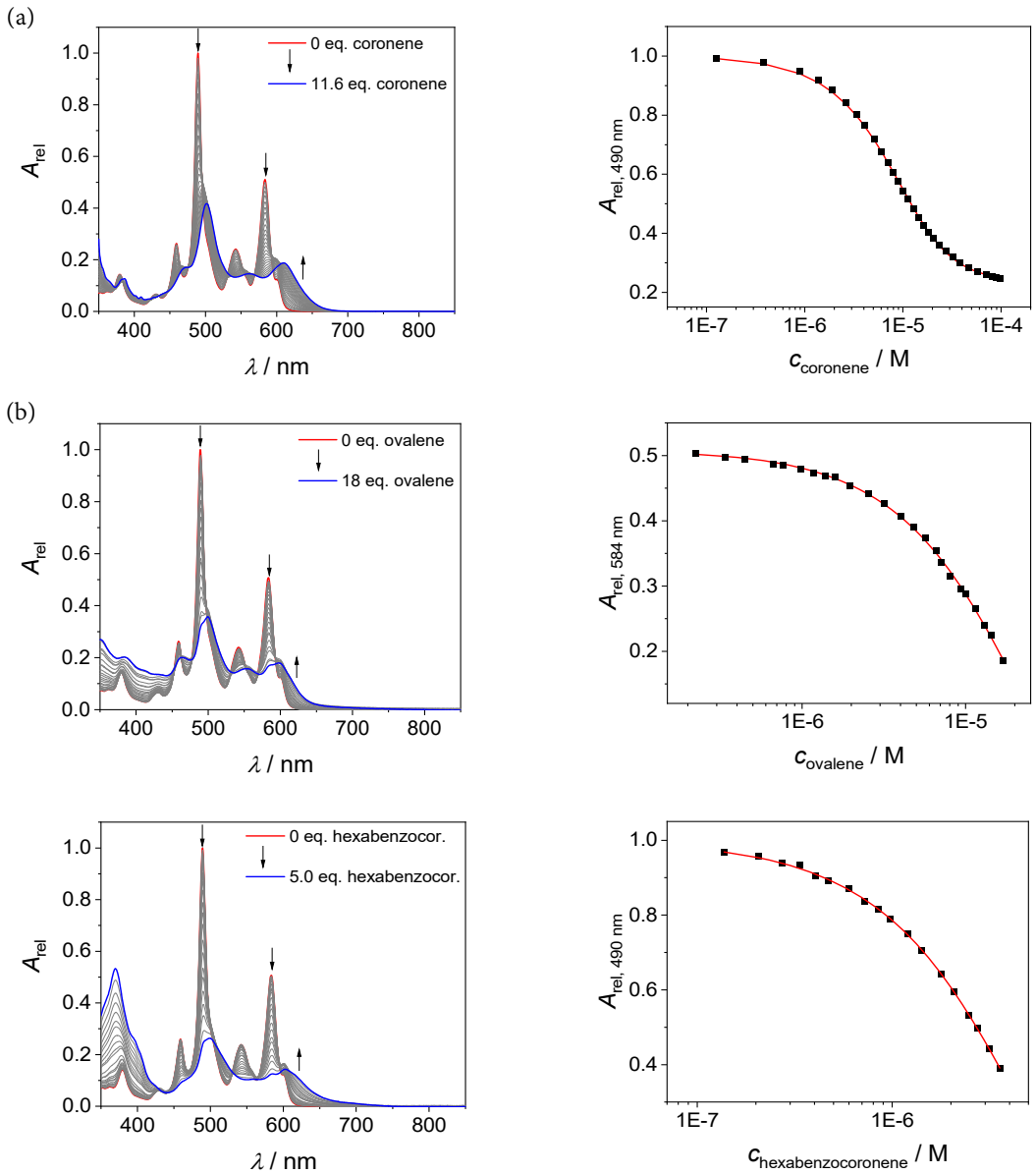

Figure A167. Left: Normalized UV–vis titration experiments of nanographene **257** in chloroform solutions (c(**257**) = 1.0–6.0·10^{-6} M, 295 K) with (a) coronene, (b) ovalene and (c) hexabenzocoronene as guests. Right: Respective plots of UV–vis titration experiment at a certain wavelength for a 1:2 binding model.

Table A30. Summary of the obtained binding constants $K_{1/2}$ from the UV–vis titration experiments and the corresponding Gibbs free energy $\Delta G_{1/2}$ (295 K) for nanographene **257** as obtained from global-fit analysis (fitting range: λ = 480–520 nm) using a 1:2-binding model.

	K_1 / M^{-1}	K_2 / M^{-1}	ΔG_1 (295 K) / kJ mol^{-1}	ΔG_2 (295 K) / kJ mol^{-1}
naphthalene	10.27 ± 0.03	3.03 ± 0.01	–5.71	–2.72
anthracene	$(1.62 \pm 0.01)\cdot 10^2$	$(4.24 \pm 0.01)\cdot 10$	–12.5	–9.19
pyrene	$(5.36 \pm 0.04)\cdot 10^2$	$(2.10 \pm 0.02)\cdot 10^2$	–15.4	–13.1
perylene[a]	$(1.20 \pm 0.01)\cdot 10^4$	$(3.38 \pm 0.01)\cdot 10^3$	–23.0	–19.9
coronene	$(2.73 \pm 0.01)\cdot 10^5$	$(6.14 \pm 0.03)\cdot 10^4$	–30.7	–27.0
ovalene[a]	$(6.81 \pm 0.17)\cdot 10^5$	$(3.03 \pm 0.02)\cdot 10^4$	–32.9	–25.3
hexabenzocoronene	$(8.05 \pm 0.04)\cdot 10^5$	$(1.61 \pm 0.01)\cdot 10^5$	–33.4	–29.4

[a]Fitting range: λ = 580–620 nm.

Fluorescence spectroscopy

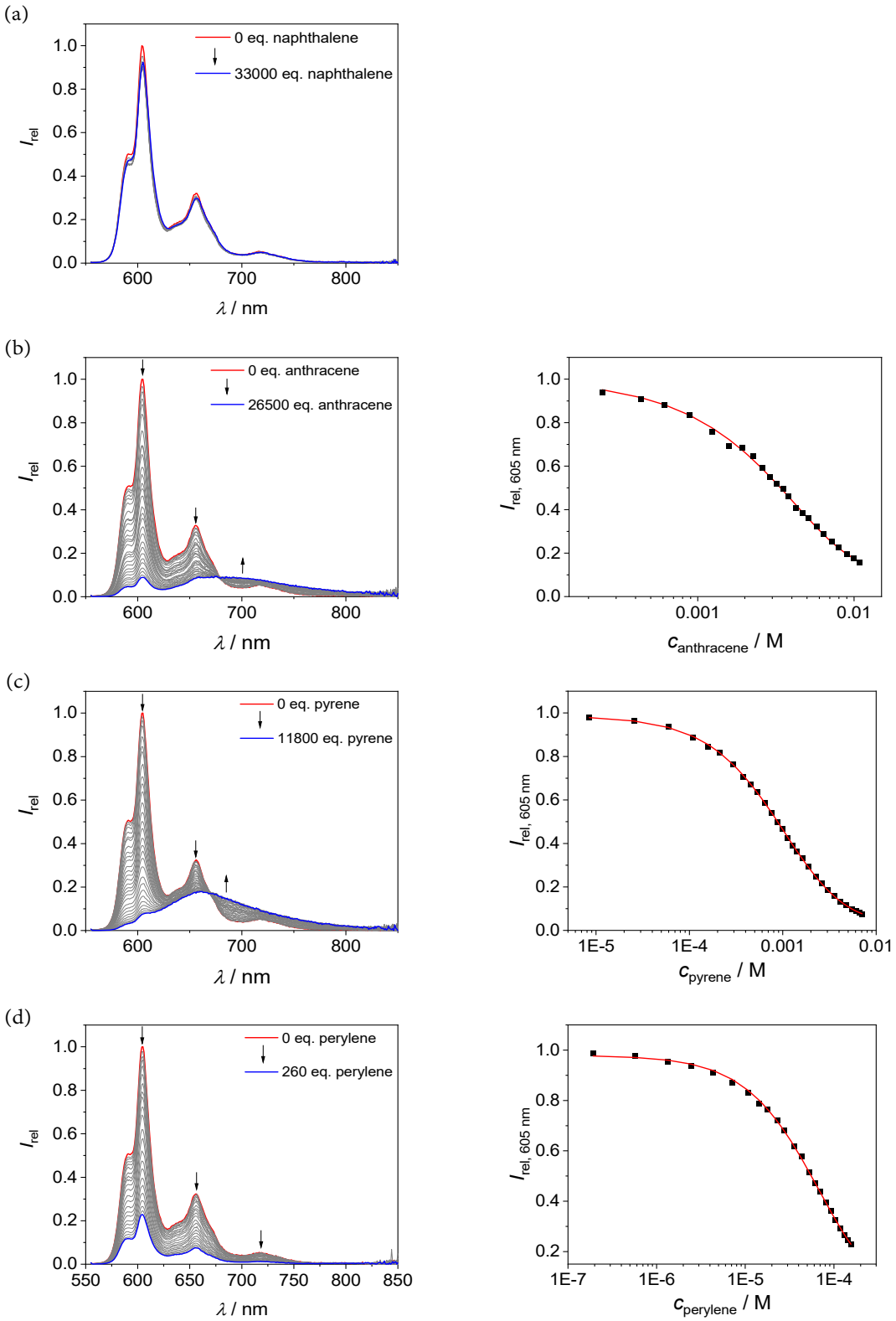

Figure A168. Left: Normalized fluorescence titration experiments of nanographene **257** (c(**257**) = $6.0 \cdot 10^{-7}$ M, λ_{ex} = 550 nm, 295 K) with (a) naphthalene, (b) anthracene, (c) pyrene and (d) perylene in chloroform at 295 K. Right: Respective plots of fluorescence titration experiment at a certain wavelength for a 1:2 binding model (for naphthalene: only negligible changes).

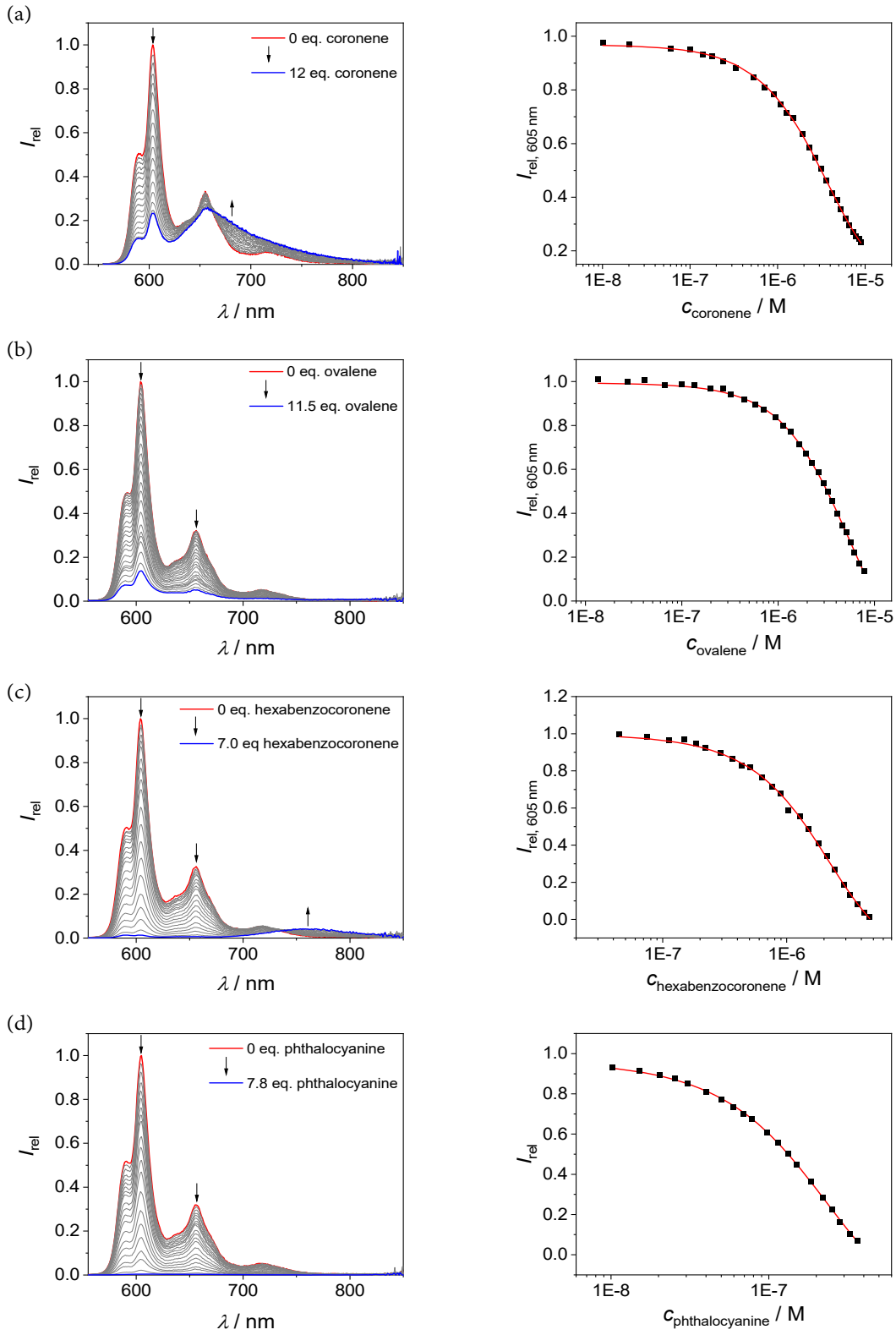

Figure A169. Left: Normalized fluorescence titration experiments of nanographene **257** (c(**257**) = $6.0 \cdot 10^{-7}$–10^{-8} M, λ_{ex} = 550 nm) with (a) coronene, (b) ovalene, (c) hexabenzocoronene and (d) phthalocyanine (λ_{ex} = 500 nm) in chloroform at 295 K. Right: Respective plots of fluorescence titration experiment at a certain wavelength for a 1:2 binding model.

Table A31. Summary of the obtained binding constants $K_{1/2}$ from the fluorescence titration experiments (λ_{ex} = 550 nm) and the corresponding Gibbs free energy $\Delta G_{1/2}$ (295 K) for nanographene **257** as obtained from global-fit analysis (fitting range: λ = 580–620 nm) using a 1:2-binding model.

	K_1 / M^{-1}	K_2 / M^{-1}	ΔG_1 (295 K) / kJ mol^{-1}	ΔG_2 (295 K) / kJ mol^{-1}
naphthalene	-[a]	-[a]	-	-
anthracene	$(1.06 \pm 0.01)\cdot 10^2$	$(7.79 \pm 0.17)\cdot 10$	–11.4	–10.7
pyrene	$(9.47 \pm 0.04)\cdot 10^2$	$(2.14 \pm 0.04)\cdot 10^2$	–16.8	–13.2
perylene[b]	$(1.51 \pm 0.01)\cdot 10^4$	$(3.09 \pm 0.06)\cdot 10^3$	–23.6	–14.1
coronene	$(2.92 \pm 0.06)\cdot 10^5$	$(7.09 \pm 0.63)\cdot 10^4$	–30.9	–27.4
ovalene	$(1.03 \pm 0.02)\cdot 10^6$	$(1.63 \pm 0.01)\cdot 10^5$	–34.0	–29.4
hexabenzocoronene	$(1.11 \pm 0.02)\cdot 10^6$	$(6.08 \pm 0.09)\cdot 10^5$	–34.1	–32.6
phthalocyanine[b]	$(9.24 \pm 0.07)\cdot 10^6$	$(5.09 \pm 0.04)\cdot 10^6$	–39.3	–37.9

[a]Only negligible changes. [b]λ_{ex} = 500 nm

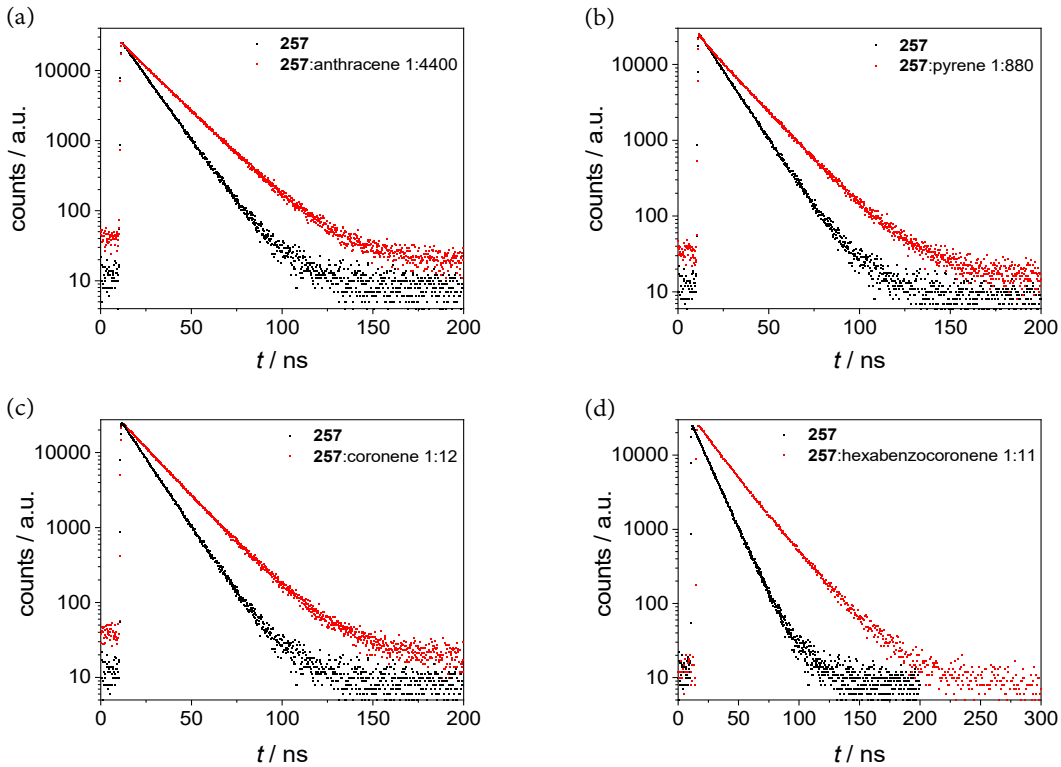

Figure A170. Lifetime decays (λ_{ex} = 505 nm) of chloroform-solutions of **257** with guest: (a) anthracene [λ_{det} = 686 nm; 4400 equiv], (b) pyrene [λ_{det} = 667 nm; 880 equiv], (c) coronene [λ_{det} = 686 nm; 12 equiv] and (d) hexabenzocoronene [λ_{det} = 775 nm; 11 equiv]

Table A32. Comparison of fluorescence lifetime decays (λ_{ex} = 505 nm) of chloroform-solutions of **257** with various guests.

guest	equiv guest	λ_{det} / nm	τ /ns
-	-	604	12.00 ± 0.01
anthracence	4400	686	17.34 ± 0.01
pyrene	880	667	17.01 ± 0.01
coronene	12	686	17.15 ± 0.01
hexabenzocoronene	11	775	17.46 ± 0.37 [56%] 25.98 ± 0.57 [44%]

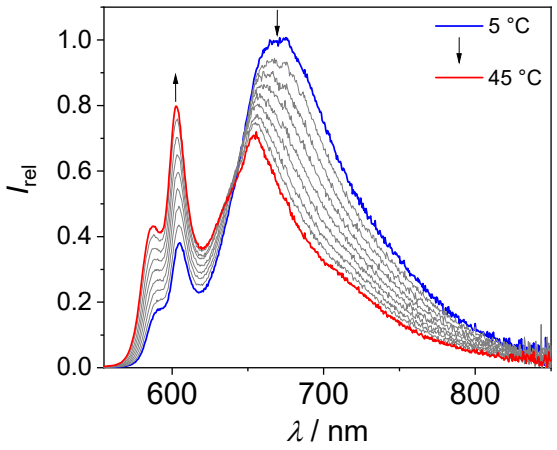

Figure A171. Temperature-dependent fluorescence spectra of **257** with 10 equiv coronene in chloroform (c(**257**) = 6.0·10^{-7} M; λ_{ex} = 510 nm).

NMR spectroscopy

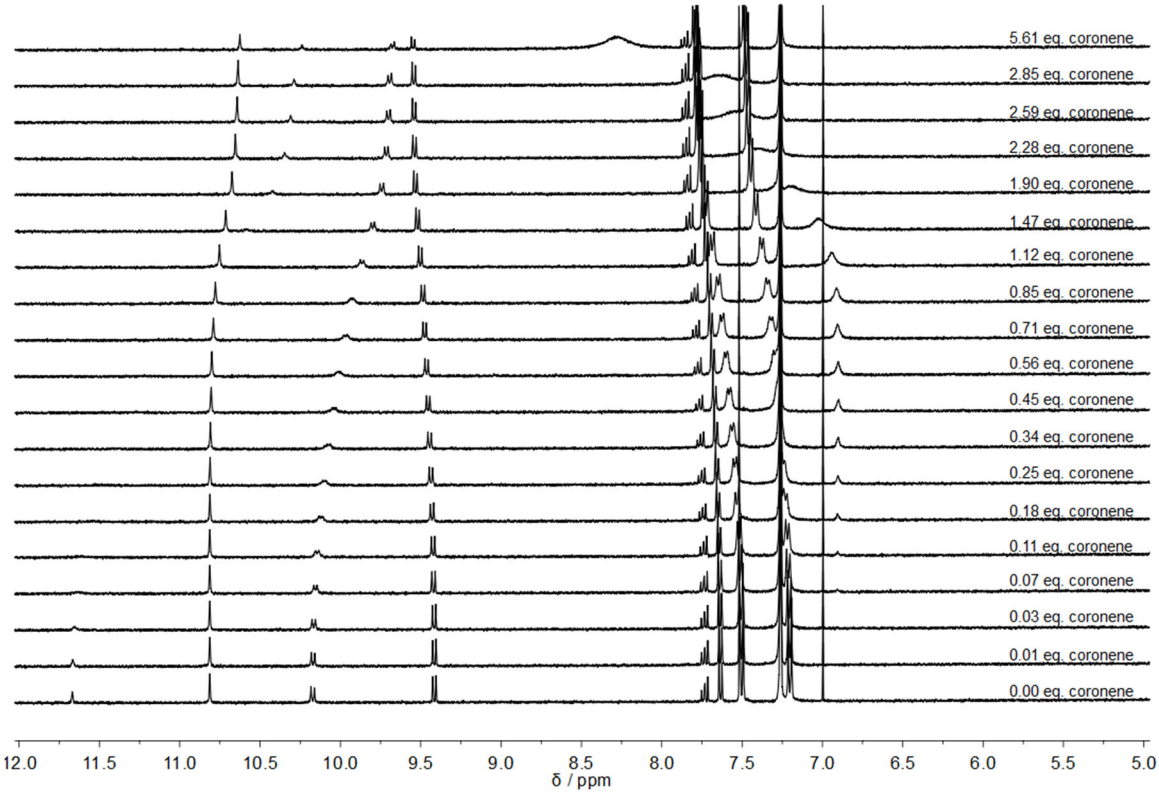

Figure A172. ^{1}H NMR (400 MHz, 295 K, $CDCl_3$) constant host titration experiment of **257** (c(**257**) = $1.0 \cdot 10^{-4}$ M) with coronene.

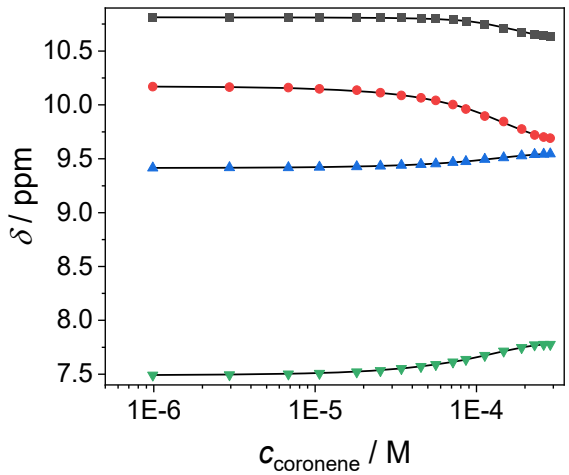

Figure A173. Fit of four different proton signals from a ^{1}H NMR (400 MHz, 295 K, $CDCl_3$) constant host titration experiment of **257** (c(**257**) = $1.0 \cdot 10^{-4}$ M) and coronene with a 1:2 binding model using the program *bindfit*[377].

For clarification of the stoichiometry, we used low temperature ^{1}H NMR spectroscopy to reach the slow exchange region and obtain signal for complexed and free coronene (Figure A174). The ratio of the integrals from these signals gives direct access to the stoichiometry of host to guest. Therefore, we had to change the solvent from $CDCl_3$ to CD_2Cl_2 due to the lower melting point of dichloromethane (the slow exchange region could not be reached with $CDCl_3$ at 220 K). The conducted experiment confirmed the stoichiometry of the used 1:2 binding model.

d

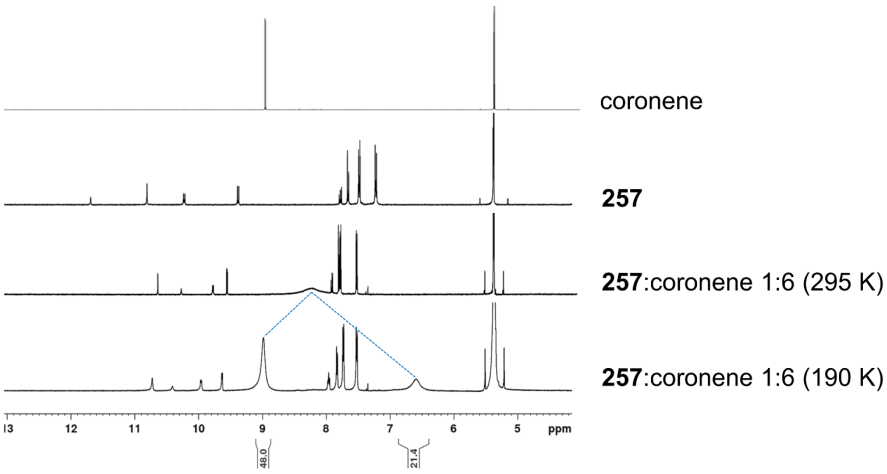

Figure A174. ^{1}H NMR (400 MHz) spectra of coronene (first), **257** (second), **257**:coronene [ratio 1:6; 295 K; 600 MHz] (third) and **257**:coronene [ratio 1:6; 295 KM; 600 MHz] (fourth) in CD_2Cl_2.

We used 2D diffusion ordered spectroscopy (DOSY, 600 MHz) for the determination of diffusion coefficients of parent **257** (c(**257**) = 5.0·10^{-4} M, $CDCl_3$, 295 K) and 1:2 complex (c(**257**) = 5.0·10^{-4} M, 6.0 equiv coronene, CD_2Cl_2, 194 K). With the help of the Stokes-Einstein equation, the hydrodynamic radii for spherical particles were determined, while the measurement at 194 K were referenced internally to residual solvent signals. These measurements further proof the existence of monomeric species/this complex in solution and exclude larger assembled structures.

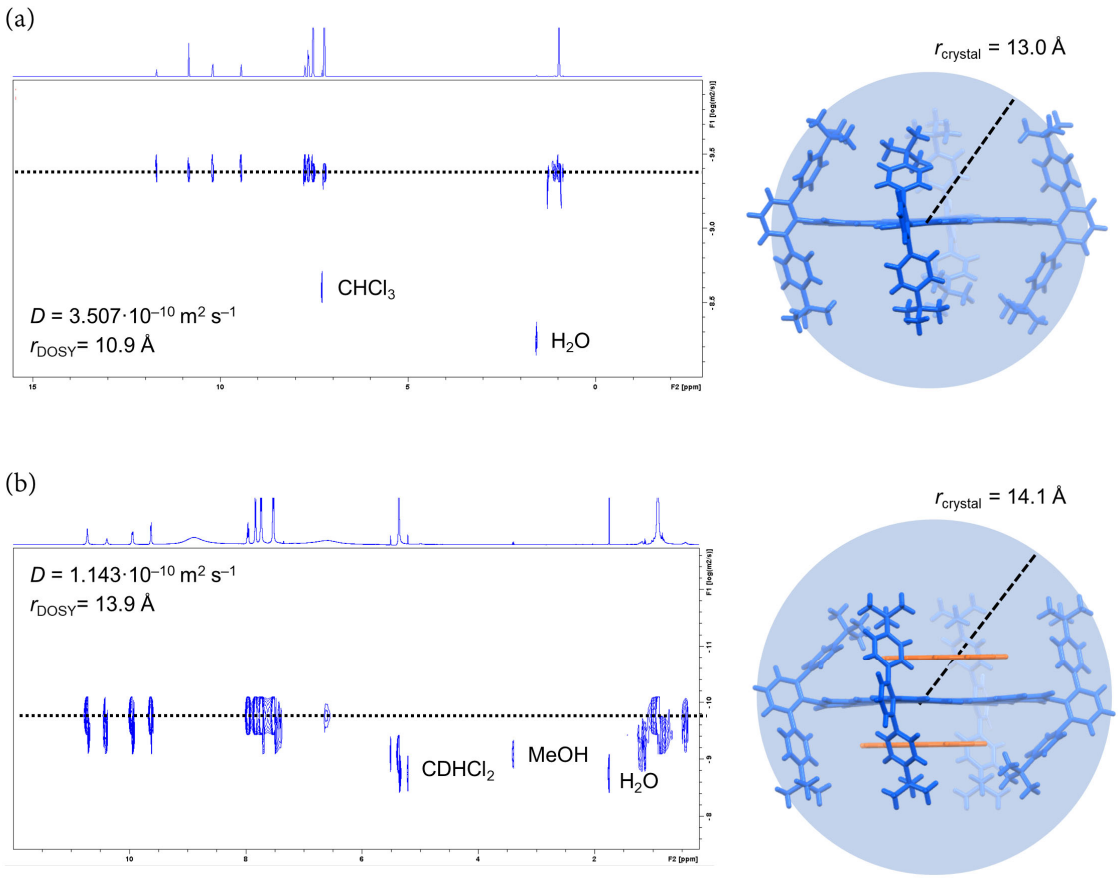

Figure A175. 2D plot of DOSY NMR (600 MHz) of (a) **257** (c(**257**) = 5.0·10^{-4} M, 298 K, $CDCl_3$) and (b) **257** (c(**257**) = 5.0·10^{-4} M, 194 K, CD_2Cl_2) and 6.0 equiv of coronene.

Crystallographic Analysis

Single crystals of **257** suitable for X-ray diffraction could be grown by slow diffusion of *n*-hexane into a toluene/chloroform (1/1) solution of **257**. All co-crystals were grown by slow diffusion of *n*-hexane into a chloroform solution of **257** and coronene with different ratios and concentrations (details see Table A38 – Table A42).

Table A33. Crystallographic data and structure refinement for **257**.

Empirical formula	$(C_{168}H_{130}N_4O_8)$, 6.124(C_7H_8), 0.238 (C_6H_{14}), 2.649$(CHCl_3)$ [+ solvent]
Formula weight	3233.75
Temperature	100(2) K
Wavelength	1.54178 Å
Crystal system, space group	Monoclinic, *C*2/*c*
Unit cell dimensions	*a* = 39.676(3) Å
	b = 26.6879(18) Å
	c = 55.958(3) Å
	α = 90 °
	β = 104.008(4) °
	γ = 90 °
Volume	57491(6) Å^3
Z	12
Calculated density	1.121 Mg/m^3
Absorption coefficient	1.506 mm^{-1}
F(000)	20421.1
Crystal size	0.500 × 0.340 × 0.190 mm
Theta range for data collection	2.274 to 80.901 °
Limiting indices	–50 <= *h* <= 50, –26 <= *k* <= 33, –70 <=*l* <= 68
Reflections collected / unique	325306 / 61582 [R_{int} = 0.1564]
Completeness	100.0%
Absorption correction	Semi-empirical from equivalents
Max. and min. transmission	0.7542 and 0.5704
Refinement method	Full-matrix least-squares on F^2
Data / restraints / parameters	61582 / 8769 / 3839
Goodness-of-fit	1.032
Final *R* indices [$I > 2\sigma(I)$]	R_1 = 0.1179, wR_2 = 0.3382
R indices (all data)	R_1 = 0.1966, wR_2 = 0.4122
Largest diff. peak and hole	0.615 and –0.501 e·Å^{-3}

Table A34. Crystallographic data and structure refinement for *Polymorph A* of 1:2 co-crystal from **257**:coronene.

Empirical formula	$(C_{168}H_{130}N_4O_8)$, $2(C_{24}H_{12})$, $0.418(CHCl_3)$
Formula weight	2983.34
Temperature	100(2) K
Wavelength	1.54178 Å
Crystal system, space group	Triclinic, $P\bar{1}$
Unit cell dimensions	a = 10.9263(5) Å
	b = 19.2350(7) Å
	c = 22.0652(8) Å
	α = 111.498(2) °
	β = 100.854(2) °
	γ = 99.776(2) °
Volume	4090.3(3) Å^3
Z	1
Calculated density	1.211 Mg/m^3
Absorption coefficient	0.746 mm^{-1}
F(000)	1566.2
Crystal size	0.272 × 0.154 × 0.097 mm
Theta range for data collection	2.237 to 68.500°
Limiting indices	$-13 \leq h \leq 13$, $-22 \leq k \leq 23$, $-26 \leq l \leq 26$
Reflections collected / unique	63999 / 14992 [R_{int} = 0.0766]
Completeness	99.6%
Absorption correction	Semi-empirical from equivalents
Max. and min. transmission	0.7536 and 0.6251
Refinement method	Full-matrix least-squares on F^2
Data / restraints / parameters	14992 / 780 / 1120
Goodness-of-fit	1.355
Final R indices [$I > 2\sigma(I)$]	R_1 = 0. 1224, wR_2 = 0.3607
R indices (all data)	R_1 = 0. 607, wR_2 = 0.3907
Largest diff. peak and hole	0.573 and –0.3907 e·Å^{-3}

Table A35. Crystallographic data and structure refinement for *Polymorph B* of 1:2 co-crystal from **257**:coronene.

Empirical formula	$(C_{168}H_{130}N_4O_8)$, $2(C_{24}H_{12})$, (C_6H_{14})
Formula weight	3019.61
Temperature	102(2) K
Wavelength	1.54178 Å
Crystal system, space group	Triclinic, $P\bar{1}$
Unit cell dimensions	a = 20.4024(16) Å
	b = 23.0355(18) Å
	c = 25.661(2) Å
	α = 103.973(5) °
	β = 110.669(5) °
	γ = 107.052(5) °
Volume	9953.4(15) Å^3
Z	2
Calculated density	1.008 Mg/m^3
Absorption coefficient	2.356 mm^{-1}
F(000)	3184
Crystal size	0.480 × 0.300 × 0.200 mm
Theta range for data collection	2.174 to 79.773°
Limiting indices	$-25 \leq h \leq 25$, $-29 \leq k \leq 27$, $-32 \leq l \leq 32$
Reflections collected / unique	178778 / 42410 [R_{int} = 0.0948]
Completeness	99.9%
Absorption correction	Semi-empirical from equivalents
Max. and min. transmission	0.7542 and 0.4771
Refinement method	Full-matrix least-squares on F^2
Data / restraints / parameters	42410 / 2164 / 2668
Goodness-of-fit	1.029
Final R indices [$I > 2\sigma(I)$]	R_1 = 0.1152, wR_2 = 0.3048
R indices (all data)	R_1 = 0.1867, wR_2 = 0.3948
Largest diff. peak and hole	0.778 and –0.491 e·Å^{-3}

Table A36. Crystallographic data and structure refinement for 2:2 co-crystal from **257**:coronene.

Empirical formula	$(C_{168}H_{130}N_4O_8)$, $(C_{24}H_{12})$, $2(CHCl_3)$
Formula weight	2871.82
Temperature	100(2) K
Wavelength	1.54184 Å
Crystal system, space group	Monoclinic, C2/c
Unit cell dimensions	a = 63.621(2) Å
	b = 34.696(3) Å
	c = 35.481(2) Å
	α = 90 °
	β = 123.211(4) °
	γ = 90 °
Volume	65528(8) Å^3
Z	16
Calculated density	1.164 Mg/m^3
Absorption coefficient	1.419 mm^{-1}
F(000)	24032
Crystal size	0.408 × 0.078 × 0.024 mm
Theta range for data collection	2.425 to 68.499°
Limiting indices	–76 <= h <= 76, –41 <= k <= 34, –42 <= l <= 42
Reflections collected / unique	708239 / 60304 [R_{int} = 0.1782]
Completeness	100.0%
Absorption correction	Semi-empirical from equivalents
Max. and min. transmission	0.7536 and 0.6026
Refinement method	Full-matrix least-squares on F^2
Data / restraints / parameters	60304 / 1179 / 4279
Goodness-of-fit	1.106
Final R indices [$I > 2\sigma(I)$]	R_1 = 0.1035, wR_2 = 0.2914
R indices (all data)	R_1 = 0.1549, wR_2 = 0.3445
Largest diff. peak and hole	1.535 and –0.648 e·Å^{-3}

Table A37. Crystallographic data and structure refinement for 1:2 co-crystal from **257**:phthalocyanine.

Empirical formula	$(C_{168}H_{130}N_4O_8)$, $2(C_{32}H_{18}N_8)$ [+ solvent]
Formula weight	3361.86
Temperature	100(2) K
Wavelength	1.54178 Å
Crystal system, space group	Monoclinic, $P2_1/n$
Unit cell dimensions	a = 42.763(3) Å
	b = 47.730(3) Å
	c = 44.804(3) Å
	α = 90 °
	β = 114.632(4) °
	γ = 90 °
Volume	83127(11) Å^3
Z	16
Calculated density	1.074 Mg/m^3
Absorption coefficient	0.517 mm^{-1}
F(000)	28192
Crystal size	0.353 × 0.154 × 0.067 mm
Theta range for data collection	2.146 to 70.395°
Limiting indices	–52 <= h <= 51, –57 <= k <= 57, –53 <= l <= 54
Reflections collected / unique	1265972 / 154602 [R_{int} = 0.2382]
Completeness	99.9%
Absorption correction	Semi-empirical from equivalents
Max. and min. transmission	0.7531 and 0.5568
Refinement method	Full-matrix least-squares on F^2
Data / restraints / parameters	154602 / 24633 / 9183
Goodness-of-fit	1.138
Final R indices [$I > 2\sigma(I)$]	R_1 = 0.2203, wR_2 = 0.5465
R indices (all data)	R_1 = 0.3397, wR_2 = 0.6418
Largest diff. peak and hole	1.146 and –0.449 e·Å^{-3}

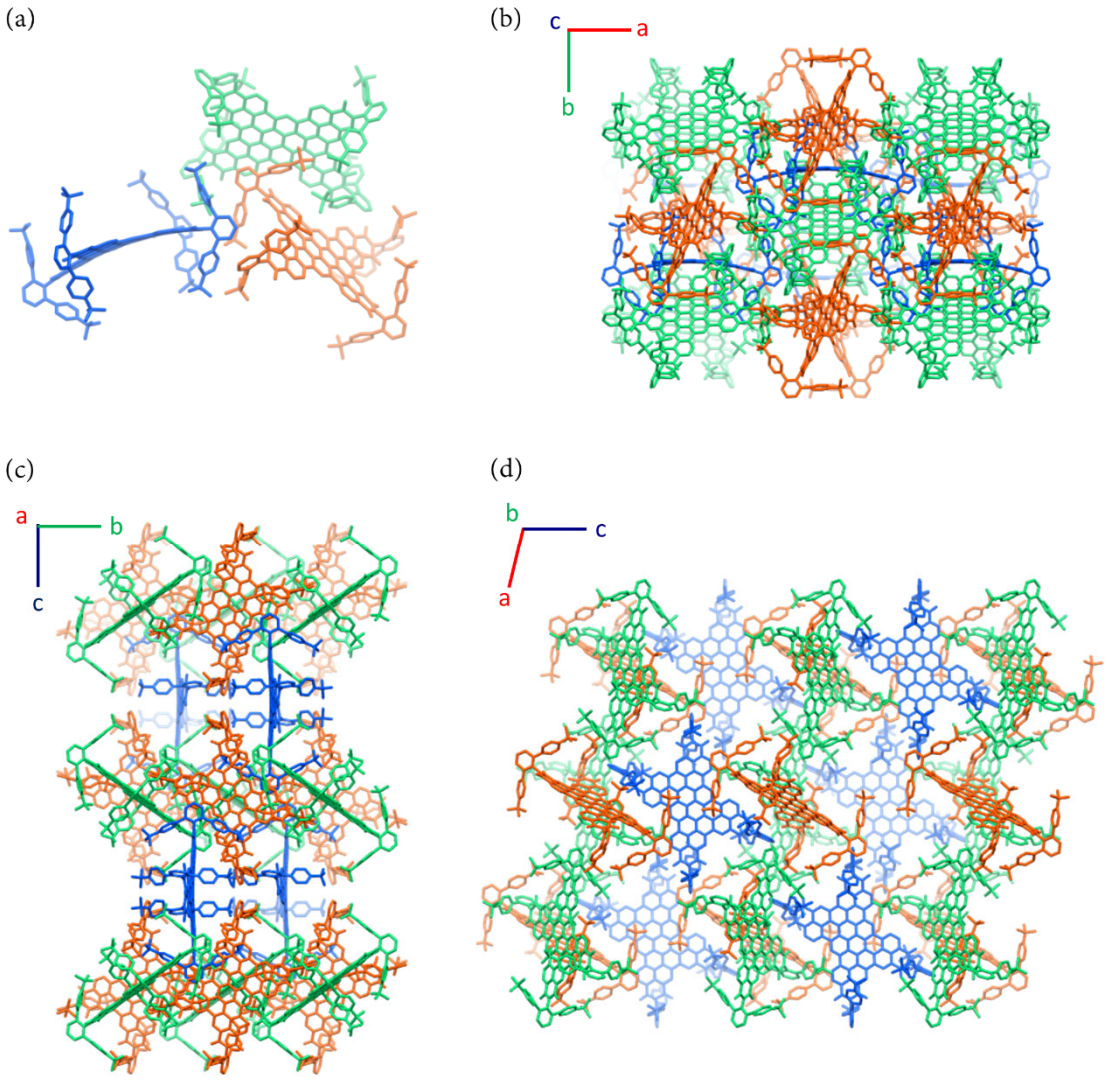

Figure A176. Molecular structure of **257** in the solid-state as obtained by single crystal X-ray diffraction. (a) Three crystallographic independent structures of **257**. (b–d) Packing arrangement of **257**.

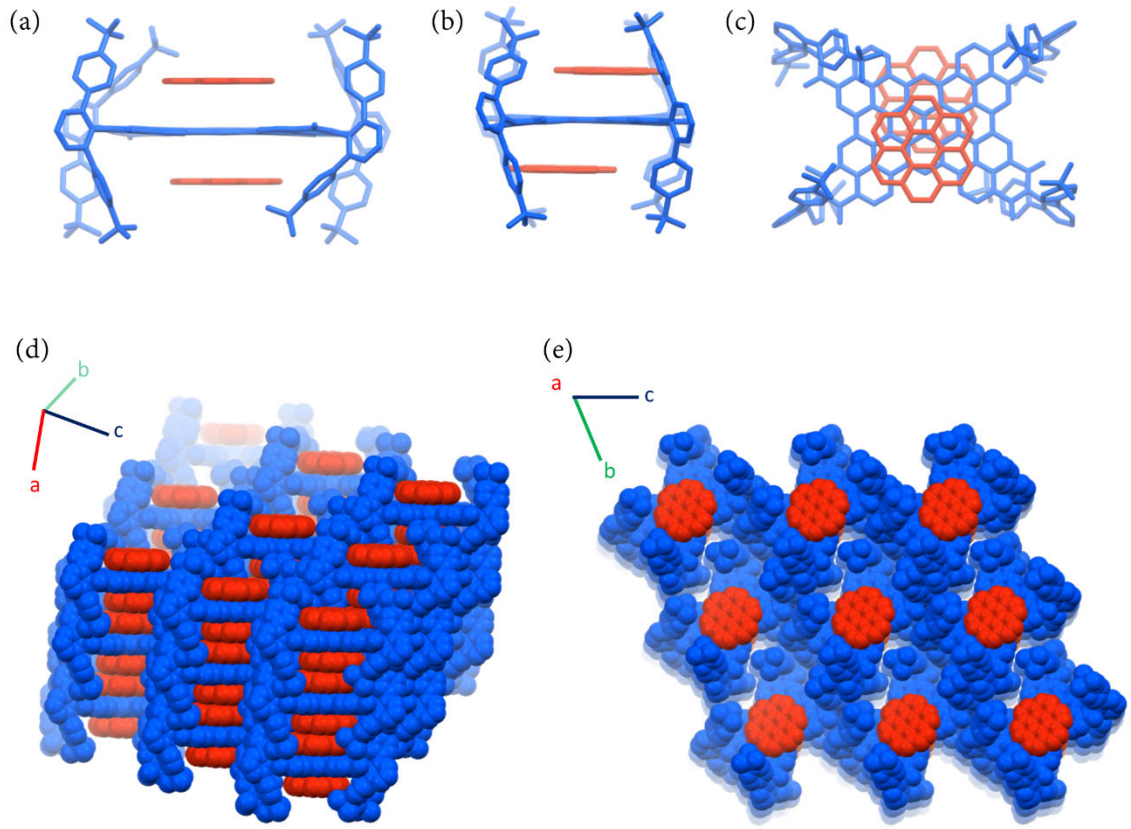

Figure A177. Molecular structure of *Polymorph A* of 1:2 co-crystal from **257** with coronene in the solid-state as obtained by single crystal X-ray diffraction. (a) Front view, (b) side view and (c) top view of 1:2 complex. (d–e) Packing arrangement of *Polymorph A*.

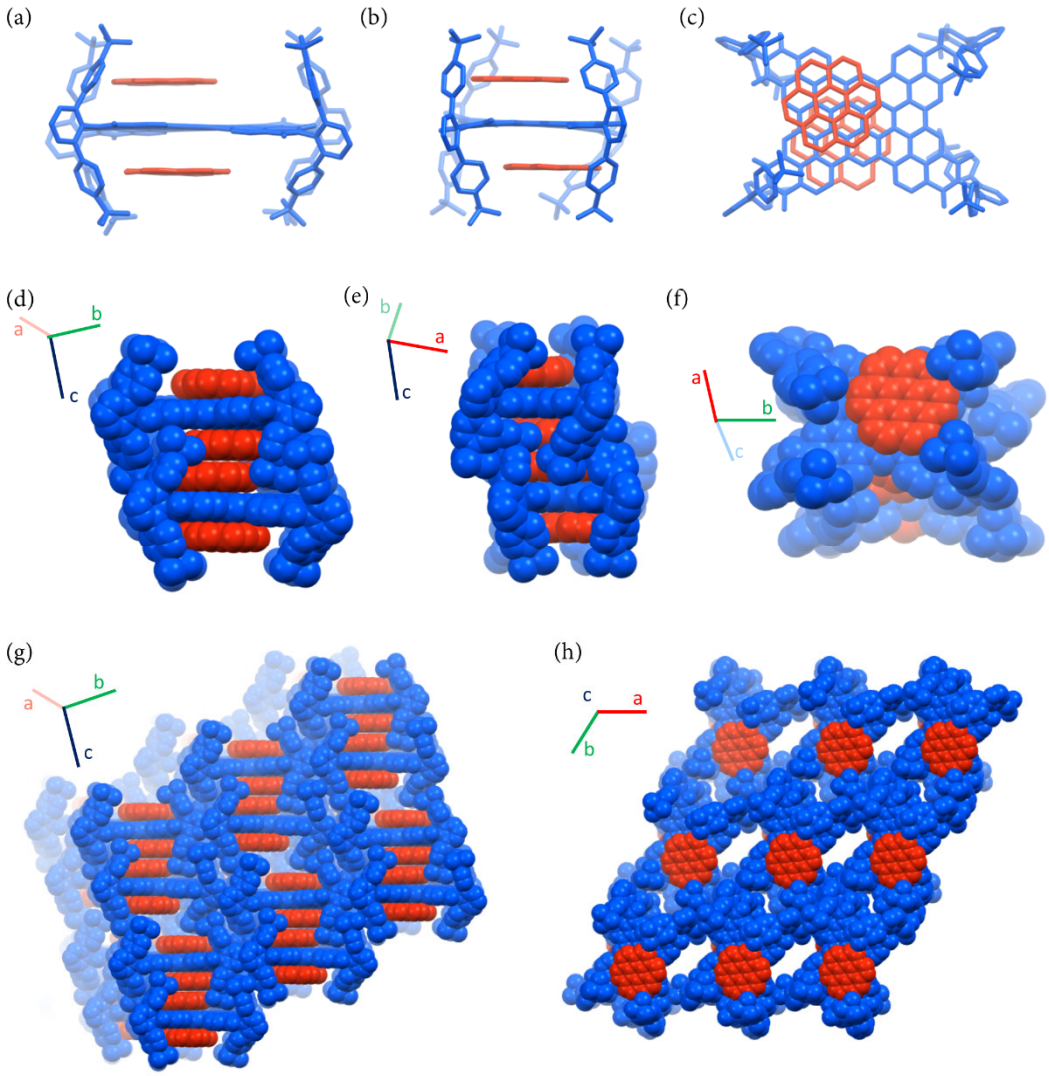

Figure A178. Molecular structure of *Polymorph B* of 1:2 co-crystal from **257** with coronene in the solid-state as obtained by single crystal X-ray diffraction. (a) Front view, (b) side view and (b) top view of 1:2 complex (*Polymorph B*). (d) Front view, (e) side view and (f) top view of dimeric arrangement and (g–h) packing arrangement of *Polymorph B*.

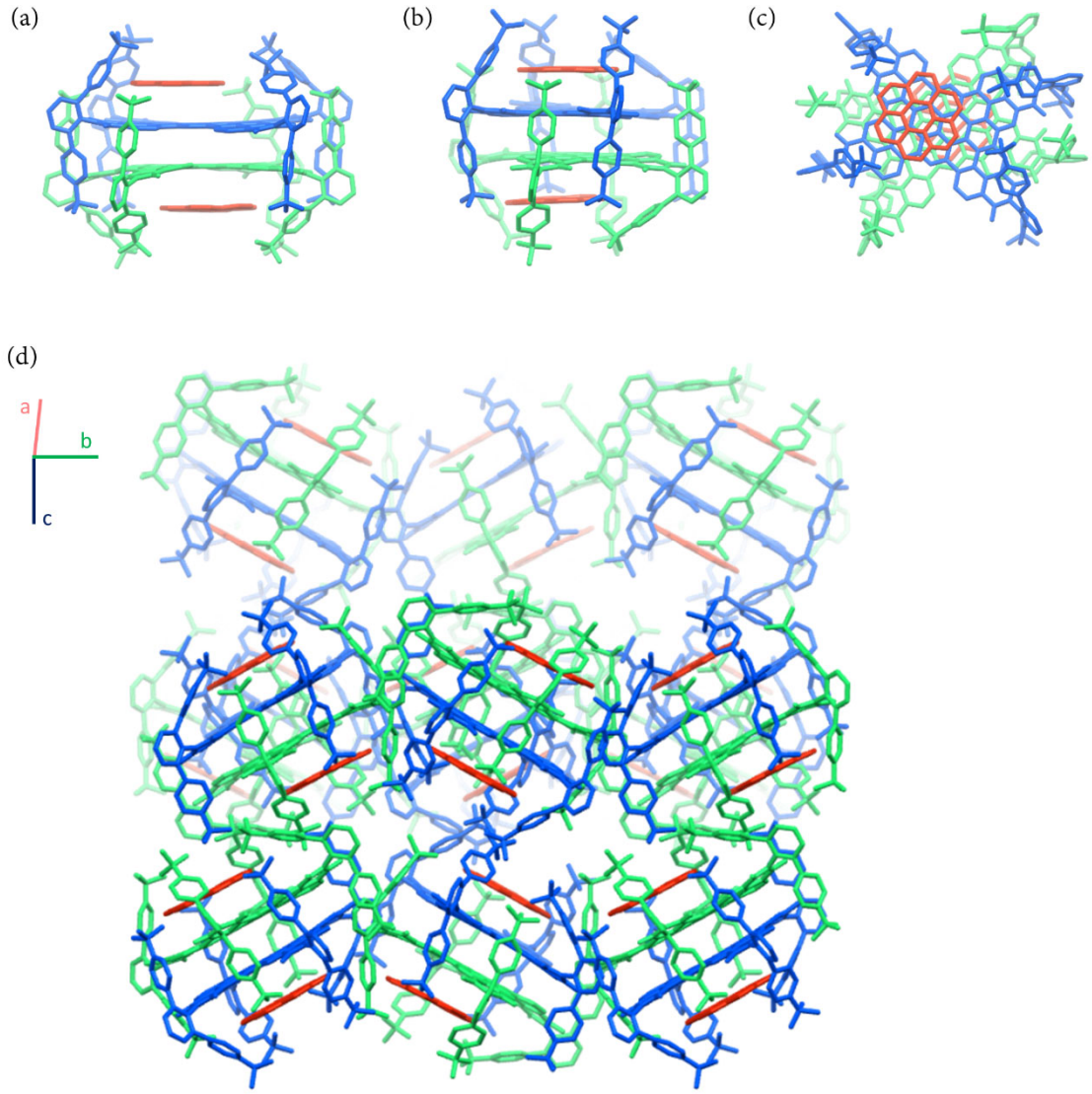

Figure A179. Molecular structure of a 2:2 co-crystal from **257** with coronene in the solid-state as obtained by single crystal X-ray diffraction. (a) Front view, (b) side view and (c) top view of 2:2 complex. (d) Packing arrangement of 2:2 complex.

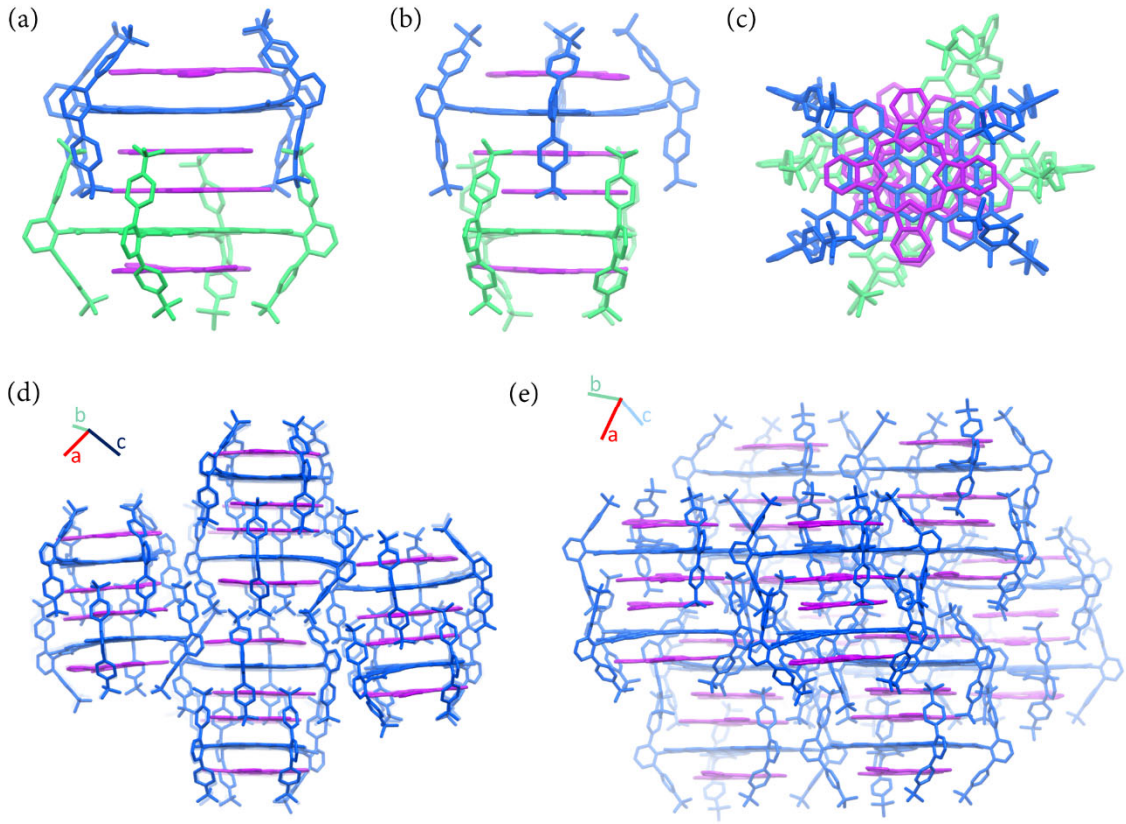

Figure A180. Molecular structure of a co-crystal from **257** with phthalocyanine in the solid-state as obtained by single crystal X-ray diffraction. (a) Front view, (b) side view and (c) top view of dimeric 1:2 complexes. (d–e) Packing arrangement of dimeric 1:2 complexes.

For elucidation of the co-crystal formation, we used different ratios of **257** and coronene as well as various concentrations (Table A38–Table A42). Therefore, a mixture of **257** and coronene (ratios: 1:0.5, 1:1, 1:2, 1:4 and 1:6) were dissolved in chloroform (C1: *c*(**257**) = 1.0 mg/mL, C2: *c*(**257**) = 0.5 mg/mL, C3: *c*(**257**) = 0.1 mg/mL) and passed through syringe filters. Appling the vapor-diffusion method with *n*-hexane gave after 3–14 days in most cases suitable co-crystals for crystallographic analysis. From all samples at least two independent crystallization experiments were performed. Subsequently, the unit cells from the obtained co-crystals were determined and compared to our initial X-ray data (Table A34–Table A36). For 1:0.5 and 1:1 ratios only 2:2 co-crystals could be observed, while ratios of 1:4 and 1:6 yielded only one of the two 1:2 co-crystal polymorphs. A ratio of 1:2 gave at higher concentration 1:2 co-crystals (*Polymorph B*) and at lower concentrations the 2:2 co-crystals.

Table A38. Unit cell determination of co-crystals grown from a molar ratio of **257**:coronene with 1:0.5.

conc.	crystal shape	*a* / Å	*b* / Å	*c* / Å	*α* / °	*β* / °	*γ* / °	unit cell
C1	needle	63.94	34.74	36.07	90	123.46	90	2:2 co-crystal (Table A36)
C1	needle	63.40	34.68	35.38	90	123.46	90	2:2 co-crystal (Table A36)
C2	needle	63.79	34.79	35.56	90	123.22	90	2:2 co-crystal (Table A36)
C2	needle	63.59	34.72	35.48	90	123.27	90	2:2 co-crystal (Table A36)
C3	-[a]	-[a]	-[a]	-[a]	-[a]	-[a]	-[a]	-[a]
C3	-[a]	-[a]	-[a]	-[a]	-[a]	-[a]	-[a]	-[a]

[a]No suitable co-crystals for X-ray diffraction could be obtained.

Table A39. Unit cell determination of co-crystals grown from a molar ratio of **257**:coronene with 1:1.

conc.	crystal shape	*a* / Å	*b* / Å	*c* / Å	*α* / °	*β* / °	*γ* / °	unit cell
C1	needle	63.58	34.75	35.43	90	123.21	90	2:2 co-crystal (Table A36)
C1	needle	63.55	34.73	35.34	90	123.24	90	2:2 co-crystal (Table A36)
C2	needle	63.82	34.57	35.90	90	123.60	90	2:2 co-crystal (Table A36)
C2	needle	63.54	34.72	35.07	90	123.34	90	2:2 co-crystal (Table A36)
C3	needle	63.77	34.72	35.69	90	123.36	90	2:2 co-crystal (Table A36)
C3	needle	63.59	34.72	35.42	90	123.19	90	2:2 co-crystal (Table A36)

Table A40. Unit cell determination of co-crystals grown from a molar ratio of **257**:coronene with 1:2.

conc.	crystal shape	*a* / Å	*b* / Å	*c* / Å	*α* / °	*β* / °	*γ* / °	unit cell
C1	block	20.49	23.49	25.30	115.03	100.14	105.38	1:2 co-crystal (*Polymorph B*, Table A35)
C1	block	20.30	22.84	25.15	114.56	100.45	105.42	1:2 co-crystal (*Polymorph B*, Table A35)
C2	-[a]	-[a]	-[a]	-[a]	-[a]	-[a]	-[a]	-[a]
C2	-[a]	-[a]	-[a]	-[a]	-[a]	-[a]	-[a]	-[a]
C3	needle	63.43	34.53	35.65	90	123.36	90	2:2 co-crystal (Table A36)
C3	needle	63.76	34.73	35.62	90	123.48	90	2:2 co-crystal (Table A36)

[a]No suitable co-crystals for X-ray diffraction could be obtained.

Table A41. Unit cell determination of co-crystals grown from a molar ratio of **257**:coronene with 1:4.

conc.	crystal shape	*a* / Å	*b* / Å	*c* / Å	*α* / °	*β* / °	*γ* / °	unit cell
C1	block	20.61	23.12	25.66	114.04	100.83	105.89	1:2 co-crystal (*Polymorph B*, Table A35)
C1	block	20.61	23.07	25.71	114.03	100.77	105.90	1:2 co-crystal (*Polymorph B*, Table A35)
C2	-[a]	-[a]	-[a]	-[a]	-[a]	-[a]	-[a]	-[a]
C2	-[a]	-[a]	-[a]	-[a]	-[a]	-[a]	-[a]	-[a]
C3	-[a]	-[a]	-[a]	-[a]	-[a]	-[a]	-[a]	-[a]
C3	-[a]	-[a]	-[a]	-[a]	-[a]	-[a]	-[a]	-[a]

[a]No suitable co-crystals for X-ray diffraction could be obtained.

Table A42. Unit cell determination of co-crystals grown from a molar ratio of **257**:coronene with 1:6.

conc.	crystal shape	*a* / Å	*b* / Å	*c* / Å	*α* / °	*β* / °	*γ* / °	unit cell
C1	-[a]	-[a]	-[a]	-[a]	-[a]	-[a]	-[a]	-[a]
C1	block	11.44	20.02	22.96	110.55	102.47	99.87	1:2 co-crystal (*Polymorph A*, Table A34)
C2	-[a]	-[a]	-[a]	-[a]	-[a]	-[a]	-[a]	-[a]
C2	-[a]	-[a]	-[a]	-[a]	-[a]	-[a]	-[a]	-[a]
C3	-[a]	-[a]	-[a]	-[a]	-[a]	-[a]	-[a]	-[a]
C3	-[a]	-[a]	-[a]	-[a]	-[a]	-[a]	-[a]	-[a]

[a]No suitable co-crystals for X-ray diffraction could be obtained.

Theoretical Calculations

Decomposition of the non-covalent interaction ($E_{interaction}$) into electrostatics ($E_{electrostatic}$), dispersion ($E_{dispersion}$), Pauli repulsion ($E_{Pauli\text{-}repulsion}$), polarization ($E_{polarization}$) and charge-transfer ($E_{charge\text{-}transfer}$) contributions (equation 4) was performed with second generation absolutely localized molecular orbitals (ALMO) energy decomposition analysis[383] (EDA). This method was chosen as the appropriate decomposition scheme as it allows supramolecular structures larger than dimers and provides information on the charge-transfer contribution.

$$E_{interaction} = E_{electrostatic} + E_{dispersion} + E_{Pauli\text{-}repulsion} + E_{polarization} + E_{charge\text{-}transfer} \quad (4)$$

The program Q-Chem 5.1[413] was used to perform the ALMO-EDA for the 1:2-crystal structure geometry of nanographene:coronene (*Polymorph A*) at B3LYP-D3/ 6-311G(d) level of theory.

NMR Spectroscopy

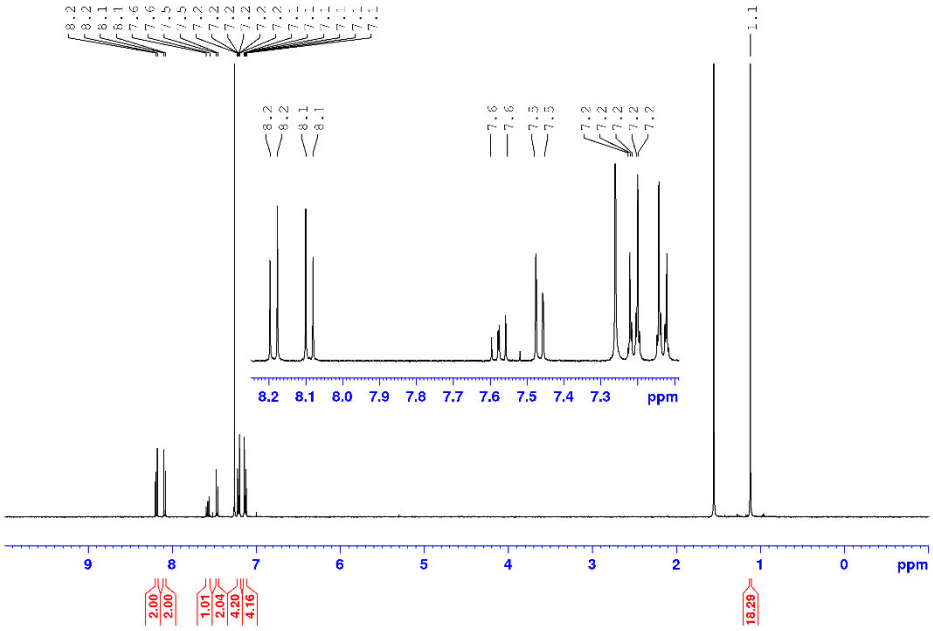

Figure A181. ^{1}H NMR (400 MHz) spectrum of **259** in $CDCl_3$ at room temperature.

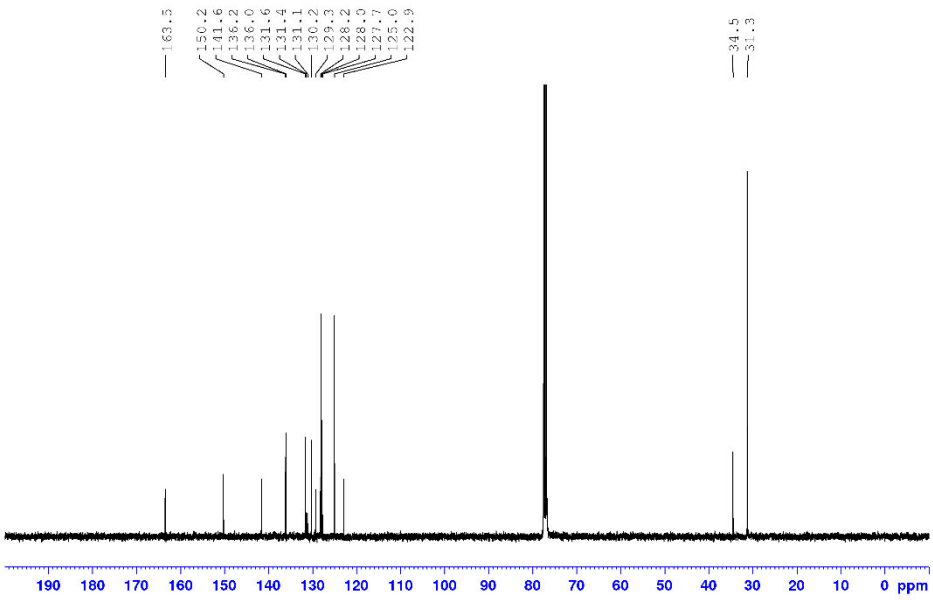

Figure A182. ^{13}C NMR (101 MHz) spectrum of **259** in $CDCl_3$ at room temperature.

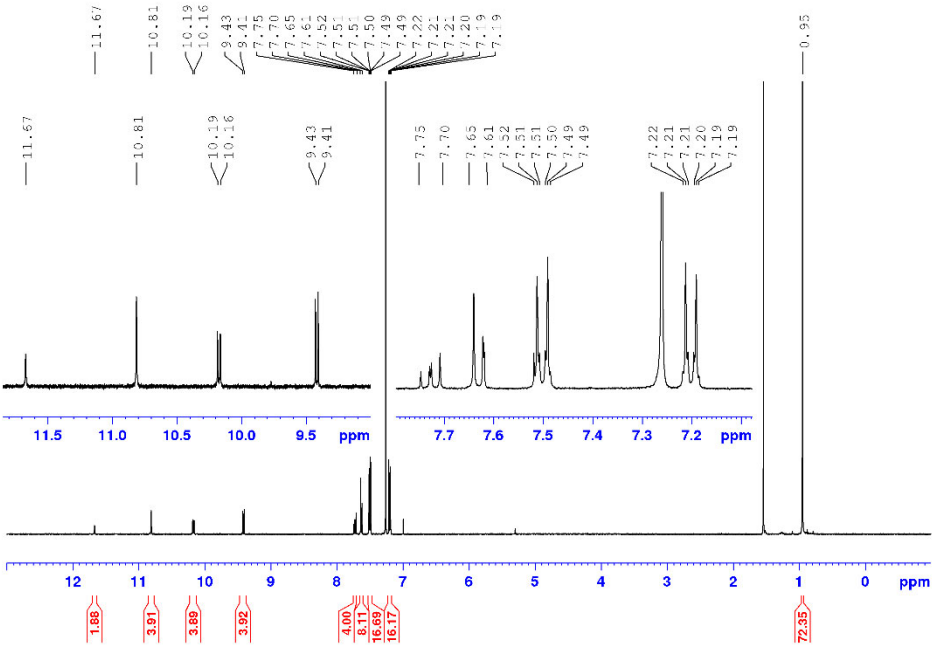

Figure A183. ^{1}H NMR (400 MHz) spectrum of **257** in $CDCl_3$ at room temperature.

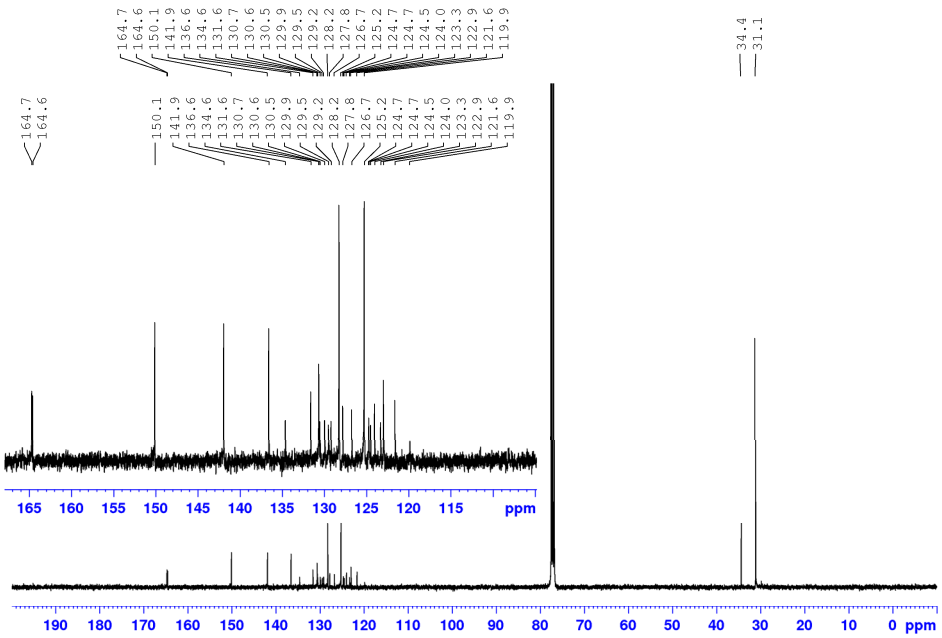

Figure A184. ^{13}C NMR (101 MHz) spectrum of **257** in $CDCl_3$ at room temperature.

Mass Spectrometry

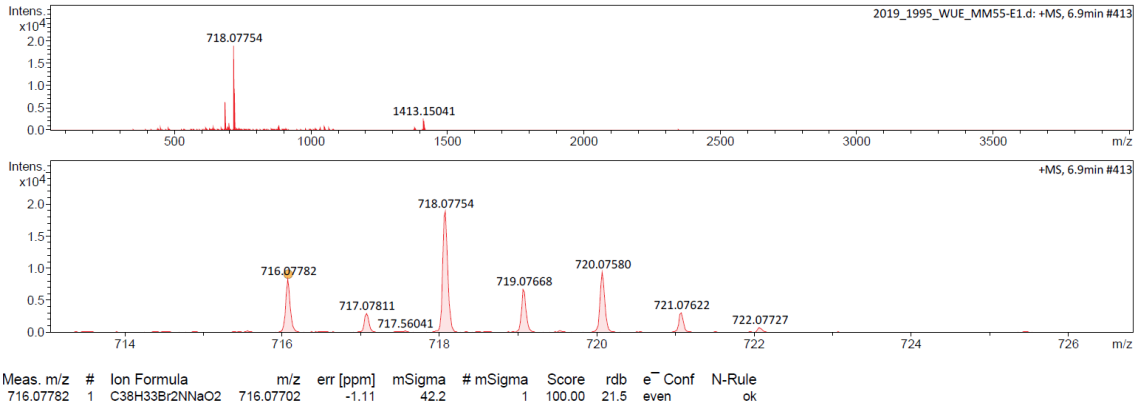

Meas. m/z	#	Ion Formula	m/z	err [ppm]	mSigma	# mSigma	Score	rdb	e¯ Conf	N-Rule
716.07782	1	C38H33Br2NNaO2	716.07702	-1.11	42.2	1	100.00	21.5	even	ok

Figure A185. HRMS (ESI-TOF, positive mode, acetonitrile/chloroform) spectrum of **259**.

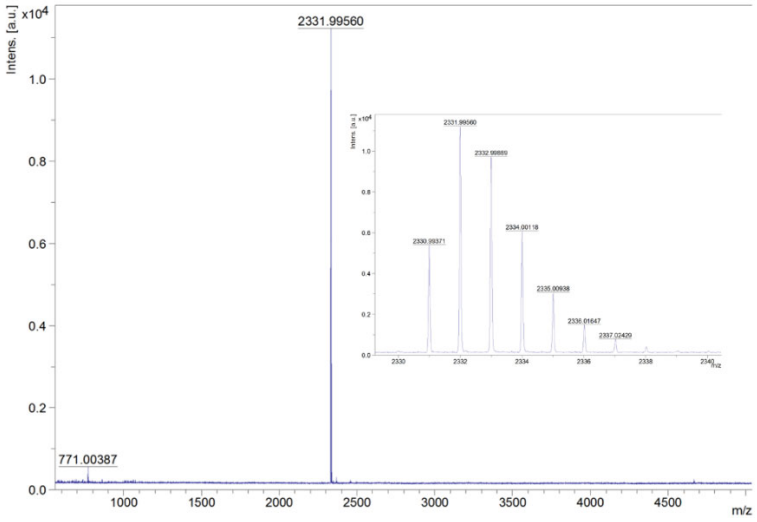

Figure A186. HRMS (MALDI-TOF, negative mode, DCTB in chloroform) spectrum of **257**.

Bibliography

[1] W. Herbst, K. Hunger, *Industrial Organic Pigments: Production, Properties, Applications*, 3 ed., Wiley VCH, Weinheim, **2004**.

[2] H. Zollinger, *Color Chemistry: Synthesis, Properties, and Applications of Organic Dyes and Pigments*, 3 ed., Verlag Helvetica Chimica Acta, Zürich, **2003**.

[3] J. O. Escobedo, O. Rusin, S. Lim, R. M. Strongin, *Curr. Opin. Chem. Biol.* **2010**, *14*, 64–70.

[4] S. Luo, E. Zhang, Y. Su, T. Cheng, C. Shi, *Biomaterials* **2011**, *32*, 7127–7138.

[5] S. Zhu, R. Tian, A. L. Antaris, X. Chen, H. Dai, *Adv. Mater.* **2019**, *31*, 1900321.

[6] A. J. C. Kuehne, M. C. Gather, *Chem. Rev.* **2016**, *116*, 12823–12864.

[7] I. D. W. Samuel, G. A. Turnbull, *Chem. Rev.* **2007**, *107*, 1272–1295.

[8] G.-W. Wei, X.-D. Wang, L.-S. Liao, *Adv. Funct. Mater.* **2019**, *29*, 1902981.

[9] M. Gsänger, D. Bialas, L. Huang, M. Stolte, F. Würthner, *Adv. Mater.* **2016**, *28*, 3615–3645.

[10] Y. Avlasevich, C. Li, K. Müllen, *J. Mater. Chem.* **2010**, *20*, 3814–3826.

[11] O. Ostroverkhova, *Chem. Rev.* **2016**, *116*, 13279–13412.

[12] K. Hunger, *Industrial Dyes: Chemistry, Properties, Applications*, WILEY-VCH Verlag GmbH & Co. KGaA, Weinheim, **2003**.

[13] P. Bamfield, M. G. Hutchings, *Chromic Phenomena: Technological Applications of Colour Chemistry*, 2 ed., The Royal Society of Chemistry, Cambridge, **2010**.

[14] R. M. Christie, *Colour Chemistry*, The Royal Society of Chemistry, Cambridge, **2001**.

[15] T. Weil, T. Vosch, J. Hofkens, K. Peneva, K. Müllen, *Angew. Chem. Int. Ed.* **2010**, *49*, 9068–9093.

[16] F. Würthner, *Chem. Commun.* **2004**, 1564–1579.

[17] M. A. Kobaisi, S. V. Bhosale, K. Latham, A. M. Raynor, S. V. Bhosale, *Chem. Rev.* **2016**, *116*, 11685–11796.

[18] A. Nowak-Król, K. Shoyama, M. Stolte, F. Würthner, *Chem. Commun.* **2018**, *54*, 13763–13772.

[19] L. Chen, C. Li, K. Müllen, *J. Mater. Chem. C* **2014**, *2*, 1938–1956.

[20] W. Jiang, Y. Li, Z. Wang, *Acc. Chem. Res.* **2014**, *47*, 3135–3147.

[21] M. Gsänger, J. H. Oh, M. Könemann, H. W. Höffken, A.-M. Krause, Z. N. Bao, F. Würthner, *Angew. Chem. Int. Ed.* **2010**, *49*, 740–743.

[22] C. Li, H. Wonneberger, *Adv. Mater.* **2012**, *24*, 613–636.

[23] M. G. Ramírez, S. Pla, P. G. Boj, J. M. Villalvilla, J. A. Quintana, M. A. Díaz-García, F. Fernández-Lázaro, A. Sastre-Santos, *Adv. Optical Mater.* **2013**, *1*, 933–938.

[24] N. G. Pschirer, C. Kohl, T. Nolde, J. Qu, K. Müllen, *Angew. Chem. Int. Ed.* **2006**, *45*, 1401–1404.

[25] C. Liu, S. Zhang, J. Li, J. Wei, K. Müllen, M. Yin, *Angew. Chem. Int. Ed.* **2018**, 1638–1642.

[26] V. M. Blas-Ferrando, J. Ortiz, K. Ohkubo, S. Fukuzumi, F. Fernández-Lázaro, A. Sastre-Santos, *Chem. Sci.* **2014**, *5*, 4785–4793.

[27] F. C. De Schryver, T. Vosch, M. Cotlet, M. Van der Auweraer, K. Müllen, J. Hofkens, *Acc. Chem. Res.* **2005**, *38*, 514–522.

[28] M. R. Wasielewski, *Acc. Chem. Res.* **2009**, *42*, 1910–1921.

[29] F. Würthner, C. R. Saha-Möller, B. Fimmel, S. Ogi, P. Leowanawat, D. Schmidt, *Chem. Rev.* **2016**, *116*, 962–1052.

[30] H.-W. Schmidt, F. Würthner, *Angew. Chem. Int. Ed.* **2020**, *59*, 8766–8775.

[31] H. Langhals, R. Ismael, O. Yürük, *Tetrahedron* **2000**, *56*, 5435–5441.

[32] H. Langhals, *Helv. Chim. Acta* **2005**, *88*, 1309–1343.

[33] D. Schmidt, M. Stolte, J. Süß, A. Liess, V. Stepanenko, F. Würthner, *Angew. Chem. Int. Ed.* **2019**, *58*, 13385–13389.
[34] J. Royakkers, A. Minotto, D. G. Congrave, W. Zeng, A. Patel, A. D. Bond, D.-K. Bučar, F. Cacialli, H. Bronstein, *J. Org. Chem.* **2019**, *85*, 207–214.
[35] B. Zhang, H. Soleimaninejad, D. J. Jones, J. M. White, K. P. Ghiggino, T. A. Smith, W. W. H. Wong, *Chem. Mater.* **2017**, *29*, 8395–8403.
[36] J. L. Banal, H. Soleimaninejad, F. M. Jradi, M. Y. Liu, J. M. White, A. W. Blakers, M. W. Cooper, D. J. Jones, K. P. Ghiggino, S. R. Marder, T. A. Smith, W. W. H. Wong, *J. Phys. Chem. C* **2016**, *120*, 12952–12958.
[37] F. O. Holtrup, G. R. J. Müller, H. Quante, S. De Feyter, F. C. De Schryver, K. Müllen, *Chem. Eur. J.* **1997**, *3*, 219–225.
[38] F. Nolde, J. W. Qu, C. Kohl, N. G. Pschirer, E. Reuther, K. Müllen, *Chem. Eur. J.* **2005**, *11*, 3959–3967.
[39] Y. Geerts, H. Quante, H. Platz, R. Mahrt, M. Hopmeier, A. Böhm, K. Müllen, *J. Mater. Chem.* **1998**, *8*, 2357–2369.
[40] H. Quante, K. Müllen, *Angew. Chem. Int. Ed. Engl.* **1995**, *34*, 1323–1325.
[41] X. Zhao, Y. Xiong, J. Ma, Z. Yuan, *J. Phys. Chem. A* **2016**, *120*, 7554–7560.
[42] S. K. Lee, Y. Zu, A. Herrmann, Y. Geerts, K. Müllen, A. J. Bard, *J. Am. Chem. Soc.* **1999**, *121*, 3513–3520.
[43] J. Fabian, H. Nakazumi, M. Matsuoka, *Chem. Rev.* **1992**, *92*, 1197–1226.
[44] G. Qian, Z. Y. Wang, *Chem. Asian J.* **2010**, *5*, 1006–1029.
[45] V. Pansare, S. Hejazi, W. Faenza, R. K. Prud'homme, *Chem. Mater.* **2012**, *24*, 812–827.
[46] C. Liu, K. Wang, X. Gong, A. J. Heeger, *Chem. Soc. Rev.* **2016**, *45*, 4825–4846.
[47] P. Brogdon, H. Cheema, J. H. Delcamp, *ChemSusChem* **2018**, *11*, 86–103.
[48] A. Zampetti, A. Minotto, F. Cacialli, *Adv. Funct. Mater.* **2019**, *29*, 1807623.
[49] J. Vollbrecht, H. Bock, C. Wiebeler, S. Schumacher, H. Kitzerow, *Chem. Eur. J.* **2014**, *20*, 12026–12031.
[50] S. Kumar, J. Shukla, Y. Kumar, P. Mukhopadhyay, *Org. Chem. Front.* **2018**, *5*, 2254–2276.
[51] Y. Fukutomi, M. Nakano, J. Y. Hu, I. Osaka, K. Takimiya, *J. Am. Chem. Soc.* **2013**, *135*, 11445–11448.
[52] Z. Sun, Q. Ye, C. Chi, J. Wu, *Chem. Soc. Rev.* **2012**, *41*, 7857–7889.
[53] S. Seifert, D. Schmidt, K. Shoyama, F. Würthner, *Angew. Chem. Int. Ed.* **2017**, *56*, 7595–7600.
[54] C. S. Sample, E. Goto, N. V. Handa, Z. A. Page, Y. D. Luo, C. J. Hawker, *J. Mater. Chem. C* **2017**, *5*, 1052–1056.
[55] T. V. Pho, F. M. Toma, M. L. Chabinyc, F. Wudl, *Angew. Chem. Int. Ed.* **2013**, *52*, 1446–1451.
[56] J. Kelber, M. F. Achard, F. Durola, H. Bock, *Angew. Chem. Int. Ed.* **2012**, *51*, 5200–5203.
[57] H. Zhylitskaya, M. Stępień, *Org. Chem. Front.* **2018**, *5*, 2395–2414.
[58] S. Seifert, K. Shoyama, D. Schmidt, F. Würthner, *Angew. Chem. Int. Ed.* **2016**, *55*, 6390–6395.
[59] S. Seifert, D. Schmidt, F. Würthner, *Org. Chem. Front.* **2016**, *3*, 1435–1442.
[60] P. Osswald, F. Würthner, *J. Am. Chem. Soc.* **2007**, *129*, 14319–14326.
[61] B. Pagoaga, L. Giraudet, N. Hoffmann, *Eur. J. Org. Chem.* **2014**, *2014*, 5178–5195.
[62] J. W. Steed, J. L. Atwood, *Supramolecular Chemistry*, 2 ed., John Wiley & Sons Ltd, Chichester, West Sussex, **2009**.
[63] J. L. Atwood, J. W. Steed, *Encyclopedia of Supramolecular Chemistry*, Marcel Dekker, Inc., New York, **2004**.
[64] H. J. Schneider, *Angew. Chem. Int. Ed. Engl.* **1991**, *30*, 1417–1436.
[65] E. Persch, O. Dumele, F. Diederich, *Angew. Chem. Int. Ed.* **2015**, *54*, 3290–3327.
[66] H. Lodish, A. Berk, S. L. Zipursky, P. Matsudaira, D. Baltimore, J. Darnel, *Molecular Cell Biology*, W. H. Freeman & Co., New York, **2000**.
[67] K. Wang, J. H. Jordan, X.-Y. Hu, L. Wang, *Angew. Chem. Int. Ed.* **2020**, *59*, 13712–13721.
[68] D. B. Amabilino, D. K. Smith, J. W. Steed, *Chem. Soc. Rev.* **2017**, *46*, 2404–2420.
[69] T. L. Mako, J. M. Racicot, M. Levine, *Chem. Rev.* **2019**, *119*, 322–477.

[70] L. You, D. Zha, E. V. Anslyn, *Chem. Rev.* **2015**, *115*, 7840–7892.
[71] Z. Liu, S. K. M. Nalluri, J. F. Stoddart, *Chem. Soc. Rev.* **2017**, *46*, 2459–2478.
[72] P. Spenst, F. Würthner, *J. Photochem. Photobiol. C* **2017**, *31*, 114–138.
[73] F.-G. Klärner, B. Kahlert, *Acc. Chem. Res.* **2003**, *36*, 919–932.
[74] M. Hardouin-Lerouge, P. Hudhomme, M. Sallé, *Chem. Soc. Rev.* **2011**, *40*, 30–43.
[75] M. Yoshizawa, J. K. Klosterman, M. Fujita, *Angew. Chem. Int. Ed.* **2009**, *48*, 3418–3438.
[76] Y. Xu, M. von Delius, *Angew. Chem. Int. Ed.* **2019**, *59*, 559–573.
[77] R. Rieger, K. Müllen, *J. Phys. Org. Chem.* **2010**, *23*, 315–325.
[78] A. Narita, X. Y. Wang, X. Feng, K. Müllen, *Chem. Soc. Rev.* **2015**, *44*, 6616–6643.
[79] X. L. Feng, W. Pisula, K. Müllen, *Pure Appl. Chem.* **2009**, *81*, 2203–2224.
[80] M. Stępień, E. Gońka, M. Żyła, N. Sprutta, *Chem. Rev.* **2017**, *117*, 3479–3716.
[81] M. K. Hargreaves, J. G. Pritchard, H. R. Dave, *Chem. Rev.* **1970**, *70*, 439–469.
[82] H. Langhals, *Heterocycles* **1995**, *40*, 477–500.
[83] M. Kardos, *Ber. Dtsch. Chem. Ges.* **1913**, *46*, 2086–2091.
[84] C. Liebermann, M. Kardos, *Ber. Dtsch. Chem. Ges.* **1914**, *47*, 1203–1210.
[85] G. Geissler, H. Remy (Hoechst AG), *DE1130099,* **1959**.
[86] A. Nowak-Król, F. Würthner, *Org. Chem. Front.* **2019**, *6*, 1272–1318.
[87] C. Huang, S. Barlow, S. R. Marder, *J. Org. Chem.* **2011**, *76*, 2386–2407.
[88] Z. Sun, K. W. Huang, J. S. Wu, *Org. Lett.* **2010**, *12*, 4690–4693.
[89] Z. Sun, K.-W. Huang, J. Wu, *J. Am. Chem. Soc.* **2011**, *133*, 11896–11899.
[90] P. de Echegaray, M. J. Mancheño, I. Arrechea-Marcos, R. Juárez, G. López-Espejo, J. T. L. Navarrete, M. M. Ramos, C. Seoane, R. P. Ortiz, J. L. Segura, *J. Org. Chem.* **2016**, *81*, 11256–11267.
[91] Z. Lin, C. Li, D. Meng, Y. Li, Z. Wang, *Chem. Asian J.* **2016**, *11*, 2695–2699.
[92] Y. Hashikawa, M. Murata, A. Wakamiya, Y. Murata, *J. Am. Chem. Soc.* **2017**, *139*, 16350–16358.
[93] J. Feng, Y. Wu, Q. Yu, Y. Liu, W. Jiang, D. Wang, Z. Wang, *CCS Chem.* **2020**, *2*, 271–279.
[94] J. Feng, H. Fu, W. Jiang, A. Zhang, H. S. Ryu, H. S. Woo, Y. Sun, Z. Wang, *ACS Appl. Mater. Interfaces* **2020**, *12*, 29513–29519.
[95] K. Shoyama, F. Würthner, *J. Am. Chem. Soc.* **2019**, *141*, 13008–13012.
[96] W. Yue, J. Gao, Y. Li, W. Jiang, S. Di Motta, F. Negri, Z. Wang, *J. Am. Chem. Soc.* **2011**, *133*, 18054–18057.
[97] S. L. Suraru, U. Zschieschang, H. Klauk, F. Würthner, *Chem. Commun.* **2011**, *47*, 11504–11506.
[98] S. L. Suraru, C. Burschka, F. Würthner, *J. Org. Chem.* **2014**, *79*, 128–139.
[99] J. Gao, Y. Li, Z. Wang, *Org. Lett.* **2013**, *15*, 1366–1369.
[100] Y. Avlasevich, S. Müller, P. Erk, K. Müllen, *Chem. Eur. J.* **2007**, *13*, 6555–6561.
[101] W. Jiang, Y. Li, W. Yue, Y. Zhen, J. Qu, Z. Wang, *Org. Lett.* **2010**, *12*, 228–231.
[102] Y. Li, W. Xu, S. Di Motta, F. Negri, D. B. Zhu, Z. Wang, *Chem. Commun.* **2012**, *48*, 8204–8206.
[103] H. Qian, Z. Wang, W. Yue, D. Zhu, *J. Am. Chem. Soc.* **2007**, *129*, 10664–10665.
[104] H. Qian, F. Negri, C. Wang, Z. Wang, *J. Am. Chem. Soc.* **2008**, *130*, 17970–17976.
[105] Y. Zhen, C. Wang, Z. Wang, *Chem. Commun.* **2010**, *46*, 1926–1928.
[106] W. Yue, A. Lv, J. Gao, W. Jiang, L. Hao, C. Li, Y. Li, L. E. Polander, S. Barlow, W. Hu, S. Di Motta, F. Negri, S. R. Marder, Z. Wang, *J. Am. Chem. Soc.* **2012**, *134*, 5770–5773.
[107] G. Liu, C. Xiao, F. Negri, Y. Li, Z. Wang, *Angew. Chem. Int. Ed.* **2020**, *59*, 2008–2012.
[108] H. Zhong, C.-H. Wu, C.-Z. Li, J. Carpenter, C.-C. Chueh, J.-Y. Chen, H. Ade, A. K.-Y. Jen, *Adv. Mater.* **2016**, *28*, 951–958.
[109] A. Wadsworth, M. Moser, A. Marks, M. S. Little, N. Gasparini, C. J. Brabec, D. Baran, I. McCulloch, *Chem. Soc. Rev.* **2018**, *48*, 1596–1625.
[110] C. Yan, S. Barlow, Z. Wang, H. Yan, A. K.-Y. Jen, S. R. Marder, X. Zhan, *Nat. Rev. Mater.* **2018**, *3*, 18003.
[111] G. Zhang, J. Zhao, P. C. Y. Chow, K. Jiang, J. Zhang, Z. Zhu, J. Zhang, F. Huang, H. Yan, *Chem. Rev.* **2018**, *118*, 3447–3507.

[112] N. J. Schuster, D. W. Paley, S. Jockusch, F. Ng, M. L. Steigerwald, C. Nuckolls, *Angew. Chem. Int. Ed.* **2016**, *55*, 13519–13523.
[113] D. Meng, G. Liu, C. Xiao, Y. Shi, L. Zheng, L. Jiang, K. K. Baldridge, Y. Li, J. S. Siegel, Z. Wang, *J. Am. Chem. Soc.* **2019**, *141*, 5402–5408.
[114] A. R. Mohebbi, C. Munoz, F. Wudl, *Org. Lett.* **2011**, *13*, 2560–2563.
[115] S. Katsuta, K. Tanaka, Y. Maruya, S. Mori, S. Masuo, T. Okujima, H. Uno, K. Nakayama, H. Yamada, *Chem. Commun.* **2011**, *47*, 10112–10114.
[116] H. Zhylitskaya, J. Cybińska, P. Chmielewski, T. Lis, M. Stępień, *J. Am. Chem. Soc.* **2016**, *138*, 11390–11398.
[117] M. Żyła-Karwowska, H. Zhylitskaya, J. Cybińska, T. Lis, P. J. Chmielewski, M. Stępień, *Angew. Chem. Int. Ed.* **2016**, *55*, 14658–14662.
[118] M. Żyła-Karwowska, L. Moshniaha, Y. Hong, H. Zhylitskaya, J. Cybińska, P. J. Chmielewski, T. Lis, D. Kim, M. Stępień, *Chem. Eur. J.* **2018**, *24*, 7525–7530.
[119] M. Navakouski, H. Zhylitskaya, P. J. Chmielewski, T. Lis, J. Cybińska, M. Stępień, *Angew. Chem. Int. Ed.* **2019**, *58*, 4929–4933.
[120] S. Kumar, Y. K. Maurya, S. Kang, P. Chmielewski, T. Lis, J. Cybińska, D. Kim, M. Stępień, *Org. Lett.* **2020**, *22*, 7202–7207.
[121] L. L. Moshniaha, M. Żyła-Karwowska, P. J. Chmielewski, T. Lis, J. Cybińska, E. Gońka, J. Oschwald, T. Drewello, S. M. Rivero, J. Casado, M. Stępień, *J. Am. Chem. Soc.* **2020**, *142*, 3626–3635.
[122] M. Navakouski, H. Zhylitskaya, P. J. Chmielewski, M. Żyła-Karwowska, M. Stępień, *J. Org. Chem.* **2020**, *85*, 187–194.
[123] Q. Bai, B. Gao, W. Ai, Y. Wu, X. Ba, *Org. Lett.* **2011**, *13*, 6484–6487.
[124] Y. Avlasevich, K. Müllen, *Chem. Commun.* **2006**, 4440–4442.
[125] D. Désilets, P. M. Kazmaier, R. A. Burt, G. K. Hamer, *Can. J. Chem.* **1995**, *73*, 325–335.
[126] Y. Li, Y. Li, J. Li, C. Li, X. Liu, M. Yuan, H. Liu, S. Wang, *Chem. Eur. J.* **2006**, *12*, 8378–8385.
[127] N. Sakai, J. Mareda, E. Vauthey, S. Matile, *Chem. Commun.* **2010**, *46*, 4225–4237.
[128] C. Li, Z. Lin, Y. Li, Z. Wang, *Chem. Rec.* **2016**, *16*, 873–885.
[129] B. Fimmel, M. Son, Y. M. Sung, M. Grüne, B. Engels, D. Kim, F. Würthner, *Chem. Eur. J.* **2015**, *21*, 615–630.
[130] S. Demmig, H. Langhals, *Chem. Ber.* **1988**, *121*, 225–230.
[131] Z. J. Chen, B. Fimmel, F. Würthner, *Org. Biomol. Chem.* **2012**, *10*, 5845–5855.
[132] D. Görl, X. Zhang, F. Würthner, *Angew. Chem. Int. Ed.* **2012**, *51*, 6328–6348.
[133] M. Sun, K. Müllen, M. Yin, *Chem. Soc. Rev.* **2016**, *45*, 1513–1528.
[134] C. W. Struijk, A. B. Sieval, J. E. J. Dakhorst, M. van Dijk, P. Kimkes, R. B. M. Koehorst, H. Donker, T. J. Schaafsma, S. J. Picken, A. M. van de Craats, J. M. Warman, H. Zuilhof, E. J. R. Sudhölter, *J. Am. Chem. Soc.* **2000**, *122*, 11057–11066.
[135] R. Schmidt, J. H. Oh, Y. S. Sun, M. Deppisch, A.-M. Krause, K. Radacki, H. Braunschweig, M. Könemann, P. Erk, Z. Bao, F. Würthner, *J. Am. Chem. Soc.* **2009**, *131*, 6215–6228.
[136] Z. Guo, S. Park, J. Yoon, I. Shin, *Chem. Soc. Rev.* **2014**, *43*, 16–29.
[137] F.-P. Gao, Y.-X. Lin, L.-L. Li, Y. Liu, U. Mayerhöffer, P. Spenst, J.-G. Su, J.-Y. Li, F. Würthner, H. Wang, *Biomaterials* **2014**, *35*, 1004–1014.
[138] M. Emmelius, G. Pawlowski, H. W. Vollmann, *Angew. Chem. Int. Ed.* **1989**, *28*, 1445–1471.
[139] H. M. D. Bandara, S. C. Burdette, *Chem. Soc. Rev.* **2012**, *41*, 1809–1825.
[140] M. Dong, A. Babalhavaeji, S. Samanta, A. A. Beharry, G. A. Woolley, *Acc. Chem. Res.* **2015**, *48*, 2662–2670.
[141] G. G. Dias, A. King, F. de Moliner, M. Vendrell, E. F. da Silva, Jr., *Chem. Soc. Rev.* **2018**, *47*, 12–27.
[142] S. Hiroto, Y. Miyake, H. Shinokubo, *Chem. Rev.* **2017**, *117*, 2910–3043.
[143] C. G. Claessens, U. Hahn, T. Torres, *Chem. Rec.* **2008**, *8*, 75–97.
[144] J. Mack, N. Kobayashi, *Chem. Rev.* **2011**, *111*, 281–321.
[145] Q. Chen, L. Brambilla, L. Daukiya, K. S. Mali, S. De Feyter, M. Tommasini, K. Müllen, A. Narita, *Angew. Chem. Int. Ed.* **2018**, *57*, 11233–11237.

[146] N. Kobayashi, H. Ogata, N. Nonaka, E. A. Luk'yanets, *Chem. Eur. J.* **2003**, *9*, 5123–5134.
[147] A. C. S. Lobo, A. D. Silva, V. A. Tomé, S. M. A. Pinto, E. F. F. Silva, M. J. F. Calvete, C. M. F. Gomes, M. M. Pereira, L. G. Arnaut, *J. Med. Chem.* **2016**, *59*, 4688–4696.
[148] A. Muranaka, M. Yonehara, M. Uchiyama, *J. Am. Chem. Soc.* **2010**, *132*, 7844–7845.
[149] N. Kobayashi, S. Nakajima, H. Ogata, T. Fukuda, *Chem. Eur. J.* **2004**, *10*, 6294–6312.
[150] B. Pigulski, K. Shoyama, F. Würthner, *Angew. Chem. Int. Ed.* **2020**, *59*, 15908–15912.
[151] C. Jiao, K.-W. Huang, J. Luo, K. Zhang, C. Chi, J. Wu, *Org. Lett.* **2009**, *11*, 4508–4511.
[152] C. Kohl, S. Becker, K. Müllen, *Chem. Commun.* **2002**, 2778–2779.
[153] A. Mishra, R. K. Behera, P. K. Behera, B. K. Mishra, G. B. Behera, *Chem. Rev.* **2000**, *100*, 1973–2011.
[154] F. Würthner, *Acc. Chem. Res.* **2016**, *49*, 868–876.
[155] K. Ilina, W. M. MacCuaig, M. Laramie, J. N. Jeouty, L. R. McNally, M. Henary, *Bioconjugate Chem.* **2020**, *31*, 194–213.
[156] D. Keil, H. Hartmann, C. Reichardt, *Liebigs Ann. Chem.* **1993**, *1993*, 935–939.
[157] A. Loudet, K. Burgess, *Chem. Rev.* **2007**, *107*, 4891–4932.
[158] K. Rurack, M. Spieles, *Anal. Chem.* **2011**, *83*, 1232–1242.
[159] C. Würth, M. Grabolle, J. Pauli, M. Spieles, U. Resch-Genger, *Nat. Protoc.* **2013**, *8*, 1535–1550.
[160] A. Zitzler-Kunkel, M. R. Lenze, N. M. Kronenberg, A.-M. Krause, M. Stolte, K. Meerholz, F. Würthner, *Chem. Mater.* **2014**, *26*, 4856–4866.
[161] U. Mayerhöffer, B. Fimmel, F. Würthner, *Angew. Chem. Int. Ed.* **2012**, *51*, 164–167.
[162] M. Tian, S. Tatsuura, M. Furuki, Y. Sato, I. Iwasa, L. S. Pu, *J. Am. Chem. Soc.* **2003**, *125*, 348–349.
[163] A. Martin, C. Long, R. J. Forster, T. E. Keyes, *Chem. Commun.* **2012**, *48*, 5617–5619.
[164] G. M. Fischer, A. P. Ehlers, A. Zumbusch, E. Daltrozzo, *Angew. Chem. Int. Ed.* **2007**, *46*, 3750–3753.
[165] S. Mathew, N. A. Astani, B. F. E. Curchod, J. H. Delcamp, M. Marszalek, J. Frey, U. Rothlisberger, M. K. Nazeeruddin, M. Grätzel, *J. Mater. Chem. A* **2016**, *4*, 2332–2339.
[166] C. Jiao, N. Zu, K.-W. Huang, P. Wang, J. Wu, *Org. Lett.* **2011**, *13*, 3652–3655.
[167] M. Rémond, J. Hwang, J. Kim, S. Kim, D. Kim, C. Bucher, Y. Bretonniére, C. Andraud, E. Kim, *Adv. Funct. Mater.* **2020**, *30*, 2004831.
[168] G. Qian, B. Dai, M. Luo, D. Yu, J. Zhan, Z. Zhang, D. Ma, Z. Y. Wang, *Chem. Mater.* **2008**, *20*, 6208–6216.
[169] D. F. Perepichka, M. R. Bryce, C. Pearson, M. C. Petty, E. J. L. McInnes, J. P. Zhao, *Angew. Chem. Int. Ed.* **2003**, *42*, 4636–4639.
[170] P. A. Gale, J. W. Steed, *Supramolecular Chemistry: From Molecules to Nanomaterials, Vol. 8: Concepts*, John Wiley & Sons Inc, New York, **2012**.
[171] S. I. Stupp, L. C. Palmer, *Chem. Mater.* **2014**, *26*, 507–518.
[172] P. A. Gale, J. W. Steed, *Supramolecular Chemistry: From Molecules to Nanomaterials, Vol. 8: Supramolecular Materials Chemistry*, John Wiley & Sons Inc, New York, **2012**.
[173] K. P. Goetz, D. Vermeulen, M. E. Payne, C. Kloc, L. E. McNeil, O. D. Jurchescu, *J. Mater. Chem. C* **2014**, *2*, 3065–3076.
[174] A. Das, S. Ghosh, *Angew. Chem. Int. Ed.* **2014**, *53*, 2038–2054.
[175] R. Foster, *Organic Charge-Transfer Complexes*, Academic Press, London, **1969**.
[176] L. Sun, W. Zhu, F. Yang, B. Li, X. Ren, X. Zhang, W. Hu, *Phys. Chem. Chem. Phys.* **2018**, *20*, 6009–6023.
[177] H.-C. Lin, B.-Y. Jin, *Materials* **2010**, *3*, 4214–4251.
[178] H. J. Wörner, A. C. Arrell, N. Banerji, A. Cannizzo, M. Chergui, A. K. Das, P. Hamm, U. Keller, P. M. Kraus, E. Liberatore, P. Lopez-Tarifa, M. Lucchini, M. Meuwly, C. Milne, J.-E. Moser, U. Rothlisberger, G. Smolentsev, J. Teuscher, J. A. van Bokhoven, O. Wenger, *Struct. Dynm.* **2017**, *4*, 061508.
[179] L. Sun, Y. Wang, F. Yang, X. Zhang, W. Hu, *Adv. Mater.* **2019**, *31*, 1902328.
[180] H. Li, P. Shao, S. Chen, G. Li, X. Feng, X. Chen, H.-J. Zhang, J. Lin, Y.-B. Jiang, *J. Am. Chem. Soc.* **2020**, *142*, 3712–3717.

[181] A. S. Filatov, M. V. Ferguson, S. N. Spisak, B. Li, C. F. Campana, M. A. Petrukhina, *Cryst. Growth Des.* **2014**, *14*, 756–762.
[182] Y.-Y. Xu, H.-R. Tian, S.-H. Li, Z.-C. Chen, Y.-R. Yao, S.-S. Wang, X. Zhang, Z.-Z. Zhu, S.-L. Deng, Q. Zhang, S. Yang, S.-Y. Xie, R.-B. Huang, L.-S. Zheng, *Nat. Commun.* **2019**, *10*, 485.
[183] D. J. Cram, *Nature* **1992**, *356*, 29–36.
[184] G. Briegleb, *Elektronen-Donator-Acceptor-Komplexe*, Springer-Verlag, Berlin, **1961**.
[185] E. J. Dale, N. A. Vermeulen, M. Juríček, J. C. Barnes, R. M. Young, M. R. Wasielewski, F. F. Stoddart, *Acc. Chem. Res.* **2016**, *49*, 262–273.
[186] A. Blanco-Gómez, P. Cortón, L. Barravecchia, I. Neira, E. Pazos, C. Peinador, M. D. García, *Chem. Soc. Rev.* **2020**, *49*, 3834–3862.
[187] G. W. Gokel, W. M. Leevy, M. E. Weber, *Chem. Rev.* **2004**, *104*, 2723–2750.
[188] G. Crini, *Chem. Rev.* **2014**, *114*, 10940–10975.
[189] E. S. Español, M. M. Villamil, *Biomolecules* **2019**, *9*, 90.
[190] S. J. Barrow, S. Kasera, M. J. Rowland, J. del Barrio, O. A. Scherman, *Chem. Rev.* **2015**, *115*, 12320–12406.
[191] T. Ogoshi, T. Yamagishi, Y. Nakamoto, *Chem. Rev.* **2016**, *116*, 7937–8002.
[192] B. Odell, M. V. Reddington, A. M. Z. Slawin, N. Spencer, J. F. Stoddart, D. J. Williams, *Angew. Chem. Int. Ed. Engl.* **1988**, *27*, 1547–1550.
[193] J. C. Barnes, M. Juríček, N. L. Strutt, M. Frasconi, S. Sampath, M. A. Giesener, P. L. McGrier, C. J. Bruns, C. L. Stern, A. A. Sarjeant, J. F. Stoddart, *J. Am. Chem. Soc.* **2013**, *135*, 183–192.
[194] I. Roy, S. Bobbala, J. Zhou, M. T. Nguyen, S. K. M. Nalluri, Y. Wu, D. P. Ferris, E. A. Scott, M. R. Wasielewski, J. F. Stoddart, *J. Am. Chem. Soc.* **2018**, *140*, 7206–7212.
[195] J. C. Barnes, E. J. Dale, A. Prokofjevs, A. Narayanan, I. C. Gibbs-Hall, M. Juríček, C. L. Stern, A. A. Sarjeant, Y. Y. Botros, S. I. Stupp, J. F. Stoddart, *J. Am. Chem. Soc.* **2015**, *137*, 2392–2399.
[196] I. Roy, S. Bobbala, R. M. Young, Y. Beldjoudi, M. T. Nguyen, M. M. Cetin, J. A. Cooper, S. Allen, O. Anamimoghadam, E. A. Scott, M. R. Wasielewski, J. F. Stoddart, *J. Am. Chem. Soc.* **2019**, *141*, 12296–12304.
[197] J. Zhou, Y. Wu, I. Roy, A. Samanta, J. F. Stoddart, R. M. Young, M. R. Wasielewski, *Chem. Sci.* **2019**, *10*, 4282–4292.
[198] M. Juríček, J. C. Barnes, E. J. Dale, W.-G. Liu, N. L. Strutt, C. J. Bruns, N. A. Vermeulen, K. C. Ghooray, A. A. Sarjeant, C. L. Stern, Y. Y. Botros, W. A. Goddard, J. F. Stoddart, *J. Am. Chem. Soc.* **2013**, *135*, 12736–12746.
[199] R. Kaur, S. Sen, M. C. Larsen, L. Tavares, J. Kjelstrup-Hansen, M. Ishida, A. Zieleniewska, V. M. Lynch, S. Bähring, D. M. Guldi, J. L. Sessler, A. Jana, *J. Am. Chem. Soc.* **2020**, *142*, 11497–11505.
[200] P. Spenst, F. Würthner, *Angew. Chem. Int. Ed.* **2015**, *54*, 10165–10168.
[201] P. Spenst, R. M. Young, M. R. Wasielewski, F. Würthner, *Chem. Sci.* **2016**, *7*, 5428–5434.
[202] M. Sapotta, A. Hofmann, D. Bialas, F. Würthner, *Angew. Chem. Int. Ed.* **2019**, *58*, 3516–3520.
[203] T. A. Barendt, W. K. Myers, S. P. Cornes, M. A. Lebedeva, K. Porfyrakis, I. Marques, V. Félix, P. D. Beer, *J. Am. Chem. Soc.* **2020**, *142*, 349–364.
[204] T. Uchikura, M. Oshima, M. Kawasaki, K. Takahashi, N. Iwasawa, *Angew. Chem. Int. Ed.* **2020**, *59*, 7403–7408.
[205] L. R. MacGillivray, J. L. Atwood, *Angew. Chem. Int. Ed.* **1999**, *38*, 1019–1034.
[206] B. Dietrich, J.-M. Lehn, J.-P. Sauvage, *Tetrahedron Lett.* **1969**, *10*, 2889–2892.
[207] D. J. Cram, S. Karbach, Y. H. Kim, K. Baczynskyj, K. Marti, R. M. Sampson, G. W. Kalleymeyn, *J. Am. Chem. Soc.* **1988**, *110*, 2554–2560.
[208] J. Rebek, Jr., *Acc. Chem. Res.* **2009**, *42*, 1660–1668.
[209] D. Ajami, J. Rebek, Jr., *Acc. Chem. Res.* **2013**, *46*, 990–999.
[210] Y. Fang, J. A. Powell, E. R. Li, Q. Wang, Z. Perry, A. Kirchon, X. Yang, Z. Xiao, C. Zhu, L. Zhang, F. Huang, H.-C. Zhou, *Chem. Soc. Rev.* **2019**, *48*, 4707–4730.

[211] M. Fujita, D. Oguro, M. Miyazawa, H. Oka, K. Yamaguchi, K. Ogura, *Nature* **1995**, *378*, 469–471.
[212] S. Tashiro, M. Tominaga, M. Kawano, B. Therrien, T. Ozeki, M. Fujita, *J. Am. Chem. Soc.* **2005**, *127*, 4546–4547.
[213] M. Yoshizawa, T. Kusukawa, M. Fujita, K. Yamaguchi, *J. Am. Chem. Soc.* **2000**, *122*, 6311–6312.
[214] M. Yoshizawa, T. Kusukawa, M. Fujita, S. Sakamoto, K. Yamaguchi, *J. Am. Chem. Soc.* **2001**, *123*, 10454–10459.
[215] M. Yoshizawa, S. Miyagi, M. Kawano, K. Ishiguro, M. Fujita, *J. Am. Chem. Soc.* **2004**, *126*, 9172–9173.
[216] M. Yoshizawa, Y. Takeyama, T. Okano, M. Fujita, *J. Am. Chem. Soc.* **2003**, *125*, 3243–3247.
[217] M. Yoshizawa, M. Tamura, M. Fujita, *Science* **2006**, *312*, 251–254.
[218] A. Das, I. Mandal, R. Venkatramani, I. Dasgupta, *Sci. Adv.* **2019**, *5*, eaav4806.
[219] E. J. Dale, N. A. Vermeulen, A. A. Thomas, J. C. Barnes, M. Juríček, A. K. Blackburn, N. L. Strutt, A. A. Sarjeant, C. L. Stern, S. E. Denmark, J. F. Stoddart, *J. Am. Chem. Soc.* **2014**, *136*, 10669–10682.
[220] N. Hafezi, J. M. Holcroft, K. J. Hartlieb, E. J. Dale, N. A. Vermeulen, C. L. Stern, A. A. Sarjeant, J. F. Stoddart, *Angew. Chem. Int. Ed.* **2015**, *54*, 456–461.
[221] H. Duan, Y. Li, Q. Li, P. Wang, X. Liu, L. Cheng, Y. Yu, L. Cao, *Angew. Chem. Int. Ed.* **2019**, *59*, 10101–10110.
[222] W. Liu, S. Bobbala, C. L. Stern, J. E. Hornick, Y. Liu, A. E. Enciso, E. A. Scott, J. F. Stoddart, *J. Am. Chem. Soc.* **2020**, *142*, 3165–3173.
[223] L. Zhao, J. Wei, J. Zhang, C. He, C. Duan, *Angew. Chem. Int. Ed.* **2017**, *56*, 15284–15288.
[224] X. Jing, C. He, L. Zhao, C. Duan, *Acc. Chem. Res.* **2019**, *52*, 100–109.
[225] M. D.-E. Murr, *ChemCatChem* **2020**, *12*, 53–62.
[226] S. Toyota, E. Tsurumaki, *Chem. Eur. J.* **2019**, *25*, 6878–6890.
[227] S. Adachi, M. Shibasaki, N. Kumagai, *Nat. Commun.* **2019**, *10*, 3820.
[228] T. Matsuno, M. Fujita, K. Fukunaga, S. Sato, H. Isobe, *Nat. Commun.* **2018**, *9*, 3779.
[229] Y. Xu, B. Wang, R. Kaur, M. B. Minameyer, M. Bothe, T. Drewello, D. M. Guldi, M. von Delius, *Angew. Chem. Int. Ed.* **2018**, *57*, 11549–11553.
[230] Y. Xu, R. Kaur, B. Wang, M. B. Minameyer, S. Gsänger, B. Meyer, T. Drewello, D. M. Guldi, M. von Delius, *J. Am. Chem. Soc.* **2018**, *140*, 13413–13420.
[231] H. A. Staab, F. Diederich, *Chem. Ber.* **1983**, *116*, 3487–3503.
[232] T. Kawase, H. R. Darabi, M. Oda, *Angew. Chem. Int. Ed. Engl.* **1996**, *35*, 2664–2666.
[233] J. Xia, R. Jasti, *Angew. Chem. Int. Ed.* **2012**, *51*, 2474–2476.
[234] G. Povie, Y. Segawa, T. Nishihara, Y. Miyauchi, K. Itami, *Science* **2017**, *356*, 172–175.
[235] Y. Xu, S. Gsänger, M. B. Minameyer, I. Imaz, D. Maspoch, O. Shyshov, F. Schwer, X. Ribas, T. Drewello, B. Meyer, M. von Delius, *J. Am. Chem. Soc.* **2019**, *141*, 18500–18507.
[236] M. Ball, B. Fowler, P. Li, L. A. Joyce, F. Li, T. Liu, D. Paley, Y. Zhong, H. Li, S. Xiao, F. Ng, M. L. Steigerwald, C. Nuckolls, *J. Am. Chem. Soc.* **2015**, *137*, 9982–9987.
[237] M. Ball, B. Zhang, Y. Zhong, B. Fowler, S. Xiao, F. Ng, M. Steigerwald, C. Nuckolls, *Acc. Chem. Res.* **2019**, *52*, 1068–1078.
[238] T. A. Barendt, M. L. Ball, Q. Xu, B. Zhang, B. Fowler, A. Schattman, V. C. Ritter, M. L. Steigerwald, C. Nuckolls, *Chem. Eur. J.* **2020**, *26*, 3744–3748.
[239] R. Frydrych, T. Lis, W. Bury, J. Cybińska, M. Stępień, *J. Am. Chem. Soc.* **2020**, *142*, 15604–15613.
[240] M.-Z. Asfari, V. Böhmer, J. Harrowfield, J. Vicens, *Calixarenes 2001*, Springer Netherlands, Dordrecht, **2001**.
[241] P. D. Sala, C. Talotta, A. Capobianco, A. Soriente, M. De Rosa, P. Neri, C. Gaeta, *Org. Lett.* **2018**, *20*, 7415–7418.
[242] E. M. Pérez, N. Martín, *Pure Appl. Chem.* **2010**, *82*, 523–533.
[243] E. M. Pérez, N. Martín, *Chem. Soc. Rev.* **2008**, *37*, 1512–1519.
[244] E. M. Pérez, N. Martín, *Chem. Soc. Rev.* **2015**, *44*, 6425–6433.
[245] T. Kawase, H. Kurata, *Chem. Rev.* **2006**, *106*, 5250–5273.

[246] K. Yoshida, A. Osuka, *Chem. Eur. J.* **2016**, *22*, 9396–9403.
[247] Z. Zhou, Y. Qin, W. Xu, D. Zhu, *Chem. Commun.* **2014**, *50*, 4082–4084.
[248] D.-C. Yang, M. Li, C.-F. Chen, *Chem. Commun.* **2017**, *53*, 9336–9339.
[249] M. Takeda, S. Hiroto, H. Yokoi, S. Lee, D. Kim, H. Shinokubo, *J. Am. Chem. Soc.* **2018**, *140*, 6336–6342.
[250] S. Selmani, D. J. Schipper, *Chem. Eur. J.* **2019**, *25*, 6673–6692.
[251] G. Zango, M. Krug, S. Krishna, V. Mariñas, T. Clark, M. V. Martinez-Diaz, D. M. Guldi, T. Torres, *Chem. Sci.* **2020**, *11*, 3448–3459.
[252] D. V. Konarev, R. N. Lyubovskaya, N. Drichko, E. I. Yudanova, Y. M. Shul'ga, A. L. Litvinov, V. N. Semkin, B. P. Tarasov, *J. Mater. Chem.* **2000**, *10*, 803–818.
[253] H. Yokoi, Y. Hiraoka, S. Hiroto, D. Sakamaki, S. Seki, H. Shinokubo, *Nat. Commun.* **2015**, *6*, 8215.
[254] S. Ito, Y. Tokimaru, K. Nozaki, *Angew. Chem. Int. Ed.* **2015**, *54*, 7256–7260.
[255] K. Thakur, D. N. Wang, S. V. Lindeman, R. Rathore, *Chem. Eur. J.* **2018**, *24*, 13106–13109.
[256] M. Mahl, K. Shoyama, J. Rühe, V. Grande, F. Würthner, *Chem. Eur. J.* **2018**, *24*, 9409–9416.
[257] D. Alberico, M. E. Scott, M. Lautens, *Chem. Rev.* **2007**, *107*, 174–238.
[258] J. Wu, W. Pisula, K. Müllen, *Chem. Rev.* **2007**, *107*, 718–747.
[259] A. Sygula, *Eur. J. Org. Chem.* **2011**, *2011*, 1611–1625.
[260] M. Grzybowski, K. Skonieczny, H. Butenschön, D. T. Gryko, *Angew. Chem. Int. Ed.* **2013**, *52*, 9900–9930.
[261] W. Wang, G. Sun, P. Routh, D.-H. Kim, W. Huang, P. Chen, *Chem. Rev. Soc.* **2014**, *43*, 7067–7098.
[262] M. Ball, Y. Zhong, Y. Wu, C. Schenck, F. Ng, M. Steigerwald, S. Xiao, C. Nuckolls, *Acc. Chem. Res.* **2015**, *48*, 267–276.
[263] X. Li, F. Kang, M. Inagaki, *Small* **2016**, *12*, 3206–3223.
[264] H. Ito, K. Ozaki, K. Itami, *Angew. Chem. Int. Ed.* **2017**, *56*, 11144–11164.
[265] S. Alibert-Fouet, I. Seguy, J.-F. Bobo, P. Destruel, H. Bock, *Chem. Eur. J.* **2007**, *13*, 1746–1753.
[266] H. Li, F. S. Kim, G. Ren, E. C. Hollenbeck, S. Subramaniyan, S. A. Jenekhe, *Angew. Chem. Int. Ed.* **2013**, *52*, 5513–5517.
[267] D. Wu, H. Ge, Z. Chen, J. Liang, J. Huang, Y. Zhang, X. Chen, X. Meng, S. H. Liu, J. Yin, *Org. Biomol. Chem.* **2014**, *12*, 8902–8910.
[268] X. Cui, C. Xiao, L. Zhang, Y. Li, Z. Wang, *Chem. Commun.* **2016**, *52*, 13209–13212.
[269] Z.-H. Wu, Z.-T. Huang, R.-X. Guo, C.-L. Sun, L.-C. Chen, B. Sun, Z.-F. Shi, X. Shao, H. Li, H.-L. Zhang, *Angew. Chem. Int. Ed.* **2017**, *56*, 13031–13035.
[270] K. Shoyama, D. Schmidt, M. Mahl, F. Würthner, *Org. Lett.* **2017**, *19*, 5328–5331.
[271] F. Würthner, M. Stolte, *Chem. Commun.* **2011**, *47*, 5109–5115.
[272] X. Zhan, A. Facchetti, S. Barlow, T. J. Marks, M. A. Ratner, M. R. Wasielewski, S. R. Marder, *Adv. Mater.* **2011**, *23*, 268–284.
[273] J. Mei, Y. Diao, A. L. Appleton, L. Fang, Z. Bao, *J. Am. Chem. Soc.* **2013**, *135*, 6724–6746.
[274] Z. Liu, G. Zhang, Z. Cai, X. Chen, H. Luo, Y. Li, J. Wang, D. Zhang, *Adv. Mater.* **2014**, *26*, 6965–6977.
[275] J. Feng, W. Jiang, Z. Wang, *Chem. Eur. J.* **2018**, *13*, 20–30.
[276] D. Uersfeld, S. Stappert, C. Li, K. Müllen, *Adv. Synth. Catal.* **2017**, *359*, 4184–4189.
[277] K. Shoyama, M. Mahl, S. Seifert, F. Würthner, *J. Org. Chem.* **2018**, *83*, 5339–5346.
[278] F. Barrios-Landeros, B. P. Carrow, J. F. Hartwig, *J. Am. Chem. Soc.* **2009**, *131*, 8141–8154.
[279] R. Kalescky, E. Kraka, D. Cremer, *J. Phys. Chem. A* **2014**, *118*, 223–237.
[280] K. Nagarajan, A. R. Mallia, K. Muraleedharan, M. Hariharan, *Chem. Sci.* **2017**, *8*, 1776–1782.
[281] Z. Chen, M. G. Debije, T. Debaerdemaeker, P. Osswald, F. Würthner, *ChemPhysChem* **2004**, *5*, 137–140.
[282] I. Seguy, P. Jolinat, P. Destruel, R. Mamy, H. Allouchi, C. Courseille, M. Cotrait, H. Bock, *ChemPhysChem* **2001**, *2*, 448−452.

[283] Y.-Z. Tan, B. Yang, K. Parvez, A. Narita, S. Osella, D. Beljonne, X. Feng, K. Müllen, *Nat. Commun.* **2013**, *4*, 2646.
[284] Y. He, Y. Li, *Phys. Chem. Chem. Phys.* **2011**, *13*, 1970–1983.
[285] C. R. Newman, C. D. Frisbie, D. A. da Silva Filho, J.-L. Bredas, P. C. Ewbank, K. R. Mann, *Chem. Mater.* **2004**, *16*, 4436–4451.
[286] A. M. Kolesnikov, F. A. Mikhailenko, *Russ. Chem. Rev.* **1982**, *56*, 275–287.
[287] Y. Khan, E. E. Ostfeld, C. M. Lochner, A. Pierre, A. C. Arias, *Adv. Mater.* **2016**, *28*, 4373–4395.
[288] P. Kumar, S. Singh, B. K. Gupta, *Nanoscale* **2016**, *8*, 14297–14340.
[289] L. Meng, Y. Zhang, X. Wan, C. Li, X. Zhang, Y. Wang, X. Ke, Z. Xiao, L. Ding, R. Xia, H.-L. Yip, Y. Cao, Y. Chen, *Science* **2018**, *361*, 1094–1098.
[290] J. V. Caspar, E. M. Kober, B. P. Sullivan, T. J. Meyer, *J. Am. Chem. Soc.* **1982**, *104*, 630–632.
[291] J. V.Caspar, T. J. Meyer, *J. Phys. Chem.* **1983**, *87*, 952–957.
[292] R. Englman, J. Jortner, *Mol. Phys.* **1970**, *18*, 145–164.
[293] W. Qiu, S. Chen, X. Sun, Y. Liu, D. Zhu, *Org. Lett.* **2006**, *8*, 867–870.
[294] M. Queste, C. Cadiou, B. Pagoaga, L. Giraudet, N. Hoffmann, *New J. Chem.* **2010**, *34*, 2537–2545.
[295] Y. Zagranyarski, L. Chen, D. Jänsch, T. Gessner, C. Li, K. Müllen, *Org. Lett.* **2014**, *16*, 2814–2817.
[296] D. Dotcheva, M. Klapper, K. Müllen, *Macromol. Chem. Phys.* **1994**, *195*, 1905–1911.
[297] W. Yang, G. Longhi, S. Abbate, A. Lucote, M. Tommasini, C. Villani, V. J. Catalano, A. O. Lykhin, S. A. Varganov, W. A. Chalifoux, *J. Am. Chem. Soc.* **2017**, *139*, 13102–13109.
[298] W. Yang, R. R. Kazemi, N. Karunathilake, V. J. Catalano, M. A. Alpuche-Aviles, W. A. Chalifoux, *Org. Chem. Front.* **2018**, *5*, 2288–2295.
[299] L. Feiler, H. Langhals, K. Polborn, *Liebigs Ann.* **1995**, *1995*, 1229–1244.
[300] K.-H. Koch, K. Müllen, *Chem. Ber.* **1991**, *124*, 2091–2100.
[301] P. Osswald, M. Reichert, G. Bringmann, F. Würthner, *J. Org. Chem.* **2007**, *72*, 3403–3411.
[302] M.-J. Lin, M. Schulze, K. Radacki, F. Würthner, *Chem. Commun.* **2013**, *49*, 9107–9109.
[303] J. Kumar, T. Nakashima, T. Kawai, *J. Phys. Chem. Lett.* **2015**, *6*, 3445–3452.
[304] J. P. Riehl, F. S. Richardson, *Chem. Rev.* **1986**, *86*, 1–16.
[305] E. M. Sánchez-Carnerero, A. R. Agarrabeitia, F. Moreno, B. L. Maroto, G. Muller, M. J. Ortiz, S. de la Moya, *Chem. Eur. J.* **2015**, *21*, 13488–13500.
[306] Y. Cai, L. Huo, X. Sun, D. Wei, M. Tang, Y. Sun, *Adv. Energy Mater.* **2015**, *5*, 1500032.
[307] Y. Cai, X. Guo, X. Sun, D. Wei, M. Yu, L. Huo, Y. Sun, *Sci. China Mater.* **2016**, *59*, 427–434.
[308] K. Shoyama, M. Mahl, M. A. Niyas, M. Ebert, V. Kachler, C. Keck, F. Würthner, *J. Org. Chem.* **2020**, *85*, 142–149.
[309] A. Mishra, P. Bäuerle, *Angew. Chem. Int. Ed.* **2012**, *51*, 2020–2067.
[310] W. Ni, X. Wan, M. Li, Y. Wang, Y. Chen, *Chem. Commun.* **2015**, *51*, 4936–4950.
[311] F. Würthner, R. Wortmann, K. Meerholz, *ChemPhysChem* **2002**, *3*, 17–31.
[312] H. Bürckstümmer, E. V. Tulyakova, M. Deppisch, M. R. Lenze, N. M. Kronenberg, M. Gsänger, M. Stolte, K. Meerholz, F. Würthner, *Angew. Chem. Int. Ed.* **2011**, *50*, 11628–11632.
[313] X. Che, C.-L. Chung, C.-C. Hsu, F. Liu, K.-T. Wong, S. R. Forrest, *Adv. Energy Mater.* **2018**, *8*, 1703603.
[314] S. Zhang, Y. Guo, H. Fan, Y. Liu, H.-Y. Chen, G. Yang, X. Zhan, Y. Liu, Y. Li, Y. Yang, *J. Polym. Sci., Part A: Polym. Chem.* **2009**, *47*, 5498–5508.
[315] F. Zhao, S. Dai, Y. Wu, Q. Zhang, J. Wang, L. Jiang, Q. Ling, Z. Wei, W. Ma, W. You, C. Wang, X. Zhan, *Adv. Mater.* **2017**, *29*, 1700144.
[316] S. Steinberger, A. Mishra, E. Reinold, J. Levichkov, C. Uhrich, M. Pfeiffer, P. Bäuerle, *Chem. Commun.* **2011**, *47*, 1982–1984.
[317] M. Privado, P. de la Cruz, S. Biswas, R. Singhal, G. D. Sharma, F. Langa, *J. Mater. Chem. A* **2018**, *6*, 11714–11724.

[318] X. Wen, A. Nowak-Król, O. Nagler, F. Kraus, N. Zhu, N. Zheng, M. Müller, D. Schmidt, Z. Xie, F. Würthner, *Angew. Chem. Int. Ed.* **2019**, *58*, 13051–13055.
[319] L.-Y. Lin, Y.-H. Chen, Z.-Y. Huang, H.-W. Lin, S.-H. Chou, F. Lin, C.-W. Chen, Y.-H. Liu, K.-T. Wong, *J. Am. Chem. Soc.* **2011**, *133*, 15822–15825.
[320] Y.-J. Cheng, Y.-J. Ho, C.-H. Chen, W.-S. Kao, C.-E. Wu, S.-L. Hsu, C.-S. Hsu, *Macromolecules* **2012**, *45*, 2690–2698.
[321] K. Takimiya, M. Nakano, *Bull. Chem. Soc. Jpn.* **2018**, *91*, 121–140.
[322] T. Jeffery, *Tetrahedron Lett.* **1994**, *35*, 3051–3054.
[323] K. Masui, H. Ikegami, A. Mori, *J. Am. Chem. Soc.* **2004**, *126*, 5074–5075.
[324] N.-N. Li, Y.-L. Zhang, S. Mao, Y.-R. Gao, D.-D. Guo, Y.-Q. Wang, *Org. Lett.* **2014**, *16*, 2732–2735.
[325] A. Nowak-Król, R. Wagener, F. Kraus, A. Mishra, P. Bäuerle, F. Würthner, *Org. Chem. Front.* **2016**, *3*, 545–555.
[326] A. Yassin, T. Rousseau, P. Leriche, A. Cravino, J. Roncali, *Sol. Energy Mater. Sol. Cells* **2011**, *95*, 462–468.
[327] J. Pommerehne, H. Vestweber, W. Guss, R. F. Mahrt, H. Bässler, M. Porsch, J. Daub, *Adv. Mater.* **1995**, *7*, 551–554.
[328] L. E. Polander, S. P. Tiwari, L. Pandey, B. M. Seifried, Q. Zhang, S. Barlow, C. Risko, J.-L. Bredas, B. Kippelen, S. R. Marder, *Chem. Mater.* **2011**, *23*, 3408–3410.
[329] T. L. Bahers, C. Adamo, I. Ciofini, *J. Chem. Theory Comput.* **2011**, *7*, 2498–2506.
[330] M. Savarese, C. A. Guido, E. Brémond, I. Ciofini, C. Adamo, *J. Phys. Chem. A* **2017**, *121*, 7543–7549.
[331] M. Mahl, K. Shoyama, A.-M. Krause, D. Schmidt, F. Würthner, *Angew. Chem. Int. Ed.* **2020**, *59*, 13401–13405.
[332] W. Herbst, K. Hunger, *Industrial Organic Pigments: Production, Properties, Applications*, 2 ed., Wiley-VCH, Weinheim, **1997**.
[333] S.-L. Suraru, F. Würthner, *Angew. Chem. Int. Ed.* **2014**, *53*, 7428–7448.
[334] G. Seybold, G. Wagenblast, *Dyes Pigm.* **1989**, *11*, 303–317.
[335] S. Nakazono, Y. Imazaki, H. Yoo, J. Yang, T. Sasamori, N. Tokitoh, T. Cédric, H. Kageyama, D. Kim, H. Shinokubo, A. Osuka, *Chem. Eur. J.* **2009**, *15*, 7530–7533.
[336] M. Schlosser, *Pure Appl. Chem.* **1988**, *60*, 1627–1634.
[337] R. Schwesinger, H. Schlemper, C. Hasenfratz, J. Willaredt, T. Dambacher, T. Breuer, C. Ottaway, M. Fletschinger, J. Boele, H. Fritz, D. Putzas, H. W. Rotter, F. G. Bordwell, A. V. Satish, G. Z. Ji, E.-M. Peters, K. Peters, H. G. von Schnering, L. Walz, *Liebigs Ann.* **1996**, *1996*, 1055–1081.
[338] K. Brady, A. F. Hegarty, *J. Chem. Soc., Perkin Trans. 2* **1980**, 121–126.
[339] K. Kurita, Y. Suzuki, T. Enari, M. Kikuchi, S.-I. Nishimura, S. Ishii, *J. Polym. Sci., Part A: Polym. Chem.* **1994**, *32*, 393–396.
[340] J. S. P. Schwarz, *J. Org. Chem.* **1972**, *37*, 2906–2908.
[341] S. Sengupta, R. K. Dubey, R. W. M. Hoek, S. P. P. van Eeden, D. D. Gunbas, F. C. Grozema, E. J. Sudholter, W. F. Jager, *J. Org. Chem.* **2014**, *79*, 6655–6662.
[342] R. Ramakrishnan, M. A. Niyas, M. P. Lijina, M. Hariharan, *Acc. Chem. Res.* **2019**, *52*, 3075–3086.
[343] S. Maniam, H. F. Higginbotham, T. D. M. Bell, S. J. Langford, *Chem. Eur. J.* **2019**, *25*, 7044–7057.
[344] B. Ventura, A. Bertocco, D. Braga, L. Catalano, S. d'Agostino, F. Grepioni, P. Taddei, *J. Phys. Chem. C* **2014**, *118*, 18646–18658.
[345] F. C. Spano, *Acc. Chem. Res.* **2010**, *43*, 429–439.
[346] B. Valeur, M. N. Berberan-Santos, *Molecular Fluorescence, Principles and Application*, 2 ed., Wiley-VCH, Weinheim, **2013**.
[347] H. Saigusa, E. C. Lim, *J. Phys. Chem.* **1995**, *99*, 15738–15747.
[348] V. Wintgens, P. Valat, J. Kossanyi, L. Biczok, A. Demeter, T. Bérces, *J. Chem. Soc., Faraday Trans.* **1994**, *90*, 411–421.
[349] A. M. Philip, S. K. Manikandan, A. Shaji, M. Hariharan, *Chem. Eur. J.* **2018**, *24*, 18089–18096.

[350] S. Mukherjee, P. Thilagar, *Chem. Eur. J.* **2014**, *20*, 8012–8023.
[351] D. W. Cho, A. Fujitsuka, A. Sugimoto, T. Majima, *J. Phys. Chem. A* **2008**, *112*, 7208–7213.
[352] E. A. Margulies, L. E. Shoer, S. W. Eaton, M. R. Wasielewski, *Phys. Chem. Chem. Phys.* **2014**, *16*, 23735–23742.
[353] J. Shi, L. E. A. Suarez, S.-J. Yoon, S. Varghese, C. Serpa, S. Y. Park, L. Lüer, D. Roca-Sanjuán, B. Milián-Medina, J. Gierschner, *J. Phys. Chem. C* **2017**, *121*, 23166–23183.
[354] P. Lova, V. Grande, G. Manfredi, M. Patrini, S. Herbst, F. Würthner, D. Comoretto, *Adv. Optical Mater.* **2017**, *5*, 1700523.
[355] S. I. Stupp, V. LeBonheur, K. Walker, L. S. Li, K. E. Huggins, M. Keser, A. Amstutz, *Science* **1997**, *276*, 384–389.
[356] T. Aida, E. W. Meijer, S. I. Stupp, *Science* **2012**, *335*, 813–817.
[357] P. A. Gale, J. W. Steed, *Supramolecular Chemistry: From Molecules to Nanomaterials, Vol. 3: Molecular Recognition*, John Wiley & Sons Inc, New York, **2012**.
[358] C. J. Pedersen, *J. Am. Chem. Soc.* **1967**, *89*, 2495–2496.
[359] D. J. Cram, S. Karbach, Y. H. Kim, L. Baczynskyj, G. W. Kalleymeyn, *J. Am. Chem. Soc.* **1985**, *107*, 2575–2576.
[360] K. Kondo, M. Akita, M. Yoshizawa, *Chem. Eur. J.* **2016**, *22*, 1937–1940.
[361] W. Liu, C. Lin, J. A. Weber, C. L. Stern, R. M. Young, M. R. Wasielewski, J. F. Stoddart, *J. Am. Chem. Soc.* **2020**, *142*, 8938–8945.
[362] M. Yoshizawa, L. Catti, *Acc. Chem. Res.* **2019**, *52*, 2392–2404.
[363] S. Origuchi, M. Kishimoto, M. Yoshizawa, S. Yoshimoto, *Angew. Chem. Int. Ed.* **2018**, *57*, 15481–15485.
[364] K. Kondo, M. Akita, T. Nakagawa, Y. Matsuo, M. Yoshizawa, *Chem. Eur. J.* **2015**, *21*, 12741–12746.
[365] T. Tsutsui, S. Kusaba, M. Yamashina, M. Akita, M. Yoshizawa, *Chem. Eur. J.* **2019**, *25*, 4320–4324.
[366] K. Ono, M. Yoshizawa, T. Kato, K. Watanabe, M. Fujita, *Angew. Chem. Int. Ed.* **2007**, *46*, 1803–1806.
[367] J. Freudenreich, C. Dalvit, G. Süss-Fink, B. Therrien, *Organometallics* **2013**, *32*, 3018–3033.
[368] Y.-L. Zhao, J. F. Stoddart, *Acc. Chem. Res.* **2009**, *42*, 1161–1171.
[369] V. Georgakilas, M. Otyepka, A. B. Bourlinos, V. Chandra, N. Kim, K. C. Kemp, P. Hobza, R. Zboril, K. S. Kim, *Chem. Rev.* **2012**, *112*, 6156–6214.
[370] V. Georgakilas, J. N. Tiwari, K. C. Kemp, J. A. Perman, A. B. Bourlinos, K. S. Kim, R. Zboril, *Chem. Rev.* **2016**, *116*, 5464–5519.
[371] J. A. Mann, J. Rodríguez-López, H. D. Abruña, W. R. Dichtel, *J. Am. Chem. Soc.* **2011**, *133*, 17614–17617.
[372] M. Garrido, J. Calbo, L. Rodríguez-Pérez, J. Aragó, E. Orti, M. Herranz, N. Martín, *Chem. Commun.* **2017**, *53*, 12402–12405.
[373] Y.-M. Liu, H. Hou, Y.-Z. Zhou, X.-J. Zhao, C. Tang, Y.-Z. Tan, K. Müllen, *Nat. Commun.* **2018**, *9*, 1901.
[374] Z. Wang, F. Dotz, V. Enkelmann, K. Müllen, *Angew. Chem. Int. Ed.* **2005**, *44*, 1247–1250.
[375] S. Ibáñez, E. Peris, *Angew. Chem. Int. Ed.* **2019**, *58*, 6693–6697.
[376] D. Lozano, R. Álvarez-Yebra, R. López-Coll, A. Lledó, *Chem. Sci.* **2019**, *10*, 10351–10355.
[377] The program *bindfit* is avialable free of charge *via* http://supramolecular.org (10.12.2020).
[378] P. Thordarson, *Chem. Soc. Rev.* **2011**, *40*, 1305–1323.
[379] M. A. Slifkin, *Nature* **1963**, *200*, 766–767.
[380] J. R. Lakowicz, *Principles of Fluorescence Spectroscopy*, 2 ed., Springer US, New York, **1999**.
[381] J. Zhang, J. Jin, H. Xu, Q. Zhang, W. Huang, *J. Mater. Chem. C* **2018**, *6*, 3485–3498.
[382] P. Dauber, A. T. Hagler, *Acc. Chem. Res.* **1980**, *13*, 105–112.
[383] P. R. Horn, Y. Mao, M. Head-Gordon, *Phys. Chem. Chem. Phys.* **2016**, *18*, 23067–23079.

[384] O. A. Melville, B. H. Lessard, T. P. Bender, *ACS Appl. Mater. Interfaces* **2015**, *7*, 13105–13118.
[385] E. Arunkumar, C. C. Forbes, B. D. Smith, *Eur. J. Org. Chem.* **2005**, *2005*, 4051–4059.
[386] J. Zhou, Q. Liu, W. Feng, Y. Sun, F. Li, *Chem. Rev.* **2015**, *115*, 395–465.
[387] R. Chakrabarty, P. S. Mukherjee, P. J. Stang, *Chem. Rev.* **2011**, *111*, 6810–6918.
[388] Y. Zhao, Y. Cotelle, L. Liu, J. López-Andarias, A.-B. Bornhof, M. Akamatsu, N. Sakai, S. Matile, *Acc. Chem. Res.* **2018**, *51*, 2255–2263.
[389] S. Y. Hyun, S. U. Jung, D. K. Kim, *KR2016032521* **2016**.
[390] M. N. Eliseeva, L. T. Scott, *J. Am. Chem. Soc.* **2012**, *134*, 15169–15172.
[391] S. S. Zalesskiy, V. P. Ananikov, *Organometallics* **2012**, *31*, 2302–2309.
[392] C. Wang, C. Li, *CN104418856* **2015**.
[393] Y. Zagranyarski, L. Chen, Y. Zhao, H. Wonneberger, C. Li, K. Müllen, *Org. Lett.* **2012**, *14*, 5444–5447.
[394] T. Lu, F. Chen, *J. Comput. Chem.* **2012**, *33*, 580–592.
[395] G. M. Sheldrick, *Acta Cryst. A* **2015**, *71*, 3–8.
[396] G.-F. Zhang, H. Wang, M. P. Aldred, T. Chen, Z.-Q. Chen, X. Meng, M.-Q. Zhu, *Chem. Mater.* **2014**, *26*, 4433–4446.
[397] N. Zink-Lorre, E. Font-Sanchis, Á. Sastre-Santos, F. Fernández-Lázaro, *Org. Chem. Front.* **2017**, *4*, 2016–2021.
[398] C.-Y. Yu, C.-Y. Wu, *Dyes Pig.* **2014**, *106*, 81–86.
[399] M. J. Frisch, G. W. Trucks, H. B. Schlegel, G. E. Scuseria, M. A. Robb, J. R. Cheeseman, G. Scalmani, V. Barone, B. Mennucci, G. A. Petersson, H. Nakatsuji, M. Caricato, X. Li, H. P. Hratchian, A. F. Izmaylov, J. Bloino, G. Zheng, J. L. Sonnenberg, M. Hada, M. Ehara, K. Toyota, R. Fukuda, J. Hasegawa, M. Ishida, T. Nakajima, Y. Honda, O. Kitao, H. Nakai, T. Vreven, J. J. A. Montgomery, J. E. Peralta, F. Ogliaro, M. Bearpark, J. J. Heyd, E. Brothers, K. N. Kudin, V. N. Staroverov, R. Kobayashi, Normand, K. Raghavachari, A. Rendell, J. C. Burant, S. S. Iyengar, J. Tomasi, M. Cossi, N. Rega, J. M. Millam, M. Klene, J. E. Knox, J. B. Cross, V. Bakken, C. Adamo, J. Jaramillo, R. Gomperts, R. E. Stratmann, O. Yazyev, A. J. Austin, R. Cammi, C. Pomelli, J. W. Ochterski, R. L. Martin, K. Morokuma, V. G. Zakrzewski, G. A. Voth, P. Salvador, J. J. Dannenberg, S. Dapprich, A. D. Daniels, Ö. Farkas, J. B. Foresman, J. V. Ortiz, J. Cioslowski, D. J. Fox, *Gaussian 09, revision D.01,*, Gaussian, Inc, Wallingford CT, **2009**.
[400] Y. Zhao, X. Zhou, K. Wu, H. Wang, S. Qu, F. He, C. Yang, *Dyes Pigm.* **2016**, *130*, 282–290.
[401] Y. Miura, H. Oka, M. Momoki, *Synthesis* **1995**, *1995*, 1419–1422.
[402] D. Meinhard, M. Wegner, G. Kipiani, A. Hearley, P. Reuter, S. Fischer, O. Marti, B. Rieger, *J. Am. Chem. Soc.* **2007**, *129*, 9182–9191.
[403] I. Göttker-Schnetmann, P. Wehrmann, C. Röhr, S. Mecking, *Organometallics* **2007**, *26*, 2348–2362.
[404] Y. Li, C. Wang, C. Li, S. Di Motta, F. Negri, Z. Wang, *Org. Lett.* **2012**, *14*, 5278–5281.
[405] H. Langhals, L. Feiler, *US5650513A* **1994**.
[406] R. H. Mitchell, M. Chaudhary, R. V. Williams, R. Fyles, J. Gibson, M. J. Ashwood-Smith, A. J. Fry, *Can. J. Chem.* **1992**, *70*, 1015–1021.
[407] A. L. Spek, *Acta Cryst. C* **2015**, *71*, 9–18.
[408] A. L. Spek, *J. Appl. Cryst.* **2003**, *36*, 7–13.
[409] H. Wonneberger, H. Reichelt, Y. Zagranyarki, C. Li, K. Müllen, L. Chen, *WO 2014/033620 A2* **2014**.
[410] R. S. Sprick, J.-X. Jiang, B. Bonillo, S. Ren, T. Ratvijitvech, P. Guiglion, M. A. Zwijnenburg, D. J. Adams, A. I. Cooper, *J. Am. Chem. Soc.* **2015**, *137*, 3265–3270.
[411] E. Clar, *Nature* **1948**, *161*, 238–239.
[412] J. Cao, Y.-M. Liu, X. Jing, J. Yin, J. Li, B. Xu, Y.-Z. Tan, N. Zheng, *J. Am. Chem. Soc.* **2015**, *137*, 10914–10917.
[413] Y. Shao, Z. Gan, E. Epifanovsky, A. T. B. Gilbert, M. Wormit, J. Kussmann, A. W. Lange, A. Behn, J. Deng, X. Feng, D. Ghosh, M. Goldey, P. R. Horn, L. D. Jacobson, I. Kaliman, R. Z. Khaliullin, T. Kuś, A. Landau, J. Liu, E. I. Proynov, Y. M. Rhee, R. M. Richard, M.

A. Rohrdanz, R. P. Steele, E. J. Sundstrom, H. L Woodcock III, P. M. Zimmerman, D. Zuev, B. Albrecht, E. Alguire, B. Austin, G. J. O. Beran, Y. A. Bernard, E. Berquist, K. Brandhorst, K. B. Bravaya, S. T. Brown, D. Casanova, D.-M. Chang, Y. Chen, S. H. Chien, K. D. Closser, D. L. Crittenden, M. Diedenhofen, R. A. DiStasio, Jr., H. Do, A. D. Dutoi, R. G. Edgar, S. Fatehi, L. Fusti-Molnar, A. Ghysels, A. Golubeva-Zadorozhnaya, J. Gomes, M. W. D. Hanson-Heine, P. H. P. Harbach, A. W. Hauser, E. G. Hohenstein, Z. C. Holden, T.-C. Jagau, H. Ji, B. Kaduk, K. Khistyaev, J. Kim, J. Kim, R. A. King, P. Klunzinger, D. Kosenkov, T. Kowalczyk, C. M. Krauter, K. U. Lao, A. D. Laurent, K. V. Lawler, S. V. Levchenko, C. Y. Lin, F. Liu, E. Livshits, R. C. Lochan, A. Luenser, P. Manohar, S. F. Manzer, S.-P. Mao, N. Mardirossian, A. V. Marenich, S. A. Maurer, N. J. Mayhall, E. Neuscamman, C. M. Oana, R. Olivares-Amaya, D. P. O'Neill, J. A. Parkhill, R. M. Perrine, R. Peverati, A. Prociuk, D. R. Rehn, E. Rosta, N. J. Russ, S. M. Sharada, S. Sharma, D. W. Small, A. Sodt, T. Stein, D. Stück, Y.-C. Su, A. J. W. Thom, T. Tsuchimochi, V. Vanovschi, L. Vogt, O. Vydrov, T. Wang, M. A. Watson, J. Wenzel, A. White, C. F. Williams, J. Yang, S. Yeganeh, S. R. Yost, Z.-Q. You, I. Y. Zhang, X. Zhang, Y. Zhao, B. R. Brooks, G. K. L. Chan, D. M. Chipman, C. J. Cramer, W. A. Goddard III, M. S. Gordon, W. J. Hehre, A. Klamt, H. F. Schaefer III, M. W. Schmidt, C. D. Sherrill, D. G. Truhlar, A. Warshel, X. Xu, A. Aspuru-Guzik, R. Baer, A. T. Bell, N. A. Besley, J.-D. Chai, A. Dreuw, B. D. Dunietz, T. R. Furlani, S. R. Gwaltney, C.-P. Hsu, Y. Jung, J. Kong, D. S. Lambrecht, W. Z. Liang, C. Ochsenfeld, V. A. Rassolov, L. V. Slipchenko, J. E. Subotnik, T. V. Voorhis, J. M. Herbert, A. I. Krylov, P. M. W. Gill, M. Head-Gordon, *Mol. Phys.* **2015**, *113*, 184–215.

Individual Contributions

The coauthors of the publications included in this partially cumulative thesis are informed and agree with the reprint within this thesis and individual contributions as stated below.

Tetrachlorinated Polycyclic Aromatic Dicarboximides: New Electron-Poor π-Scaffolds and NIR Emitters by Palladium-Catalyzed Annulation Reaction

M. Mahl, K. Shoyama, J. Rühe, V. Grande, F. Würthner, *Chem. Eur. J.* **2018**, *24*, 9409–9416.

author	**M.M.**	**K.S.**	**J.R.**	**V.G.**	**F.W.**
Design of research	45%	10%	-	-	45%
Synthesis	85%	5%	10%	-	-
Characterization of the compounds	85%	-	15%	-	-
Optical investigations	85%	-	15%	-	-
Electronic investigations	85%	-	15%	-	-
Theoretical calculations	-	-	-	100%	-
Publication writing	50%	10%	-	-	40%
Publication correction	15%	30%	-	-	55%
Publication coordination	30%	10%	-	-	60%

Palladium-Catalyzed [3 + 2] Annulation of Naphthalimide Acceptors and Thiophene Donors

K. Shoyama,* M. Mahl,* M. A. Niyas, M. Ebert, V. Kachler, C. Keck, F. Würthner, *J. Org. Chem.* **2020**, *85*, 142–149.

author	**K.S.**	**M.M.**	**M.A.**	**M.E.**	**V.K.**	**C.K.**	**F.W.**
Design of research	35%	35%	-	-	-	-	30%
Synthesis	35%	35%	-	10%	10%	10%	-
Characterization of the compounds	50%	50%	-	-	-	-	-
Optical investigations (UV/vis)	50%	50%	-	-	-	-	-
Electronic investigations (CV/SWV)	50%	50%	-	-	-	-	-
DFT calculations	-	-	100%	-	-	-	-
Publication writing	35%	35%	5%	-	-	-	25%
Publication correction	15%	15%	15%	-	-	-	55%
Publication coordination	20%	20%	-	-	-	-	60%

Base-Assisted Imidization: A Synthetic Method for the Introduction of Bulky Imide Substituents to Control Packing and Optical Properties of Naphthalene and Perylene Imides

M. Mahl, K. Shoyama, A.-M. Krause, D. Schmidt, F. Würthner, *Angew. Chem. Int. Ed.* **2020**, *59*, 13401–13405.

author	**M.M.**	**K.S.**	**A.K.**	**D.S.**	**F.W.**
Design of research	45%	10%	-	-	45%
Synthesis	100%	-	-	-	-
Characterization of the compounds	100%	-	-	-	-
Optical investigations	100%	-	-	-	-
Crystallographic analysis	-	-	50%	50%	-
Publication writing	50%	10%	-	-	40%
Publication correction	10%	35%	-	-	55%
Publication coordination	30%	10%	-	-	60%

Parts of Chapter 4 and the corresponding Supporting Information were submitted for publication:

M. Mahl, H. Reichelt, A. Rausch, B. Mahlmeister, K. Shoyama, M. Stolte, F. Würthner, *submitted for publication*.

author	**M.M.**	**H.R.**	**A.R.**	**B.M.**	**K.S.**	**M.S.**	**F.W.**
Design of research	30%	30%	-	-	-	-	40%
Synthesis	60%	-	35%	5%	-	-	-
Characterization of the compounds	80%	-	20%	-	-	-	-
Optical investigations	80%	-	-	10%	-	10%	-
Theoretical calculations	100%	-	-	-	-	-	-
Crystallographic analysis	-	-	-	-	100%	-	-
Publication writing	45%	-	-	-	10%	-	45%
Publication correction	10%	20%	-	-	15%	5%	50%
Publication coordination	20%	-	-	-	10%	-	70%

Acknowledgment/Danksagung

Mein besonderer Dank gilt meinem Doktorvater Prof. Dr. Frank Würthner für die Überlassung des sehr interessanten und spannenden Forschungsthemas und das damit entgegengebrachte Vertrauen. Des Weiteren danke ich Ihm für die zahlreichen wissenschaftlichen Diskussionen, hilfreichen Ratschläge, stete Unterstützung und die Bereitstellung eines exzellenten Arbeitsumfeldes.

Der BASF SE mit Dr. Helmut Reichelt und Dr. Hans Reichert danke ich für die wissenschaftliche Begleitung des in Kapitel 4 beschriebenen Kooperationsprojektes über NIR-Farbstoffe sowie den konstruktiven Diskussionen und Anregungen.

Dr. David Schmidt, Dr. Chantu Saha-Möller, Dr. Matthias Stolte und Dr. Kazutaka Shoyama bin ich für die Hilfe bei fachlichen Fragestellungen, den wissenschaftlichen Austausch und Anregungen im Rahmen der Subgroups und darüber hinaus zu großem Dank verpflichtet. Auch danke ich Dr. Chantu Saha-Möller und Dr. Kazutaka Shoyama für die Hilfe bei der Ausarbeitung der Manuskripte.

Auch möchte ich mich besonders bei Dr. Kazutaka Shoyama für die zahllosen Ratschläge, Anregungen und Hilfestellungen bei allen synthetischen, kristallographischen, theoretischen und sonstigen Fragestellungen sowie seiner fortwährenden Unterstützung bedanken.

Petra Seufert-Baumbach, Anja Rausch und Maximilian Roth danke ich für ihre stete Hilfsbereitschaft und der Organisation eines reibungslosen Laboralltags. Für jegliche Art von bürokratischen und organisatorischen Belangen danke ich Christiana Toussaint, Eleonore Klaus, Rodger Rausch, Sarah Bullnheimer und Lisa Weidner.

Für die Durchführung und Auswertung der zahllosen Kristallstrukturanalysen (mit jedem noch so kleinen Kristall) bin ich Dr. David Schmidt, Olga Anhalt und im Besonderen Ana-Maria Krause und Dr. Kazutaka Shoyama zu außerordentlichem Dank verpflichtet. Auch möchte ich Niyas Mundakkamattathil Abdul Salam für seine wertvollen Hinweise zur Kristallzucht sowie der Kristallisation von zwei Co-Kristallen danken.

Dr. Matthias Grüne und Patricia Altenberger danke ich für die Aufnahme zahlreicher NMR-Experimente. Bei Dr. Michael Büchner und Juliane Adelmann bedanke ich mich für die massenspektrometrischen Untersuchungen.

Für die Durchführung von theoretischen Berechnungen sowie die Hilfestellungen und Erläuterungen zu diesen, möchte ich mich bei Dr. Vincenzo Grande, Dr. Kazutaka Shoyama und Niyas Mundakkamattathil Abdul Salam bedanken.

Für die synthetische Unterstützung bedanke ich mich bei Julius Albert und meinem Auszubildendem Maximilian Roth. In diesem Zusammenhang gilt mein ganz besonderer Dank Anja Rausch für Ihre unermüdliche synthetische Hilfe. Auch bedanke ich mich hierfür bei meinen Praktikanten Valentin Kachler, Tobias Tröster und Mai Linh Vu, wie auch meinen Bachelor-Studenten Jessica Rühe, Matthias Schnitzlein und Christoph Keck.

Auch möchte ich mich im Besonderen bei dem gesamten Arbeitskreis Würthner und den Arbeitskreisen Beuerle und Nowak-Król für die schöne Zeit, die hervorragende Arbeitsatmosphäre und die stete Hilfsbereitschaft untereinander bedanken.

Zuletzt möchte ich mich auch bei meiner Familie, Freunden und Johanna bedanken, welche mir während meiner Promotionszeit durch ihre uneingeschränkte und unablässige Unterstützung immer zur Seite standen.

List of Publications

Electron-Poor Bowl-Shaped Polycyclic Aromatic Dicarboximides: Synthesis, Crystal Structures, and Optical and Redox Properties

K. Shoyama, D. Schmidt, M. Mahl, F. Würthner, *Org. Lett.* **2017**, *19*, 5328–5331.

A General Synthetic Route to Polycyclic Aromatic Dicarboximides by Palladium-Catalyzed Annulation Reaction

K. Shoyama, M. Mahl, S. Seifert, F. Würthner, *J. Org. Chem.* **2018**, *83*, 5339–5346.

Tetrachlorinated Polycyclic Aromatic Dicarboximides: New Electron-Poor π-Scaffolds and NIR Emitters by Palladium-Catalyzed Annulation Reaction

M. Mahl, K. Shoyama, J. Rühe, V. Grande, F. Würthner, *Chem. Eur. J.* **2018**, *24*, 9409–9416.

Palladium-Catalyzed [3+2] Annulation of Naphthalimide Acceptors and Thiophene Donors

K. Shoyama,* M. Mahl,* M. A. Niyas, M. Ebert, V. Kachler, C. Keck, F. Würthner, *J. Org. Chem.* **2020**, *85*, 142–149.

Base-Assisted Imidization: A Synthetic Method for the Introduction of Bulky Imide Substituents to Control Packing and Optical Properties of Naphthalene and Perylene Imides

M. Mahl, K. Shoyama, A.-M. Krause, D. Schmidt, F. Würthner, *Angew. Chem. Int. Ed.* **2020**, *59*, 13401–13405; *Angew. Chem.* **2020**, *132*, 13503–13507.